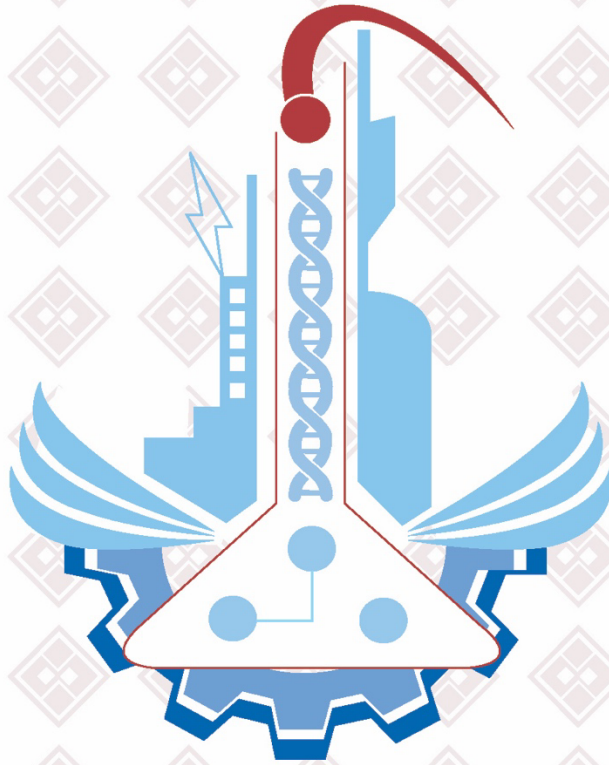


PRINTED ISSN: 1308-9080 / OLINE ISSN: 1308-9099

Volume: 17 / Number: 2 / Year: 2022

TURKISH JOURNAL OF SCIENCE & TECHNOLOGY



TURKISH JOURNAL OF SCIENCE AND TECHNOLOGY (TJST)

Year: 2022 Vol: 17 Number: 2

Address:

Fırat Universitesi
Fen Bilimleri Enstitüsü
23119, Elazig - TURKEY

Tel: 0 424 212 27 07

Fax: 0 424 236 99 55

e-mail: fenbilim@firat.edu.tr

New ISSN

Online: 1308-9099

Printed: 1308-9080

Old ISSN

Online: 1306 – 8555

Printed: 1306 – 8547

Refereed journal. Published twice a year

<https://dergipark.org.tr/tr/pub/tjst>

TURKISH JOURNAL OF SCIENCE & TECHNOLOGY (TJST)
Published by Firat University

Owner

Prof Dr. Fahrettin GÖKTAŞ
Rector of Firat University

Editor in Chef

Assoc. Prof. Dr. Fatih ÖZKAYNAK
Firat University, Faculty of Technology
Department of Software Engineering

Responsible Director

Assoc. Prof. Dr. Kürşat Esat ALYAMAÇ
Firat University, Faculty of Engineering
Department of Civil Engineering

Editor

Assoc. Prof. Dr. Emrah YILMAZ
Firat University, Faculty of Science
Department of Mathematic

ADVISORY BOARD

Eyüp BAĞCI

Firat University, Department of Biology,
Elazig-Turkey

Eres SOYLEMEZ

Middle East Technical University,
Department of Engineering Science,
Ankara-Turkey

Coskun BAYRAK

UALR Donaghey Collage of Eng. and
Information Tech.Dept. of Computer
Science, Little Rock, AR, USA

Hikmet GECKIL

Inonu University, Department of Biology,
Malatya-Turkey

Metin CALTA

Firat University, Fisheries Faculty,
Elazig-Turkey

Ertan GOKALP

Karadeniz Technical University,
Department of Geodesy and
Photogrametry Engineering, Trabzon-
Turkey

Abdulkadir ŞENGÜR

Firat University, Department of
Electronics and Computer Education,
Elazig-Turkey

Hasan EFEOGLU

Ataturk University, Department of
Electrical-Electronics Engineering,
Erzurum-Turkey

Yanhui GUO

St. Thomas University, School of Science
and Technology, Miami, FL, USA

İbrahim TURKMEN

Bahkesir University, Department of
Geology Engineering, Bahkesir-Turkey

Deniz UNER

Middle East Technical University,
Department of Chemical Engineering,
Ankara-Turkey

M.Polat SAKA

Bahreyn University, Department of Civil
Engineering, Bahrain

Siqing XIA

Tongji Univ, State Key Lab Pollut Control
& Resource Reuse, Coll Environm Sci &
Engn, Shanghai 200092, R China

Zihni DEMIRBAG

Karadeniz Technical University,
Department of Biology, Trabzon-Turkey

Hanifi GULDEMİR

Firat University, Department of Electronics
and Computer Education, Elazig-Turkey

Nilgun GULEC

Middle East Technical University,
Department of Geology Engineering,
Ankara-Turkey

Erdogan GUNEL

West Virginia University, Department of
Statistics, Morgontown, USA

Sedigheh GHOFRANI

Islamic Azad University, Electrical
Engineering Department, Tehran South
Branch, Iran

Wang XIBAO

Tianjin University, The School of
Materials Science and Engineering, China

Brain WOERNER

West Virginia University, Department of
Computer Sciences & Electrical
Engineering, Morgontown, WV, USA

A. Kadri CETIN

Firat University, Department of Biology,
Elazig-Turkey

Yusuf Kağan KADIOĞLU

Ankara University, Department of Geology
Engineering, Ankara-Turkey

Sezgin BAKIRDERE

Yıldız Technical University, Department of
Chemistry, Ankara-Turkey.

Tuncay OREN

Ottawa Univ, Fac Eng, Inform Technol.
McLeod Inst Sim.t Sci, Ottawa, ON KIN
6N5 Canada

Halil ONDER

Middle East Technical University,
Department of Civil Engineering, Ankara-
Turkey

Nazmi POLAT

Ondokuz Mayıs University, Department of
Biology, Samsun-Turkey

Mustafa DORUCU

Firat University, Fisheries Faculty,
Elazig-Turkey

Binod Chandra TRIPATHY

Mathematical Sciences Division, Institute
of Advanced Study Science and Tech.
Paschim Boragaon; Guwahati, India

Eoin CASEY

University College Dublin, Chemical and
Bioprocess Engineering, Dublin, Ireland

Farid El-TANTAWY

Suez Canal University, Faculty of
Science, Department of Physics, Ismailia,
Egypt

Saleem HASHMI

International College of Technology,
Dublin, Ireland

Sakir ERDOĞDU

Karadeniz Technical University,
Department of Civil Engineering, Trabzon-
Turkey

Serdar SALMAN

Marmara University, Metallurgical and
Materials Engineering, İstanbul-Turkey

Firat University Turkish Journal of Science & Technology (TJST)
17-2, 2022

CONTENTS / İÇİNDEKİLER

- 1. Determination Some Physical Properties of Ground NiMnCoSn Magnetic Shape Memory Alloy Powders**
Öğütülmüş NiMnCoSn Manyetik Şekil Hafızalı Alaşım Tozlarının Bazı Fiziksel Özelliklerinin Belirlenmesi
Muhammed KANCA, Ecem ÖZEN ÖNER, Yakup SAY..... 151-160
- 2. Multilingual Text Mining Based Open Source Emotional Intelligence**
Çok Dilli Metin Madenciliği Tabanlı Açık Kaynak Duygusal Zeka
Aytuğ BOYACI, Shahin AHMADOV..... 161-166
- 3. A New Algorithmic Trading Approach Based on Ensemble Learning and Candlestick Pattern Recognition in Financial Assets**
Finansal Varlıklarda Topluluk Öğrenmesi ve Şamdan Örüntüsü Tanıma Temelli Yeni Algoritmik Ticaret Yaklaşımı
Üzeyir AYCEL, Yunus SANTUR..... 167-184
- 4. A Novel Histological Dataset and Machine Learning Applications**
Yeni Bir Histoloji Veriseti ve Makine Öğrenmesi Uygulamaları
Kübra UYAR, Merve SOLMAZ, Sakir TASDEMİR, Nejat ÜNLÜKAL..... 185-196
- 5. Mathematical Analysis of The Hash Functions as a Cryptographic Tools for Blockchain**
Blok Zincir için bir Kriptografik Araç Olarak Hash Fonksiyonlarının Matematiksel Analizi
Muharrem Tuncay GENÇOĞLU..... 197-201
- 6. A Deep Learning Model Collaborates with an Expert Radiologist to Classify Brain Tumors from MR Images**
MR Görüntülerinden Beyin Tümörlerini Sınıflandırmak İçin Uzman Bir Radyolog ile İşbirliği Yapan Derin Öğrenme Modeli
Tülin ÖZTÜRK, Oğuzhan KATAR..... 203-210
- 7. Classification of Hotspots in Photovoltaic Modules with Deep Learning Methods**
Fotovoltaik Modüllerdeki Sıcak Noktaların Derin Öğrenme Yöntemleriyle Sınıflandırılması
Hakan AÇIKGÖZ, Deniz KORKMAZ, Çiğdem DANDIL..... 211-221
- 8. A Performance Analysis of Current Multi-Objective Metaheuristic Optimization Algorithms for Unconstrained Problems**
Güncel Çok Amaçlı Metasezgisel Optimizasyon Algoritmalarının Kısıtsız Problemler için Performans Analizi
Eyüp ERÖZ, Erkan TANYILDIZI..... 223-232
- 9. A Defense Mechanism Against DoS Attacks on Unmanned Aerial Vehicle Communication**
İnsansız Hava Araçların Haberleşmesine Yönelik Saldırlara Yönelik bir Savunma Mekanizması
Vedat TÜMEN, Kubilay DEMİR..... 233-239

- 10. Comparison of the Machine Learning Methods to Predict Wildfire Areas**
Makine Öğrenmesi Yöntemlerini Kullanarak Orman Yangınlarını Tahminleme
Gözde BAYAT, Kazım YILDIZ..... 241-250
- 11. Deep Learning Based Recognition of Turkish Sign Language Letters with Unique Data Set**
Özgün Veri Seti ile Derin Öğrenme Temelli Türk İşaret Dili Harflerinin Tanınması
Mustafa KAYA, Fatih BANKUR..... 251-260
- 12. Antioxidant and Antimicrobial Effects of Trametes versicolor (L.) Lloyd Extracts in Different Solvents**
Trametes versicolor (L.) Lloyd'un Farklı Çözücülerdeki Ekstraktlarının Antioksidan ve Antimikrobiyal Etkileri
Şule İNCİ, Mehmet AKYÜZ, Sevda KIRBAĞ..... 261-265
- 13. A Study on Uniaxial Compressive Strength and Ultrasonic Non-Destructive Analysis of Fine- Grained Soil in Seasonally Frozen Regions**
Mevsimsel Donmuş Bölgelerde İnce Taneli Zeminlerin Tek Eksenli Basınç Dayanımları ve Ultrasonik Tahribatsız Analizleri Üzerine Bir Çalışma
İbrahim Haruna UMAR 1, Müge Elif ORAKOĞLU FIRAT..... 267-277
- 14. Effect of Different Drill Bits on Delamination in Drilling Composite Materials**
Kompozit Malzemelerin Delinmesinde Farklı Matkap Uçlarının Delaminasyona Etkisi
Haşim PIHTILI..... 279-297
- 15. Classification of Chest X-ray COVID-19 Images Using the Local Binary Pattern Feature Extraction Method**
Chest X-ray COVID-19 Görüntülerinin Yerel İkili Model Özellik Çıkarımı Yöntemi Kullanılarak Sınıflandırılması
Narin Aslan, Sengul Dogan, Gonca Ozmen Koca..... 299-308
- 16. The Investigation of Mechanical Properties of Polycrystalline Nb Nanowire Under Applied Tensile Deformation by Molecular Dynamics Simulation**
Kriptoloji Uygulamaları için Rastgele Seçime Dayalı İkame Kutusu Yapıları Veri Kümesi
Sefa KAZANÇ, Canan AKSU CANBAY..... 309-319
- 17. Artificial Intelligence Based Smart Interchange System In Smart Urbanization**
Akıllı Şehircilikte Yapay Zeka Tabanlı Akıllı Kavşak Sistemi
Emrullah EZBERCİ, Derya AVCI..... 321-328
- 18. Photo-electrical Characterization of New CuAlNi/n-Si/Al Schottky Photodiode Fabricated by Coating Thin-film Smart Material**
İnce Film Akıllı Malzeme Kaplamasıyla Üretilen Yeni CuAlNi/n-Si/Al Schottky Fotodiyotunun Foto-elektriksel Karakterizasyonu
Oktay KARADUMAN, Canan Aksu CANBAY..... 329-341
- 19. Some Quantum Integral Inequalities Based on Left-Right Quantum Integrals**
Sol Sağ Kuantum İntegrallerine Dayalı Bazı Kuantum İntegral Eşitsizlikleri
Mehmet KUNT, Abdul Wakil BAIDAR, Zeynep ŞANLI..... 343-356

20. **Dynamic Response of Concentrically Braced Steel Frames to Pulse Period in Near-Fault Ground Motions**
Merkezi Çaprazlı Çelik Çerçevelerin Yakın-Fay Yer Hareketlerinin Darbe Periyoduna Dinamik Tepkisi
Zeliha TONYALI, Muhammet YURDAKUL, Hasan SESLİ..... 357-373
21. **Improving the Flux-Weakening Capability of Interior Permanent Magnet Machines by Number of Turns Changing Methodology**
Gömülü Tip Mıknatıslı Makinaların Sipir Sayısı Değişirme Metodolojisi ile Akı Zayıflatma Kapasitesinin Geliştirilmesi
Tayfun GÜNDOĞDU..... 375-394
22. **Optimized YOLOv4 Algorithm for Car Detection in Traffic Flow**
Trafik Akışında Araba Algılama için Optimize Edilmiş YOLOv4 Algoritması
AlzubairALQARAGHULİ, Oğuz ATA..... 395-403
23. **Automatic Diagnosis of Snoring Sounds with the Developed Artificial Intelligence-based Hybrid Model**
Geliştirilen Yapay Zeka Tabanlı Hibrit Model ile Horlama Seslerinin Otomatik Teşhisi
Muhammed YILDIRIM 405-416
24. **A Deep Learning-Based Technique for Diagnosing Retinal Disease by Using Optical Coherence Tomography (OCT) Images**
Optik Koherens Tomografi (OCT) Görüntülerini Kullanarak Retina Hastalığını Teşhis Etmek için Derin Öğrenmeye Dayalı Bir Teknik
M. Emin SAHİN..... 417-426
25. **Loxodromes On Twisted Surfaces in Euclidean 3-Space**
Öklidyen 3-Uzayında Twisted Yüzeyle Üzerinde Loksodromlar
Mustafa ALTIN..... 427-433
26. **Active Face Spoof Detection Using Image Distortion Analysis**
Yüz Tanıma Sistemleri İçin Kararlı Aktif Tabanlı Yüz Sahteciliği Tespiti
Betul AY, Peter ANTHONY..... 435-450
27. **Genetic Algorithm-Based Optimization of Mass Customization Using Hyperledger Fabric Blockchain**
Hyperledger Fabric Blok Zincirini Kullanarak Kitlesel Özelleştirmenin Genetik Algoritma Tabanlı Optimizasyonu
Nursena BAYGIN, Mehmet KARAKOSE..... 451-460
28. **A Dynamic Analysis of Historical Masonry Arch Bridges under Different Earthquakes: The Case of Murat Bey Bridge**
Tarihi Yiğma Köprülerin Farklı Depremler Altında Dinamik Analizi: Murat Bey Köprüsü Örneği
Elif Gözde ÇUBUK, Erkut SAYIN, Alper ÖZMEN..... 461-473
29. **A Response Surface Methodology to Optimize the Yield of Alkyd Resin from Jatropha (Jatropha Curcas) and Sesame (Sesamum Indicum) Seed Oils Using CaCO₃ as Catalyst**
Katalizör Olarak CaCO₃ Kullanan Jatropha (Jatropha Curcas) ve Susam (Sesamum Indicum) Tohum Yağlarından Alkid Reçinesinin Görünümünü Optimize Etmek için Tepki Yüzey Metodolojisi
Aliru Olajide MUSTAPHA, Simeon Gbenga OLADELE, Salihu Folorunsho ADİSA..... 461-473

Determination Some Physical Properties of Ground NiMnCoSn Magnetic Shape Memory Alloy Powders

Muhammed KANCA¹, Ecem ÖZEN ÖNER^{2*}, Yakup SAY³

^{1,2} Department of Physics, Faculty of Science, Fırat University, Elazığ, Turkey

³ Munzur University, Department of Metallurgical and Materials Engineering, Tunceli, Turkey

¹ msaitkanca23@gmail.com, ^{2*} e.ozen@firat.edu.tr, ³ yakupsay@gmail.com

(Geliş/Received: 09/02/2022;

Kabul/Accepted: 01/05/2022)

Abstract: In this study, NiMnCoSn alloy was produced in the arc melting furnace and then grounded into small powder particles. After this procedure, particles of alloys were pelletized and heat treatment was applied to pellet alloys for 3 different temperatures (500 °C, 700 °C and 900 °C). Differential scanning calorimetry (DSC), X-ray diffraction (XRD) and physical property measuring system (PMMS) were used for determining physical properties of samples. The biggest feature of NiMn-based shape memory alloys is that they are magnetically based. The feature that distinguishes magnetic shape memory alloys from traditional ones is that the shape memory effect is magnetic. For this reason, studies of NiMn-based alloys are becoming very popular. It was observed that, grounding procedure is effected all physical properties of NiMnSnCo shape memory alloys, seriously.

Key words: NiMnCoSn, magnetic shape memory alloy, thermal characteristics, XRD, microstructure

Öğütülmüş NiMnCoSn Manyetik Şekil Hatırlamalı Alaşım Tozlarının Bazı Fiziksel Özelliklerinin Belirlenmesi

Öz: Bu çalışmada, ark ergitme fırınında NiMnCoSn alaşımı üretilmiş ve daha sonra küçük toz parçacıklarına öğütülmüştür. Bu işlemten sonra alaşım parçacıkları pelet haline getirilmiş ve pelet alaşımlara 3 farklı sıcaklıkta (500 °C, 700 °C ve 900 °C) ısıtım işlemi uygulanmıştır. Numunelerin fiziksel özelliklerinin belirlenmesi için diferansiyel taramalı kalorimetri (DSC), X-ışını kırınımı (XRD) ve fiziksel özellik ölçüm sistemi (PMMS) kullanılmıştır. NiMn bazlı şekil hafızalı alaşımların en büyük özelliği manyetik bazlı olmalarıdır. Manyetik şekil hafızalı alaşımları geleneksel olanlardan ayıran özellik, şekil hafıza etkisinin manyetik olmasıdır. Bu nedenle NiMn esaslı alaşımlarla ilgili çalışmalar oldukça popüler hale gelmektedir. Öğütme işleminin NiMnSnCo şekil hatırlamalı alaşımların tüm fiziksel özelliklerini ciddi şekilde etkilediği görülmüştür.

Anahtar kelimeler: NiMnCoSn, manyetik şekil hafızalı alaşım, termal özellikler, XRD, mikro yapı

1. Introduction

The smart or sensitive materials can change their shape and respond with stress, moisture, electric or magnetic field, light, pH or chemical compounds [1, 2]. Shape memory alloys (SMAs) change their shape when exposed to a certain external force while in martensitic structure, and take their original shape when heated to austenite phase temperature [3-5]. SMAs frequently used in many fields such as automotive, textile, bioengineering, aviation,

* Sorumlu yazar: e.ozen@firat.edu.tr. Yazarların ORCID Numarası: ¹[0000-0002-2987-4284](https://orcid.org/0000-0002-2987-4284), ²[0000-0001-7687-9021](https://orcid.org/0000-0001-7687-9021), ³[0000-0001-5005-8516](https://orcid.org/0000-0001-5005-8516)

composites and micro electromagnetic system [6-9]. Magnetic shape memory alloys, which are developed as an alternative to traditional shape memory alloys, are materials that also show shape change with applying magnetic field [10, 11].

Magnetic shape memory alloys have a high magnetocaloric effect. When a magnetic field is applied, the entropy value of the material decreases, so the heat is dissipated from the magnetic cooling system into the environment. When the magnetic field is removed, it is observed that the magnetic entropy increases and therefore the material absorbs the heat energy from the environment [12-15]. magnetic shape memory alloy group are used as a coolant in the industry due to their magnetocaloric effect.

Nowadays, NiMnSn-based Heusler type magnetic shape memory alloys are being developed [16, 17]. Because when this type of magnetic alloys are compared with traditional magnetic alloys such as NiMnGa, it is seen that the magnetization value between the transformation phases is high. This is thought to be due to the Manganese ratio in alloy [18-20].

Haluk E. Karaca et al. observed that as the applied magnetic field effects on NiMnCoIn shape memory alloy. In their study, when the magnetic field increased from 0.05 to 5 T, the martensite start (Ms) value decreased from 230 to 165 K [21]. Han et al. investigated that the magnetization difference between the transformation phases of $Ni_{50-x}Mn_{39+x}Sn_{11}$ by increasing amount of Mn ratio. They found that magnetic entropy change to below 1 T, and because of this feature, they reported that this alloy group is used in magnetic cooling applications [22].

Among these magnetic shape memory alloys, NiCoMnIn alloys have been most extensively studied. Ni-Mn-Ga is one of the most studied MSMA. Substitution of Ga with Sn is an economical alternative for Ni-Mn-Ga alloys. In NiMn-based magnetic shape memory alloys, the magnetic moments are strongly dependent on the distance between Mn-Mn atoms. The bonding mechanism between Ni and Mn leads to a martensite transition. In these materials, especially alloys with high Mn content, the martensite transition should be affected by factors such as magnetic field, composition, temperature and should be developed for practical applications [16, 23-25]. NiCoMnSn alloys are also very promising for practical applications as they do not contain expensive elements [26]. In this study, thermal and crystal structure of grounded NiMnCoSn MSMA bulk were investigated. The aim of this study is to examine all physical properties of powdered NiMnSn alloy by heat treatment. Powdered NiMnCoSn alloy is rare.

2. Experimental Procedure

After determining the mass ratio of the $Ni_{50}Mn_{36}Sn_{12}Co_2$ (%at.) quaternary magnetic shape memory alloy, 50 g of powder mixture was prepared by using pure element powder and pelleted using a hydraulic press. The atomic and weight ratios of the alloy are given in Table 1.

Table 1. Atomic percentage ratio of NiMnSnCo alloy produced

	Ni	Mn	Sn	Co
Atomic (%)	50	36	12	2
Mass ratio in 50 g	22,73	15,32	11,035	0,913

The alloys' mixture, which became a pellet, was melted in a vacuum atmosphere using arc melter device. The alloy was homogenized on the first level by repeating the melting process several times. After that, the alloy in bulk form was kept at 900 °C for 24 hours and the second-level homogenization process was performed, and thus the production part was completed. After production it was seen that high volume of porosity was determined into bulk NiMnCoSn magnetic shape memory alloy. Alloy samples were ground in agate mortar.

For this reason, NiMnCoSn alloy was grinded into shape and macro powders of alloys were obtained as seen in Figure 1a. The alloys' powder, which was then pulverized with coarse grains, were turned into pellets (In order to see the properties of the NiMnSnCo alloy more easily, the macro powdered alloys were turned into pellets) and were kept at three different temperatures (500 °C, 700 °C, and 900 °C) for 8 hours, after these treatments aging process was carried out under both pressure and temperature (Fig. 1b).

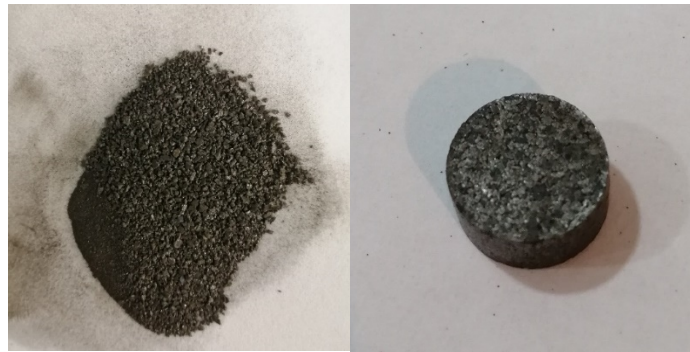


Fig. 1. a. Powder form of NiMnCoSn alloy, **b.** Pellet form of NiMnCoSn alloys' powders

The phase transformation of all samples were measured with a heating-cooling rate of 10 °C/ min. using a Perkin Elmer differential scanning calorimeter (DSC) in a nitrogen gas atmosphere. The crystal structure of main and heat treated powder alloys were determined by XRD diffractometer at room temperature. Finally, room temperature magnetization measurement was made to investigate magnetic properties of the NiMnSnCo alloy by using Quantum PPMS (physical property measurement system) device in the magnetic field range of -8T to 8T.

3. Results and Discussions

Differential scanning calorimetry (DSC) is often used to determine the phase transformation temperature of shape memory alloys. The most used and important shape memory alloy characterization device is DSC, and the transformation temperatures are found by measuring the heat absorbed or emitted by the heating and cooling of very small samples taken from the materials [27]. DSC measurements were taken in nitrogen gas atmosphere with a heating rate of 10 °C/min. to determine the transformation temperatures of non-heat treated and heat treated pelletized alloys at 500 °C, 700 °C and 900 °C for 8 hours. Figure 2 displays complete heating and cooling DSC curves of the main and heat-treated samples taken between -40 °C and 200 °C. According to the DSC measurement results, multiple peaks were observed during heating in the main ground alloys (particle alloy), and transformation was not observed during cooling procedure. As a result of the aging of the pelleted powdered NiMnCoSn alloy at 500 °C and 700 °C, phase transformation peak disappeared on the heating or cooling. However, a significant peak was observed during heating in the alloy, which was aged at 900 °C for 8 hours. This peaks that martensite→austenite transformation was occurred by heating. Austenite→martensite transformation sign did not seen for all of ageing alloys and nonageing alloys. It can be said that force which use for ground alloys effect to destroy arranging of atoms in the crystal structure.

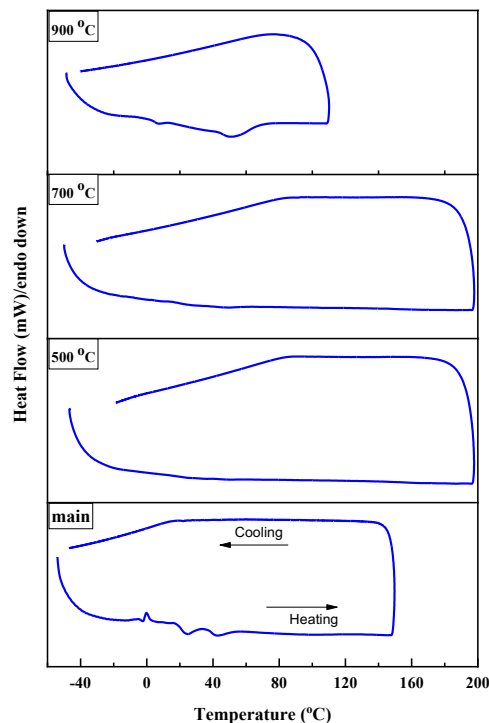
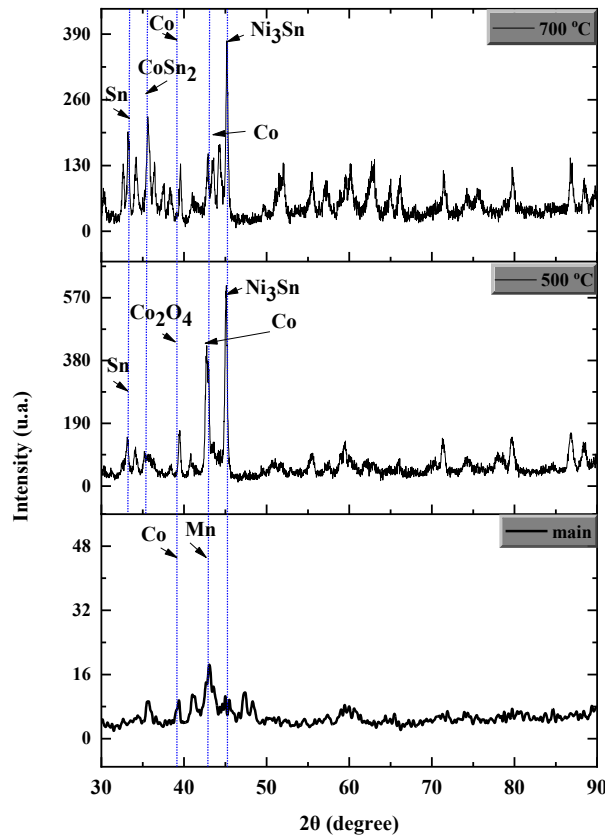


Fig. 2. The DSC curves of main and heat treated powder NiMnCoSn alloys

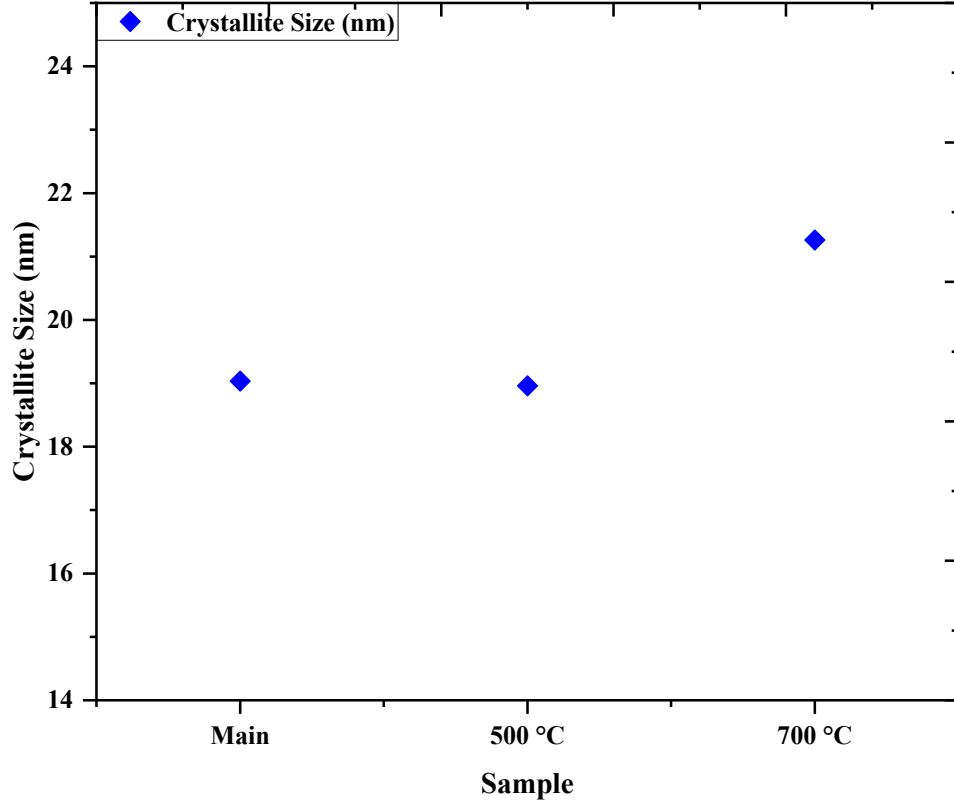
X-ray diffraction method is used to determine whether the materials are amorphous and crystalline structure. This method is based on Bragg's law. With X-ray diffraction methods, it is possible to measure the exact dimensions of the unit cell in any crystal and to determine the arrangement of the atoms in the crystalline form [28]. X-ray measurements were taken in the range of 30-90 with a scanning speed of 2 °/min for samples which nonheat treated and heat treated at 500, 700 °C. The X-ray diffractograms of the alloys are given in Fig. 3. The XRD peaks were indexed by the literature [29-31].

In this study, when the XRD diffractions are examined, the elements or compounds that the peaks belong to are shown in the Fig. 3. In particular, it is seen that the XRD diffraction is concentrated between 30 and 50 degrees. It is an expected result that the highest peaks belong to Ni and Mn elements.

The particle size was calculated with the Debye Scherrer equation ($D = K \cdot \lambda / \beta \cdot \cos\theta$) and the graph was drawn from the obtained nanometer (nm) unit. When the graph in Fig. 4 was examined, it was observed that the particle size increased with the increase of the heat treatment temperature. This can be explained that thermal expansion with heating important effect of the grain size of NiMnSnCo alloy.

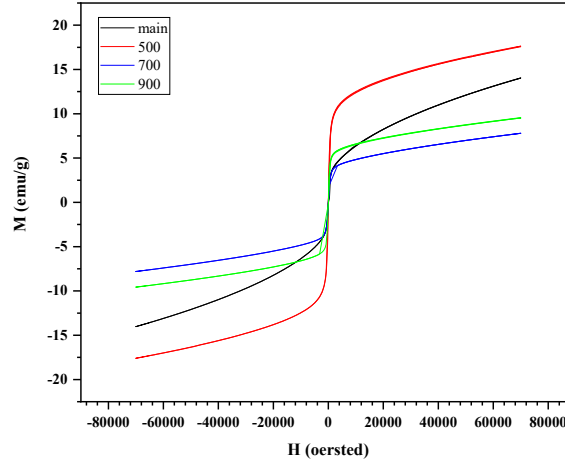


Hata! Başvuru kaynağı bulunamadı.



Hata! Başvuru kaynağı bulunamadı.

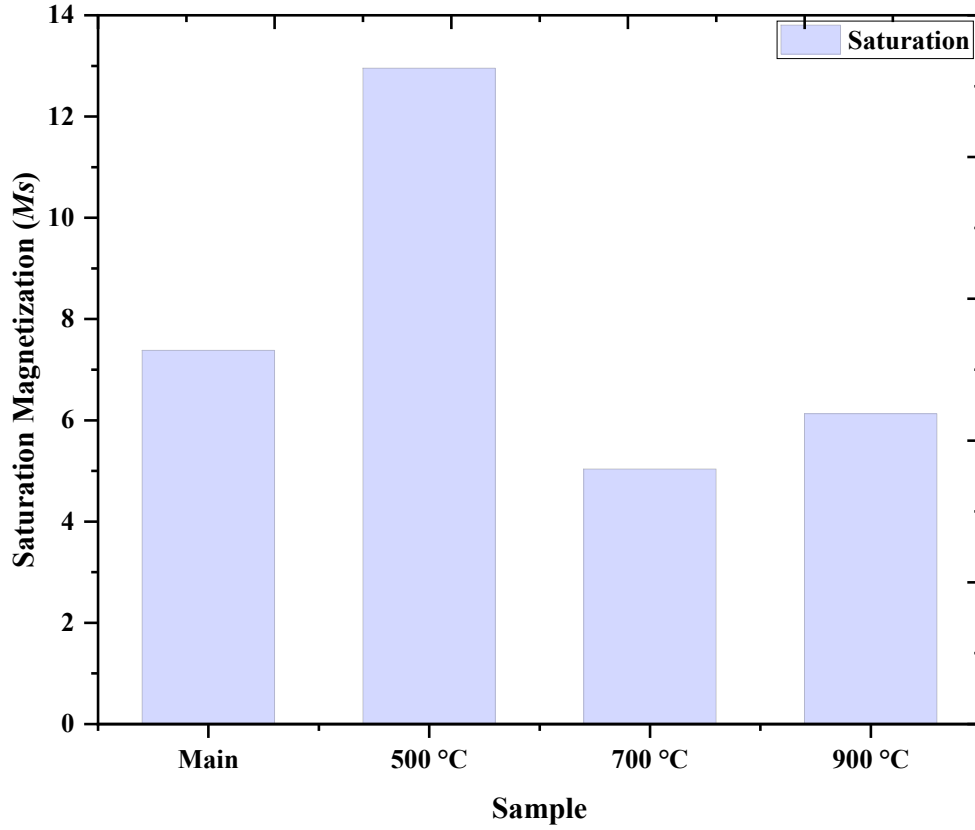
Magnetic measurements are very important in magnetic shape memory alloy analysis. Therefore, transition between phases or sudden changes in magnetic properties can be detected and evaluated. Magnetic measurements were taken with Quantum Design PPMS 7 (Physical Properties Measurement System) at room temperature, between -8 Tesla and 8 Tesla magnetic field before heat treatment and after heat treatment at 500 °C, 700 °C and 900 °C. When Fig. 5 is examined, the internal magnetic properties of the NiMnSnCo alloys changed after 500 °C heat treatment temperature. Magnetization of alloys value increased for 500 °C temperature, after this temperature, magnetization of alloy decreased. Kök et al. explained that rising oxidation amount of alloys diminished the saturation values of alloys [32, 33].



Hata! Başvuru kaynağı bulunamadı.

The difference between saturation magnetization and natural magnetization has to be made with magnetic domains. Saturation magnetization is a structural property independent of particle size but dependent on temperature. There is a big difference between paramagnetic and ferromagnetic susceptibility. Compared to paramagnetic materials, the magnetization of ferromagnetic materials reaches saturation at high temperatures and moderate magnetic fields. The flattening of the magnetization curve is interpreted as reaching saturation [34].

Fig. 6 in the magnetization graph, the slope of the fixed part of the curve gives the saturation magnetization. The difference between saturation magnetization and natural magnetization has to be made with magnetic domains. Saturation magnetization is a structural property independent of particle size but dependent on temperature. The results obtained are in agreement with the magnetization plot [34]. Kök et al. observed that the magnetic saturation decreased as a result of high temperature oxidation applied to the NiMnGa alloy and attributed the reason to the increase in the amount of oxide on the alloy [17]. While the highest magnetic saturation value is seen in the sample that is heat treated at 500 °C, it is seen that the magnetic saturation values of the samples that are heat treated at 700 °C and 900 °C are close to each other.



Hata! Başyuru kaynağı bulunamadı.

4. Conclusion

In this study, magnetocaloric, crystalline and scientific research of NiMnCoSn magnetic shape memory alloy was aimed.

- Three different temperatures were selected according to the DSC results. When the DSC analysis results are examined, it is seen that the samples do not give any transformation. It is thought that the reason is because the samples are melted first and then grinded. According to the DSC results, the absence of austenite or martensite phase means that the crystal structure of the sample did not change with temperature.
- When the XRD results were examined, a common peak was observed around 30 and 50 degrees, and it was determined that it was in agreement with the literature results [35].
- It can be seen that magnetization measurements, the most obvious result is seen in the sample, which is heat treated at 500 °C. This is followed by the main sample, 900 °C, 700 °C.

- Saturation magnetization values were calculated from the slope, and then the results were graphed. When the particle size results are examined, it is seen that it is compatible with the magnetization values.

References

- [1] Addington, D.M. and D.L. Schodek, *Smart materials and new technologies: for the architecture and design professions*. 2005: Routledge.
- [2] Gandhi, M.V. and B. Thompson, *Smart materials and structures*. 1992: Springer Science & Business Media.
- [3] Sullivan, M.R., A.A. Shah, and H.D. Chopra, *Pathways of structural and magnetic transition in ferromagnetic shape-memory alloys*. Physical Review B, 2004. **70**(9): p. 094428.
- [4] Schetky, L.M., *Shape-memory alloys*. Kirk-Othmer Encyclopedia of Chemical Technology, 2000.
- [5] Aydogdu, Y., et al., *The effect of Sn content on mechanical, magnetization and shape memory behavior in NiMnSn alloys*. Journal of Alloys and Compounds, 2016. **683**: p. 339-345.
- [6] Esmaeli, A., *New worm robot structure using the shape-memory alloy*. Majlesi Journal of Electrical Engineering, 2014. **8**(2).
- [7] Bruno, N., et al., *On the microstructural origins of martensitic transformation arrest in a NiCoMnIn magnetic shape memory alloy*. Acta Materialia, 2018. **142**: p. 95-106.
- [8] Duerig, T.W., K. Melton, and D. Stöckel, *Engineering aspects of shape memory alloys*. 2013: Butterworth-heinemann.
- [9] Xuan, H., et al., *Effect of annealing on the martensitic transformation and magnetocaloric effect in Ni_{44.1}Mn_{44.2}Sn_{11.7} ribbons*. Applied Physics Letters, 2008. **92**(24): p. 242506.
- [10] Planes, A., et al., *Magnetostructural tweed in ferromagnetic Heusler shape-memory alloys*. Materials Science and Engineering: A, 2006. **438**: p. 916-918.
- [11] Ma, Y. and J. Li, *A constrained theory on actuation strain in ferromagnetic shape memory alloys induced by domain switching*. Acta materialia, 2007. **55**(9): p. 3261-3269.
- [12] Huang, L., et al., *Large magnetic entropy change and magnetoresistance in a Ni₄₁Co₉Mn₄₀Sn₁₀ magnetic shape memory alloy*. Journal of Alloys and Compounds, 2015. **647**: p. 1081-1085.
- [13] Gschneidner Jr, K.A., V. Pecharsky, and A. Tsokol, *Recent developments in magnetocaloric materials*. Reports on progress in physics, 2005. **68**(6): p. 1479.
- [14] Zimm, C., et al., *Description and performance of a near-room temperature magnetic refrigerator*, in *Advances in cryogenic engineering*. 1998, Springer. p. 1759-1766.
- [15] Shen, B., et al., *Recent progress in exploring magnetocaloric materials*. Advanced Materials, 2009. **21**(45): p. 4545-4564.
- [16] Kainuma, R., et al., *Metamagnetic shape memory effect in a Heusler-type Ni₄₃Co₇Mn₃₉Sn₁₁ polycrystalline alloy*. Applied Physics Letters, 2006. **88**(19): p. 192513.
- [17] Kök, M., G. Pirge, and Y. Aydoğdu, *Isothermal oxidation study on NiMnGa ferromagnetic shape memory alloy at 600–1000° C*. Applied surface science, 2013. **268**: p. 136-140.
- [18] Li, D., et al., *Effects of high magnetic field annealing on texture and magnetic properties of FePd*. Journal of magnetism and magnetic materials, 2004. **281**(2-3): p. 272-275.
- [19] Oikawa, K., et al., *Phase equilibria and phase transformation of Co–Ni–Ga ferromagnetic shape memory alloy system*. Journal of phase equilibria and diffusion, 2006. **27**(1): p. 75-82.
- [20] Kainuma, R., et al., *Magnetic-field-induced shape recovery by reverse phase transformation*. Nature, 2006. **439**(7079): p. 957-960.

- [21] Karaca, H.E., et al., *Magnetic Field-Induced Phase Transformation in NiMnCoIn Magnetic Shape-Memory Alloys—A New Actuation Mechanism with Large Work Output*. *Advanced Functional Materials*, 2009. **19**(7): p. 983-998.
- [22] Han, Z., et al., *Low-field inverse magnetocaloric effect in Ni_{50-x}Mn_{39+x}Sn₁₁ Heusler alloys*. *Applied Physics Letters*, 2007. **90**(4): p. 042507.
- [23] Ma, L., et al., *Martensitic and magnetic transformation in Mn₅₀Ni_{50-x}Sn_x ferromagnetic shape memory alloys*. *Journal of Applied Physics*, 2012. **112**(8): p. 083902.
- [24] Han, Z., et al., *Phase diagram and magnetocaloric effect in Mn₂Ni_{1-64-x}CoxSn_{0.36} alloys*. *Scripta Materialia*, 2012. **66**(2): p. 121-124.
- [25] Wu, Z., et al., *Metallurgical origin of the effect of Fe doping on the martensitic and magnetic transformation behaviours of Ni₅₀Mn_{40-x}Sn₁₀Fe_x magnetic shape memory alloys*. *Intermetallics*, 2011. **19**(4): p. 445-452.
- [26] Khovaylo, V., et al., *Peculiarities of the magnetocaloric properties in Ni-Mn-Sn ferromagnetic shape memory alloys*. *Physical Review B*, 2010. **81**(21): p. 214406.
- [27] Choon, T.W., et al., *Phase transformation temperatures for shape memory alloy wire*. *World Academy of Science, Engineering and Technology*, 2007. **25**(304).
- [28] Altın, S., *Süper iletken BSCCO whiskerlerin büyüme mekanizması ve farklı katkılamalara bağlı olarak elektriksel ve manyetik özellikleri*. 2009.
- [29] Elwindari, N., et al. *Microstructure and Magnetic Properties of Optimally Annealed Ni₄₃Mn₄₁Co₅Sn₁₁Heusler Alloy*. in *IOP Conference Series: Materials Science and Engineering*. 2017. IOP Publishing.
- [30] Chen, F., et al., *Martensitic transformation and magnetic properties of Ti-doped NiCoMnSn shape memory alloy*. *Rare Metals*, 2014. **33**(5): p. 511-515.
- [31] Mishra, S.S., et al., *Rapidly Quenched Ni₄₅Fe₅Mn₄₀Sn₁₀ Heusler Alloys*. *Materials Research*, 2015. **18**: p. 101-105.
- [32] Kök, M., et al., *Effects of Aging on Magnetic and Thermal Characteristics of NiMnCoSn Magnetic Shape Memory Alloys*. *Iranian Journal of Science and Technology, Transactions A: Science*, 2021: p. 1-9.
- [33] Kök, M., G. Pirge, and Y. Aydoğdu, *Isothermal oxidation study on NiMnGa ferromagnetic shape memory alloy at 600–1000 C*. *Applied Surface Science*, 2013. **268**: p. 136-140.
- [34] Lu, H., W. Zheng, and Q. Jiang, *Saturation magnetization of ferromagnetic and ferrimagnetic nanocrystals at room temperature*. *Journal of Physics D: Applied Physics*, 2007. **40**(2): p. 320.
- [35] Hernando, B., et al., *Grain oriented NiMnSn and NiMnIn Heusler alloys ribbons produced by melt spinning: Martensitic transformation and magnetic properties*. *Journal of Magnetism and Magnetic Materials*, 2009. **321**(7): p. 763-768.

Multilingual Text Mining Based Open Source Emotional Intelligence

Aytug BOYACI^{1*}, Shahin AHMADOV²

¹ Department of Computer Engineering, , Air Force Academy, National Defence University, Istanbul, Turkey

² Department of Computer Technologies, Hezarfen Aeronautics and Space Technologies Institute, National Defence University, Istanbul, Turkey

^{1*} aboyaci@hho.msu.edu.tr, ² shahinya@code.edu.az

(Geliş/Received: 08/05/2022;

Kabul/Accepted: 31/05/2022)

Abstract: The purpose of this study is to learn how people who speak different languages interpret the same issues, and to compare the results obtained and show the difference between their perspectives. To learn this point of view, we must first turn to open source intelligence. In this execution, a sentiment analysis application was designed using the Python programming language and the Natural Language Processing algorithms in the texts, which were taken as a data set of comments in Azerbaijani, Turkish, Russian and English languages from social media. As the data set, the comments made on 4 subjects: the declaration of Hagia Sophia as a mosque, the objection events that started with the natural gas hike in Kazakhstan, the natural disasters in Turkey, the Ukraine crisis. After loading the texts in four languages from the network environment, after preprocessing, the text was divided into 8 different categories (neutral, fear, joy, anger, sadness, surprise, disgust, shame) by means of the application written in Python programming language based on Data Mining and Machine Learning topics. In the study, precision, sensitivity, accuracy and F1 score were obtained by using Random Decision Forests, K - Near Neighbor Algorithm, Decision Trees, Support Vector Machine, Naive Bayes Algorithm, Logistic Regression, which are machine learning methods. By comparing the results, it was determined that the Logistic Regression method obtained the highest result. A sentiment analysis model was created using the Logistic Regression method, and sentiment analysis was performed for each subject at separation and the results were compared.

Key words: Text mining, Emotion detection, Machine learning, Natural language processing.

Açık Kaynak Duyusal Zeka Tabanlı Çok Dilli Metin Madenciliği

Öz: Bu çalışmanın amacı farklı dillerde konuşan insanların aynı konuları nasıl yorumladıklarını öğrenmek ve elde edilen sonuçları kıyaslayarak bakış açıları arasındaki farkı ortaya koymaktadır. Bu bakış açısını öğrenmek için ilk önce açık kaynak istihbaratına başvurmamız gerekmektedir. Bu çalışmada açık kaynak istihbaratı olan sosyal medya platformu Intagram üzerinden Azerbaycan, Türk, Rus ve İngiliz dillerinde Ayasofya'nın cami olarak ilan edilmesi, Kazakistan'da doğal gaz zamyyla başlayan itiraz olayları, Türkiye'de oluşan doğal afetler, Ukrayna krizi olmak üzere 4 konuda yapılan yorumlar veri seti olarak kullanılmıştır. Veri seti üzerinde Python programlama dili ve içerisinde bulunan doğal dil işleme algoritmalarını kullanarak duygu analizi uygulaması tasarlanmıştır. Dört dilde metinler ağ ortamından yüklenerek, ön işlemlerden geçtikten sonra veri madenciliği ve makine öğrenmesi konuları baz alınarak Python programlama dilinde yazılmış uygulama vasıtasıyla metin 8 farklı kategoriye (nötr, korku, sevinç veya eğlence, öfke, üzüntü, hayret, iğrenme, utanç) ayrılmıştır. Çalışmada makine öğrenmesi yöntemlerinden olan Rastgele Karar Ormanları, K - Yakın Komşu Algoritması, Karar Ağaçları, Destek Vektör Makinesi, Naive Bayes Algoritması, Lojistik Regresyon kullanılarak kesinlik,duyarlılık, doğruluk ve F1 skoru sonuç olarak elde edilmiştir. Sonuçlar karşılaştırılmış ve Lojistik Regresyon yönteminin en yüksek netice elde ettiği tespit edilmiştir. Daha sonra Lojistik Regresyon yöntemi kullanılarak duygu analizi modeli oluşturulmuş ve her bir konu için ayrılıkta duygu analizi yapılmış ve sonuçlar karşılaştırılmıştır.

Anahtar kelimeler: Metin madenciliği, Duygu analizi, Makine öğrenmesi, Doğal dil işleme.

1. Introduction

Throughout life, people have a desire to learn about various topics and to learn ideas. Lately, we usually get this information from the Internet. Later, we would like to discuss about this information or learn the opinion of others about the said topic. So, if in ancient times people were asking their friends or books for information or ideas, now with the rapid development of information and computing technologies and especially the global internet, a valuable alternative has emerged to find the necessary information and help choose something. The leading method for obtaining this information is open source intelligence. OSINT-open source intelligence is based on online publications, chats, blogs, social networks and streaming platforms. Apart from these, open source intelligence also takes into account the print media such as magazines, newspapers, professional research articles, business data, telephone directories, and other reports that may be useful in extracting data from individuals or organizations representing the interest[1]. As an example, we can say that 80-90% of the intelligence needs of countries in our age are obtained from open source intelligence [2]. Since the aim of the study is to understand people's feelings about current events by making sentiment analysis on texts, open source intelligence helps us to achieve an efficient result. We have decided to use social media platforms as we aim to extract text data from open source intelligence.

Various texts created on social media, such as blog articles, product reviews, social media posts, news comments, etc., contain a lot of valuable information. With the help of this valuable information, we can read people's minds or direct them if needed. One of these methods is sentiment analysis [3]. In social media, sentiment is an emotional evaluation that expresses the direction of thoughts in comments and other texts. The importance of the task of identifying emotions, i.e. sentiment analysis, is that it is possible to evaluate the attitude of society towards a message, product or idea of the text based on text information. This sentiment analysis can be used, for example, to evaluate the success of an advertising campaign, political and economic reforms, or to determine the attitude of the press and media towards a particular person, organization or event. In another area, it provides information on how consumers relate to certain products, services, and organizations. Therefore, this type of information is very important for marketers, sociologists, economists, politicians and all experts whose activities depend on people's opinions [4].

The sentiment analysis conducted in this study aims to determine what people who express themselves in four languages on different topics think and how their emotions change based on the comment texts collected through social media.

This study consists of four parts. The first chapter deals with the introduction and the aim of the study. The second chapter deals with the formation of the machine learning model and the methods of collecting the data used and preprocessing the texts. The third chapter explains the results of the categorization of the text according to the sentiment analysis performed in the study and compares the results according to the applications to the data in different languages. In the last part, the results were evaluated and suggestions for future studies were presented.

2. Material and Methods

In this part of the study, information is given about the procedures before the analysis. First, it will be shown that the model we will use in the study for sentiment analysis consists of the following elements.

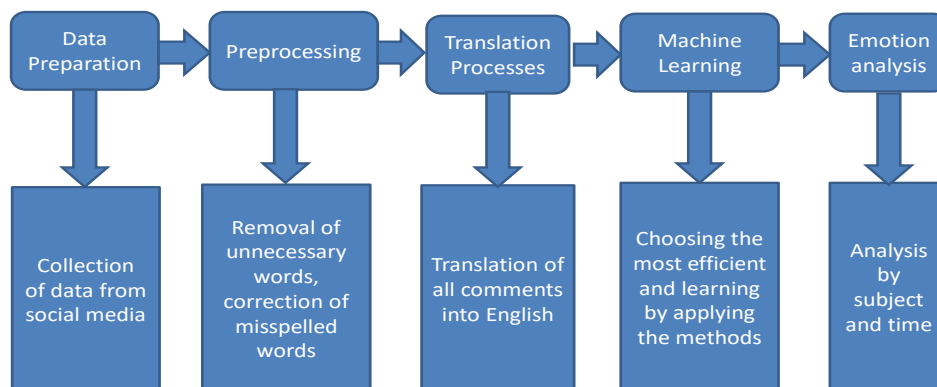


Figure 1. Creating the Model

2.1 Dataset and Preprocessing

Machine Learning algorithms produce predictive models that perform well only if they are trained with sufficient number and quality of data[5]. In this regard, the machine learning process starts with the creation of the dataset.

In the data collection phase, the social media platform Instagram, which is widely used in many countries, was used [6].

Comments on news posts on the Turkish 'Ist1hbarat', 'Haberglobal', 'BBCTurkce' pages on the Instagram platform, comments on news posts on the Russian 'Ria_novosti', 'NTVru', 'BBCRussian' pages, comments on the news shared on the English 'BBCnews' page, In Azerbaijani, the comments made on the news shared on 'BBCAzeri', 'Azerbaijan.24', 'Maraqlı.tv' pages were compiled and used manually.

At this stage, the first step is to check the correct collection of data. The collected data is reread according to the topic and time and wrong data formation is prevented. Then, incorrectly added or classified comments are manually filtered and cleaned. In the next step, the collected data is converted to a suitable format (CSV) so that it can be compiled by the Python programming language. After the format conversion, the row and column layout of the dataset is recompiled. Information loss is minimized by completing missing data. Some data sets are combined into a single data set.

The new datasets created after these preprocessing steps are classified and grouped. The preprocessed and grouped data are translated from Turkish, Russian and Azerbaijani languages into English using 'Microsoft Translator for Business' and 'Google Translate'. Each translated comment is manually compiled and the accuracy of the translation is checked. The translations that occur at this stage, resulting in incorrect or ambiguous translations, are converted into the appropriate text by manual changes. The translated texts are prepared again by applying preprocessing steps. After these steps, the dataset can now be considered ready for use.

2.2. Machine Learning

After the preprocessing steps are done, the evaluation of the operation results made by the Machine Learning methods [7] on the prepared dataset is made according to the obtained F1 score, accuracy, sensitivity and precision values. Six different Machine Learning methods were applied to the pre-prepared dataset and value results were obtained for each of them.

For the Random Decision Forests method, the Random Forest Classifier module of the Scikit-learn library in the Python programming language was used. The "Gini" index was used as the common objective function. An attempt was made to obtain the best result by changing the number of trees.

The K-neighbors Classifier module of the Python library Scikit-learn is used for the K - Near Neighbor Algorithm classification method. In this module, the number of neighbors was set to 3 and 5, and the Minkowski distance and Euclidean distance were chosen as distance measures.

The Decision Tree Classifier module of the Scikit-learn library in the Python programming language was used for the decision tree method. The "Gini" index was used as the common objective function. An attempt was made to obtain the best result by changing the maximum depth settings.

For the Support Vector Machine classification method, the SVC (Support Vector Classification) module of the Scikit-learn library was used. The kernel function is used as a Radial Based Function. The variables are set to 'auto'.

For the classification method with the Naive Bayes algorithm, the module MultinomialNB of the Scikit-learn library was used. Many variants of the Naive Bayes algorithm are used in the scikit-learn library. The main reason for using the Multinomial Naive Bayes algorithm is its application to texts.

For the Logistic Regression classification method, the Logistic Regression module of the Scikit-learn library was used. The experiments were performed by determining the random variables.

2.3. Emotion Detection

Sentiment analysis analyzes human emotions and moods on the dataset, that is, it is a method that analyzes data obtained from customer reviews, financial news, social media comments or other sources according to emotion criteria [8].

With the advent of social media, people are becoming more receptive about their experiences with online products and services through blogs, vlogs, social media stories, reviews, recommendations, reviews, hashtags, comments, direct messages, news articles, and various other platforms. Such sentimental perceptions leave a digital

footprint of how a person expresses their experience in an online space [9]. Most sentiment analysis methods can evaluate these ideas as positive, negative, or simply neutral [10]. If we want to get a more detailed result, we can use methods that include many emotions. With these methods, we can divide the data into categories such as fear, joy, anger, sadness, surprise, disgust, and so on. This helps us a lot in getting the necessary information or forming an opinion about a topic. In the mood analysis phase, the machine learning model was trained using the Logistic Regression module of the Scikit-learn library in the Python programming language [11]. Using the trained model, sentiment analysis was performed on the data categorized according to the mentioned topics.

Using the sentiment analysis, the texts were categorized into 8 sentiment categories such as neutral, fear, joy or fun, anger, sadness, surprise, disgust, and shame.

3. Findings

The results of the machine learning experiments are shown in Table 1. In this table, precision, sensitivity, f1-score and accuracy values of 6 machine learning methods were compared and it was determined that the Logistic Regression result was the highest.

Table 1. Results of Machine Learning Methods

Machine Learning Methods	Precision	Sensitivity	Accuracy	F1 score
Random Decision Forests	0.74	0.60	0.58	0.60
K Near Neighbor Algorithm	0.47	0.24	0.22	0.24
Decision Trees	0.52	0.52	0.52	0.52
Support Vector Machine	0.71	0.61	0.59	0.61
Naive Bayes Algorithm	0.61	0.57	0.54	0.57
Logistic Regression	0.65	0.63	0.60	0.63

Based on these results, the Logistic Regression method will be used for the Sentiment Analysis to be done later [12].

3.1. Comparative Analysis of the Announcement of Hagia Sophia as a Mosque

In the sentiment analysis phase, all the topics for each language were analyzed first, and in the next phase, the results of the sentiment analysis of the comments of the people speaking in different languages were compared according to the topic.

After the Sentiment Analysis of the comments made in four different languages on the subject mentioned here, the three emotions with the most comments are shown.

Table 2. Comparative Analysis of the Announcement of Hagia Sophia as a Mosque

Language	Emotions		
Turkish	Joy	Neutral	Fear
Russian	Neutral	Joy	Fear
English	Joy	Neutral	Fear
Azerbaijani	Joy	Neutral	Sadness

As shown in Table 2, we see that the emotion of joy is dominant in the comments written in all languages about the declaration of Hagia Sophia as a mosque. It is also shown that, unlike the others, the comments with a neutral emotion in the comments made in Russian are more than the emotion of joy.

For example, in Russian texts 'Church', 'Mosque', 'Tourist', 'Christian' and 'Prayer' words, in Turkish texts 'Hagia Sophia', 'Mosque', 'People', 'Allah', 'Day' and 'Satisfied' words, in English texts 'Turkey', 'Mosque', 'Muslim', 'Beautiful', 'Love', 'Erdogan', in Azerbaijani texts 'Allah', 'Acceptance', 'Prayer', 'Beautiful', 'Possible' words are used more.

3.2. Comparative Analysis of Objection Events in Kazakhstan

After the Sentiment Analysis of the comments made in four different languages on the subject mentioned in Table 3, the three emotions with the most comments are shown.

Table 3. Comparative Analysis of Objection Events in Kazakhstan

Language	Emotions		
Turkish	Fear	Neutral	Joy
Russian	Joy	Fear	Neutral
English	Fear	Neutral	Joy
Azerbaijani	Neutral	Joy	Sadness

As shown in Table 3, we see that the emotion of fear is dominant in the comments written in English and Turkish regarding the protest events that started with the natural gas hike in Kazakhstan. And we see that the emotion of joy in Russian interpretations, neutral in the Azerbaijani language.

For example, in Russian texts 'People', 'Well', 'Russia', 'Natural Gas', 'Price', 'Time', in Turkish texts 'People', 'Kazakhstan', 'Russia', 'Will', 'Turkish' and 'Street', in English texts 'People', 'Kazakhstan', 'Russia', 'Demand', 'Terrorist', 'State', in Azerbaijani texts 'Nation', 'Power', 'Russia', 'Day', 'Demand' words are used more often.

3.3. Comparative Analysis of Natural Disasters in Turkey

In Table 4, after the Sentiment Analysis of the comments made in four different languages about the natural disasters that have occurred in Turkey in recent years, the three emotions that contain the most comments are shown.

Table 4. Comparative Analysis of Natural Disasters in Turkey

Language	Emotions		
Turkish	Joy	Neutral	Fear
Russian	Joy	Neutral	Fear
English	Joy	Sadness	Fear
Azerbaijani	Neutral	Joy	Fear

As shown in Table 4, we see that the emotion of joy is dominant in the comments written in English, Russian and Turkish about natural disasters in Turkey. In the Azerbaijani, we see that the emotions of neutrality and later joy is superior. It is used in large numbers in comments that contain a emotion of fear, usually in all interpretations.

For example, in Russian Texts 'God', 'Turkey', 'Always', 'Good', 'Pain', in Turkish texts 'Hotel', 'Aim', 'Fire', 'Burn', 'Immediate', In English texts, 'People', 'Care', 'Smooth', 'God', and 'Walk', in Azerbaijani texts the words 'Allah', 'Help', 'Prayer', 'Protect' and 'Remember' are used more often.

3.4. Comparative Analysis of the Ukraine Crisis

In Table 5, after the Sentiment Analysis of the comments made in four different languages regarding the crisis in Ukraine in 2022, the three emotions with the most comments are shown.

As shown in Table 5, we see comments that contain more sadness in the comments written in English and Azerbaijani on the subject. Neutral and fearful interpretations are used a lot in Turkish, while interpretations containing fear are used a lot in Russian.

For example, in Russian texts 'Ukraine', 'Russia', 'War', 'People' and 'Thinking', in Turkish texts 'World War', 'Russia', 'Putin', 'Countries', in English texts 'War', 'Russia', 'Stop', 'Need', in Azerbaijani texts 'War', 'Ukraine', 'Soldier', 'Nation', 'World' and 'Persistence' words are used more common.

Table 5. Comparative Analysis of the Ukraine Crisis

Language	Emotions		
Turkish	Neutral	Fear	Joy
Russian	Fear	Neutral	Joy
English	Sadness	Fear	Anger
Azerbaijani	Sadness	Neutral	Joy

4. Conclusion

We see that open source intelligence is very important to understand the emotions of people speaking different languages, which is our in four languages: Turkish, Russian, English and Azerbaijani. The second chapter talks in the study. It is easy to access all kinds of data and information we need on the Internet. However, the open-source nature of this data creates the opportunity to act within the legal framework. For this reason, intelligence data collected on the Internet should be open source. More than six thousand comments were collected on the social media platform Instagram, which has open-source intelligence data in four languages, Turkish, Russian, English, and Azerbaijani, because it is legal and contains information on the topics needed for the study. After the preprocessing steps were done on the collected data set, machine learning methods were used for sentiment analysis and the results were compared. In this phase, machine learning methods such as Random Decision Forests, KNN algorithm, Decision Trees, Support Vector Machine, Naive Bayes algorithm and Logistic Regression were used. Logistic Regression was selected with the highest result, an F1 score of 0.63. A machine learning model was created and preparations for sentiment analysis were seen. Sentiment analysis was performed according to the timing and announcement of Hagia Sophia as a mosque, the objection events that started with the natural gas surge in Kazakhstan, the natural disasters that occurred in Turkey, and the Ukraine crisis. The sentiment analysis was performed separately for the comments made in four languages on each topic and the results were displayed. As a result of the sentiment analysis, we see that the indicator of the emotion of joy we obtained is the highest. The reason is that the sentiment analysis perceives the allusions and ironic expressions used in the comments as joy. For example, in the comparative analysis of natural disasters in Turkey, many comments about the construction of hotels in fire areas were rated as feelings of joy. For future studies, it is suggested to develop models to detect such expressions.

References

- [1] Eliot Higgins, "We Are Bellingcat: An Intelligence Agency for the People", Bloomsbury Publishing, 2021, pp. 9-63.
- [2] Stevyn Gibson, "Open Source Intelligence, An Intelligence Lifeline", Royal United Services Institute Journal, 2004, pp 5-6.
- [3] Svetlana Tupikova, "Cognitive Foundations of Communicative Tonality", Lambert Academic Publishing, 2020, pp. 28-44.
- [4] A.G. Dodonov, D.V. Lande, V.V. Prishchepa, V.G. Putyatin, "Computer competitive intelligence", Engineering, 2021, pp. 15-18.
- [5] F. Pedregosa, G. Varoquaux, A. Gramfort, V. Michel, B. Thirion, O. Grisel, M. Blondel, P. Prettenhofer, R. Weiss, V. Dubourg, et al., "Scikit-learn: Machine learning in Python", J. Mach. Learn. Res. 2012, pp. 2825–2830.
- [6] We are social and Hootsuite, "Digital 2020" report, 2021.
- [7] Engin Sorhun, "Machine Learning with Python", Abakus, 2021, pp. 9-43.
- [8] Hassan Saif, "Semantic Sentiment Analysis in Social Streams", IOS Press, 2017, pp. 26-36.
- [9] Harkamal Preet Pal Singh Ubhi, "The Social Media Guide", Rakuten, 2019, pp. 7-31.
- [10] Bing Liu, "Sentiment Analysis", Cambridge University Press, 2020, pp. 16-46.
- [11] Michael Bowles, "Machine Learning with Spark and Python: Essential Techniques for Predictive Analytics", Wiley, 2019, pp. 129-166.
- [12] Joseph M. Hilbe, "Practical Guide to Logistic Regression", CRC Press, 2016, pp. 49-70.

A New Algorithmic Trading Approach Based on Ensemble Learning and Candlestick Pattern Recognition in Financial Assets

Üzeyir AYCEL^{1*}, Yunus SANTUR¹

¹ Software Engineering, Institute of Science, Firat University, Elazig, Turkey

*¹ uzeyir.aycel@hotmail.com, ² ysantur@firat.edu.tr

(Geliş/Received: 31/05/2022;

Kabul/Accepted: 31/08/2022)

Abstract: Financial assets considered as time series are chaotic in nature. The main goal of investors is to take a position at the right time and in the right direction by making predictions about the future of this chaotic series. These time series consist of the opening, low, high, and closing prices of a certain period. The approaches used to make predictions about trend direction and strength using moving averages and indicators based on them have noise and lag problems as they are obtained statistically. Candlestick charts, on the other hand, reflect the price-based psychology of bear and bull investors, and facilitate the interpretation of price movements by consolidating the said opening, closing, lowest and highest prices in a single image. It is known that it was applied to Japanese rice markets for the first time in history and there are more than 100 candle patterns. In this study, an extensible architecture software framework using factory patterns and an object-oriented approach is proposed for defining candlestick patterns and developing intelligent learning algorithms based on them. In the studies carried out for financial assets, the profit factor, which shows the portfolio gain of the strategy, is used. It is desirable that this number of wins be greater than 1. When the proposed approach is tested for 5 major financial assets, this value was obtained as greater than 1 for all assets. The proposed software framework can also be used in the development of new robotic approaches in terms of being applicable to all kinds of financial assets in every period.

Key words: Algorithmic trading, Ensemble learning, Financial forecasting, Pattern recognition, XGBoost.

Finansal Varlıklarda Topluluk Öğrenme ve Mum Grafiği Patern Tanıma Dayalı Yeni Bir Algoritmik Ticaret Yaklaşımı

Öz: Zaman serileri olarak ele alınan finansal varlıklar yapısı gereği kaotiktir. Kaotik olan bu seri üzerinde geleceğe yönelik tahminlerde bulunarak doğru zamanda, doğru yönde pozisyon almak yatırımcıların temel hedefidir. Bu zaman serileri belirli bir periyotta ki açılış, en düşük, en yüksek ve kapanış fiyatından oluşmaktadır. Hareketli ortalamalar ve bunlara dayalı olarak göstergeleri kullanarak trend yönü ve gücü hakkında tahminler yapmak için kullanılan yaklaşımlar istatistiksel olarak elde edildiğinden gürültü ve gecikme problemlerine sahiptir. Mum grafikler ise bahsi edilen açılış, kapanış, en düşük ve en yüksek fiyatları tek bir görselde konsolide ederek, fiyat hareketlerinin yorumlanmasını kolaylaştırmalarının yanı sıra ayı ve boğa yatırımcılarının fiyat temelli psikolojilerini de yansıtır. Tarihte ilk defa Japon pirinç piyasalarına uygulandığı ve 100'den fazla mum patern olduğu bilinmektedir. Bu çalışmada mum grafik paternlerinin tanımlanması ve bunlara dayalı akıllı öğrenme algoritmalarının geliştirilmesi için fabrika deseni ve nesne tabanlı yaklaşım kullanan genişleyebilir mimaride bir yazılım çatısı önerilmiştir. Finansal varlıklar için gerçekleştirilen çalışmalarda stratejinin portföy kazancını gösteren kazanç katsayısı kullanılmaktadır. Bu kazanç sayısının 1'den büyük olması arzu edilmektedir. Önerilen yaklaşım 5 major finansal varlık için test edildiğinde, tüm varlıklarda bu değer 1'den büyük olarak elde edilebilmiştir. Önerilen yazılım çatısı her türlü finansal varlığa her periyotta uygulanabilir olması açısından yeni robotik yaklaşımların geliştirilmesinde de kullanılabilir olacaktır.

Anahtar kelimeler: Algoritmik ticaret, Desen tanıma, Finansal tahmin, Topluluk öğrenimi, XGBoost.

1. Introduction

An exchange is an organized market in which tradeable securities, commodities, foreign Exchange, and futures are bought or sold. The stock market is one of the most popular investment environments that work with the principle of capital exchange due to its regular trading mechanism, up-to-date prices, and real-time trading, as well as creating a safe environment for its investors. Another tool that can be shown as an investment tool is stock market stocks [1]. Stocks and sector indices such as banking, construction and health are examples of financial time series. The future values of financial time series have a complex and chaotic structure that changes dynamically due to instant decisions of investors. Therefore, the estimation process on these time series is considered to be a challenging task based on more than one condition [2].

* Corresponding author: uzeyir.aycel@hotmail.com. ORCID Number of authors: ¹ 0000-0003-0847-9418, ² 0000-0002-8942-4605

There are two main approaches where attempting to predict stock prices and investors get information before investing. These are called technical analysis and fundamental analysis. The technical analysis develops statistical-based approaches to predict future prices using past price movements and trading volumes. Fundamental analysis, on the other hand, is to have an idea about whether to invest or not by taking into account other factors, especially economic, environmental, political, and financial factors in addition to these statistical approaches [3]. Fundamental analysis can be used to examine a company's balance sheet such as assets, liabilities and earnings, and even the company's management and competitive conditions. In technical analysis, it is generally used for short-term transactions, but also instant, minute, 5 minute, hourly, daily, weekly and monthly transactions. For this purpose, online platforms such as Tradingview and Investing and package programs called data terminals are also used [4]. In addition, stock charts containing previous price movements are used to predict future price movements of stocks [2].

Understanding how to use and interpret charts with technical analysis is of paramount importance to any trader. The starting point of technical analysis is to read the charts correctly and to choose a chart type suitable for the analysis style. These charts consist of price and date information in their most basic form. Thanks to the graphs, the trend, the resistance, and support levels that the price has difficulty in passing, the pattern formations can be determined and the decision is made to enter a buy or sell position using various analysis tools. Therefore, charts are the final point of departure in the decision mechanism for every investor.

There are basically three types of charts on trading platforms. These charts are called line, bar, and candlestick charts. The line chart, as seen in Figure 1, is the simplest form of chart used to observe price development information at a glance. These charts, which are usually drawn over the closing prices, can be drawn over the opening, lowest or highest price. However, in any case, it only refers to a single data.



Figure 1. An example line graph representation

The bar graph, also known as the bar graph, has the representation in Figure 2. It is the type of chart that shows the opening, closing, lowest and highest prices in the session and is widely used in technical analysis. In the bar chart, the top of the bar shows the highest price the share has reached throughout the day. The lowest point of the bar also indicates the lowest price that the share has gone through throughout the day. The lengthening of the bar indicates that the volatility of the share has increased, while the shortening of the neck indicates that the volatility of the share has decreased. In a bar chart, the closing price is a line to the right on the bar, and the opening is a line to the left. The fact that the lowest price of the stock and the closing price are close to each other indicates that there is selling pressure in the stock in the short term, but this indicates that the stock has technically weakened. On the contrary, the closeness of the highest price reached during the day with the closing price indicates that the stock is technically stronger in the short run [5].



Figure 2. An example bar graph representation

The use of candlestick patterns in time series has been very popular around the world lately because they are more visually appealing and generally easier to read and interpret than the bar or line charts. However, candlestick charts give investors and analysts a clearer view, as well as give a more accurate depiction of market sentiment. Many traders are able to trade using candlestick charts, exemplified in Figure 3, without any helpful indicators. Candlestick charts, in addition to showing the market movements in detail, make it easy to see the relationship between the opening (Open) and closing (Close) and the highest (High) and lowest (Low) price movements in a single visual, and it is called OHLC for short [6].



Figure 3. An example candlestick chart

Candlestick charts were learned and used by the whole world when Steve Nison went to Japan and did research [6]. The traditional Japanese candlestick interpretation technique has the potential to be a unique approach that can be used in the development of financial forecasting models. Traders use candlesticks as in Figure 3 and can analyze the OHLC data, which includes all price movements, in a single visual [7]. As seen in Figure 4, the green candle indicates an upward trend in the market. Since the closing price is higher than the opening price, it is considered positive for the uptrend and indicates the fact that the bulls are in control. The longer the candle body, the stronger the buying interest. The red candle indicates that the market has a downward trend. This indicates that there is more selling than buying. It indicates the fact that the downtrend is also under the control of the bears as the closing price is lower than the opening price. The longer the candle body, the stronger the supply-demand balance between bears and bulls is assumed. The lines above and below the candle body are called “Shadow” or “Wick”. The upper shadow represents the tested but failed high point of the price, while the lower shadow represents the tested but failed low point of the price. There are more than 104 candle formations that support candlestick charts. Japanese candlesticks have been affected by noisy stock prices [6].

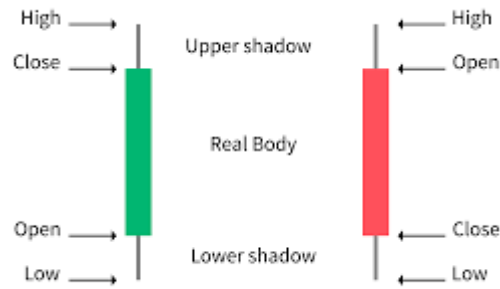


Figure 4. Candlestick description

The work will proceed as follows: Chapter 2 provides a summary of the work in the field of financial forecasting. Chapter 3 presents the architecture of the proposed model and the proposed system. In Chapter 4, the experimental study of the proposed approach is mentioned. The results of the study and future studies are given in Chapter 5.

2. Background

Prediction of financial time series is of primary importance for investors. In recent years, there has been a noticeable increase in the publications published in this field. In this context, different algorithms and methods have been developed. Research in this area will be outlined below.

Kusuma et al. (2019) investigated the predictability of the stock market using deep convolutional network and candlestick charts. In this study, different neural networks such as convolutional neural network, residual network and visual geometry group network are used. Consequently, it has been used to design a decision support framework that can be used by traders to provide suggested indicators of future stock price direction [8].

Hung et al. (2021), taking a new approach, proposed a deep predictive (DPP) method for price action by using candlestick charts in stock historical data. This method consists of three steps: 1. parsing a particular candlestick chart into sub-charts; 2. Using the CNNautoencoder to get the best representation of subcharts; 3. Application of RNN to predict price movements from a collection of sub-chart representations [9].

Sadeghi and Farid (2021) aim to design a stock market prediction based on candle patterns and use fuzzy logic to model market rules and candles. It explores how a trading algorithm should be designed using trading information analysis and signaling techniques and how they should be combined with the capabilities of fuzzy logic. In this study, the short- and medium-term benefits of the proposed method have been demonstrated in various markets. Again, this study enables investors to use private information to make safer investments. Also, in this study, fuzzy logic is used to implement trading systems based on candlestick patterns [10].

Yee et al. (2021) prefer to examine the states of the Ichimoku Kinko Hyo and Japanese Candlestick indicators to generate strong bullish and strong bearish signals. This model using real data determined from Bursa Malaysia, three counters NOTION, ADVENTA and RANHILL have been selected with a strong fundamental background through fundamental analysis and technical analysis in a short-term trade. Comparative work has been done on the performance of this combination analysis for 8 months of daily data market price action. It was determined that the experimental results revealed that the combination algorithm was successfully predicted for the short term. Therefore, this study has been a promising method for traders and investors who are interested in estimating the stock price to make a profit [11].

Lin et al (2021) proposed the PRML model, a new candlestick pattern recognition model that uses machine learning methods to make stock trading decisions even better. Four popular machine learning methods and 11 different feature types were applied to all possible cases of everyday patterns to initiate the pattern recognition scheme. The PRML model was applied to forecast all Chinese market stocks from January 1, 2000 to October 30, 2020 [12].

Ardianti et al. (2021), in their study, performed the estimation of the trading strategy by analyzing the candlestick pattern using Artificial Neural Network (ANN). Technical indicator tools and candlestick pattern were created as features and label data during the modeling process. The method has been applied to four stocks from IDX for a certain period of time through their technical indicators. In the 28-day period, the model was found to

produce the highest accuracy, reaching 85.96%. In addition, K-Fold Cross-Validation was used to evaluate the result of the model performance [13].

To highlight its capabilities, Chen and Tsai (2020) proposed a two-step approach to automatically recognize candlestick patterns. As a first step, Gramian Angular Field (GAF) was used to encode the time series as different image types. The second step was to use a Convolutional Neural Network (CNN) with GAF images to learn the eight critical types of candlestick patterns. In this paper, his approach is named GAF-CNN [14].

Yassini et al. (2019) analyzed the existence of different candlestick patterns in this study. It can predict trends in the foreign exchange market. The first set of minor hypotheses includes whether a candle with an inverted color is advancing with these patterns. The second group analyzes the trading profit significantly profitable transaction after various patterns. In this study, the three “open” prices of the First candles are considered as different possible stop points. These three different points have different consequences, so we have divided them into three different scenarios and discussed about them separately. Based on the small hypotheses in the end, it is concluded that there is no evidence to predict the strength of candlestick patterns in trend recognition.

Gökül (2021), in his work, focuses on the prediction of stock price using a technical analysis tool (candlestick chart). In this study, one-year stock price data of 30 companies, which are the leading companies in the individual sector, on the NSE (National Stock Exchange) are used to predict share prices. Example charts are from moneycontrol.com. In this study, the stock price is estimated using previous price changes in the stock market. Comparing these with a real price, it was found that how many were true and how many were false [16].

Ho and Huang (2021), on the other hand, proposed a multi-channel collaboration network by combining candlestick charts and social media data for stock trend forecasts. First, social media sentiment features were extracted from Twitter using the Natural Language Toolkit and sentiment analysis data. Next, the stock's historical time series data is converted into a candlestick chart to illuminate patterns in the stock's movement. Finally, the stock's sentiment features and candlestick chart are integrated to predict stock price action over 4-, 6-, 8-, and 10-day timeframes. We evaluated our model for five high-demand stocks (Apple, Tesla, IBM, Amazon, and Google) and found that our collaborative network achieved promising results, comparing favorably with single-network models using sentiment data or candlesticks alone [17].

Lin et al (2021), a simple eight-trigram feature engineering schema approach of inter-day candlestick patterns, a new approach to daily stock pattern prediction, which combines traditional candlestick charting with current artificial intelligence, is an ensemble machine learning framework. Various machine learning methods, including deep learning methods, are applied to stock data to predict the closing price direction [18].

Ananthi and Vijayakumar (2021) make predictions on the stock prices of any company determined by users in their proposed system for the next few days. It estimates the general condition of the stock by using estimated stock price and data sets obtained from different data regarding a particular stock. It is done by regression and candlestick pattern detection to make stock price prediction. In this proposed system, it generates signals to predict the market on the candlestick chart [19].

Aycel and Santur (2022), in their study, developed a new hybrid approach that can be used as an alternative to moving averages such as SMA, WMA and EMA used in the literature. Their performance was compared with the PSAR, BB, MACD, RSI and Stoch RSI indicators, which are widely used in the literature. The proposed approach has been validated by backtesting 30 stocks in BIST30 [20].

3. Material and Method

In this study, a software framework was created to develop algorithmic strategies supported by statistical pattern analysis. As shown in Figure 5, the proposed approach has four stages. In the first stage, the software framework was created with object-based coding for the 18 wax patterns used in the study. At this stage, object-oriented programming and factory design cover were used in order to increase the patterns to be used in the future with minimum code cost for future studies. In the second stage, one-hot encoding was done to determine the candle type. Thus, in the third stage, a data set labeled with candle types was created. In the fourth stage, which is the last stage, algorithmic buy/sell strategies based on patterns and/or statistical buy/sell strategies supported by candlestick patterns will be developed and portfolio return and buy&wait strategies will be compared.

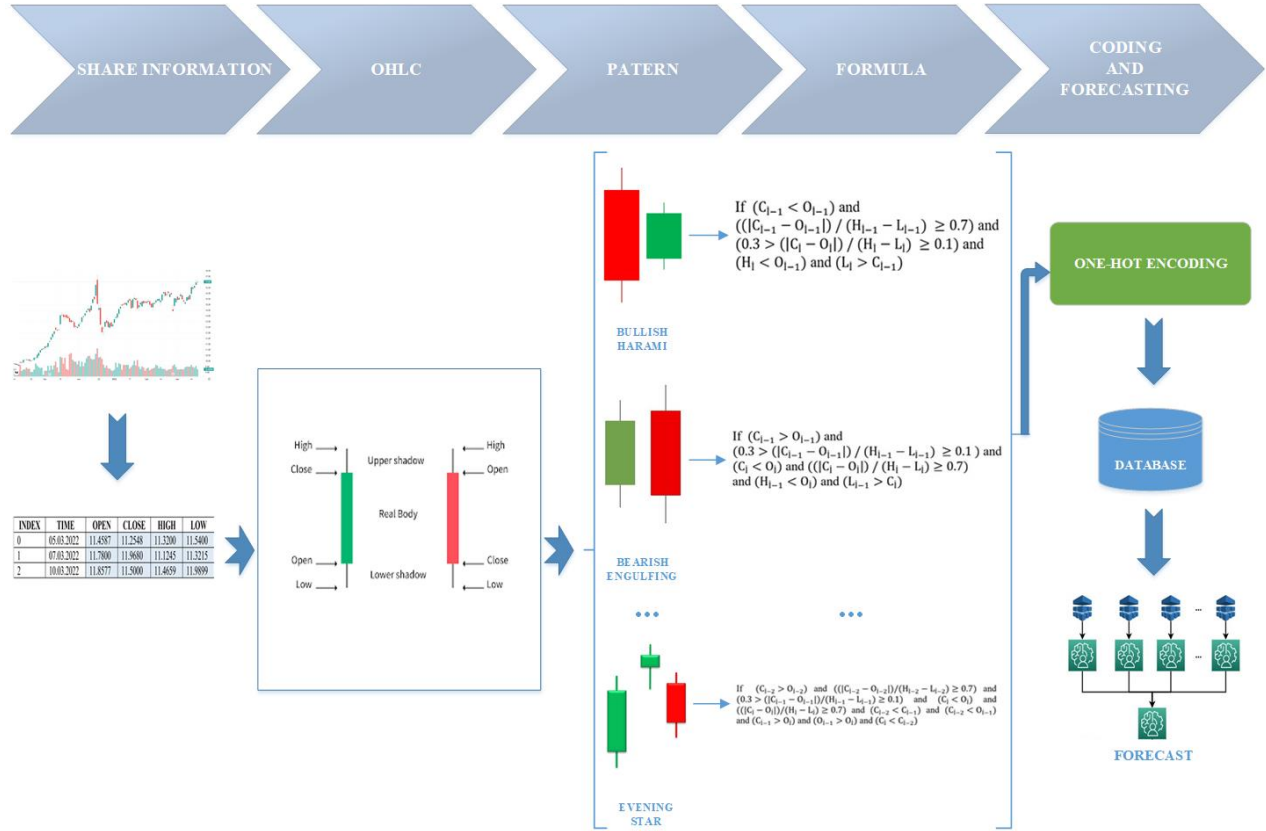


Figure 5. Proposed approach

3.1. Candlestick math

$$v_i = [O_i, C_i, H_i, L_i]$$

$$\Delta v_i = C_i - O_i$$

$$\max_{v_i} = \max(C_i, O_i)$$

$$\min_{v_i} = \min(C_i, O_i)$$

3.1.1. Doji

As in Figure 6a, candlesticks formed when the opening and closing prices are very close to each other or are exactly equal, are called doji. If the current stock has the same opening and closing prices, a doji occurs. Doji looks like a straight line in appearance. It is a term used to describe the equal power of buyers and sellers in the market. The formulation of the Doji candlestick pattern is shown below.

$$Doji(v_i) = \begin{cases} 1, & \text{if } \left[\begin{array}{l} \left(\frac{|\Delta v_i|}{H_i - L_i} < 0.1 \right) \text{ and} \\ \left(\frac{H_i - \max_{v_i}}{3 * |\Delta v_i|} > 1 \right) \text{ and} \\ \left(\frac{\min_{v_i} - L_i}{3 * |\Delta v_i|} > 1 \right) \end{array} \right] \\ 0, & \text{otherwise} \end{cases} \quad (1)$$

3.1.2. Doji star

As seen in Figure 6b, it is an undecided candle whose lower and upper wicks are equal and the opening and closing values are close to each other. Like the doji formation, the doji star formation is similar in appearance to a straight line.

The formulation of the Doji star candlestick pattern is shown below.

$$DojiStar(v_i, v_{i-1}) = \begin{cases} 1, & \text{if } \left[\begin{array}{l} C_{i-1} > O_{i-1} \quad \text{and} \quad \frac{|\Delta v_{i-1}|}{H_i - L_i} \geq 0.7 \quad \text{and} \\ \frac{|\Delta v_i|}{H_i - L_i} < 0.1 \quad \text{and} \quad C_{i-1} < C_i \quad \text{and} \\ C_{i-1} < O_i \quad \text{and} \quad \frac{H_i - \max_{v_i}}{3 * |\Delta v_i|} > 1 \quad \text{and} \\ \frac{\min_{v_i} - L_i}{3 * |\Delta v_i|} > 1 \end{array} \right] \\ 0, & \text{otherwise} \end{cases} \quad (2)$$

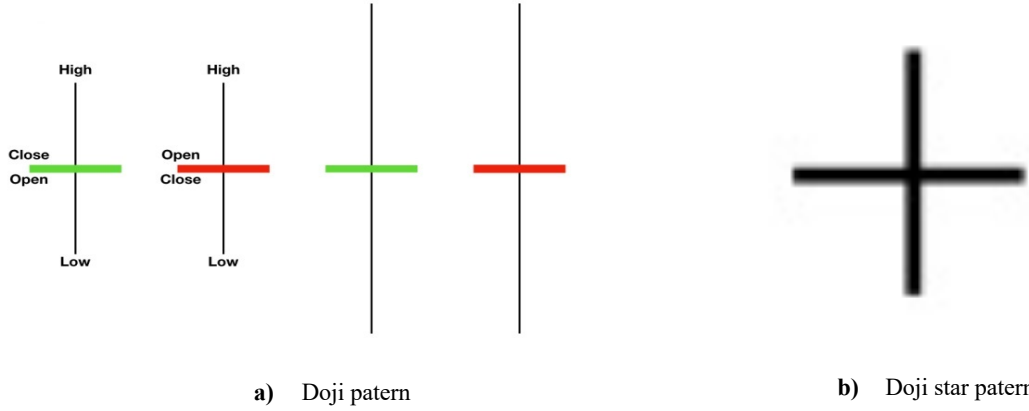


Figure 6. Doji and doji star candlestick pattern description

3.1.3. Dragonfly doji

The dragonfly doji, also known as the dragonfly doji, is a particular Doji where both the open and closed price is at or relatively close to the high of a particular day. It is a bearish or bullish (depending on context) candle with a long lower wick and open/close near the upper end as shown in Figure 7a.

The formulation of the Dragonfly doji candlestick pattern is shown below.

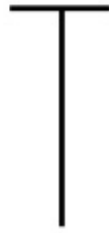
$$DragonFly(v_i) = \begin{cases} 1, & \text{if } \left[\begin{array}{l} \left(\frac{|\Delta v_i|}{H_i - L_i} < 0.1 \right) \quad \text{and} \\ \left(\frac{H_i - \max_{v_i}}{|\Delta v_i|} < 1 \right) \quad \text{and} \\ \left(\frac{\min_{v_i} - L_i}{3 * |\Delta v_i|} > 1 \right) \end{array} \right] \\ 0, & \text{otherwise} \end{cases} \quad (3)$$

3.1.4. Gravestone doji

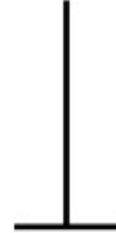
The Bears version of the Dragonfly Doji is the Gravestone Doji (Tombstone Doji). It is a bearish reversal candle with a long upper wick and an open/close near the lower end as shown in Figure 7b.

The formulation of the Gravestone doji candlestick pattern is shown below.

$$GraveStone(v_i) = \begin{cases} 1, & \text{if } \left[\begin{array}{l} \left(\frac{|\Delta v_i|}{H_i - L_i} < 0.1 \right) \text{ and} \\ \left(\frac{H_i - \max_{v_i}}{3 * |\Delta v_i|} > 1 \right) \text{ and} \\ \left(\frac{\min_{v_i} - L_i}{|\Delta v_i|} \leq 1 \right) \end{array} \right] \\ 0, & \text{otherwise} \end{cases} \quad (4)$$



a) Dragonfly doji pattern



b) Gravestone doji pattern

Figure 7. Dragonfly doji and gravestone doji candle pattern description

3.1.5. Hammer

This pattern is formed at the bottom of a trend or during a downtrend. As it can be seen in Figure 8a, since it shows a bottom-beating uptrend, this formation is called a hammer. The upper shadow is almost absent. The lower shadow of the candlestick must be at least twice the length of the body.

The formulation of the Hammer candle mold is shown below.

$$Hammer(v_i) = \begin{cases} 1, & \text{if } \left[\begin{array}{l} \left(\frac{H_i - L_i}{3 * |\Delta v_i|} < 1 \right) \text{ and} \\ \left(\frac{C_i - L_i}{0.001 + H_i - L_i} > 0.6 \right) \text{ and} \\ \left(\frac{O_i - L_i}{0.001 + H_i - L_i} > 0.6 \right) \end{array} \right] \\ 0, & \text{otherwise} \end{cases} \quad (5)$$

3.1.6. Hanging man

Hanging Man acts as a reversal signal of an uptrend. As seen in Figure 8b, it has the same structure as the hammer. The difference between them is seen at the end of the hammer downtrend; hanging man is seen at the end of an uptrend. Both are a reversal candlestick pattern.

The formulation of the Hanging man candlestick is shown below.

(6)

$$HangingMan(v_i, v_{i-1}, v_{i-2}) = \begin{cases} 1, & \text{if } \left[\begin{array}{l} \left(\frac{H_i - L_i}{-4 * \Delta v_i} > 1 \right) \quad \text{and} \\ \left(\frac{C_i - L_i}{0.001 + H_i - L_i} > 0.75 \right) \quad \text{and} \\ \left(\frac{O_i - L_i}{0.001 + H_i - L_i} > 0.75 \right) \quad \text{and} \\ (H_{i-1} < O_i) \quad \text{and} \quad (H_{i-2} < O_i) \end{array} \right] \\ 0, & \text{otherwise} \end{cases}$$



a) Hammer pattern



b) Hanging man pattern

Figure 8. Hammer and hanging man candle pattern description

3.1.7. Inverted hammer

The Inverted Hammer pattern is formed at the end of a downtrend and gives a bullish signal. Their bodies are below, their shadows are above, and the drop shadow is almost absent as in figure 9a.

The formulation of the Inverted hammer candle mold is shown below.

$$InvHammer(v_i) = \begin{cases} 1, & \text{if } \left[\begin{array}{l} \left(\frac{H_i - L_i}{-3 * \Delta v_i} > 1 \right) \quad \text{and} \\ \left(\frac{H_i - C_i}{0.001 + H_i - L_i} > 0.6 \right) \quad \text{and} \\ \left(\frac{H_i - O_i}{0.001 + H_i - L_i} > 0.6 \right) \end{array} \right] \\ 0, & \text{otherwise} \end{cases} \quad (7)$$

3.1.8. Shooting star

The Shooting Star has the opposite view of the Hammer pattern. It is seen at the end of an uptrend. In the Shooting Star candle, the opening and closing are very close to each other, as in figure 9b. It is a candle formation at the end of an uptrend that will move the trend down.

The formulation of the Shooting star candlestick pattern is shown below.

$$ShootingStar(v_i, v_{i-1}) = \begin{cases} 1, & \text{if } \left[\begin{array}{l} (O_{i-1} < C_{i-1} < O_i) \quad \text{and} \\ \left(\frac{H_i - \max_{v_i}}{|\Delta v_i|} \geq 3 \right) \quad \text{and} \\ \left(\frac{\max_{v_i} - L_i}{|\Delta v_i|} \leq 1 \right) \end{array} \right] \\ 0, & \text{otherwise} \end{cases} \quad (8)$$

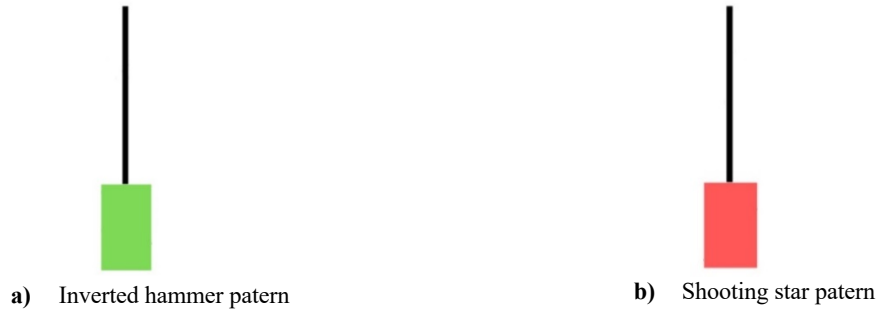


Figure 9. Inverted hammer and shooting star candle pattern description

3.1.9. Bullish harami

The Bullish harami (Pregnant Bull) formation is formed by first a red body as in figure 10a, and a green body that stays within the boundaries of this red body and then emerges completely inside the red body. It occurs during a downtrend in the market. The second small green body formed indicates that the bears' strength is decreasing.

The formulation of the Bullish harami candle pattern is shown below.

$$BullishHarami(v_i, v_{i-1}) = \begin{cases} 1, & \text{if } \left[\begin{array}{l} (C_{i-1} < O_{i-1}) \quad \text{and} \quad \left(\frac{|\Delta v_{i-1}|}{H_{i-1} - L_{i-1}} \geq 0.7 \right) \quad \text{and} \\ \left(0.3 > \frac{|\Delta v_i|}{H_i - L_i} \geq 0.1 \right) \quad \text{and} \quad (H_i < O_{i-1}) \quad \text{and} \\ (L_i > C_{i-1}) \end{array} \right] \\ 0, & \text{otherwise} \end{cases} \quad (9)$$

3.1.10. Bearish harami

The Bearish harami (Pregnant Bear) pattern consists of a first green body, as in figure 10b, and a red body that falls within the boundaries of this green body and then occurs. It occurs in an uptrend in the market. The formation basically resembles a pregnant woman.

The formulation of the Bearish harami candle pattern is shown below.

$$BearishHarami(v_i, v_{i-1}) = \begin{cases} 1, & \text{if } \left[\begin{array}{l} (C_{i-1} > O_{i-1}) \quad \text{and} \quad \left(\frac{|\Delta v_{i-1}|}{H_{i-1} - L_{i-1}} \geq 0.7 \right) \quad \text{and} \\ \left(0.3 > \frac{|\Delta v_i|}{H_i - L_i} \geq 0.1 \right) \quad \text{and} \quad (H_i < C_{i-1}) \quad \text{and} \\ (L_i > O_{i-1}) \end{array} \right] \\ 0, & \text{otherwise} \end{cases} \quad (10)$$



Figure 10. Bullish harami and bearish harami candle pattern views

3.1.11. Bullish engulfing

The most important factor in the formation of Bullish engulfing (Bull Engulfing) formation is that the red candle formed on the first day remains inside the green candle formed on the second day, as in figure 11a. The formation of the formation in a falling or correcting market gives us a bearish signal in this formation.

The formulation of the Bullish engulfing candle pattern is shown below.

$$BullishEngulfing(v_i, v_{i-1}) = \begin{cases} 1, & \text{if } \left[\begin{array}{l} (C_{i-1} < O_{i-1}) \quad \text{and} \quad \left(\frac{|\Delta v_i|}{H_i - L_i} \geq 0.7 \right) \quad \text{and} \\ \left(0.3 > \frac{|\Delta v_{i-1}|}{H_{i-1} - L_{i-1}} \geq 0.1 \right) \quad \text{and} \quad (C_i > O_i) \quad \text{and} \\ (H_{i-1} < C_i) \quad \text{and} \quad (L_{i-1} > O_i) \end{array} \right] \\ 0, & \text{otherwise} \end{cases} \quad (11)$$

3.1.12. Bearish engulfing

The Bearish engulfing pattern is the combination in which the body boundaries of the red candle are larger than the body boundaries of the green candle, as seen in figure 11b. The red candle is formed after the green and swallows the green completely. This indicates that the asset price has fallen more than its previous rise. Generally, this pattern indicates an uptrend end and a downtrend start.

The formulation of the Bearish engulfing candle pattern is shown below.

$$BearishEngulfing(v_i, v_{i-1}) = \begin{cases} 1, & \text{if } \left[\begin{array}{l} (C_{i-1} > O_{i-1}) \quad \text{and} \quad \left(\frac{|\Delta v_i|}{H_i - L_i} \geq 0.7 \right) \quad \text{and} \\ \left(0.3 > \frac{|\Delta v_{i-1}|}{H_{i-1} - L_{i-1}} \geq 0.1 \right) \quad \text{and} \quad (C_i < O_i) \quad \text{and} \\ (H_{i-1} < O_i) \quad \text{and} \quad (L_{i-1} > C_i) \end{array} \right] \\ 0, & \text{otherwise} \end{cases} \quad (12)$$



Figure 11. Bullish engulfing and bearish engulfing candle pattern description

3.1.13. Dark cloud cover

The dark cloud cover pattern is a top return pattern. When the market is in an uptrend, a green candlestick is observed on the first day of the pattern as seen in figure 12a. The second day gaps up and opens higher, but closes lower than the middle of the body of the previous candlestick, creating a strong red candlestick. The second day does not close under the body of the first day.

The formulation of the dark cloud cover candle mold is shown below.

$$DarkCloudCover(v_i, v_{i-1}) = \begin{cases} 1, & \text{if } \left[\begin{array}{l} (C_{i-1} > O_{i-1}) \quad \text{and} \quad \left(\frac{|\Delta v_{i-1}|}{H_{i-1} - L_{i-1}} \geq 0.7 \right) \quad \text{and} \\ \left(\frac{|\Delta v_i|}{H_i - L_i} \geq 0.7 \right) \quad \text{and} \quad (C_i < O_i) \quad \text{and} \\ (O_i \geq C_{i-1}) \quad \text{and} \quad (O_{i-1} < C_i < \frac{O_{i-1} + C_{i-1}}{2}) \end{array} \right] \\ 0, & \text{otherwise} \end{cases} \quad (13)$$

3.1.14. Piercing pattern

Piercing Pattern (Piercing Candles) pattern has an opposite structure to the Dark Cloud Cover pattern. Piercing pattern is formed at the end of a downtrend. It is a bottom reversal pattern. As in Figure 12b, a red candlestick appears first. A green candlestick gaps down and closes in the upper half of the body of the first candlestick. The second candle does not close above the body of the first candle.

The formulation of the piercing pattern wax pattern is shown below.

$$DarkCloudCover(v_i, v_{i-1}) = \begin{cases} 1, & \text{if } \left[\begin{array}{l} (C_{i-1} < O_{i-1}) \quad \text{and} \quad \left(\frac{|\Delta v_{i-1}|}{H_{i-1} - L_{i-1}} \geq 0.7 \right) \quad \text{and} \\ \left(\frac{|\Delta v_i|}{H_i - L_i} \geq 0.7 \right) \quad \text{and} \quad (C_i > O_i) \quad \text{and} \\ (O_i \leq C_{i-1}) \quad \text{and} \quad (C_i < \frac{O_{i-1} + C_{i-1}}{2}) \end{array} \right] \\ 0, & \text{otherwise} \end{cases} \quad (14)$$

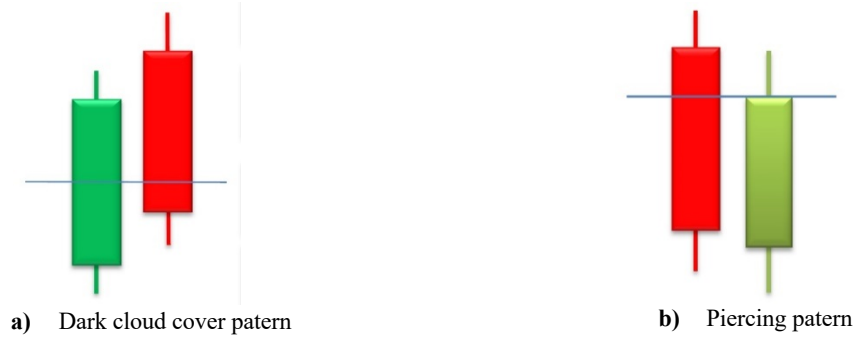


Figure 12. Dark cloud cover and piercing wax pattern description

3.1.15. Evening star

Evening star is a candle formation that indicates the possible reversal of an uptrend. As seen in Figure 13a, a short candlestick comes after the first green candle. Finally, a red candlestick appears.

The formulation of the Evening star candlestick pattern is shown below.

$$EveningStar(v_i, v_{i-1}, v_{i-2}) = \begin{cases} 1, & \text{if } \left[\begin{array}{l} (C_{i-2} > O_{i-2}) \quad \text{and} \quad \left(\frac{|\Delta v_{i-2}|}{H_{i-2} - L_{i-2}} \geq 0.7 \right) \quad \text{and} \\ \left(0.3 > \frac{|\Delta v_{i-1}|}{H_{i-1} - L_{i-1}} \geq 0.1 \right) \quad \text{and} \quad (C_i < O_i) \quad \text{and} \\ \left(\frac{|\Delta v_i|}{H_i - L_i} \geq 0.7 \right) \quad \text{and} \quad (C_{i-2} < C_{i-1}) \quad \text{and} \\ (C_{i-2} < O_{i-1}) \quad \text{and} \quad (C_{i-1} > O_i) \quad \text{and} \\ (O_{i-1} > O_i) \quad \text{and} \quad (C_i < C_{i-2}) \end{array} \right] \\ 0, & \text{otherwise} \end{cases} \quad (15)$$

3.1.16. Evening doji star

Evening doji star means the end of the uptrend and is a sell signal for traders trading in the forex market. It consists of a doji following a green bullish candle as in Figure 13b. The doji following the green candle is formed by creating a gap in the upward direction. On the third day, a red bearish candle is formed, which is inside the green bullish candle formed on the first day.

The formulation of the Evening doji star candlestick pattern is shown below.

$$EveningDojiStar(v_i, v_{i-1}, v_{i-2}) = \begin{cases} 1, & \text{if} \\ 0, & \text{otherwise} \end{cases} \left[\begin{array}{l} (C_{i-2} > O_{i-2}) \quad \text{and} \quad \left(\frac{|\Delta v_{i-2}|}{H_{i-2} - L_{i-2}} \geq 0.7 \right) \quad \text{and} \\ \left(\frac{|\Delta v_{i-1}|}{H_{i-1} - L_{i-1}} < 0.1 \right) \quad \text{and} \quad \left(\frac{|\Delta v_i|}{H_i - L_i} \geq 0.7 \right) \quad \text{and} \\ (C_{i-2} < C_{i-1}) \quad \text{and} \quad (C_{i-2} < O_{i-1}) \quad \text{and} \\ (C_{i-1} > O_i) \quad \text{and} \quad (O_{i-1} > O_i) \quad \text{and} \\ \left(\frac{H_{i-1} - \max_{v_{i-1}}}{3 * |\Delta v_{i-1}|} > 1 \right) \quad \text{and} \quad \left(\frac{\min_{v_{i-1}} - L_{i-1}}{3 * |\Delta v_{i-1}|} > 1 \right) \quad \text{and} \\ (C_i < C_{i-2}) \end{array} \right. \quad (16)$$

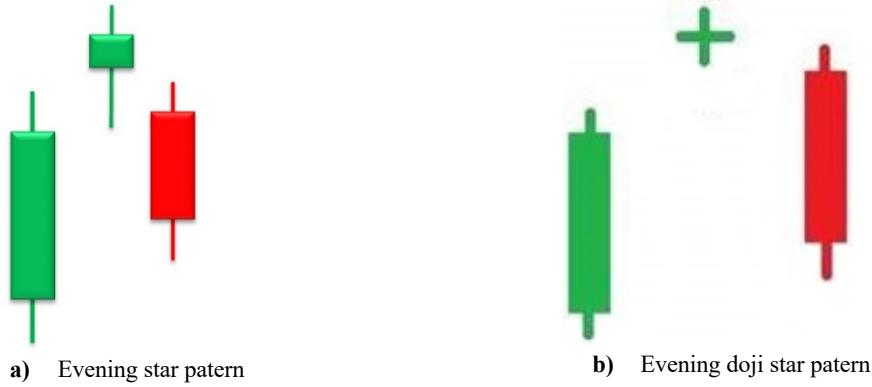


Figure 13. Evening star and evening doji star candle pattern description

3.1.17. Morning star

This candle formation is the downtrend counterpart of the Evening Star candlestick formation in an uptrend. For the Morning Star formation to occur, the characteristics of the three candles should be as follows; The first candle should be a long bearish or bearish candle, the second candle should be a small body bullish or doji that closes below the first candle, and the third candle should be a bullish or bullish candle that opens above the second candle.

The formulation of the Morning star candlestick pattern is shown below.

$$MorningStar(v_i, v_{i-1}, v_{i-2}) = \begin{cases} 1, & \text{if} \\ 0, & \text{otherwise} \end{cases} \left[\begin{array}{l} (C_{i-2} > O_{i-2}) \quad \text{and} \quad \left(\frac{|\Delta v_{i-2}|}{H_{i-2} - L_{i-2}} \geq 0.7 \right) \quad \text{and} \\ \left(0.3 > \frac{|\Delta v_{i-1}|}{H_{i-1} - L_{i-1}} \geq 0.1 \right) \quad \text{and} \quad (C_i > O_i) \quad \text{and} \\ \left(\frac{|\Delta v_i|}{H_i - L_i} \geq 0.7 \right) \quad \text{and} \quad (C_{i-2} > C_{i-1}) \quad \text{and} \\ (C_{i-2} > O_{i-1}) \quad \text{and} \quad (C_{i-1} < O_i) \quad \text{and} \\ (O_{i-1} < O_i) \quad \text{and} \quad (C_i > C_{i-2}) \end{array} \right. \quad (17)$$

3.1.18. Morning doji star

The Morning Doji Star is a bullish reversal pattern seen in a downtrend very similar to the Morning Star. The only difference is that the Morning Doji Star must have a doji candle in the second line. As can be seen in Figure 14b, it is an inverse pattern of the Evening Doji Star pattern. The first candle is a downtrend candle and the second candle is a doji below the body of the first candle. The last candle should close between the body of the first candle.

The formulation of the Morning doji star candlestick pattern is shown below.

$$\text{MorningDojiStar}(v_i, v_{i-1}, v_{i-2}) = \begin{cases} 1, & \text{if} \\ 0, & \text{otherwise} \end{cases} \left[\begin{array}{l} (C_{i-2} < O_{i-2}) \quad \text{and} \quad \left(\frac{|\Delta v_{i-2}|}{H_{i-2} - L_{i-2}} \geq 0.7 \right) \quad \text{and} \\ \left(\frac{|\Delta v_{i-1}|}{H_{i-1} - L_{i-1}} \geq 0.1 \right) \quad \text{and} \quad (C_i > O_i) \quad \text{and} \\ \left(\frac{|\Delta v_i|}{H_i - L_i} \geq 0.7 \right) \quad \text{and} \quad (C_{i-2} > C_{i-1}) \quad \text{and} \\ (C_{i-2} > O_{i-1}) \quad \text{and} \quad (C_{i-1} < O_i) \quad \text{and} \\ (O_{i-1} < O_i) \quad \text{and} \quad (C_i > C_{i-2}) \quad \text{and} \\ \left(\frac{H_{i-1} - \max_{v_{i-1}}}{3 * |\Delta v_{i-1}|} > 1 \right) \quad \text{and} \quad \left(\frac{\min_{v_{i-1}} - L_{i-1}}{3 * |\Delta v_{i-1}|} > 1 \right) \end{array} \right] \quad (18)$$

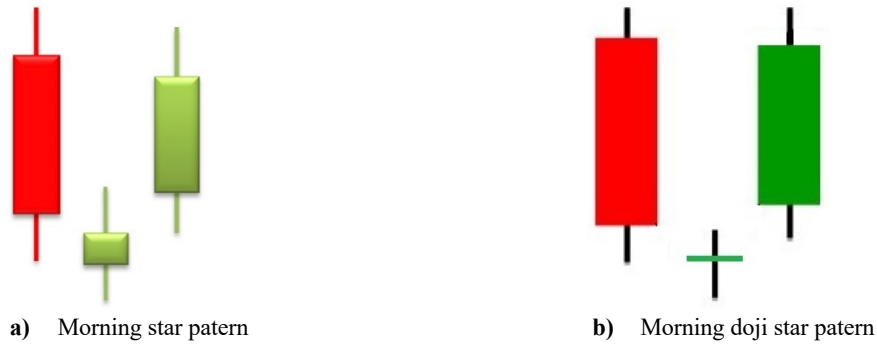


Figure 14. Morning star and morning doji star candlestick patterns

4. Experimental Results

To validate the proposed approach, gold, Brent oil, BIST100 index, Bitcoin (BTC), and USD were used. In the experimental studies, the first stage involves labeling the trend (1: increase, 0: decrease) and the candle pattern type of the daily bar with one-hot encoding, using the daily closing values of the relevant financial assets. At this stage, the raw data set is transformed and used as in Figure 15.

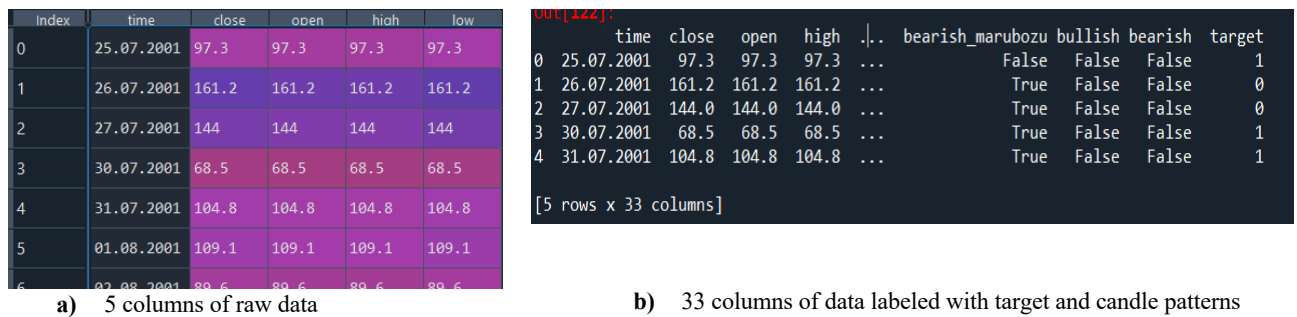


Figure 15. Preparation of the data set

In the second stage, the data set was divided into training and testing and trained with the XGBoost algorithm. In the training phase, the system learns the rise and fall patterns by using the labeled data set. The XGBoost algorithm used at this stage is a learning algorithm that uses collective learning and is widely used in data science problems. Written in C++ language, XGBoost C++ can work with high performance on big data such as financial data because it works with the parallel programming principle, and it is more convenient than other collective learning methods against overfitting/underfitting problems. The tree-based XGBoost algorithm is typically as in Figure 16.

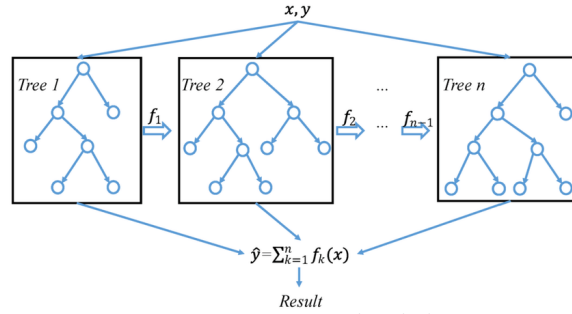


Figure 16. XGBoost description

Table 1. Hyperparameters selected for XGBoost

MAX_DEPTH	ETA	ERROR FUNCTION	GAMMA	ESTIMATORS
5	0.1	rmse	0.05	100

In the test phase, the bars in this period that were not used before were subjected to Backtest using the previously learned system. Backtest is expressed as making buy/sell transactions according to the rules determined in manual or algorithmic transactions in financial markets. Backtesting typically calculates PF (Profit Factor - coefficient of gain) by obtaining GF (Gross Profit – Gross Profit), GL (Gross Loses – Gross Loss) values on historical data (19). In the ideal Backtest, it aims to have a PF value greater than 1, a low number of transactions (for paying less commission), a low slippage value (price difference between trading), and a linear yield curve instead of a fluctuating one. In this study, commission and slippage are ignored since a robot that trades with daily bars and stays in the trend direction is considered instead of a high-frequency algorithmic robot.

$$PF = GP/GL \tag{19}$$

In all charts, the GP yield curve is shown in green and the GL curve in red.

4.1. Experimental studies for Bist100 index, BTC, gold, Dollar and Brent oil

In recent years, there has been an increase in the number of approaches based on machine learning for popular financial assets such as the Bist100 index, BTC, gram gold, dollar, and Brent oil [21-29].

The Bist100 index represents the 100 most valuable companies in the Borsa Istanbul index. The data set obtained for Bist100 consists of 4792 pieces of data covering daily bars in the range of 11.04.2003 – 10.05.2022. When the training and testing ratio is selected as 50%, PF=1.43 as seen in Figure 17a, 162 of the transactions resulted a profit, and 74 of them resulted in loss. An approach that can be used to reduce the amount of loss is the stop loss strategy (stop loss when the threshold value is reached) when entering the position, but the main motivation of this study is to prove the performance of algorithmic transactions that will only be performed with pattern recognition, so stop loss and technical / fundamental indicators are not used.

The data set for btc, the most popular blockchain-based cryptocurrency, was used between 18.07.2010 – 10.05.2022 with 4315-day bar closing. Since the data set is relatively small, the training:test partitioning was used as 0.85:0.15. As can be seen in Figure 17b, PF=35 could be obtained in experimental studies, 143 of the transactions were closed with profit and only 13 with loss. With the high PF value obtained, commission and slippage have also become insignificant. It is also effective that cryptocurrencies are in a bullish trend and are very popular in the high PF value and linear yield curve. Cohen (2021), the PF value in his study is much lower than

this study, but in addition to the difference in the approach, it differs from each other in the selected periods for training and testing. In this context, no one-to-one comparison has been made [30].

For gram gold, one of the financial assets that are considered an important investment tool and can be considered the least volatile, 2780-day bar closing data between 11.04.2013 and 10.05.2022 was used, and the data set was divided equally. As can be seen in Figure 17c, PF= 33.44 was obtained, and only 37 lossy transactions were realized against 316 profitable transactions.

The 5000-day bar closing between 11.04.2000 and 13.06.2019 was used for the dollar, which is one of the important investment instruments in our country and can be extremely volatile from time to time due to the socio-economic structure. PF=12.1 was obtained when a short test period was selected. As can be seen in Figure 17d, when training:test is divided as 50% in experimental studies, more than 90% profitable transactions are obtained in the Backtest phase.

Sudden changes in brent oil, which is an important indicator in international markets, is one of the most important commodities that has the power to deeply affect especially emerging markets. In the study, the data set was chosen as 600-day bar closing between 13.04.2020 – 10.05.2022. When the training and testing rate was chosen as 50%, PF=2.01 as seen in figure 17e. Despite 28 profitable transactions, 16 lossy transactions were carried out.

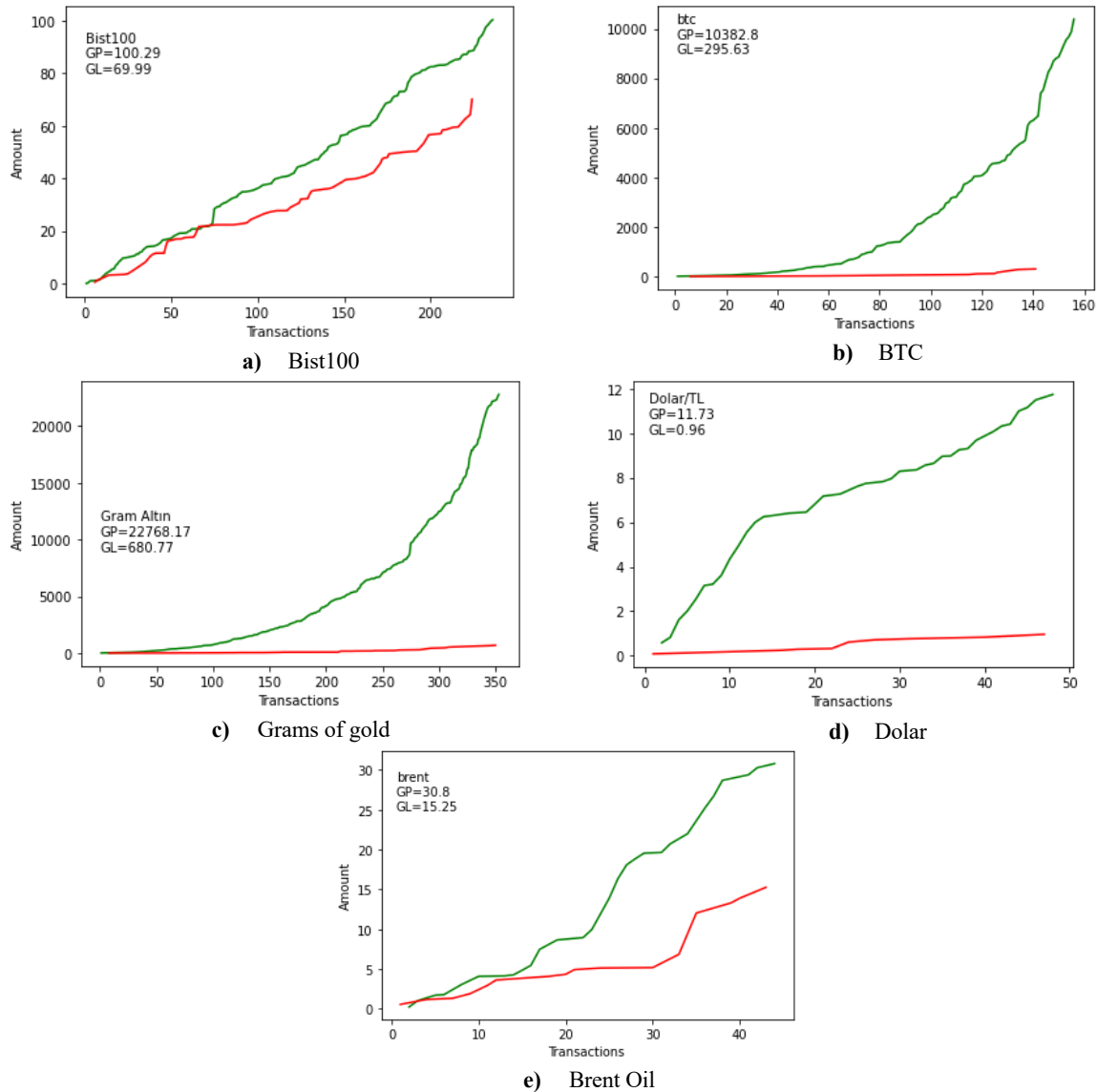


Figure 17. GP and GL values of datasets

5. Discussion, Conclusion and Future Works

This study, which was carried out to identify only candlestick patterns for both the bist100 index and global financial assets, revealed the success of an algorithmic trading strategy based solely on candlestick charts. Candlestick charts can be used in almost any period, from minute to daily bars. Although only 21 of the most popular patterns were used in the proposed study, the earnings coefficient could be obtained above 1 in all major financial assets and the profit/loss ratio could be above 90%.

It is aimed to expand this study in two main ways in the future and thus to increase its originality. The first of these is to increase the number of candlestick patterns. In fact, only 21 of the patterns known to be over 100 were used and typically 40-60% of all bars were recognized in the study. Despite this, the results obtained are quite satisfactory, and it is predicted that the performance will be increased by increasing the number of patterns. In this study, only buy/sell strategies based on candlestick patterns were produced. In time series, the number and quality of input attributes can be increased by obtaining technical indicators, basic ratios of assets, visual formations, and trends in different time periods. In this context, the approach proposed in this study and the other approaches mentioned will be combined in a hybrid way. Thus, when commission and slippage losses are combined with take profit and loss situation strategies, a more effective algorithmic robot system will be brought to the literature.

Acknowledgement

This work was supported by the Scientific and Technological Research Council of Turkey (TUBITAK, Grant No. 121E733).

References

- [1] Filiz, E., Karaboğa, H. A., Akoğul, S. (2017). Bist-50 endeksi değişim değerlerinin sınıflandırılmasında makine öğrenmesi yöntemleri ve yapay sinir ağları kullanımı, Çukurova Üniversitesi Sosyal Bilimler Enstitüsü Dergisi, 26(1), 231-241.
- [2] Pabuçcu, H. (2019). Borsa endeksi hareketlerinin tahmini: trend belirleyici veri, Selçuk Üniversitesi Sosyal Bilimler Meslek Yüksekokulu Dergisi, 22(1), 246-256.
- [3] Şişmanoğlu, G., Koçer, F., Önde, M. A., Sahingöz, O. K. (2020). Derin Öğrenme yöntemleri ile borsada fiyat tahmini, Bitlis Eren Üniversitesi Fen Bilimleri Dergisi, 9(1), 434-445.
- [4] Santur, Y. Deep learning based regression approach for algorithmic stock trading: A case study of the Bist30, Gümüşhane Üniversitesi Fen Bilimleri Enstitüsü Dergisi, 10(4), 1195-1211.
- [5] Budak, C. (2019). Teknik analiz indikatörlerinin performans karşılaştırması üzerine bir araştırma (Doctoral dissertation), Marmara Üniversitesi
- [6] Bozkurt, Y. (2021). Piyasa performans oranlarına göre oluşturulmuş portföylerin getiri oranlarının değerlendirilmesi: BİST 100 endeksi firmaları üzerine bir uygulama (Master's thesis), Aydın Adnan Menderes Üniversitesi, Sosyal Bilimler Enstitüsü.
- [7] Madbouly, M. M., Elkholy, M., Gharib, Y. M., Darwish, S. M. (2020, April). Predicting stock market trends for japanese candlestick using cloud model, In The International Conference on Artificial Intelligence and Computer Vision (pp. 628-645), Springer, Cham.
- [8] Kusuma, R. M. I., Ho, T. T., Kao, W. C., Ou, Y. Y., Hua, K. L. (2019). Using deep learning neural networks and candlestick chart representation to predict stock market, arXiv preprint arXiv:1903.12258.
- [9] Hung, C. C., Chen, Y. J. (2021). DPP: Deep predictor for price movement from candlestick charts, Plos one, 16(6), e0252404.
- [10] Sadeghi, M., Farid, D. (2021). Investigating candlestick patterns using fuzzy logic in the stock trading system, Turkish Journal of Computer and Mathematics Education (TURCOMAT), 12(13), 7786-7806.
- [11] Yee, L. L., Mei, H. L., Isharuddin, L. (2021). Ichimoku cloud and japanese candlestick prediction combination pattern approached: the case study of malaysia stock market, Multidisciplinary Applied Research and Innovation, 2(2), 190-196.
- [12] Lin, Y., Liu, S., Yang, H., Wu, H., Jiang, B. (2021). Improving stock trading decisions based on pattern recognition using machine learning technology, PloS one, 16(8), e0255558.
- [13] Ardiyanti, N. P. W., Palupi, I., Indwiarti, I. (2021). Trading strategy on market stock by analyzing candlestick pattern using artificial neural network (ann) method, Jurnal Media Informatika Budidarma, 5(4), 1273-1282.
- [14] Chen, J. H., Tsai, Y. C. (2020). Encoding candlesticks as images for pattern classification using convolutional neural networks, Financial Innovation, 6(1), 1-19.
- [15] Yassini, S. B., Rahnamay Roodposhti, F., Fallahshams, M. (2019). Analyzing the effectiveness of candlestick technical trading strategies in foreign exchange market, International Journal of Finance & Managerial Accounting, 4(15), 25-41.
- [16] Gökül, U. (2021). Forecast share price using technical analysis tool, Pacific International Journal, 4(1), 01-06.

- [17] Ho, T. T., Huang, Y. (2021). Stock price movement prediction using sentiment analysis and candlestick chart representation, *Sensors*, 21(23), 7957.
- [18] Lin, Y., Liu, S., Yang, H., Wu, H. (2021). Stock trend prediction using candlestick charting and ensemble machine learning techniques with a novelty feature engineering scheme, *IEEE Access*, 9, 101433-101446.
- [19] Ananthi, M., Vijayakumar, K. (2021). Stock market analysis using candlestick regression and market trend prediction (CKRM), *Journal of Ambient Intelligence and Humanized Computing*, 12(5), 4819-4826.
- [20] Aysel, Ü., Santur, Y. (2022). A new moving average approach to predict the direction of stock movements in algorithmic trading, *Journal of New Results in Science*, 11(1), 13-25.
- [21] Kaynar, T., Yiğit, Ö. E. (2021). Öznitelik mühendisliği ile makine öğrenmesi yöntemleri kullanılarak bıst 100 endeksi değişiminin tahminine yönelik bir yaklaşım, *Yaşar Üniversitesi E-Dergisi*, 16(64), 1741-1762.
- [22] Koç, Y. (2021). Makine öğrenmesi ile çok terimli hisse senedi yönlü tahmini; BIST100 örneği/Multinomial direction forecast with machine learning algorithms; BIST100 example (Doctoral dissertation), Kadir Has Üniversitesi.
- [23] Santur, Y. (2022). Candlestick chart based trading system using ensemble learning for financial assets, *Sigma Journal of Engineering and Natural Sciences*, 40(2), 370-379.
- [24] Aksoy, B. (2021). Pay senedi fiyat yönünün makine öğrenmesi yöntemleri ile tahmini: Borsa İstanbul örneği, *Business and Economics Research Journal*, 12(1), 89-110.
- [25] Akdağ, M., Bozma, G. (2021). Stok akış modeli ve facebook prophet algoritması ile bitcoin fiyatı tahmini/Prediction of bitcoin price with stock to flow model and facebook prophet algorithm, *Uluslararası Ekonomi İşletme ve Politika Dergisi*, 5(1), 16-30.
- [26] Demirel, A. C., Hazar, A. (2021). Kripto para değerlerine dayanılarak bıst 100 endeks hareketi tahmininde destek vektör makineleri uygulaması, *Başkent Üniversitesi Ticari Bilimler Fakültesi Dergisi*, 5(1), 27-35.
- [27] Altunbaş, C. (2021). Derin öğrenme ile hisse senedi piyasası tahmini (Master's thesis), Aydın Adnan Menderes Üniversitesi Sosyal Bilimler Enstitüsü.
- [28] Ustali, N. K., Tosun, N., Tosun, Ö. (2021). Makine öğrenmesi teknikleri ile hisse senedi fiyat tahmini, *Eskişehir Osmangazi Üniversitesi İktisadi ve İdari Bilimler Dergisi*, 16(1), 1-16.
- [29] Tanışman, S., Karcıoğlu, A. A., Aybars, U. G. U. R., Bulut, H. (2021). LSTM sinir ağı ve arıma zaman serisi modelleri kullanılarak bitcoin fiyatının tahminlenmesi ve yöntemlerin karşılaştırılması, *Avrupa Bilim ve Teknoloji Dergisi*, (32), 514-520.
- [30] Cohen, G. (2021). Optimizing candlesticks patterns for Bitcoin's trading systems, *Review of Quantitative Finance and Accounting*, 57(3), 1155-1167.

A Novel Histological Dataset and Machine Learning Applications

Kübra UYAR^{1*}, Merve SOLMAZ², Sakir TASDEMİR³, Nejat ÜNLÜKAL⁴

¹ Selcuk University, Computer Engineering Department, Konya, Turkey

² Department of Histology, Selcuk University, Medical School, Konya, Turkey

³ Selcuk University Computer Engineering Department, Konya, Turkey

⁴ Selcuk University, Histology and Embryology Department, Konya, Turkey

*¹ kubrayyar@selcuk.edu.tr, ² merve.solmaz@selcuk.edu.tr, ³ stasdemir@selcuk.edu.tr, ⁴ nunlukal@selcuk.edu.tr

(Geliş/Received: 22/06/2022;

Kabul/Accepted: 16/09/2022)

Abstract: Histology has significant importance in the medical field and healthcare services in terms of microbiological studies. Automatic analysis of tissues and organs based on histological images is an open problem due to the shortcomings of necessary tools. Moreover, the accurate identification and analysis of tissues that is a combination of cells are essential to understanding the mechanisms of diseases and to making a diagnosis. The effective performance of machine learning (ML) and deep learning (DL) methods has provided the solution to several state-of-the-art medical problems. In this study, a novel histological dataset was created using the preparations prepared both for students in laboratory courses and obtained by ourselves in the Department of Histology and Embryology. The created dataset consists of blood, connective, epithelial, muscle, and nervous tissue. Blood, connective, epithelial, muscle, and nervous tissue preparations were obtained from human tissues or tissues from various human-like mammals at different times. Various ML techniques have been tested to provide a comprehensive analysis of performance in classification. In experimental studies, AdaBoost (AB), Artificial Neural Networks (ANN), Decision Tree (DT), Logistic Regression (LR), Naive Bayes (NB), Random Forest (RF), and Support Vector Machines (SVM) have been analyzed. The proposed artificial intelligence (AI) framework is useful as educational material for undergraduate and graduate students in medical faculties and health sciences, especially during pandemic and distance education periods. In addition, it can also be utilized as a computer-aided medical decision support system for medical experts to minimize spent-time and job performance losses.

Key words: Classification, computer-aided diagnosis, histological image, image processing, machine learning.

Yeni Bir Histoloji Veriseti ve Makine Öğrenmesi Uygulamaları

Öz: Histoloji, tıp alanında ve sağlık hizmetlerinde mikrobiyolojik çalışmalar açısından önemli bir yere sahiptir. Histolojik görüntülere dayalı doku ve organların otomatik analizi, gerekli araçların olmaması nedeniyle açık bir sorundur. Ayrıca hücrelerin bir araya gelmesiyle oluşan dokuların doğru tanımlanması ve analizi, hastalıkların mekanizmalarını anlamak ve tanı koymak için çok önemlidir. Makine öğrenmesi (MÖ) ve derin öğrenme (DÖ) yöntemlerinin etkin performansı çeşitli son teknoloji tıbbi sorunlara çözüm sağlamıştır. Bu çalışmada Histoloji ve Embriyoloji Anabilim Dalında hem laboratuvar derslerinde öğrenciler için hazırlanan hemde kendimizin elde ettiği preparatlar kullanılarak yeni bir histoloji veriseti oluşturulmuştur. Hazırlanan veriseti kan, bağ, epitel, kas ve sinir dokusundan oluşmaktadır. Kan, bağ, epitel, kas ve sinir dokusu preparatları insan dokularından veya dokuları insana benzer çeşitli memeli hayvanlardan farklı zamanlarda alınmıştır. Sınıflandırmada kapsamlı bir performans analizi sunmak amacıyla çeşitli MÖ teknikleri test edilmiştir. Deneysel çalışmalarda AdaBoost (AB), Yapay Sinir Ağları (YSA), Karar Ağacı (KA), Lojistik Regresyon (LR), Naive Bayes (NB), Rastgele Orman (RO) ve Destek Vektör Makineleri (DVM) yöntemleri analiz edilmiştir. Geliştirilen yapay zekâ (YZ) uygulaması, özellikle pandemi ve uzaktan eğitim dönemlerinde, tıp fakülteleri ve sağlık bilimlerindeki lisans ve lisansüstü öğrencileri için bir eğitim materyali olarak faydalı olmaktadır. Ayrıca, bu uygulama tıp uzmanlarının harcadığı zamanı ve iş performans kayıplarını en aza indirmek amacıyla bilgisayar destekli tıbbi karar destek sistemi olarak da kullanılabilir.

Anahtar kelimeler: Bilgisayar destekli teşhis, görüntü işleme, histolojik görüntü, makine öğrenmesi, sınıflandırma.

1. Introduction

Histology is a term derived from the Greek words histos (tissue) and logia (science) and refers to the science of the structure and function of tissues. Physicians' basic science education makes a significant contribution to the accuracy of the decisions they make in their profession.

* Sorumlu yazar: kubrayyar@selcuk.edu.tr. Yazarların ORCID Numarası: ¹0000-0001-5345-3319, ²0000-0003-4144-4647, ³0000-0002-2433-246X, ⁴0000-0002-8107-4882

Histology knowledge is critical in medical science because accurate identification and analysis of tissues are necessary for comprehending disease mechanisms and diagnosing patients. The recent global pandemic has had a significant impact on medical education, particularly on face-to-face education practices. Histology education, in particular, is severely lacking in the process of face-to-face laboratory applications, in which students learn to differentiate tissue types.

From this vantage point, the effectiveness of ML methods has provided the solution to numerous state-of-the-art medical problems. AI frameworks may be beneficial as educational material for undergraduate and graduate students studying histology, medicine, and health sciences, particularly during distance education and pandemic periods. Additionally, it can be also utilized as a computer-assisted medical decision support system for medical experts to help them save time and perform better on the job.

AI has rapidly emerged method of choice for medical image analysis applications. Classification [1], detection [2-3], segmentation [4], etc. problems in the medical field can be solved more easily due to the fast and robust side of the AI approaches. In the literature, computer-aided analysis of histological and histopathological tissues and organs has been performed using different AI techniques. Codella et al. [5] studied lymphoma recognition in hematoxylin and eosin (H&E) stained histopathology slides. Each of the over 200 descriptors has been trained by non-linear SVMs. They demonstrated a 38.4% reduction in residual error over the current state-of-the-art dataset. Mazo et al. [6] developed a framework to categorize normal cardiovascular tissues and organs from histological images using a transfer learning mechanism. Convolutional Neural Network (CNN) architectures trained to recognize visual objects in natural images were fitted and modified for this problem. They claimed the idea that CNNs are very suitable for improving tissue and organ classification. Niemann et al. [7] compared various image segmentation techniques which are texture-based clustering, filter and threshold-based segmentation, and DL for histologic images of intracranial aneurysms. Finally, they analyzed the performance of the approaches depending on the experimental results. Xu et al. [8] proposed an unsupervised Tissue Cluster Level Graph Cut (TisCut) approach for histological image partition using three different histology image sets with different color staining methods. They proved that TisCut can effectively partition the histological images into meaningful compartments. Sato et al. [9] proposed an unsupervised approach combining CNNs and a visualization algorithm to cluster the images of the glomerulus of kidney biopsy samples stained with (H&E). Taylor-Weiner et al. [10] described an ML-based method for liver histology assessment to characterize disease severity and heterogeneity. They measured key histological features such as steatosis, inflammation, hepatocellular ballooning, and fibrosis. Varalakshmi et. al [11] proposed a classification and prediction model based on the XGBoost algorithm which is an ensemble learning algorithm that uses a gradient boosting framework. The proposed model has been compared with other classification algorithms such as AB, DT, Gradientboost, and NB. They classified osteosarcoma with an accuracy of 94.84%.

Normal fundamental tissues are analyzed by histology experts or others with a similar background. However, there are not enough systems that can recognize tissues automatically. Thanks to the designed AI framework that classifies histological images automatically, people who do not work in the field of histology such as biology, dentistry, and veterinary medicine can utilize and pathological analysis can be performed after determining which image belongs to which tissue. As a result, the designed AI framework has a support system mechanism that can be used by students and experts in the medical faculty minimizing the loss of time and energy.

The rest of this paper is structured as follows. Section 2 describes the created novel histological dataset in detail. Section 3 gives experimental results and discussion of ML applications for the classification of histological images. Finally, Section 4 summarizes the main conclusions of this work.

2. Material and Method

2.1. Histological data

Cell groups that are specialized to perform a specific task with a similar structure in the living body are called tissues. The main structures that make up the tissue are the cells and the substances that lie between the cells. Since tissues perform different tasks, they differ from each other in many respects. There are more intercellular substances, in some tissues, there are fewer. This causes the tissues to be different from each other. The tissue consists of cellular and intercellular elements organized to perform specific functions. There are four basic types of tissue: epithelial, connective, muscle, and nervous. There are samples of these four basic tissues in every organ and there are many subtypes of these four basic tissues [12]. Tissue types are summarized in Figure 1.

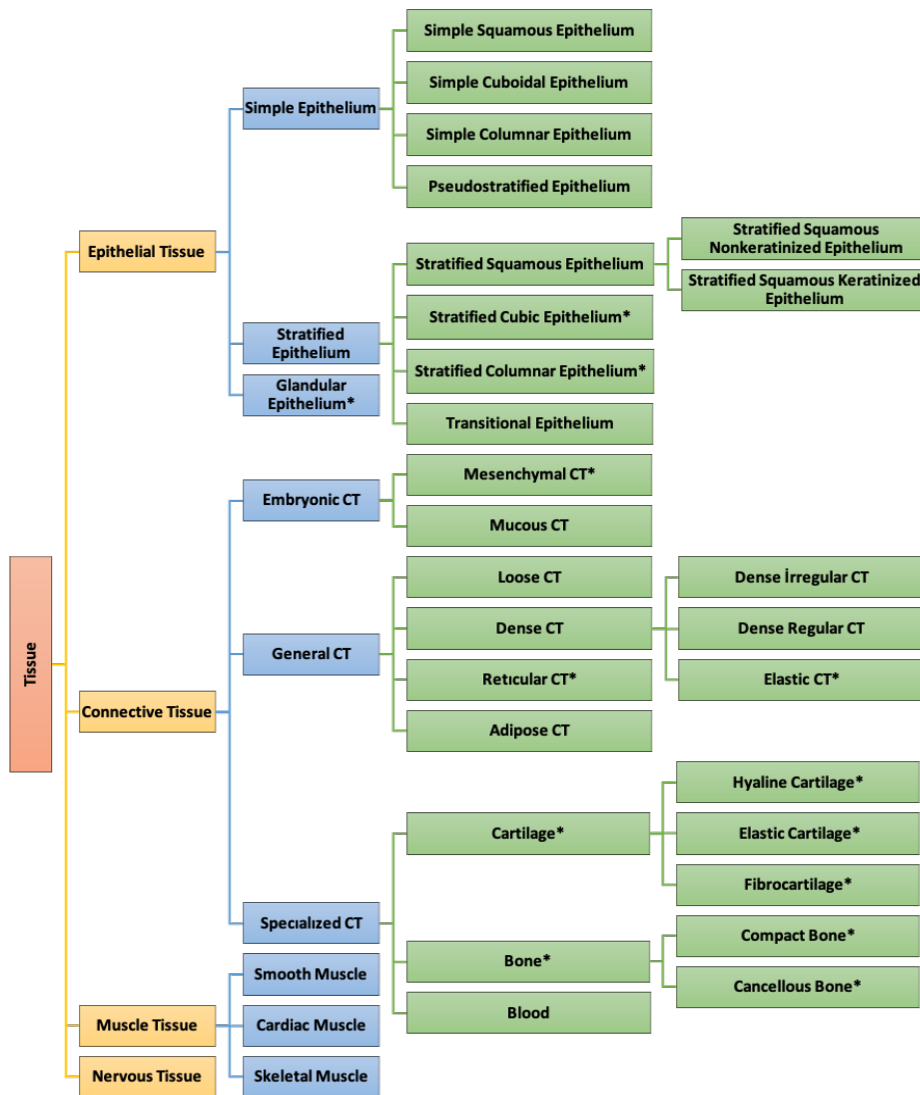


Figure 1. Tissue types (* Tissue types are excluded from the dataset).

Four basic tissue types are present in almost all organs, with different subtypes and in varying amounts. However, the locations of some specialized tissue subtypes are specific. For example, smooth muscle, which is a subtype of muscle tissue, is located on the walls of visceral organs, while the cardiac muscle is specific to the heart [13]. Epithelial tissue serves as a protective covering for the body and organs by covering the inner surface of all lumen organs as well as the exterior surface of the body and organs [14]. Connective tissues comprise the majority of the body's structural components. While specific connective tissue types, such as bone, cartilage, and blood, play significant functions in the skeletal and circulatory systems, general connective tissue types provide support for all organs [15]. While the majority of nervous tissue is concentrated in the central nervous system, which serves as the decision-maker, the peripheral nervous system also includes the nerve network that extends throughout the body to gather information and transmit commands [16]. The need for histological image classification can be expressed as follows:

- To analyze pathological images known as abnormal tissue, histological images must be analyzed first. After determining which image belongs to which tissue, pathological analysis can be performed.
- There is a system that can be easily utilized by people who do not work in the field of histology. It provides convenience in some areas such as biology, dentistry, and veterinary medicine to identify histological images.

- AI frameworks have a support system mechanism that can be used by students and experts in the medical faculty. These kinds of systems minimize the loss of time and energy.

All of the tissue subtypes that can be detected using standard staining and are not exceedingly rare were photographed at various microscope magnifications and transferred to digital media in this histological data set. Tissue types marked with an * in Figure 1 are excluded from the dataset.

The dataset was generated using educational slides prepared for the laboratory courses of ***** University Faculty of Medicine, Department of Histology and Embryology. The preparations were obtained from human tissues or tissues from various human-like mammals at different times. Tissues were fixed with formaldehyde, embedded in paraffin, and stained with H&E. Blood preparations were taken as smears and stained with Wright-Giemsa (WG). Figure 2 shows the dissection of the visceral organs in the rat and Figure 3 demonstrates the dissected rat cerebrum and cerebellum. In the continuation of this section, the process of obtaining histological images is explained in detail.



Figure 2. Dissection of the visceral organs in the rat.



Figure 3. Dissected rat cerebrum and cerebellum.

2.1.1 Data preparation processes

2.1.1.1. Preparation of slides

The basic steps in the preparation of tissues were fixation, washing, dehydration, clearing, embedding, sectioning, and attaching sections to slides. These steps can be summarized as follows:

1. Fixation: Tissues were taken into 10% formaldehyde solution with a fixative/tissue ratio of 10/1 and fixed at +4 °C for 24 hours.
2. Washing: Tissues were washed under running tap water for 1 night.
3. Dehydration:
 - Sections were dehydrated by soaking in 50-60-70-80-90% alcohol, for 45 minutes each.
 - Then, 96% and 100% alcohol for 45 minutes each.
4. Clearing:
 - 20 minutes in alcohol+xylene (1/1),
 - 1 hour in xylene,
 - Tissues were cleared by soaking in the second xylene for 1.5 hours.
5. Embedding:
 - Sections were kept for 20 minutes in xylene+paraffin (1/1) in an oven at 57 °C.
 - Then kept in paraffin in an oven at 57 °C for 15 minutes.
 - Then the tissues were embedded in paraffin blocks in metal cassettes and allowed to cool at room temperature. Figure 4 displays the tissue cassette embedded in paraffin.
6. Sectioning: Sections of 4-5µm thickness were taken from the tissues embedded in paraffin blocks with a microtome device as shown in Figure 5.
7. Putting the sections on the slide: The 4 µm sections taken were left in the water pool, left to open, and labeled on the slides with lysine.

To prepare blood tissue preparations:

1. A small drop of blood was placed on the midline, 1 cm from one end of the slide. Then the lamella is brought in front of the drop at an angle of 30-45° and after contacting the drop backward, it is driven forward with a smooth and rapid movement of the hand.
2. The smear was dried in the air for 5-10 minutes.



Figure 4. The tissue cassette embedded in paraffin.



Figure 5. Microtome device.

2.1.1.2. Staining of preparations

For the prepared preparations, the dying phase was started. At this stage, the tissues were first freed from paraffin, then rehydrated and made ready for staining. After the staining steps, the sections were made transparent again and closed with entellan and made ready for imaging. The H&E protocol is summarized below:

1. Deparaffinization:
 - Tissue sections were deparaffinized by incubating at 57 °C overnight,
 - And keep it in xylene at room temperature for 2x30 minutes.
2. Rehydration: Sections were passed through a series of ethyl alcohol in decreasing concentrations (96%, 90%, 80%, 70%, 60%). (2 minutes each) and 5 minutes under running tap water.
3. Staining:
 - Sections were kept in hematoxylin for 5 minutes and washed under running tap water for 5 minutes.
 - Sections were dipped in acid alcohol for a few seconds and washed under running tap water for 5 minutes.
4. Sections were kept in eosin for 2-3 minutes and washed under running tap water for 2 minutes.
5. Sections were passed through a series of increasing concentrations of alcohol.
6. Clearing: Sections were kept in xylene for 1 hour.
7. Mounting: 1 drop of entellan was dropped on the tissue and closed with a coverslip.

Smear and dried blood preparations were stained with WG according to the following protocol:

1. Wright's dye was poured on the preparation and left for 1 minute.
2. Washed with distilled water.
3. Giemsa paint was poured on the preparation and left for 7 minutes.
4. The paint was poured from the preparation and left in an upright position to dry.
5. For the preparations to be used for a long time, entellan was dripped onto the tissue and covered with a coverslip.

The produced preparations for various tissue classes are depicted in Figure 6.

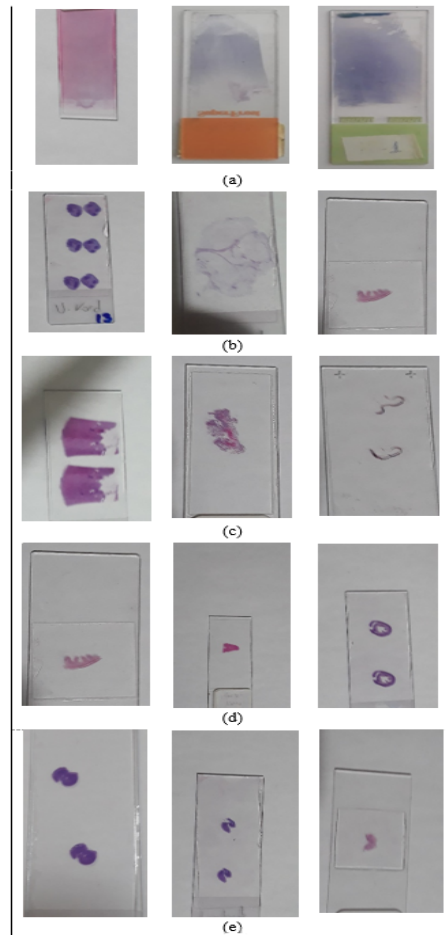


Figure 6. Prepared samples of preparations for histological tissue classification (a: Blood, b: Connective, c: Epithelium, d: Muscle, e: Nerve).

2.1.1.3. Digital display of slides

The prepared and stained preparations were viewed using an Olympus BX51 microscope and a data pool was created by photographing all sections at 4x, 10x, and 40x magnifications using the Olympus DP72 camera and Olympus DP2-BSW program. Since the general evaluation of blood tissue preparations was made with 100x magnifications, photographs were taken with 100x magnifications as well as 4x, 10x, and 40x magnifications. The Olympus BX51 microscope, the Olympus DP72 camera, and the Olympus DP2-BSW program used to digitize the images are shown in Figure 7. Photo examples of histological data classes at 4x, 10x, 20x, 40x, and 100x magnification are shown in Figure 8.

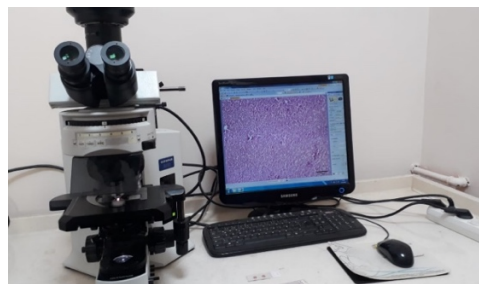


Figure 7. The Olympus BX51 microscope, the Olympus DP72 camera, and the Olympus DP2-BSW program.

2.1.1.4. Dataset description

In this paper, a novel histological RGB image dataset that involves blood, connective, epithelium, muscle, and nerve tissue images was created to perform various medical image analysis tasks such as classification, detection, localization, and semantic segmentation. Sample images of the histological tissues are depicted in Figure 9. As listed in Table 1, the dataset consists of 4031 blood tissue, 4118 connective tissue, 4063 epithelium tissue, 4023 muscle tissue, and 4113 nerve tissue images.

The ethics committee report for the experimental studies was taken from the Histology and Embryology Department of Faculty of Medicine at ***** University with the date and number 26.06.2019 and 2019/175.

The proposed histological image dataset is not publicly available due to ethical restrictions. However, some information about the previous studies that use this dataset can be explained as follows: In the first study, detection and classification of leucocyte types on the histological blood tissue images were performed. The positions and types of leucocytes were determined and the classification process was carried out [17]. In the second study, a novel three-dimensional image filter-based CNN approach which is based on three-dimensional object images with different perspectives was developed. The efficiency of the filter generation approach was proved on the proposed histological dataset [18].

Table 1. Distribution of the dataset.

Tissue class	Number of images
Blood	4031
Connective	4118
Epithelium	4063
Muscle	4023
Nerve	4113

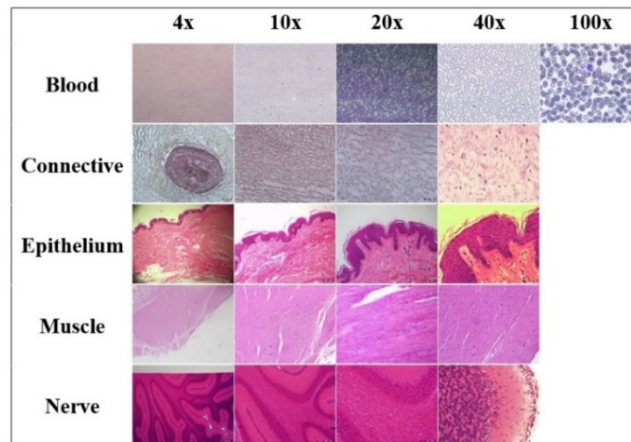


Figure 8. Photo examples of histological data classes at 4x, 10x, 20x, 40x, and 100x magnifications.

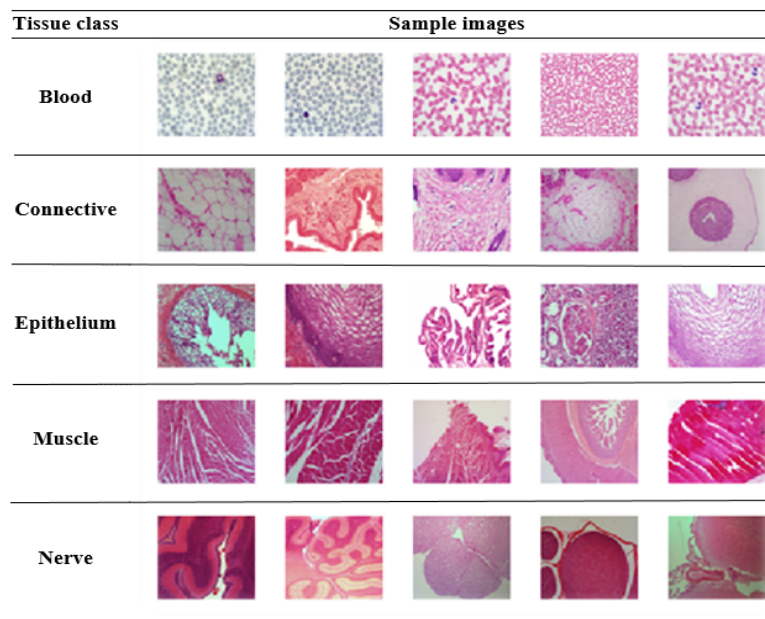


Figure 9. Histological image samples.

2.2. ML methods

ML aims to design models which enable computer systems to mimic the learning process of human beings from the available data. The main task of designing an ML system is to fit the data to the model by tuning the model's hyperparameters. Unlike the DL approaches, ML methods have less learnable parameters. Considering both training and testing processes and computational complexity, ML methods are preferable approaches.

To provide a comprehensive performance analysis in the classification problem, frequently used seven various ML techniques which are AB, ANN, DT, LR, NB, RF, and SVM were discussed. Successful implementation of feature extraction directly affects the classification result. Therefore, features should summarize most of the information of the original dataset. The parameters of the methods used during the training are given in Table 2 in detail, the pseudocode for comparing ML models to make the designed system more understandable is given below.

```

import the histology dataset
scale the dataset
store various ML models in a variable 'models'
set scoring equal to accuracy, precision, recall, f1-score
set name as name of the ML models
for name, model in models:
    store value of model_selection using 10 splits in a variable
    calculate and store results using cross_val_score method of model_selection (train and test data)
    append results in a list of existing results
    calculate the mean of the performance metrics
end for

```

3. Experimental Results and Discussion

The analysis of medical images on time is extremely important to get treatment on time and maintain a healthy lifestyle. In particular, the manual classification of large dimensions of medical image data by medical experts is tiring, time-consuming, and prone to error. With ML prediction, the time that medical professionals will devote to diagnosis, prognosis, image examination, and treatment processes is increased. With discoveries in AI and ever-increasing technological development, ML techniques can analyze medical data efficiently.

3.1. Results

To show the efficiency of classification performances of ML methods, AB, ANN, DT, LR, NB, RF, and SVM methods experimented. Training parameters of the ML methods are listed in Table 2.

Table 2. ML methods and training parameters.

ML method	Training parameters
AB	The number of estimators: 100 The initial learning rate: 0.01 The classification algorithm: Stagewise Additive Modeling using a Multi-class Exponential for Real Loss function for regression: Linear Hidden layer count: 40
ANN	The activation function: Rectified Linear Unit (ReLU) The optimization algorithm: Stochastic Gradient Descent The number of iterations (maximum): 80
DT	The number of instances in leaves (minimum): 2 The tree depth limit (maximum):100
LR	L1 normalization
NB	-
RF	The number of trees: 35 The split limit for subsets smaller than: 5
SVM	SVM with Radial Basis Function (Gaussian kernel) The number of iterations: 350

The feature extraction process directly affects the classification result. Therefore, the features of the experimental histological image dataset should summarize most of the information of the original dataset. For this study, SqueezeNet model trained on ImageNet dataset was used for the feature extraction process with Orange Data Mining software. The feature matrix that consists of 1000 image features including five target values (blood, connective, epithelium, muscle, nerve) was obtained using 20348 histological image samples.

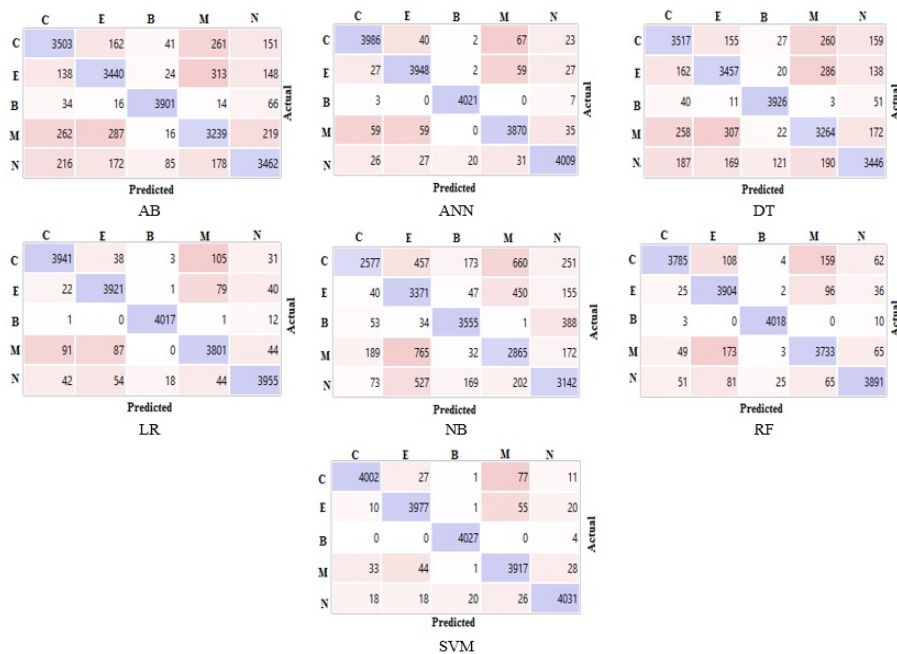


Figure 10. Confusion matrices of ML methods (C: Connective, E: Epithelium, B: Blood, M: Muscle, N: Nerve).

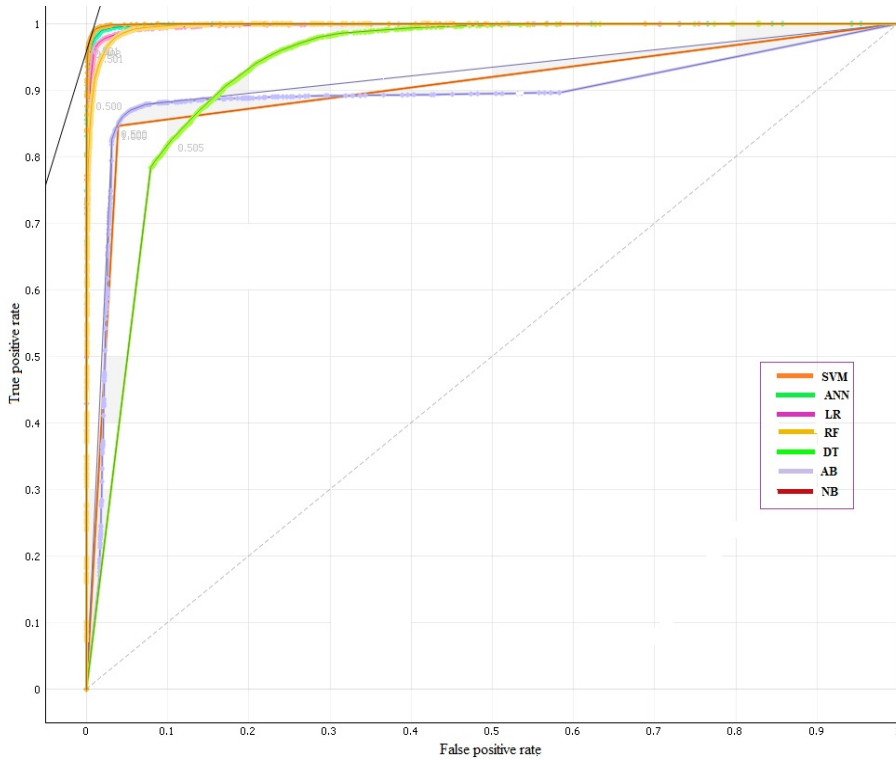


Figure 11. AUC/ROC of ML methods.

The classification performances of ML methods were evaluated using well-known performance metrics such as accuracy, precision, recall, and f1-score. In addition, 10-fold cross-validation was used to improve the validity of the experimental results. Moreover, area under curve (AUC) values and receiver operating characteristic (ROC) curves of all methods were obtained. Figure 10 illustrates the confusion matrices and Figure 11 shows the AUC/ROC of ML methods at the end of the test process.

Table 3. Classification performances of ML methods.

ML method	Measurement metrics (%)				
	Accuracy	Precision	Recall	F1-score	AUC
AB	86.20	86.20	86.20	86.20	91.40
ANN	97.50	97.50	97.50	97.50	99.90
DT	86.50	86.50	86.50	86.50	90.90
LR	96.50	96.50	96.50	96.50	99.70
NB	76.20	77.60	76.20	76.30	93.10
RF	95.00	95.10	95.00	95.00	99.60
SVM	98.10	98.10	98.10	98.10	99.90

Table 3 lists the accuracy, precision, recall, f1-score, and AUC performance metrics of ML methods for the image classification task. SVM outperformed other ML methods with an accuracy of 98.10% as seen in Table 3. Besides, SVM obtained the best values for all calculated performance metrics. SVM obtained a sensitivity of 98.10% with a specificity of 98.10%, which was significantly better than the worst performing method (NB), with a sensitivity of 77.60%, and specificity of 76.20%. SVM is an effective model in high-dimensional spaces and it provides memory efficiency using a subset of training points in the decision function, also called support vectors. The classification accuracy values of ML methods obtained for each class are illustrated in Figure 12.

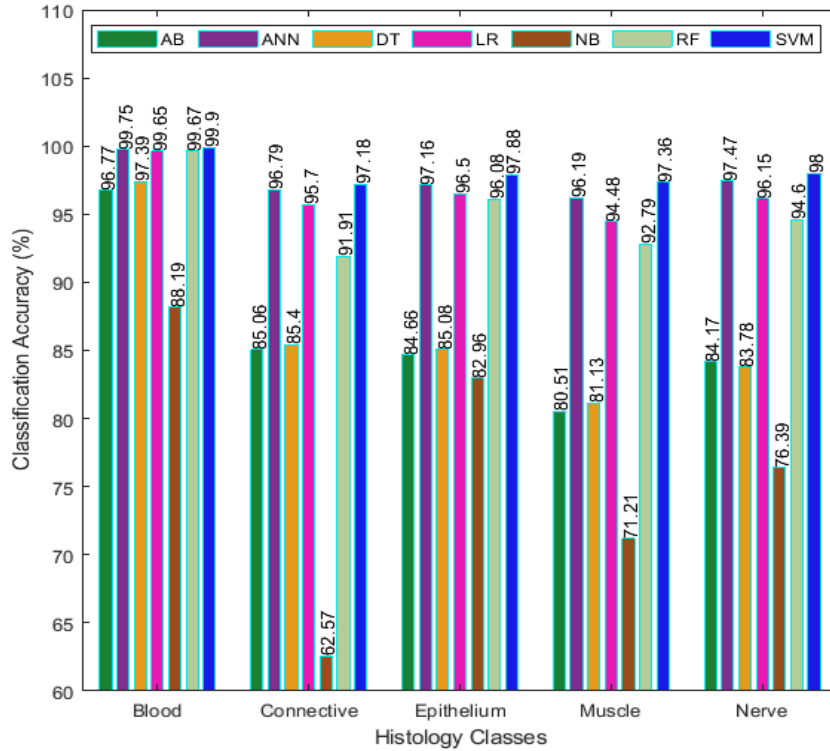


Figure 12. The classification accuracy rates of ML methods obtained for each histology class.

Blood tissue images are the class with the highest classification success. However, connective and muscle tissue images have a structure that can hardly be detected even by most medical experts. While the most successful ML method to classify blood tissue was SVM with an accuracy of 99.90%, the worst classification model was NB with 88.19%. Moreover, ANN has proved that it is a competitive model with an accuracy of 99.75% by taking second place in the classification task.

3.2. Discussion

The proposed approach conducted using real-world data enables a preliminary outline for the clinical studies and the designed AI framework can be utilized as a computer-aided medical decision support system.

The medical image analysis field has complex and massive data and the importance of the decisions made by medical experts makes it one of the fields in which ML techniques can have the greatest impact. Because microscopic examination of histological images is difficult and time-consuming. As seen in this study, histological data were classified with almost 99% success with SVM without needing more complex classification models. In order to analyze the histopathological data, it must first be determined which basic tissue class the image belongs to. After the tissue is determined, more detailed analyzes can be performed. Thanks to this study, the classification of basic tissues can be done quickly. The most important advantage of this study is that ML methods are fast and have a less complex structure compared to DL methods. As a result, the proposed AI framework that provides the automatic classification of histological data, the workload will be alleviated and it will be possible for medical professionals to focus on critical cases.

4. Conclusions

This study presents a novel histological dataset and the implementation of ML methods to analyze histological images. The experimental results of the classification of histological data obtained using ML methods were presented within the scope of this study. The proposed study eliminates the expert's bias with 98% success achieved with the most successful ML model (SVM). Considering the problems such as the fact that the expert's

error is more in real life, and the need for two or more expert evaluations to reduce this error, the proposed AI system has provided a significant advantage.

It is obvious that this dataset will be highly useful in the computer vision field. Among the applications that can be made with the existing dataset, the studies listed below can be given as examples:

- Classification of histological tissues and the classification of the subgroups of each histological tissue
- Detection and grouping of leukocytes in blood tissue
- Detection and classification of histopathological formations in different tissues and organs
- Histological tissue segmentation

Acknowledgment

This project has been funded by ***** University and OYP with Project 2017-OYP-047.

References

- [1] Ozyurt F, Tuncer T, Avci E, Koç M, Serhatlioğlu İ. A novel liver image classification method using perceptual hash-based convolutional neural network. *Arabian Journal for Science and Engineering* 2019; 44 (4): 3173-3182.
- [2] Tuncer T, Dogan S, Ozyurt F. An automated residual exemplar local binary pattern and iterative reliefF based COVID-19 detection method using chest X-ray image. *Chemometrics and Intelligent Laboratory Systems* 2020; 203: 104054.
- [3] Baygin M, Yaman O, Barua PD, Dogan S, Tuncer T, Acharya UR. Exemplar Darknet19 feature generation technique for automated kidney stone detection with coronal CT images. *Artificial Intelligence in Medicine* 2022; 127: 102274.
- [4] Aljabri M. AlGhamdi M. A review on the use of deep learning for medical images segmentation. *Neurocomputing* 2022; 506: 311-335.
- [5] Codella N, Moradi M, Matasar M, Sveda-Mahmood T, Smith JR. Lymphoma diagnosis in histopathology using a multi-stage visual learning approach. *Proceedings of the SPIE Medical Imaging* 2016; 9791.
- [6] Mazo C, Bernal J, Trujillo M, Alegre E. Transfer learning for classification of cardiovascular tissues in histological images. *Computer Methods and Programs in Biomedicine* 2018; 165: 69-76.
- [7] Niemann A, Talagini A, Kandapagari P, Preim B, Saalfeld S. Tissue segmentation in histologic images of intracranial aneurysm wall. *Interdisciplinary Neurosurgery* 2021; 26: 101307.
- [8] Xu H, Liu L, Lei X, Mandal M, Lu C. An unsupervised method for histological image segmentation based on tissue cluster level graph cut. *Computerized Medical Imaging and Graphics* 2021; 93: 101974.
- [9] Sato N, Uchino E, Kojima R, Sakuragi M, Hiragi S, Minamiguchi S, Haga H, Yokoi H, et al. Evaluation of kidney histological images using unsupervised deep learning. *Kidney International Reports* 2021; 6(9): 2445-2454.
- [10] Taylor-Weiner A, Pokkalla H, Han L, Jia C, Huss R, Chung C, Elliott H, Glass B, et al. A Machine learning approach enables quantitative measurement of liver histology and disease monitoring in NASH. *Hepatology* 2021; 74(1): 133-147.
- [11] Varalakshmi P, Priyamvadan AV, Rajakumar BR. Predicting osteosarcoma using extreme gradient boosting model. *International Conference on Advances in Computing, Communication and Applied Informatics (ACCAI)* 2022; 1-6.
- [12] Kierszenbaum AL, Tres LL. *Histology and cell biology: an introduction to pathology in Philadelphia*. Elsevier Saunders, 2016. pp. 123, 217, 239.
- [13] Gartner LP, Hiatt JL, Gartner LP. *Color atlas and text of histology in Philadelphia: Wolters Kluwer Health/Lippincott Williams Wilkins*, 2013. pp.126-148.
- [14] Mescher AL, Junqueira LCU. *Junqueira's basic histology: Text and atlas*, New York: McGraw-Hill, 2021. pp.73-98.
- [15] Ovalle WK, Nahirney PC, Netter FH. *Netter's essential histology with correlated histopathology*, 2021. pp. 51-71.
- [16] Pawlina W, Ross MH. *Histology: A text and atlas in correlated cell and molecular biology*, 2020. pp.356-404.
- [17] Uyar K, Taşdemir Ş. Detection and classification of leucocyte types in histological blood tissue images using deep learning approach. *The European Journal of Science and Technology* 2021; 24:130-137.
- [18] Uyar K, Taşdemir Ş, Ülker E, Ünlükal N, Solmaz M. Improving efficiency in convolutional neural networks with 3D image filters. *Biomedical Signal Processing and Control* 2022; 74: 103563.

Mathematical Analysis of The Hash Functions as a Cryptographic Tools for Blockchain

Muharrem Tuncay GENÇOĞLU^{1*}

¹ Firat University, Vocational School of Technical Sciences, Elazığ, Turkey

*¹ mtgencoglu23@gmail.com

(Geliş/Received: 05/07/2022;

Kabul/Accepted: 02/09/2022)

Abstract- Blockchain is one of the most interestingly developing technologies today, with its applications in many fields from smart contracts to cryptocurrencies. In this respect, blockchain is a hot modern topic nowadays. This study presents a mathematical analysis of cryptographic hash functions, which are one of the most important elements for understanding the security foundations of this technology. In this analysis presented; Hash functions, which are one of the building blocks of blockchain technology, used to ensure information integrity, have proven to be resistant to collision resistance, which is very important in data mining. Thus, a theory has been put forward that will contribute to time and energy saving, which is one of the important problems in data mining, in which blockchain technology is used.

Keywords: hash functions, blockchain, cryptographic hash functions, mathematical analysis

Blok Zincir için bir Kriptografik Araç Olarak Hash Fonksiyonlarının Matematiksel Analizi

Öz: Blockchain, akıllı sözleşmelerden kripto paralara kadar birçok alanda uygulamalarıyla günümüzde en ilginç gelişen teknolojilerden biridir. Bu bağlamda, blockchain günümüzde sıcak ve modern bir konudur. Bu çalışma, bu teknolojinin güvenlik temellerini anlamak için en önemli unsurlardan biri olan kriptografik özet fonksiyonlarının matematiksel bir analizini sunmaktadır. Sunulan bu analizde; Bilgi bütünlüğünü sağlamak için kullanılan blockchain teknolojisinin yapı taşlarından biri olan hash fonksiyonlarının veri madenciliğinde oldukça önemli olan çarpışma direncine karşı dirençli olduğu kanıtlanmıştır. Böylece blockchain teknolojisinin kullanıldığı veri madenciliğinde önemli sorunlardan biri olan zaman ve enerji tasarrufuna katkı sağlayacak bir teori ortaya konulmuştur.

Anahtar kelimeler: Hash fonksiyonları, blok zincir, kriptografik hash fonksiyonları, matematiksel analiz

1. Introduction

Blockchain is one of the most popular and developing technologies in recent years. This technology is briefly; It can be defined as an interconnected chain of data blocks that allows the creation of transaction records based on a managed distributed consensus protocol without a central authority. Thanks to this structure, any of the participants cannot change the content of the blocks that have been agreed upon. Therefore, only new transactions can be added or merged to eliminate or modify existing ones. In this structure, three basic features complete the principle of immutability;

1. A summary of the state of the entire chain should be available at any time to prevent and detect manipulation of any block of the chain.
2. It is necessary to verify whether a transaction is included in the blockchain.
3. Parties involved in a transaction in any block should be allowed to do so in a so-called anonymous manner.

Conceivably one of the best-known applications of this technology, bitcoin, the cryptocurrency so named for its use makes several cryptographic primitives, and ensures the pseudo-anonymity of participants, and the immutability of stored records, and distributed consensus without recourse to a central authority[1].

In this study, the most basic cryptographic concept of blockchain technology and the concept of the hash function, which is the primary tool in providing information integrity, are reviewed. In addition, the mathematical proof that it is a collision-resistant function is presented.

The remainder of this article is organized as follows; In the second chapter, the definition and properties of the hash function used in verifying data integrity and the definition and properties of the concept of modular arithmetic are given. In the third part, a theorem that can be a solution to the computational problem of data miners

* Sorumlu yazar: mtgencoglu23@gmail.com. Yazarların ORCID Numarası: ¹0000 -0002-8784-9634

using blockchain technology, which includes finding partial collisions of a certain hash function, has been proved. Finally, the results of the study are presented in the fourth chapter.

2. Hash Functions

Hash functions are among the cryptographic primitives that have grown in relevance in recent years. It is important to point out that such functions do not encrypt or decrypt messages. However, they are an indispensable tool for verifying data integrity, apart from other applications equally interesting, hash functions can be defined as functions that are capable of transforming any block of binary data into another fixed-size binary block[2,3]. The result of such a transformation is called has hor digest.

In addition to this initial use, hash functions have been applied to other areas concerned with the protection of information in general, and its integrity in particular. Therefore, it can detect corrupt data, the presence of viruses, etc. They are also used to detect.

One-way functions that take any variable-length input and convert it to a fixed-length output are called hash functions[3].

The hash function is the operation that creates a fixed-length unique value with mathematical functions of various lengths of data. In other words, hash functions, which have a very important place in cryptography, compress data of any size to a fixed length. It is a one-way function and although a relationship is established between the processed text and the summary value, the original data cannot be obtained from the summary value. In the hashing process, the same value is produced for the same data, but when there is the slightest change, the value created by the hash function changes. Hash functions are widely used in areas such as verifying the integrity of data, storing passwords, digital signatures, message authentication code, and blockchain.

In hash functions, different inputs can produce the same output. This situation is called conflict. This is not desirable for hash functions and compromises their security. Hash functions have advantages such as guaranteeing data integrity, producing fixed and small-sized outputs, and producing fast output for each input length.

Mathematically, the hash function is expressed using the concept of a One Way Function.

m ; variable size and predetermined message,

M ; a particular set that gives a summary of the message m

n ; dimension provided that;

$$\begin{aligned} h: M &\rightarrow \{0,1\}^n, \\ h(m) &= \hat{m}. \end{aligned}$$

In other words; At $Y = f(x)$, They are functions that are easy to find when x is known, but difficult to find when Y is known. Hash functions with this property are collision-proof functions.

2.1. Properties

For an ideal cryptographic hash function to be considered secure, it should have the following three properties[4];

I. *Collision Resistance*: Messages should be difficult to find when the digest of two separate messages is the same.

For $m_1 \neq m_2$, when $\hat{m}_1 = \hat{m}_2$, calculating m_1, m_2 should be difficult.

II. *Inverse Image resistance*: The original data cannot be found from the hash function generated by the hash function. That is, it should be difficult to find m when the summary \hat{m} is given.

$f^{-1}(\hat{m})$ must not be computable.

III. *Secondary Reverse Image Resistance*: It must be very difficult to have the same digest of two separate messages.

For $m_1 \neq m_2$, it should be $\hat{m}_1 \neq \hat{m}_2$.

As stated earlier, blockchains are chains of information blocks where each block has an associated hash value. These hashes are used to create a data index. If each data block contains the hash of the block previously

added to the chain, a linked blockchain is obtained, where the hashes play the role of pointers. In this context, it is important to define a method by which it is possible to determine whether a particular block has been obtained. This can be done with the hash function[5].

For quite some time, the most widely-used hash function was MD5 (Message Digest 5), proposed by Rivest[4], which generates hashes of 128 bits. However, when some security vulnerabilities were published in 2005, the use of the MD5 function was discontinued[6]. Although still used in insecure contexts such as checking the integrity of downloaded files, it is prohibited in environments where security is a critical element. The SHA-1 (Secure Hash Algorithm-1) function, which produces 160-bit hashes, was adopted by the National Institute of Standards and Technology (NIST) in 1995[7]. Although there are collisions, SHA-1 continues to be used quite frequently today[8]. As in the MD5 example, its use is discarded by most international institutions and organizations within the scope of secure applications. Another function that provides 160-bit hashes and is still used in some scenarios today is the RIPEMD-160 (RACE Integrity Primitives Assessment Message Digest) function[9]. The SHA-2 family of hash functions is the successor to the SHA-1 function. The SHA-2 specification includes the functions SHA-224, SHA-256, SHA-384, and SHA-512, which provide hashes of 224, 256, 384, and 512 bits, respectively; where SHA-224 and SHA-384 are shortened versions of SHA-256 and SHA-512 functions, respectively. This range of hash sizes significantly improves security compared to the output lengths of MD5 and SHA-1[6].

2.2. Modular Arithmetic

The set of remaining classes according to the module m , $m \in \mathbb{Z}^+$,

$$\mathbb{Z}/m = \{\bar{0}, \bar{1}, \bar{2}, \dots, \overline{m-1}\},$$

$$\mathbb{Z}/n = \{\bar{0}, \bar{1}, \bar{2}, \dots, \overline{n-1}\}.$$

Explanation:

If $x, y \in \mathbb{Z}$, $x \equiv y \pmod{m}$,

1. The remainder of x and y divided by m are equal.
2. The difference between x and y is divisible by m . $x \equiv y \pmod{m} \Rightarrow x - y = k \cdot m$,
3. The remainder in the division of a sum equals the sum of the individual remainders.

$$\overline{x+y} = \bar{x} + \bar{y}.$$

4. The remainder in the division of multiplication is equal to the multiplication of the individual remainders.
- $$\overline{x \cdot y} = \bar{x} \cdot \bar{y}.$$

$$5. \left. \begin{array}{l} a \equiv b \pmod{m} \\ c \equiv d \pmod{m} \end{array} \right\} \Rightarrow \begin{array}{l} a + c \equiv b + d \pmod{m} \\ a \cdot c \equiv b \cdot d \pmod{m} \end{array} ,$$

$$6. a \equiv b \pmod{m} \text{ and } k \in \mathbb{Z} \Rightarrow a \equiv b \pm km.$$

$$7. a \equiv b \pmod{m} \text{ and } n \in \mathbb{Z}^+ \text{ while}$$

$$a^n \equiv b^n \pmod{m}.$$

3. Collisions Problem of Hash Functions

Miners using blockchain technology are accountable for figure out the computationally arduous problem, which involves finding partial collisions of a given hash function. A collision consists of finding two different messages m_1 and m_2 , $m_1 \neq m_2$, such that $\tilde{m}_1 = \tilde{m}_2$. In this case, the chosen hash function is SHA-256[6].

To find a partial collision, each miner takes into account the values (titles and transactions) that make up a block, then uses the difficulty corresponding to the moment he did his computations and tries different nonces until the resulting hash value is lesser a certain threshold. This threshold value is equivalent to a certain number of leading zero hashes. Such several zeros are determined by the number of miners in the network (and their computing power), so the time required to find a solution is about 10 minutes on average. It is obvious that the higher the number of leading zeros, the more difficult it is to solve the problem.

The mathematical problem of finding partial collisions guarantees not to use of the same block. This is known in the cryptocurrency literature as Proof of Work (PoW)[10,11].

3.1. Theorem

While p is a prime number, $q = \frac{p-1}{2}$ is also prime. This situation is called absolute primality.

α and β , primitive roots of $\alpha^a \equiv \beta \pmod{p}$,

a ; being unknown

Let a hash function be defined as $h: \mathbb{Z}/q^2\mathbb{Z} \rightarrow \mathbb{Z}/p\mathbb{Z}$. This function, for the message

$m = r_0 + r_1q$ ($0 \leq r_0, r_1 \leq q - 1$) expressed as $h(m) = \alpha^{r_0}\beta^{r_1} \pmod{p}$. This h function is highly resistant to collision resistance.

3.2. Proof

Let's assume that; for $m = r_0 + r_1q$ ve $m_1 = r_0' + r_1'q$,

$$\alpha^{r_0}\beta^{r_1} \equiv 1 \pmod{p}. \quad (1)$$

Since $\beta \equiv \alpha^a \pmod{p}$ the above equivalence can be written as

$$\alpha^{a(r_1-r_1')-(r_0'-r_0)} \equiv 1 \pmod{p}. \quad (2)$$

However, since there is a primitive root in $\alpha \pmod{p}$, the following result is obtained;

$$\alpha^b \equiv 1 \pmod{p} \Leftrightarrow b = 0 \pmod{p-1}. \text{ Therefore;}$$

$$a(r_1 - r_1') \equiv (r_0' - r_0) \pmod{p-1}.$$

If $g = \text{OBEB}(r_1 - r_1', p - 1)$, then using the properties of modular arithmetic we can say that equivalence (2) has exactly g solutions[2].

Since $\frac{p-1}{2}$ is prime and $0 \leq r_1, r_1' \leq q - 1$, it must be $-(q - 1) \leq r_1 - r_1' \leq q - 1$.

So if $r_1 - r_1' \neq 0$ then $q > |r_1 - r_1'|$. Therefore, there are solutions g_1 and g_2 .

From the equivalence $\alpha^a \equiv \beta$, we can say that only two possible values of a , and one of them will give β . If we can show that is hidden, that is, unknown, of a , we have proved the theorem.

$r_1 - r_1' \Rightarrow r_0 = r_0' \pmod{p-1}$ becomes $r_0 \equiv r_0'$ from the inequality $-(q - 1) \leq r_1 - r_1' \leq q - 1$ means. This indicates that messages m ve m_1 are the same. That is, $m = m_1$, which contradicts the assumption that messages m ve m_1 are different. Then it is $r_1 - r_1' \neq 0$. This indicates that a is hidden, that is, unknown. Therefore, the function $h(m) = \alpha^{r_0}\beta^{r_1} \pmod{p}$ is a strong collision-resistant function.

4. Conclusions

As a result; It is thought that this study will contribute to the solution of the computationally difficult problem, which includes finding the collisions of hash functions, which is very important for data mining in which the blockchain technology used in the crypto money system, which is very popular today, is very important. Also, miners compare the obtained hashes using one-time keys to find partial collisions of a particular hash function. They spend a lot of time and energy making these comparisons. Considering the methods and concepts used in mathematical analysis, they will save time and therefore save energy.

When dealing with blockchains, hash functions appear in a few places. On the one hand, they are used as part of numerical signature algorithms. On the other hand, hash functions play a significant role in implementing Merkle trees, a notion that allows to efficiently check whether a particular block exists in a blockchain. Thanks to the combination of these elements, it has been possible to form a promising trustworthy technology - a blockchain.

Finally; We have shown mathematically that the above-mentioned partial collisions can be found mathematically, namely PoW, and that double spending can be detected in a short time.

References

- [1] Martínez, V.G., Hernández-Álvarez, L., and Hernández Encinas, L, Analysis of the Cryptographic Tools for Blockchain and Bitcoin, *Mathematics* 2020; 8: 131.
- [2] Menezes, A.J.; van Oorschot, P.C.; Vanstone, S.A. *Handbook of Applied Cryptography*; USA: CRC Press, Inc.: Boca Raton, FL, 1996.
- [3] Paar, C., Pelzl, J. *Understanding Cryptography. A Textbook for Students and practitioners*; Germany: Springer-Heidelberg, 2010.
- [4] Rosen, K. *An INTRODUCTION to CRYPTOGRAPHY*. USA: Taylor&Francis Group, 2007.
- [5] Merkle, R.C. Method of Providing Digital Signatures. U.S. Patent 4,309,569, 5 January 1982. Available online: <https://patents.google.com/patent/US4309569A/en> (accessed on 15 August 2022).
- [6] Wang, X.; Yu, H. *How to break MD5 and other hash functions*. Germany: Springer, 2005.
- [7] NIST. Secure Hash Standard (SHS). Federal Information Processing Standard Publication. FIPS 180-4. 2015. Available online: <https://nvlpubs.nist.gov/nistpubs/FIPS/NIST.FIPS.180-4.pdf> (accessed on 15 August 2021).
- [8] Wang, X.; Yin, Y.L.; Yu, H. Finding collisions in the full SHA-1. German: Springer, 2005.
- [9] Dobbertin, H.; Bosselaers, A.; Preneel, B. RIPEMD-160: A strengthened version of RIPEMD. In *Fast Software Encryption*; Germany: Springer, 1996.
- [10] Dwork, C.; Naor, M. Pricing via Processing or Combatting Junk Mail. In *Advances in Cryptology-Proceedings of Crypto'92* Germany: Springer, 1993.
- [11] Jakobsson, M.; Juels, A. Proofs of Work and Bread Pudding Protocols (Extended Abstract). In *Secure Information Networks*, USA: Springer, 1999.

A Deep Learning Model Collaborates with an Expert Radiologist to Classify Brain Tumors from MR Images

Tülin ÖZTÜRK¹, Oğuzhan KATAR^{2*}

¹ Department of Radiology, Medikal Park Hospital, Elazığ, Turkey

² Department of Software Engineering, Faculty of Technology, Firat University, Elazığ, Turkey

¹ tulin58@hotmail.com, ^{2*} okatar@firat.edu.tr

(Geliş/Received: 12/07/2022;

Kabul/Accepted: 12/09/2022)

Abstract: The brain, which consists of nerve cells called neurons, is the center of the nervous system. The rapid and abnormal growth of nerve cells by interacting with each other is called a brain tumor. Undiagnosed or delayed diagnosis of brain tumors lead to death. Although it depends on experience, manually diagnosing and classifying brain tumors is challenging for physicians. Artificial intelligence-based computer systems can help doctors detect brain tumors using the developments in hardware technology and the amount of data increasing daily. This study proposes a deep learning-based system to classify brain MRI images as tumorous or normal using the pre-trained EfficientNet-B0 model. Our radiologist validated a public dataset containing 3000 brain MRI images. The dataset is divided into 70% train, 20% validation, and 10% test. In the test phase after the training, the pre-trained EfficientNet-B0 model achieved high performance with 99.33% accuracy, 99.33% sensitivity, and 99.33% F1 score. In addition, in the evaluation of the test images, the heat maps obtained by the Grad-CAM method were examined by our radiology specialist. The result of evaluations shows that the pre-trained EfficientNet-B0 deep model chooses the right focus areas in its predictions and can be used for clinical tumor detection due to its explainable structure.

Key words: Brain tumor, MRI, Deep learning, EfficientNet, Grad-CAM.

MR Görüntülerinden Beyin Tümörlerini Sınıflandırmak İçin Uzman Bir Radyolog ile İşbirliği Yapan Derin Öğrenme Modeli

Öz: Nöron adı verilen sinir hücrelerinden oluşan beyin, sinir sisteminin merkezidir. Sinir hücrelerinin birbirleriyle etkileşerek hızlı ve anormal büyümesine beyin tümörü denir. Beyin tümörlerinin teşhis edilmemiş veya gecikmiş teşhisi ölüme yol açmaktadır. Tecrübeye bağlı olmakla birlikte, beyin tümörlerini manuel olarak teşhis etmek ve sınıflandırmak hekimler için zordur. Yapay zeka tabanlı bilgisayar sistemleri, donanım teknolojisindeki gelişmeleri ve her geçen gün artan veri miktarını kullanarak doktorların beyin tümörlerini tespit etmelerine yardımcı olabilir. Bu çalışma, ön eğitilmiş EfficientNet-B0 modelini kullanarak beyin MRG görüntülerini tümörlü veya normal olarak sınıflandırmak için derin öğrenme tabanlı bir sistem önermektedir. Radyoloğumuz, 3000 beyin MRG görüntüsü içeren halka açık bir veri setini doğruladı. Veri seti %70 eğitim, %20 doğrulama ve %10 teste bölünmüştür. Eğitim sonrası test aşamasında, ön eğitilmiş EfficientNet-B0 modeli %99.33 doğruluk, %99.33 hassasiyet ve %99.33 F1 puanı ile yüksek performans elde etti. Ayrıca test görüntülerinin değerlendirilmesinde Grad-CAM yöntemi ile elde edilen ısı haritaları radyoloji uzmanımız tarafından incelendi. Değerlendirmelerin sonucunda, ön eğitilmiş EfficientNet-B0 derin modelinin tahminlerinde doğru odak alanlarını seçtiğini ve açıklanabilir yapısı sayesinde klinik olarak tümör tespiti için kullanılabileceğini göstermektedir.

Anahtar kelimeler: Beyin tümörü, MRG, Derin öğrenme, EfficientNet, Grad-CAM.

1. Introduction

The incidence of brain tumors is five to 13 cases per 100,000, with a five-year survival rate of %33.4. The incidence of brain tumors increases with age. The most common symptoms of these tumors are headache, nausea, vomiting, and seizures [1]. As the tumor grows, focal neurological findings can be seen. In some patients, there may be no symptoms at all, and the patient may be detected incidentally by medical imaging methods taken for some other reasons. The present findings of the patient are usually first evaluated with CT, MRI [2]. Magnetic Resonance Imaging (MRI) technology is widely applied to create high-resolution images for brain tumor diagnosis. It has been shown that the treatments applied when brain tumors are detected early in small size are very effective. Radiologically, the diagnosis is difficult because the tumors are small in size, resemble blood vessels, and can be easily missed in non-contrast series. In addition, manual image reading takes a lot of time and effort [3]. The diagnosis process becomes an error-prone process with the emergence of human factors such as

* Corresponding author: okatar@firat.edu.tr. ORCID Number of authors: ¹ 0000-0001-8942-5264, ² 0000-0002-5628-3543

fatigue due to the excess time spent. Computers with fast processing capacity and the ability to be unaffected by human factors can help radiologists in this process [4].

Artificial intelligence-based systems are actively used to detect various diseases or monitor the process of treatments [5]. Today, studies involving the use and development of deep learning models for disease-based classification of medical images and marking important disease areas on the image have gained attention [6]. Khan et al. [7] proposed a method for automatic detection of brain tumors with the help of a deep learning-based system. They used a publicly available MRI dataset to detect brain tumors containing 253 images; 155 of them were labeled as tumor, while the remaining 98 images were marked as normal. They used the Canny Edge Detection method to contain minimal background area. Due to the small dataset, synthetic images were produced by data multiplexing. Using these images, four different models, including the CNN-based deep model proposed by the authors. The proposed model correctly classified all 28 test images.

Singh et al. [8] proposed a CNN model to classify MR images. They used a pre-trained VGG-16 model to classify brain tumor MR images into the tumor or normal classes. The dataset was resized to 224x224 and used in model training for 16 epochs. When the test images were examined, it was seen VGG-16 model reached %90 accuracy.

Pundir and Kumar [9] proposed a deep model that can classify normal and tumor brain MRI images. Training dataset consists of images produced by data multiplexing methods. The pre-trained VGG-16 model was trained for 100 epochs. 431 out of 500 tumor images and 487 of 500 normal images allocated for the test phase were predicted correctly by the trained classifier model. Therefore, the VGG-16 model reached 91.8% accuracy.

The primary purpose of this study is to automatically classify tumor and normal images on brain MRI images by a deep learning model and to visualize which areas are focused on the image in the classification predictions it has made. In this way, it is aimed to explain the black-box structure of deep models and to spread the use of deep models in the health sector. The rest of this paper is organized as follows. Section 2 contains information about the method proposed for this study, the used dataset, the classifier deep learning model, and the performance metrics used in classification studies. The numerical values obtained during the training phase of the classifier and the Grad-CAM outputs are given in Section 3. The conclusion part of the study is in Section 4.

2. Materials and Methods

This study proposes a deep learning model to detect brain tumors from MR images. A large number of training data and high-capacity hardware that can process the given data are needed to train deep learning models from scratch. For this reason, it is very costly to train a model from scratch. In order to reduce the computational cost during the training process, CNN models that have been pre-trained on a different dataset are used on the current task. The pre-trained models have learned various features and have optimized weights for the classification task. In this study, a deep learning system is designed to classify brain MRI images with or without tumor. Using the Grad-CAM algorithm, which areas on the image the CNN model pays attention to in its predictions are visualized using the heat map technique. In this way, it was determined by an expert radiologist whether the areas that the deep learning model focuses on are the areas that play an active role in determining the class. Fig.1 shows a block representation of the proposed approach employed in this study.

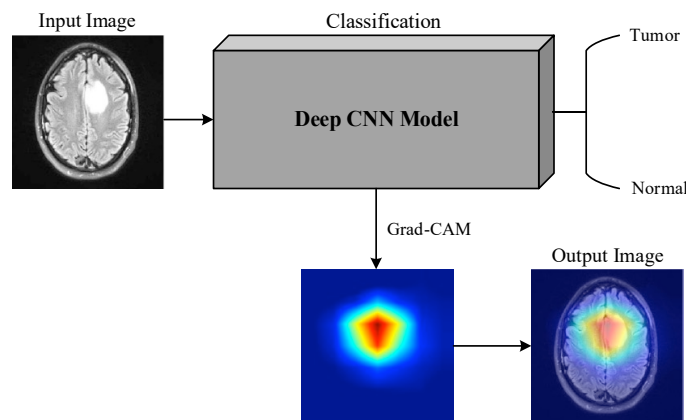


Figure 1. A block representation of the proposed method in this study.

2.1. Brain MRI Dataset

A publicly available dataset called Br35H was used in this study [10]. This dataset includes 1500 tumor and 1500 normal brain MRI images. The experts verified the class labels of the images in the dataset. Sample brain MR images with tumor and normal labels are shown in Fig.2.

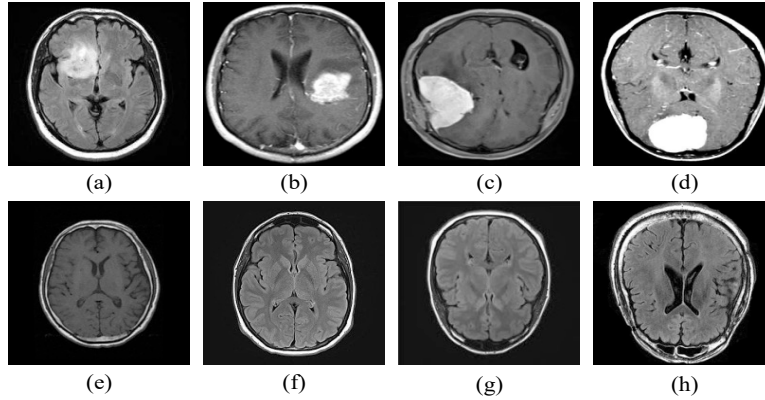


Figure 2. (a), (b), (c), (d) Brain Tumor Axial MR slices, (e), (f), (g), (h) Normal Axial Brain MR slices.

2.2. Proposed Classification Method

This study uses a CNN-based EfficientNet-B0 architecture as the classifier deep learning model. The selected model is state-of-the-art in ImageNet classification computation. The models trained on large datasets achieve significantly higher performance than model training with small data. Tan M. et al. [11] proposed a new method to scale CNNs in a structured way. In the proposed method, a fixed size scaling was used instead of traditional approaches such as increasing the depth, width, or input resolution. The EfficientNet model family, which is smaller and faster than the current computing models, has been developed in the specified new scaling method. This family has eight members, sequentially named from EfficientNet-B0 to EfficientNet-B7. EfficientNet-B0 is designed as the base model, and all other models have scaled versions. The architecture of the EfficientNet-B0 model is given in Table 1.

Table 1. EfficientNet-B0 Model Architecture [11].

Stage	Operators	Resolutions	Channels	Layers
1	Conv3×3	224×224	32	1
2	MBCConv1,3×3	112×112	16	1
3	MBCConv6,3×3	112×112	24	2
4	MBCConv6,5×5	56×56	40	2
5	MBCConv6,3×3	28×28	80	3
6	MBCConv6,5×5	14×14	112	3
7	MBCConv6,5×5	14×14	192	4
8	MBCConv6,3×3	7×7	320	1
9	Conv1×1 & Pooling & FC	7×7	1280	1

The basic network structure block diagram of the EfficientNet-B0 deep learning model is shown in Fig.3.

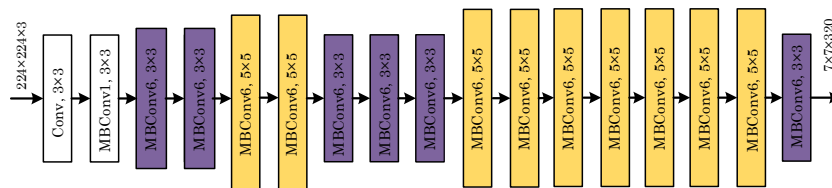


Figure 3. The Block diagram of the EfficientNet-B0 model.

2.3. Experimental Setups

EfficientNet-B0, the basic model of the EfficientNet model family, was used in training the classifier deep learning model. The model with a default input size of 224x224 pixels was trained using the Keras library created with the Python programming language. During the model training, we preferred to use ImageNet [12] weights instead of random initial weights to optimize the parameters. The last layers of the model have been revised to produce only two values in accordance with the binary classification method at the output. In the final layer of the model, the softmax activation function is used as the activation function. Adam optimization was carried out for the training process with cross-entropy loss, batch size of 16, and early termination function active for 50 epochs with a learning rate of 0.001. The performance value followed during training was the accuracy rate. When the verified accuracy rate does not exceed the highest value for five consecutive rounds, the early stop function was activated, and the step with the highest value was saved in the '.hd5' format. This way, it aims to reach the step with the most successful classification ability. All of these processes were carried out in the Google Colab environment.

Since the images in the dataset are of different resolutions, they have been resized to 224x224px. Before starting the training of the model, 70% of the resized dataset samples were randomly divided to be used in the training, 20% validation, and 10% testing phases, preserving the class distribution. The visual setup of the data splitting process is shown in Fig.4.

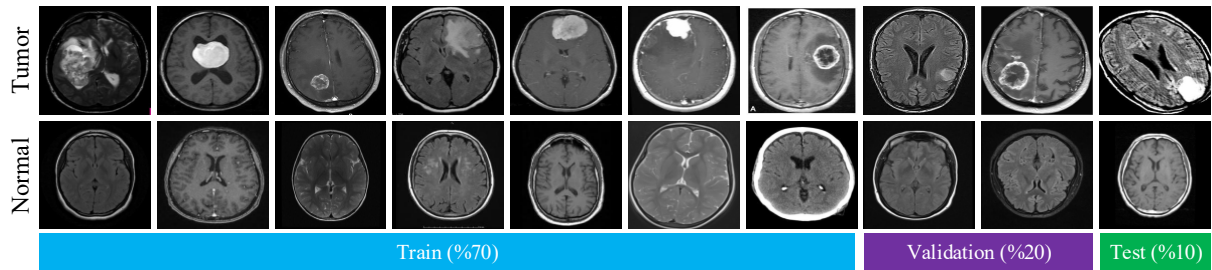


Figure 4. A representation of brain MRI images showing the division rates during model training and testing phases.

The detailed information about the numerical distributions of the data set samples after data division is given in Table 2.

Table 2. Numerical distribution of MR images after data distribution.

Phase	Number of Tumor MR Images	Number of Normal MR Images	Total
Train	1050	1050	2100
Validation	300	300	600
Test	150	150	300
Total	1500	1500	3000

2.4. Performance Evaluation Metrics

In artificial intelligence-based classification studies, confusion matrix-based performance measurements are commonly used to evaluate the performance of the deep learning model in the testing phase. The confusion matrix provides information about the relationship between the predicted label and the actual class label, with reference to the image given as input to the deep learning model. In the studies carried out on the binary classification setup, the model can only predict two different classes at the output. For this reason, only four different situations can arise by examining the predictions of the model. These situations and their details are as follows.

- The prediction of an image with a tumor labeled as tumorous by the classifier deep learning model is called True Positive (TP).
- The prediction of an image with a normal label as tumorous by the classifier deep learning model is called False Positive (FP).

- Normal prediction of an image with tumor label by the classifier deep learning model is called False Negative (FN).
- Normal prediction of an image labeled Normal by the classifier deep learning model is called True Negative (TN).

In order to represent the confusion matrix visually, the values of TP, FP, FN, and TN must be placed in a 2×2 matrix. It is understood that the classification ability of the classifier deep learning model is developed when the TP and TN values are higher than the values of other cases. Various performance metrics have been standardized to express this classification ability mathematically. Some standardized metrics and the equations used for their calculations are as follows.

$$Accuracy = \frac{TP+TN}{TP+FP+FN+TN} \quad (1)$$

$$Sensitivity = \frac{TP}{TP+FN} \quad (2)$$

$$Precision = \frac{TP}{TP+FP} \quad (3)$$

$$Specificity = \frac{TN}{TN+FP} \quad (4)$$

$$F1\ Score = \frac{2*(Precision*Sensitivity)}{(Precision+Sensitivity)} \quad (5)$$

$$Matthews\ Correlation\ Coefficient\ (MCC) = \frac{(TP*TN)-(FP*FN)}{\sqrt{(TP+FP)(TP+FN)(TN+FP)(TN+FN)}} \quad (6)$$

3. Experimental Results

For automatic detection of tumor and normal brain MR images, the pre-trained EfficientNet-B0 model was trained for 50 epochs with the help of the early termination function. The EfficientNet-B0 model achieved the highest validation accuracy rate of 0.9967 in the 10th epoch. The loss and accuracy graphs of EfficientNet-B0 model obtained during training are shown in Fig. 5.

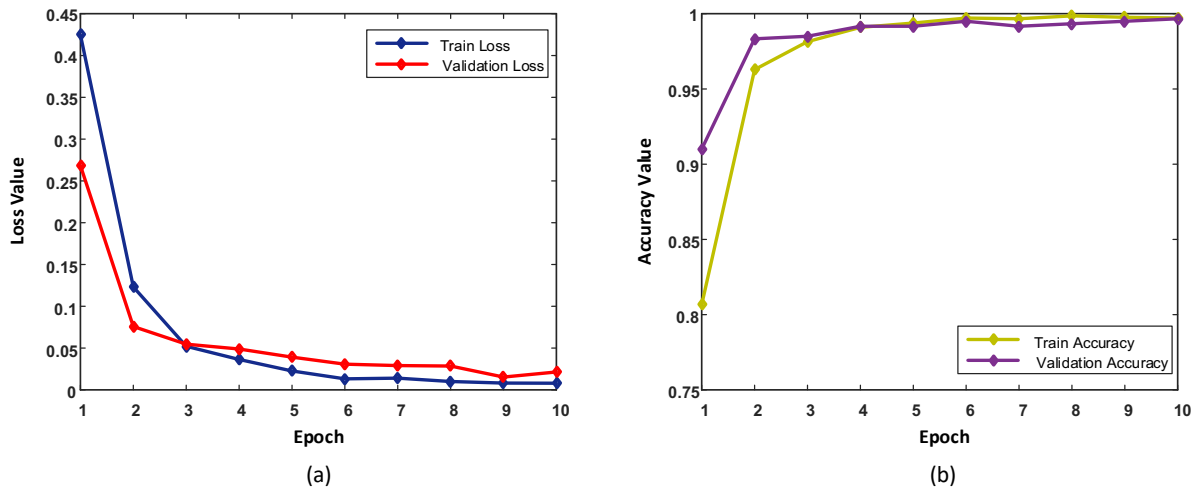


Figure 5. Training graphs EfficientNet a) loss graph b) accuracy graph.

The images reserved for use only in the testing phase are given as input to the EfficientNet-B0 model. The confusion matrix created by reference to the predictions made by the model for the test images is shown in Fig.6.

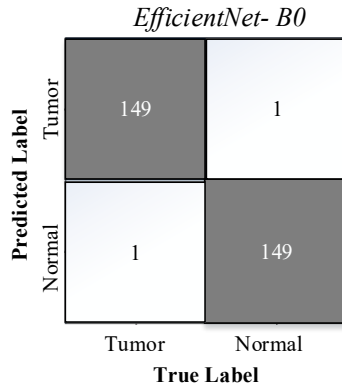


Figure 6. The confusion matrix was obtained by the model on the test images.

It seems that the EfficientNet-B0 model can gain the ability to classify brain MRI images as tumorous or normal according to the findings it contains. In Table 3, the values of the performance metrics achieved by the model during the testing phase are given.

Table 3. Performance values of the classifier model on test data.

Accuracy	Sensitivity	Specificity	Precision	F1 Score	MCC
0.9933	0.9933	0.9933	0.9933	0.9933	0.9867

When the performances of deep learning models are examined, the specified mathematical equations are usually used. However, it is not known which feature of the deep learning model takes into account the class prediction on the image, so the deep models are in a black-box structure. Especially in areas that directly affect human life, such as health, proving that deep learning models focus on which areas in predictions will lead to the emergence of more reliable systems. In this study, Grad-CAM [13] method was applied to examine whether the EfficientNet-B0 model focuses on tumor areas while deciding on brain MRI images. A visualization of the use of the Grad-CAM algorithm in this study is given in Fig.7.

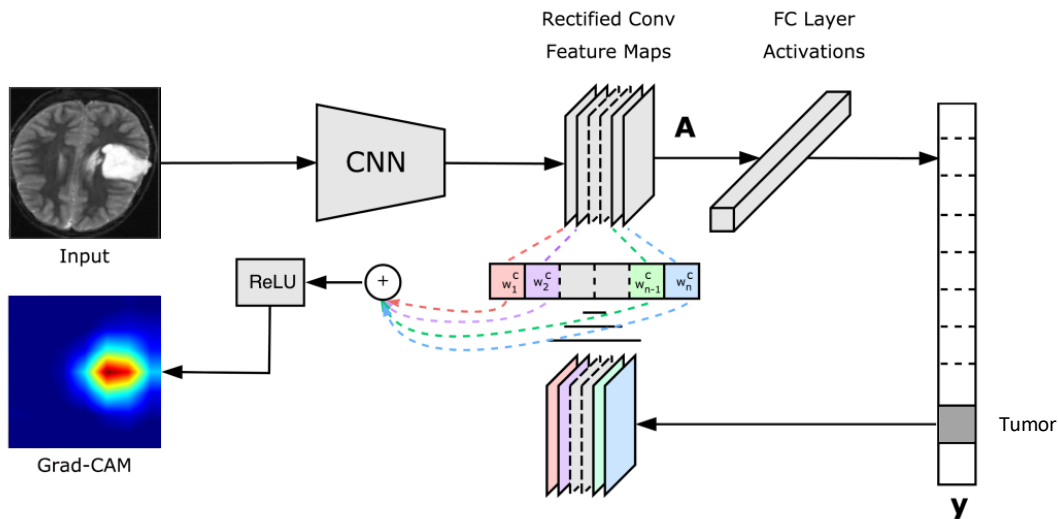


Figure 7. An illustration of the use of the Grad-CAM algorithm.

The Grad-CAM algorithm processes the feature maps generated in the last convolution layer in the CNN architecture. For this reason, the last convolution layer of the classifier model is referenced with the naming of the Grad-CAM algorithm. The heat map corresponding to the input image is created with the help of feature maps and

gradients in the relevant layer. The areas expressed in red and yellow in these heat maps represent the areas that the classifier deep learning model focuses on in class prediction. The comparison of the areas focused on by the radiologist and the classifier model on some randomly selected test images in the study is shown in Fig.8.

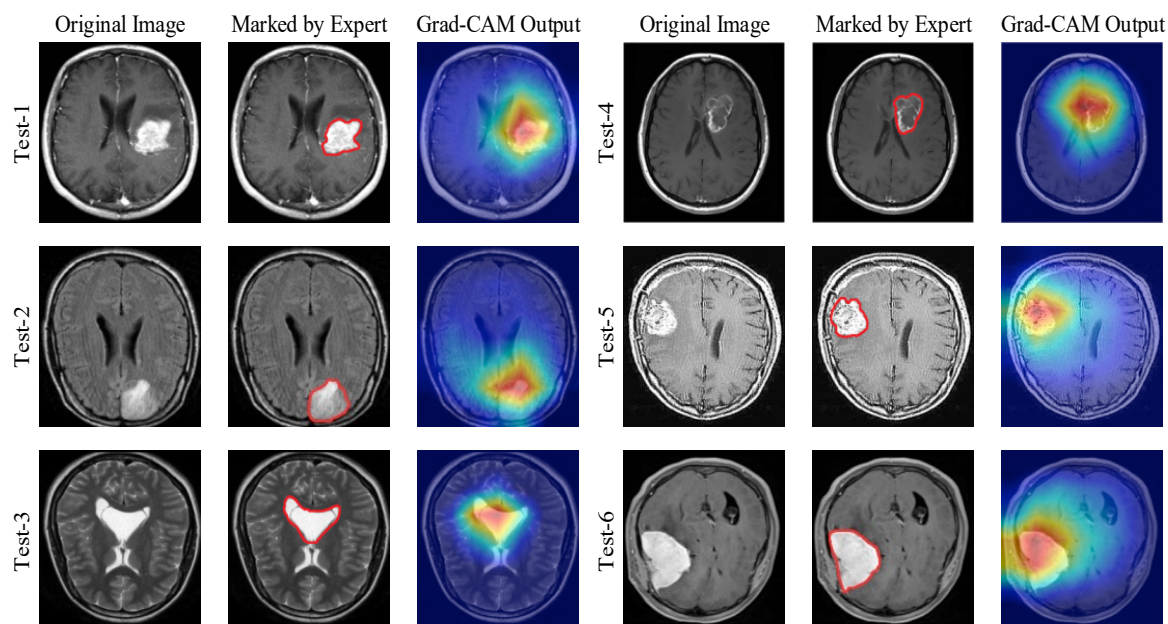


Figure 8. The output of the Grad-CAM algorithm and marks of the expert radiologist.

The comments of the radiologist regarding the areas focused by each original image and deep learning model in Fig.8 are as follows.

- The mass lesion detected by the radiologist in the T1W axial MR image, named Test-1, was correctly focused by the model.
- The mass lesion detected by the radiologist in the non-contrast T1W axial MR image called Test-2 was correctly focused by the model.
- The mass lesion detected by the radiologist in the FLAIR axial MR images, named Test-3, was correctly focused by the model.
- The model correctly focused on the mass lesion detected by the radiologist in the non-contrast T1W axial MR image called Test-4.
- The mass lesion detected by the radiologist in the T2W axial MR image, named Test-5, was correctly focused by the model.
- The model is correctly focused on the mass lesion detected by the radiologist in the contrast-enhanced T1W axial MR image called Test-6.

The model accurately focused on brain tumors that the radiologist detected and localized on the available MR images. The model also detected existing brain tumors in the unenhanced series. In addition, the model marked the masses without distinguishing between benign and malignant.

4. Conclusion

The use of machine learning methods in the health field is becoming more common daily, with the computer having more substantial computational power and increased labeled health data daily. Computer-based automatic detection systems have gained importance in processes such as diagnosing disease and monitoring the progression of the disease by physicians. Since the approaches developed in this context directly affect human life, they must have a high success rate and an explainable structure to gain trust of physicians. In this study, brain MRI images were classified as a tumor or normal with the help of the pre-trained EfficientNet-B0 deep model. The classification performance of the model and the consistency of its focus areas on the image were verified by the radiology

specialist. In this way, a reliable artificial intelligence-based system that can help physicians clinically detect brain tumors has been presented. In future studies, we aim to perform model training and testing on larger datasets by using different deep learning models.

References

- [1] Perkins A, Liu G. Primary brain tumors in adults: diagnosis and treatment. *American family physician*, 2016; 93(3): 211-217.
- [2] Villanueva-Meyer J. E, Mabray M. C, Cha S. Current clinical brain tumor imaging. *Neurosurgery*, 2017; 81(3): 397-415.
- [3] Zhang Y, Wang S, Wu H, Hu K, Ji S. Brain Tumors Classification for MR images based on Attention Guided Deep Learning Model. 43rd Annual International Conference of the IEEE Engineering in Medicine & Biology Society (EMBC), 2021; 3233-3236.
- [4] Chartrand G, Cheng P. M, Vorontsov E, Drozdal M, Turcotte S, Pal C. J, Tang A. Deep learning: a primer for radiologists. *Radiographics*, 2017; 37(7): 2113-2131.
- [5] Arsalan M, Owais M, Mahmood T, Choi J, Park K. R. Artificial intelligence-based diagnosis of cardiac and related diseases. *Journal of Clinical Medicine*, 2020; 9(3): 871.
- [6] Biswas M, Kuppili V, Saba L, Edla D. R, Suri H. S, Cuadrado-Godia, E, Suri J. S. State-of-the-art review on deep learning in medical imaging. *Front Biosci (Landmark Ed)*, 2019; 24: 392-426.
- [7] Khan, H. A, Jue W, Mushtaq M, Mushtaq M. U. Brain tumor classification in MRI image using convolutional neural network. *Math. Biosci. Eng.*, 2020; 17(5): 6203-6216.
- [8] Singh V, Sharma S, Goel S, Lamba S, Garg N. Brain Tumor Prediction by Binary Classification Using VGG-16. *Smart and Sustainable Intelligent Systems*, 2021; 127-138.
- [9] Pundir A, Kumar R. Brain Tumor Classification in MRI Images Using Transfer Learning. *Machine Learning for Intelligent Multimedia Analytics*, 2021; 307-319.
- [10] A. Hamada, Br35h: Brain Tumor Detection 2020, version 5, 2020, <https://www.kaggle.com/ahmedhamada0/brain-tumordetection>.
- [11] Tan M, Le Q. Efficientnet: Rethinking model scaling for convolutional neural networks. *International conference on machine learning*, 2019; 6105-6114.
- [12] Deng J, Dong W, Socher R, Li L. J, Li K, Fei-Fei L. Imagenet: A large-scale hierarchical image database. *Computer vision and pattern recognition*, 2009; 248-255.
- [13] Selvaraju R. R, Cogswell M, Das A, Vedantam R, Parikh D, Batra D. Grad-cam: Visual explanations from deep networks via gradient-based localization. *International conference on computer vision*, 2017; 618-626.

Classification of Hotspots in Photovoltaic Modules with Deep Learning Methods

Hakan AÇIKGÖZ^{1*}, Deniz KORKMAZ^{2*}, Çiğdem DANDIL³

¹ Electrical and Electronics Engineering, Faculty of Engineering and Natural Sciences, Gaziantep Islamic Science and Technology University, Gaziantep, Turkey

² Electrical and Electronics Engineering, Faculty of Engineering, Malatya Turgut Özal University, Malatya, Turkey
³ hakan.acikgoz@gibtu.edu.tr, ²deniz.korkmaz@ozal.edu.tr, ³cdandil@gmail.com

(Geliş/Received: 07/08/2022;

Kabul/Accepted: 07/09/2022)

Abstract: Solar energy systems are increasing their capacity in the energy industry day by day by operating with higher efficiency in parallel with technological developments. The functional operation of photovoltaic (PV) module contributes greatly to the optimal performance of these systems. On the other hand, detection and classification of faults occurring in PV modules are of vital importance in the operation and maintenance of solar energy systems. In this study, the classification of hotspots, which is one of the most common faults in Photovoltaic (PV) modules, is carried out by deep learning methods. First, data augmentation is applied to the images in the training dataset to improve the classification performance. Then, pre-trained deep learning models namely AlexNet, GoogLeNet, ShuffleNet, SqueezeNet, ResNet-50, and MobileNet-v2 are compared on the same test dataset. According to the obtained experimental results, AlexNet has the best performance with an accuracy value of 98.65%, while ResNet-50 provides the worst result with 94.59%.

Key words: Classification, Deep Learning, Hotspot, Photovoltaic Module

Fotovoltaik Modüllerdeki Sıcak Noktaların Derin Öğrenme Yöntemleriyle Sınıflandırılması

Öz: Güneş enerji sistemleri teknolojik gelişmelere paralel olarak daha yüksek verimlilikte çalışarak enerji endüstrisindeki kapasitesini her geçen gün arttırmaktadır. Fotovoltaik (PV) modül hücrelerinin işlevsel bir şekilde çalışması bu sistemlerin en uygun performansı göstermesine büyük katkı sağlamaktadır. Öte yandan, PV modül hücrelerinde meydana gelen arızaların teşhisi ve sınıflandırılması güneş enerji sistemlerinin çalışmasında ve bakımında hayati öneme sahiptir. Bu çalışmada, Fotovoltaik (PV) modül hücrelerindeki en yaygın arızalardan biri olan sıcak noktaların sınıflandırılması derin öğrenme yöntemleriyle gerçekleştirilmiştir. İlk olarak, sınıflandırma performansını arttırmak için eğitim veri setindeki görüntülere veri artırma işlemi uygulanmıştır. AlexNet, GoogLeNet, ShuffleNet, SqueezeNet, ResNet-50 ve MobileNet-v2 gibi ön eğitilmiş derin öğrenme modelleri aynı test veri seti üzerinde karşılaştırılmıştır. Elde edilen deneysel sonuçlara göre AlexNet %98.65'lik bir doğruluk değeri ile en iyi performansa sahipken ResNet-50 ise %94.59 ile en kötü sonucu sağlamıştır.

Anahtar kelimeler: Sınıflandırma, Derin öğrenme, Sıcak nokta, Fotovoltaik modül

1. Introduction

In the last decade, renewable energy sources have started to attract increasing interest, with the consumption of fossil fuels causing severe diseases and environmental pollution [1,2]. Among these renewable energy source types, one of the remarkable clean and reliable energy sources is photovoltaic (PV) based energy systems [3,4]. PV energy systems come to the fore with many advantages such as silent operation, global availability, easy installation, low cost, and pollution-free. However, the PV panels may be influenced by different types of anomalies that impress the credibility and safety of the system operation [5,6]. In addition, Uneven increases in the temperature of their cells, known as PV hotspots, can occur. Hotspot defects appear as highlighted areas in infrared images captured by the thermal Infrared (IR) imaging camera. In hotspot conditions, the affected cells begin to dissipate heat energy instead of generating electrical energy [7,8]. Therefore, early and automated hotspot detection is a crucial defect to provide the reliability of the panels.

Recently, the literature has focused on the detection and classification of hotspots. Le et al. [6] developed a hybrid feature-based support vector machine (SVM) model using infrared thermography technique for hotspots detection and classification of PV panels. They analyzed the PV panels into three different classes as healthy, non-

* Sorumlu yazar: hakan.acikgoz@gibtu.edu.tr. Yazarların ORCID Numarası: ¹0000 -0002-6432-7243, ²0000 -0002-5159-0659, ³0000 -0002-1698-1806

faulty hotspot, and faulty. Their method achieved 92% testing accuracy with low computational complexity structure. Cipriani et al. [9] proposed a convolutional neural network (CNN) model to classify the losses related to PV systems using thermographic non-destructive tests. They achieved an accuracy of 98% in tests that last a couple of minutes. In another study, Ali et al. [7] introduced an early hotspot detection using red-green scale-invariant feature transform descriptor with k-nearest neighbor (KNN) method. In this method, the thermographic is divided into non-overlapping regions and then color image descriptors are calculated for the regions. Their method outperformed all other image descriptors and machine learning combinations with 98.7% accuracy. Dhimish [10] analyzed the machine learning algorithms to early detect PV hotspots. four effective machine learning classifiers as decision tree (DT), SVM, KNN, and discriminant classifiers (DC) were used. The highest detection accuracy was obtained with DC as 98%. Su et al. [11] also proposed a deep learning-based hotspot defect detection method for PV farms. In the model, a residual channel wise attention gate network was designed and distinctive features were extracted. The global average pooling and multilayer perceptron (MLP) were used to dimension reduction of the extracted features. Their method was validated through a real defect detection system and the recall of the hotspot defects reached to 97.06%. Manno et al. [12] introduced a CNN model for use in the effective classification of thermographic images. To decrease image noise, various pre-processing strategies were assessed and they reached an accuracy of 99%. Oliveira et al. [13] presented an aerial infrared thermography analysis for four utility-scale PV plants in the northeast of Brazil. The flight campaign applied different techniques and sensors for each PV power plant. As a result, automated early hotspot defect detection and classification methods have been still studied by designing effective and robust approaches, and also their accuracy performance may still be increased.

This paper presents a comprehensive study on the classification of PV panel hotspot defects using pre-trained deep learning models on infrared thermographic images. These models with two-class classification are applied to define which model reaches a higher hotspot detection accuracy from PV modules. The used dataset is one of the publicly available datasets and it was collected from various large-scale PV farms. In addition, effective offline augmentation methods are utilized to increase and balance the class distribution. In the experimental studies, the metric results are compared and the effectiveness of the deep networks are evaluated. The rest of the paper is presented as: Section 2 describes the classification approach and collected the dataset. In Section 3, the general structures of pre-trained deep learning models are given in detail. Section 4 presents experimental studies and results. Finally, the results obtained from experimental studies are evaluated in Section 5.

2. Classification Approach and Dataset

The scheme of the developed method for the classification of hotspot faults in PV modules is shown in Figure 1. As can be seen in Figure 1, the hotspot and No-Anomaly images are obtained and data augmentation is performed. The obtained dataset is divided into training, validation, and testing dataset. Comparison studies are realized using the most widely used pre-trained deep learning models and metric results are obtained.

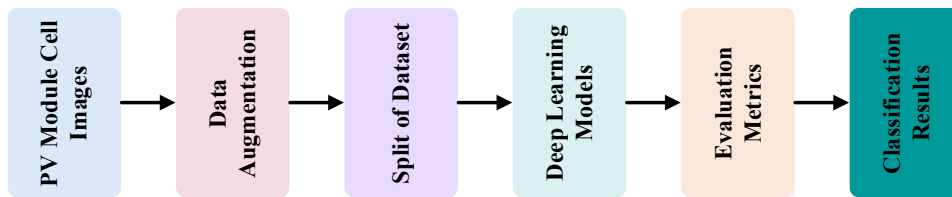


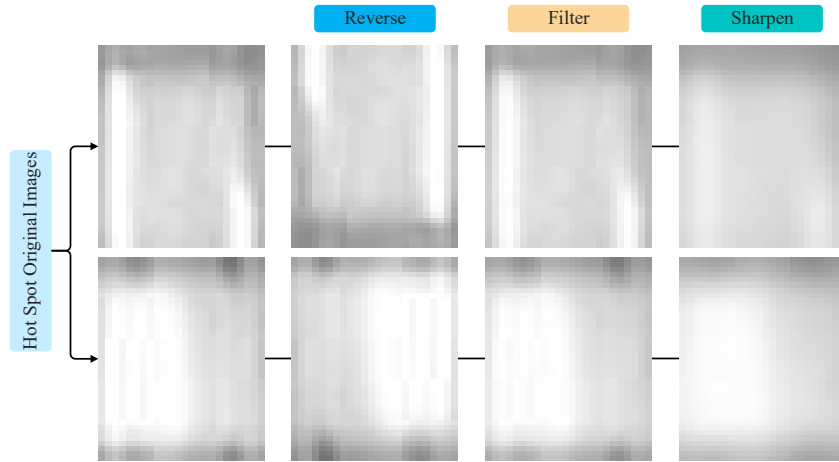
Figure 1. Overview of classification approach used in this study

A publicly available dataset is used in this study [14]. The dataset is obtained from the Raptor Maps Inc team using infrared camera modules [14]. The dataset contains a total of 10,495 images representing 495 hotspot class and 10,000 No-Anomaly class. The each of image in the dataset has 24x40 pixels. The general information about the classes in the dataset is presented in Table 1. As can be seen from Table 1, there is an imbalance in the dataset, which is directly related to the classification performance. The data augmentation is made to deal with this imbalance problem [14].

Table 1. Description of classes in dataset

Class	Number of images	Description
Hotspot	495	Hotspot and multiple hotspots on a thin-film modules
No-Anomaly	10,000	Functional solar module
Total	10,495	Total number of images

First of all, 70% of the hotspot images are divided to training, and the rest equally to validation and testing dataset. The reversing, filtering and sharpening processes are applied to images in the hotspot class. After data augmentation process, a total of 1041 synthetic hotspot images are obtained. The sample images of the data augmentation process are shown in Figure 2. Furthermore, 1388 images are obtained for the hotspot class. In the reversing, the hotspot images are rotated 180° counter clockwise. In the filtering process, two-dimensional Gaussian filtering is used. In sharpening process, a Gaussian low-pass filter with a standard deviation of 1.5 is determined.

**Figure 2.** The sample images obtained from data augmentation

In order to eliminate the imbalance in the dataset, the number of images in the No-Anomaly class is equalized to the number of images in the Hot-Spot class, providing a total of 2776 images for the training dataset. In Figure 3, the samples of the dataset divided into training, validation, and testing are presented.

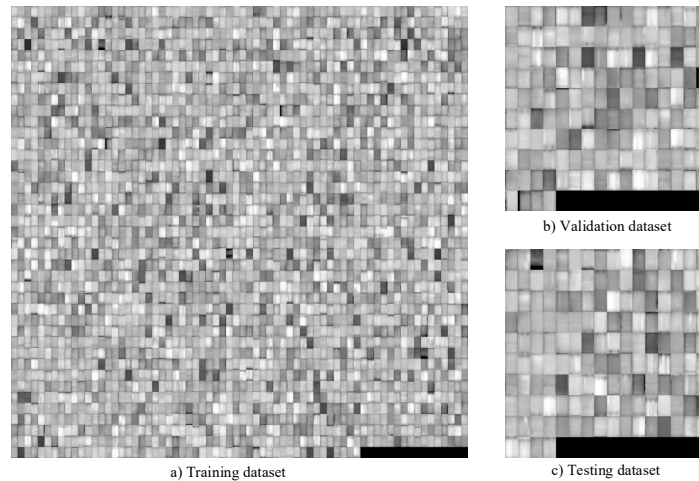


Figure 3. The images of training, validation, and testing in the dataset

3. Deep Learning Models

The deep learning models are widely used in many image processing problems. In this study, deep learning models commonly used in the literature such as AlexNet [15], ShuffleNet [16], SqueezeNet [17], ResNet-50 [18], GoogLeNet [19], and MobileNet-v2 [20] are selected. In this section, the brief information about the general features of pre-trained deep learning models is presented. The structures of the pre-trained deep models used in this study are presented in detail in Figures 4-9.

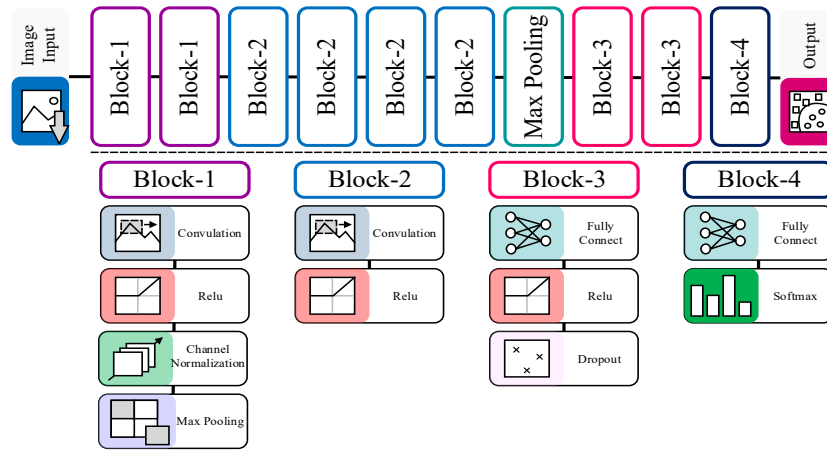


Figure 4. The general structure of AlexNet

AlexNet was proposed by Alex Krizhevsky [15] in 2012 and has features such as superior generalization ability, fast training time and high stability. AlexNet basically includes five convolution layers and three fully connected layers. The input of the AlexNet is $227 \times 227 \times 3$ with RGB depth and the size of each input image is resized according to the input of the network. The convolutions in AlexNet have filters of 96 kernels of size 11×11 , 48 kernels of size 5×5 , 384 kernels of size 3×3 , 384 kernels of size 3×3 , and 256 kernels of size 3×3 , respectively. While the first two fully-connected layers have 4096 neurons, the last one has 1000 neurons. AlexNet performs 3×3 max-pooling with a stride of 2 after convolution-1, convolution-2, and convolution-5.

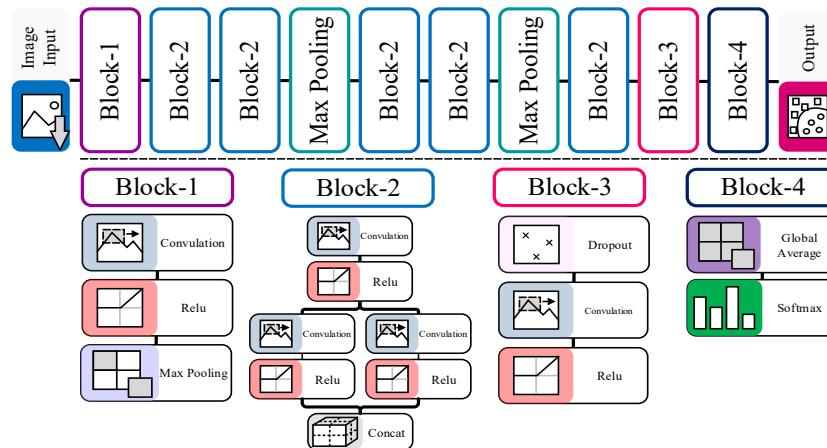


Figure 5. The general structure of SqueezeNet

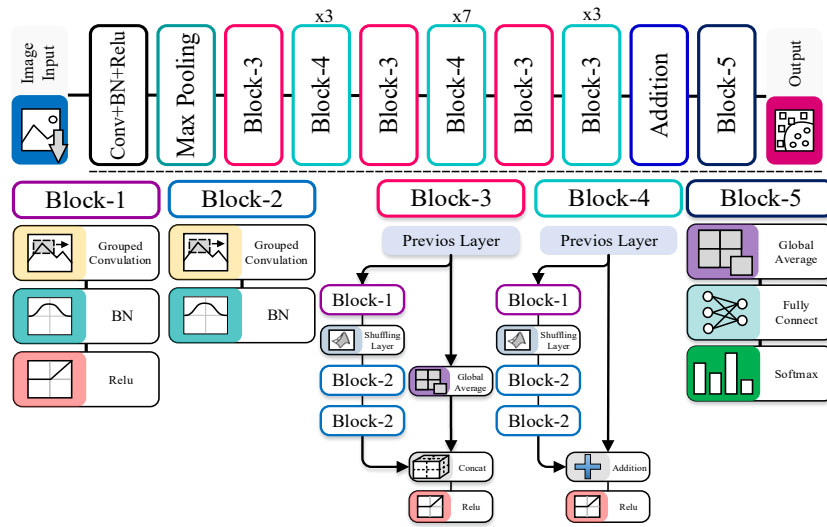


Figure 7. The general structure of ShuffleNet

ShuffleNet was developed for the use of mobile devices with very limited computing power [18]. ShuffleNet performs two operations such as pointwise group convolution and channel shuffle simultaneously to decrease the network computation cost. Through the channel shuffle process used in the network, more durable structures can be obtained with many convolution layers. The input image size of the ShuffleNet is 224×224 and it has fifty layers. The filter sizes of the grouped convolutions in the structure of the network are set as 1×1 , 3×3 , and 1×1 , respectively. The 3×3 average pooling with stride 2 is added in parallel to some units of the network.

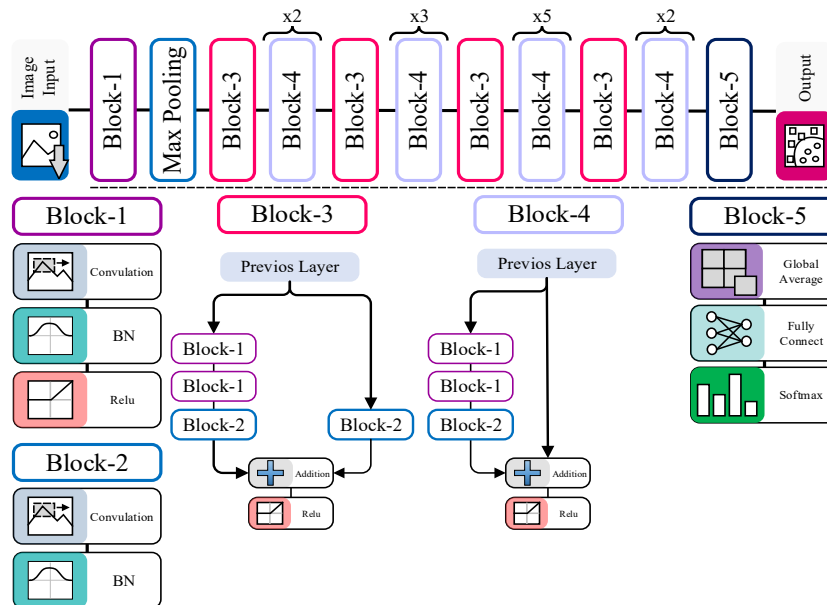


Figure 8. The general structure of ResNet-50

It is known that ResNet-50 has fifty layers [19]. The input image size of the ResNet-50 is 224×224 . The batch normalization layer is used after each convolution and before relu activation. There is a convolution with a kernel size of 7×7 with a stride of 2 at the input of the network. After adding batch normalization and relu to this convolution, the maximum pooling layer with a stride size of 2 is connected. The 1×1 , 3×3 and 1×1 filters are used in convolutions in a building blocks. An average pooling, a fully connected layer and a softmax function are used at the end of the network.

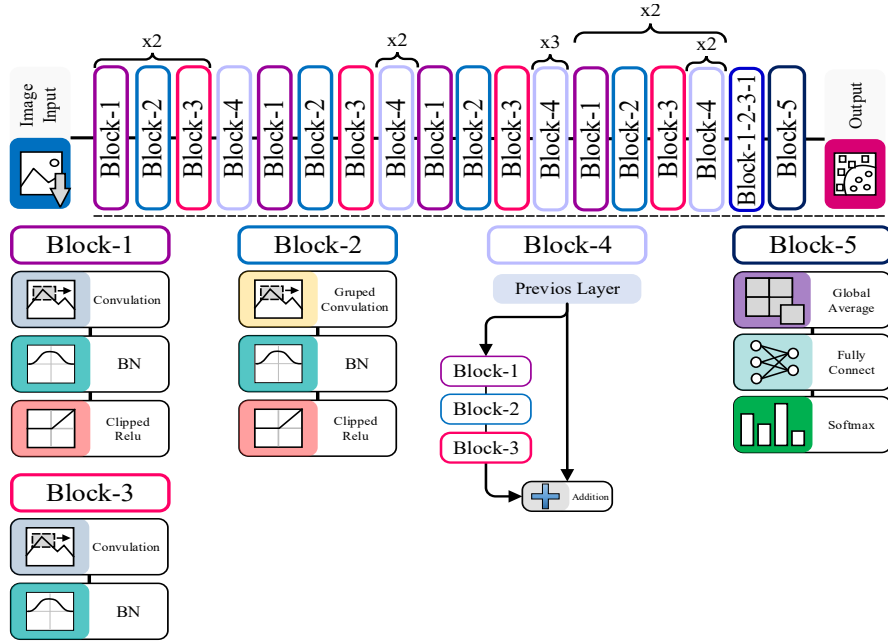


Figure 9. The general structure of MobileNet-v2

MobileNet-v2 is known as a new network developed for mobile and resource-constrained environments [20]. The network is designed to have a new module through the inverted residual with linear bottleneck. This module provides the network with a low-dimensional compressed representation feature that is expanded to high-dimensionality and filtered with a slight depth-based convolution. The input of the network is $224 \times 224 \times 3$ with RGB depth. While the 3×3 filter sizes are used in grouped convolutions in the network, the 1×1 filter sizes are used in others. MobileNet-v2 has only one global average pooling. Some parameters of the deep learning models used in this study are compared in Table 2. As can be seen from the Table 2, while AlexNet has the most parameters among models, SqueezeNet has about 50 times fewer parameters.

Table 2. Comparison of pre-trained deep learning models

Models	Input Size	No. of Layers	Parameters
ResNet-50	224x224	50	25.6M
SqueezeNet	227x227	18	1.24M
GoogLeNet	224x224	22	7M
ShuffleNet	224x224	50	1.4M
MobileNet-v2	224x224	53	3.5M
AlexNet	227x227	8	61M

AlexNet is the first main deep learning model to use GPUs for training. Since AlexNet has less depth, it needs more computation time to learn the features of the images in the dataset. ShuffleNet has less computational cost and comparatively better performance. Although GoogLeNet has relatively few parameters thanks to inception modules, it may not guarantee satisfactory results. Among the deep learning models used in this study, SqueezeNet has the least parameter. MobileNet-V2 with about 3.5M parameters can be considered as a lightweight network which has the deep separable convolution, which increases the computation cost. ResNet-50, which has relatively more parameters, uses residual blocks for better results.

4. Experimental Studies and Results

In this section, the experimental comparison studies are carried out for the classification of hotspots in photovoltaic modules. In these studies, AlexNet, ShuffleNet, SqueezeNet, ResNet-50, GoogLeNet, and

MobileNet-v2, which are commonly used pre-trained deep learning models, are preferred. The same training, validation, and test datasets are applied to each deep learning model. All of our models and studies are carried out on a computer with an Intel (R) i7-10750H CPU @2.60 GHz, NVIDIA Quadro P620 GPU, and 16 GB RAM. Experimental studies are carried out with the help of the R2022a version of Matlab. The stochastic gradient descent with momentum (SGDM) optimizer is used for error minimization with a learning rate of 1e-3. All pre-trained deep learning models are trained for 40 epochs. During training, MiniBatch size is selected as 32.

In order to statistically evaluate the obtained classification results, some performance metric values such as Accuracy, Precision, Sensitivity, Specificity, and F1-score are calculated. These metric values can be expressed mathematically as follows.

$$\text{Accuracy} = \frac{TP+TN}{TP+TN+FP+FN} \quad (1)$$

$$\text{Precision} = \frac{TP}{TP+FP} \quad (2)$$

$$\text{Sensitivity} = \frac{TP}{TP+FN} \quad (3)$$

$$\text{Specificity} = \frac{TN}{TN+FP} \quad (4)$$

$$\text{F1_score} = 2 * \frac{\text{Sensitivity} * \text{Precision}}{\text{Sensitivity} + \text{Precision}} \quad (5)$$

In the equations, expressions such as True Positive, True Negative, False Positive, and False Negative are symbolized as TP, TN, FP, and FN, respectively. Where, TP and TN represent numbers that are actually positive and actually negative, and are correctly predicted, respectively. FP and FN show the numbers that are actually in the negative and positive classes, and that is incorrectly predicted, respectively.

The main target of this study is effectively the classification of hotspots in PV modules. For this purpose, the comparison studies are carried out by deep learning models. First, all deep learning models are trained with the same training dataset and then tested. From these results, the confusion matrix is obtained. The confusion matrices of all deep learning models are presented in Figure 10. As can be clearly seen from Figure 10, AlexNet misclassifies only two images while MobileNet-v2, and ShuffleNet, GoogLeNet, SqueezeNet, and ResNet-50 misclassify 4, 4, 6, 7 and 8 images, respectively.

	AlexNet		MobileNet-v2		ShuffleNet	
Hot Spot	97.4% 74	0.0% 0	98.6% 71	3.9% 3	96.1% 73	1.4% 1
No-Anomaly	2.6% 2	100.0% 72	1.4% 1	96.1% 73	3.9% 3	98.6% 71
	Hot Spot	No-Anomaly	Hot Spot	No-Anomaly	Hot Spot	No-Anomaly
	GoogLeNet		SqueezeNet		ResNet-50	
Hot Spot	95.9% 71	4.1% 3	93.5% 72	2.8% 2	94.6% 70	5.4% 4
No-Anomaly	4.1% 3	95.9% 71	6.5% 5	97.2% 69	5.4% 4	94.6% 70
	Hot Spot	No-Anomaly	Hot Spot	No-Anomaly	Hot Spot	No-Anomaly

Figure 10. The confusion matrices

To highlight the classification performance of deep learning models, statistical evaluation metrics are calculated. The obtained results are listed in Table 3. Moreover, the bar graphs are presented in Figure 11 to better analyze the results in table 3. When the metric results in Table 3 are analyzed in terms of accuracy values, AlexNet provides the best result with 0.9865 among all deep learning models, while ResNet-50 gives the worst result with 0.9459. The accuracy values of SqueezeNet, GoogLeNet, ShuffleNet, and MobileNet-v2 are calculated as being 0.9527, 0.9595, 0.9730, and 0.9730, respectively. The AlexNet achieves 1.39%, 1.39%, 2.81%, 3.55%, and 4.29% improvement in accuracy compared to MobileNet-v2, ShuffleNet, GoogLeNet, SqueezeNet, and ResNet-50, respectively.

Table 3. The metric value comparison of deep learning models

Models	Accuracy	Precision	Sensitivity	Specificity	F1-score
ResNet-50	0.9459	0.9459	0.9459	0.9459	0.9459
SqueezeNet	0.9527	0.9351	0.9730	0.9324	0.9536
GoogLeNet	0.9595	0.9595	0.9595	0.9595	0.9595
ShuffleNet	0.9730	0.9605	0.9865	0.9595	0.9733
MobileNet-v2	0.9730	0.9861	0.9595	0.9865	0.9726
AlexNet	0.9865	0.9737	1.00	0.9730	0.9867

When deep learning models are compared in terms of error, the MobileNet-v2 achieves 0.9861 value. Those of AlexNet, ShuffleNet, GoogLeNet, SqueezeNet, and ResNet-50 are 0.9737, 0.9605, 0.9595, 0.9351, and 0.9459, respectively. Moreover, the MobileNet-v2 shows that the performance improvement of 1.27%, 2.66%, 2.77%, 5.45%, and 4.25% in precision than the AlexNet, ShuffleNet, GoogLeNet, SqueezeNet, and ResNet-50 respectively. Table 3 compares the sensitivity values of deep learning models. As can be seen, AlexNet outperforms other models with a value of 1.00. While ShuffleNet gives the best-second result with 0.9865, ResNet-50 has the worst value, which is 0.9459. The sensitivity values of SqueezeNet, GoogLeNet, and MobileNet-v2 are 0.9730, 0.9595, 0.9595, respectively.

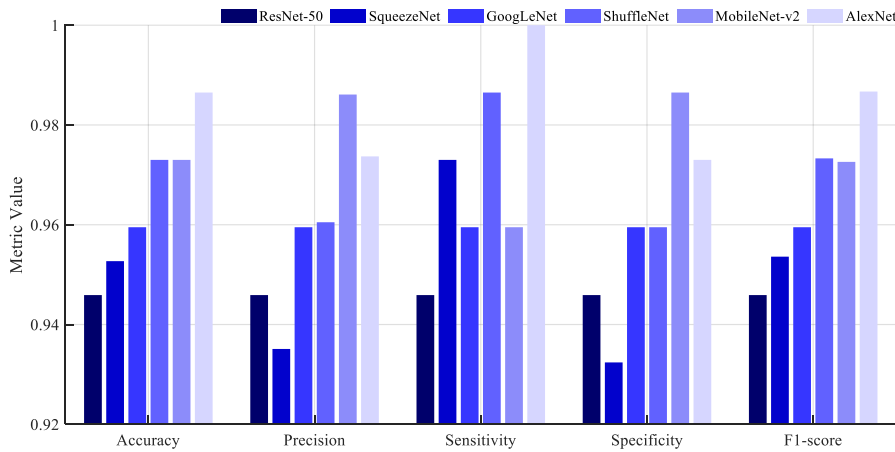


Figure 11. Comparison results of metric values for each deep learning models

When deep learning models are compared in terms of specificity values, when deep learning models are compared in terms of specificity values, MobileNet-v2 provides the best performance among all models. While AlexNet reaches the second-best result with a value of 0.9730, ResNet-50 shows the worst result with 0.9459. the MobileNet-v2 has an increase of approximately 1.39%–4.29% in terms of specificity compared to other models. When deep learning models are analyzed in terms of F1-score, AlexNet reaches the highest result with 0.9867. This result shows that the AlexNet is feasible. Those of MobileNet-v2, ShuffleNet, GoogLeNet, SqueezeNet, and ResNet-50 are calculated as being 0.9726, 0.9733, 0.9595, 0.9536, and 0.9459, respectively.

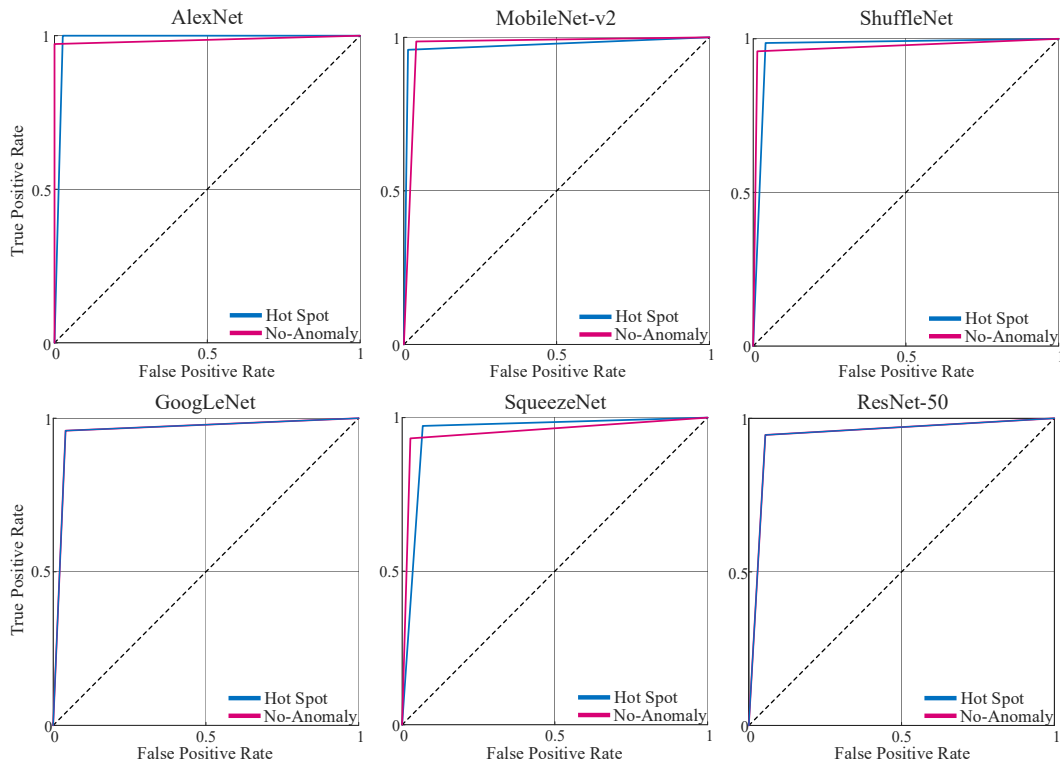


Figure 12. ROC curves of deep learning models

To get a better understanding and visualizing of the classification performances of deep learning models, Receiver Operating Characteristic (ROC) curves are given in Figure 12. As can be seen from Figure 11, AlexNet not only shows better classification ability, but also guarantees more effective results.

5. Conclusion

The fault-free operation of the PV modules directly affects the efficiency of the whole system. Although it is known that there are many fault classes in these modules, the most common fault class is the hotspot, which has an active role in the energy production of that module. For this reason, the detection and classification of hotspots in PV modules is considered as an important task. In recent years, deep learning, which is widely used in almost every sector and gives satisfactory results, has also taken its place in the solar energy sector. In this study, deep learning models namely AlexNet, MobileNet-v2, ShuffleNet, GoogLeNet, SqueezeNet, and ResNet-50 are used to classify hotspots in PV modules. All models are applied to the training dataset using the pre-trained model in the Matlab environment. The comparison studies are carried out by obtaining the values of performance evaluation metrics through experimental studies. AlexNet provides the highest accuracy, precision, and F1-score values, which are 0.9865, 1.00, and 0.9867, respectively. MobileNet-v2 reaches the highest precision and specificity values with 0.9861, and 0.9864, respectively. In future study, it is aimed to achieve better results by developing lightweight deep learning methods with different structures.

References

- [1] Korkmaz D, Acikgoz H, Yildiz C. A Novel Short-Term Photovoltaic Power Forecasting Approach based on Deep Convolutional Neural Network. *Int J Green Energy* 2021;1–15.
- [2] Korkmaz D, Acikgoz H. An efficient fault classification method in solar photovoltaic modules using transfer learning and multi-scale convolutional neural network. *Eng Appl Artif Intell* 2022;113:104959.
- [3] Korkmaz D. SolarNet: A hybrid reliable model based on convolutional neural network and variational mode decomposition for hourly photovoltaic power forecasting. *Appl Energy* 2021;300:117410.
- [4] Acikgoz H. A novel approach based on integration of convolutional neural networks and deep feature selection for short-

- term solar radiation forecasting. *Appl Energy* 2022;305:117912.
- [5] Wang Q, Paynabar K, Pacella M. Online automatic anomaly detection for photovoltaic systems using thermography imaging and low rank matrix decomposition. *J Qual Technol* 2021;0:1–14.
- [6] Ali MU, Khan HF, Masud M, Kallu KD, Zafar A. A machine learning framework to identify the hotspot in photovoltaic module using infrared thermography. *Sol Energy* 2020;208:643–51.
- [7] Ali MU, Saleem S, Masood H, Kallu KD, Masud M, Alvi MJ, et al. Early hotspot detection in photovoltaic modules using color image descriptors: An infrared thermography study. *Int J Energy Res* 2022;46:774–85.
- [8] Rahaman SA, Urmee T, Parlevliet DA. PV system defects identification using Remotely Piloted Aircraft (RPA) based infrared (IR) imaging: A review. *Sol Energy* 2020;206:579–95.
- [9] Cipriani G, D'Amico A, Guarino S, Manno D, Traverso M, Di Dio V. Convolutional neural network for dust and hotspot classification in PV modules. *Energies* 2020;13.
- [10] Dhimish M. Defining the best-fit machine learning classifier to early diagnose photovoltaic solar cells hot-spots. *Case Stud Therm Eng* 2021;25:100980.
- [11] Su B, Chen H, Liu K, Liu W. RCAG-Net: Residual Channelwise Attention Gate Network for Hot Spot Defect Detection of Photovoltaic Farms. *IEEE Trans Instrum Meas* 2021;70.
- [12] Manno D, Cipriani G, Ciulla G, Di Dio V, Guarino S, Lo Brano V. Deep learning strategies for automatic fault diagnosis in photovoltaic systems by thermographic images. *Energy Convers Manag* 2021;241:114315.
- [13] Kirsten Vidal de Oliveira A, Aghaei M, Rütther R. Aerial infrared thermography for low-cost and fast fault detection in utility-scale PV power plants. *Sol Energy* 2020;211:712–24.
- [14] Matthew M, Edward O, Vadhavkar N. Infrared Solar Module Dataset for Anomaly Detection. *Int Conf Learn Represent*. Published online 2020:1-5.
- [15] Krizhevsky, A, Sutskever, I, Hinton, GE. Imagenet classification with deep convolutional neural networks. In *Proceedings of the 25th International Conference on Neural Information Processing Systems*. 2012:1097-1105.
- [16] Zhang X, Zhou X, Lin M, Sun J. ShuffleNet: An extremely efficient convolutional neural network for mobile devices. *Proc. IEEE/CVF Conf. Comput. Vis. Pattern Recognit*. 2018:6848-6856.
- [17] Iandola FN, Han S, Moskewicz MW, Ashraf K, Dally WJ, Keutzer K. Squeezenet: Alexnet-level accuracy with 50x fewer parameters and <0.5 mb model size. *arXiv preprint arXiv:1602.07360*, 2016.
- [18] He, Kaiming, Xiangyu Zhang, Shaoqing Ren, and Jian Sun. Deep residual learning for image recognition. *Proc IEEE Comput Soc Conf Comput Vis Pattern Recognit*. 2016:770-778.
- [19] Szegedy C, Liu W, Jia Y, et al. Going deeper with convolutions. *Proc IEEE Comput Soc Conf Comput Vis Pattern Recognit*. 2015:1-9.
- [20] Sandler M, Howard A, Zhu M, Zhmoginov A, Chen LC. MobileNetV2: Inverted Residuals and Linear Bottlenecks. *Proc. IEEE/CVF Conf. Comput. Vis. Pattern Recognit*. 2018:4510-4520.

Performance Analysis of Current Multi-Objective Metaheuristic Optimization Algorithms for Unconstrained Problems

Eyüp ERÖZ^{1*}, Erkan TANYILDIZI²

¹ Software Engineering, Technology Faculty, Firat University, Elazig, Turkey

² Software Engineering, Technology Faculty, Firat University, Elazig, Turkey

*¹ eeroz@firat.edu.tr, ² etanyildizi@firat.edu.tr

(Geliş/Received: 11/08/2022;

Kabul/Accepted: 13/09/2022)

Abstract: Multi-objective optimization is a method used to produce suitable solutions for problems with more than one Objective. Various multi-objective optimization algorithms have been developed to apply this method to problems. In multi-objective optimization algorithms, the pareto optimal method is used to find the appropriate solution set over the problems. In the Pareto optimal method, the Pareto optimal set, which consists of the solutions reached by the multi-objective optimization, includes all the best solutions of the problems in certain intervals. For this reason, the Pareto optimal method is a very effective method to find the closest value to the optimum. In this study, the Multi-Objective Golden Sine Algorithm we developed (MOGoldSA), the recently published Multi-Objective Artificial Hummingbird Algorithm (MOAHA), and the Non-Dominant Sequencing Genetic Algorithm II (NSGA-II), which has an important place among the multi-objective optimization algorithms in the literature, are discussed. In order to see the performance of the algorithms on unconstrained comparison functions and engineering problems, performance comparisons were made on performance metrics

Key words: Multi-objective optimization, Pareto Optimal, unconstrained benchmark functions, performance metrics

Güncel Çok Amaçlı Metasezgisel Optimizasyon Algoritmalarının Kısıtsız Problemler için Performans Analizi

Öz: Çok amaçlı optimizasyon, birden fazla amacı bulunan problemlere uygun çözümler üretmek için kullanılan bir yöntemdir. Bu yöntemi problemlere uygulamak amacıyla çeşitli çok amaçlı optimizasyon algoritmaları geliştirilmiştir. Çok amaçlı optimizasyon algoritmalarında problemler üzerinden uygun çözüm kümesi bulmak için pareto optimal yöntemi kullanılmıştır. Pareto optimal yönteminde, çok amaçlı optimizasyonun ulaştığı çözümlerden oluşan pareto optimal kümesi, problemlerin belli aralıklardaki tüm en iyi çözümlerini içermektedir. Bu nedenle pareto optimal yöntemi, optimuma en yakın değeri bulmak için oldukça etkili bir yöntemdir. Bu çalışmada, geliştirdiğimiz Çok Amaçlı Altın Sinüs Algoritmasının (MOGoldSA), son zamanlarda yayınlanan Çok Amaçlı Yapay Sinekkuşu Algoritması (MOAHA) ve literatürde çok amaçlı optimizasyon algoritmaları içerisinde önemli yere sahip Baskın Olmayan Sıralama Genetik Algoritması II (NSGA-II) ele alınmıştır. Algoritmaların kısıtsız kıyaslama fonksiyonları ve mühendislik problemleri üzerindeki başarımını görmek için performans metrikleri üzerinde performans karşılaştırılması yapılmıştır.

Anahtar kelimeler: Çok amaçlı optimizasyon, Pareto Optimal, kısıtsız kıyaslama fonksiyonları, performans metrikleri

1. Introduction

From past to present, people have had to struggle with many problems. Problems have become more complex and difficult to solve with classical (stochastic and deterministic) methods. For this reason, the importance of modeling, calculation and algorithm studies carried out by experts on solving problems is increasing [1].

The heuristic optimization method is one of the leading methods developed to solve problems. Optimization, which is the process of producing suitable solutions in line with the objective of the problem, has an important place for the solution of problems in many areas encountered in daily life. Vehicle routing, logistics, engineering, business plan, mapping, etc. fields and engineering and benchmarking functions are examples of places where optimization is effective [2].

Various optimization algorithms have been developed for the implementation of the optimization method. In order for algorithms to produce solutions on the problem, they need to create a mathematical model for the Objective. Since mathematical modeling in complex problems is very costly and difficult, algorithms that need

* Corresponding author: eeroz@firat.edu.tr. ORCID Number of authors: ¹ [0000-0003-2670-0606](https://orcid.org/0000-0003-2670-0606), ² [0000-0003-2973-9389](https://orcid.org/0000-0003-2973-9389)

modeling are insufficient to produce solutions. Since the same is true for most linear optimization models, metaheuristic methods have been used.

Since metaheuristic methods examine the search space efficiently and actively regardless of the problem, they find the most appropriate solutions to the problems that deterministic methods cannot solve in a reasonable time. Metaheuristic methods do not always find the global optimum, but they are very useful because they produce the most effective solution to the global optimum in the fastest time [3,4]. In general, metaheuristic methods are evaluated in seven different categories: physics, mathematics, chemistry, biology, social, music and herd-based. These algorithms produce solutions by mimicking ethological, biological and physical behaviors [5].

Multi-objective optimization algorithms are being developed to produce effective solutions to problems with multiple Objectives encountered in daily life. Examples of these algorithms are the Arrow Dragonfly Algorithm (MODA)[6], Multi-Objective Ant Lion Optimization (MOALO)[7], Multi-Objective Differential Evolution (MODE)[8], Multi-Objective Gray Wolf Optimization (MOGWO)[9], Algorithms such as Multi-Objective Particle Swarm Optimization (MOPSO)[10], Non-Dominant Sequence Genetic Algorithm II (NSGA)[11] and Multi-Objective Artificial Hummingbird Algorithm (MOAHA)[12] can be given as examples of current multi-objective optimization algorithms[13].

In this study, the effects of the MOGoldSA algorithm we developed, the newly developed MOAHA and the NSGA-II metaheuristic multi-objective optimization algorithms, which have an important place in the literature, on unconstrained comparison functions and engineering problems are examined through success criteria.

2. Performance Comparison Optimization Algorithms

2.1 Multi-Objective Golden Sine Algorithms (MOGoldSA)

It is the version of Gold-SA developed for single-objective optimization algorithms, which has been made applicable to problems with more than one purpose. It is a mathematics-based metaheuristic optimization algorithm developed based on the sine function. The sine function can be defined as the coordinate of a point to the y-axis on a 1-unit radius circle whose center is the origin. It is calculated using the angle that the line drawn from the origin to the point makes with the y-axis. Since the values of the sine function with a definition range of $[-1,1]$ are repeated at regular intervals, it is characterized as a periodic function [14].

Scanning all values of the sine function in the unit circle is similar to scanning the search space in optimization problems. Based on this similarity, Gold-SA was developed. Like all other swarm-based optimization algorithms, Gold-SA starts with a randomly generated population. For population-based algorithms, it is very important to choose the first population well. As shown in Equation 1, the Gold-SA initial population aims to better scan the search space by generating a random distribution for each dimension.

$$V = \text{rand}(\text{agent_no, size}) * (\text{ub} - \text{lb}) + \text{lb} \quad (1)$$

The main purpose of metaheuristic methods is to search for the regions considered to be the best in the search area and to make sure that these areas are scanned as much as possible. Gold-SA uses the gold section method to do this as best as possible. The MOGoldSA method has been introduced in order to apply Gold-SA to multi-purpose problems due to its important features such as wide scanning of the search space, producing near-optimal results and fast working while producing solutions to problems. The pseudo-code of MOGoldSA is given in Figure 2 [12].

```

Calculate the initial population by Equation 2.1.
generate randomly based on uniform distribution as the number of search agents for each
dimension
Calculate availability of search agents
Assign top search agent as target
Create archive
while maximum iteration
    Get function values
    Find the best search agents and update Archive with Roulette wheel
    if archive is full
        Run the archive maintenance mechanism to remove one of the existing archive
    members
    Update archive by adding new solutions to archive
    else
        Update archive by adding new solutions to archive
    end if
    for search agent no
        r ← rand(0,1)
        r1 ← 2π * r
        r2 ← π * r
        for size number
            V(i,j) = V(i,j) * |sin r1| - r2 * sin r1 * |x1 * D(j) - x2 * V(i,j)|
        end for
    end for
    Find the best solution (search agent) and assign D(j) as target value
    if V(i,j) < D(j)
        then b ← x2, x2 = x1
            x1 ← a * φ + b * (1 - φ)
        else a ← x1, x1 = x2
            x2 ← a * (1 - φ) + b * φ
        if x1 == x2
            then a = random1, b = random2
                x1 = a * φ + b * (1 - φ)
                x2 = a * (1 - φ) + b * φ
        end if
    end if
end while
return The best solution set and the global optimum result obtained

```

Figure 2.1 Pseudo code of MOGoldSA

2.1 Multi-Objective Artificial Hummingbird Algorithms (MOAHA)

MOAHA is an algorithm developed by Artificial Hummingbird Algorithm (AHA) for multi-objective optimization problems[15]. MOAHA starts with a random solution set and a random artificial hummingbird population by creating a fixed number of external archives. All non-dominant solutions are archived and the visit table is initialized. The visitation chart monitors the level of hummingbird visitation of each food source and is a very important component of the MOAHA algorithm. When the food source is not visited by the hummingbird for a long time, the value in the visitation table is high. In this case, the priority of visiting hummingbirds will be increased as the food source is more voluminous. During each iteration, the MOAHA has a 50% probability of performing a guided foraging or regional foraging. During the guided search, each hummingbird updates the location for the selected target food source and the dominance relationship for the visit table. In regional foraging, updates are made according to the local population. As a result of the search, an NDS-based solution update is applied and the visit table is updated. In every 2n iterations, a migration search is performed and the solutions on the worst front are randomly started and the visit table is changed. At the end of the iteration, if the non-dominant solutions in the new population exceed the size, they are added to the archive according to the external archiving procedure based on DECD. All these processes are repeated until the maximum number of iterations is reached. Finally, the archive with the optimal solution set is returned [12].

Non-Dominant Ranking (NDS); The basic principle is that solutions dominated by fewer solutions have a higher dominance hierarchy. All solutions are ranked according to their dominance level. There are three different solution update states in NDS. These situations are shown in Figure 2.1.

- (1) If the candidate solution front is better than the current solution front, the candidate solution replaces the current solution
- (2) If the candidate solution and the current solution front are equal, the probability of being selected is 50%.
- (3) If the candidate solution front is worse than the current solution front, there is no change and the next iteration continues.

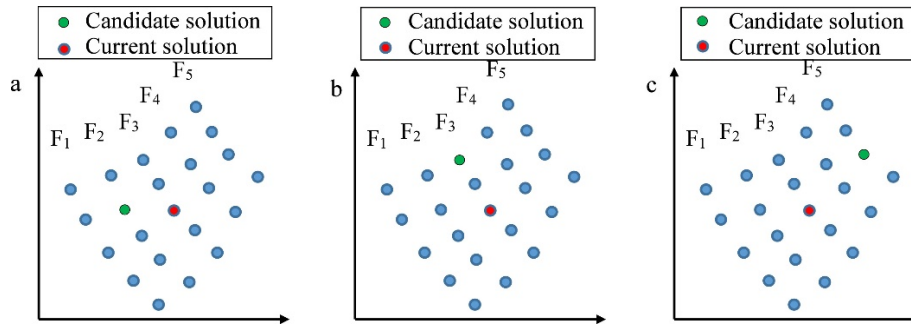


Figure 2.2 a) The front of the candidate solution is better than the front of the current solution, b) The probability of choosing between the candidate and existing solutions is 50%, c) The front of the current solution is better than the front of the candidate solution [12]

DECD method; The crowd distance method is an effective parameterless method to increase the variety of solutions [16]. For this reason, it is used in most multi-objective optimization algorithms to maintain a fixed size external archive by removing excessive solutions with smaller crowd distance. When a solution is removed, the order of the crowd distance of the remaining solutions will change. Therefore, the next solution to be removed in terms of the initial crowd order may not have the current crowd order, reducing the variety of solutions in the archive. The crowd-distance-based archiving procedure is ineffective in maintaining the sustainable diversity of the optimal solution set. Therefore, an external archive with DECD is recommended. In the DECD method, when the solution with the minimum crowd distance present in the optimal solution set is removed, only the crowd distances of the solutions adjacent to the removed solution need to be updated and the crowd distances of the remaining solutions do not change. To generate n solutions to create an external archive using the DECD method, the crowd distances of the $2n$ solutions need to be recalculated.

While adding multiple strategies, the theoretical analysis is as follows;

- (1) An external archive is created to record non-dominant optimal solutions. Using the archive for storage can greatly benefit all multi-objective optimization algorithms [17]. The DECD method is used to manage the solutions in the archive. It has been proven in the literature that the translation distance is suitable for maintaining solution diversity. A phase out strategy can significantly improve solution delivery [18]. Therefore, DECD can benefit uniformity and solution diversity.
- (2) The NDS method can count the distribution of all solutions on the fronts that can be easily compared while performing the sorting [16]. Thus, better non-dominant solutions may be kept in the archive. It can be passed to the next iteration to allow other individuals to search. In other words, NDS can facilitate the algorithm to reach optimal solutions.

2.3 Non-Dominant Sorting Genetic Algorithm II (NSGA-II)

Non-Dominant Sorting Genetic Algorithm II (NSGA-II) is a multi-objective genetic algorithm proposed by Deb et al. in 2002. It is an extension and development of the NSGA previously proposed by Srinivas and Deb in 1995. In the structure of NSGA-II, in addition to genetic operators, crossover and mutation, two special multi-objective operators and mechanisms have been defined and used.

Non-dominated Sorting: Population is sorted and sorted by F_1, F_2 , etc. is partitioned. Here F_1 (first front part) shows the approximate Pareto front. Crowding Distance: It is a sorting mechanism between members of a front where each other dominates or dominates. These sequencing mechanisms are used in conjunction with genetic selection operators (usually Tournament Selection Operator) to create the next generation population [11]. The pseudo code of NSGA II is given in Table 4.3.

```

Initialize population: P
Generate random population size: N
Evaluate Goal Values
Assign Sort (level) by Pareto order
Create Child Population
    Binary Tournament Selection
    Recombination and Mutation
For fi = 1 to g do
    For Every Parent and Child of the Population
        Sort (level) assignment according to Pareto order
        Creates sets of non-dominant solutions
        Determine crowd distance
        Cycle adding new solutions to the next generation, from the first front to N
    individuals
    end
    Choose spots on lower levels with high crowd distance
    create next generation
        Binary Tournament Selection
        Recombination and Mutation
    end
end
    
```

Figure 2.3 Psuedo code of NSGA-II

3. Experiments and Results

In order to test the success of the developed method, the performance values of 11 different unconstrained comparison functions (unconstrained function and engineering problems) in the literature were examined. The mathematical expressions of some of the functions used are given in Table 3.1.

Table 3.1 Mathematical representation of the Unconstrained functions used

F	LIMIT OF VARIABLE	OBJECTIVE FUNCTIONS
ZDT1	$x_i \in [0,1]$ $i = 1, \dots, n$ $n = 30$	$f_1(x) = x_1$ $f_2(x) = g(x) \left(-\sqrt{f_1/g(x)} \right)$ $g(x) = 1 + 9 \left(\sum_{i=2}^m x_i \right) / (n - 1)$
ZDT6	$x_i \in [0,1]$ $i = 1, \dots, n$ $n = 10$	$f_1(x) = 1 - \exp(-4x_1) \sin^6(\pi x_1)$ $f_2(x) = g(x) (1 - (x_1/g(x))^2)$ $g(x) = 1 + 9 \left[\left(\sum_{i=2}^m x_i / (n - 1) \right) \right]^{0.25}$
FON	$x_i \in [-4,4]$ $i = 1, \dots, n$ $n = 10$	$f_1(x) = 1 - \exp \left(- \sum_1^3 \left(x_i - \frac{1}{\sqrt{3}} \right)^2 \right)$

Table 3.1 Mathematical representation of the Unconstrained functions used (continued)

F	LIMIT OF VARIABLE	OBJECTIVE FUNCTIONS
KUR	$x_i \in [-5,5]$ $i = 1, \dots, n$ $n = 3$	$f_1(x) = \sum_{i=1}^{n-1} \left(-10 \exp \left(-0.2 \sqrt{x_i^2 + \sqrt{x_{i+1}^2}} \right) \right)$ $f_2(x) = \sum_{i=1}^n (x_i ^{0.8} + 5 \sin x_i^3)$
POLO	$x_i \in [-\pi, \pi]$ $i = 1, \dots, n$ $n = 2$	$f_1(x) = [1 + (A_1 - B_1)^2 + (A_2 - B_2)^2]$ $f_2(x) = [(x_1 + 3)^2 + (x_2 + 1)^2]$ $A_1 = 0.5 \sin 1 - 2 \cos 1 + \sin 2 - 1.5 \cos 2$ $A_2 = 1.5 \sin 1 - \cos 1 + 2 \sin 2 - 0.5 \cos 2$ $B_1 = 0.5 \sin x_1 - 2 \cos x_1 + \sin x_2 - 1.5 \cos x_2$ $B_2 = 1.5 \sin x_1 - \cos x_1 + 2 \sin x_2 - 0.5 \cos x_2$
FBTP	$1 \leq x_1, x_4 \leq 3$ $\sqrt{2} \leq x_2, x_3 \leq 3$ $F=10, E=2e5, L=200$	$\min f_1(x) = L(2x_1 + \sqrt{2x_2} + \sqrt{x_3} + x_4)$ $\min f_2(x) = (F \frac{L}{E}) \left(\frac{2}{x_2} + 2 \frac{\sqrt{2}}{x_2} - 2 \frac{\sqrt{2}}{x_3} + \frac{2}{x_4} \right)$
GEAR	$x_i \in [12,60]$ $i = 1, \dots, n$ $n = 4$	$f_1(x) = \left(\left(\frac{1}{6.931} \right) - \left(\frac{x_1 x_2}{x_3 x_4} \right) \right)^2$ $f_2(x) = \max ([x_1, x_2, x_3, x_4])$

The criteria used to evaluate the success of the developed algorithms are called performance criteria. In our study, performance criteria, which have taken place in the literature and are frequently used in the comparison of multi-objective optimization algorithms, are used. These; Distance Distance (SE)[19], Inverse Distance Distance (RGD)[19,20], Space(S)[21], Spread (SP)[22], Maximum Spread(MS)[22,23] and High Volume Indicator (HV)[19] are performance measurement metrics. The explanations of the metrics are given in Table 3.2.

Table 3.2 Performance Criteria Used

Metric Name	Criteria	Definition
GD	Convergence	The lower the GD value, the better for convergence.
RGD	Convergence	The lower the RGD value, the better for convergence.
S	Variation	The lower the S value, the better for convergence.
SP	Spread	The higher the SP value, the better for propagation.
MS	Spread	The higher the MS value, the better for propagation.
HV	Convergence and Diversity	Higher HV value is better for all criteria

When Table 3.3 is looked at, statistical data are seen according to GD and RGD criteria. According to the GD criterion, MOGoldSA achieved 9/11 and MOAHA 2/11 success out of 11 comparison functions. When compared according to the RGD criterion, the MOAHA algorithm was successful at a rate of 9/11, and the MOGoldSA was successful at a rate of 2/11. In this case, the superiority of MOGoldSA according to the GD success metric and MOAHA according to the RGD criterion is clearly seen.

Looking at Table 3.4, statistical data according to MS and S criteria can be seen. In these criteria, as seen in Table 3.2, higher for MS and lower for S means better. Accordingly, MOGoldSA 4/11 and NSGA-II 7/11 were successful for the MS criterion. In the S criterion, 4/11 MOGoldSA, 6/11 MOAHA and 1/11 NSGA-II algorithms were successful.

Table 3.3 Statistical data according to GD and RGD criteria

F	I	MOGOLDSA	MOAHA	NSGA-II	MOGOLDSA	MOAHA	NSGA-II
		GD			RGD		
FBTP	Best	1,3538	22,2135	1,522E+04	4,8131	100,4478	1,344E+04
	Mean	1,7139	22,2268	1,724E+06	5,3122	113,8351	4,596E+04
	Worst	2,2770	22,2396	3,301E+07	6,0131	127,9738	2,770E+05
	Standart	0,2163	0,0059	7,365E+06	0,3271	0,0855	6,400E+04
	Time	394,6623	207,6105	4236,8051	394,6623	207,6105	4236,8051
GEAR	Best	4,852E+04	519,4864	1,371E+10	5,431E+04	364,8572	1,746E+07
	Mean	1,179E+05	573,0392	3,826E+10	7,558E+04	402,6668	5,789E+09
	Worst	3,278E+05	626,3775	1,324E+11	1,368E+05	489,9123	3,884E+10
	Standart	6,615E+04	266,1139	3,176E+10	2,339E+04	285,6714	1,052E+10
	Time	299,9048	215,4202	4523,8692	299,9048	215,4202	4523,8692
FON	Best	0,0010	0,0046	0,0022	0,0056	0,0014	0,0046
	Mean	0,0013	0,0049	0,0025	0,0062	0,0018	0,0049
	Worst	0,0018	0,0051	0,0030	0,0076	0,0020	0,0057
	Standart	0,0002	0,0001	0,0003	0,0004	0,0001	0,0003
	Time	430,5992	167,6028	4338,8464	430,5992	167,6028	4338,8464
KUR	Best	16,0989	15,6197	16,1477	15,5874	16,1614	15,6148
	Mean	16,1460	15,6336	16,1936	15,5995	16,1736	15,6299
	Worst	16,1950	15,6388	16,2691	15,6140	16,1922	15,6399
	Standart	0,0289	0,0047	0,0270	0,0060	0,0086	0,0077
	Time	213,2565	131,9476	4406,5289	213,2565	131,9476	4406,5289
POL	Best	0,0303	0,0687	0,3466	0,1083	0,0216	1,2796
	Mean	0,2755	0,0745	0,4699	0,1468	0,0566	3,0514
	Worst	0,5155	0,0827	0,6717	0,1838	0,0876	9,6327
	Standart	0,1651	0,0036	0,1122	0,0234	0,0243	3,3753
	Time	224,9433	189,4781	4294,0028	224,9433	189,4781	4294,0028
VIE	Best	0,0067	0,0506	16,2128	0,0472	0,0017	0,1080
	Mean	0,0124	0,0550	18,5965	0,0711	0,0020	0,1323
	Worst	0,0221	0,0611	19,8853	0,1124	0,0024	0,1779
	Standart	0,0048	0,0028	0,9337	0,0138	0,0002	0,0175
	Time	545,3776	183,1814	4870,8179	545,3776	183,1814	4870,8179
ZDT1	Best	0,0007	0,0046	7,6003	0,0065	0,0012	6,0681
	Mean	0,0017	0,0049	8,8265	0,0076	0,0016	6,9284
	Worst	0,0038	0,0052	9,6329	0,0103	0,0022	7,6887
	Standart	0,0007	0,0002	0,6086	0,0010	0,0003	0,4094
	Time	662,2493	141,3644	4053,5786	662,2493	141,3644	4053,5786
ZDT2	Best	0,0004	0,0047	6,223E+07	0,0059	0,0005	1,757E+03
	Mean	0,0005	0,0049	1,508E+11	0,0073	0,0012	4,575E+05
	Worst	0,0006	0,0053	2,645E+12	0,0083	0,0022	7,931E+06
	Standart	0,0000	0,0002	5,921E+11	0,0005	0,0004	1,762E+06
	Time	702,9784	157,1703	4786,8025	702,9784	157,1703	4786,8025
ZDT3	Best	0,0011	0,0052	1,4137	0,0068	0,0009	1,8811
	Mean	0,0015	0,0053	7,7594	0,0086	0,0011	7,1750
	Worst	0,0024	0,0056	12,3287	0,0144	0,0012	12,6277
	Standart	0,0003	0,0097	3,2963	0,0016	0,0008	3,0546
	Time	442,1689	142,1434	4218,0993	442,1689	142,1434	4218,0993
ZDT4	Best	0,0021	0,0047	1,5646	0,0070	0,0010	0,7822
	Mean	0,0036	0,0048	4,2266	0,0090	0,0013	3,5352
	Worst	0,0061	0,0050	17,4885	0,0112	0,0017	17,6962
	Standart	0,0010	0,0074	5,4102	0,0012	0,0002	5,7539
	Time	347,9827	152,1434	4269,7994	347,9827	152,1434	4269,7994
ZDT6	Best	0,0003	0,0036	7,877E+36	0,0055	0,0003	7,878E+36
	Mean	0,0003	0,0036	1,449E+44	0,0068	0,0402	1,449E+44
	Worst	0,0004	0,0038	1,408E+45	0,0091	0,1488	1,408E+45
	Standart	0,0000	0,0002	4,323E+44	0,0009	0,0408	4,323E+44
	Time	683,4443	207,2610	5032,5692	683,4443	207,2610	5032,5692

Table 3.4 Statistical data according to MS and S criteria

F	I	MOGOLDSA	MOAHA	NSGA-II	MOGOLDSA	MOAHA	NSGA-II
		MS			S		
FBTP	Best	545,7294	0,6163	8,839E+02	78,7184	80,5914	2,442E+02
	Mean	551,7484	0,5908	1,735E+06	134,2362	121,2974	2,897E+05
	Worst	553,3824	0,5627	3,380E+07	176,2839	157,2897	5,550E+06
	Standart	1,9343	0,0146	7,547E+06	26,9925	17,3091	1,238E+06
	Time	394,6623	207,6105	4236,8051	394,6623	207,6105	4236,8051
GEAR	Best	1,021E+07	0,4672	3,283E+10	1,964E+06	205,1385	1,746E+09
	Mean	1,167E+07	0,3276	6,638E+10	2,628E+06	279,4360	8,706E+09
	Worst	1,282E+07	0,2764	1,271E+11	3,357E+06	317,7173	3,110E+10
	Standart	8,638E+05	0,0469	2,844E+10	3,650E+05	299,9545	7,029E+09
	Time	299,9048	215,4202	4523,8692	299,9048	215,4202	4523,8692
FON	Best	1,3732	0,1784	0,0022	0,0785	0,0626	0,0747
	Mean	1,3832	0,1411	0,0025	0,0939	0,0826	0,0981
	Worst	1,3884	0,1149	0,0030	0,1144	0,0970	0,1124
	Standart	0,0054	0,0152	0,0003	0,0087	0,0085	0,0097
	Time	430,5992	167,6028	4338,8464	430,5992	167,6028	4338,8464
KUR	Best	12,6658	0,8029	16,1477	1,2163	1,1087	1,8929
	Mean	12,8601	0,7923	16,1936	1,6905	1,5875	2,1941
	Worst	12,8978	0,7842	16,2691	2,1380	2,0207	2,6364
	Standart	0,0541	0,0050	0,0270	0,2524	0,2989	0,1932
	Time	213,2565	131,9476	4406,5289	213,2565	131,9476	4406,5289
POL	Best	29,2133	0,4224	0,3466	2,6133	3,0190	3,5888
	Mean	31,4311	0,2931	0,4699	4,7876	3,7678	4,5154
	Worst	32,8554	0,1967	0,6717	6,2262	5,0254	5,5066
	Standart	1,2887	0,0863	0,1122	0,9793	0,5071	0,4832
	Time	224,9433	189,4781	4294,0028	224,9433	189,4781	4294,0028
VIE	Best	8,0552	0,7767	16,2128	1,4520	1,7465	15,8646
	Mean	8,3637	0,7223	18,5965	1,9821	2,0917	20,4540
	Worst	8,4388	0,6566	19,8853	2,6379	2,5596	25,8887
	Standart	0,0800	0,0349	0,9337	0,3704	0,2333	2,4413
	Time	545,3776	183,1814	4870,8179	545,3776	183,1814	4870,8179
ZDT1	Best	1,3606	0,1841	7,6003	0,0559	0,0505	0,1332
	Mean	1,3917	0,1522	8,8265	0,0717	0,0697	0,6825
	Worst	1,4088	0,1210	9,6329	0,0912	0,0882	0,9233
	Standart	0,0125	0,0161	0,6086	0,0100	0,0089	0,2263
	Time	662,2493	141,3644	4053,5786	662,2493	141,3644	4053,5786
ZDT2	Best	1,3643	0,1764	6,223E+07	0,0625	0,0568	2,457E+06
	Mean	1,3941	0,1517	1,508E+11	0,0769	0,0749	1,324E+11
	Worst	1,4111	0,1140	2,645E+12	0,0883	0,0955	2,621E+12
	Standart	0,0152	0,0158	5,921E+11	0,0061	0,0089	5,857E+11
	Time	702,9784	157,1703	4786,8025	702,9784	157,1703	4786,8025
ZDT3	Best	1,9235	0,2551	1,4137	0,1825	0,1515	0,0000
	Mean	1,9466	0,2186	7,7594	0,2211	0,1946	1,5494
	Worst	1,9648	0,1931	12,3287	0,2711	0,2371	7,4420
	Standart	0,0122	0,0192	3,2963	0,0264	0,0236	1,8608
	Time	442,1689	142,1434	4218,0993	442,1689	142,1434	4218,0993
ZDT4	Best	1,3938	0,1821	1,5646	0,0535	0,0576	0,2266
	Mean	1,4117	0,1609	4,2266	0,0690	0,0695	0,5705
	Worst	1,4141	0,1403	17,4885	0,0886	0,0810	1,0606
	Standart	0,0046	0,0136	5,4102	0,0092	0,0063	0,2767
	Time	347,9827	152,1434	4269,7994	347,9827	152,1434	4269,7994
ZDT6	Best	1,1466	1,7003	7,877E+36	0,0697	0,0443	3,938E+21
	Mean	1,1670	0,9235	1,449E+44	0,0864	0,2547	3,662E+40
	Worst	1,1687	0,1086	1,408E+45	0,1085	0,7843	4,127E+41
	Standart	0,0049	0,7189	4,323E+44	0,0113	0,2629	1,034E+41
	Time	683,4443	207,2610	5032,5692	683,4443	207,2610	5032,5692

A high value in these criteria indicates the ideal solution. While NSGA-II 6/11, MOAHA 3/11 and MOGoldSA 2/11 were successful according to SP criteria, MOAHA 4/11 and NSGA-II 7/11 success rates were statistically successful according to HV criteria.

Table 3.5 Statistical results according to SP and HV criteria

F	I	MOGOLDSA	MOAHA	NSGA-II	MOGOLDSA	MOAHA	NSGA-II
		SP			HV		
FBTP	Best	0,8277	1,0506	0,9921	0,0000	0,0000	1,0000
	Mean	0,9161	1,0506	1,1328	0,0000	0,0000	1,0000
	Worst	0,9899	1,0506	1,4065	0,0000	0,0000	1,0000
	Standart	0,0525	0,0456	0,1524	0,0000	0,0000	0,0000
	Time	394,6623	207,6105	4236,8051	394,6623	207,6105	4236,8051
GEAR	Best	0,7453	0,7890	1,1597	0,8910	0,9040	0,9920
	Mean	0,8089	0,7936	1,3023	0,6582	0,6859	0,2377
	Worst	0,8954	0,8023	1,3753	0,0000	0,0000	0,0000
	Standart	0,0445	0,0024	0,0628	0,2848	0,3312	0,3811
	Time	299,9048	215,4202	4523,8692	299,9048	215,4202	4523,8692
FON	Best	0,6229	0,3619	0,2776	0,0785	0,0040	0,0747
	Mean	0,7041	0,3623	0,3284	0,0939	0,0009	0,0981
	Worst	0,7831	0,3626	0,3669	0,1144	0,0000	0,1124
	Standart	0,0491	0,0002	0,0293	0,0087	0,0010	0,0097
	Time	430,5992	167,6028	4338,8464	430,5992	167,6028	4338,8464
KUR	Best	0,8811	0,9901	0,8316	1,2163	1,0000	1,8929
	Mean	0,9085	0,9901	0,8418	1,6905	0,8983	2,1941
	Worst	0,9276	0,9901	0,8590	2,1380	0,8550	2,6364
	Standart	0,0156	0,0005	0,0069	0,2524	0,0465	0,1932
	Time	213,2565	131,9476	4406,5289	213,2565	131,9476	4406,5289
POL	Best	1,0821	1,0812	0,7580	2,6133	0,7750	3,5888
	Mean	1,1438	1,0832	1,0109	4,7876	0,1133	4,5154
	Worst	1,1919	1,0884	1,1176	6,2262	0,0000	5,5066
	Standart	0,0320	0,0030	0,1217	0,9793	0,2768	0,4832
	Time	224,9433	189,4781	4294,0028	224,9433	189,4781	4294,0028
VIE	Best	0,7333	0,8686	0,9875	1,4520	1,0000	15,8646
	Mean	0,8610	0,8686	1,0218	1,9821	0,6671	20,4540
	Worst	0,9945	0,8686	1,0582	2,6379	0,4160	25,8887
	Standart	0,0654	0,0000	0,0186	0,3704	0,2061	2,4413
	Time	545,3776	183,1814	4870,8179	545,3776	183,1814	4870,8179
ZDT1	Best	0,6312	0,2776	0,8175	0,0559	0,2430	0,1332
	Mean	0,7551	0,2776	0,8601	0,0717	0,0975	0,6825
	Worst	0,8869	0,2776	1,0232	0,0912	0,0000	0,9233
	Standart	0,0695	0,0000	0,0432	0,0100	0,1121	0,2263
	Time	662,2493	141,3644	4053,5786	662,2493	141,3644	4053,5786
ZDT2	Best	0,6657	0,2293	1,0127	0,0625	0,0000	2,457E+06
	Mean	0,7834	0,2293	1,2470	0,0769	0,0000	1,324E+11
	Worst	0,8453	0,2293	1,3996	0,0883	0,0000	2,621E+12
	Standart	0,0430	0,0000	0,1175	0,0061	0,0000	5,857E+11
	Time	702,9784	157,1703	4786,8025	702,9784	157,1703	4786,8025
ZDT3	Best	0,8497	0,9671	0,7542	0,1825	1,0000	0,0000
	Mean	0,9385	0,9671	0,9655	0,2211	0,9500	1,5494
	Worst	1,0533	0,9671	1,3790	0,2711	0,0000	7,4420
	Standart	0,0580	0,0000	0,1483	0,0264	0,2236	1,8608
	Time	442,1689	142,1434	4218,0993	442,1689	142,1434	4218,0993
ZDT4	Best	0,6315	0,2770	0,9092	0,0535	0,2690	0,2266
	Mean	0,6956	0,2770	0,9555	0,0690	0,1332	0,5705
	Worst	0,7693	0,2770	1,0041	0,0886	0,0000	1,0606
	Standart	0,0379	0,0000	0,0304	0,0092	0,1241	0,2767
	Time	347,9827	152,1434	4269,7994	347,9827	152,1434	4269,7994
ZDT6	Best	0,7094	0,1692	0,8813	0,0697	0,0000	3,938E+21
	Mean	0,8393	0,5665	0,9938	0,0864	0,0000	3,662E+40
	Worst	0,9498	0,8606	1,0613	0,1085	0,0000	4,127E+41
	Standart	0,0714	0,3338	0,0378	0,0113	0,0000	1,034E+41
	Time	683,4443	207,2610	5032,5692	683,4443	207,2610	5032,5692

4. Conclusion

In the study, the performance of current multi-objective optimization algorithms on unconstrained comparison functions and unconstrained engineering problems has been evaluated. While evaluating, MOAHA, which is the most up-to-date multi-objective optimization algorithm, NSGA-II, which is a very useful algorithm with its success in multi-objective problems, and MOGoldSA algorithms, which we brought to the literature in our master's study and which revealed very efficient results, were used. The studies were carried out equally for each algorithm and were evaluated according to the success metrics based on the literature while comparing the performance. According to this evaluation, on unconstrained comparison functions and engineering problems, MOGoldSA according to GD and S criteria, NSGA-II according to MS, SP and HV criteria, and finally MOAHA multi-objective optimization algorithms according to RGD criteria were superior.

References

- [1] K. Murty, "Optimization Models For Decision Making", http://wwwpersonal.umich.edu/~murty/books/opti_model/junior-0.pdf), 2003.
- [2] E. Eröz and E. Tanyildizi, "Çok Amaçlı Metasezgisel Optimizasyon Algoritmalarının Performans Karşılaştırması," 2019 International Artificial Intelligence and Data Processing Symposium (IDAP), 2019, pp. 1-11, doi: 10.1109/IDAP.2019.8875955.
- [3] E. Talbi, "Metaheuristic: Design to Implementation, 2nd Edition", New Jersey: Wiley, 2009.
- [4] Alataş. B., "Kaotik Haritalı Parçacık Sürü Optimizasyonu Algoritmaları Geliştirme" 2007.
- [5] S. Mirjalili, "Dragonfly Algorithm: a new meta-heuristic optimization technique for solving single-objective, discrete, and multi-objective problems" *Neural Comput & Applic* 27, pp. 1053-1073, 2016.
- [6] S. Mirjalili, "Dragonfly Algorithm: a new meta-heuristic optimization technique for solving single-objective, discrete, and multi-objective problems" *Neural Comput & Applic* 27, pp. 1053-1073, 2016.
- [7] S. M. P. J. S. S., "Multi-objective ant lion optimizer: a multi-objective optimization algorithm for solving engineering problems," *Appl Intell*, DOI 10.1007/s10489-016-0825-8, 2016.
- [8] K. P. Rainer S., "Differential Evolution – A Simple and Efficient Heuristic for Global Optimization over Continuous Spaces," *Journal of Global Optimization* 11, pp. 341-359, 1997.
- [9] S. S. S. M. L. S. C. Seyedali M., "Multi-objective grey Wolf optimizer: A novel Algorithm for multi-criterion Optimization," *Expert Systems With Applications* 47, pp. 106-119, 2016.
- [10] G. P. M. L. C.A.C. Coello, "Handling multiple objectives with particle swarm Optimization," *IEEE Transactions on Evolutionary Computation* Volume: 8, Issue: 3, 2004.
- [11] K. D. N. Sirinivas, "Multiobjective Optimization Using Nondominated Sorting in Genetic Algorithms," *Journal of Evolutionary Computation*, Vol. 2, No. 3, pp. 221-248, 1994.
- [12] Zhao W, Zhang Z, Mirjalili S, Wang L, Khodadadi N, Mirjalili SM, "An effective multi-objective artificial hummingbird algorithm with dynamic elimination-based crowding distance for solving engineering design problems", *Computer Methods in Applied Mechanics and Engineering*, 2022; 398, <https://doi.org/10.1016/j.cma.2022.115223>
- [13] A. B., "Kaotik Haritalı Parçacık Sürü Optimizasyonu Algoritmaları Geliştirme, Doktora
- [14] Tanyıldızı E, Demir G. Golden Sine Algorithm: A Novel Math-Inspired Algorithm. *Adv Electr Comput En*, 2017; 17(2):71-78.
- [15] W. Zhao, L. Wang, S. Mirjalili, Artificial hummingbird algorithm: A new bio-inspired optimizer with its engineering applications, *Comput. Methods Appl. Mech. Engrg.* 388 (2022) 318
- [16] .K. Deb, A. Pratap, S. Agarwal and T. Meyarivan, "A fast and elitist multiobjective genetic algorithm: NSGA-II," in *IEEE Transactions on Evolutionary Computation*, vol. 6, no. 2, pp. 182-197, April 2002, doi: 10.1109/4235.996017.
- [17] M.B. Patil, Using external archive for improved performance in multi-objective optimization, 2018, arXiv preprint arXiv:1811.09196.
- [18] Patil, M.B. (2018). Using External Archive for Improved Performance in Multi-Objective Optimization. ArXiv, abs/1811.09196.
- [19] Deb K. Multi-objective optimization using evolutionary algorithms. New York: John Wiley&Sons, 2001.
- [20] Van Veldhuizen, DA and Lamont GB. Multiobjective evolutionary algorithm research: A history and analysis. Technical Report TR-98-03, Department of Electrical and Computer Engineering, Graduate School of Engineering, Air Force Institute of Technology, WrightPatterson AFB, Ohio, 1998
- [21] Zitzler E. Evolutionary Algorithms for Multiobjective Optimization: Methods and Applications, Ph.D Thesis, Swiss Federal Institute of Technology, Switzerland. 1999.
- [22] Miettinen K. Nonlinear multiobjective optimization, Kluwer Academic Publishers, Boston: SpringerScience& Bus Media. 1999.
- [23] Schott JR. Fault Tolerant Design Using Single and Multi-Criteria Genetic Algorithms. Master of Science Thesis, Massachusetts Institute of Technology, Cambridge, 1995.

A Defense Mechanism Against DoS Attacks on Unmanned Aerial Vehicle Communication

Vedat TÜMEN^{1*}, Kubilay DEMİR²

¹Department of Computer Engineering, Faculty of Engineering

²Architecture, Bitlis Eren University, Bitlis, Turkey

*¹vtumen@beu.edu.tr, ²kdemir@beu.edu.tr

(Geliş/Received: 06/01/2022)

Kabul/Accepted: 04/06/2022)

Abstract: The use of Unmanned Aerial Vehicles (UAV) in every field is increasing rapidly. In order for UAVs to perform their duties correctly, they must be able to maintain continuous communication with ground stations. The use of WiFi wireless communication protocol has increased due to its high bandwidth. One of the most important threats that can threaten this type of communication is Denial of Service (DoS) attacks. In the event of such an attack, the UAV becomes inaccessible and may crash. Especially when the open port number is known, it becomes much easier to perform attacks that consume the resources of the drone. In this study, a mechanism is proposed to eliminate or at least mitigate the attack risk. This mechanism enables UAVs using wireless communication (WiFi) to communicate using TCP over UDP using middleware. In addition, by periodically changing the UDP open ports with a secret port number sequence known to both parties, it prevents the attacker from using the open port for a long time and renders the attack ineffective. In this study, the effects of the port hopping method on UAVs are evaluated. Test results on real systems shows that the proposed system makes the communication system of UAVs more resistant to DoS attacks by 91.2%.

Key words: Unmanned aerial vehicle, DoS, Defense mechanism.

İnsansız Hava Araçların Haberleşmesine Yönelik Saldırlara Yönelik bir Savunma Mekanizması

Öz: İnsansız Hava Araçlarının (İHA) her alanda kullanımı hızlı bir şekilde artmaktadır. İHA'ların doğru bir şekilde görevlerini yerine getirebilmeleri için yer istasyonları ile devamlı olarak haberleşmelerini sürdürebilmeleri gerekir. WiFi kablosuz haberleşme metodu yüksek bant genişliği nedeni ile kullanımı artmıştır. Bu haberleşme tipini tehdit edebilecek en önemli tehditlerden biri Hizmet Reddi (DoS) saldırıdır. Bu tip bir saldırı durumunda İHA ulaşılmaz olur ve düşebilir. Özellikle açık port numarasının bilinme surumun da dronun kaynaklarını tüketen ataklar gerçekleştirmek çok daha kolay hale gelir. Bu tehlikeyi gidermek veya en azından hafifletmek amacıyla bu çalışmada bir mekanizma önerilmiştir. Bu mekanizma kablosuz haberleşme (WiFi) kullanan İHA'ların TCP kullanarak gerçekleştiği haberleşmeyi arabir yazılım (middleware) kullanılarak UDP üzerinden yapmasını sağlar. Ayrıca UDP açık portlarını iki tarafın bildiği gizli bir port numarası dizilimi ile periyodik olarak değiştirerek saldırganın açık portu bulması durumunda uzun süre kullanımını engeller ve saldırıyı etkisiz kılar. Bu çalışmada port atlama (port hopping) metodunun İHA'lar üzerine uygulamasını ve etkileri incelenecektir. Gerçek sistemler üzerinde yapılan testler önerilen sistemin İHA'ların haberleşme sistemini %91.2'ye kadar daha fazla DoS ataklarına dayanıklı kıldığını göstermiştir.

Anahtar kelimeler: İnsansız hava aracı, DoS, Savunma mekanizması.

1. Introduction

The usage area of Unmanned Aerial Vehicles (UAV) has expanded to many areas from personal use to flying base stations. As examples of recently popular usage areas; agriculture, mapping, security, search and rescue, filming, etc. In addition, we witness the introduction of a new usage area every day [1].

Commercial mini and micro UAVs use WiFi communication protocol due to video transmission requirements [2]. WiFi protocol is a promising protocol whose features are being developed day by day. Supporting a communication distance of around one hundred meters, WiFi supports data transfer up to seven hundred bits per second. Due to these superior features, it is widely used in commercial UAVs [3]. The widespread use of the WiFi protocol in UAVs creates opportunities in many ways, as well as opportunities for attackers.

Such an attack on UAVs will be a common problem, since a Denial of Service (DoS) attack does not require a high level of specialized knowledge and hardware. When a DoS attack is made, the UAV is inaccessible to the

¹ Corresponding author: vtumen@beu.edu.tr. ORCID Number of authors: ¹0000-0003-0271-216X, ²0000-0001-5355-2472

ground station. There are many types of DoS attacks [4]. Someone can make the device inaccessible by filling the entire communication channel with malicious packets, or can make the system inaccessible by consuming the system's resources with much less malicious packets. A powerful hardware is required to generate a large enough number of packets to fill the entire channel. These attacks can rarely be performed on UAVs. Attacks performed at higher Open Systems Interconnection (OSI) layers, such as Transmission Control Protocol (TCP) SYN attack, can be performed more easily with lower packet count [5].

In this study, a study was carried out to prevent attacks at the upper levels of OSI layers. The proposed defense approach prevents attacks on the 4th layer and above with a method applied in the 3rd layer (network layer). For this purpose, one of the most effective methods proposed in the literature is the port hopping method. This method is not suitable for use in all communication networks as it requires mutual secret sharing and can only be applied on the User Datagram Protocol (UDP) protocol [6-8]. For this reason, there are some applications in the literature for areas where high-level security is required in local networks or private wide area networks [9-11]. In this study, the application and evaluation of the port hopping mechanism on UAVs are performed. Although there are studies mentioning that port hopping mechanisms can be applied on UAVs, its application and evaluation has not been fulfilled [12].

The proposed model does not require changes in the software of commercial UAVs. It is assumed to allow commercial UAVs to install middleware on flight computers. On the ground station side, there are usually mobile phones. A separate middleware is also installed on this mobile phone side. These middlewares on both sides catch and forward TCP based messages to UDP. In addition, open UDP port numbers change in a known order only between the UAV and the mobile phone. The security provided by the proposed method has been tested with a test system. In the comprehensive evaluations, it has been observed that the system can withstand up to 91.2% more attacks when the proposed method is applied.

In the remainder of this article, the relevant studies in the literature in Section 2 and the model proposed in Section 3 are explained. In Section 4, the tests of the system were carried out, and finally, in Section 5, the results were given.

2. Related Works

With the widespread use of the Internet, DoS and (Distributed Denial of Service: DDoS) attacks seriously damage both the end users and the servers these users are connected to. Many different studies have been developed in the literature to prevent these damages.

Lee et al. proposed a new practical technique called port hopping to detect and block DoS/DDoS attacks. According to the method he proposed, based on the fact that the port numbers of the server change dynamically according to time and a cryptographic key shared between the server and the client, authorized clients stated that they could determine the valid port number used by the server, while malicious users stated that they could not find the valid port number [6]. The server can then easily filter out illegitimate packets by examining the port number found in the UDP/TCP headers. In the real-time experiment conducted on two computers, a port hopping mechanism was applied between client and server. With this mechanism, it sends UDP packets from client to server. The attacker fills the server with different rates of UDP packets at different rates. The filling speed of UDP packets to the server was determined and measures were taken. In this study, successful results were obtained depending on the traffic density in the network.

For a structure where cloud storage technology is used for smart electrical networks, both a hierarchical cloud structure and a port-hopping-based defense mechanism have been developed to prevent DoS attacks [7,8]. It also provides a structure for distinguishing aggressive and non-aggressive clients by using the port hopping structure.

Shi et al., using port and address skipping methods in network systems, suggested different methods aiming to establish a healthy communication under DoS/DDoS attacks and eavesdropping on the network in sending confidential information between departments and agents [9]. In this method, the client replicator performs data transfer via the data module and aims to provide secure information transfer by creating a jump address list between the server and the trusted client. When the results of this work he proposed were examined, he determined that the system he developed with the jump tactic had difficulties in getting the information from the audience and that he had to receive and analyze all the information. In this case, it has developed a system that examines much more and repetitive redundant data and causes great delays or difficulties in finding the useful data packet.

Shoufan et al. stated that the address hopping method can be used in the transmission of information packets in communication between UAV vehicles. In this study, different encryption methods have been developed and a more secure communication protocol has been tried to be made. As a result of the proposed study, it has been

shown that DoS/DDoS attacks can have serious effects on UAV vehicles, therefore a secure communication protocol can be developed [12].

3. Proposed Method

In this study, a defense method is proposed to mitigate DoS attacks that can target vital communication systems for UAVs, the use of which is increasing rapidly today. In this method, the main goal is to block malicious connection requests at the network layer before they reach the upper layers. In order to achieve this, the open port numbers in the UAV and the end-user computer (smartphone, tablet, etc.) are changed periodically, according to a hidden secret. Thus, when an attacker who does not know the open port sends packets with the wrong port number, these packets are dropped at the network interface card. The proposed method for the realization of the scenario is presented in two stages, the attack and defense model.

3.1. Attack model

In this study, it is aimed to protect against DoS attacks targeting the layers above the network layer. As it is known, OSI layers consists of 7 layers, as denoted in Figure 1.

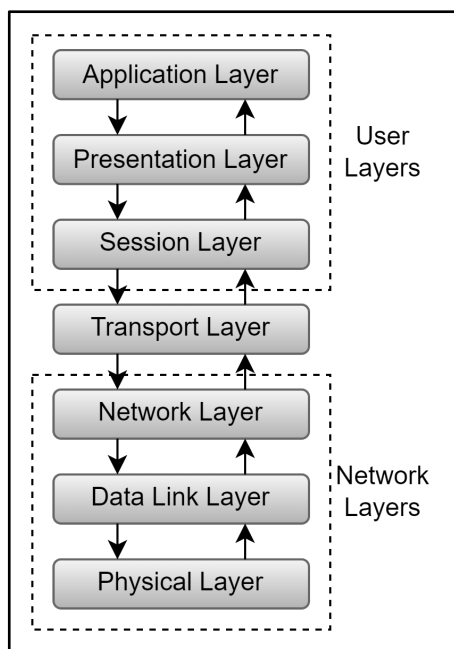


Figure 1. OSI network layers

With the low number of data packets, it is possible to completely consume computer resources (RAM, CPU, Eran Card, etc.) in the layers above the network layer. For this reason, it seems very risky for malicious packets to reach layers above Layer 3.

For example, the most well-known of these types of attacks are TCP SYN attacks. This type attack(TCP syn flood, 2021) can be expressed as: “In a TCP SYN attack, the attacker sends repeated SYN packets using a fake IP address to open a TCP connection on the targeted computer. The attacked computer receives a connection request, which it sees as bona fide, to communicate. It responds with a SYN-ACK packet for each connection request. But the malicious computer does not send the expected ACK. The attacked server waits for a while for the SYN-ACK packet to be acknowledged. During this time, the server cannot close the connection by sending an RST packet and the connection remains open. Before the connection times out, the attacker sends another SYN packet. This leaves more and more connections half-open. Eventually, as the server's connection tables fill up, legitimate clients are denied service and the server may even fail or crash” [13].

3.2. Proposed defence model

The proposed method suggests changing the open port number over time. However, in the basic system, due to the TCP connection structure, communication must be made over the same IP address and port during the session established. This makes port switching impossible on TCP. The proposed method to overcome this problem carries the communication over TCP over UDP with the help of a middleware (Middleware) installed on both the UAV side and the computer that acts as the remote controller. The proposed approach is illustrated visually in Figure 2.

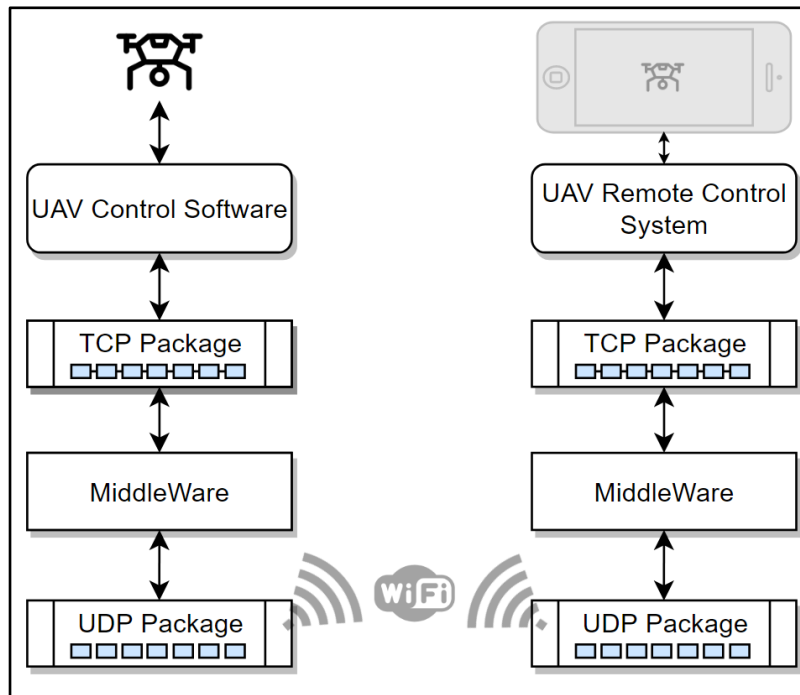


Figure 2. Proposed model.

As it can be seen in Figure 1, TCP packets coming out of the UAV control software on the remote controller are picked up by the developed middleware. This packet is sent to the known open UDP port of the other party over the currently open UDP port. On the UAV side, the middleware reads the open UDP port and receives these packets, then converts them to TCP format and delivers them to the control software. In this way, the proposed defence mechanism runs without the need for any changes in the UAV software.

It is an extremely demanding task for two parties to open and close the same ports at the same time. To achieve this, the middleware first periodically sends synchronized packets for clock synchronization. After the clock is synchronized, the port number is generated in the random number generator using a secret key password placed between the two parties during the setup. Since the same numbers are generated at the same time on both sides, the same ports are open at the same time. Therefore, both sides know which port to send the data to, but the attacker does not know this. Thus, the attacker's packets are dropped at the network layer. Figure 3 shows a DoS attack on a UAV in a field.



Figure 3. Image of the DoS attack on the UAV

4. System Test and Evaluation Results

In order to test the proposed method, the system is tested from several aspects: 1) the effect of the proposed system on the maximum communication capacity, 2) the resistance of the defense system against attacks. Figure 4 shows the effect of the proposed model on the maximum communication performance of the system

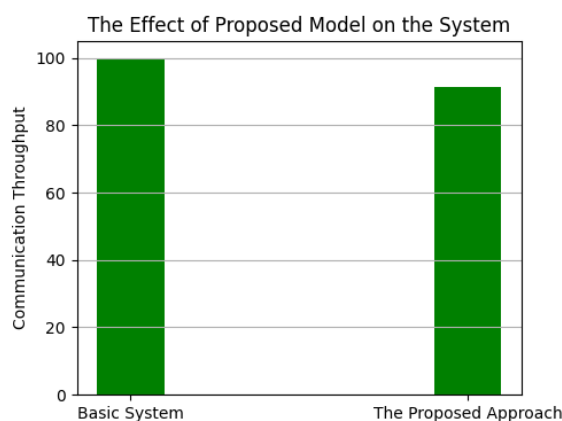


Figure 4. The effect of the proposed model on the maximum communication performance of the system

4.1. Communication throughput test

The burden of a proposed defense methodology on the current system should not exceed an acceptable level. Therefore, the system was tested without installing the developed software and then the maximum communication capacity (throughput) was measured. Afterwards, once the developed software is installed, how much decrease in the maximum communication capacity occurs is tested. As can be seen in Figure 5, a negligible (2%) performance drop was detected. This result shows that the proposed system can provide defense without a high overhead.

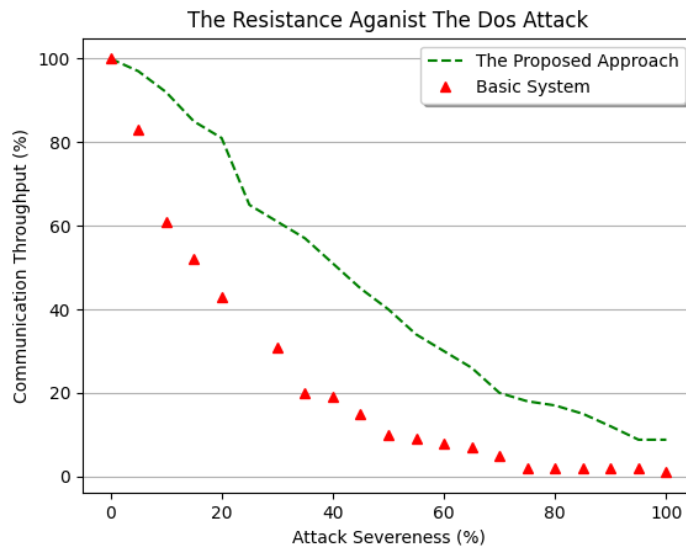


Figure 5. The resilience of the basic system and the system protected by the proposed model against attacks

4.2. System performance test

Secondly, we examined the effects of attacks on UAVs and on the UAV communication system for two cases: 1) Not using the proposed defense system and 2) Using the proposed defense system. In the event of an attack, it is compared how many malicious packets the UAV communication system can withstand. As it can be seen from Figure 4, 10% of the number of malicious packages that make the system with the proposed defense mechanism inaccessible becomes inaccessible when the proposed system is not used. This shows that if the proposed method is used, the system can withstand 91.2% stronger attacks.

5. Results

In this study, a defense system is presented against DoS attacks targeting the communication systems of UAVs. This defense system can be installed using a middleware without changing the software on the UAVs and on the controller. This middleware receives incoming packets over TCP and converts them to UDP format and sends the packets to the other party over the open port determined according to a secret between the UAV and the Remote Controller, the other party converts the packets back to TCP format and delivers them to the software. Open ports are changed over time according to the secret between the two parties. Thus, the open port is closed in the time required for the attacker to find the open port. It has been seen in the tests of the system that the proposed model provides an extra protection of 91.2% and brings a reasonable overhead for the system. As a future work, we plan to develop a mitigation method to address physical layer attacks such as jamming, interference vb.

References

- [1] Savkin, A. V., & Huang, H. (2018). "Deployment of unmanned aerial vehicle base stations for optimal quality of coverage," *IEEE Wireless Communications Letters*, 8(1), 321-324.
- [2] Bernal, S. A. S. (2016). "Detection solution analysis for simplistic spoofing attacks in commercial mini and micro UAVs" (Doctoral dissertation, MS thesis, University Of Tartu).
- [3] Lin, H. Y., Tu, K. C., & Li, C. Y. (2020). "VAID: An aerial image dataset for vehicle detection and classification," *IEEE Access*, 8, 212209-212219.
- [4] Huseinović, A., Mrdović, S., Bicakci, K., & Uludag, S. (2020). "A survey of denial-of-service attacks and solutions in the smart grid". *IEEE Access*, 8, 177447-177470.
- [5] Zeebaree, S. R., Jacksi, K., & Zebari, R. R. (2020). "Impact analysis of SYN flood DDoS attack on HAProxy and NLB cluster-based web servers". *Indones. J. Electr. Eng. Comput. Sci*, 19(1), 510-517.
- [6] Lee, H. C., & Thing, V. L. "Port hopping for resilient networks". In *IEEE 60th Vehicular Technology Conference*, 2004. VTC2004-Fall. 2004: Vol. 5, pp. 3291-3295.

- [7] Demir, K., “A Secure and Reliable Communication Platform for the Smart Grid”. Ph.D. Thesis, Darmstadt, Technische Universität, 2017.
- [8] Demir, K., Ismail, H., Vateva-Gurova, T., & Suri, N. “Securing the cloud-assisted smart grid”. *International Journal of Critical Infrastructure Protection*, 2018; 23, 100-111.
- [9] Shi, L., Cui, Y., Liu, X., Sun, H., Xue, Z., & Zhang, S. “A covert communication scheme based on DNA microdots for port hopping”. *International Journal of Performability Engineering*, 2017; 13(5), 598.
- [10] Luo, Y. B., Wang, B. S., & Cai, G. L. “Analysis of port hopping for proactive cyber defence.” *International Journal of Security and Its Applications*, 2015; 9(2), 123-134.
- [11] Luo, Y. B., Wang, B. S., Wang, X. F., Hu, X. F., Cai, G. L., & Sun, H. “RPAH: Random Port and Address Hopping for Thwarting Internal and External Adversaries”. *IEEE Trustcom/BigDataSE/ISPA*, 2015; Helsinki, Finland, Vol. 1, pp. 263-270.
- [12] Shoufan, A., Yeob Yeun, C., & Taha, B. “eSIM-Based Authentication Protocol for UAV Remote Identification”. *Security and Privacy in the Internet of Things: Architectures, Techniques, and Applications*, 2021; 91-122.
- [13] TCP syn flood: Ddos attack glossary: Imperva. Learning Center. Retrieved December 24, 2021, from <https://www.imperva.com/learn/ddos/syn-flood/>

Comparison of the Machine Learning Methods to Predict Wildfire Areas

Gözde BAYAT^{1*}, Kazım YILDIZ²

¹ Department of Computer Engineering, Institute of Pure and Applied Sciences, Marmara University, Istanbul, Turkey

² Department of Computer Engineering, Technology Faculty, Marmara University, Istanbul, Turkey
^{*}gozdebayat@marun.edu.tr, ² kazim.yildiz@marmara.edu.tr

(Geliş/Received: 26/01/2022)

Kabul/Accepted:21/04/2022)

Abstract: In the last decades, global warming has changed the temperature. It caused an increasing the wildfire in everywhere. Wildfires affect people's social lives, animal lives, and countries' economies. Therefore, new prevention and control mechanisms are required for forest fires. Artificial intelligence and neural networks(NN) have been benefited from in the management of forest fires since the 1990s. Since that time, machine learning (ML) methods have been used in environmental science in various subjects. This study aims to present a performance comparison of ML algorithms applied to predict burned area size. In this paper, different ML algorithms were used to forecast fire size based on various characteristics such as temperature, wind, humidity and precipitation, using records of 512 wildfires that took place in a national park in Northern Portugal. These algorithms are Multilayer perceptron(MLP), Linear regression, Support Vector Machine (SVM), K-Nearest Neighbors (KNN), Decision Tree and Stacking methods. All algorithms have been implemented on the WEKA environment. The results showed that the SVM method has the best predictive ability among all models according to the Mean Absolute Error (MAE) metric.

Key words: Machine Learning, Random Forest, Support Vector Machine, Decision Tree, WEKA.

Makine Öğrenmesi Yöntemlerini Kullanarak Orman Yangınlarını Tahminleme

Öz: Son on yılda, küresel ısınma sıcaklığı değiştirdi. Orman yangınlarının her yerde artmasına neden oldu. Orman yangınları insanların sosyal yaşamlarını, hayvan yaşamlarını ve ülke ekonomilerini etkiler. Bu nedenle orman yangınları için yeni önleme ve kontrol mekanizmalarına ihtiyaç duyulmaktadır. 1990'lı yıllardan itibaren orman yangınlarının yönetiminde yapay zeka ve sinir ağlarından yararlanılmaktadır. O zamandan beri, çevre biliminde çeşitli konularda makine öğrenmesi (ML) yöntemleri kullanılmıştır. Bu çalışma, yanan alan boyutunu tahmin etmek için uygulanan ML algoritmalarının performans karşılaştırmasını sunmayı amaçlamaktadır. Bu yazıda, Kuzey Portekiz'deki bir milli parkta meydana gelen 512 orman yangınının kayıtları kullanılarak sıcaklık, rüzgar, nem ve yağış gibi çeşitli özelliklere dayalı olarak yangın boyutunu tahmin etmek için farklı ML algoritmaları kullanılmıştır. Bu algoritmalar Lineer regresyon, Destek Vektör Makineleri (SVM), Çok Katmanlı Algılayıcı, K-En Yakın Komşular (KNN), Karar Ağacı ve Yığınlama yöntemleridir. Tüm algoritmalar WEKA ortamında gerçekleştirilmiştir. Sonuçlar, Ortalama Mutlak Hata (MAE) metriğine göre tüm modeller arasında SVM yönteminin en iyi tahmin yeteneğine sahip olduğunu göstermiştir.

Anahtar kelimeler: Makine Öğrenmesi, Random Forest, Destek Vektör Makineleri, Karar Ağacı, WEKA.

1. Introduction

Forests are one of the most important resources of the world's ecological balance. Also, it provides oxygen for people and natural living areas for animals. The world has been losing its forests rapidly as a consequence of wildfires and tree cutting uncontrollably. Wildfire as a natural disaster has severe effects on all living creatures. Also, it has extremely large economic and social consequences. During the last few decades, gigantic wildfires have occurred in various places of the world. Creating a trustworthy model to predict the size of the burned area in a forest fire is necessary to allocate resources optimally for fire departments. In this paper, ML models have been used to predict how much fire will grow using the dataset that includes wind speed, humidity, location information, temperature, etc. The output of prediction is the burning area and its unit hectares.

A wildfire susceptibility map for the two fire seasons in the Liguria region in Italy was created and validated by using the Random Forest (RF) method [1]. The susceptibility map was investigated considering the dataset of mapped fire environments covering a 21-year period (1997-2017) and different environmental susceptibility factors. Also, the authors aim to compare the performance of ML models. The proposed model is better than the other models to predict areas which were affected by a fire. Hung Van Le and friends [2] suggested a novel deep

* Corresponding author: gozdebayat@marun.edu.tr. ORCID Number of authors: ¹ 0000-0003-1116-1881, ² 0000-0001-6999-1410

neural network model for the prediction of wildfires in a tropical region. They proposed 3 hidden layers to create a wildfire susceptibility map for the Gia Lai province in Vietnam which is called deep neural computing.

A literature review covering 300 publications by the end of 2019 was investigated in [3] to show that ML methods can be used in wildfires. It is shown that the common methods are RF, NN, SVM, Decision trees. Stella and friends use machine learning to address the next day forest fire prediction problem. An ML method utilizing Tree Ensemble and NN, where a large parameter search procedure is performed through cross-validation, has been applied to determine powerful models that are expected to generalize fine on the new data[4]. Meteorological parameters such as temperature, average rains to understand scale of a forest fire can be used. These parameters have been used as a input values for these forecast models, such as long short-term memory (LSTM) backpropagation neural network (BPNN) and recurrent neural network (RNN). The experimental results show, the scale of fire can be predict at the onset occurrence with these informations [5]. ML techniques such as RF, SVM and Logistic Regression (LR) have been exploited to build susceptibility map and compared for the study area of Northern Iran. It was revealed that RF has the highest accuracy and suited for wildfire sensitivity evaluation[6]. Novel gradient boosting models have been applied to predict wildfire activity trained with loss function Extreme-Value theory have been exploited for generate loss function. In the study, the benchmarked against boosting scheme was designed and shown to provide a better proxy for test set performance than pure cross validation. Estimates are compared against reinforcement approaches with different loss functions[7]. BPNN, RNN and LSTM techniques have been applied to data set which include Alberta region meteorological parameters taken from Canadian National Fire Database (CNFDB) [8]. In the study, length of fire time have been exploited along with meteorological parameters to predict burning area.

Authors recommend that to have placed sensors that has massive resolution at the initial phase of fire to predict scale of wildfire. Different synthetic data generation techniques and different ML models have been applied the created synthetic dataset. Results have shown that SVM method has most accuracy to predict large forest fires [9]. Uncertainty is big problem to predict fire, in literature multi-fidelity techniques have become attractive from wildfire researchers, recently. Multi-fidelity techniques have been used to understand fire spread als Monte-Carlo and multi level Monte-Carlo simulation methods have been compared[10]. Not only weather parameters also smoke information has been used to predict wildfire events in early stage. LSTM has been applied with convolutional layers for smoke detection and reached high accuracy 97.8% [11]. Forecast future wildfires is vital point as well in forest fires management. Daily forest fire probability map forecast has been carried out using deep fully convolutional neural network called AllConvNet. Authors estimated future burn probability map for next seven days using 2006-2017 wildfire period for Australia[12].

Predictive models such as RF, LR, Ridge Regression have been applied for estimate burning area size in [13]. The dataset contains parameters measured in wildfires between 1911-2015 in the United States. RF algorithm has better performance than LR and Ridge Regression. Beşli and Tenekeci used the data obtained from the satellites for prediction. Forest fires were estimated using Normalized Difference Vegetation Index (NDVI), Land Surface Temperature (LST) and Thermal anomaly (TA) data calculated from satellite data. Decision trees were used to make predictions from the mentioned data. 70% of the data was used to be used as training and remaining as a test. The average performance of the applied method was determined by repeating the training and testing process 10 times with different data. In the experiments carried out, the fires were predicted correctly with an average sensitivity of 98.62%. The actual situation was determined with an average accuracy of 93.11% [14]. RF, linear regression, Stacked Regressor, NN, SVM and KNN algorithms have been used for forecast the burned areas with two different data set. Algorithms have been implemented on the Python environment. Also Data sets have taken from Kaggle and UCI, respectively. Performance of used ML algorithms compared each other. MAE and MAPE error metrics have been used to evaluate the performance of the models[15]. Logistic regression has been applied for predicting areas that can be burned using past meteorological parameters. This technique is easy to implement and also facilitates interpretation of the results obtained and possible duplication of the methodology in other regions or countries. [16]. Trucchia and friends proposed a study which is RF based. Their approach is about to obtain national susceptibility maps in Italy. Each pixel of the study are is classified by the model. Experimental results show the ability of RF to notice the most sensitive areas with defined factors[17].

It is aimed to demonstrate the performance comparison of ML algorithms applied to estimate the burned area size. For this purpose, Linear Regression, SVM, MLP, KNN, Decision Tree and Stacked Regressor methods were applied in WEKA environment. The estimation performance of these methods is compared to the MAE performance metric. In addition, the obtained results are presented by comparing with Moore's study[15].

2. Material and Methods

2.1. Dataset

The dataset was taken from the UCI site. The dataset consists of fires in a national park in northern Portugal between January 2000 and December 2003. It was collected using two different sources. The first of these sources were prepared by the inspector responsible for forest fires in the park. The inspector recorded time, date, location (x and y), Fine Fuel Moisture Code (FFMC), Duff Moisture Code (DMC), Drought Code (DC), Initial Emission Index (ISI), and total burned area data for each fire. The second source was prepared using the meteorological station in the park. The meteorological station recorded various weather information like temperature (Celsius), relative humidity, rain, wind speed. The datas were collected from two sources and converted into a single dataset with a total of 512 entries [18]. In this study, the burning area size attribute was tried to be estimated. The sample dataset content is shown in Table 1. The distribution histogram of the features are given in Figure 1.

Table1. Example of UCI dataset file[18]

X	Y	Month	Day	FFMC	DMC	DC	ISI	Temp	RH	Wind	Rain	Area
7	5	Mar	Fri	86.2	26.2	94.3	5.1	8.2	51	6.7	0	0
7	4	Oct	Tue	90.6	35.4	669.1	6.7	18	33	0.9	0	0
7	4	Oct	Sat	90.6	43.7	686.9	6.7	14.6	33	1.3	0	0
8	6	Mar	Fri	91.7	33.3	77.5	9	8.3	97	4	0.2	0
8	6	Mar	Sun	89.3	51.3	102.2	9.6	11.4	99	1.8	0	0
8	6	Aug	Sun	92.3	85.3	488	14.7	22.2	29	5.4	0	0
8	6	Aug	Mon	92.3	88.9	495.6	8.5	24.1	27	3.1	0	0
8	6	Aug	Mon	91.5	145.4	608.2	10.7	8	86	2.2	0	0
8	6	Sep	Tue	91	129.5	692.6	7	13.1	63	5.4	0	0
7	5	Sep	Sat	92.5	88	698.6	7.1	22.8	40	4	0	0
7	5	Sep	Sat	92.5	88	698.6	7.1	17.8	51	7.2	0	0
7	5	Sep	Sat	92.8	73.2	713	22.6	19.3	38	4	0	0
6	5	Aug	Fri	63.5	70.8	665.3	0.8	17	72	6.7	0	0
6	5	Sep	Mon	90.9	126.5	686.5	7	21.3	42	2.2	0	0
6	5	Sep	Wed	92.9	133.3	699.6	9.2	26.4	21	4.5	0	0
6	5	Sep	Fri	93.3	141.2	713.9	13.9	22.9	44	5.4	0	0
5	5	Mar	Sat	91.7	35.8	80.8	7.8	15.1	27	5.4	0	0
8	5	Oct	Mon	84.9	32.8	664.2	3	16.7	47	4.9	0	0
6	4	Mar	Wed	89.2	27.9	70.8	6.3	15.9	35	4	0	0
6	4	Apr	Sat	86.3	27.4	97.1	5.1	9.3	44	4.5	0	0
6	4	Sep	Tue	91	129.5	692.6	7	18.3	40	2.7	0	0
5	4	Sep	Mon	91.8	78.5	724.3	9.2	19.1	38	2.7	0	0
7	4	Jun	Sun	94.3	96.3	200	56.1	21	44	4.5	0	0
7	4	Aug	Sat	90.2	110.9	537.4	6.2	19.5	43	5.8	0	0
7	4	Aug	Sat	93.5	139.4	594.2	20.3	23.7	32	5.8	0	0
7	4	Aug	Sun	91.4	142.4	601.4	10.6	16.3	60	5.4	0	0

It was considered that some parameters such as temperature, wind, and humidity would be very correlated with the burning area. However, during the preliminary research phase on the data, it was observed that even these highest correlated features of the data set were low correlated with the burning field. As represented in Figure 2(a), the wind has a low relationship to the burning area in the data set. Small-scale fires occur all months of a year whereas large-scale occurred mostly during the summer seasons. This relationship has been shown in Figure 2(b).

The correlation matrix was generated with the help of Python program to measure the correlation between dataset features which can be seen in Figure 3. The correlation value of -0.076 between burned area and relative humidity (RH) indicates an inverse relationship between these data. In this case, it can be seen that the RH data is one of the weak indicators in estimating the fire size. Examining the correlation matrix, the lack of high correlation between burning areas and other data complicates it difficult to predict fire size. Besides, Figure 3 shows the importance of weather parameters such as temperature, wind for estimating burning areas size, which has a high correlation.

Comparison of the Machine Learning Methods to Predict Wildfire Areas

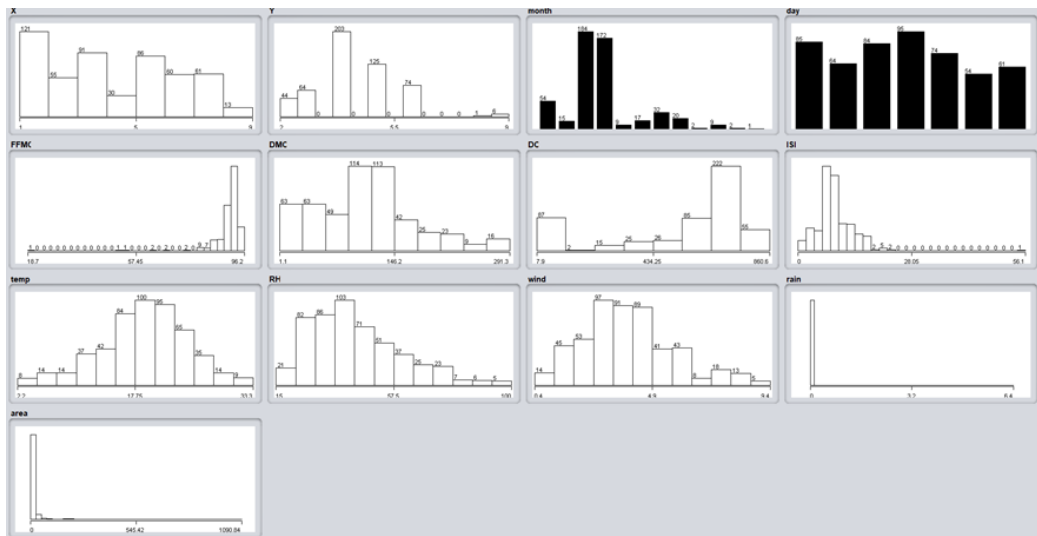


Figure 1. The distribution histogram of dataset features

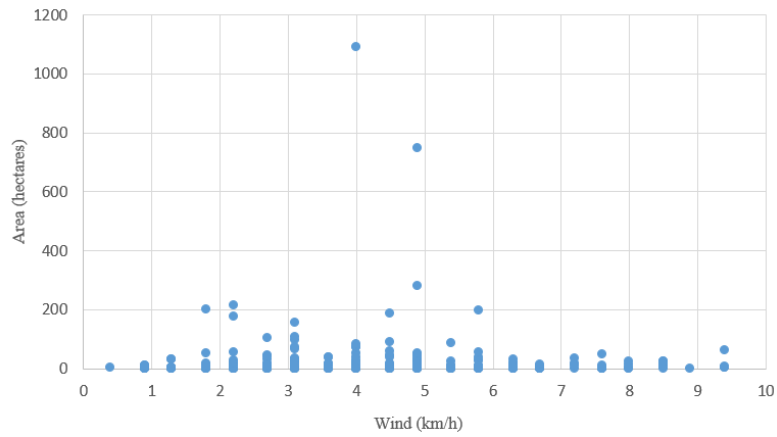


Figure 2(a). Relationship between wind (km/h) and burned area (hectares)

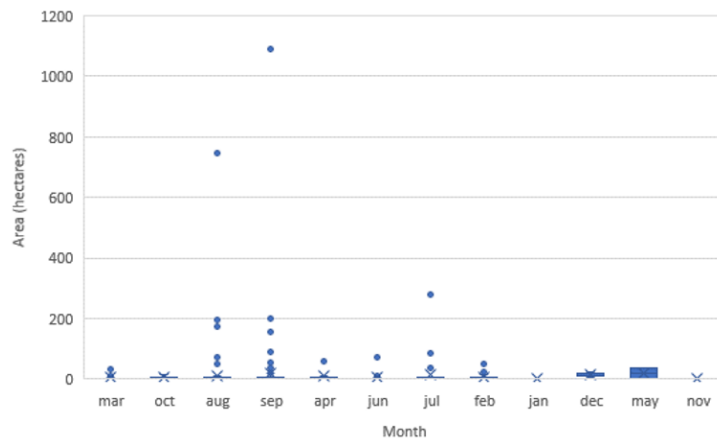


Figure 2(b). Relationship between the months of the fire and the burning area as hectare.

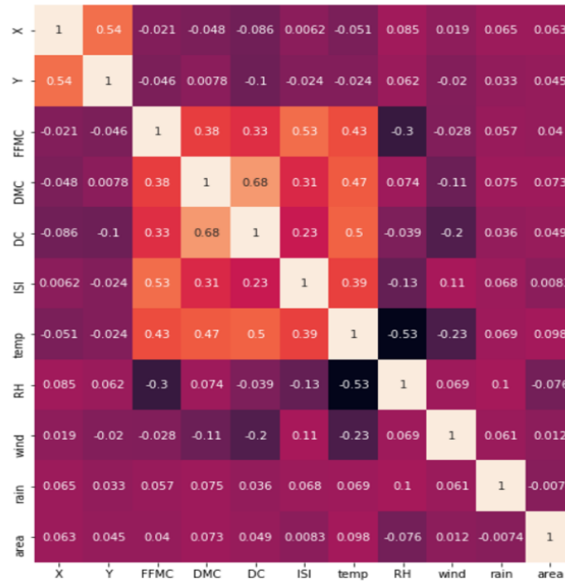


Figure 3. Correlation matrix of features for area estimation

2.2. WEKA

WEKA is a modular data mining tool produced by New Zealand's University of Waikato under a free GNU license [19]. It contains many methods, algorithms, libraries, and ready-made functions. Many features that are newly developed or not included with the standard program can be downloaded free of charge from the WEKA platform and can be integrated into the program as requested by the user. Since WEKA program is produced using Java, during development, its libraries have .jar extensions which provides convenience in the integration process of many programs produced with Java. Data preprocessing, classification, clustering, association and visualization can be done easily on the WEKA platform. In order to perform these operations, the extension of the file must be arff. However, the conversion of data in different extensions can be done easily. So the methods were tested in WEKA environment and 10 fold cross validation was chosen to trained the test pattern.

2.3. Linear Regression

Representing the relationship between two or more variables with a straight line is called Linear Regression [20]. Figure 4 shows an example linear regression model. The blue points describe the data, the red line defines the relationships between these variables. The closest linear result to the connection between the two variables is obtained. A line equation is obtained that will pass to cover as much of the sample data as possible which predicts future data [21].

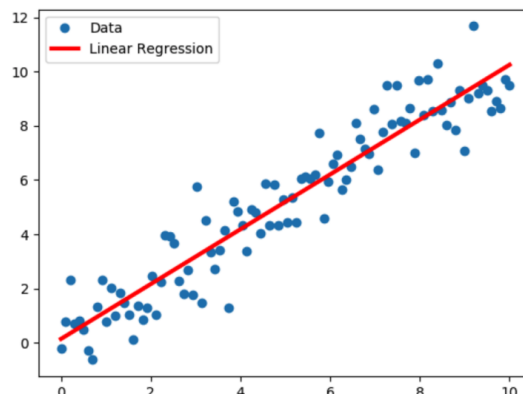


Figure 4. Example a linear regression model [22]

2.4. SVM

SVM [23-24] is frequently used in classification problems which aims to find the line that has the maximum distance between the points placed on a hyper plane. In order to draw the border, two lines close and parallel to each other are drawn for both groups and these lines are brought closer together to produce the borderline. The most appropriate function is to try to be estimated for separating the data from each other [25]. If a linear boundary cannot be found for classification, the boundary is searched by moving the data to another multidimensional space. It is more common to use for complex small and medium sized datasets [26]. The presented dataset in this study is medium-sized.

2.5. Neural Networks

NN is a ML model built in layers[27-28]. MLP[29] is one of the neural network methods which is proposed in the study. It tries to automatically realize abilities such as deriving new information, creating and discovering through learning. Classification can be made using threshold values. MLP have an input layer, one or more hidden layers, an output layer, and transitions between layers called back-and-forward propagation. The input layer gets the data and sends it to the middle layer. Then this information is send to the next layer. The number of hidden layers is adjusted between at least and need. Each layer's output, becomes the input of the next layer. Thus, the output is reached[30].

2.6. KNN

KNN is one of the ML methods used for regression and classification in supervised learning[31-32]. It is considered the simplest machine learning algorithm. KNN is based on estimating the class of the vector formed by the independent variables of the value to be estimated, based on the information in which class the nearest neighbors are dense [33]. KNN makes predictions on two basic values such as distance and number of neighbors [34]. An example KNN model is shown with three classes in figure 5. In this study, the number of neighbors is selected as $n=1$, $n=5$, $n=10$ and $n=50$ respectively and the results were compared.

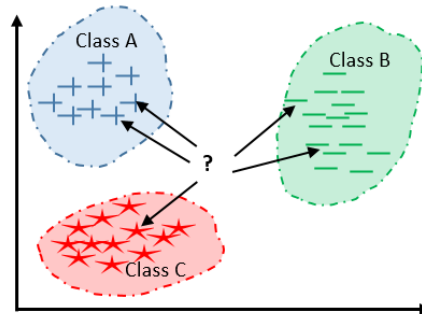


Figure 5. Example a KNN model [35]

2.7. Decision Tree

Decision tree is the tree-based algorithm which is commonly used in regression and classification problems [36]. It can be used in complex datasets [37]. The tree model is created by dividing possible decision groups into small sub groups by applying simple decision-making steps. The first node of the decision tree is the root and the other nodes connected to the roots are leaf nodes [38]. An example decision tree model is given in figure 6.

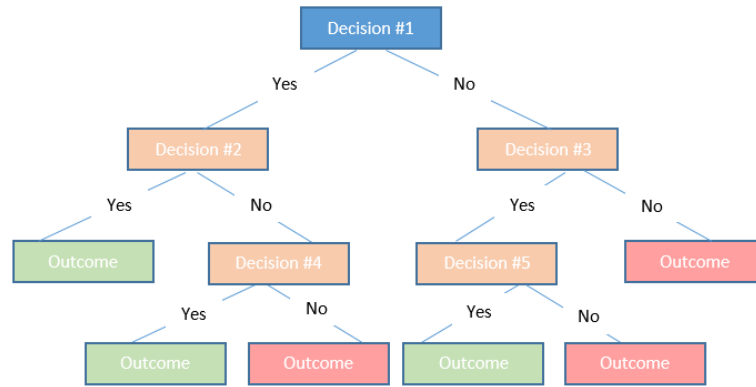


Figure 6. Example a Decision Tree model [39]

2.8. Stacked Regressor

Stacked regressor is used to combine multiple predictors which has been applied since a set of models performs better at burning areas at different places [40]. The principal concept of this technique is to assemble the complementary merits of multiple models to boost the total performance of the ensemble model [41]. Ensemble is one of the machine learning methods that combines the prediction results of more than one base model in order to obtain more powerful and generalizable results compared to a single model. An example stacked regressor model is given in figure 7. The figure illustrates that, the training data is tested on three different models in the first stage and predictions are obtained. At the second level, these predictions are generalized and expressed as a single output.

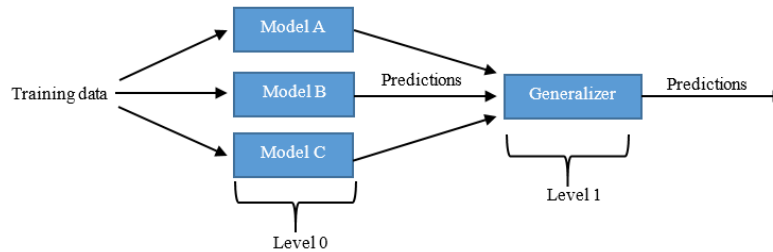


Figure 7. Example a Stacked regressor model [42]

3. Results and Discussion

The identified models were trained on the UCI dataset and the models were evaluated based on the MAE metric on the respective test sets. MAE is a performance metric calculated by dividing the sum of the absolute values of the differences between the actual and the predicted results by the total number of data. Since MAE is easily interpreted, it is frequently used in the fields of machine learning and artificial neural network. Table 2 shows the performance results which are obtained comparatively. The best value of the MAE is obtained with SVM as 12.8879 and the worst one is MLP is 38.7481. SVM has the best overall prediction ability among all models for the MAE metric in the dataset. However, when all the results are examined, it is seen that very high accuracy results are not achieved. This shows that the parameters used cannot predict fire sizes with high accuracy. It means that the correlations between the lit fields and the input parameters are weak. SVM performed better as the values in the UCI dataset were likely to be distributed over a small range. Considering the results in Table 2, the least accurate results are obtained from the MLP according to the MAE metric. This is thought to be due to the small amount of data and insufficient features.

Table 2. Model performances of according to the MAE metric

ML MODELS	MAE
Linear Regression	20.0857
SVM	12.8879
NN	38.7481
KNN (N=1)	23.8073
KNN (N=5)	20.6596
KNN (N=10)	20.3174
KNN (N=50)	18.9255
Decision Tree	19.1364
Stacking	18.5918

In addition, the obtained results were compared with the results obtained in which was performed in Python[15]. The same data set and methods were used. Table 3 shows the comparison results. When Table 3 is examined, although the results obtained from the Linear regression, SVM, KNN, Stacking methods are compatible, the results obtained from the MLP and Decision tree methods are completely inconsistent. Our proposed approach was carried out in the WEKA program. For this reason, it is thought that one of the reasons for the differences in the results obtained may be the difference in the program used. In addition, it is thought that the other reason for the difference may be the difference in the data preprocessing stage. Finally, in the study of [15], more than one dataset was used, but in this study it was studied on a single dataset. For these reasons, it was concluded that there may be differences between the results obtained.

Table 3. Comparison of study results with [15]

	MAE (Our study)	MAE [15]
Linear Regression	20.0857	15.547
SVM	12.8879	6.334
NN	38.7481	8.264
KNN	18.9255	15.53
Decision Tree	19.1364	31.5
Stacking	18.5918	9.45

4. Conclusion

In this study, various machine learning methods were used to estimate fire size based on various characteristics such as temperature, wind, humidity and precipitation using 512 wildfire records that took place in a national park in Northern Portugal. These methods are Linear regression, SVM, MLP, KNN, Decision Tree and Stacking. Models were evaluated based on the MAE metric in the relevant test sets. It has been seen that the SVM method has the best predictive ability among all models for the MAE metric in the data set. According to the MAE metric, it was observed that the least accurate results were obtained from the MLP method.

In this study a dataset from Northern Portugal was used. For future work if a similar dataset belonging Turkey can be found then It will be able to possible to estimate the size of the burning area over the dataset with the

alternative ML methods. In addition, the number of data and more parameters such as weather and environmental factors in the dataset used in this study can be increased to improve the prediction success.

References

- [1] Tonini, M.; D'Andrea, M.; Biondi, G.; Degli Esposti, S.; Trucchia, A.; Fiorucci, P. A Machine Learning-Based Approach for Wildfire Susceptibility Mapping. The Case Study of the Liguria Region in Italy. *Geosciences* 2020, 10, 105.
- [2] Le, H. V., Hoang, D. A., Tran, C. T., Nguyen, P. Q., Tran, V. H., Hoang, N. D., Amiri, M., Ngo, T. P., Nhu, H. V., Hoang, T. V., & Tien Bui, D. A new approach of deep neural computing for spatial prediction of wildfire danger at Tropical Climate Areas. *Ecological Informatics*, 2021, 63
- [3] Jain, P., Coogan, S.C., Subramanian, S.G., Crowley, M., Taylor, S., & Flannigan, M.D. A review of machine learning applications in wildfire science and management. *ArXiv*, 2020,abs/2003.00646.
- [4] S. Girtsou, A. Apostolakis, G. Giannopoulos and C. Kontoes, A Machine Learning Methodology for Next Day Wildfire Prediction, 2021 IEEE International Geoscience and Remote Sensing Symposium IGARSS, 2021, pp. 8487-8490
- [5] Liang Hç, Zhang M. and Wang H., "A Neural Network Model for Wildfire Scale Prediction Using Meteorological Factors," in *IEEE Access*, vol. 7, pp. 176746-176755, 2019
- [6] Gholamnia, K.; Gudiyangada Nachappa, T.; Ghorbanzadeh, O.; Blaschke, T. Comparisons of Diverse Machine Learning Approaches for Wildfire Susceptibility Mapping. *Symmetry* 2020, 12, 604.
- [7] Jonathan K., "Gradient boosting with extreme-value theory for wildfire prediction," *arXiv*, 2021.
- [8] V. Zope, T. Dadlani, A. Matai, P. Tembhurnikar and R. Kalani, "IoT Sensor and Deep Neural Network based Wildfire Prediction System," 2020 4th International Conference on Intelligent Computing and Control Systems (ICICCS), 2020, pp. 205-208
- [9] Pérez-Porras, F.-J.; Triviño-Tarradas, P.; Cima-Rodríguez, C.; Meroño-de-Larriva, J.-E.; García-Ferrer, A.; Mesas-Carrascosa, F.-J. Machine Learning Methods and Synthetic Data Generation to Predict Large Wildfires. *Sensors* 2021, 21, 3694.
- [10] Valero, M. M., Jofre, L., & Torres, R. Multifidelity prediction in wildfire spread simulation: Modeling, uncertainty quantification and sensitivity analysis. *Environmental Modelling & Software*, 141, 2021.
- [11] Cao Y., Yang F., Tang Q. and Lu X., An Attention Enhanced Bidirectional LSTM for Early Forest Fire Smoke Recognition. *IEEE Access*, vol. 7, pp. 154732-154742, 2019
- [12] Bergado J. R, Persello C., Reinke K., Stein A. Predicting wildfire burns from big geodata using deep learning. *Safety Science*, 140, 2021.
- [13] Qin L , Shao W. , Du G., Mou J. ve Bi R., Predictive Modeling of Wildfires in the United States. 2021 2nd International Conference on Computing and Data Science (CDS);2021 Stanford, pp. 562-567
- [14] Beşli N. And Tenekeci M. Uydu verilerinden karar ağaçları kullanarak orman yangını tahmini. *DÜMF Mühendislik Dergisi*; 2020.
- [15] Moore S. A. Wildfire Burn Area Prediction. 2019. 33rd Conference on Neural Information Processing Systems. Vancouver, Canada,.
- [16] Raffaello Bergonse, Sandra Oliveira, Ana Gonçaves, Sílvia Nunes, Carlos DaCamara & José Luis Zêzere (2021) Predicting burnt areas during the summer season in Portugal by combining wildfire susceptibility and spring meteorological conditions, *Geomatics, Natural Hazards and Risk*, 12:1, 1039-1057, DOI: 10.1080/19475705.2021.1909664.
- [17] Trucchia, A.; Meschi, G.; Fiorucci, P.; Gollini, A.; Negro, D. Defining Wildfire Susceptibility Maps in Italy for Understanding Seasonal Wildfire Regimes at the National Level. *Fire* 2022, 5, 30. <https://doi.org/10.3390/fire5010030>.
- [18] Cortez, Paulo & Morais, A.. (2007). A Data Mining Approach to Predict Forest Fires using Meteorological Data.
- [19] Witten, I.H., Frank, E.: *Data Mining: Practical machine learning tools and techniques*, 2nd Edition, Morgan Kaufmann, San Francisco (2005).
- [20] Vetter TR, Schober P. Regression: The Apple Does Not Fall Far From the Tree. *Anesth Analg*. 2018 Jul;127(1):277-283.
- [21] Seber, G. A. ve Lee, A. J., "Linear regression analysis", Vol. 329, John Wiley & Sons, 2012.
- [22] Tran, Hieu. (2019). A survey of machine learning and data mining techniques used in multimedia system.
- [23] Willsch D., Willsch M., De Raedt H. , Michielsen K., Support vector machines on the D-Wave quantum annealer. *Computer Physics Communications*, Volume 248, 2020, 107006, ISSN 0010-4655.
- [24] Huang, Y., Zhao, L. Review on landslide susceptibility mapping using support vector machines. 2018. *CATENA*, 165, 520–529.
- [25] Karakoyun, M. ve Hacıbeyoğlu, M., "Biyomedikal Veri Kümeleri ile Makine Öğrenmesi Sınıflandırma Algoritmalarının İstatistiksel Olarak Karşılaştırılması", *Dokuz Eylül Üniversitesi Mühendislik Fakültesi Fen ve Mühendislik Dergisi*, 2014.
- [26] Support Vector Machine - Regression (SVR), http://www.saedsayad.com/support_vector_machine_reg.htm. 27.02.2022.
- [27] Zhang, Y., Tuo, M., Yin, Q., Qi, L., Wang, X., & Liu, T. Keywords extraction with deep neural network model. *Neurocomputing*. 2020 383, 113-121.
- [28] Zhang, G., Wang, M., & Liu, K. Forest fire susceptibility modeling using a convolutional neural network for Yunnan province of China. 2019. *International Journal of Disaster Risk Science*, 10(3), 386-403.

- [29] Heidari, A. A., Faris, H., Mirjalili, S., Aljarah, I., & Mafarja, M. Ant lion optimizer: theory, literature review, and application in multi-layer perceptron neural networks. 2020 *Nature-Inspired Optimizers*, 23-46.
- [30] Meha Desai, Manan Shah, "An anatomization on breast cancer detection and diagnosis employing multi-layer perceptron neural network (MLP) and Convolutional neural network (CNN)," *Clinical eHealth*, Volume 4, 2021, Pages 1-11, ISSN 2588-9141, <https://doi.org/10.1016/j.ceh.2020.11.002>.
- [31] Abu Alfeilat, H. A., Hassanat, A. B., Lasassmeh, O., Tarawneh, A. S., Alhasanat, M. B., Eyal Salman, H. S., & Prasath, V. S. Effects of distance measure choice on k-nearest neighbor classifier performance: a review. 2019, *Big data*, 7(4), 221-248.
- [32] Ali, N., Neagu, D., & Trundle, P. Evaluation of k-nearest neighbour classifier performance for heterogeneous data sets. 2019. *SN Applied Sciences*, 1(12), 1-15.
- [33] M. Toğaçar , "Detection of Phishing Attacks on Websites with Lasso Regression, Minimum Redundancy Maximum Relevance Method, Machine Learning Methods, and Deep Learning Model", *Turkish Journal of Science and Technology*, c. 16, sayı. 2, ss. 231-243, Eyl. 2021.
- [34] Damien Chanal, Nadia Yousfi Steiner, Raffaele Petrone, Didier Chamagne, Marie-Cécile Péra, "Online Diagnosis of PEM Fuel Cell by Fuzzy C-Means Clustering", *Reference Module in Earth Systems and Environmental Sciences*, Elsevier, 2021, ISBN 9780124095489, <https://doi.org/10.1016/B978-0-12-819723-3.00099-8>.
- [35] Atallah, Dalia & Badawy, Mohammed & El-Sayed, Ayman & Ghoneim, Mohamed. (2019). Predicting kidney transplantation outcome based on hybrid feature selection and KNN classifier. *Multimedia Tools and Applications*. 78. 20383–20407. 10.1007/s11042-019-7370-5.
- [36] Yıldız, Olcay Taner, et al. *Bagging Soft Decision Trees*. Springer Verlag, 2017. EBSCOhost, https://doi.org/10.1007/978-3-319-50478-0_2.
- [37] Jaafari, A., Zenner, E. K., & Pham, B. T. Wildfire spatial pattern analysis in the Zagros Mountains, Iran: A comparative study of decision tree based classifiers. 2018. *Ecological informatics*, 43, 200-211.
- [38] Altaş, D. & Gülpınar, V. (2012). Karar Ağaçları Ve Yapay Sinir Ağlarının Sınıflandırma Performanslarının Karşılaştırılması . *Trakya Üniversitesi Sosyal Bilimler Dergisi* , 14 (1) , 1-22 .
- [39] Decision tree diagrams: what they are and how to use them, <https://blog.mindmanager.com/blog/2021/05/11/decision-tree-diagrams/> 27.02.2022.
- [40] Pavlyshenko, B. Using stacking approaches for machine learning models. 2018. 2018 IEEE Second International Conference on Data Stream Mining & Processing .255-258. IEEE.
- [41] Kaibing Zhang, Shuang Luo, Minqi Li, Junfeng Jing, Jian Lu, and Zenggang Xiong. 2020. Learning stacking regressors for single image super-resolution. *Applied Intelligence* 50, 12 (Dec 2020), 4325–4341. DOI:<https://doi.org/10.1007/s10489-020-01787-0>
- [42] Divina, F., Gilson, A., Gómez-Vela, F., García Torres, M., & Torres, J. (2018). Stacking Ensemble Learning for Short-Term Electricity Consumption Forecasting. *Energies*, 11(4), 949. doi:10.3390/en11040949.

Deep Learning Based Recognition of Turkish Sign Language Letters with Unique Data Set

Mustafa KAYA^{1*}, Fatih BANKUR²

^{1,2}Department of Digital Forensics Engineering, Fırat University, Elazığ, Turkey

^{1*} mkaya@firat.edu.tr, ² fth.bnkr23@gmail.com

(Geliş/Received: 14/02/2022;

Kabul/Accepted: 01/05/2022)

Deep Learning Based Recognition of Turkish Sign Language Letters with Unique Data Set

Abstract: With its development, artificial intelligence has formed the basis for many studies aimed at facilitating people's lives. More successful results have been tried to be obtained with the increasing data and developing equipment in these studies. It is seen that these developments in artificial intelligence are reflected in the studies related to sign language conversion.

In this study, a data set belonging to the letters in the Turkish Sign Language Alphabet was created, and the classification process was carried out with both the deep learning model we created and VGG16, Inceptionv3, Resnet, and Mobilnet models, which are frequently used in image classification. In addition, an open-source data set containing the letters in the American Sign Language Alphabet was organized similar to the data set containing the letters in the Turkish Sign Language Alphabet we created, and Deep Learning models were used to classify the letters in the American Sign Language Alphabet by using this data set. Performance evaluations of the classifications made by Deep Learning Models using both data sets were made. With this study, the results obtained from training Deep Learning methods with different data sets were compared. In addition, it is thought that the study will be useful in determining both the data set and the deep learning method to be used for the studies on the recognition of Sign Language Letters.

Key words: Turkish Sign Language Alphabet, Deep Learning, SSD Mobilenet, EfficientNet, YOLOv5.

Özgün Veri Seti ile Derin Öğrenme Temelli Türk İşaret Dili Harflerinin Tanınması

Öz: Derin Öğrenme kavramı, artan veri miktarı ve geliştirilen kapsamlı donanımlarla birlikte önem kazanmaya başlamıştır. Derin Öğrenme yöntemleri birçok farklı alanda kullanılmış ve başarılı sonuçlar alınmıştır. Bu alanlar doğal dil işleme, görüntü işleme, sanal veri üretme, otonom araçlar, ses tanıma ve sağlık, sanayi ve savunma sanayi gibi birçok alanı kapsamaktadır. İnsan hayatını kolaylaştırma adına birçok alanda kullanılmakta olan derin öğrenme yöntemleri yapılan bu çalışma ile Türk İşaret Dili (TİD) Harflerinin tanınması amacı ile kullanılmıştır.

Bu çalışmada TİD harflerine ait özgün bir veri seti oluşturulmuş, oluşturulan bu veri seti içerisindeki verileri çeşitlendirmek ve arttırmak için farklı veri çoğaltma yöntemleri de kullanılmıştır. Sonuç olarak toplamda 10.000 adet resimden oluşan özgün bir veri seti elde edilmiştir. Hazırlanan özgün veri seti, TİD harflerinin hızlı bir şekilde tanınması amacıyla tek aşamalı nesne tespiti modelleri olan SSD Mobilenet, EfficientNet ve YOLO modelleri ile eğitime tabi tutulmuştur. Yakın eğitim süreleri sonucunda YOLOv5 modelinin diğer nesne tespiti modellerine oranla daha hızlı ve daha doğru sonuçlar verdiği gözlemlenmiştir. Bu sebeple hazırlanan özgün veri seti ile YOLOv5 modeli daha uzun süreli olarak eğitilmiş ve sonuç olarak YOLOv5 modeli ile TİD harflerinin tanınması %92,3 oranında başarı ile gerçekleştirilmiştir. TİD harflerinin hızlı bir şekilde tanınmasını sağlayan bu çalışma daha sonra yapılacak olan gerçek zamanlı TİD çevirmen uygulamalarına hem veri seti, hem de kullanılacak derin öğrenme yönteminin belirlenmesi açısından fayda sağlayacaktır.

Anahtar kelimeler: Türk İşaret Dili Alfabeti, Derin Öğrenme, SSD Mobilenet, EfficientNet, YOLOv5.

1. Introduction

Speech is the most important way of human communication. It is seen that people who are deaf, mute or have difficulty in speaking mostly communicate with TSL. With the recent developments in the field of object recognition, TSL signs can also be recognized as objects, which constitutes the source of motivation for this study.

* Corresponding author: mkaya@firat.edu.tr. ORCID Number of authors: ¹ 0000-0002-0160-4469, ² 0000-0002-2455-1195

Since 1990, signs and data in sign language have been started to be processed. In one of the first studies conducted for this purpose, Charahpayan and Marble developed a computer vision-based system based on the use of the speed of the hand for the creation of ASL (American Sign Language) [1]. Takahashi and Kishimo tried to classify and recognize the Japanese Sign Language alphabet over 46 samples taken through the data glove [2]. In 1995, Waldron and Kim performed the recognition of 14 ASL words using the artificial neural network method, using hand shape, hand position, and movement [3]. Allen et al. performed a spelling system for ASL. This system could recognize 24 of 26 hand shapes [4]. In 2004, Wang, ÖZ et al. implemented an ASL hand shape recognition system. Data gloves and motion tracking are used in the system, and artificial neural networks and HMM (Hidden Markov Model) are used in classification [5]. In the study conducted in 2018, after the hands in the images were detected using skin color discrimination, it was observed that real-time sign recognition was performed using deep learning methods with an accuracy rate of 98.05% [6]. It has been observed that there are studies on many foreign sign languages.

When we overview the studies conducted by Haberdar and Albayrak in 2005 on the TSL, a classification was conducted with the HMM and a success rate of 95.7% was achieved [7]. In the study conducted by Işıkdoğan and Albayrak in 2011, achieved a 99.39% classification success by using feature extraction with Histograms of Oriented Gradients (HOG), and then reducing dimensions Principal Components Analysis (PCA) has been applied to the extracted features [8]. In 2013, the recognition of motion pictures was carried out by Albayrak and Memiş using discrete cosine transformation of RGB video data and data received with Kinect device, and 90% success was achieved [9]. In the study conducted by Demircioğlu et al. in 2016, basic hand movements selected from Turkish sign language were recognized with a 99.03% success rate using the Leap Motion device [10]. In 2017, the classification process of the data obtained using the data glove on TSL was carried out [11]. In the study carried out by Fırat and Uğurlu in 2018, it is seen that some of the words in the Turkish sign language are recognized from the images obtained by using the Kinect device [12]. In the study presented by Çelik and Odabaş in August 2020, it was observed that a 97% success rate was achieved in estimating 10 numbers and 29 letters by using CNN + LSTM models trained with obtained hand images in front of the camera [13].

As a result of the literature review, it is seen that systems with extra equipment such as data glove and Kinect sensor used in the studies have high-performance rates, but it is evaluated that the systems to be created will not be sufficient in terms of their contribution to daily life due to the cost. Although it is seen that the 97% success rate of the work done against the normal camera will make more contribution to daily life, there are more usable and easier systems to perform. It can be observed that determining the skin color and hands in the study will not achieve the desired success as a result of the change in people's clothes.

In this study, the process of recognizing the letters in the TSL alphabet in front of a normal camera was carried out using deep learning models. Unlike other studies, the letters of the TSL alphabet created in front of a normal camera are recognized without any preprocessing. In addition, SSD Mobilenet, EfficientNet, and YOLO models, which are one-stage object detection models used in object recognition, were trained with the original data set. It is observed that the performance values obtained from the object detection models as a result of the training will be beneficial in the selection of the model to be used in further studies on object detection.

This study consists of 6 parts. In the introduction, general information about the study and studies on the recognition of TSL were presented. In Chapter 2, general information about deep learning as well as content about single and two-stage models used in object recognition were included. In Chapter 3, information about the data set created by us for the letters TSL was presented. In Chapter 4, the original data set containing the letters TSL was trained with SSD Mobilenet, EfficientNet and YOLO models, one of the one-stage models used in object detection, and the performance values obtained as a result of the training were compared. With the YOLOv5 model, which has better performance values than the other models trained in Chapter 5, the training period was increased, and the training results were indicated. Chapter 6 includes conclusions and evaluations.

2. Deep Learning and Single Stage Object Detection Models

2.1. Deep learning

Artificial intelligence systems are systems that observe the existing situation and process these observations in line with the predetermined parameters and react to the desired situations to solve the problem. The concept of machine learning has emerged as artificial intelligence allows it to learn from the data in a certain system. Machine learning algorithms determine collecting data from many data sources, transforming these data sets, and processing

according to the results. With the development of these algorithms, artificial neural network models have emerged with logical software that imitates the working mechanism of the human brain and can derive new information by learning, remembering, and generalizing.

With the increasing importance of large amounts of data, deep neural network models have been developed to facilitate feature extraction. Deep learning is a type of artificial neural network consisting of many specialized hidden layers and processing elements, eliminating the cost of feature extraction in classification problems by using large amounts of unsupervised data.

Deep learning methods have gained more importance with the development of graphics cards. Deep learning methods are used in many areas such as natural language processing, image processing, virtual data generation, autonomous vehicles, voice recognition, health, industry, and defense industry. In this study, object recognition, which is one of the fields of image processing, has been performed. Two different methods were used while performing the object recognition process. It has been evaluated that it would be appropriate to use one-stage object detection models, where more efficient results in terms of speed were obtained from these methods, which were distinguished as two-stage and one-stage object detection models.

2.2. One-stage object detection models

The importance of faster detection of objects in object detection applications is increasing day by day for realtime implementation. For this reason, one-stage object detection models, which detect objects much faster than two-stage object detection models, have been developed. In one-stage object recognition models, unlike two-stage object detection models, the whole picture is handled as a whole and object detection is made in this way. The general structure of one-stage object detection applications consists of the backbone, which is called the spine, the neck, which is called the neck between the spine and the head, and the head, which is defined as the head. The process, which starts with the given input image, reaches its final goal with the determination of the class of the object and the coordinates in the head part. One-stage object detection models include models such as SSD, EfficientNet, and YOLO. The general structure of one-stage object detection models is shown in Figure1. [14].

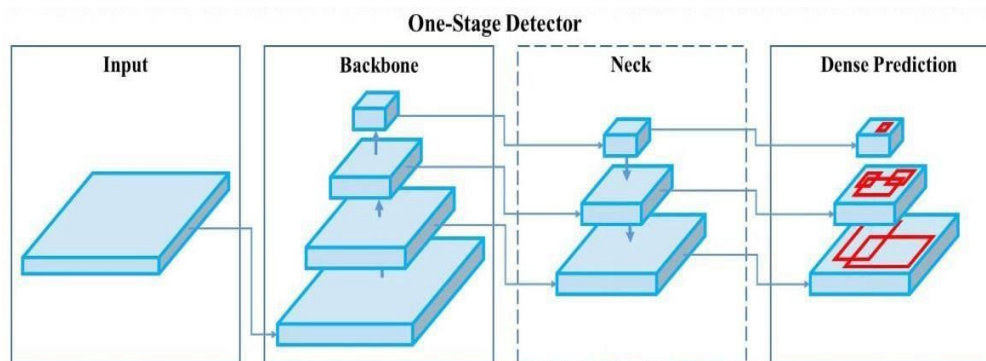


Figure 1. The General structure of one-stage object detection [14]

2.2.1. Single Shot Multibox Detector (SSD)

The SSD model has emphasized that a regression problem to be solved to perform the object detection process would be useful. It has been argued that it would be beneficial not to make proposals for the region containing the object, but instead to consider the picture as a whole. In order to train the SSD model, besides the input images, the bounding box information indicating the locations of the objects is needed. The image given as input is divided into matrix cells by using matrices arranged in different sizes from each other. The maps of the features contain these matrices as a part of the content. Object detection is performed using bounding boxes with different properties from these feature maps.

2.2.2. EfficientNet

The EfficientNet model has two different features compared to other models. The first is the use of a twoway feature pyramid network that offers learnable weights to learn how different input images can make a difference in the model. Secondly, the developed model uses a combined scaling method in the form of resolution, depth, and width as a class prediction network and as a backbone network.

2.2.3. Yolo Models

The biggest advantage of YOLO models over other models is that they can detect objects faster. In the developed YOLO models, the class of the object and its location information are obtained by performing only one operation on the input picture, without any suggestion of a place where the object to be detected can be found. While YOLO extracts this information, it tackles a regression problem and tries to solve it. This regression process combines the coordinates of a bounding box containing the object from the pixels in the picture and the probabilistic classification of which class the object will be included in. The convolutional neural network created with the YOLO model allows us to find the class probabilities of many different objects and the bounding boxes of these objects at the same time in the picture content given as inputs. In this way, the YOLO model, which performs both operations together, stands out a little more than other models with its speed as well as fewer errors in background extraction and more generalizable inferences.

The latest developed version of the YOLO model is the YOLOv5 model. It includes different models such as Yolov5s, Yolov5m, Yolov5l, and Yolov5x. The YOLOv5 model is a model created by implementing the YOLOv4 model developed in the Darknet library on the PyTorch Library. The biggest difference of the Yolov5 model is that it uses the PyTorch structure, unlike the Darknet structure used in previous models. The PyTorch ecosystem is easier to deploy and simpler to support. One of its newest features is that it is simpler to deploy, especially to mobile devices. The weight files created for the YOLOv5 model are quite small compared to other YOLO models. The file includes weights for the YOLOv5 is 27 megabytes, while the weight file for the YOLOv4 model is 244 megabytes. The YOLOv5 model has shown that it can be applied to embedded devices more easily with this feature.

3. Material and Method

3.1. The development process of the proposed model

The model used in the application to be developed for the recognition of the letters in the TSL Alphabet must be satisfactory in terms of both fast and accurate results. The block diagram regarding the development process and performance evaluations of the models is given in Figure 2 below.

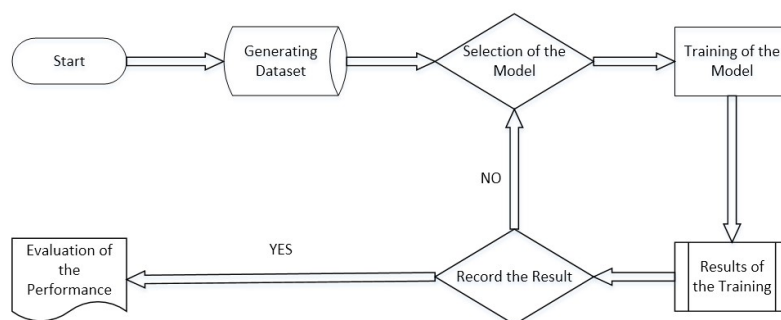


Figure 2. The development process of the models

After the dataset is created and the model is selected, the data is randomly divided into 3 separate groups for training, validation, and test data. Then, the training process is started for the selected model to learn. As a result of the training, model and parameter selection and improvements continued until the system learned enough and the results were satisfactory. The performance evaluation of the system obtained the best performance values is presented in the results section.

3.2. Dataset

TSL is a new and untouched field in terms of applying computer science and artificial intelligence models. With the development of deep learning methods, datasets have started to be created for the recognition of TSL. However, it is seen that the datasets prepared in the studies examined are mostly not open to the public, it has been seen that the datasets are specific to the study. For this reason, it was decided to create a new dataset. Therefore, it was decided to generate a new dataset. While generating the new dataset, it was aimed to prepare a dataset consisting of 29 classes, corresponding to 29 letters in our alphabet. The original dataset creation process consists of four steps. In the first step, videos that can be viewed publicly and that contain the TSL alphabet were detected and downloaded. In the second step, a total of 1000 416x416 pictures were obtained by adding the videos we took to the letters where the downloaded videos were insufficient. The images obtained in the third step are tagged with www.roboflow.com.

Since there is no Turkish character support, the letter 'Ç' is labeled as 'CCC', 'I' as 'III', 'Ğ' as 'GGG', 'Ö' as 'OOO', 'Ş' as 'SSS' and ' The letter 'Ü' is labeled as 'UUU'. In the last step, 1000 tagged images were subjected to data duplication by keeping the same proportions, and a total of 10000 tagged original datasets were obtained with the brightness, contrast, color, saturation, noise, and geometric changes. Some images of the original dataset prepared are shown in Figure 3 and Figure 4 below.

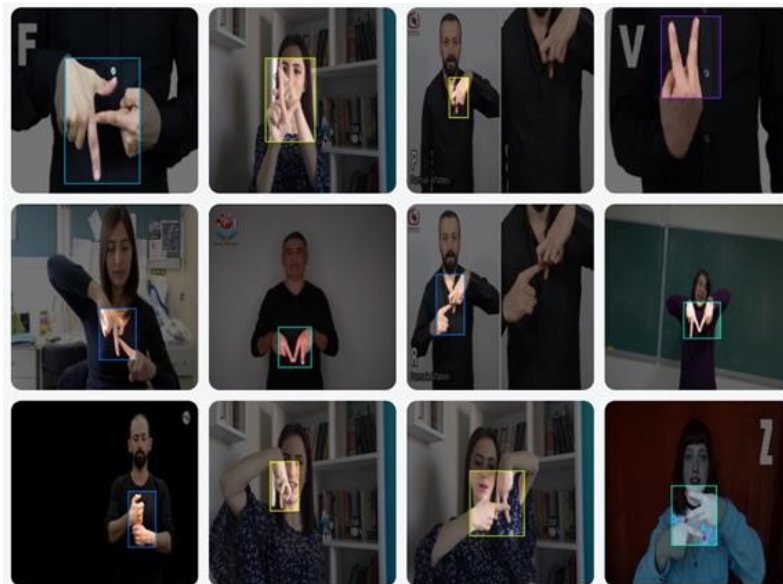


Figure 3. Some TSL image examples before augmentation

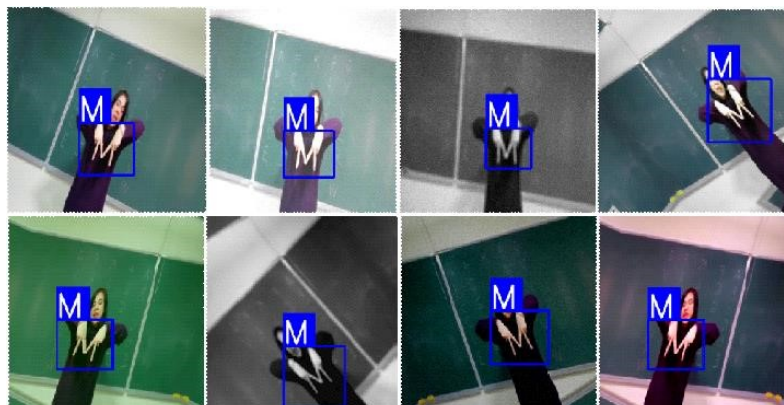


Figure 4. A sample augmentation of “M” letters

The data set, which was preprocessed, labeled, and reproduced, was randomly grouped as 70% training, 20% validation, 10% testing, and the training process was started.

At this stage of the study, the original data set containing the letters TSL was trained with SSD Mobilenet, EfficientNet, and YOLOv5s models, which are one-stage object detection models. The training process of all models was carried out in Google Colab environment using Tesla T4 GPU. Loss values were calculated for the models. Classification/cls_loss loss value was calculated to determine whether the detected sign is in the correct class. In order to determine whether the position and size of the frame (BBox) are correct, the Loss value of Localization (box_loss), the loss value of Confidence (Regularization/obj_loss) related to the confidence value of the box performing the detection operation, and finally the Total (Total) loss values were calculated. Graphs were drawn regarding the variation of these calculated values. The parameters were updated for each model, taking into account the parameter values with the highest performance.

3.3. SSD Mobilenet

The SSD Mobilenet model was designed with the Tensorflow API, which includes many trained network structures in the field of object recognition and classification. With the arrangement made, files in the form of record and .pbtxt were created. 7000 trained and 2000 valid images are set as input data to the designed model. In the model, the input images were resized, the size of the input data was resized to 640x640, the Batch Size was determined as 14 and the training process was provided in 5000 steps. Total training time is 2 hours and 5 minutes. The total loss value calculated as a result of the training was calculated as 0.84 and is shown in Figure 5 below along with the other loss values.

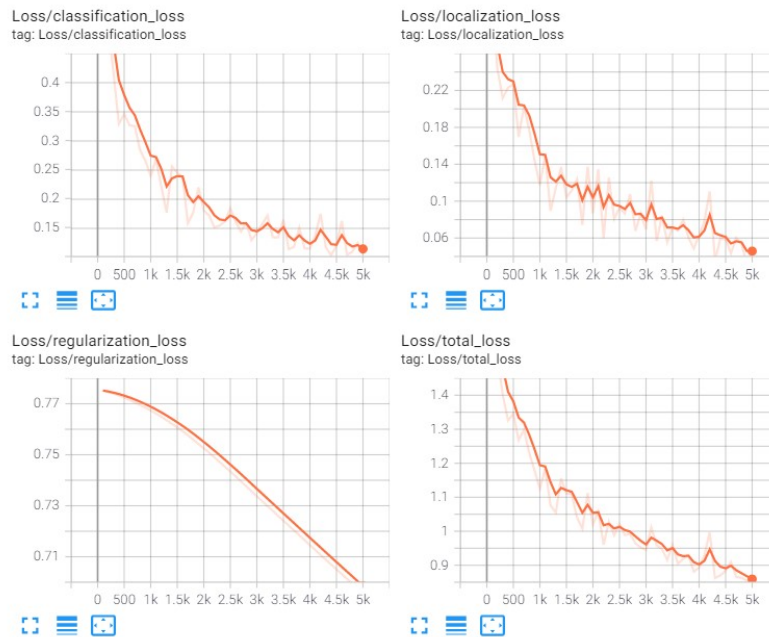


Figure 5. SSD Mobilenet loss values

3.4. EfficientNet

In this model, which was created using Tensorflow API, the input images were resized, the size of the input data was reduced to 512x512 by the model, the Batch Size was determined as 16 and the training process was provided in 5000 steps. The training process was completed in 2 hours. The total loss value calculated as a result of the training was calculated as 0.78 and is shown separately in Figure 6 below along with the other loss values.

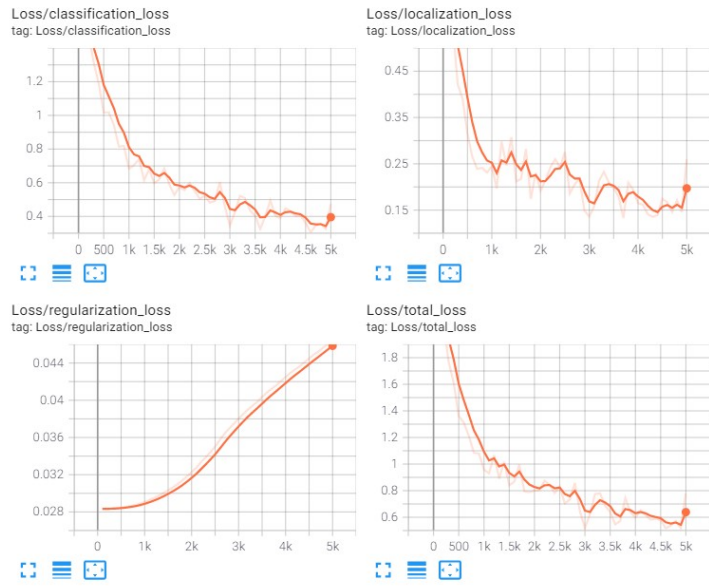


Figure 6. EfficientNet loss values

3.5. YOLOv5s

The YOLOv5s model is a one-stage object detection model using the Pytorch library. In this model, input images are resized to 416x416, Batch Size is set to 16 and, the training process is defined as 100 epochs. The total training was completed in 1 hour 59 minutes and 47 seconds. The total loss value was calculated as 0.04 at the end of the training and results are shown separately in Figure 7 below along with the other loss values.

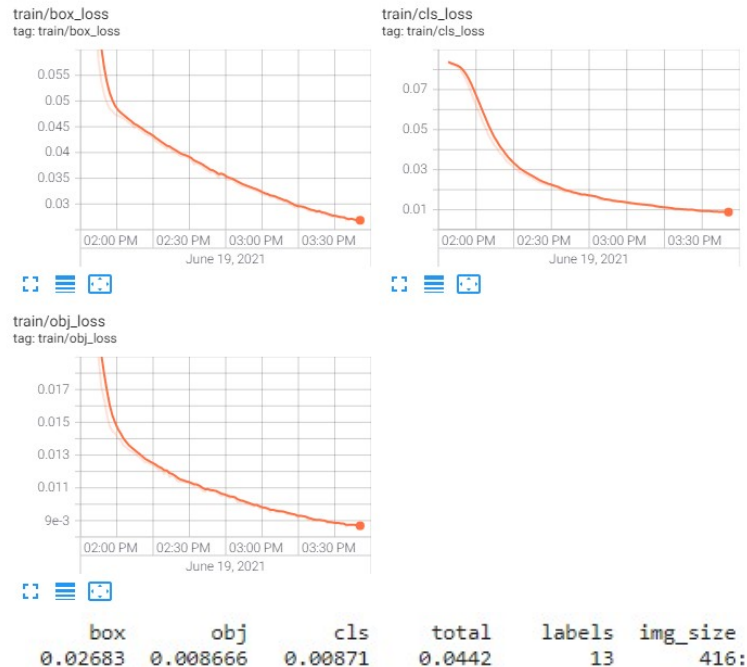


Figure 7. YOLOv5s loss values

Considering that all the developed models take approximately 2 hours and the input dimensions are close to each other, it is seen that the YOLOv5s model with a total loss value of 0.04 comes to the fore. Then, in the trials

with the Yolov5s model, a Colab file running Tesla K4 extracted an image in approximately 0.009 seconds. In other words, approximately 110 FPS operations are performed per second. When compared with other models, it was found appropriate to use the YOLOv5s model in the application to be prepared for recognizing the letters in the Turkish Sign Language Alphabet, since it has the lowest loss value and operates faster than other models. Information about all the models prepared is shown in Table 1.

Table 1. Performance values of implemented models

Model	Size of inputs	Step / Epoch	Batch Size	Cls Loss	Lclzsn /Bbox Loss	Total Loss	Training time
SSD Mobilenet	640x640	5000	14	0,10	0,04	0,84	2 h 5 min.
EfficientdetD0	512x512	5000	16	0,47	0,25	0,78	2 h
YOLOv5s	416x416	100	16	0,008	0,02	0,04	1 h 59 min. 47 sec.

3.6. Classification of TSL letters based on YOLOv5s Model

As a result of the training process of the original dataset of TSL letters, it was understood that the model with the highest success rate was the YOLOv5s model. It recognized the TSL letters of the YOLOv5 model at 110 FPS per second, with a success rate of 92.3.

To recognize TSL letters, the training process was carried out by changing only the number of epochs as 200 from the above-mentioned parameters in the YOLOv5s model. Each epoch performed, the training process averaged 1 minute for 438 groups and 11 seconds for evaluation on 63 groups. The total duration of the training was calculated as 4 hours and 43 seconds. As a result of the training, Precision (Precision), Recall (Sensitivity) and Mean Average Precision (Mean Average Precision) performance values are calculated both in total and separately for each class. The formulas used to calculate the performance values are given in formulas 1,2 and 3, respectively. The expression presented with Formula 1 was used to calculate the Accuracy value.

$$Acc = (TP+TN)/(TP+TN+FN+FP) \tag{1}$$

Precision shown by Formula 2 is expressed as the ratio of correctly classified data to all classified data.

$$P = TP/(TP+FP) \tag{2}$$

Recall, also known as sensitivity value, this value presented by Formula 3. expresses the ratio of correctly classified data to all correctly classified and misclassified data.

$$SN = TP/(TP+FN) \tag{3}$$

Precision Value 0.921, Recall Value 0.89, and mAP@.5 Value 0.923 after training performed at 200 epochs. Some numerical information about these calculated values is presented in Figure 8, and the complexity matrix is shown in Figure 9.

Mustafa KAYA, Fatih BANKUR

Epoch	gpu_mem	box	obj	cls	total	labels	img_size
199/199	1.73G	0.02332	0.007587	0.005633	0.03654	13	416: 100% 438/438 [01:00<00:00, 7.23it/s]
	Class	Images	Labels	P	R	mAP@.5	mAP@.5: 95: 100% 63/63 [00:11<00:00, 5.27it/s]
	all	2000	2000	0.921	0.893	0.923	0.505
	A	2000	70	0.977	0.843	0.937	0.454
	B	2000	70	0.868	1	0.968	0.527
	C	2000	70	0.882	0.957	0.987	0.649
	CCC	2000	70	0.976	0.857	0.932	0.493
	D	2000	70	0.836	0.726	0.794	0.518
	E	2000	70	0.966	0.9	0.93	0.248
	F	2000	70	0.946	0.843	0.914	0.6
	G	2000	70	0.983	0.971	0.994	0.635
	GGG	2000	70	0.976	1	0.995	0.55
	H	2000	70	0.867	0.935	0.88	0.538
	I	2000	60	0.925	0.983	0.969	0.48
	III	2000	60	0.846	0.983	0.931	0.505
	J	2000	60	0.731	0.867	0.703	0.351
	K	2000	80	0.962	0.487	0.845	0.36
	L	2000	60	0.999	0.95	0.993	0.574
	M	2000	70	0.843	0.857	0.76	0.432
	N	2000	70	0.99	0.857	0.935	0.625
	O	2000	70	0.984	0.882	0.991	0.569
	OOO	2000	70	0.994	1	0.995	0.536
	P	2000	70	0.92	1	0.988	0.501
	R	2000	70	1	0.948	0.985	0.329
	S	2000	70	0.985	0.943	0.994	0.513
	SSS	2000	70	0.877	1	0.994	0.571
	T	2000	70	1	0.995	0.995	0.454
	U	2000	70	0.752	0.986	0.909	0.578
	UUU	2000	70	1	0.547	0.765	0.417
	V	2000	70	0.813	0.957	0.97	0.638
	Y	2000	70	0.955	0.914	0.912	0.527
	Z	2000	70	0.861	0.714	0.814	0.461

200 epochs completed in 3.833 hours.

Optimizer stripped from runs/train/yolov5s_results15/weights/last.pt, 14.9MB
 Optimizer stripped from runs/train/yolov5s_results15/weights/best.pt, 14.9MB
 CPU times: user 2min 57s, sys: 22.1 s, total: 3min 19s
 Wall time: 4h 43s

Figure 8. YOLOv5s loss values

In the confusion matrix shown in Figure 9. below, the TP (True Positive) class was predicted correctly, TN (True Negative) was predicted correctly if it should not be in the relevant class, FP (False Positive) was incorrectly predicted in a class even though it should not be, and FN (False Negative) indicates that it was incorrectly guessed when it should not be in the relevant class.

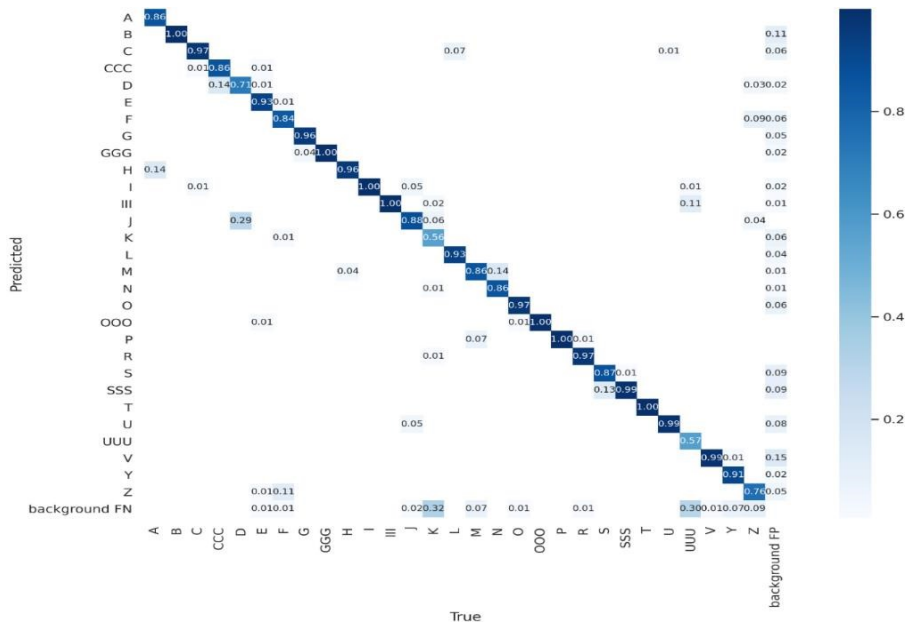


Figure 9. YOLOv5s Confusion Matrix

When the values obtained for each letter were checked after the training, it was determined that there were letters with mAP@.5 value below 0.9. It is seen that these detected letters are D, H, J, K, M, Ü, and Z. It is evaluated

that the most important factors in the confusion of these letters in the TSL by the model are the movements that make up these letters using both hands and the positions of the fingers.

4. Conclusion and Evaluation

It is aimed to recognize the letters in the TSL alphabet quickly and accurately. It has been understood that there is no publicly shared data set suitable for the application to be carried out in line with this goal. Thereupon, videos shared publicly by 15 different people to learn the letters in TSL were used to generate a data set. In cases where the images obtained from the videos were not sufficient, new videos were prepared. Using all the videos recorded, a new and unique data set was generated with a total of 10000 images containing 29 letters in our alphabet. As a result of the research, it was found appropriate to use the YOLO model, which can reach 140 FPS in the fields of object recognition and object tracking. The generated data set was trained in the Google-Colab environment with the latest version of the YOLO model, YOLOv5, and a success rate of 92.3% was achieved.

Although 92.3% success was achieved with the implemented application, one of the biggest factors affecting this success rate is the data set. The dataset used in the application was generated by people of different genders in many different age groups. It is thought that the improvements to be made in the data set can increase the performance of the model since most of the movements that make up the TSL alphabet are made using both hands and that the movements that make up some letters are not fixed.

References

- [1] Charayaphan, C., & Marble, A. E. (1992). Image processing system for interpreting motion in American Sign Language, *Journal of Biomedical Engineering*, 14(5), 419-425.
- [2] Takahashi, T., & Kishino, F. (1991). Hand gesture coding based on experiments using a hand gesture interface device. *Acm Sigchi Bulletin*, 23(2), 67-74.
- [3] Waldron, M. B., & Kim, S. (1995). Isolated ASL sign recognition system for deaf persons. *IEEE Transactions on rehabilitation engineering*, 3(3), 261-271.
- [4] Allen, J. M., Asselin, P. K., & Foulds, R. (2003, March). American Sign Language finger spelling recognition system. In *2003 IEEE 29th Annual Proceedings of Bioengineering Conference* (pp. 285- 286). IEEE.
- [5] Wang, H. G., Sarawate, N. N., & Leu, M. C. (2004, July). Recognition of American sign language gestures with a sensory glove. In *Japan USA Symposium on Flexible Automation*, Denver, CO (pp. 102-109).
- [6] M. Taskiran, M. Killioglu and N. Kahraman, (2018) "A Real-Time System for Recognition of American Sign Language by using Deep Learning," *2018 41st International Conference on Telecommunications and Signal Processing* (pp. 1-5)
- [7] Haberdar, H., & Albayrak, S. (2005, October). Real time isolated turkish sign language recognition from video using hidden markov models with global features. In *International Symposium on Computer and Information Sciences* (pp. 677687). Springer, Berlin, Heidelberg.
- [8] Işıkdoğan F., Albayrak S., 2011, June, Automatic recognition of Turkish fingerspelling, In *Innovations in Intelligent Systems and Applications (INISTA)*, 2011 International Symposium on (pp. 264-267), IEEE.
- [9] Memiş, A., & Albayrak, S. (2013, April). Turkish Sign Language recognition using spatio-temporal features on Kinect RGB video sequences and depth maps. In *2013 21st Signal Processing and Communications Applications Conference (SIU)* (pp. 1-4). IEEE.
- [10] Demircioglu, Burcak & Bülbül, Güllü & Kose, Hatice. (2016). Leap Motion ile Türk İşaret Dili Tanıma / Turkish Sign Language Recognition with Leap Motion. 10.13140/RG.2.1.4923.3529.
- [11] Ceber, Y. E., Karacaoğlan, E., Uysaf, F., & Tokmakçı, M. (2017, October). The design of glove that can translate sign language to Turkish language. In *2017 Medical Technologies National Congress (TIPTEKNO)* (pp. 1-4). IEEE.
- [12] Firat, Yelda & Uğurlu, Taşkın. (2018). LATİS TABANLI ANLAM ÇÖZÜMLENMESİ İLE TÜRKÇE İŞARET DİLİ TERCÜME SİSTEMİ. Ömer Halisdemir Üniversitesi Mühendislik Bilimleri Dergisi. 10.28948/ngumuh.443157. [13] Çelik, Ö , Odabas, A . (2020). Sign2Text: Konvolüsyonel Sinir Ağları Kullanarak Türk İşaret Dili Tanıma . *Avrupa Bilim ve Teknoloji Dergisi* , (19) , 923-934 .
- [14] <https://towardsdatascience.com/yolo-v4-optimal-speed-accuracy-for-object-detection-79896cd47b50> Erişim Tarihi 06/06/2021.

Antioxidant and Antimicrobial Effects of *Trametes versicolor* (L.) Lloyd Extracts in Different Solvents

Şule İNCİ^{1*}, Mehmet AKYÜZ², Sevda KIRBAĞ³

^{1*} Department of Biology, Science Faculty, Fırat University, Elazığ, Turkey

² Department of Biology, Science & Arts Faculty, 3Bitlis Eren University, Bitlis, Turkey

³ Department of Biology, Science Faculty, Fırat University, Elazığ, Turkey

*¹ sule.inci@hotmail.com, ² makyuz@beu.edu.tr, ³ skirbag@firat.edu.tr

(Geliş/Received: 20/02/2022;

Kabul/Accepted: 27/06/2022)

Abstract: *Trametes versicolor* (L.) Lloyd known as turkey tail, is a medicinal mushroom belonging to the Polyporaceae. Although the consumption and commercial sale of this mushroom in our country is new, it has been used for centuries as a medicine in some countries, especially in China. In this study, it was aimed to determine the antimicrobial and antioxidant effects of ethanol and methanol extracts of *T. versicolor*. Its antimicrobial effects were determined by disk diffusion and microdilution method using pathogenic microorganisms such as *Escherichia coli*, *Klebsiella pneumoniae*, *Pseudomonas aeruginosa*, *Bacillus megaterium*, *Staphylococcus aureus*, *Candida albicans* and *Trichophyton* sp. Total antioxidant level, total oxidant level and DPPH radical scavenging capacity were detected for the antioxidant activity of the mushroom. According to the results obtained, it was seen that these extracts inhibit the growth of microorganisms at different rates (10-21 mm) according to the disk diffusion method. The minimal inhibitory concentrations of *T. versicolor* against microorganisms used were determined to be between 62.5-250 µg/mL. The TAS and TOS values of the methanol extract were 0.72 mmol Trolox Equiv./L and 18.39, respectively, the TAS and TOS values of the ethanol extract were detected 0.88 mmol Trolox Equiv./L and 16.71 µmol H₂O₂ Equiv./L, respectively.

Key words: Medicinal mushrooms, *Trametes versicolor*, antimicrobial, antioxidant.

Trametes versicolor (L.) Lloyd'un Farklı Çözücülerdeki Ekstraktlarının Antioksidan ve Antimikrobiyal Etkileri

Öz: Hindi kuyruğu olarak bilinen *Trametes versicolor* (L.) Lloyd, Polyporaceae familyasına ait tıbbi bir mantardır. Bu mantarın ülkemizde tüketimi ve ticari satışı yeni olmasına rağmen Çin başta olmak üzere bazı ülkelerde yüzyıllardır ilaç olarak kullanılmaktadır. Bu çalışmada, *T. versicolor*'un etanol ve metanol ekstraktlarının antimikrobiyal ve antioksidan etkilerinin belirlenmesi amaçlanmıştır. Antimikrobiyal etkileri, *Escherichia coli*, *Klebsiella pneumoniae*, *Pseudomonas aeruginosa*, *Bacillus megaterium*, *Staphylococcus aureus*, *Candida albicans*, *Trichophyton* sp. gibi patojenik mikroorganizmalar kullanılarak disk difüzyon ve mikrodilüsyon yöntemi ile belirlendi. Mantarın antioksidan aktivitesi için toplam antioksidan seviyesi, toplam oksidan seviyesi ve DPPH radikal süpürme kapasitesi tespit edildi. Elde edilen sonuçlara göre bu ekstraktların disk difüzyon yöntemine göre bazı mikroorganizmaların büyümesini farklı oranlarda (10-21 mm) engellediği görülmüştür. *T. versicolor*'un kullanılan mikroorganizmalara karşı minimum inhibitör konsantrasyonları. 62.5-250 µg/mL arasında olduğu belirlendi. Metanol ekstraktının TAS ve TOS değerleri sırasıyla 0.72 mmol Trolox Equiv./L ve 18.39 µmol H₂O₂ Equiv./L, etanol ekstraktının TAS ve TOS değerleri sırasıyla 0.88 mmol Trolox Equiv./L ve 16.71 µmol H₂O₂ Equiv./L tespit edildi.

Anahtar kelimeler: Tıbbi mantarlar, *Trametes versicolor*, antimikrobiyal, antioksidan.

1. Giriş

Mushrooms are increasingly appreciated for their medicinal properties as well as their use as functional foods [1]. Since ancient times, mushrooms are benefited in the treatment of many diseases. In many studies conducted today, it has been reported that mushrooms have antioxidant, antimicrobial, antiproliferative, anticancer, DNA protective, antiinflammatory, immunomodulatory and antihypertensive activities [2, 3]. Extracts are prepared from, macrofungi and actinomycetes, which are used in the treatment of many diseases [4]. *Trametes versicolor* (commonly known as turkey tail), which is among the macrofungi, draws attention due to its wide use in the food and pharmaceutical industry [5]. *T. versicolor* (L.) Lloyd, known as turkey tail, is a woody mushroom that grows on different trees such as oak and Prunus, and on different conifers such as fir or pine trees [6]. Although it is a non-edible species, it has traditionally been used in Asia as an alternative source for the treatment of many diseases,

* Corresponding author: sule.inci@hotmail.com. ORCID Number of authors: ¹ 0000-0002-4022-5269, ² 0000-0003-3986-3498, ³ 0000-0002-4337-8236

including cancer and some infections [7]. In our country, *T. versicolor* has commercially been produced by a company since 2000. It is sold in natural form, as ground and sliced in 100 g packages [8]. Generally, 2-5 g of dried mushrooms are boiled in 1 L of water and consumed 2-3 times a day. The tea of this mushroom is used to strengthen immunity, regulate blood sugar, reduce stress and fatigue, anti-aging, increase probiotic microorganisms, reduce oxidative stress of cells and strengthen memory [8].

However, although the medicinal effects of this species are remarkable, its antimicrobial and antioxidant effects are not sufficient in the literature. More emphasis is placed on the anticancer effect of polysaccharides. Therefore, in this study, it was aimed to detect the antimicrobial effect against some pathogenic microorganisms and antioxidant capacity of ethanol and methanol extracts of *T. versicolor*.

2. Materials and Methods

2.1. Material

T. versicolor was collected in April 2017 in Sivrice district of Elazig. The species was identified by performing macroscopic and microscopic studies. After the mushroom was ground, 0.5 g was weighed. 100 mL of 96% methanol (MetOH) and ethanol (EtOH) were added to the samples and left in an orbital shaker at 100 rpm for 72 h. Then, samples were filtered with blank disc.

2.2. Antimicrobial effect

2.2.1. Microorganisms

In this study; *E. coli* ATCC25922, *K. pneumoniae* ATCC700603, *P. aeruginosa* DMS 50071, *B. megaterium* DSM32, *S. aureus* COWAN1, *C. albicans* FMC17 and *Trichophyton sp.* were used. Microorganism were obtained from Firat-University, Department of Biology.

2.2.2. Preparation of microorganism cultures and antimicrobial testing

The antimicrobial activity was determined by the disc diffusion method [9]. Mueller Hinton Agar, Yeast Malt Extract Agar and Sabouraud Dextrose Agar were sterilized separately in an erlen, then cooled to 45-50°C and inoculated with culture of bacteria, yeast and dermatophyta (10^6 cells / mL of bacteria, 10^4 cells / mL yeast and 10^4 cells/mL dermatophyta as per Mc Farland standard). After shaking well, they were poured into sterile petri dishes and homogeneously dispersed. Discs (6 mm diameter) impregnated with 100 μ L (1000 μ g) of extracts were placed on microorganism-inoculated plates. Then the plates were kept at 4°C for 2 h. The inoculated petri dishes were incubated at $37 \pm 0.1^\circ\text{C}$ at 24 h for bacteria and at $25 \pm 0.1^\circ\text{C}$ at 72 h for yeasts and dermatophyta fungi. Standard discs were used for bacteria (Streptomycin sulphate 10 μ g / disc) and yeasts (Nystatin 30 μ g / disc). The antimicrobial effect was detected by measuring the inhibition zone in mm.

2.2.3. The minimum inhibitory concentration (MIC)

The minimum inhibitory concentration (MIC) of MetOH and EtOH extracts of *T. versicolor* was detected using macro-broth dilution techniques [10]. A two fold serial dilution of the reconstituted extract was prepared in Mueller Hinton Broth. Each dilution was seeded with 100 μ L of the standardized suspension of the test organisms and incubated for 24 h at 37°C. All extracts were tested at 1000-15.625 μ g/mL concentrations.

2.3. Antioxidant effect

2.3.1. Total antioxidant activity (TAS) and total oxidant activity (TOS)

TAS and TOS levels of MetOH and EtOH extracts of sample were determined with Rel Assay kits (Rel Assay Kit Diagnostics). TAS value was given as mmol Trolox equiv./L and Trolox was used as the calibrator [11]. The TOS value was expressed as μ mol H₂O₂ equiv./L and hydrogen peroxide was used as the calibrator [12].

2.3.2. 2,2-diphenyl-1-picrylhydrazyl radical scavenging capacity (DPPH)

The antioxidant activity of different concentrations of MetOH and EtOH extracts of *T. versicolor* was detected according to the DPPH radical scavenging capacity method [13]. The solution was prepared in methanol and ethanol at a concentration of 25 mg/mL of the obtained extract and diluted 4 times to obtain the calibration curve of DPPH. 40 µL of the solution was taken and 160 µL of DPPH solution was added. After mixing well, the plate left in the dark for 30 min. Methanol and ethanol were used as controls. At the end of the period, absorbances of each mixture were read at 570 nm in the spectrophotometer. percent inhibition values were calculated;

$$\% \text{ DPPH inhibition} = [(AbsControl - AbsSample) / AbsControl] \times 100 \quad (1)$$

2.4. Statistical analysis

The statistical analysis was performed according to the Kruskal Wallis test.

3. Results

3.1. Antimicrobial effect

Antimicrobial activities of *T. versicolor* extracts obtained from MetOH and EtOH against, used microorganisms are given in Table 3.1. According to the results obtained from, methanol and ethanol extracts of *T. versicolor*, it inhibited the development of *C. albicans* the most.

Table 3.1. Inhibition zones of extracts of *T. versicolor* against some microorganisms (mm)

	<i>T. versicolor</i> -MetOH	<i>T. versicolor</i> -EtOH	Standard antibiotics
<i>E.coli</i>	15.66 ± 0.33 ^{ab}	12.33 ± 0.33 ^b	20.21 ± 0.57*
<i>K. pneumoniae</i> .	16.33 ± 0.33 ^{ab}	21.75 ± 0.46 ^{ab}	19.13 ± 0.43*
<i>P. aeruginosa</i>	11.66 ± 0.33 ^b	12.33 ± 0.33 ^b	10.33 ± 0.33*
<i>B. megaterium</i>	12.66 ± 0.33 ^b	10.23 ± 0.33 ^b	20.25 ± 0.57*
<i>S. aureus</i>	15.66 ± 0.33 ^{ab}	10.23 ± 0.33 ^b	20.23 ± 0.33*
<i>C. albicans</i>	26.76 ± 0.46 ^{ab}	24.74 ± 0.48 ^{ab}	21.32 ± 0.42**
<i>Tricophyton sp.</i>	24.76 ± 0.46 ^{ab}	11.26 ± 0.33 ^b	12.24 ± 0.33**

(Streptomycin sulphate *10 µg/disc for bacteria, Nystatin** 30 µg/disc for yeast and dermatophyta), Means in the same column with the different superscript are significantly different (p<0.05)

In the results obtained, minimum inhibitory concentration values of extracts against some microorganisms were determined. Minimum inhibitory concentration values between 62.5 -125µg/mL were determined in the MetOH extract. The MIC value of the EtOH extract of *T. versicolor* against microorganisms were detected between 62.5-250 µg/mL (Table 3.2).

Table 3.2. MIC values of extracts of *T. versicolor* against some microorganisms (µg/mL)

Microorganisms	<i>T. versicolor</i> -MetOH	<i>T. versicolor</i> -EtOH
<i>E.coli</i>	62.5	125
<i>K. pneumoniae</i>	62.5	62.5
<i>P. aeruginosa</i>	125	250
<i>B. megaterium</i>	62.5	250
<i>S. aureus</i>	62.5	125
<i>C. albicans</i>	125	250
<i>Tricophyton sp.</i>	125	125

3.2. Antioxidant effect

The TAS and TOS values of the MetOH extract of mushroom was found to be 0.72 mmol and 18.39 µmol, respectively and the EtOH extract of mushroom was 0.88 mmol and 16.71 µmol, respectively (Table 3.3).

Table 3.3. TAS and TOS values of *T. versicolor*

	TAS(mmol Trolox equiv./L)	TOS ($\mu\text{mol H}_2\text{O}_2$ equiv./L)
<i>T. versicolor</i> -MetOH	0.72 \pm 0.231	18.39 \pm 0.187
<i>T. versicolor</i> -EtOH	0.88 \pm 0.235	16.71 \pm 0.131

Values are means \pm S.D.n:3, $p < 0.05$ importantly dissimilar

The percent inhibition of the DPPH of *T. versicolor* is seen in Table 3.4. It was detected that the antioxidant effects of MetOH and EtOH extracts increased with increasing concentration.

Table 3.4. Percent inhibition of the DPPH radical of *T. versicolor*

	<i>T. versicolor</i> -MetOH	<i>T. versicolor</i> -EtOH
1000 $\mu\text{g/mL}$	62.80 \pm 0.231	64.84 \pm 0.724
500 $\mu\text{g/mL}$	50.60 \pm 0.724	60.03 \pm 0.645
250 $\mu\text{g/mL}$	26.82 \pm 0.440	38.78 \pm 0.732
125 $\mu\text{g/mL}$	10.97 \pm 0.635	22.42 \pm 0.724

Values are means \pm S.D.n:3, $p < 0.05$ importantly dissimilar with Kruskal Wallis's test

4. Discussion

Methanol extract of *T. versicolor* was detected to form inhibition zones (24.14-30.18 mm) at different rates against *E. coli*, *K. pneumoniae*, *P. aeruginosa* and *S. aureus* [5]. It was detected that the methanol extract of *T. gibbosa* at 30 mg/mL inhibited the growth of *E. coli*, *S. aureus*, *K. pneumoniae* and *C. albicans* at different rates (zones of inhibition, respectively 19.50, 20.67, 17.00, 20.80 mm) The methanol extract of *T. elegans* (30 mg/mL) showed different antimicrobial effects against similar microorganisms (18.00 \pm 0.75-23.50 \pm 0.55mm). Methanol extracts of *T. gibbosa* and *T. elegans* have been reported to have MIC ranging from 6 to 20 mg/mL against microorganism used [14]. MIC values of the methanol extract of *T. versicolor* were determined against *E. coli*, *P. aeruginosa* and *C. albicans* [15]. Inhibition zones of *T. versicolor* extract at 150 μL concentration were found between 7-8 mm against *B. subtilis*, *C. albicans*, *K. pneumoniae* (MDR) and *S. aureus* [16]. Mycelial extracts of *T. versicolor*, *T. gibbosa*, *T. hirsuta* have been reported to inhibit the growth of *C. albicans* at a concentration of 32.0 mg/mL [17]. When the obtained results are compared with previous studies, it is seen that there are differences. The results seem to vary depending on the species used, the habitat of the species, the microorganism, the solvent and most importantly the concentrations [5, 14-17].

Antioxidant effect of the methanol extract of *T. versicolor* at different concentrations was determined in the range of 32.62-72.32% [5]. The IC₅₀ values of the DPPH of the water and ethanol extracts of the same species were calculated as 11.9 \pm 1.1 and 5.6 \pm 0.8 $\mu\text{g/mL}$, respectively [7]. The IC₉₀ values of methanol and aqueous extracts of *T. versicolor* were determined as 178.83 $\mu\text{g/mL}$ and 518.06 $\mu\text{g/mL}$, respectively [18]. It has been reported that the percent inhibition of DPPH of the ethanol extract of the same species at different concentrations is between 5.26% and 26.77%. In the same study, TAS and TOS values were calculated as 0.820 \pm 0.063 mmol Trolox equiv./L and 17.760 \pm 0.456 $\mu\text{mol H}_2\text{O}_2$ equiv./L, respectively [19]. The antioxidant effects of *T. versicolor* at 250, 500, 1000 and 5000 $\mu\text{g/mL}$ concentrations were determined as 2.97% \pm 0.14, 5.14 \pm 0.27%, 8.20 \pm 0.40% and 28.69 \pm 0.50%, respectively [20]. Study results compared with previous studies, it was determined that some were higher than others [7, 18-20]. The main reason for this might depend on the habitat of the fungus, the time of collection and the concentrations used.

5. Conclusion

It was detected that the methanol extract of *T. versicolor* showed the best antimicrobial activity against *C. albicans*. In addition, methanol extract showed antimicrobial effect at lower concentrations compared to ethanol extract. It was determined that *T. versicolor*'s methanol and ethanol extracts had good TAS values, but high TOS values. Therefore, it can be said that the presence of oxidant compounds in methanol and ethanol extracts of *T. versicolor* is high. It was determined that the scavenging effect of DPPH radical of *T. versicolor* was lower than the controls. It is known that in the region where this species is collected, it is boiled for healing purposes and its water is consumed. We think that *T. versicolor* has little medical effects in literature studies and this study is important in terms of bringing it into the literature. We predict that the results obtained are important in terms of pharmacology and that mushroom extracts can be used as antimicrobial and antioxidant agents.

Acknowledgements

This study has been presented at 8th International Conference on Materials Science and Nanotechnology For Next Generation. MA and SK: conceptualization, supervision, methodology, writing, review and editing of the final manuscript, Şİ: formal analysis, methodology, editing of manuscript. All authors have read the final manuscript and approved the submission.

References

- [1] Venturella G, Ferraro V, Cirlincione F, Gargano ML. Medicinal mushrooms: bioactive compounds, use, and clinical trials. *Int J Molecular Sci* 2021; 22(2): 634.
- [2] İnci Ş, Kirbag, S. *Terfezia claveryi* Chatin'ın besinsel içeriği, antioksidan ve antimikrobiyal aktivitesi. *Artvin Çoruh Üni Orman Fak Derg* 2018; 19(2): 138-143.
- [3] Akyüz M, Karagöz ID, İnci S, Kilic IH, Kirbag S, Simitcioglu B. Cytotoxicity and DNA protective effects of the *Terfezia* and *Picoa* species from the eastern region of Turkey. *J Fac Pharmacy of Istanbul Uni* 2021; 51(2): 198-204.
- [4] Sevim E, Sevim, A. (2021). Kırşehir ilinden toplanan *Morchella esculenta* (L.) Pers (Kuzu Göbeği) mantarlarının moleküler karakterizasyonu ve antimikrobiyal aktivitelerinin belirlenmesi. *J Advanced Re in Natural and Applied Sci* 2021; 7(1): 48-59.
- [5] Bains A, Chawla P. In vitro bioactivity, antimicrobial and anti-inflammatory efficacy of modified solvent evaporation assisted *Trametes versicolor* extract. *3 Biotech* 2020; 10(9): 1-11.
- [6] Pop R, Pop RM, Puia IC, Puia A, Chedea VS, Leopold N, Bocsan IC, Buzoianu AD. Characterization of *Trametes versicolor*: medicinal mushroom with important health benefits. *Not Bot Horti Agrobo* 2018; 46(2): 343-349.
- [7] Rašeta M, Popović M, Knežević P, Šibul F, Kaišarević S, Karaman M. Bioactive phenolic compounds of two medicinal mushroom species *Trametes versicolor* and *Stereum subtomentosum* as antioxidant and antiproliferative agents. *Chem Biodiver* 2020; 17(12): e2000683.
- [8] Anonymous, 2021. <https://www.agromantar.com>. (03.09.2021)
- [9] Collins CH, Lyne PM. *Mikrobiyological Methods*. London, Butter Morths and Co (Publishers) Ltd, 1987. pp. 450
- [10] National Committee for Clinical Laboratory Standard. *Methods for dilution in Antimicrobial Susceptibility Test. Approved Standard*, National Committee for Clinical Laboratory Standard (NCCLS), Villanova, P.A. 1998.
- [11] Erel O. A novel automated direct measurement method for total antioxidant capacity using a new generation, more stable ABTS radical cation. *Clinical biochem* 2004; 37(4): 277-285.
- [12] Erel O. A new automated colorimetric method for measuring total oxidant status. *Clinical biochem* 2005; 38(12): 1103-1111.
- [13] Cuendet M, Hostettmann K, Potterat O, Dyatmiko W. Iridoid glucosides with free radical scavenging properties from *Fagraea blumei*. *Helvetica Chimica Acta* 1997; 80(4): 1144-1152.
- [14] Appiah T, Boakye YD, Agyare C. Antimicrobial activities and time-kill kinetics of extracts of selected Ghanaian mushrooms. *Evidence-Based Complementary and Alternative Med* 2017.
- [15] Hleba L, Vuković N, Petrová J, Kačániová M. Antimicrobial activity of crude methanolic extracts from *Ganoderma lucidum* and *Trametes versicolor*. *Scientific Papers: Animal Sci Biotechnol* 2014; 47: 89-93.
- [16] Canlı K, Benek A, Şenturan M, Akata I, Altuner EM. In vitro antimicrobial activity of *Morchella esculenta* and *Trametes versicolor*. *Mantar Derg* 2019; 10(3): 28-33.
- [17] Knežević A, Stajić M, Sofrenić I, Stanojković T, Milovanović I, Tešević V, Vukojević J. Antioxidative, antifungal, cytotoxic and antineurodegenerative activity of selected *Trametes* species from Serbia. *PloS one* 2018; 13(8): e0203064.
- [18] Hossen SM, Tanim MAH, Hossain MS, Sami SA, Emon NU. Deciphering the CNS anti-depressant, antioxidant and cytotoxic profiling of methanol and aqueous extracts of *Trametes versicolor* and molecular interactions of its phenolic compounds. *Saudi J Biological Sci* 2021; 28(11): 6375-6383.
- [19] Akgul H, Sevindik M, Coban C, Alli H, Selamoglu Z. New approaches in traditional and complementary alternative medicine practices: *Auricularia auricula* and *Trametes versicolor*. *J Tradit Med Clin Natur* 2017; 6(2): 239.
- [20] Orhan I, Üstün O. Determination of total phenol content, antioxidant activity and acetylcholinesterase inhibition in selected mushrooms from Turkey. *J Food Composition and Analysis* 2011; 24(3): 386-390.

A Study on Uniaxial Compressive Strength and Ultrasonic Non-Destructive Analysis of Fine-Grained Soil in Seasonally Frozen Regions

Ibrahim Haruna UMAR¹, Müge Elif ORAKOĞLU FIRAT^{2*}

¹ Science and Technology, Kano University, Kust Wudil, Nigeria

² Technology Faculty, Civil Engineering, Firat University, Turkey

¹ ibrahimharunaumar@yahoo.com, ^{2*} morakoglu@firat.edu.tr

(Geliş/Received: 01/03/2022;

Kabul/Accepted: 30/05/2022)

Abstract: Understanding the physical and mechanical properties of soils subjected to freeze-thaw cycles, including both micro and macrostructures, is critical for achieving the required performance of structures employing it as a structural or support material. An experimental study was carried out on clay soil with varying water content (18%, 21.5%, and 23%) after repeated freeze-thaw cycles (0, 2, 5, 7, 12, and 15). The performance of soil was evaluated using unconfined compressive strength (UCS) and ultrasonic pulse velocity (UPV) tests. The experimental results demonstrated that UCS peak values were observed at the lowest water content before and after the freeze-thaw cycles. The stress-strain curves exhibited strain-softening behavior, and this condition transitioned to strain hardening behavior after freeze-thaw cycles with increment in the water content. Moreover, the highest values of UPV were observed to increase UCS values due to capillary forces at minimum water content. Also, an increase in the number of freeze-thaw cycles resulted in a decrease in the UPV. According to correlations between UPV and UCS values, the highest correlations for water contents were obtained at optimum water content, and a decreasing trend was observed after experiencing a number of freeze-thaw periods. In addition, the Grey Correlation Analysis was performed to show the degree of correlation between the UCS and UPV, water content as well as the freeze-thaw cycles. The results demonstrated that the UPV values have a greater impact on the UCS than other parameters.

Key words: Clay soil, uniaxial compression test, ultrasonic pulse velocity test, seasonally frozen region.

Mevsimsel Donmuş Bölgelerde İnce Taneli Zeminlerin Tek Eksenli Basınç Dayanımları ve Ultrasonik Tahribatsız Analizleri Üzerine Bir Çalışma

Öz: Mikro yapı ve makro yapı dahil olmak üzere donma-çözülme döngülerine maruz kalan zeminlerin fiziksel ve mekanik özelliklerini anlamak, onu yapısal veya destek malzemesi olarak kullanan yapıların gerekli performansını elde etmek için kritik öneme sahiptir. Bu sebeple, 0, 2, 5, 7, 12 ve 15 donma-çözülme döngüsünden sonra farklı su içeriklerine sahip (%18, %21,5 ve %23) killi zemin üzerinde deneysel bir çalışma yapılmıştır. Zeminin performansı, serbest basınç dayanımı (UCS) ve ultrasonik dalga hızı (UPV) testleri ile değerlendirilmiştir. Deneysel sonuçlar, donma-çözülme döngülerinden önce ve sonra en düşük su içeriğinde UCS pik değerlerinin gözlemlendiğini göstermiştir. Gerilme-şekil değiştirme eğrileri, kırılma davranış sergilemiş ve bu durum, donma-çözülme döngülerinden sonra ve su içeriğindeki bir artışla kırılma davranışına doğru değişiklik göstermiştir. Ayrıca, minimum su içeriği değerlerinde kılcal kuvvetler nedeniyle artan UCS değerlerinde en yüksek UPV değerleri gözlemlenmiştir. Ayrıca, donma-çözülme döngülerinin sayısındaki artışla UPV'de bir düşüş gözlemlenmiştir. UPV ve UCS değerleri arasındaki korelasyonlara göre, optimum su içeriğinde su içerikleri için en yüksek korelasyonlar elde edilmiş ve artan donma-çözülme döngü sayısı ile azalma eğilimi gözlemlenmiştir. Ayrıca, serbest basınç dayanımı ile ultrasonik darbe hızı, su içeriği ve ayrıca donma-çözülme döngüleri arasındaki korelasyon derecesini göstermek için Grey korelasyon analizi yapılmıştır. Sonuçlar, UPV değerlerinin UCS üzerinde diğer parametrelerden daha büyük bir etkiye sahip olduğunu ortaya koydu.

Anahtar kelimeler: Killi zemin, serbest basınç dayanımı, ultrasonik darbe hızı testi, mevsimsel donma bölgeleri.

1. Introduction

Fine-grained soil is a difficult material to work with in a variety of civil engineering applications. High clay content in a fine-grained soil tends to shrink and expand as the volume of water changes. The change in volume can lead to structural problems for buildings hence posing critical threats to geotechnical engineers [1-2]. Due to the variation of mechanical properties exhibited by these soils, frost susceptibility, excessive compression, high swelling potential, low strength, and collapse behavior are examples of possible structural damages to be encountered [3-5]. Dry density and water content were proved to significantly impact the unconfined compressive strength (UCS), shear strength, and brittle against plastic behavior of these soils [6-7]. Furthermore, the water content is said to strongly influence the strength and structural stability of the soil grains [8-11]. Depending on the

* Corresponding author: morakoglu@firat.edu.tr. ORCID Number of authors: ¹ 0000-0002-8623-4785, ² 0000-0002-5391-5859

moisture content of a fine-grained compacted soil, it may behave brittle or plastic under loading. The water content at which softening to hardening behavior transitions happen is based on the plasticity level of clay and the type and amount of clay minerals [7].

Freezing and thawing cycles throughout the changes in seasonal temperature have destructive effects on soil behavior. Mineral composition, moisture content and dry density all influences the physical and mechanical behavior of the frozen soils. The arrangement and structure of soil particles changes as a result of the freezing-thawing cycles, hence the changes in the soil's physical and mechanical properties [12-17]. According to studies of previous tests on the soils after repeated freezing-thawing cycles, compacted soil would become loose and thaw settlement would increase after thawing or vice versa [12, 18, 19]. The volume of water increases to about 9% when it freezes in fine-grained soil, exerting great pressure on the pore walls of the fine-grained soil, also changing its physical and mechanical properties [20]. Destruction of these soils by freezing and thawing occurs as water migrates into the soil. The extent of the destructive effect depends on factors such as freezing depth, surface freezing temperature, duration of freezing, and negative variations in the amount of snow on the surface during the winter [21, 22].

In seasonally frozen regions, the occurrence of variations in freezing-thawing cycles should be taken into account while determining stability analysis parameters and deformational problems. While utilizing UCS tests, deformation changes in the soil, changes in the mass due to changes in water content and passing wave velocity, and the influence of freezing-thawing cycles on the mechanical behavior of soils were investigated in this study. Also, the most significant parameters affecting the UCS values of the soil were revealed with the Grey correlation analysis.

2. Materials and Method

2.1. Soil

The soil specimens were collected from Ataçehir district, Elazığ city (Turkey), and fine-grained soil was used in the experiments. Grain Size Distribution Test, Atterberg Limit Tests, and Proctor Tests were carried out to obtain the soil's physical properties. The maximum dry density is 1.656 gr/cm³, the optimum water content is 21.50% and the plasticity index has been found 45.67%. The collected samples were found to be high plasticity clay (CH) soils according to the Unified Soil Classification System (USCS). Also, the grain size distribution is presented in Figure 1.

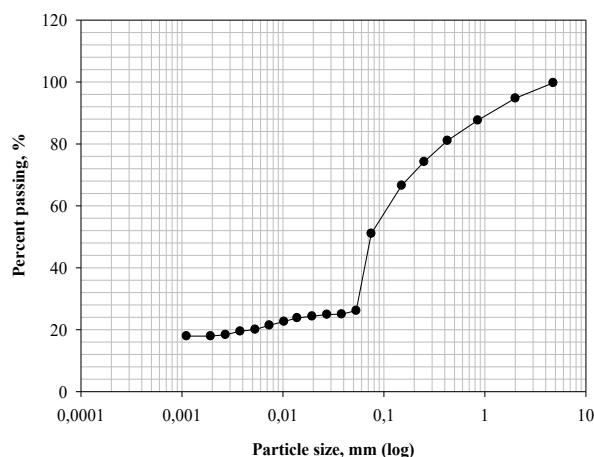


Figure 1. Grain size distribution of the studied soil.

2.2. Specimens preparation

Physical, uniaxial mechanical properties and non-destructive analysis results were determined on the fine-grained soil for various water contents and after experiencing a number of freeze-thaw cycles. While preparing the soil specimens, the following steps were followed; (i) The soil specimens were put in an oven at 105 ± 5 °C for 12 hours in order to obtain specimens with desired water content and to prevent water loss. After the required drying,

all soils were placed in the humidity cabinet to cool. (ii) According to the optimum water content determined by the Proctor test, water was slowly added to the soil specimens and mixed. (iii) Then, the soil-water mixture was placed in plastic bags and kept for 24 hours in order to ensure homogeneous distribution of the water content in the mixture. (iv) The water contents of the soils were checked again before starting the experiments. (v) Soil-water mixtures were compacted in three layers with the apparatus for preparing the test specimens shown in Figure 2(a), 3.80 cm in diameter and 7.60 cm in height, as in Figure 2(b). The first layer of the specimens is placed in the mold and compacted. Then, the remaining two layers were added and placed separately and compacted in the same way, and the test sample was prepared as in Figure 2 (c). (vi) After preparation of the samples, they were quickly covered with plastic wraps and placed in humidity cabinets to preserve the water contents. Table 1 depicts the experimental plan of the test specimens.



Figure 2. Preparation of soil specimens.

Table 1. The experimental plan for the specimens.

Test/Series	Dimension of test specimen		Soil Type	Water contents	N	Temperature		TT°	
	D (mm)	H (mm)				F	T		
Physical properties	-	-	CH soil	18%, 21.5%, 23%	0, 2, 5, 7, 12, 15	Unfrozen condition	-	-	~20 °C
UCS tests	38	76					-18 °C	20 °C	~20 °C
UPV tests	38	76					-18 °C	20 °C	~20 °C

Note: UCS is uniaxial compression test, UPV is ultrasonic pulse velocity test, F is the freezing, T is the thawing, D is the diameter, H is the height, N is the number of freeze-thaw cycles, TT° is the tested temperature.

2.3. Freeze-thaw test

As presented in Table 1, for all series in the tests in this study, the freeze-thaw tests were operated at 0, 2, 5, 7, 12, and 15 freeze-thaw cycles. For all tests, the freezing temperature was -18 °C, the thawing temperature was 20 °C. Also, the experiments for all specimens were conducted at about 20 °C. Due to the continental climate affecting eastern Turkey, most of the region is exposed to the effects of freezing. Considering the average annual temperatures, the freezing periods of the region are between November and March [23].

The prepared soil specimens were subjected to various numbers of freeze-thaw cycles (0, 2, 5, 7, 12, and 15) by placing them in a closed system freezing cabinet without water before their UCS and UPV tests. Freezing temperatures were chosen considering the approximate mean minimum temperature of the region ($T_{\text{freezing}} = -18$ °C). As seen in (a) to (d) as in Figure 3, the soil samples were frozen for 12 hours at a temperature of -18 °C in a freezing cabinet. The temperature of the freezing cabinet was maintained for 12 hours after it reached the predetermined degree to maintain the temperature balance between the specimens and the environment. Then, the soil specimens were put in humidity cabinets and exposed to the thawing process for 12 hours. All these processes were considered as one freeze-thaw cycle. In addition, Figure 3 (e) shows the time-dependent variations of temperature control processes and freeze-thaw cycles of soil specimens.

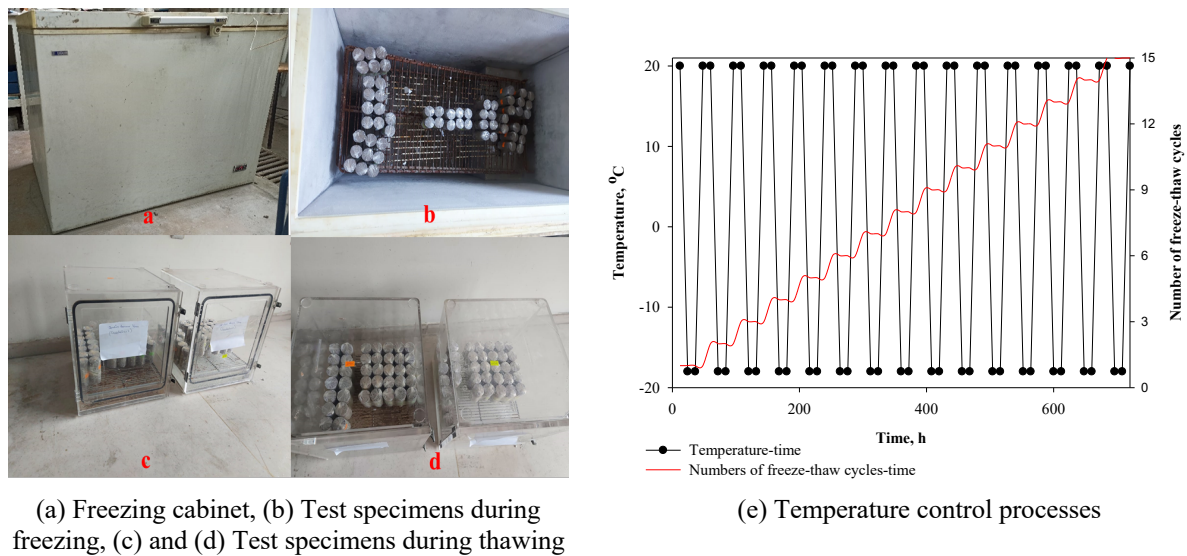


Figure 3. Freeze-thaw tests.

2.4. Principle of uniaxial compression behaviors of the soil

In this study, the uniaxial compression test was carried out according to ASTM D2166 [24]. After freezing-thawing cycles, the uniaxial compression strengths of the specimens were determined with a Triaxial test machine (ELE brand) at the Firat University- Faculty of Technology-Civil Engineering Department-Soil Mechanics Laboratory. The same machine was also used for uniaxial compression tests. A strain rate of 0.760 mm per minute was used to apply the load to the specimens. The loading procedure was repeated until either the specimen failed or the strain reached 25.0% (presented as Figure 4).



Figure 4. The appearance of the specimen before and after the UCS test.

2.5. Principle of UPV behaviors of the soil

An ultrasonic non-destructive digital tester apparatus was utilized to determine the ultrasonic pulse velocity (UPV) of the specimens. The Ultrasonic Wave tests were conducted in accordance with ASTM C 597-09 [25] after 0, 2, 5, 7, 12, and 15 freeze-thaw cycles (Figure 5). The transducers were positioned at appropriate positions on the circular surface of the specimens once the apparatus had been calibrated. The measurements of the UPV were taken with an accuracy of 0.1 μ s. Previous research has found that ultrasonic wave frequencies in the 40-80 Hz range are effective for evaluating stabilized soils. The goal of this experiment was to find a link between the UCS of the soil and the UPV. According to the display unit, the pulse frequency and the pulse transmission time were 54 Hz and 0.1 microseconds, respectively. The UPV for the specimen can be computed using Eq. (1) taking into account the sample length:

$$V = \frac{L}{t} \times 10^6 \quad (1)$$

where V is the ultrasonic wave velocity (m/s), L is the sample's pulse transmission path distance (m), and t is the sample's pulse transmission time.



Figure 5. The appearance of the specimen during the UPV test.

2.6. Grey correlation analysis

Grey correlation analysis is a method for determining how different sequences inside a structure approach each other geometrically [26]. The relationship between water content, freeze-thaw cycles, and UPV was derived using the Grey correlation theory to reveal the primary parameters impacting the UCS of clayey soil. The UCS values were taken as the reference sequences (RefSeq) and water contents, freeze-thaw cycles, and UPV values were used as the comparison sequences (ComSeq). Eqs. (2) and (3) can be used to define the reference and comparison sequences, respectively:

$$x_0(f_k) = \{x_0(f_1), x_0(f_2), \dots, x_0(f_n)\} \quad (2)$$

$$x_i(f_k) = \{x_i(f_1), x_i(f_2), \dots, x_i(f_n)\} \quad (3)$$

where $x_0(f_k)$ and $x_i(f_i)$ are the RefSeq, the ComSeq, respectively and k shows the number of RefSeq or ComSeq.

The RefSeq and ComSeq were normalized using Eqs. (4) and (5) since the parameters in the sequences had different dimensions.

$$x'_0(f_k) = x'_0(f_k) / x_0(f_1) = \{x'_0(f_1), x'_0(f_2), \dots, x'_0(f_n)\} \quad (4)$$

$$x'_i(f_k) = x'_i(f_k) / x_i(f_1) = \{x'_i(f_1), x'_i(f_2), \dots, x'_i(f_n)\} \quad (5)$$

where $x'_0(f_k)$ and $x'_i(f_k)$ the normalized reference and comparison sequences, respectively. Eq. (6) was used to calculate the correlation coefficient after normalizing the sequences.

$$\xi_i(f_k) = \frac{\min_i \min_k |x_0(f_k) - x_i(f_k)| + \rho \max_i \max_k |x_0(f_k) - x_i(f_k)|}{|x_0(f_k) - x_i(f_k)| + \rho \max_i \max_k |x_0(f_k) - x_i(f_k)|} \quad (6)$$

where ξ shows the correlation coefficient and taken equal to 0.50 in this study. The Grey correlation degree (r_{0i}) can be determined from Eq. (7), using the correlation coefficient calculated from Eq. (6):

$$r_i = \frac{1}{n} \sum_{k=1}^n \xi_{0i}(f_k) \quad (7)$$

3. Results and Discussions

3.1. Evaluation of unconfined compression test results and effects of water contents

Figure 6 shows the compressive strength - strain behavior of the soil specimens with various water contents before and after freeze-thaw cycles. The UCS failure strength of clayey soil declined with an increment in water content. Some researchers [27] found a similar trend in water content, however, some of them [28, 29] presented that as water content increases, the compressive strength rises at first and then decreases. Their results showed that the maximum UCS was observed at the optimum moisture content value. Further, the UCS of all specimens after freeze-thaw cycles decreased. Moreover, in clayey soil, the stress-strain curves exhibited strain-softening behavior, and this condition transitioned from strain-softening to strain-hardening behavior after freeze-thaw cycles and with an increment in water content.

Also, Figure 7 depicts the variation of peak values of UCS versus freeze-thaw cycles (N) for different water content (w). The UCS of the soil with an 23.0% water content was observed little less than the soil with a 18.0% water content before freeze-thaw cycles, but after the maximum freeze-thaw cycle, it was observed that this ratio approached each other. Moreover, the compressive strength decreased at the rate of 62.03% for an increase in the water content to 21.5%, and 59.25% for a 23.0% water content. Generally, when the water content rises, the friction resistance and interfacial force between soil grains decrease. This drop could be attributed to a decrease in soil absorption, which happens simultaneously as the water content rises and the potential for the formation of excess pore water pressure [30].

3.2. Influence of the freeze-thaw cycles on the UCS strength

Due to probable moisture movement and ice development below 0 °C, soil engineering qualities change significantly after the repeated freeze-thaw cycles. As a result, the determination of engineering features is a requirement for stability analysis and solutions in seasonally frozen regions [20]. Figure 6 shows the UCS-strain relationships prior to and following repeated freeze-thaw cycles. As shown in Figure 6, the soil compressive strength is greatly affected by water content and freeze-thaw cycles. Before freeze-thaw cycles, UCS peak values varied from 442.45 to 1085.63 kPa with an increase in water content from 18.5% to 23.0%. However, after the 15th freeze-thaw cycle, UCS peak values decreased from 183.20 to 159.88 kPa with an increase in water content from 18.5% to 23.0%. The pore water within the soil freezes when it is exposed to a freezing process. Soil particles separate from one another due to the ice force, raising pore water pressure. The increased pore water pressure, on the other hand, cannot return to its original state during thawing. As a result, freeze-thaw cycles frequently weaken soil [31].

In this study, to demonstrate the impacts of freeze-thaw cycles on soil failure strength, a ratio ($qu-N/qu-0$) was calculated by dividing the UCS peak values of the soil after the freeze-thaw cycles ($qu-N$) by the UCS peak values of soil that had not been experienced to any freezing-thawing cycles ($qu-0$). Figure 8 depicts the failure strength ratio of all specimens experienced with freeze-thaw cycles at different water contents.

The failure strength ratio of the clayey soil reduced as the number of freeze-thaw cycles increased, as illustrated in Figure 8. Also, the compressive strength of the soil decreased by 40.82% to 80.09% for 18.0% water content; this drop was about 14.44 % to 58.57 % for 21.5% water content and 38.18% to 63.87 % for 23.0% water content between 2 and 15 freeze-thaw cycles.

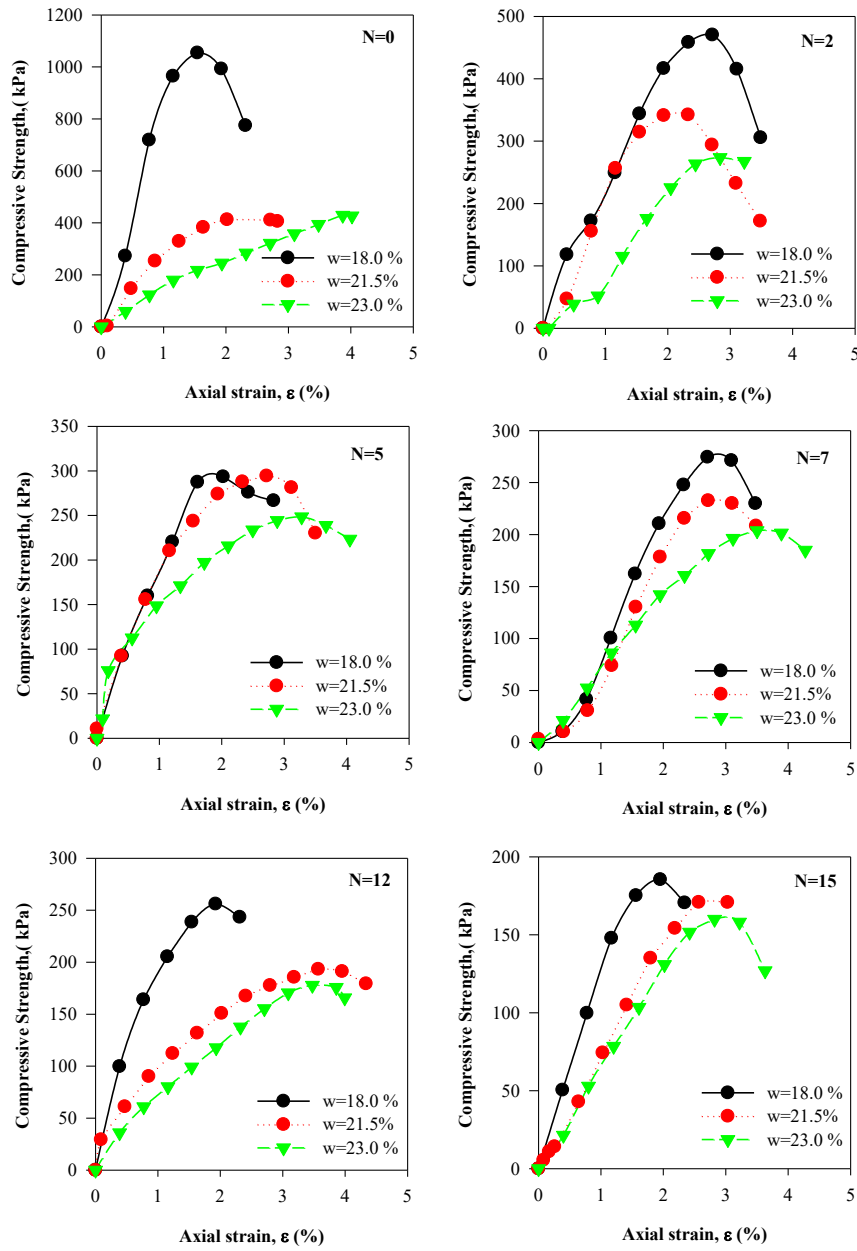


Figure 6. The UCS versus axial strain of the specimens for different w and N.

3.3. Effects of the freeze-thaw cycles and water contents on the ultrasonic pulse velocity

The UPV is regarded to be a useful tool for determining the material's overall quality and elasticity [32]. As presented in Figure 9, the water content and UPV of the specimens were inversely proportional. That is, the water content rises while the UPV of the soil specimen's decreases. Since velocities of solids are greater than velocities of liquids, which are greater than air velocities, the velocity of ultrasonic pulses are transmitted rapidly in voids and a high frequency is more easily transmitted in the clay soil with lower water and air content. The UPV measurements before the freeze-thaw tests varied from 593 to 916 m/s, indicating the degree of very low velocity suggested by prior research. This low degree of strength and elasticity could be related to the material type (clay) used in this study. According to other research, ultrasonic velocities are higher in clayey soils at low water content

[33, 34], which confirms the findings of this study. This is due to the fact that waves propagate at a fast speed in low-water-content soils [35]. This could be because voids in soil samples reduce as water content decreases, resulting in higher UPV.

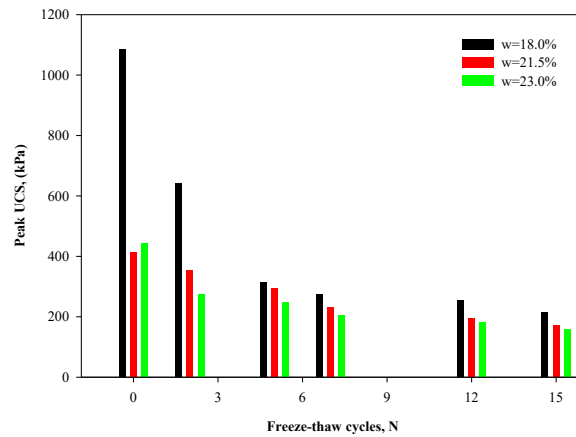


Figure 7. Change of peak values of UCS versus N for different w .

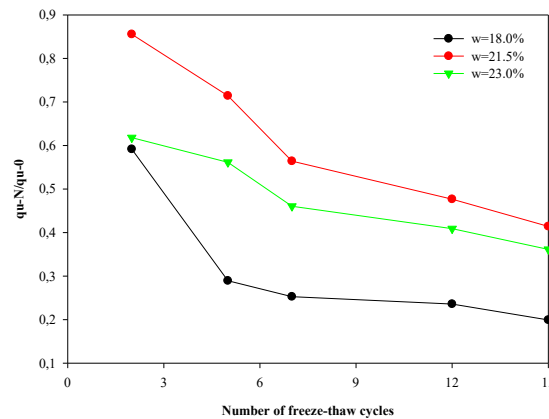


Figure 8. Variation of q_u-N/q_{u-0} ratio with freezing-thawing cycles for different w .

In addition, when the number of freeze-thaw cycles increases, the UPV values decline. Soil samples showed a velocity variation of 515 m/s for samples with 18.0% water content, 490 m/s for samples with 21.5% water content, and 406 m/s for samples with 23.0% water content after the freeze-thaw tests with the maximum number of cycles. As previously explained by [36, 37] the soil has a decrease in the UPV during thaw cycles, while the soil has a slight rise in the UPV during freeze cycles. The water inside the pores and voids between the soil particles tends to freeze when the temperature is lowered to negative during the freezing process, reducing the volume and raising the internal pressure on the soil particles. The UPV is increased by filling the pores in the soil with ice, resulting in a more compacted soil with improved interlocking. By allowing the ultrasonic waves to pass through the soil sample in a shorter time, a higher UPV value is obtained. Micro-cracks occur as the ice melts, resulting in a drop in the UPV.

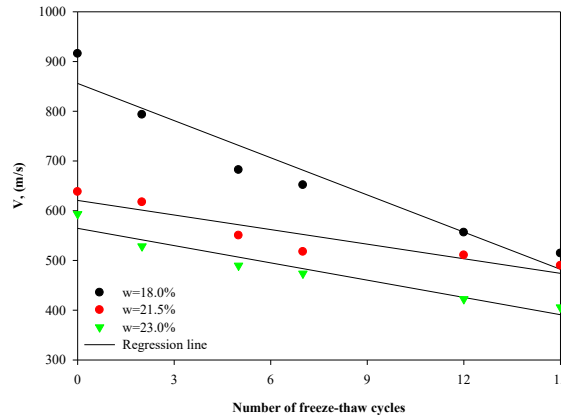


Figure 9. Comparison of the impact of freeze-thaw cycles on the UPV.

As Figure 10 shows, an increase in the UCS values was observed with increasing the UPV values for clayey soil. This conclusion is in agreement with that of [33]. Figure 10 further shows that for all soil specimens, the UCS against the UPV relationships result in good correlations ($R^2 > 0.87$). The number of freeze-thaw cycles (N) and water contents (w) have a clear impact on the relationships. The highest correlations for water contents were obtained at optimum water content. On the other hand, low correlations were obtained with the increasing number of freeze-thaw cycles. The correlations for the 15th freeze-thaw cycle were lower, whereas the correlations for the 2nd freeze-thaw cycle were higher.

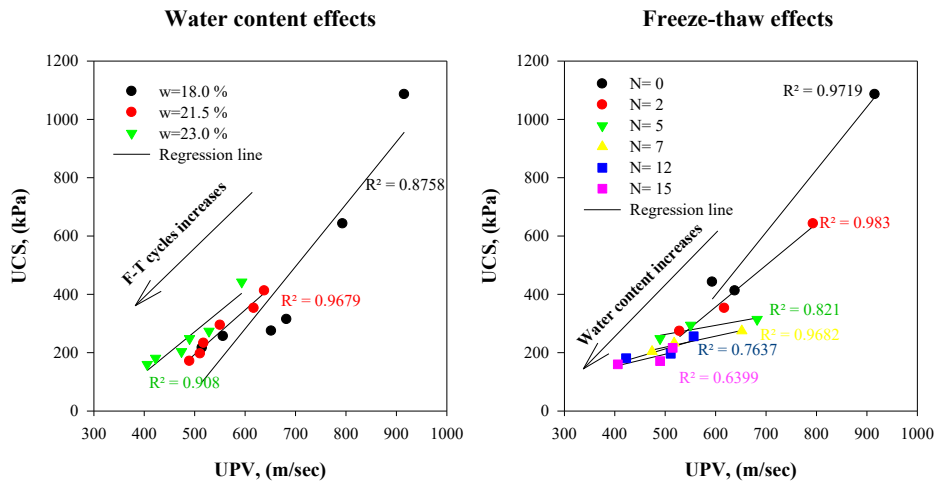


Figure 10. The correlations of UCS versus UPV for different w and N.

3.4. Results of Grey correlation analysis

Temperature changes in a year significantly influence the water migration of soils. Because a significant quantity of latent heat must be removed in soil with high unfrozen water content, the freezing phase takes longer to penetrate. Describing the soil water conditions can make it easier and is essential for specifying the strength properties of soil in the seasonally frozen region. The strength characteristics and water content of the subgrade soil are not directly considered in evaluating the performance or usability of the pavement. However, the increased water content in subgrade soil in seasonal freezing regions, coupled with increased pavement loads often leads to pavement problems. In this study, the UCS was described as the reference sequence, and the water content, the ultrasonic pulse velocity, and freeze-thaw cycles, (w, UPV, and N) were used as the comparison sequences. While soil water content is related to internal properties, ultrasonic wave velocity, temperature, and freeze-thaw cycle

are external parameters for the soil. Therefore, Grey correlation analysis was used to assess the significance of these parameters on the UCS of the soils. Table 2 presented the Grey correlation coefficients.

Table 2. Grey correlation coefficients.

Reference sequences	Comparison sequences		
	<i>w</i>	<i>F-T</i>	<i>UPV</i>
q_u	0.898	0.604	0.958

qu: Unconfined compressive strength, w: water content, F-T: number of freeze-thaw cycles, UPV: ultrasonic pulse velocity

The sequence of Grey correlation for several parameters was found to be $UPV > w > F-T$. It is clear that the UPV has more influence on the q_u than the freeze-thaw cycles and water contents for clayey soil. The UPV values are mainly related to the composition of soils, namely the mineralogical structure. The soil's composition is proportional to the lower number of voids, thus the higher its strength. In contrast to freeze-thaw cycles, the water content has a greater impact on the q_u . This was due to the limits enshrined by the soil's inherent properties exhibited while experiencing both the freezing and thawing processes.

Moreover, the highest mean correlation coefficients of the reference sequence, ξ_{max} , were calculated as $\xi_{max1}=0.9479$, $\xi_{max2}=0.9261$, $\xi_{max3}=0.9686$. Thus, the best gradation for the reference sequences (q_u) of clayey soil under the examined condition is proved for 18%, 0 freeze-thaw cycles, and 916 m/sec respectively.

4. Conclusions

In this study, the impact of water content and freeze-thaw cycle on the unconfined compressive strength and non-destructive testing behavior using the UPV test of the soil specimens was investigated. Conclusions were made within the scope of the study. These are as follows:

The UCS of specimens prepared with water contents less than the optimum water content was greater than the other values. Also, UCS peak values were observed at the lowest water content prior to and post the freeze-thaw cycles. The stress-strain curves exhibited a strain-softening behavior, and this condition transitioned from brittle to ductile behavior after the freeze-thaw cycles, with an increment in the water content.

According to the unconfined compression test results, the soil's strength decreases with an increase in the freeze-thaw cycles. A decrease in the UCS of soils due to freeze-thaw cycles was derived with the highest values of the samples prepared below the optimum water content, while it was seen the least values in the soil specimen prepared at the optimum water content. After the maximum freeze-thaw cycle, with a water content rise from 18.5% to 23.0%, UCS peak values decreased from 183.20 to 159.88 kPa.

To show the impacts of freeze-thaw cycles on the soil failure strength, a ratio (q_u-N/q_u-0) was determined and a decline in the compressive strength was found by 80.09% for 18.0% water content; 58.57 % for 21.5% water content, and 63.87% for 23.0% water content after maximum freeze-thaw cycles, respectively.

The highest values of UPV were observed for UCS values increasing due to capillary forces at minimum values of water content. Moreover, a decrease in the UPV was observed with increments in the number of freeze-thaw cycles. According to correlations between UCS and UPV values, the highest correlations for water contents were obtained at 21.5% (optimum water content), and a decreasing trend was observed with the increasing number of freeze-thaw cycles.

The Grey correlation sequence of various parameters on the UCS values was determined to be ultrasonic pulse velocity > water content > freeze-thaw cycles.

References

- [1] Bulolo S, Leong EC, Kizza R. Tensile strength of unsaturated coarse and fine-grained soils. Bull Eng Geol Environ 2021; 80(3); 2727–2750.
- [2] Safi W, Singh S. Efficient & effective improvement and stabilization of clay soil with waste materials. Mater Today: Proc 2022; 51(1); 947-955.
- [3] Yarbaşı N, Kalkan E. The mechanical performance of clayey soils reinforced with waste pet fibers. Int J Earth Sci Knowl Appl 2020; 2(1); 19–26.
- [4] Indiramma P, Sudharani C, Needhidasan S. Utilization of fly ash and lime to stabilize the expansive soil and to sustain pollution free environment - An experimental study. Mater Today Proc 2020; 22(3); 694-700.
- [5] Kalkan E, Yarbaşı N, Bilici Ö. Strength performance of stabilized clayey soils with quartzite material. Int J Earth Sci Knowl Appl 2019; 1; 1-5.

- [6] Das BM. Principles of Geotechnical Engineering. Sacramento, California. USA, Cengage Learning, 2020.
- [7] Malizia JP, Shakoor A. Effect of water content and density on strength and deformation behavior of clay soils. *Eng Geol* 2018; 244;125-131.
- [8] Huang S, He Y, Yu S, Cai C. Experimental investigation and prediction model for UCS loss of unsaturated sandstones under freeze-thaw action. *Int J Min Sci Technol* 2022; 32(1); 41-49.
- [9] Huang S, He Y, Liu X, Xin Z. Experimental investigation of the influence of dry-wet, freeze-thaw and water immersion treatments on the mechanical strength of the clay-bearing green sandstone. *Int J Rock Mech Min* 2021; 138; 104613.
- [10] Wang P, Zhou G. Frost-heaving pressure in geotechnical engineering materials during freezing process, *Int J Min Sci Technol* 2018; 28 (2); 287-296.
- [11] Liu Y, Cai Y, Huang S, Guo Y, Liu G. Effect of water saturation on uniaxial compressive strength and damage degree of clay-bearing sandstone under freeze-thaw. *B Eng Geol Environ* 2020; 79(4); 2021-2036.
- [12] Zhang L, Ren F, Li H, Cheng D, Sun B. The influence mechanism of freeze-thaw on soil erosion: A review. *Water* 2021; 13(8); 1010.
- [13] Orakoglu ME, Liu J, Tutumluer E. Frost depth prediction for seasonal freezing area in Eastern Turkey. *Cold Reg Sci Technol* 2016; 124; 118-126.
- [14] Chen Z, Ge S, Zhang Z, Du Y, Yao B, Xie H, Liu P, Zhang Y, Wang W, Zhou H. Soil moisture but not warming dominates nitrous oxide emissions during freeze–thaw cycles in a Qinghai–Tibetan plateau alpine meadow with discontinuous permafrost. *Front Ecol Evol* 2021; 9; 676027.
- [15] Luo L, Ma W, Zhang Z, Zhuang Y, Zhang Y, Yang J, Cao X, Liang S, Mu Y. Freeze/thaw-induced deformation monitoring and assessment of the slope in permafrost based on terrestrial laser scanner and GNSS. *Remote Sens* 2017; 9(3);1-20.
- [16] Jiang H, Zheng G, Yi Y, Chen D, Zhang W, Yang K, Miller CE. Progress and challenges in studying regional permafrost in the Tibetan plateau using satellite remote sensing and models. *Front Earth Sci* 2020; 8; 560403.
- [17] Zeinali A, Dagli D, Edeskär T. Freezing-thawing laboratory testing of frost susceptible soils. In *Nordic Geotech Meet Challenges in Nordic Geotechnics* 2016 ; 267-276.
- [18] Yarbasi N, Doğal bir materyal olarak keçi kili lifleriyle modifiye edilen kohezyonlu zeminlerin donma-çözülme direnci. *Adıyaman Üniversitesi Mühendislik Bilimleri Dergisi*. 2020; 7(13); 157-166.
- [19] Nguyen TTH, Cui YJ, Ferber V, Herrier G, Ozturk T, Plier F, Puiatti D, Salager S, Tang AM. Effect of freeze-thaw cycles on mechanical strength of lime-treated fine-grained soils. *Transp Geotech* 2019; 21;100281.
- [20] Andersland OB, Branko L. *Frozen Ground Engineering*. 2nd Ed. Hoboken, NJ, John Wiley & Sons, Inc. 2004.
- [21] Shirmohammadi S, Jahromi SG, Payan M, Senetakis K. Effect of lime stabilization and partial clinoptilolite zeolite replacement on the behavior of a silt-sized low-plasticity soil subjected to freezing-thawing cycles. *Coatings* 2021; 11(8); 994.
- [22] Liu J, Chang D, Yu Q. Influence of freeze-thaw cycles on mechanical properties of a silty sand. *Eng Geol* 2016; 210; 23-32.
- [23] Kış mevsimi yağış değerlendirilmesi. <https://www.mgm.gov.tr/veridegerlendirme/yagis-raporu.aspx?b=m>, Yayın tarihi Ocak 2020, Erişim tarihi: Şubat 11, 2020.
- [24] ASTM D2166, 2006. Standard test method for unconfined compressive strength of cohesive soil. *Annual Book of ASTM Standards*.
- [25] ASTM C 597-09, 2009. Standard test method for pulse velocity through concrete. *Annual Book of ASTM Standards*.
- [26] Deng JL. Introduction to grey system theory. *J Grey Syst* 1989; 1(1): 1-24.
- [27] Mirzababaei M, MirafTAB M, Mohamed M, McMahon P. Unconfined compression strength of reinforced clays with carpet waste fibers. *J Geotech Geoenviron Eng* 2013; 139(3); 483-493.
- [28] Patel SK, Singh B. Strength and deformation behavior of fiber-reinforced cohesive soil under varying moisture and compaction states. *Geotech Geol Eng* 2017; 35(4);1767-1781.
- [29] Nataraj M, McManis K. Strength and deformation properties of soils reinforced with fibrillated fibers. *Geosynth Int* 1997; 4(1):65-79.
- [30] Qu Y, Chen G, Niu F, Ni W, Mu Y, Luo J. Effect of freeze-thaw cycles on uniaxial mechanical properties of cohesive coarse-grained soils. *J Mt Sci* 2019; 16 (9); 2159-2170.
- [31] Konrad JM, Morgenstern NR. Mechanistic theory of ice lens formation in fine-grained soils. *Can Geotech J* 1980; 17(4); 473-486.
- [32] Marfisi E, Burgoyne CJ, Amin MHG, Hall LD. The use of MRI to observe the structure of concrete. *Mag Concr Res* 2005; 57 (2); 101-109.
- [33] Güllü H, Canakci H, Al Zangana IF. Use of cement based grout with glass powder for deep mixing. *Constr Build Mater* 2017; 137; 12-20.
- [34] Sarro WS, Assis GM, Ferreira GCS. Experimental investigation of the UPV wavelength in compacted soil. *Constr Build Mater* 2021; 272; 121834.
- [35] Kramer SL. *Geotechnical Earthquake Engineering*. Prentice-Hall Inc., Upper Saddle River, NJ, 1996.
- [36] Eskişar T, Altun S, Kalıpcılar İ. Assessment of strength development and freeze–thaw performance of cement treated clays at different water contents. *Cold Reg Sci Technol* 2015; 111; 50-59.
- [37] Roshan K, Choobbasti AJ, Kutanaei SS, Fakhraei A. The effect of adding polypropylene fibers on the freeze-thaw cycle durability of lignosulfonate stabilised clayey sand. *Cold Reg Sci Technol* 2022; 193; 103418.

Effect of Different Drill Bits on Delamination in Drilling Composite Materials

Haşim PIHTILI^{1*}

¹ Department of Mechanical Engineering, Firat University, Engineering Faculty, 23279 Elazığ, Turkey

*¹ hpihtili@firat.edu.tr

(Geliş/Received: 13/03/2022;

Kabul/Accepted: 27/06/2022)

Abstract: The most important problem of composite materials, which have been started to be used in every field of technology, is the ability to perform machining operations such as drilling and cutting. In this respect, in this experimental study, its performance in drilling different composite materials with different reinforcements and thicknesses with drills of different types and different diameters was investigated. Three different types of drills were used in drilling operations, namely HSS, TiN and Carbide. Reinforced composites of different types and properties were used as materials. As a result of the drilling processes, the surface roughness of the drilled surface, drilling performance, hole quality and different cutting parameters were examined depending on the rotation and feed rate. The same drilling conditions were applied for each composite material. All result values obtained were transferred to graphs and tables. In addition, photographs of all samples were taken under Scanning electron microscopy (SEM) and the surface roughness of these photographs was examined.

Key words: Drill Bits, Drilling, Reinforced Composites, Roughness

Kompozit Malzemelerin Delinmesinde Farklı Matkap Uçlarının Delaminasyona Etkisi

Öz: Teknolojinin her alanında kullanılmaya başlanan kompozit malzemelerin en önemli problemi, delme, kesme gibi talaşlı işlemin gerçekleştirilebilme durumudur. Bu bakımdan, bu deneysel çalışmada, değişik tür ve farklı çaplara sahip olan matkaplarla, değişik takviyeli ve kalınlıktaki farklı kompozit malzemelerin delinmesindeki performansı incelendi. Delme işlemlerinde, HSS, TiN ve Karbür olmak üzere üç çeşit değişik matkap kullanıldı. Malzeme olarak değişik tip ve özelliklerdeki takviyeli kompozitler kullanıldı. Yapılan delme işlemlerinin sonucunda, devir ve ilerleme hızına bağlı olarak, delinmiş yüzeydeki yüzey pürüzlülüğü, delme performansı ile delik kalitesi ve değişik kesme parametreleri incelendi. Her bir kompozit malzeme için aynı delme şartları uygulandı. Hem matkap hem de kompozit malzemede meydana gelen delaminasyon incelendi. Elde edilen tüm sonuç değerleri, grafiklere ve tablolara aktarıldı. Ayrıca, tüm numunelerin fotoğrafları taramalı elektron mikroskobu (SEM) altında çekildi ve bu fotoğraflardaki yüzey pürüzlülük durumu incelendi.

Anahtar kelimeler: Matkap ucu, Delme, Takviyeli Kompozitler, Yüzey pürüzlülüğü

1. Introduction

In today's technology, the use of composite materials in all areas is increasing day by day. Especially, it has become an indispensable material in the aerospace and aircraft industry, automotive industry, and sports and marine materials. Composite materials have numerous characteristics such as lightness, rigidity, heat resistance, high strength, and good abrasion resistance. However, despite the manufacturing industry has developed modern machining methods, traditional drilling method is still the most widely used machining process due to the reasons such as its economy and simple applicability. Fibre reinforced composites are widely recognized for their superior mechanical properties and advantages for applications in aerospace, defence and transportation sectors (Hocheng, 2005). However, composite materials have characteristics which drive their machining behaviour, therefore, the mechanisms involved while cutting composite materials have been regarded as considerably distinct from those observed when cutting homogeneous materials (Hocheng, 2006).

Carbon fiber-reinforced composites are well recognized for their superior mechanical properties and are widely used in aerospace, defense and transportation applications. Composite materials possess peculiar characteristics during machining. The reference of drilling of fiber-reinforced plastics reports that the quality of the machined parts is strongly dependent on drilling parameter (W. Koenig, 1985), (R. Komanduri, 1991). Numerous studies have examined the delamination in drilling (G. Caprino, 1995), (J.A. Miller, 1984), (K. Sakuma, 1984), (F. Veniali, 1995), (W. Koenig, 1984). In Fig. 1, the center of the circular plate is loaded by a twist drill of diameter d . F_A is the thrust force, X is the displacement, H is the workpiece thickness, h is the uncut depth under tool, $2b$ is the diameter of pilot hole, and a is the radius of existing delamination, (C.C.Tsao, H.Hocheng, 2003).

Fig.2 shows the delamination damage at the drill entrance and exit of a laminate composite material (Koenig, 1984). When the studies on the processing of composites are examined, mostly the metal matrix composites (MMC) are

encountered. Pihtili and Canpolat, in the study, drilling performance and cutting parameters with holes having different qualities, drill kinds, and drill diameters are examined in different composite materials. As a result of the drilling operations, it is found that as rotation and progress speed increases, surface roughness on the processed surface increases as well. Better results in terms of surface roughness are obtained with small-scaled drills (Pihtili,2009). Schafer, as a whole, it is observed in the drilling tests performed on MMC that when conventional high speed steel (HSS) drills are used, tool wear is high and the surface roughness of the hole is weak (Schaefer,1969). Chamber, In the study of Chamber and Stepfens, MMCs are processed in the lathe by using different cutting tools. It was observed that Polly Crystal Diamond(PCD)drills have high wearing resistance, longer tool life, and the best surface roughness values are obtained when the machining process is performed by using these drills (Chamber,1991). Joshi et al. analyzed the wearing of the carbide tool and chips that are ruptured during the machining of the metal matrix composite on the lathe. In the current study, chips with a larger diameter were obtained by decreasing the angle of shear (Joshi,1999). In the study of El-Gallab and Sklad, the surface roughness of the metal matrix with machined particles is emphasized. They investigated the effect of cutting parameters on surface roughness by performing dry turning tests at different cutting speeds, different feed rates, and different cutting depths (El-Gallab,1998). Lin et al. examined the forms of chips at different cutting rates of aluminum-matrix composite. In the present study, the decrease in brittleness via the addition of SiC particles to the Al alloy caused semi-continuous chips to be formed during the machining of MMCs (Lin,1998). S.Arul et al. examined the effect of vibrated drilling on the quality of the holes in the polymeric composites. Especially, they emphasized on a new drilling method by applying low frequency and high voltage on the part in the direction of the feed during drilling. As a result of literature reviews, studies on the machining of composites are generally focused on the drill life. However, it has been observed that there are no further examinations conducted on the material after machining. The effects of feed rate, number of cycles, type of drill, and the drill diameter on the surface roughness of the workpiece are examined while drilling the composite material (Arul, 2006).Senol B. investigated the drillability of CuSn10 and GGG40 MMCs having different reinforcement rates (10%–20%–30%–40%) under dry cutting conditions with carbide drill. As the reinforcement ratio is increased, the Stronsiyum (SR)is also increased, whereas the feed force is decreased. During cutting process, GGG 40 metallic chips act as fillers with different hardness values than the matrix (Şenol,2021Kosedag,E.,et all.he low-velocity impact behavior of SiC nanoparticle-glass fiber-reinforced polymer matrix composites (PMC) in terms of different weight fraction of nanoparticle, artificial aging time, and impact energy was investigated in this study (2021). Kosedag,M.,Aydin,and Ekici, in another study was to reveal the effect of stacking sequence (SS), metal volume fraction (MVF), and number of layers on ballistic resistance in fiber metal laminates (FMLs). Four types of FMLs in different sequences and MVF (25% and 50%) were produced with hot press and vacuum(2021).

The aim of this study, the surface roughness of the composite materials is examined depending on the effect of drill type, diameter of the drill, rotational speed, and feed rate regarding the machinability of various composite materials in the drilling process.

2. Model of delamination analysis

During drilling-induced delamination, the drill movement of distance dX is associated with the work done by the thrust force F_A , which is used to deflect the plate, as well as to propagate the interlaminar crack. The energy balance equation gives

$$G_{IC} \cdot dA = F_A \cdot dX \cdot dU \quad (1)$$

Where dU is the infinitesimal strain energy, dA is the increase in the area of the delamination crack, and G_{IC} is the critical crack propagation energy per unit area in mode I. The value of G_{IC} is assumed a constant to be a mild function of strain rate by Saghizadeh and Dhahran, (1986). Fig. 1 depicts the schematics of delamination with a pre-drilled central hole. The diameter of the pilot hole is selected equal to the chisel length of drill, in order to eliminate the disadvantage of the chisel-induced thrust force and avoids the threat of creating large delamination by large pre-drilled hole. In Fig. 1, the center of the circular plate is loaded by a twist drill of diameter d . F_A is the thrust force, X is the displacement, H is the workpiece thickness, h is the uncut depth under tool, $2b$ is the diameter of pilot hole, and a is the radius of existing delamination, (C.C.Tsao, H.Hocheng,2003).

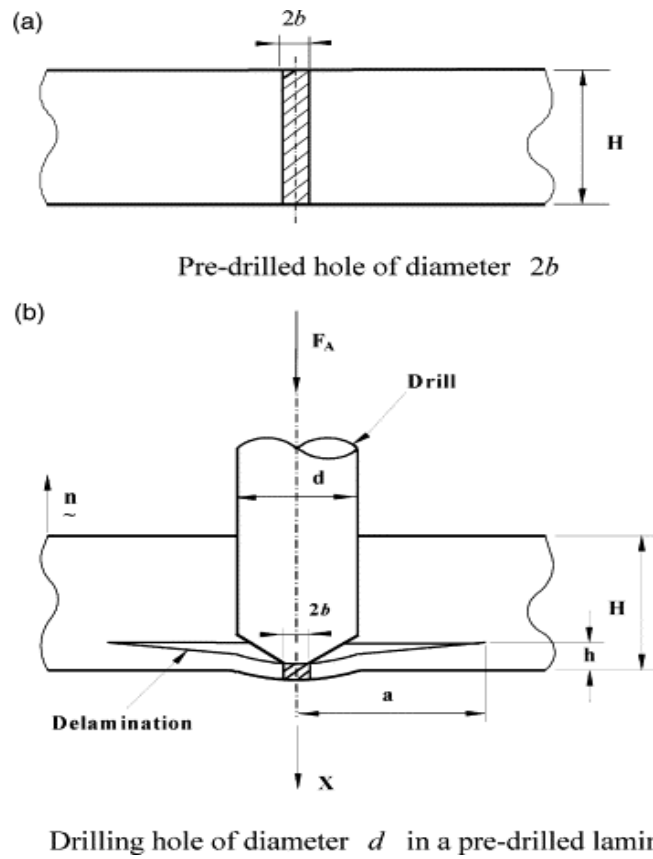


Figure 1. Circular plate model for delamination analysis of a pre-drilled specimen [11]

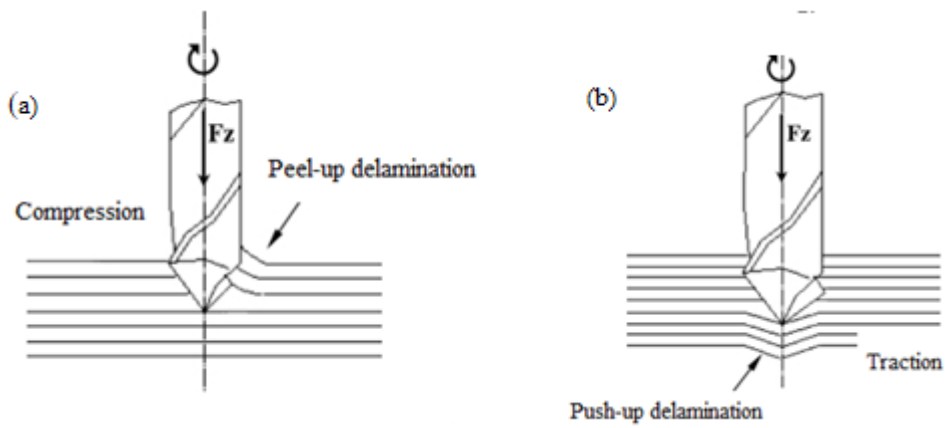


Figure 2. Delamination at the tool entry (a) and exit (b) when drilling Composite laminate [3]

3 . Materials and Method

CYCOM 7701 and CYCOM 7714 epoxy resins were used as matrix material in the tests. These resins are self-destructive resins that resist dissolving, designed specifically for use in structural laminates and honeycomb core sandwich panels for aircraft. Formulated for autoclaving or process printing. It can be absorbed into all suitable structures by the dissolution process. They are generally applied on aramid and glass fiber. ISOVAL11 is made of glass fabric impregnated with a heat resistant version of the epoxy system. The layers show excellent thermal and chemical resistance as well as mechanical strength at high temperatures (Pihtili, 2009). Plastic matrix composites produced in different forms are used in the tests to be used in the drilling process. Materials were produced from various companies as semi-finished and finished products. Semi-finished materials are made ready for use in tests as finished products by going through various processes. Table 1 shows the composite materials used in the tests. Semi-finished materials in the size of 21x29.7 cm, which were previously supplied from private companies, were cut to certain dimensions for perforation. Afterwards, the prepared samples were kept in a 10-ton press at 80 degrees for 2 minutes, and then kept in a 5 tons of hot press at 80 degrees for 15 minutes, and 80x110 mm composite materials were obtained. In order for all the produced materials to turn into a homogeneous structure, they were stored in the refrigerator for 20-30 minutes after the hot pressing process and allowed to cool rapidly

Table 1 The composite materials used in experiments.

Material	Characteristics	Texture	Thickness (mm)	status
CYCOM7701-A	Epoksi/E-glass fiber	170 g/m ²	0.1	Semi-finished product
CYCOM7701-B	Epoksi/E-glass fiber	485 g/m ²	0.25	Semi-finished product
CYCOM7701-C	Epoksi/E-glass fiber	610 g/m ²	0.35	Semi-finished product
CYCOM7714-A	Epoksi/Kevlar 49	370 g/m ²	0.27	Semi-finished product
CYCOM7714-B	Epoksi/Kevlar 49	142 g/m ²	0.105	Semi-finished product
ISOVAL11-A	Epoksi/E-glass fiber	0.2 g/cm ³	2	Finished materials
ISOVAL11-B	Epoksi/E-glass fiber	0.2 g/cm ³	3.5	Finished materials
ISOVAL11-C	Epoksi/E-glass fiber	0.2 g/cm ³	5	Finished materials
ISOVAL11-D	Epoksi/E-glass fiber	0.2 g/cm ³	7	Finished materials
ISOVAL11-E	Epoksi/E-glass fiber	0.2 g/cm ³	10	Finished materials

ISOVAL11-F	Epoksi/E-glass fiber	0.2 g/cm ³	14	Finished materials
------------	----------------------	--------------------------	----	-----------------------

3.1 Drilling Processes

In order to achieve optimum results in the drilling process, the maximum size of the drilling length was chosen as 15 mm in order to comply with the requirement that it should be three times or less than three times of the hole diameter in the literature. Coolant is not used to reduce the possible heat shock in the tools during the test (Durante, 1997). During the drilling processes, the experiments are conducted via dry drilling the Stanke import brand radial drilling machine, which operates between 20 rpm and 2000 rpm, and has a feed range of 0.056 mm/rev and 2.5 mm/rev.

3.2 Cutting Tools

In the tests, N-type drills with a helix angle of $30^{\circ} \pm 3$ and a point angle of 118° are used. A new drill is used in every test (Fig. 3). In drilling operations, 3 different types of drills, HSS, TIN and Carbide, with the diameter of 5 mm are used. Experiments are conducted with dry drilling at cutting speed of 125 rpm and progresses of feed rate 0.056 mm/rev.

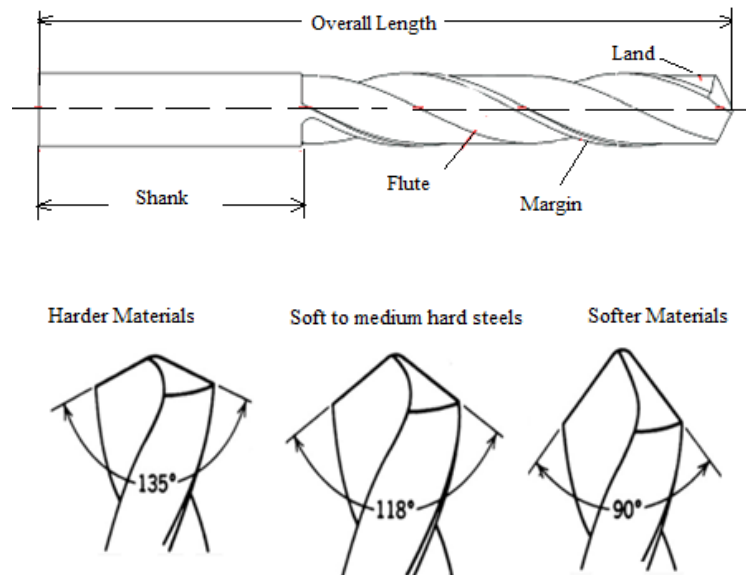


Figure 3. Drill type used in the Drilling Process

After the type of drill is selected, process parameters are specified. These are feed rate drilling speeds, and coolant, if used. Progress is expressed in s mm/rev or mm/min, and it is the distance the drill travels in the axial direction in one revolution. For a sufficient drilling and economical tool life, it is necessary to use the highest feed rate possible. The drilling speed gives the circumferential or surface speed of the drill in m/min. The correlation between the rotating speed of the drill and the drilling speed is given below.

$$V = \frac{\pi \cdot d \cdot n}{1000} \quad (2)$$

$$n = \frac{1000 \cdot V}{\pi \cdot d} \quad (3)$$

Where;

V = drilling speed m/min.

d = diameter of the drill

n= rotating speed of the drill rev/min.

Ra values were calculated with the following formula:

$$Ra = 0.58 - 0.013 \times KM + 0.273 - \text{snd} + 0.276 \times MM \quad (\text{micron}) \quad (4)$$

where;

KM is the composite material, MM is the drill material, and snd =rpm.

In addition,

TW=3, HSS=2, and carbide=1 values were considered.

These values are constant values used in the solution of Ra.

4. Transferring and Analyzing the Test Results to Graphics

4.1 Examination of Surface Roughness

The composite samples, which are drilled, were then sheared right in the middle parallel to the hole axis. Surface roughness of the materials around the hole is measured by the Mitutoyo Sufstest-211 device in order to examine the drilling performance depending on different drilling parameters. Surface roughness is determined by taking three measurements for each of Ra and Ry values from every surface and taking their averages. Table 2 shows the test parameters and surface roughness values of the workpiece obtained as a result of the tests performed under different drilling conditions (Pihtili,2009).

4.2 CYCOM7714 Composite Sample Plates used in Drilling

Kevlar 49 is used as the reinforcement material (Fig.4). A total of 8 drilling are applied to CYCOM7714 Composite sample plates. Overheating occurred in the drill during the material drilling process. It is determined that the material is torn and holes are found at the inlet and outlet of the material, however, the surface roughness in the intermediate layer is lower, especially the Ry values are much lower than the fiber glass reinforcement. Good results are especially obtained in carbide tools in terms of surface roughness. It is observed that the diameter

of the drill had no effect on the surface roughness, and some burns are observed on the surface that are caused by heat generated in the material during drilling.

Table 2. Test parameters and results.

Material	Drill Type	Average surface roughness Ra (μ)	Maximum surface roughness Ry (μ)
CYCOM7701-C	Carbide	1,13	5,1
CYCOM7701-C	TiN	2,27	6,8
CYCOM7701-C	HSS	3,01	6,1
CYCOM7714-A	Carbide	0,83	3,8
CYCOM7714-A	TiN	1,47	3,8
CYCOM7714-A	HSS	1,71	5,1
CYCOM7714-B	Carbide	0,64	2,1
CYCOM7714-B	TiN	1,11	3,7
CYCOM7714-B	HSS	1,84	2,9
ISOVAL11-A	Carbide	1,02	5,1
ISOVAL11-A	TiN	1,44	5,7
ISOVAL11-A	HSS	1,37	6,9

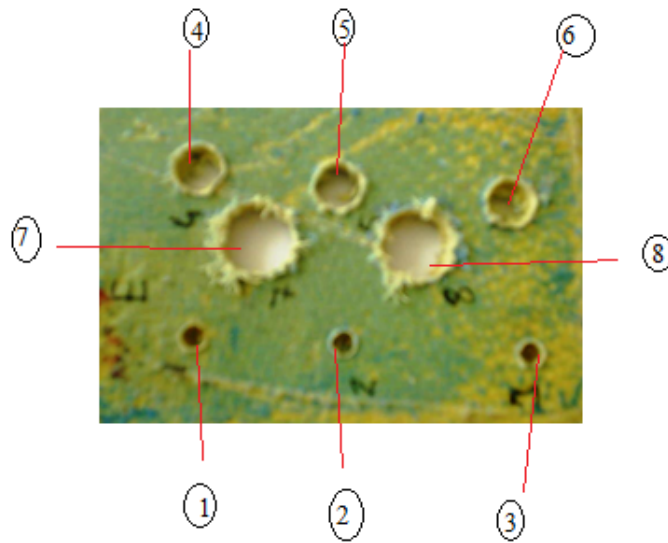


Figure 4. CYCOM7714-A Composite materials used in experiments.(8 holes of different diameter)

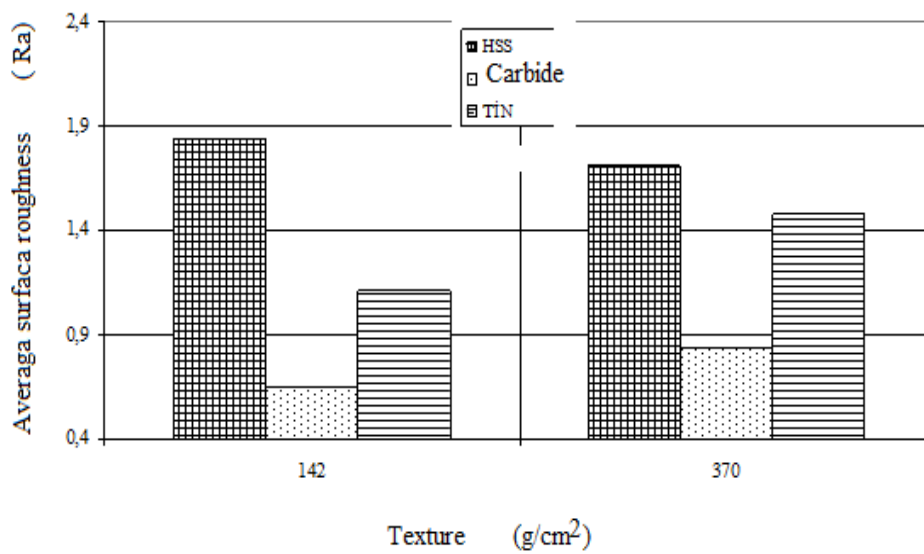


Figure 5. Variation of the average surface roughness with the weave density of the CYCOM7714 epoxy / Kevlar49 composite ($s=0.056$ mm/rev, $n=125$ rpm, $d=5$ mm)

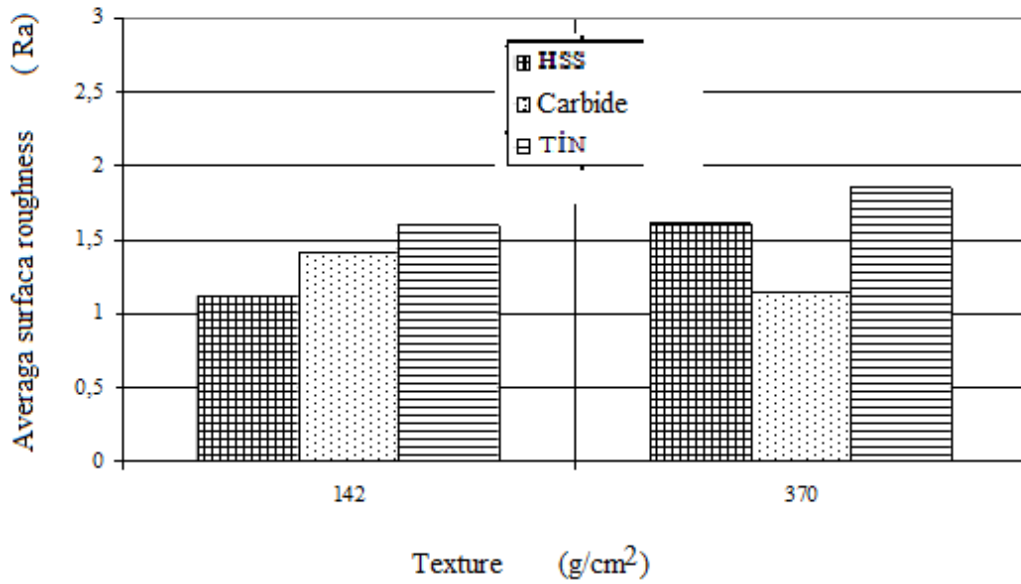


Figure 6. Variation of the average surface roughness with the weave density of the CYCOM7714 epoxy / Kevlar49 composite (s=0.112 mm/rev, n=250 rpm, d=10 mm)

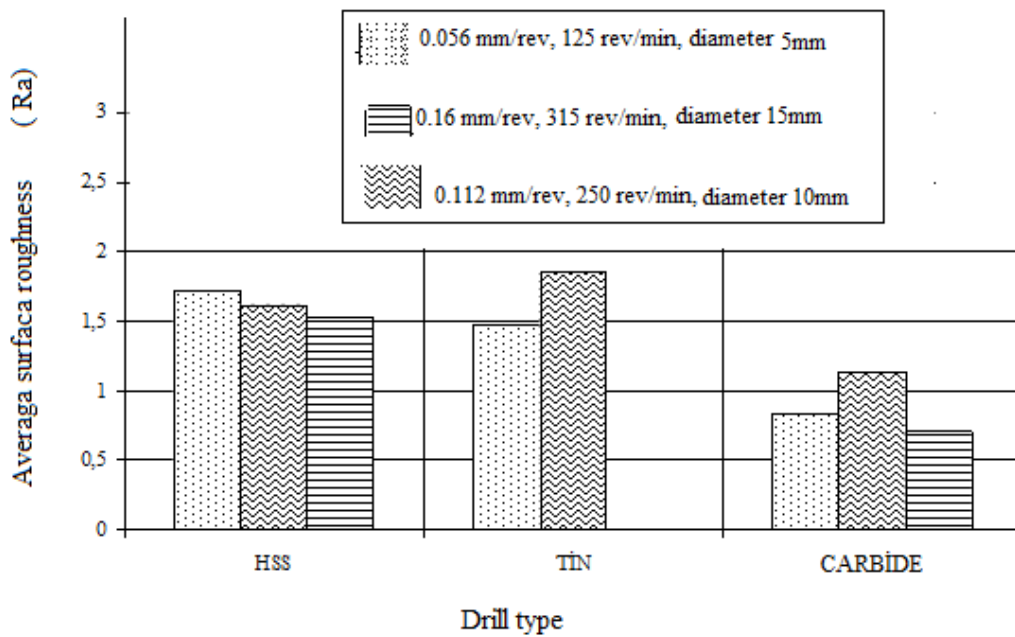


Figure 7. The change in drill material and the average surface roughness for CYCOM7714 Epoxy/ Kevlar49 fiber composite (texture densit 485 g/m², semi-finished material thickness 0.25 mm)

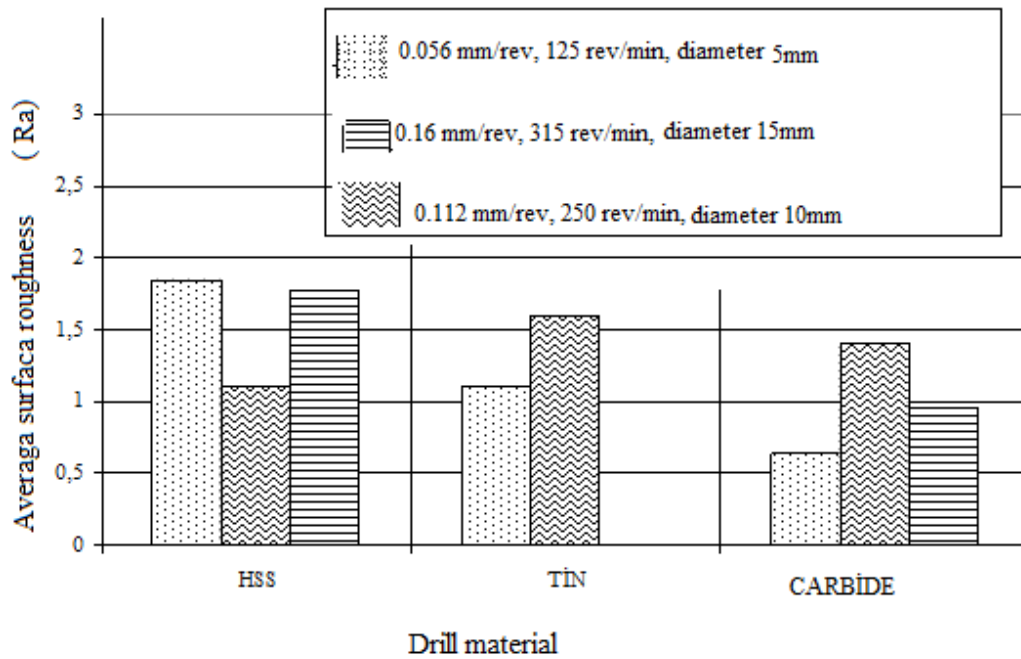


Figure 8. The change in drill material and the average surface roughness for CYCOM7714 Epoxy/ Kevlar49 fiber composite (texture densit 142 g/m², semi-finished material thickness 0.15 mm)

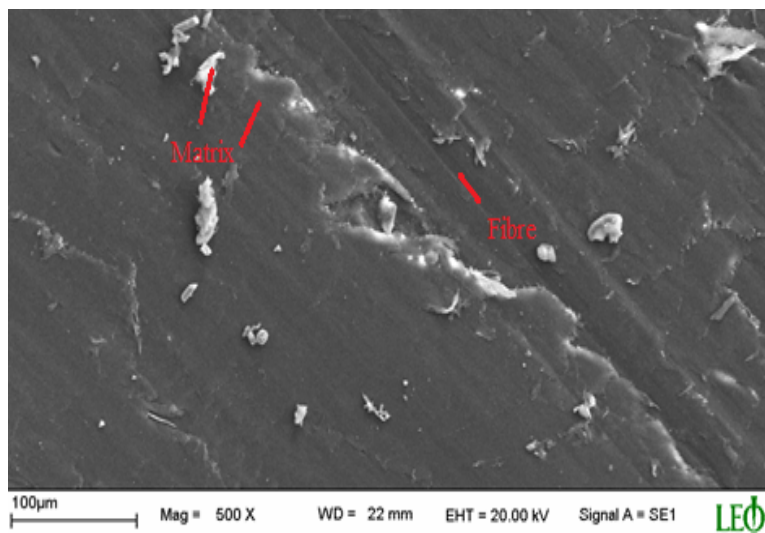


Figure 9. 500x enlarged SEM photo of middle point of hole section for CYCOM7714 Epoxy/ Kevlar49 fiber composite drilled with HSS drill (texture density 142 g/m², semi-finished material thickness 0.105 mm, s=0.16 mm/rev, n=315 rpm, d=15 mm)

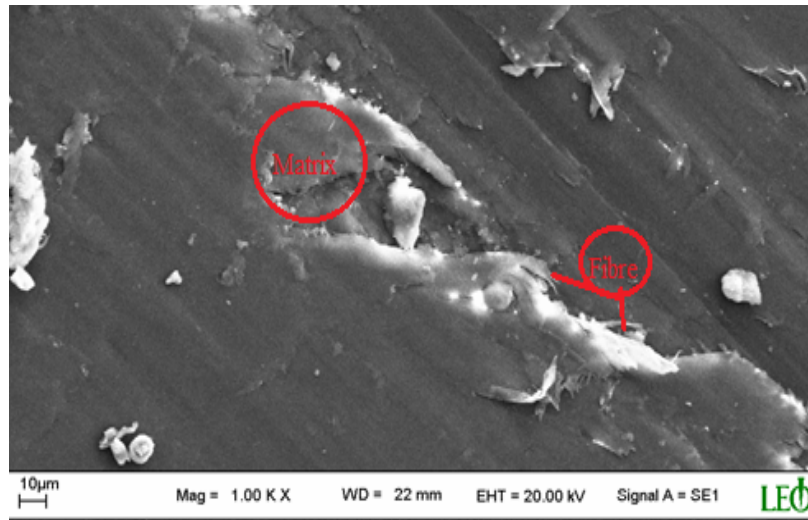


Figure 10. 1000x enlarged SEM photo of middle point of hole section for CYCOM7714 Epoxy/ Kevlar49 fiber composite drilled with HSS drill (texture density 142 g/m^2 , semi-finished material thickness 0.105 mm, $s=0.16 \text{ mm/rev}$, $n=315 \text{ rpm}$, $d=15 \text{ mm}$)

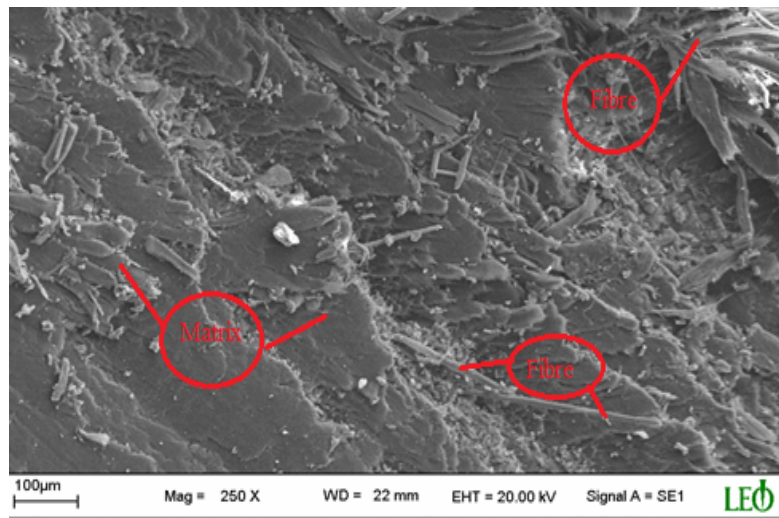


Figure 11. 250x enlarged SEM photo of middle point of hole section for CYCOM7714 Epoxy/ Kevlar49 fiber composite drilled with HSS drill (texture density 142 g/m^2 , semi-finished material thickness 0.105 mm, $s=0.16 \text{ mm/rev}$, $n=315 \text{ rpm}$, $d=15 \text{ mm}$)

4.3 CYCOM7701 Composite Plate Sample used in Drilling

Figure 12 shows the CYCOM7701 series type composite layer material. 8 drilling processes are conducted in total Carbide, TiN and HSS drills are used for the drilling processes having diameters of 5mm and 10 mm. It is observed that more sensitive surface was obtained in the drilling processes performed by using carbide drills at the

same revolution and progress, and the same situation was also present in the drills having diameters of 10 mm and 15 mm. Figure 13 and 14 show the maximum surface roughness values obtained as a result of drilling.

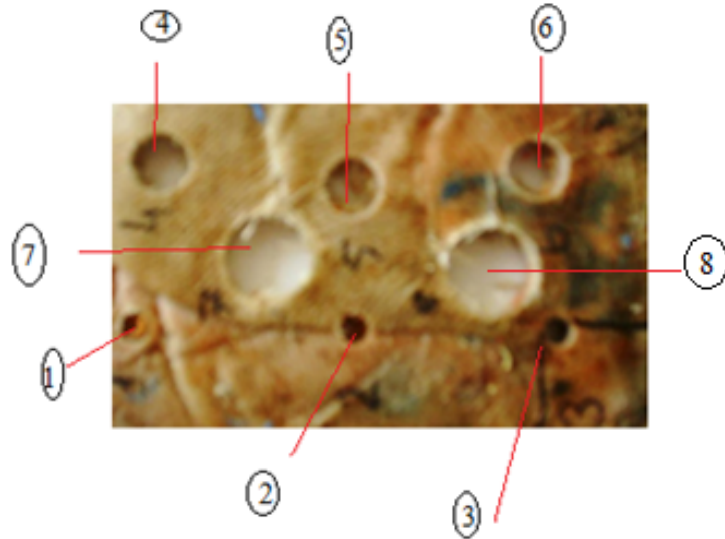


Figure 12. CYCOM7701-C Composite materials used in experiments

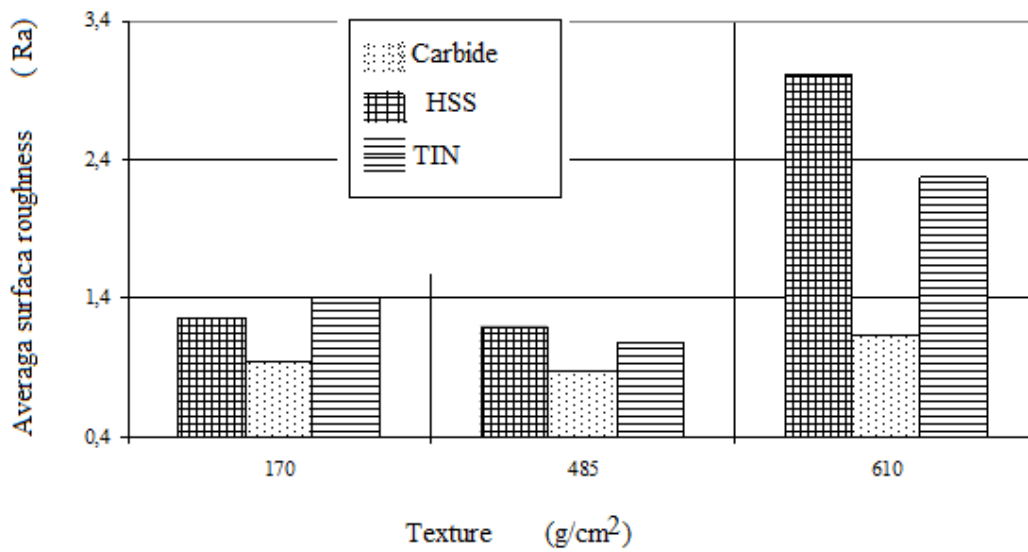


Figure 13. The change in Texture (g/cm²) and the average surface roughness for CYCOM7701 Epoxy/E-glass fiber composite (s=0.056 mm/rev, n=125 rpm, d=5 mm)

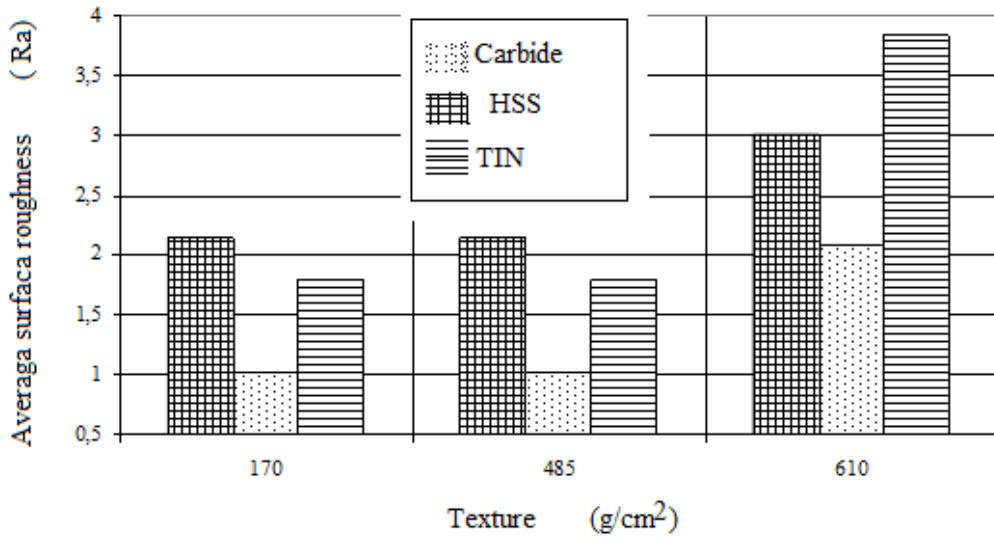


Figure 14. The change in Texture (g/cm^2) and the average surface roughness for CYCOM7701 Epoxy/E-glass fiber composite ($s=0.112$ mm/rev, $n=250$ rev/min, $d=10$ mm)

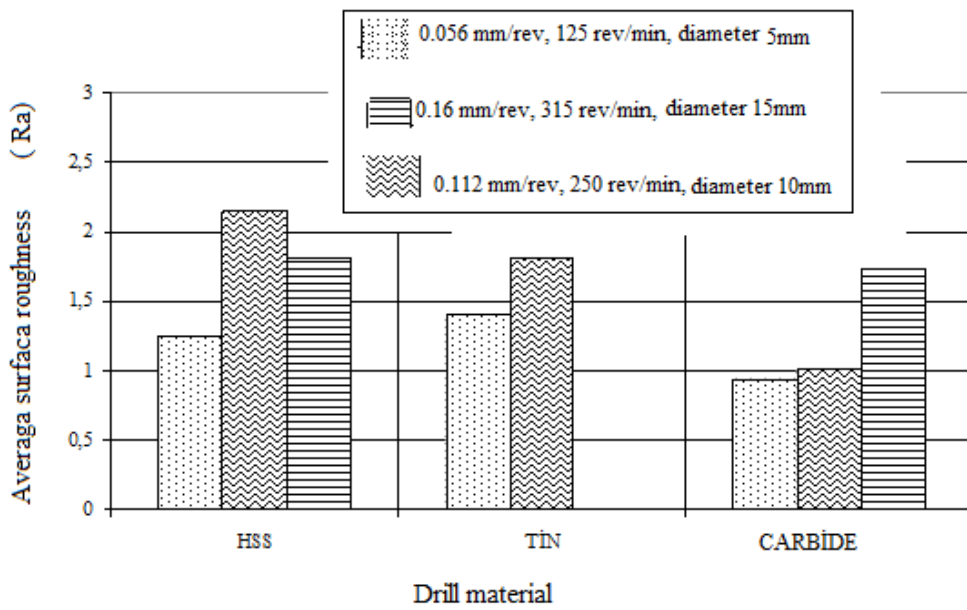


Figure 15. The change in Texture (g/cm^2) and the average surface roughness for CYCOM7701 Epoxy/E-glass fiber composite (texture density 170 g/m^2 , semi-finished material thickness 0.1 mm).

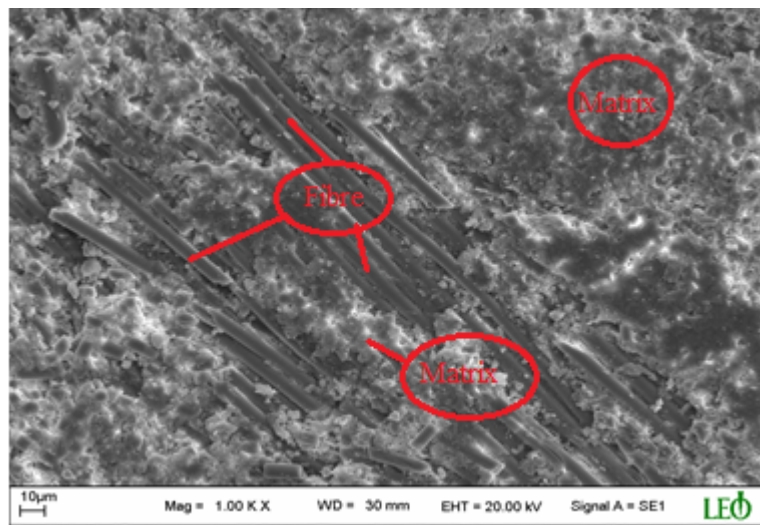


Figure 16. 1000x enlarged SEM photo of middle point of hole section for CYCOM7701 Epoxy/ E-glass fiber composite drilled with HSS drill (texture density 485 g/m², semi-finished material thickness 0.25 mm, s=0.16 mm/rev, n=315 rpm, d=15 mm)

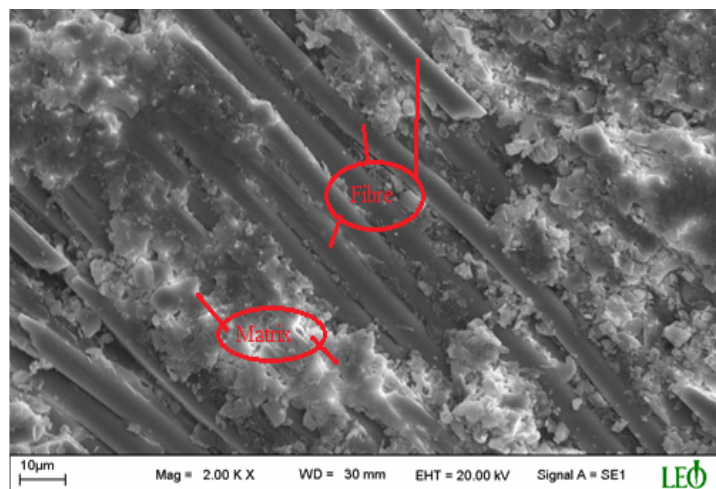


Figure 17. 2000x enlarged SEM photo of middle point of hole section for CYCOM7701 Epoxy/ E-glass fiber composite drilled with HSS drill (texture density 485 g/m², semi-finished material thickness 0.25 mm, s=0.16 mm/rev, n=315 rpm, d=15 mm)

4.4 ISOVAL11 Composite Plate used in Drilling

Figure 18 shows the ISOVAL11 series type composite material. A total of 8 drilling processes are applied with the ISOVAL11 material having a thickness of 3.5 mm. It is observed that more sensitive surface is obtained in the drilling processes performed by using carbide drills at the same revolution and progress, and the same

situation was also present in the drills having diameters of 10 mm and 15 mm. It is observed that there is little heating on the tool, where the chips are formed in the powder form. Ry value is found to be high in the holes with a diameter of 15 mm.

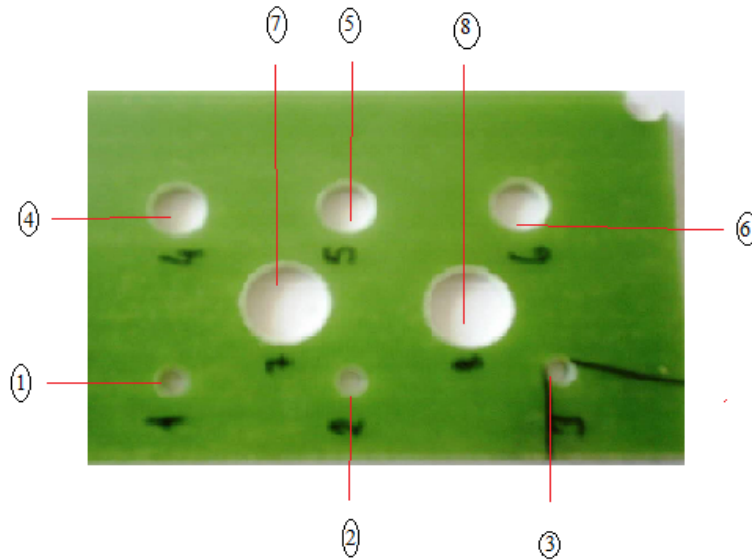


Figure 18. ISOVAL11 Composite materials used in experiments

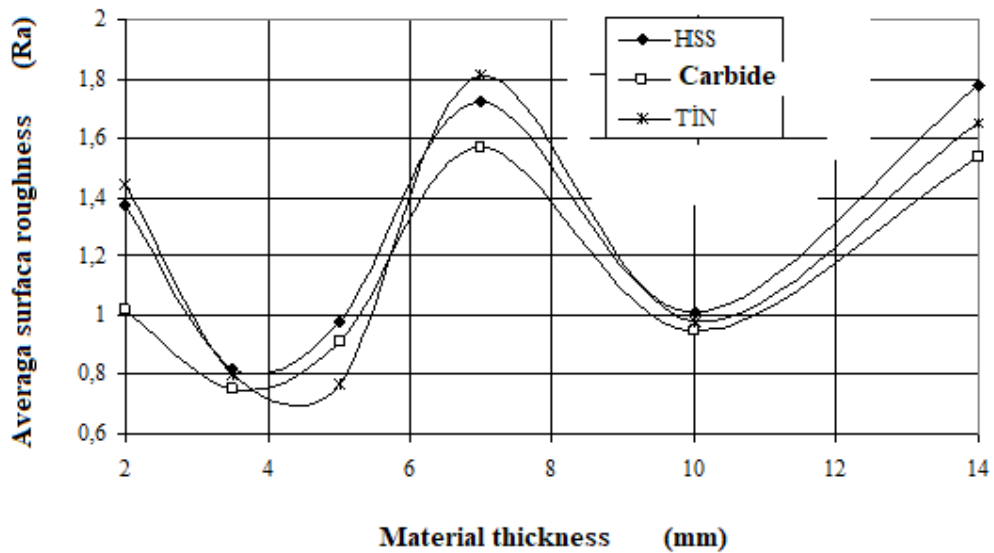


Figure 19. The change in material thickness and the average surface roughness for ISOVAL11 Epoxy/E-glass fiber composite ($s=0.056$ mm/rev, $n=125$ rpm, $d=5$ mm)

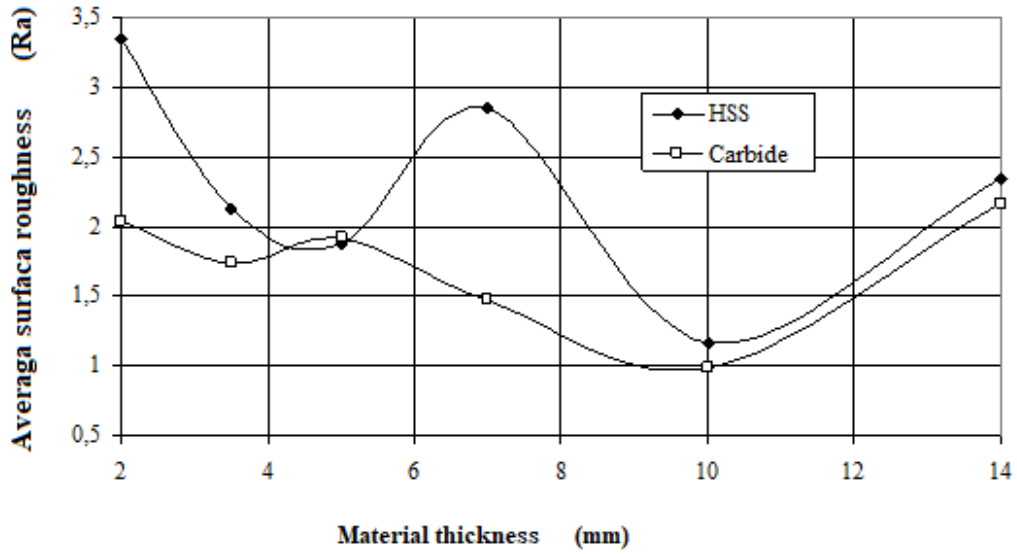


Figure 20. The change in material thickness and the average surface roughness for ISOVAL11 Epoxy/E-glass fiber composite ($s=0.056$ mm/rev, $n=315$ rpm, $d=15$ mm)

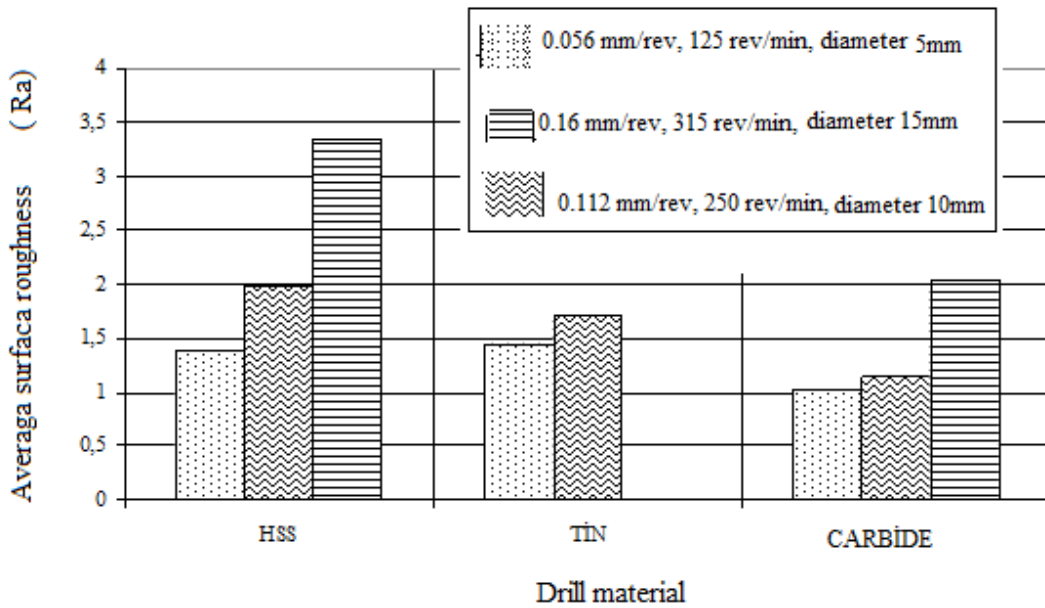


Figure 21. The change in drill material and the average surface roughness for ISOVAL 11 Epoxy/E-glass fiber composite (texture density =0.2 g/m³, composite material thickness 2mm)

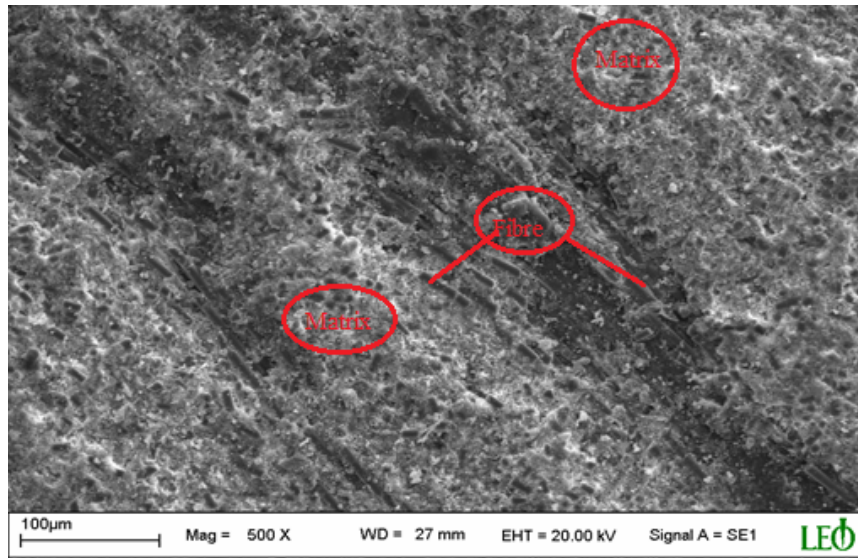


Figure 22. 500x enlarged SEM photo of middle point of hole section for ISOVAL11 Epoxy/ E-glass fiber composite drilled with HSS drill (texture density= 0.2 g/m^3 , composite material thickness =5, mm, $s=0.16 \text{ mm/rev}$, $n=315 \text{ rpm}$, $d=15 \text{ mm}$)

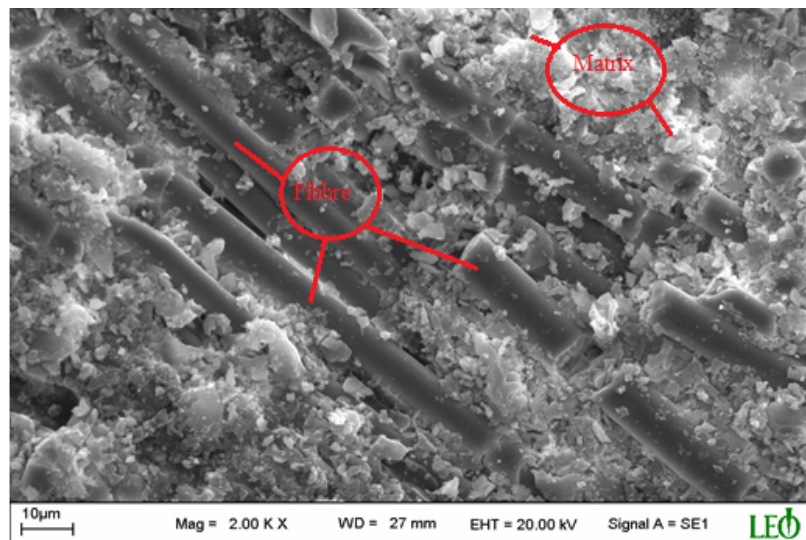


Figure 23 . 2000x enlarged SEM photo of middle point of hole section for ISOVAL11 Epoxy/ E-glass fiber composite drilled with HSS drill (texture density= 0.2 g/m^3 , composite material thickness =5, mm, $s=0.16 \text{ mm/rev}$, $n=315 \text{ rpm}$, $d=15 \text{ mm}$)

5. Test Results and Discussion

In the present study, the surface roughness of the composite materials is examined depending on the effect of drill type, diameter of the drill, rotational speed, and feed rate regarding the machinability of various composite materials in the drilling process. Below-mentioned results are obtained as a result of the test studies:

- Since the coolant is not used, it caused the softening of the matrix material as a result of the heating around the hole. In all the drilling operations conducted by using drills, matrix condensation occurred on the surface edges of the holes.
- With the increase in the feed rate, sudden ruptures occurred between the lattices in the composite material and it is found that the values of surface roughness increased in the study.
- When the surface roughness values depending on the rotation speed are considered, it is observed that the surface roughness values increased as the speed increased in all the drilling processes conducted by using all types of drills.
- In general, it is observed that the surface roughness increased as the thickness of the material increased, and drilling became difficult, and the tool heating increased.
- Due to the increase of the shearing surface in contact with the material surface, it will cause an enlargement of the cutting area and thus create larger chips during drilling and will also increase the surface roughness. It is observed that the best results for all the drill types are obtained with the drills having small diameters and thus, the surface roughness increased as the drill diameter increased. This situation also gave the same results for CYCOM7714 and ISOVAL11 materials.
- Generally it is seen that, the biggest Ra value is obtained in HSS drill materials. During drilling of the materials extreme levels of heat were generated on the drill. Both ends of the segment are torn while they are drilled. As the material gets ruptured a hole is formed at that point. However, surface roughness is lower in middle layer, and especially Ra values are found to be much lower than fiber glass reinforcement.
- When an examination is performed among the materials, it is seen that the rupture strength of Kevlar reinforced material is higher than the fiber glass material, so it is more difficult to drill the Kevlar reinforced materials.

References

- [1] Hocheng H, Tsao CC.: The path towards delamination – free drilling of composite materials. *J Mater Process Technol*; DOI: 10.1016/j.jmatprotec.2005.06.039-167:251–64, 2005.
- [2] Hocheng H, Tsao CC.: Effects of special drill bits on drilling-induced delamination of composite materials. *Int J Mach Tools Manuf*;46,11,12): DOI:10.1016/j.ijmachtools.2005.10.004-1403–16 ,2006.
- [3] W. Koenig, C. Wulf, P. Grass, H. Willerscheid Machining of fiber reinforced plastics *Annals of the CIRP*,34 (2) , pp. 538-548, 1985.
- [4] R. Komanduri, B. Zhang, C.M. Vissa Machining of fiber reinforced composites *Proceedings Manufacture Composite Materials*, 49/27 pp. 1-36,1991.
- [5] G. Caprino, V. Tagliaferri Development in drilling glass fiber reinforced plastics *International Journal of Machine Tools & Manufacture*, 35 (6) pp. 817-829,1995.
- [6] J.A. Miller, Drilling graphite/epoxy at lockheed, *American Machine Automatic Manufacture* 70–71,1987.
- [7] K. Sakuma, Y. Yokoo, M. Seto, Study on drilling of reinforced plastics—relation between tool material and wear behavior, *Bulletin of the JSME* 27 (228) 1237–1244,1984.
- [8] F. Veniali, A. DiLlio, V. Tagliaferri, An experimental study of the drilling of aramid composites, *Transactions of the ASME, Journal of Energy Resources Technology* 117 271–278,1995.
- [9] W. Koenig, P. Grass, A. Heintze, F. Okcu, C. Schmitz-Justin, Developments in drilling, contouring composites containing Kevlar, *Production Engineer* 5 6–61,1984.
- [10] H. Saghizadeh, C.K.H. Dharan, Delamination fracture toughness of graphite and aramid epoxy composites, *Transactions of the ASME, Journal of Engineering Materials and Technology* 108 290–295,1986.
- [11] C.C.Tsao,H.Hocheng, The effect of chisel length and associated pilot hole on delamination when drilling composite materials, *International Journal of Machine Tools and Manufacture*,doi.org/10.1016/S0890-6955(03)00127-5,Volume 43, Issue 11, Pages 1087-1092,2003.
- [12] Kosedag, E.,Caliskan,and Ekici, The effect of artificial aging on the impact behavior of SiC nanoparticle-glass fiber-reinforced polymer matrix composites, *polymer composite*, Vol:43, Issue2, doi.org/10.1002/pc.26426,2021.

- [13] Kosedag, M.,Aydin,and Ekici, Effect of stacking sequence and metal volume fraction on the ballistic impact behaviors of ARALL fiber-metal laminates: An experimental study, polymer composite, doi.org/10.1002/pc.26474, Vol:43, Issue 3,2021.
- [14] Koenig W, Grass P, Heintze A, Okcu F, Schmitz-Justin C. Developments in drilling, contouring composites containing Kevlar. *Prod Engineer*;DOI:10.34218/IJM.12.5.2021..024-63(8):56–7. 60–1,1984.
- [15] Pihtili H,Canpolat, N., Investigation of Different Reinforced Composite Materials for Surface Roughness and Capacity of Being Drilled *Journal of Composite Materials*, Vol. 43, No. 19 DOI:10.1177/0021998314532668 -2009.
- [16] Schaefer, W.H., Christion, J.L.,Evaluation of the Structural Behavior of Filament Reinforced Metal Matrix Composites, Technical Report No. AFML-TR-69-36, Vol. 3, Air Force Materials Laboratory, ISBN 0-12-136504-2-1969.
- [17] Chamber, A.R., Stephens, S.E. Machining of Al-5Mg Reinforced with 5 Vol.%Saffil and 15 Vol. % SiC, *Materials Science and Engineering*, [https://doi.org/10.1016/0921-5093\(91\)90577-A-A135](https://doi.org/10.1016/0921-5093(91)90577-A-A135): 287_290,1991.
- [18] Joshi, S.S., Ramakrishnan, N., Ramakrishnan, P. Analysis of Chip Breaking During Orthogonal Machining of Al/SiCp Composites, *Journal of Materials Processing Technology*, ISSN: 2276-9919 © E3 Journals 2014-88: 90_96,1999.
- [19] El-Gallab, M., Sklad, M. Machining of Al/SiC Particulate Metal-matrix Composites Part I: Tool Performance, *Journal of Materials Processing Technology*, [https://doi.org/10.1016/S0924-0136\(98\)00054-5-83](https://doi.org/10.1016/S0924-0136(98)00054-5-83): 151_158.,1998.
- [20] Lin, J.T., Bhattacharyya, D., Ferguson, W.G. Chip Formation in the Machining of SiC-particle-reinforced Aluminum-matrix Composites, *Composites Science and Technology*, DOI:10.1016/S0266-3538(97)00126-7-58(2):285_291 ,1998.
- [21] Arul, S., Vijayaraghavan, L., Malhotra, S.K.,Krishnamurthy, R. The Effect of Vibratory Drilling on Hole Quality in Polymeric Composites, *International Journal of Machine Tools & Manufacture*, DOI:10.1016/j.ijmachtools.2005.05.023-46: 252_259, 2006.
- [22] Şenol, B., Dry cutting: a sustainable machining technology, in *Sustainable Manufacturing*- DOI: 10.1016/b978-0-12-818115-7.00004-3 ,2021.
- [23] Bernt, S. Aadnøy, Reza Looyeh, *Wellbore Instability Analysis*, in *Petroleum Rock Mechanics (Second Edition)*- ISBN 9780128159040, 2019.
- [24] Xingru, Wu, *A Special Focus on Formation Damage in Offshore and Deepwater Reservoirs*, in *Formation Damage During Improved Oil Recovery* - ISBN: 9780128137826, 2018.

Classification of Chest X-ray COVID-19 Images Using the Local Binary Pattern Feature Extraction Method

Narin Aslan^{1*}, Sengul Dogan², Gonca Ozmen Koca¹

¹Department of Mechatronic Engineering, College of Technology, Firat University, Elazig/ Turkey

²Department of Digital Forensics Engineering, College of Technology, Firat University, Elazig/ Turkey

^{1*}narin.aslan@firat.edu.tr, ²sdogan@firat.edu.tr, ¹gozmen@firat.edu.tr

(Geliş/Received: 24/03/2022;

Kabul/Accepted: 09/08/2022)

Abstract: *Background and Purpose:* COVID-19, which started in December 2019, caused significant loss of life and economic losses. Early diagnosis of the COVID-19 is important to reduce the risk of death. Therefore, studies have increased to detect COVID-19 with machine learning methods automatically. *Materials and Methods:* In this study, the dataset consists of 15153 X-ray images for 4961 patient cases in three classes: Viral Pneumonia, Normal and COVID-19. Firstly, the dataset was preprocessed. And then, the dataset was given to the Cubic Support Vector Machine (Cubic SVM), Linear Discriminant (LD), Quadratic Discriminant (QD), Ensemble, Kernel Naive Bayes (KNB), K-Nearest Neighbor Weighted (KNN Weighted) classification methods as input data. Then, the Local Binary Model (LBP) texture operator was applied for feature extraction. *Results:* These values were increased from 94.1% (without LBP) to 98.05% using the LBP method. The Cubic SVM method's highest accuracy was observed in these two applications. *Conclusions:* This study demonstrates that the performance of the presented methods with LBP feature extraction is improved.

Keywords: Covid-19, local binary pattern, feature extraction, machine learning, classification.

Chest X-ray COVID-19 Görüntülerinin Yerel İkili Model Özellik Çıkarımı Yöntemi Kullanılarak Sınıflandırılması

Öz: *Arka Plan ve Amaç:* Aralık 2019'da başlayan COVID-19, önemli can ve ekonomik kayıplara neden oldu. Ölüm riskini azaltmak için COVID-19'un erken teşhisi çok önemlidir. Bu nedenle, COVID-19'u makine öğrenmesi yöntemleriyle otomatik olarak tespit etmeye yönelik çalışmalar artmaktadır. *Materyal ve Metod:* Bu çalışmada veri seti, Viral Pnömoni, Normal ve COVID-19 olmak üzere üç sınıftaki 4961 hasta vakası için 15153 X-ray görüntüsünden oluşmaktadır. Öncelikle, veri seti ön işlemden geçirildi. Daha sonra, Cubic Support Vector Machine (Cubic SVM), Linear Discriminant (LD), Quadratic Discriminant (QD), Ensemble, Kernel Naive Bayes (KNB), K-Nearest Neighbor Weighted (KNN Weighted) sınıflandırma metodlarına girdi datası olarak verildi. Daha sonra özellik çıkarımı için Yerel İkili Model (LBP) doku operatörü uygulandı. *Bulgular:* Bu değerler LBP yöntemi kullanılarak %94,1'den (LBP kullanılmadan) %98,05'e yükseltildi. Bu iki farklı uygulamada en yüksek doğruluk Cubic SVM yönteminde gözlemlendi. *Sonuçlar:* Bu çalışma, LBP öznitelik çıkarımı ile sunulan yöntemlerin performansının arttığını göstermektedir.

Anahtar kelimeler: Covid-19, yerel ikili model, özellik çıkarma, makine öğrenimi, sınıflandırma.

1. Introduction

Coronavirus 2019 (COVID-19), a pandemic virus type, causes respiratory tract infections in humans. This epidemic, which emerged in Wuhan city of China in December 2019, caused the death of millions of people. COVID-19 poses a danger to global health and should be detected early. Therefore, it is important to facilitate the early diagnosis of this disease, predict the recovery day of the patient, and help the specialists who diagnose the disease [1, 2]. Due to these necessary reasons, studies on the machine learning method for the specification of COVID-19 have gained momentum. In addition, studies on lung computed tomography (CT) and X-ray images were analyzed [3]. Some related studies in the literature are shortly mentioned below:

Hasoon et al. [4] used feature extractors with Local Binary Pattern (LBP), Gradient Histogram, and Haralick texture features after preprocessing the COVID-19 data. KNN and SVM were applied in classification methods. An average of 98.66% accuracy performance was observed in the LBP-KNN model. Jawahar et al. [5] suggested a Local Binary Model technique to predict COVID-19 disease using X-ray images and extract the images distinctive features. The features were given as input data to various classifiers. As a result of the study, 77.7%

^{1*}Corresponding author: narin.aslan@firat.edu.tr. ORCID Number of authors: ^{1*} 0000-0002-7609-1557, ² 0000-0001-9677-5684, ¹ 0000-0003-1750-8479

accuracy was obtained in the Random Forest classifier. Tuncer et al. [6] proposed a sample Local Binary Model (ResExLBP) feature generation method to detect COVID-19. The work consists of preprocessing, feature selection, and feature extraction. Grayscale conversion and image resizing were applied in the preprocessing stage. Iterative ReliefF (IRF) was used in the feature selection phase. In the classification phase, they worked on decision tree (DT), SVM, subspace discriminant (SD), and K-Nearest Neighbor (KNN) methods. 100% accuracy was obtained in the SVM classifier. Lakshmi et al. [7] classified 2815 COVID CT images using two different datasets, COVID and non-COVID. The logarithmic transformation of the LBP (LT-LBP) was applied in the feature extraction. KNN, SVM, Random Forest (RF), and Logistic Regression (LR) methods were used for classification. The accuracy value for the LD-LBP method combined with SVM was calculated as 95.7%. Alquran et al. [8] applied LBP, Gabor Filter, and Gray Level Co-Occurrence Matrix (GLCM) texture features extraction methods to machine learning methods to detect COVID-19. The 1929 X-ray image of the lung was analyzed. SVM, RF, KNN, ANN, and Ensemble were used for classification. The best accuracy obtained using the Ensemble classifier was observed as 93.1%. Abed et al. [9] detected COVID-19 disease using SVM, radial basis function (RBF), linear kernel, DT, KNN, CN 2 rule induction techniques, and deep learning models. 800 X-ray images were used. The best accuracy of 95% was observed in the SVM method. Barstugan et al. [10] analyzed 150 CT images for COVID-19 classification. Gray Level Working Length Matrix (GRLLM), GLCM, Discrete Wavelet Transform (DWT), Local Directional Model (LDP), and Gray Level Dimension Region Matrix (GLSZM) algorithms were applied as feature selection methods. These features extracted by SVM method are classified. With the GLSZM feature extraction method, 99.68% classification accuracy was obtained. Rohman and Bustamam [11] analyzed the classification of COVID-19 disease based on tissue feature selection using X-ray and CT scan images. GLCM, Histogram of Oriented Pattern (HOG), and LBP were implemented to select texture features. 1100 X-ray and 1100 CT images were used for analysis. SVM method was applied in classification. Predictive accuracy of 97% and 99% was observed in the classification of CT and X-ray images, respectively. Amini and Shalbah [12] determined the severe, moderate, and mild severity of COVID-19 from 956 CT images. They used second-order statistical and a number of quantitative first texture features. Variance, kurtosis, and skewness are the first-order tissue features extracted from the histogram. GLCM, GLRLM, and GLSZM constitute the quadratic texture feature extraction methods. It was detected with 90.95% accuracy in the classification made using random forest (RF).

In this study, an open-access dataset containing X-ray images was used to detect COVID-19. Local Binary Model (LBP) feature extraction method was applied to this data set. The most important features obtained in LBP feature extraction were given as input data to classification methods such as support vector machine (SVM), Linear Discriminant (LD), Quadratic Discriminant (QD), Ensemble, Naive Bayes (NB), and K-Nearest Neighbor. In the diagnosis of COVID-19, classification and performance criteria were measured, and the results were compared. We can summarize the contribution of our work as follows:

- Six different classification methods were combined Cubic SVM, LD [13], QD [14], Ensemble [15], KNN, and KNN with the LBP feature extraction operator.
- A large dataset of 15153 X-ray images obtained very high predictive values in performance criteria.
- LBP feature extraction was used to extract high-level features from images.
- Among the other five classification models, the best results were seen in the LBP-Cubic SVM model.
- We achieve the highest performance criteria with 98.05% accuracy, 90.99% sensitivity, 95.39% specificity, and 91.71% F score.

The remainder of the paper study is structured as follows: First, dataset preparation and preprocessing, feature selection, and evaluation metrics are discussed in **Section 2**. In **Section 3**, the experimental results are described. In **Section 4** provides a comprehensive discussion of similar literature studies. Finally, the conclusion and future work are discussed in **Section 5**.

2. Material and Method

2.1 Dataset

Chest X-ray images are a data set containing three classes: 10192 Normal, 3616 COVID-19, and 1345 Viral Pneumonia [16]. The resulting dataset has a total of 15153 images. These images consist of 299×299 Portable Network Graphics (PNG) image files. The original X-ray images of Normal, COVID-19, and Viral Pneumonia are presented in three classes, and textural images of the same images obtained by applying LBP are shown in Figure 1.

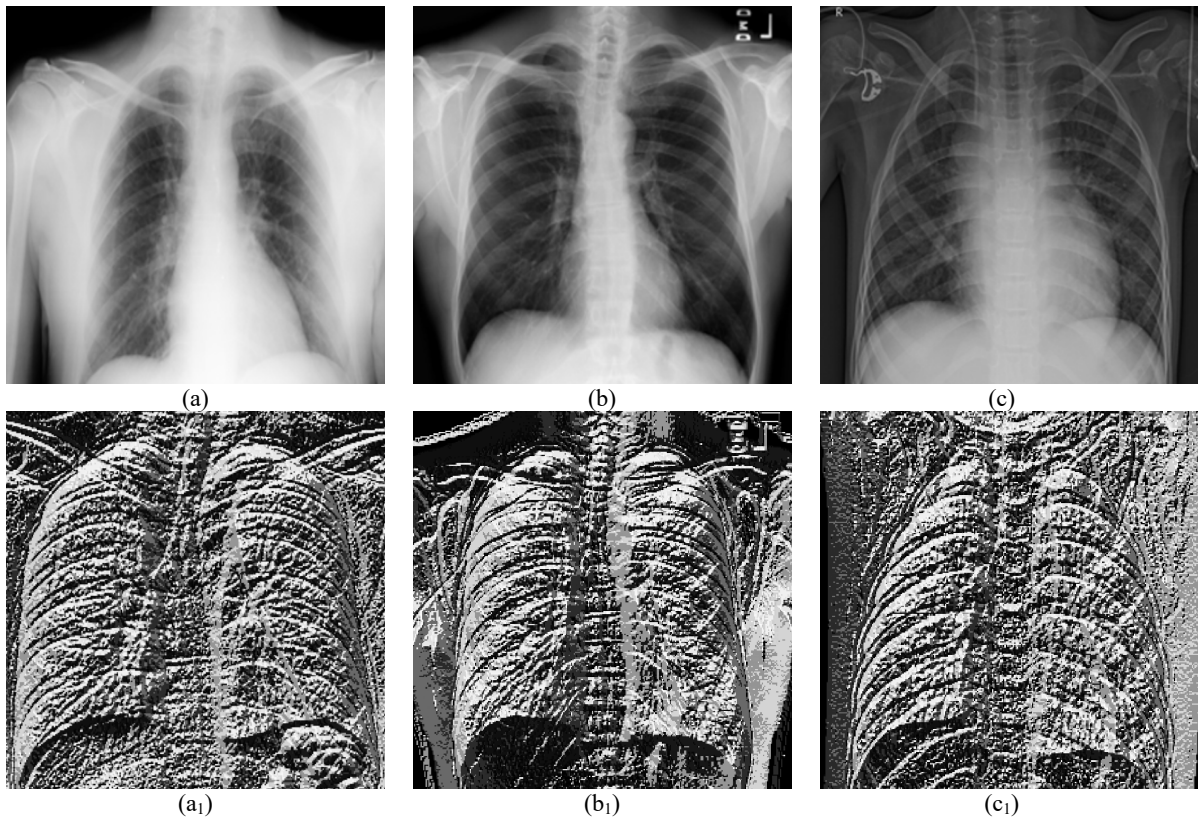


Figure 1. The original images of COVID-19 (a), Normal (b), and Viral Pneumonia (c) X-ray images and the feature images of these images obtained by applying LBP are (a₁), (b₁), and (c₁), respectively.

2.2 Method

The flow chart covering the content of the study is shown in Figure 2.

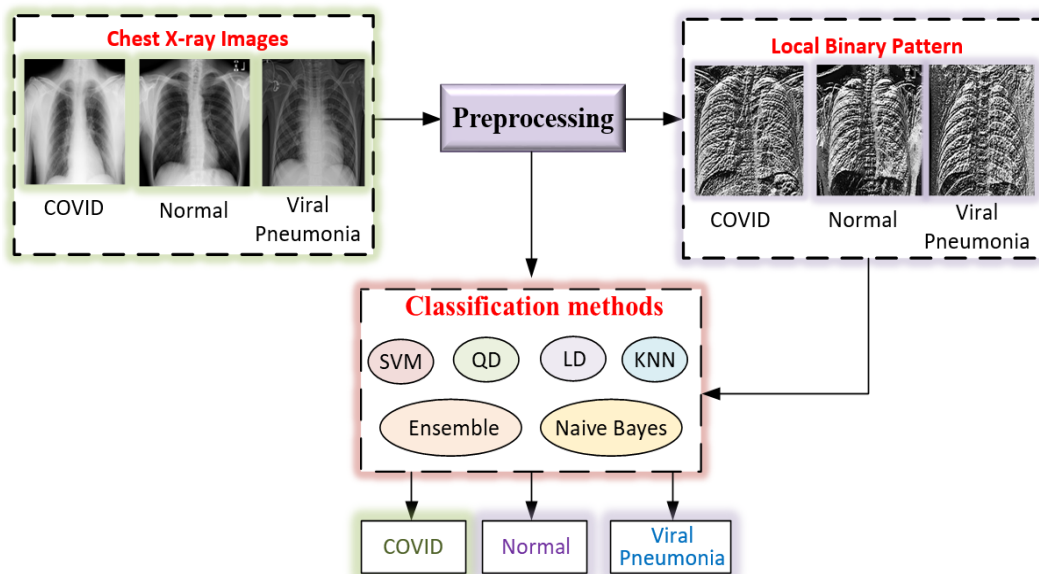


Figure 2. Workflow of proposed study framework for classifying the COVID-19 status in X-Ray images.

The steps followed in the presented study are mentioned below:

Step 1: The chest X-ray images are tagged in three classes: COVID, Normal, and Viral Pneumonia.

Step 2: Since LBP is applied to a one-dimensional image, these images containing Portable Network Graphics (PNG) of 299×299 in the preprocessing part were converted to 224×224 data size.

Step 3: These images are given as input data to SVM, QD, LD, KNN, Ensemble, and Naive Bayes classification methods.

Step 4: The performance criteria of the classification results in three classes (COVID, Normal and Viral Pneumonia) are calculated.

Step 5: The input data is reduced to one dimension before applying LBP feature extraction.

Step 6: These input data, which applied LBP feature extraction, are given as input data again to SVM, QD, LD, KNN, Ensemble, and Naive Bayes classification methods.

Step 7: After applying LBP feature extraction, performance criteria for classification results in three classes (COVID, Normal and Viral Pneumonia) are calculated.

2.2.1. Local Binary Pattern

Local Binary Pattern (LBP) is a very effective tissue operator that labels the pixels of the image and evaluates the result as a binary number. It is a texture measurement method independent of gray level. It is a common approach in various applications due to its computational simplicity and distinctive power. Computational simplicity is its most important feature, making it possible to analyze images in real-time adjustment. The original LBP operator constrains every pixel 3×3 neighborhood of every pixel to its center value. It evaluates the result as a binary number and creates labels for the image pixels [17, 18]. The following equations are used in the LBP method to obtain the feature set.

$$LBP = \sum_{n=0}^7 S(I_n - I_c) \times 2^n \quad (1)$$

$$A_{i,j}^1 = S(I_1, I_c) \times 2^7 + S(I_2, I_c) \times 2^6 \quad (2)$$

$$A_{i,j}^2 = S(I_3, I_c) \times 2^5 + S(I_4, I_c) \times 2^4 \quad (3)$$

$$A_{i,j}^3 = S(I_5, I_c) \times 2^3 + S(I_6, I_c) \times 2^2 \quad (4)$$

$$A_{i,j}^4 = S(I_7, I_c) \times 2^1 + S(I_8, I_c) \times 2^0 \quad (5)$$

$$A = A_{i,j}^1 + A_{i,j}^2 + A_{i,j}^3 + A_{i,j}^4 \quad (6)$$

$$LBP = Histogram_A \quad (7)$$

$$S(z) = \begin{cases} 0, & z < 0 \\ 1, & z \geq 0 \end{cases} \quad (8)$$

Here, I_c and I_n represent the center pixel value and the neighboring pixel value, respectively. z represents the difference between the neighboring pixel, and the center pixel $S(z)$ represents the bits produced as a result of the LBP operator. The pixel labeling scheme in the LBP operator is given in Figure 3.

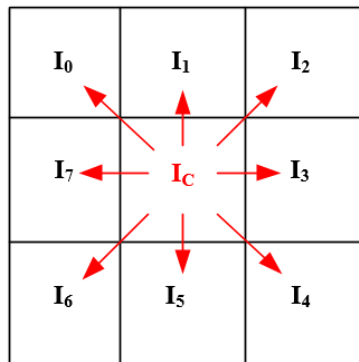


Figure 3. Labeling pixels in the LBP operator.

The performance criteria used in this study are given below:

$$Accuracy = \frac{TP + TN}{TP + TN + FP + FN} \quad (9)$$

$$Sensitivity = \frac{TP}{Positive} \quad (10)$$

$$Sensitivity = \frac{TN}{Negative} \quad (11)$$

$$F_score = \frac{((1 + \beta^2)) * (sensitivity * precision))}{((\beta^2) * (precision + sensitivity))} \quad (12)$$

where, the value of beta is 1. Also, True Negative, True Positive, False Positive, and False Negative are TN, TP, FP, and FN, respectively [19-21].

3. Experimental Results

The dataset used in this study includes 15153 Viral Pneumonia, Normal, and COVID-19 Chest X-ray images. In the first stage of this study, the dataset size consisting of 299×299 Portable Network Graphics (PNG) image files is converted to 224×224 data size. Then, Cubic SVM, LD, QD, Ensemble, Kernel Naive Bayes, and KNN Weighted classification methods are given separately as the input dataset. The classification learner of MATLAB R2020a provides this study with a personal computer with 16 GB RAM and a 3.30 GHz processor. For each classification method, 10-fold cross validation is used. In the second step, important features are selected from the dataset with LBP feature extraction, and these features are applied again as input data to the specified classification methods. Finally, the Accuracy, Sensitivity, Specificity, and F_Score performance criteria of the experimental results obtained without feature extraction are calculated, and these results are shown in Table 1.

Table 1. Classification results without applying LBP feature extraction.

	Accuracy	Sensitivity	Specificity	F_score
Cubic SVM	94.1	91.25	95.61	91.86
Linear Discriminant	87.0	80.87	89.91	81.52
Quadratic Discriminant	86.7	86.54	91.64	82.29
Ensemble	88.4	79.93	90.43	83.12
Kernel Naive Bayes	71.2	72.66	83.89	64.48
KNN Weighted	90.0	82.82	91.37	85.51

As seen in Table 1, the highest estimation accuracy of the Cubic SVM method is 94.1%. Sensitivity, Specificity, and F_score performance criteria of Cubic SVM are 91.25%, 95.61%, and 91.86%, respectively. In addition, these performance criteria are higher than the performance criteria of other classification methods. Although the lowest accuracy is seen in the Kernel Naive Bayes method with a rate of 71.2%, the Linear Discriminant and Quadratic Discriminant methods showed close values of 87.0% and 86.7%, respectively.

The confusion matrix is used to compare target feature estimates and actual values to measure the performance of classification methods [22]. The confusion matrix results obtained without LBP feature extraction are shown in Figure 4.

	Predicted Class				Predicted Class				Predicted Class			
		1	2	3		1	2	3		1	2	3
True Class	1	3221	360	35	1	2506	974	136	1	2843	689	84
	2	240	9856	96	2	338	9608	246	2	497	9060	635
	3	33	129	1183	3	65	217	1063	3	41	65	1239
	Cubic SVM				Linear Discriminant				Quadratic Discriminant			
	Predicted Class				Predicted Class				Predicted Class			
		1	2	3		1	2	3		1	2	3
True Class	1	2651	895	70	1	2096	1033	487	1	2614	890	112
	2	329	9790	73	2	1559	7539	1100	2	152	9968	72
	3	109	289	947	3	108	79	1158	3	49	242	1054
	Ensemble				Kernel Naive Bayes				KNN Weighted			
	1	COVID-19	2	Normal	3	Viral Pneumonia						

Figure 4. Confusion matrix of classification results without applying LBP feature extraction.

Confusion matrices by class Covid-19 (1), Normal (2), and Viral Pneumonia (3) are used to visualize their predictive accuracy. Pink cells correct prediction values and green cells indicate incorrect prediction values are shown. It is also understood from the confusion matrix that the best result is seen in the Cubic SVM method. Here, the Normal class achieved a classification accuracy of 96.70%, while the COVID-19 class has an accuracy of 89.08% on 3616 test samples, classifying as 360 samples Normal and 35 samples as Viral Pneumonia. In the normal class 10192 test samples, 240 samples are included COVID-19 and 96 samples of Viral Pneumonia. While the Viral Pneumonia class distribution reached an accuracy of 87.96% in 1345 test samples, 33 samples are in the COVID-19, and 129 samples are in the Normal class.

LBP feature extraction is applied to increase the predictive accuracy of disease diagnosis in Chest X-ray images and improve performance criteria. The results obtained after applying LBP feature extraction are presented in Table 2.

Table 2. Classification results applying LBP feature extraction.

	Accuracy	Sensitivity	Specificity	F_score
Cubic SVM	98.05	90.99	95.39	91.71
Linear Discriminant	95.36	80.56	89.78	81.24
Quadratic Discriminant	95.71	86.41	91.62	82.10
Ensemble	95.80	79.38	90.06	82.61
Kernel Naive Bayes	89.03	72.46	83.78	64.25
KNN Weighted	96.31	82.27	91.12	84.94

As seen in Table 2, the Cubic SVM method's highest prediction accuracy is 98.05%. The accuracy value is 94.1% in the study without LBP feature extraction. When the other methods in the table examined, an increase in the accuracy performance criterion observed. The Linear Discriminant, Quadratic Discriminant, and Ensemble classification methods have almost the same predictive accuracy, with 95.36%, 95.71%, and 95.80%, respectively. The KNN method has 96.31% predictive accuracy. After applying LBP feature extraction to the input data, the best prediction accuracy is presented in Figure 5, again with the Cubic SVM method.

	Predicted Class				Predicted Class				Predicted Class			
		1	2	3		1	2	3		1	2	3
True Class	1	3195	392	29	1	2496	984	136	1	2844	683	89
	2	243	9852	97	2	348	9596	248	2	504	9047	641
	3	31	131	1183	3	69	220	1056	3	44	66	1235
	Cubic SVM				Linear Discriminant				Quadratic Discriminant			
	Predicted Class				Predicted Class				Predicted Class			
		1	2	3		1	2	3		1	2	3
True Class	1	2604	938	74	1	2092	1037	487	1	2588	909	119
	2	352	9770	70	2	1572	7507	1113	2	166	9950	76
	3	108	292	945	3	112	78	1155	3	52	249	1044
	Ensemble				Kernel Naive Bayes				KNN Weighted			
	1	COVID-19	2	Normal	3	Viral Pneumonia						

Figure 5. Confusion matrix of classification results applying LBP feature extraction.

While classifying 392 samples as Normal and 29 samples as Viral Pneumonia out of 3616 test samples, a classification accuracy of 98.05% is achieved. 10192 test data of the normal class are contained 243 data COVID-19 and 97 Viral Pneumonia data. The Viral Pneumonia class distribution in 1345 test data are included 31 data in the COVID-19 class and 131 data in the Normal class.

4. Discussion

In this section, the classification studies of COVID-19 disease with the machine learning method in the literature are compared in Table 3.

Table 3. Comparison of machine learning methods and chest X-ray models.

Ref.	Number of Sample	Feature extraction	Method	Accuracy	Sensitivity	Specificity	F_score
[4]	5000	LBP	KNN	98.66	97.76	100	-
			SVM	94.25	99.94	88.10	-
		HOG	KNN	94.26	79.95	70.19	-
			SVM	89.20	78.61	65.30	-
		Haralick	KNN	95.51	93.98	97.88	-
			SVM	94.88	99.96	89.23	-

[10]	150	GLCM	SVM	98.91	98.52	99.23	98.81
		LDP		50.70	42.47	57.71	44.14
		GLRLM		96.41	98.78	94.38	96.20
		GLSZM		98.77	97.72	99.67	98.65
		DWT		97.81	96.8	98.66	97.60
[11]	2200	GLCM	SVM	95.4	96.8	-	-
		LBP		97.5	98.0	-	-
		HOG		97.8	100	-	-
Our study	15153	LBP	Cubic SVM	98.05	90.99	95.39	91.71
			LD	95.36	80.56	89.78	81.24
			QD	95.71	86.41	91.62	82.10
			Ensemble	95.80	79.38	90.06	82.61
			Kernel Naive Bayes	89.03	72.46	83.78	64.25
			KNN Weighted	96.31	82.27	91.12	84.94

In the study, Hasoon et al. [4] used 5000 datasets, which applied LBP, HOG, and Haralick feature extraction methods. KNN and SVM methods were used as classification methods. The performance criteria values were calculated by taking the average of the 5-fold cross-validation predictive values. The highest accuracy value was seen at 98.66% in the KNN classification made with the LBP feature extraction method. The lowest accuracy estimate was observed at 89.20% in the SVM classification made with the HOG feature extraction method. In addition, in the HOG-SVM method the lowest sensitivity and specificity values were found to be 78.61% and 65.30%, respectively. When this study is compared with ours, the number of the dataset used in classification is less than ours. Although 15153 data are used in our study, in the LBP-SVM method is 98.05%, the accuracy value and the value in the LBP-KNN method in [4] is close to the accuracy rate of 98.66%. Barstugan et al. [10] classified with the different number of patches. 150 data were used in the study, which was carried out by applying 10-fold cross-validation. The highest predictive accuracy was found to be 98.91% in the GLCM-SVM method. The lowest accuracy, sensitivity, specificity, and F_score performance criteria were observed in the LDP-SVM method as 50.70%, 42.47%, 57.71%, and 44.14%, respectively. Although 2200 data were used in the study by Rohmah and Bustamam [11], an accuracy rate of 97.5% was observed in the analysis performed using the LBP-SVM method. Our study calculated the predictive accuracy value as 98.05% in the LBP-SVM method. When our study is compared with the studies in the literature, although the number of data in the study is high, the performance criteria values calculated with the Cubic SVM, LD, QD, Ensemble, Kernel Naive Bayes, and KNN Weighted methods used in classification vary between 98.05% and 64.25%. In the Cubic SVM classification method, the performance criterion result graph in the analysis performed LBP feature extraction, and without LBP feature extraction is shown in Figure 6.

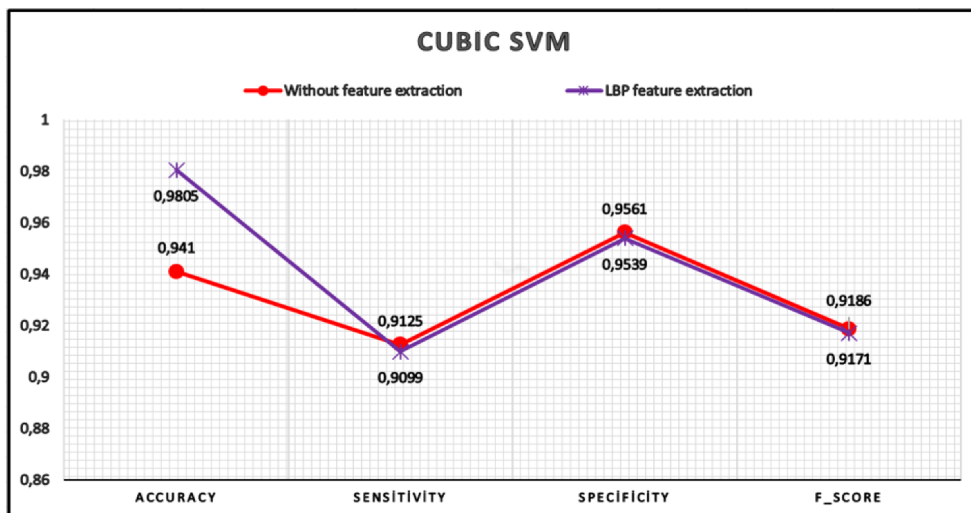


Figure 6. Performance criteria graph after feature selection in Cubic SVM classification method and LBP feature selection.

Although sensitivity, specificity, and F_score values are close, a noticeable increase in accuracy values is observed. Although the accuracy value in the analysis performed without applying feature extraction to the input data is 94.10%, the accuracy value in the analysis performed after applying LBP feature extraction is 98.05%.

5. Conclusion

In this study, classification is performed using 15153 Chest X-ray images belonging to the Normal, COVID-19, and Viral Pneumonia classes. First, the input data with the size of 229×229 is converted to the size of 224×224, and these data are applied as input data to the Cubic SVM, LD, QD, Ensemble, Kernel Naive Bayes, and KNN Weighted classification methods. Then, LBP feature extraction is applied to the input data, and these features are given as inputs to the respective classification methods. The performance criteria calculated in both applications are compared. The analysis performed after LBP feature extraction observed that the accuracy value increased from 94.1% to 98.05%. In the future, we intend to use and test variants of other feature extraction and classification operators.

References

- [1] L. Wynants *et al.*, "Prediction models for diagnosis and prognosis of covid-19: systematic review and critical appraisal," *bmj*, vol. 369, 2020.
- [2] D. Uphade and A. Muley, "Identification of parameters for classification of COVID-19 patient's recovery days using machine learning techniques," *J. Math. Comput. Sci.*, vol. 12, no. 3, p. Article ID 56, 2022.
- [3] S. H. Kassania, P. H. Kassanib, M. J. Wesolowskic, K. A. Schneidera, and R. Detersa, "Automatic detection of coronavirus disease (COVID-19) in X-ray and CT images: a machine learning based approach," *Biocybernetics and Biomedical Engineering*, vol. 41, no. 3, pp. 867-879, 2021.
- [4] J. N. Hasoon *et al.*, "COVID-19 anomaly detection and classification method based on supervised machine learning of chest X-ray images," *Results in Physics*, vol. 31, p. 105045, 2021.
- [5] M. Jawahar *et al.*, "Diagnosis of covid-19 using optimized pca based local binary pattern features," *International Journal of Current Research and Review*, pp. 37-41, 2021.
- [6] T. Tuncer, S. Dogan, and F. Ozyurt, "An automated Residual Exemplar Local Binary Pattern and iterative ReliefF based COVID-19 detection method using chest X-ray image," *Chemometrics and Intelligent Laboratory Systems*, vol. 203, p. 104054, 2020.
- [7] P. P. Lakshmi, M. Sivagami, and V. Balaji, "A novel LT-LBP based prediction model for COVID-CT images with Machine Learning," in *2021 International Conference on Information Systems and Advanced Technologies (ICISAT)*, 2021: IEEE, pp. 1-5.
- [8] H. Alquran, M. Alsleti, R. Alsharif, I. A. Qasmieh, A. M. Alqudah, and N. H. B. Harun, "Employing texture features of chest x-ray images and machine learning in covid-19 detection and classification," in *Mendel*, 2021, vol. 27, no. 1, pp. 9-17.
- [9] M. Abed *et al.*, "A comprehensive investigation of machine learning feature extraction and classification methods for automated diagnosis of COVID-19 based on X-ray images," *Computers, Materials, & Continua*, pp. 3289-3310, 2021.
- [10] M. Barstugan, U. Ozkaya, and S. Ozturk, "Coronavirus (covid-19) classification using ct images by machine learning methods," *arXiv preprint arXiv:2003.09424*, 2020.
- [11] L. N. Rohmah and A. Bustamam, "Improved classification of coronavirus disease (covid-19) based on combination of texture features using ct scan and x-ray images," in *2020 3rd International Conference on Information and Communications Technology (ICOIACT)*, 2020: IEEE, pp. 105-109.

- [12] N. Amini and A. Shalbaf, "Automatic classification of severity of COVID-19 patients using texture feature and random forest based on computed tomography images," *International Journal of Imaging Systems and Technology*, vol. 32, no. 1, pp. 102-110, 2022.
- [13] S. Balakrishnama and A. Ganapathiraju, "Linear discriminant analysis-a brief tutorial," *Institute for Signal and information Processing*, vol. 18, no. 1998, pp. 1-8, 1998.
- [14] S. Srivastava, M. R. Gupta, and B. A. Frigyik, "Bayesian quadratic discriminant analysis," *Journal of Machine Learning Research*, vol. 8, no. 6, 2007.
- [15] Y. Ren, L. Zhang, and P. N. Suganthan, "Ensemble classification and regression-recent developments, applications and future directions," *IEEE Computational intelligence magazine*, vol. 11, no. 1, pp. 41-53, 2016.
- [16] T. Rahman, M. Chowdhury, and A. Khandakar. "COVID-19 Radiography Database, COVID-19 Chest X-ray Database, <https://www.kaggle.com/tawsifurrahman/covid19-radiography-database>." (accessed).
- [17] T. Ojala, M. Pietikäinen, and D. Harwood, "A comparative study of texture measures with classification based on featured distributions," *Pattern recognition*, vol. 29, no. 1, pp. 51-59, 1996.
- [18] T. Ojala and M. Pietikäinen, "Unsupervised texture segmentation using feature distributions," *Pattern recognition*, vol. 32, no. 3, pp. 477-486, 1999.
- [19] X. Li, W. Tan, P. Liu, Q. Zhou, and J. Yang, "Classification of COVID-19 chest CT images based on ensemble deep learning," *Journal of Healthcare Engineering*, vol. 2021, 2021.
- [20] D. M. Powers, "Evaluation: from precision, recall and F-measure to ROC, informedness, markedness and correlation," *arXiv preprint arXiv:2010.16061*, 2020.
- [21] M. J. Warrens, "On the equivalence of Cohen's kappa and the Hubert-Arabie adjusted Rand index," *Journal of classification*, vol. 25, no. 2, pp. 177-183, 2008.
- [22] X. Deng, Q. Liu, Y. Deng, and S. Mahadevan, "An improved method to construct basic probability assignment based on the confusion matrix for classification problem," *Information Sciences*, vol. 340, pp. 250-261, 2016.

The Investigation of Mechanical Properties of Polycrystalline Nb Nanowire Under Applied Tensile Deformation by Molecular Dynamics Simulation

Sefa KAZANÇ^{1*}, Canan AKSU CANBAY²

¹Fırat University, Faculty of Education, Mathematics and Science Education, Elazığ, Turkey

²Fırat University, Faculty of Science, Department of Physics, Elazığ, Turkey

*¹ skazanc@firat.edu.tr, ² caksu@firat.edu.tr

(Geliş/Received: 05/04/2022;

Kabul/Accepted: 27/06/2022)

Abstract: In this study, the change in the mechanical properties of Niobium (Nb) nanowire with different grain numbers under applied uniaxial tensile deformation was tried to be investigated by Molecular Dynamics (MD) simulation method. The Embedded Atom Method (EAM), which includes many-body interactions, was used to determine the force interactions between atoms. To determine the effect of grain number on the mechanical properties of Nb nanowire, stress-strain curve, young modulus, yield strain and atomic images obtained from the common neighbor analysis method (CNA) were used. It has been determined that necking and breaking of the model nanowire occur at the grain boundaries, however, the number of grains has important effects on the mechanical properties.

Key words: Nanowire, grain boundary, molecular dynamics, mechanical properties.

Polikristal Nb Nano Telinin Uygulanan Çekme Deformasyonu Altında Mekanik Özelliklerinin Moleküler Dinamik Benzetimi ile İncelenmesi

Öz: Bu çalışmada farklı tane sayılarına sahip Niyobyum (Nb) nano telinin uygulanan tek eksenli çekme deformasyonu altında mekanik özelliklerindeki değişim Moleküler Dinamik (MD) benzetim yöntemi ile incelenmeye çalışıldı. Çok cisim etkileşmelerini içeren Gömülmüş Atom Metodu (GAM), atomlar arasındaki kuvvet etkileşmelerini belirlemek için kullanıldı. Nb nano telinin mekanik özellikleri üzerine tane sayısının etkisini belirlemek için zor-zorlanma eğrisi, elastiklik modülü, akma zorlanması ve genel komşu analiz yönteminden (Common Neighbor Analysis-CNA) elde edilen atomik görüntülerden yararlanıldı. Model nano telde boyun verme ve kopmanın tane sınırlarında meydana geldiği bununla birlikte tane sayısının mekanik özellikler üzerinde önemli etkilerinin olduğu tespit edildi.

Anahtar kelimeler: Nano tel, tane sınırı, moleküler dinamik, mekanik özellikler.

1. Introduction

The rapid technical progress in nanowire fabrication in recent years has greatly supported the development and application of nanoelectromechanical systems. The structural safety and reliability of nanoelectromechanical systems largely depend on the mechanical behavior of these newly developed nanoscale materials. The properties of nanostructured materials depend on the internal microstructure size and the external sample size. Nanostructured materials can be developed by refining the grain size [1] by embedding nanotwined lamellas in sub-micrometer sized grains [2, 3] or nanowires [4, 5] or by adjusting the layer thickness of nanoscale metallic multilayers [6, 7]. They are also used in the development of new products such as nanoelectronic devices [8-10], energy storage and conversion systems [11, 12], biomedical devices and sensors [13].

Research on the mechanical properties of polycrystalline materials is of great importance in terms of both theory and practice [14-16]. It is known that grain boundary plays an important role on the mechanical properties of polycrystalline materials [17-19]. A good understanding of crystallographic deformation in mechanical processes due to nano-dimensional effects [20, 21] is very important for devices to be developed. Atomic force microscopy [22] and high-resolution transmission electron microscopy [23] are used to experimentally examine the properties of nano-sized metallic materials at the atomic level. Nanowires always exhibit a special and unpredictable behavior under applied tensile loading as they are affected by factors such as temperature, crystallographic orientations, strain rate, multiple grain structures, surface and boundary conditions.

*Corresponding author: caksu@firat.edu.tr. ORCID Number of author: ¹ 0000-0002-8896-8571, ² 0000-0002-5151-4576

Nb element is used in both experimental and theoretical studies due to its ductility at room temperature, melting at high temperatures, low density and low neutron capture cross section [24, 25]. In addition, Nb and Nb alloys are preferred in the aerospace industry, in the production of reactor pipes, and in implants [26, 27]. Although there are many studies on bulk, clustered and thin film structures of Nb element [28-30], the number of studies on nanowire structure is few.

With the rapid development of computer technology and computational methods, atomic simulation techniques have become a popular and effective tool widely used to identify new properties of nanomaterials [31] and to detect atomic details of the deformation mechanism [32, 33]. Especially in recent years, the MD simulation method has been used effectively to examine the deformation characteristics of polycrystalline metals [34, 35]. When Wolf et al. [36] examined the deformation behavior of nanocrystalline materials, they revealed that dislocations predominate in the deformation of larger grain size materials, while grain boundaries are effective in smaller grain size materials. A study on the plastic deformation of nanocrystalline Mo showed that a large component of the strain is settling through the formation of cracks at the grain boundaries [37]. However, studies on mechanical properties have mainly focused on single-crystal metallic nanowires with fcc structure. Compared to single crystal nanowires, polycrystalline nanowires are composed of multiple grains. The deformation behavior and breakage of nanowires are highly dependent on grain size [38]. The compatibility of the results obtained in the MD simulation method with the experimental data depends on the potential energy function selected for the system to be modeled [39]. There are many potential energy functions developed for different element and alloy systems [40, 41]. EAM, which includes multi-body interactions, is one of the most preferred functions in MD studies in terms of its simple mathematical structure and effective results.

In this study, it was tried to determine the effects of uniaxial tension deformation applied to polycrystalline Nb nanowires with single and different grain numbers on the mechanical properties of the nanowire. LAMMPS (Large-scale Atomic/Molecular Massively Parallel Simulator) MD simulation program was used for calculations [42]. It was determined that the tension strain applied to the Nb nanowire caused significant changes on the mechanical and structural properties of the wire, such as the stress-strain curve, the young modulus, the yield strain, and the atomic positions, depending on the number of grains.

2. Material and Method

In the classical MD simulation method, the equations of motion of a system composed of N atoms are derived from the Lagrangian function.

$$L_{PR}(\mathbf{r}^N, \dot{\mathbf{r}}^N, \mathbf{h}, \dot{\mathbf{h}}) = \frac{1}{2} \sum_{i=1}^N m_i (\dot{\mathbf{s}}_i^t \mathbf{G} \dot{\mathbf{s}}_i) - \sum_{i=1}^N \sum_{j>i}^N \phi(|\mathbf{h} \mathbf{s}_{ij}|) + \frac{1}{2} M \text{Tr}(\dot{\mathbf{h}}^t \dot{\mathbf{h}}) - P_{ext} V \quad (1)$$

obtained. Here, the \mathbf{s}_i , \mathbf{h} , \mathbf{G} and P_{ext} parameters represent the scaled coordinate, the axes of the calculation cell, the metric tensor and the external pressure, respectively. For a system subjected to deformation, the strain is calculated by the microscopic stress tensor as given in equation (2) [43, 44].

$$\boldsymbol{\pi} = V^{-1} \left[\sum_{i=1}^N m_i \vartheta_i \vartheta_i - \sum_{i=1}^N \sum_{j>i}^N \frac{F_{ij}}{r_{ij}} \mathbf{r}_i \cdot \mathbf{r}_j \right] \quad (2)$$

An object under the influence of external forces is said to be in a strained state. The stress tensor is determined by the nine components of the state of the force at any point in the matter.

$$\sigma_{ij} = \begin{pmatrix} \sigma_{11} & \sigma_{12} & \sigma_{13} \\ \sigma_{21} & \sigma_{22} & \sigma_{23} \\ \sigma_{31} & \sigma_{32} & \sigma_{33} \end{pmatrix} \quad (3)$$

The normal components of the stress tensor σ_{11} , σ_{22} , σ_{33} (also referred to as σ_x , σ_y , σ_z , respectively) are known as the shear components of the stress. The positive and negative values of the normal components of the stress tensor correspond to the tensile stress and compression stress, respectively. Only the σ_x component changes with uniaxial loading applied along the x-axis. On the other hand, the other components are zero [45]. The expression $\varepsilon_x = (l_x - l_{x0}) / l_{x0}$ determines the strain along the x-axis. l_{x0} and l_x are the length of the wire before and under load in the x direction, respectively [46].

The Nb model nanowire system, to be applied uniaxial tensile deformation, was created in 5 different ways: single crystal and multi-grain structure. During the study, the single crystal structure was expressed as Nb1, while the 2, 3, 4 and 5 grain nanowire structures were named Nb2, Nb3, Nb4 and Nb5, respectively. Nb1, Nb2, Nb3, Nb4 and Nb5 nanowires consist of 4672, 4492, 4433, 4417 and 4463 atoms, respectively. Each grain in the model nanowire is defined as gr (grain). In the Nb1 nanowire with a single crystal structure, atoms are arranged in the x, y and z directions with $\langle 100 \rangle$, $\langle 010 \rangle$ and $\langle 001 \rangle$ crystallographic orientations, while for Nb2 $\langle 6\bar{1}0 \rangle$, $\langle 16\bar{4} \rangle$, $\langle 169 \rangle$ for Nb3, they are placed in orientations $\langle 410 \rangle$, $\langle \bar{1}40 \rangle$, $\langle 001 \rangle$ and $\langle 1\bar{1}1 \rangle$, $\langle 1\bar{1}\bar{2} \rangle$, $\langle 110 \rangle$ for Nb4, and $\langle 1\bar{1}0 \rangle$, $\langle 11\bar{2} \rangle$ and $\langle 111 \rangle$ for Nb5. While the length of the nanowire in the x direction is 12 nm, its length in the y and z directions varies between 2.59 nm and 2.71 nm due to the different orientations of the atoms.

In MD studies, it is very important to detect microstructures such as fcc, hcp, bcc, which are formed as a result of thermal or mechanical processes applied to the model system, and to determine their development. Many numerical analysing methods have been developed to determine these structures. Assigning a structural type to each particle is the main goal of these methods. In addition, these methods try to determine how close they are by matching a local structure with an idealized structure. For structure analysis in MD simulation studies, centrosymmetry parameter analysis, common neighbor analysis, bond-order analysis, bond-angle analysis, Honeycutt -Andersen, Voronoi analysis is used quite frequently [47, 48].

In this study, atoms were placed at bcc lattice points for the Nb nanowire system as the initial structure. While periodic boundary conditions were applied along the [100] direction of the nanowire, boundary conditions were not applied along the [010] and [001] directions. The initial velocities of the atoms in the model system were randomly determined in accordance with the Maxwell-Boltzman velocity distribution. By using the velocity form of the Verlet algorithm, the numerical integration of the system's equations of motion was performed in 1 fs time steps. Uniaxial drawing processes were applied to the NVT statistical ensemble, where the particle count, volume, and temperature were kept constant at certain values. Before applying tensile loading, 5×10^4 MD steps were waited for all nanowires to reach stable structure. The strain rate was chosen as $1 \times 10^9 \text{ s}^{-1}$ in the study. In addition, the EAM potential function was used to calculate the interactions between Nb atoms in the model calculation cell. Details on potential can be found in the literature [49]. The cut-off distance of the potential function used was determined as $r_c = 2a_{\text{Nb}}$.

3. Results and Discussion

In this study, the effect of uniaxial tensile deformation applied along the [100] direction at 10 K temperature and $1 \times 10^9 \text{ s}^{-1}$ strain rate on the mechanical properties of Nb nanowire system with different grain structures was tried to be investigated using the MD method. Figure 1 shows the stress-strain curve obtained until rupture occurs in a single-grained Nb1 nanowire, which is called gr1 and has the arrangement of atoms along the crystallographic orientations of $\langle 100 \rangle$, $\langle 010 \rangle$, $\langle 001 \rangle$. This graph shows two peaks and a region where the hard value changes within certain limits with the increase in the stress in the middle. The hard-strain curve exhibits an almost linear change until ϵ (tensile stress), which begins to be applied to the model system, reaches a value of 0.09. This region in the graph is referred to as the elastic region. The highest value reached by the stress before the sudden drop in stress starts is known as the yield strain and has a value of 9.8 GPa. In addition, in Figure 1, the young modulus of the model nanowire system was determined as a result of the regression analysis of the linear region where elastic deformation occurs. High values of the young modulus, which is known as a measure of elastic deformation under the applied force, indicate that the elastic property of that material decreases. The young modulus for the Nb1 nanowire was determined as 104.3 GPa. After a critical strain value is reached, a sudden decrease in strain occurs (point b). This sudden decrease in the graph is an indication of the onset of plastic deformation in the model system. When a stress above the strain corresponding to the yield strain value is applied to the material, plastic deformation begins and the sliding mechanism is activated. This is a wide strain range from point b to point e and there is no significant change in difficulty. At point e, the hard-strain curve starts to change as it did at the beginning of the strain process (e-f interval). As the strain continues, when the strain reaches 0.72 after the second maximum, the strain suddenly drops to zero (g point). This corresponds to the breaking of the nanowire. The deformation phases seen in the stress-strain graph have also been observed in studies for other metallic nanowires [50, 51].

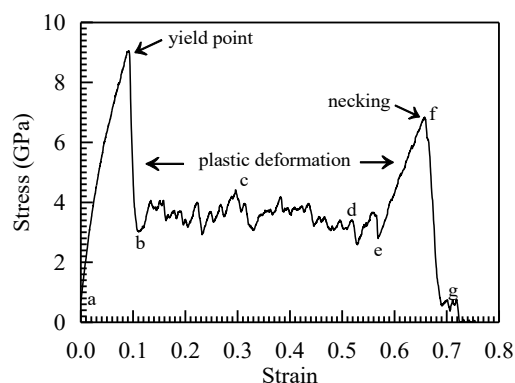


Figure 1. Stress-strain curve of Nb1 nanowire.

In this study, the CNA topological analysis method proposed by Honeycutt and Andersen was used to determine the regional structures with unit cells such as bcc, fcc, hcp that may occur around the atoms in the model system during the drawing process. CNA analysis is a characterization technique used to determine the structural evolution of crystal structures such as agglomeration defects, grain boundaries, deformation and different phases. The CNA algorithm performs a geometric analysis of the nearest neighbors around a reference atom. The minimum value of the radial distribution function between the first two peaks and the arrangement of the selected atoms within a certain distance are analyzed one by one [52]. In this analysis, each atom in the model system is classified according to regional crystal structures determined by the bonds between an atom and its nearest neighbors. Here, atoms are divided into 4 classes called bcc, fcc, hcp and “other”. Atoms in a regional bcc arrangement are considered bcc atoms, and atoms in a regional fcc arrangement are considered fcc atoms. Atoms in a regional hcp arrangement are considered as hcp atoms, which are seen as stacking defect structures formed in the fcc crystal. Atoms in all other local arrangements are called “other” atoms. Generally, blue bcc, green fcc, red hcp and white color represent atoms called “other” [53].

In Figure 2 (a-g), atomic positions taken from the (001) plane section obtained by CNA analysis from the OVITO [54] program at different MD steps for the Nb1 nanowire during the drawing process are given. In Figure 2(a), it was determined that 68% of the structure was bcc and 32% was other structures before applying tensile stress to the nanowire. Since periodic boundary conditions are not applied in the y and z directions of the nanowire, atoms on and near the surface of the wire are not considered as bcc unit cell structure. It is seen in Figure 2(b) that after the strain applied to the nanowire passes the yield point, where plastic deformation begins, regions of atomic rearrangement are formed at the top and bottom ends of the nanowire. These regions, where atoms with different orientations are located, are separated from each other by white colored atoms. Figure 2(c-d) shows the evolution of these differentially oriented regions within the structure with increasing strain. It is seen in Figure 2(e-f) that when the e and f points are reached in the stress-strain curve, the reorientations are completed and the nanowire begins to give neck in the region determined by the dotted circle. In Figure 2(g), the atomic structure of the nanowire when it is broken by thinning and stretching is given.

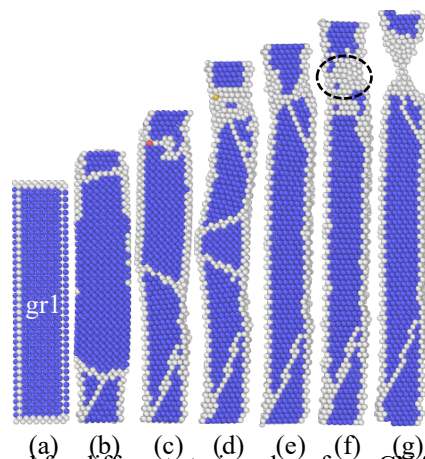


Figure 2. Atomic positions determined for different strain values from CNA analysis for Nb1 nanowire.

In Figure 3, the stress-strain curve obtained until rupture occurs in the Nb2 nanowire, which consists of two grained structures called gr1 and gr2, is given. It is seen that the yield strength is 6.02 GPa and the hard-strain curve exhibits an almost linear change until $\epsilon=0.08$ is reached. The elastic constant for Nb2 nanowire was determined as 99.07 GPa. The change in the stress-strain curve with increasing strain is almost similar to the Nb1 nanowire structure. It was determined that the rupture occurred at a value of 0.58 of the strain.

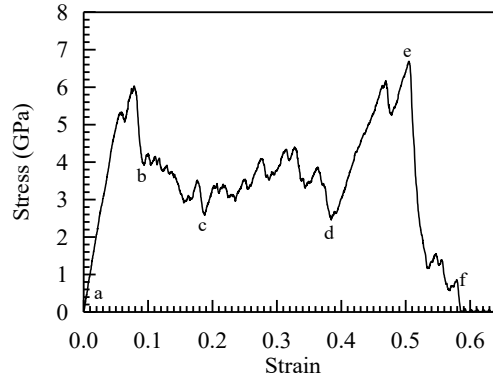


Figure 3. Stress-strain curve of Nb2 nanowire.

In Figure 4, atomic images of the nanowire obtained from CNA analysis are given for the different points (a-f) determined in the stress-strain curve. Figure 4(a) shows the initial structure composed of bcc unit cells of the Nb2 before nanowire is strain applied. Grains of gr1 and gr2, which have different atomic orientations, are separated from each other by the grain boundary indicated by white colored atoms. When the point b on the hard-strain curve, where plastic deformation occurs by increasing the strain applied on the nanowire, is reached, a region begins to form as indicated by the arrow with different crystallographic orientation by rearranging the atoms at the grain boundary, as seen in Figure 4(b), and as the strain continues to increase, this change occurs. The development of the region within the structure (Figure 4(c)) is seen. It is determined from Figure 4(d) that this reorientation and diffusion within the structure ends when the d point is reached in the strain curve. It can be seen from Figure 4(e-f) that the applied strain from this moment on creates a neck in the region marked with a dotted circle in the grain boundary region instead of creating plastic deformation in the structure, and the deformation of the nanowire ends with rupture.

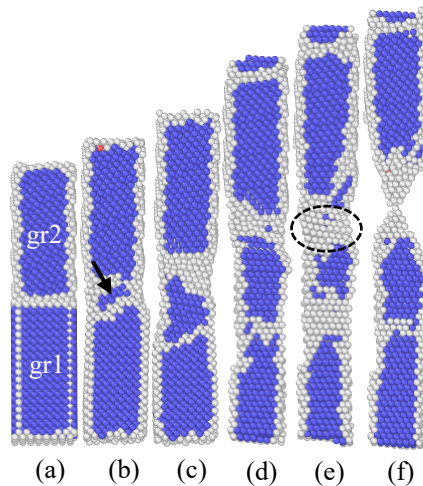


Figure 4. Atomic positions determined for different strain values from CNA analysis for Nb2 nanowire.

In Figure 5, the stress-strain curve obtained as a result of uniaxial tensile deformation applied to the Nb3 nanowire, which consists of three grained structures called gr1, gr2 and gr3, is given. The change in the stress-strain curve with increasing strain is almost similar to that of other granular nanowire structures. From the stress-

strain curve, yield strain was determined as 5.42 GPa, $\epsilon=0,068$ and elastic constant 87.2 GPa for Nb3 nanowire. It was observed that when $\epsilon=0,56$ reached the value, rupture occurred.

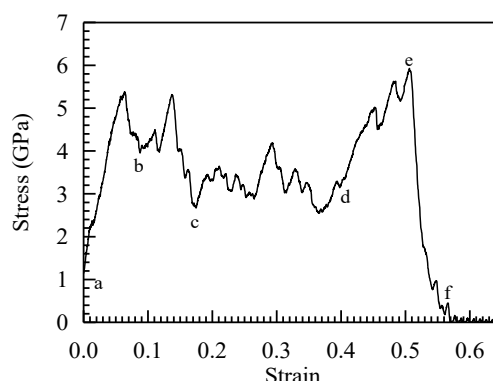


Figure 5. Stress-strain curve of Nb3 nanowire.

Figure 6 shows the atomic positions of different points on the stress-strain curve given in Figure 5 for the Nb3 nanowire. The initial structure of the Nb3 nanowire, which consists of layers with three different atomic orientations, is given in Figure 6(a). It is clearly seen in Figure 6(b-c) that when the yield point is passed and plastic deformation begins, a region in which the atoms take different orientations is formed at the grain boundary of the gr1 and gr2 grains and as a result of the increase in the strain, the atoms in this region move in the shear planes and spread into the gr1 grain structure in a way to form a twin structure. However, no change was observed in the atomic configurations of the gr2 and gr3 grains forming the nanowire, with increasing strain. With increasing strain value, the twin boundary moved until it reached the lower end of the nanowire (Figure 6(d)) and then the rearrangement of the atoms was completed. It is clearly seen from Figure 6(e-f) that the nano wire starts to give neck at the gr1 and gr2 grain boundary and that rupture occurs in this region as the strain continues to increase.

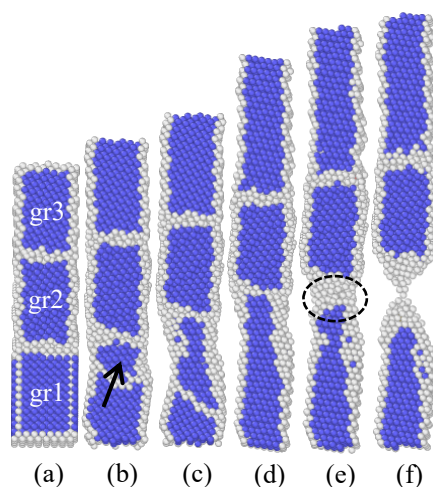


Figure 6. Atomic positions determined for different strain values from CNA analysis for Nb3 nanowire.

In Figure 7, a stress-strain curve is given for Nb4 nanowire, which contains four grained structures called gr1, gr2, gr3 and gr4. The stress-strain curve exhibits a linear change, as in other nanowire structures, until $\epsilon=0,069$, where the yield strain is 5.98 GPa. The elastic constant of the Nb4 nanowire was determined as 84.7 GPa from the regression analysis. It has been determined that the nanowire rupture occurs when it reaches the value of $\epsilon=0,45$.

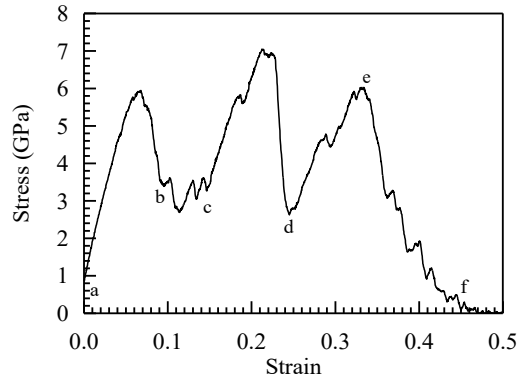


Figure 7. Stress-strain curve of Nb4 nanowire.

Figure 8 shows the atomic positions obtained at different stress values for the Nb4 nanowire. The initial structure of the Nb4 nanowire formed with 4 different crystallographic orientations of atoms is given in Figure 8(a). It is clearly seen in Figure 8(b) that a twinning occurs within the gr1 grain and the atoms take a different orientation when the yield point is passed and the plastic deformation begins. This atomic arrangement formed in the gr1 grain is completed when the strain value reaches the c point in the stress-strain curve (Figure 8c). However, the atomic orientations of the gr2, gr3 and gr4 grains that make up the nanowire did not show any change with the increase in strain. It is clearly seen from Figure 8(e-f) that the neck region begins to form at the gr2 and gr3 grain boundaries at progressive strain values, and then the atoms in this region become thinner and elongate like a chain and rupture occurs, respectively.

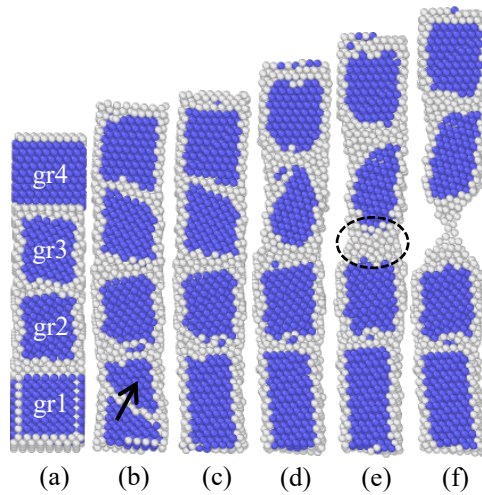


Figure 8. Atomic positions determined for different strain values from CNA analysis for Nb4 nanowire.

The stress-strain curve for five grained Nb5 nanowires called gr1, gr2, gr3, gr4 and gr5 is given in Figure 9. It is clearly seen that the stress-strain graph exhibits an almost linear change until $\epsilon=0,085$, where the yield strain is 6.2 GPa. The elastic constant of the Nb5 nanowire was found to be 82.4 GPa by using this linear region. It was determined that the nanowire rupture occurred as the strain increased and reached the value of $\epsilon=0,3$.

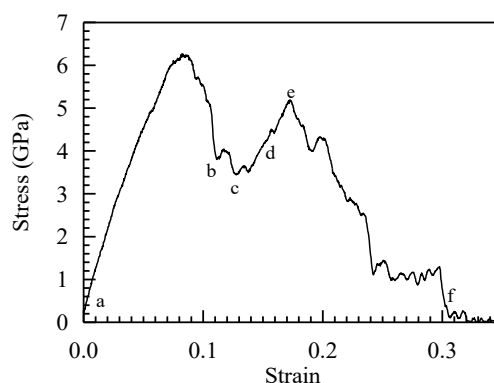


Figure 9. Stress-strain curve of Nb5 nanowire.

In Figure 10, atomic images corresponding to different values of strain are given for the Nb5 nanowire. While the initial structure of the Nb5 nanowire is given in Figure 10(a), it is clearly seen in Figure 10(b) that the atoms in the gr3 grain enter an irregular structural arrangement that does not have a specific unit cell, once the yield point is passed and the plastic deformation begins. It has been determined from Figure 10(c-d) that the irregular structure has been replaced by relatively regular bcc unit cell structures with the increase of the strain and reaching the c and d points in the stress-strain graph, respectively. However, it is seen that the atomic arrangement of the gr1, gr2, gr4 and gr5 grains that make up the nanowire do not show any change with increasing strain. It is clearly seen from Figure 10(e-f) that the neck region starts to form at the gr2 and gr3 grain boundaries and the rupture also occurs at this grain boundary with the increase of the strain.

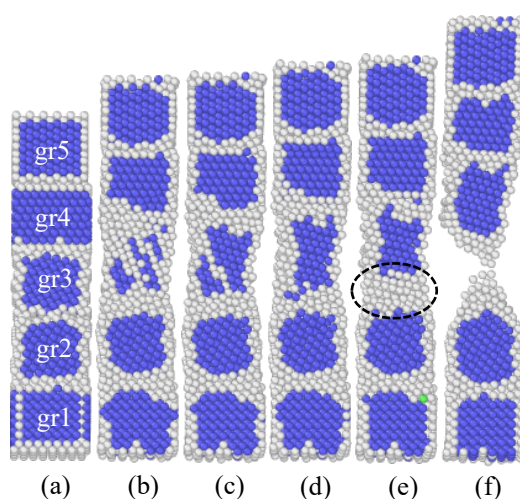


Figure 10. Atomic positions determined for different strain values from CNA analysis for Nb5 nanowire.

In the study, it is seen that single crystal and polycrystalline Nb nanowires exhibit distinctly different tensile deformation behaviors. Microstructure control plays a critical role in nanoscale wires to provide the desired mechanical properties. Grain boundaries are the most basic defects in polycrystalline materials. Material properties are greatly affected by the presence of such defects. Grain boundaries play an important role in plastic deformation since grain sizes are reduced to nanometers [55, 56]. In all model nanowires, necking started at the grain boundary and then fracture occurred with decreasing tensile ductility. High stresses in the grain boundary region clearly play a dominant role in controlling both plastic deformation and fracture processes in nanoscale materials [57]. In the study, yield strain, strain values (ϵ) and breaking strain values of Nb polycrystalline nanowires are lower than single crystal nanowires. However, yield strain and ϵ value increase for Nb4 and Nb5 nanowires.

Deformation and rupture behaviors of polycrystalline nanowires show dependence on grain size and length-diameter ratio (LDR). It shows that the polycrystalline nanowires exhibit a ductile characteristic under tensile loading and elongation before breaking. When the tensile stress reaches a certain value, the change of atomic configuration in the grains can be seen. At the elastic limit, the young modulus increases with grain size. It was found that LDR had little effect on the elastic properties, but had a significant effect on the fractures of

polycrystalline nanowires due to the surface effect. [38]. In conventional polycrystalline metals, the volumetric stresses due to interfacial tensions are negligible. However, grain boundary interfacial tensions are important for metallic nanowires with nanometer grains [38]. Because they induce bulk stresses in the order of t/d , where t is wire thickness and d is grain size. Studies have shown that as the t/d ratio increases from 1 to 4, the tensile strength of Ni, Cu and Al films [58] increases, while it decreases in Ag microwires [59]. Obviously, there is controversy regarding the size effect of nanoscale polycrystalline films/nanowires and therefore it is essential to examine this effect and deduce the underlying mechanism. It is thought that the size effect caused by the t/d ratio of 4 and above in Nb₄ and Nb₅ nanowires is the reason for the increase in yield strain and ϵ .

The stresses near the grain boundary are quite different from the stresses occurring within the grain. The highest internal stresses and high energy atoms are located at the grain boundary interface due to its heterogeneous structure. The flow mechanism is via nucleation and propagation of partial dislocations at grain boundary interfaces rather than at free surfaces. This causes the yield strain to be much lower than that of single crystal nanowires. In addition, despite the large surface-to-volume ratio, a significantly lower yield strain may also occur as a result of dislocations propagating from the free surfaces [38]. Researchers have determined from experimental and simulation studies that the cause of plastic deformation in many fcc and bcc metallic nanowires is due to partial/full dislocation shifts. However, metallic nanowires with both fcc and bcc structures with suitable orientations can also be plastically deformed by the twinning mechanism [60]. During the tensile deformation process applied to our model nanowire systems, it was determined that the plastic deformation did not occur as a result of any dislocation as a result of the dislocation defect analysis DXA (Dislocation Extraction Algorithm). However, it can be said that plastic deformation in model nanowires occurs due to nucleation, propagation and atomic rearrangements of twinning.

4. Conclusion

The effects of uniaxial tensile deformation applied to single-crystal and polycrystalline nanowires with different grain numbers, where the interactions between Nb atoms are determined by EAM, on the properties of nanowires such as yield strain, young modulus, yield strain were investigated using MD simulation method. It was determined that the number of grains significantly affects the plastic deformation of the nanowire. All nanowires used in the study are plastically deformed by twinning and their propagation. It was determined that grain boundary interfacial tensions are important for metallic nanowires with nanometer grains and necking and breaking of the nanowire occur at these grain boundaries. The size effect resulting from the increase in the number of grains shows its effect on the yield strain and strain of the nanowire. However, it can be said that the atomic orientations that make up the grains may have important structural effects on the nanowire.

References

- [1] Hansen N. Hall-Petch relation and boundary strengthening. *Scripta Materialia* 2004; 51(8): 801-806.
- [2] Jang D, Cai C, Greer JR. Influence of Homogeneous Interfaces on the Strength of 500 nm Diameter Cu Nanopillars. *Nano Letters* 2011; 11: 1743-1746.
- [3] Lu L, Chen X, Huang X, Lu K. Revealing the maximum strength in nanotwinned copper. *Science* 2009; 323: 607-610.
- [4] Afanasyev KA, Sansoz F. Strengthening in Gold Nanopillars with Nanoscale Twins. *Nano Letters* 2007; 7(7): 2056-2062.
- [5] Deng C, Sansoz F. Size-dependent yield stress in twinned gold nanowires mediated by site-specific surface dislocation emission. *Applied Physics Letters* 2009; 95: 091914.
- [6] Zhang JY, Zhang X, Liu G, Zhang GJ, Sun J. Scaling of the ductility with yield strength in nanostructured Cu/Cr multilayer films. *Scripta Materialia* 2010; 63: 101-104.
- [7] Zhu XF, Li YP, Zhang GP, Tan J, Liu Y. Understanding nanoscale damage at a crack tip of multilayered metallic composites. *Applied Physics Letters* 2008; 92: 161905.
- [8] Yan H, Choe HS, Nam S, Hu Y, Das S, Klemic JF, Ellenbogen JC, Lieber CM. Programmable nanowire circuits for nanoprocessors. *Nature* 2011; 470: 240-244.
- [9] Mourik W, Zuo K, Frolov SM, Plissard SR, Bakkers EPAM, Kouwenhoven LP. Signatures of Majorana Fermions in Hybrid Superconductor-Semiconductor Nanowire Devices. *Science* 2012; 336: 1003-1007.
- [10] Radisavljevic B, Radenovic A, Brivio J, Giacometti V, Kis A. Single-layer MoS₂ transistors. *Nature Nanotechnology* 2011; 6(3): 147-150.
- [11] Wang F, Deng R, Wang J, Wang Q, Han Y, Zhu H, Chen X, Liu X. Tuning upconversion through energy migration in core-shell nanoparticles. *Nature Materials* 2011; 10(12): 968-973.
- [12] Liu R, Duay J, Lee SB. Heterogeneous nanostructured electrode materials for electrochemical energy storage. *Chemical Communications* 2011; 47(5): 1384-1404.

- [13] Cobley CM, Chen J, Cho EC, Wang LV, Xia Y. Gold nanostructures: a class of multifunctional materials for biomedical applications. *Chemical Society Reviews* 2011; 40(1): 44-56.
- [14] Lim LC. Surface intergranular cracking in large strain fatigue. *Acta Metallurgica* 1987; 35(7): 1653-1662.
- [15] Field DP, Adams BL. Interface cavitation damage in polycrystalline copper. *Acta Metallurgica et Materialia* 1992; 40(6): 1145-1157.
- [16] Aifantis KE, Soer WA, De Hosson JTM, Willis JR. Interfaces within strain gradient plasticity: Theory and experiments. *Acta Materialia* 2006; 54: 5077-5085.
- [17] Swygenhoven HV, Farkas D, Caro A. Grain-boundary structures in polycrystalline metals at the nanoscale. *Physical Review B* 2000; 62: 831-838.
- [18] Capolungo L, Spearot DE, Cherkaoui M, McDowell DL, Qu J, Jacob KI. Dislocation Nucleation from Bicrystal Interfaces and Grain Boundary Ledges: Relationship to Nanocrystalline Deformation. *Journal of the Mechanics and Physics of Solids* 2007; 55(11): 2300-2327.
- [19] Li XF, Hu WY, Xiao SF, Huang WQ. Molecular dynamics simulation of polycrystalline molybdenum nanowires under uniaxial tensile strain: Size effects. *Physica E: Low-Dimensional Systems Nanostructures* 2008; 40(10): 3030-3036.
- [20] Cagin T, Jaramillo-Botero A, Gao G, Goddard WA. Molecular mechanics and molecular dynamics analysis of Drexler-Merkle gears and neon pump. *Nanotechnology* 1998; 9: 143-152.
- [21] Craighead HG. Nanoelectromechanical systems. *Science* 2000; 290: 1532-1535.
- [22] Marszalek PE, Greenleaf WJ, Li HB, Oberhauser AF, Fernandez JM. Atomic force microscopy captures quantized plastic deformation in gold nanowires. *PNAS* 2000; 97: 6282-6286.
- [23] Legoas SB, Galvao DS, Rodrigues V, Ugarte D. Origin of Anomalously Long Interatomic Distances in Suspended Gold Chains. *Physical Review Letters* 2002; 88: 076105.
- [24] Singh D, Sharma P, Parashar A. Atomistic simulations to study point defect dynamics in bi-crystalline niobium. *Materials Chemistry and Physics* 2020; 255: 123628.
- [25] Yang C, Qi L. Modified embedded-atom method potential of niobium for studies on mechanical properties. *Computational Materials Science* 2019; 161: 351-363.
- [26] Divya S, Avinash P. Effect of symmetric and asymmetric tilt grain boundaries on the tensile behaviour of bcc-Niobium. *Computational Materials Science* 2018; 143: 126-132.
- [27] Grill R, Gnadenberger A. Niobium as mint metal: Production-properties-processing. *Int. J. Refract. Met. Hard Mater* 2006; 24(4): 275-282.
- [28] Singh D, Sharma P, Jindal S, Kumar P, Kumar P, Parashar A. Atomistic simulations to study crack tip behaviour in single crystal of bcc niobium and hcp zirconium. *Current Applied Physics* 2019; 19: 37-43.
- [29] Abdeslam S, Chihi T. Molecular dynamics study of size and cooling rate effects on physical properties of Niobium nanoclusters. *Chinese Journal of Physics* 2018; 56: 2710-2717.
- [30] Yang XY, Wu D. The melting behaviors of the Nb(1 1 0) nanofilm: a molecular dynamics study. *Applied Surface Science* 2010; 256: 3197-3203.
- [31] Zhao JW, Murakoshi K, Yin X, Kiguchi M, Guo Y, Wang N, Liang S, Liu H. Dynamic characterization of the postbreaking behavior of a nanowire. *J. Phys. Chem. C* 2008; 112: 20088-20094.
- [32] Liu YH, Wang FY, Zhao JW, Jiang LY, Kiguchi M, Murakoshi K. Theoretical investigation on the influence of temperature and crystallographic orientation on the breaking behavior of copper nanowire. *Physical Chemistry Chemical Physics* 2009; 11: 6514-6519.
- [33] Liu YH, Zhao JW, Wang F. Influence of length on shock-induced breaking behavior of copper nanowires. *Physical Review B* 2009; 80: 115417.
- [34] Spearot DE, Tschopp MA, Jacob KI, McDowell DL. Tensile strength of <100> and <110> tilt bicrystal copper interfaces. *Acta Materialia* 2007; 55(2): 705-714.
- [35] Spearot DE, Capolungo L, Qu J, Cherkaoui M. On the elastic tensile deformation of <100> bicrystal interfaces in copper. *Computational Materials Science* 2008; 42(1): 57-67.
- [36] Wolf D, Yamakov V, Phillpot SR, Mukherjee A, Gleiter H. Molecular-Dynamics Simulation: Relationship to Experiments? *Acta Materialia* 2005; 53: 1-40.
- [37] Frederiksen SL, Jacobsen KW, Schiotz J. Simulations of intergranular fracture in nanocrystalline molybdenum. *Acta Materialia* 2004; 52: 5019-5029.
- [38] Li X, Hu W, Xiao S, Huang WQ. Molecular dynamics simulation of polycrystalline molybdenum nanowires under uniaxial tensile strain: Size effects. *Physica E* 2008; 40: 3030-3036.
- [39] Voter AF, Chen SP. Accurate Interatomic Potentials for Ni, Al, and Ni₃Al. *Mat. Res. Soc. Symp. Proc.* 1987 82: 175.
- [40] Cai J, Ye YY. Simple analytical embedded-atom-potential model including a long-range force for fcc metals and their alloys. *Physical Review B* 1996; 54: 8398.
- [41] Malins A, Williams SR, Eggers J, Royall CP. Identification of structure in condensed matter with the topological cluster classification. *The Journal of Chemical Physics* 2013; 139: 234506.
- [42] <http://lammps.sandia.gov/> LAMMPS Molecular Dynamics Simulator (Erişim Tarihi:02.04.2021).
- [43] Kazanc S. The effects on the lattice dynamical properties of the temperature and pressure in random NiPd alloy. *Canadian Journal of Physics* 2013; 91: 833-838.
- [44] Kazanc S, Ozgen S, Adiguzel O. Pressure effects on martensitic transformation under quenching process in a molecular dynamics model of NiAl alloy. *Physica B* 2003; 334: 375-381.

- [45] Jacobus K, Sehitoglu H, Balzer M. Effect of stress state on the stress-induced martensitic transformation in polycrystalline Ni-Ti alloy. *Metallurgical and Materials Transactions A* 1996; 27(A): 3066-3073.
- [46] Saitoh KI, Liu WK. Molecular dynamics study of surface effect on martensitic cubic-to-tetragonal transformation in Ni-Al alloy. *Computational Materials Science* 2009; 46: 531-544.
- [47] Malins A, Williams, SR, Eggers J, Royall CP. Identification of structure in condensed matter with the topological cluster classification. *The Journal of Chemical Physics* 2013; 139: 234506.
- [48] Stukowski A. Structure identification methods for atomistic simulations of crystalline materials. *Modelling and Simulation in Materials Science and Engineering* 2012; 20: 045021.
- [49] Feller MR, Park H, Wilkins JW. Force-matched embedded-atom method potential for niobium. *Physical Review B* 2010; 81: 144119.
- [50] Landman U, Luedtke WD, Salisbury BE, Whetten RL. Reversible Manipulations of Room Temperature Mechanical and Quantum Transport Properties in Nanowire Junctions. *Physical Review Letters* 1996; 77: 1362.
- [51] Li S, Ding X, Deng J. Superelasticity in bcc nanowires by a reversible twinning mechanism. *Physical Review B* 2010; 82: 205435.
- [52] Bañuelos EU, Aburto CC, Arce AM. A common neighbor analysis of crystallization kinetics and excess entropy of charged spherical colloids. *The Journal of Chemical Physics* 2016; 144: 094504.
- [53] Fanga R, Wanga W, Guoa L, Zhanga K, Zhanga X, Lib H. Atomic insight into the solidification of Cu melt confined in graphene Nanoslits. *Journal of Crystal Growth* 2020; 532: 125382.
- [54] Stukowski A. Visualization and analysis of atomistic simulation data with OVITO-the Open Visualization Tool. *Modelling and Simulation in Materials Science and Engineering* 2010; 18(1): 015012.
- [55] Yuan L, Jing P, Shan D, Guo B. The effect of inclination angle on the plastic deformation behavior of bicrystalline silver nanowires with $\Sigma 3$ asymmetric tilt grain boundaries. *Applied Surface Science* 2017; 392: 1153–1164.
- [56] Li J, Guo JW, Luo H, Fang QH, Wu H, Zhang LC, Liu YW. Study of nanoindentation mechanical response of nanocrystalline structures using molecular dynamics simulations. *Applied Surface Science* 2016; 364: 190-200.
- [57] Cao A, Wei YG, Ma E. Grain boundary effects on plastic deformation and fracture mechanisms in Cu nanowires: Molecular dynamics simulations. *Physical Review B* 2008; 77: 195429.
- [58] Seppala ET, Belak J, Rudd RE. Onset of Void Coalescence during Dynamic Fracture of Ductile Metals. *Physical Review Letters* 2004; 93: 245503.
- [59] Latapie A, Farkas D. Molecular dynamics simulations of stress-induced phase transformations and grain nucleation at crack tips in Fe. *Modelling Simulation in Materials Science and Engineering* 2003; 11(5): 745-753.
- [60] Paul SK. Effect of twist boundary angle on deformation behavior of $\langle 100 \rangle$ FCC copper nanowires. *Computational Materials Science* 2018; 150: 24-32.

ARTIFICIAL INTELLIGENCE BASED SMART INTERCHANGE SYSTEM IN SMART URBANIZATION

Emrullah EZBERCİ ^{1*}, Derya AVCI ²

¹ Institute of Science and Technology, Firat University, Elazığ, Turkey

² Department of Computer Technologies, Vocational School of Technical Sciences, Firat University, Elazığ, Turkey

*¹emrullah_76@hotmail.com, ²davci@firat.edu.tr

(Geliş/Received: 14/04/2022;

Kabul/Accepted: 11/07/2022)

Abstract: The duration of the smart intersection system lights is determined automatically according to the nearest busy. The vehicle at the intersection with the camera is calculated by the image processing process. Optimizing the signaling time in traffic signaling. It will be passed to be passed by a system that can be reached later. Also the system can be entered with this remote central management. Manually switch to roads. In this study, it is a smart intersection system used with special permission from Malatya Metropolitan Municipality transportation units. These studies and the benefits they have provided are highlighted. In addition, DARKNET's real-time object detection YOLOV3 deep learning model is used within the scope of in-vehicle real-time traffic system from data images on websites for traffic. The vehicles are placed in the targeted and future-determined database. Positive signaling with information from the designed Process-Based Intersection Management System. Agricultural bounty takes advantage of little stealing gases to be grown to take advantage of time and small items. A clean environment will be created.

Key words: Smart City, Smart Transportation, Smart Junction, Image Processing, Deep Learning, Darknet, Yolov3

Akıllı Şehircilikte Yapay Zeka Tabanlı Akıllı Kavşak Sistemi

Öz: Akıllı kavşak sistemlerinde trafik ışıklarının süreleri araç yoğunluğa göre otomatik olarak belirlenir. Kamera sistemi ile kavşaktaki araç sayıları görüntü işleme yöntemleriyle hesaplanmaktadır. Böylelikle araç sayısına göre sinyalizasyondaki bekleme süresi optimize edilmektedir. Daha sonra araç yoğunluğu fazla olan tarafa sistem tarafından geçiş üstünlüğü verilerek trafik yoğunluğunun önüne geçilmektedir. Ayrıca bu sistemde uzaktan merkezi yönetim ile müdahale edilebilmektedir. Yollara geçiş üstünlükleri manuel olarak verilebilir. Bu çalışmada, Malatya Büyük Şehir Belediyesi ulaşım biriminden alınan özel izinle kullanılan akıllı kavşak sistemi incelenmiştir. Bu sistemin çalışması ve sağlamış olduğu faydalar vurgulanmıştır. Ayrıca kavşaklardaki veri görüntülerinden araç tespiti için açık kaynaklı sinir ağı çerçevesi olan DARKNET'in gerçek zamanlı nesne algılama sistemi YOLOV3 derin öğrenme modeli kullanılmıştır. Araçların sayımı ve sınıflandırılması anlık tespit edilerek veri tabanına kaydedilmiştir. Tasarlanan Görüntü İşleme Tabanlı Kavşak Yönetim Sistemi ara yüzü ile anlık bilgilerle sinyalizasyonun dinamik olması sağlanmıştır. Böylelikle yakıt tasarrufu, zaman ve araçların egzozlarından çevreye daha az zehirli gazların yayılması sağlanmaktadır. Temiz çevre oluşumuna katkı sağlanmış olacaktır.

Anahtar kelimeler: Akıllı Şehir, Akıllı Ulaşım, Akıllı Kavşak, Görüntü İşleme, Derin Öğrenme, Darknet, Yolov3.

1. Introduction

Due to the increase in population in urbanization, there is a significant increase in the number of vehicles used in cities. This traffic density causes problems such as time, environmental pollution and unnecessary fuel consumption. In order to solve these problems, intelligent systems developed by using information technologies are needed, especially in order to prevent the densities of vehicles waiting at the lights and to provide fast transition. There are many parameters for making transportation in cities smart. The most important of these is to reduce the waiting times of vehicles at traffic lights and to prevent vehicle density in these areas. As a result, smart intersection applications have been developed. Magnetic-based, ultrasonic-based and image-based systems are used in smart junction applications [1]. In particular, image-based systems are preferred due to the versatility of functionality, ease of installation, simplicity of management and long durability. The images taken in real time with the camera in these systems are detected instantly with the image processing software, and the traffic flow is directed. The lights that control the traffic flow do not have a certain duration, but the duration of the lights is determined according to the vehicle density. The increasing population in urban areas and the number of vehicles make it difficult to control the roads. The most important reason for this problem is the lack of instant control [2].

* Corresponding author: emrullah_76@hotmail.com ORCID Number of authors: ¹ 0000-0002-8960-1456, ² 0000-0002-5204-0501

Today, they are systems created with signal detectors laid under the road to control traffic signaling. Since the installation, operation, maintenance and cost of this system is high, artificial intelligence-based camera and vehicle detection systems have been developed [3].

In recent years, a high level of success has been achieved in studies on image processing. Deep learning algorithms play an important role in this success. These algorithms are used in many fields with great accuracy, especially in the detection and classification of objects in the field of image, sound analysis, robotics, gene, autonomous systems and medicine [4].

Many areas from transportation to finding parking spaces, from traffic density to autonomous vehicle development and target detection in the defense field are carried out with vehicle detection systems [5]. The necessity of using deep learning, machine learning methods and image processing algorithms has emerged in order to provide faster and more accurate description of the performance and scalability of the systems, especially in the images coming from drones and traffic cameras [6]. Convolutional network model in deep learning methods and YOLO algorithms in image processing and object detection methods come to the fore [7,8].

Studies in the literature on smart intersection applications were examined. In one study, an autonomous traffic light control was performed. In the study based on image processing technology prepared with Python software language and an open source microscopic software, SUMO, comparisons were made over four different traffic density scenarios [9]. In the study using image processing techniques, an online software that can generate statistical data by looking at the current traffic has been developed. Vehicle detection and tracking were performed using deep learning and machine learning techniques on the videos of five selected intersections and nine highways [10]. He conducted a study using deep Q learning technique to combine on a four-way intersection to solve traffic congestion. The traffic intersection environment and traffic scenario in which this model will be applied has been created on the traffic simulation software SUMO [11]. He did a study against the problems caused by some traffic methods based on timers or human control. In the study, a real-time traffic management system using contrast enhancement and fuzzy logic controller was created for morphological operators [12]. A study based on LSTM (Long Short-Term Memory) neural network has been carried out for non-relational cases of traffic flow. By using the data obtained from connected and autonomous devices as inputs, the density of traffic during free flow, vehicle transit and congested times was estimated [13]. It has developed an adaptive, real-time and density-based traffic light control system. According to the model, with the help of cameras, the lanes on the roads are monitored and images, the number of vehicles in each lane and the queue length are determined by using image processing techniques [14]. He conducted a study using real data for the intelligent control of traffic signaling at a four-way intersection. In the study, the traffic flow was controlled with fuzzy logic, classical fixed time management [15]. As a solution proposal to traffic congestion, a smart and automatic traffic control system and a system that determines the light durations by optimizing the traffic light time becomes the traffic controller [16]. In order to minimize the waiting time and queue length in traffic, a combination of optimal general type-2 fuzzy logic controller and modified backtracking search algorithm techniques is used [17].

The smart intersection system, which is used with a special permission from the Malatya Metropolitan Municipality transportation unit, has been examined. Classical image processing technologies are used in smart intersection systems of Malatya Metropolitan Municipality. In this study, contrary to traditional image processing algorithms, with deep learning, which is an artificial intelligence technology, the vehicles in the lights are detected, the number of vehicles is found and the light durations are changed dynamically. In addition, with the designed Image Processing Based Intersection Management System interface, it is ensured that the signaling is dynamic with instant information.

2. Material Method

In this study, traffic video images taken from Malatya Metropolitan Municipality were detected and counted by using deep learning model. In addition, YOLO, which uses the convolutional neural network model, was used for object detection and recognition. Then, a model was developed for adjusting the waiting times of traffic lights by looking at the vehicle density in the traffic. In order to realize a model with deep learning, the system was created by first preparing the data set, structuring the convolutional neural network to be used in the training, and finally obtaining the model weights. With its designed interface, it is ensured that the signaling is dynamic with instant information.

2.1. Preparation of the Data Set

Within the scope of the study, traffic videos were taken from certain intersections of the city with a camera system by taking special permission from Malatya Metropolitan Municipality Transportation Department. These images were transformed into separate image frames every 10 seconds by going through certain processes. A data set consisting of 7200 images in total was obtained. Then, each image frame was examined and repetitive and inappropriate images were removed from the data set. At the end of the process, approximately 1650 images were used for training. Of these images, 80% were adjusted randomly for training and 20% for testing. Thus, it was tried to prevent the occurrence of data memorization error of the artificial neural network model. Examples of data sets used are shown in Figure 1. In Figure 2, examples of inappropriate data extracted from the data set are shown.



Figure 1. Dataset example



Figure 2. Inappropriate data

2.2. Labeling of Data

The prepared data must be labeled in order to be able to use it in education with the supervised learning method. The object belonging to the "tool" class in each image is labeled with bounding boxes, and a file with the txt extension is created in which the coordinates with the same file name as the image file are kept. Figure 3 shows the labeling of the data.

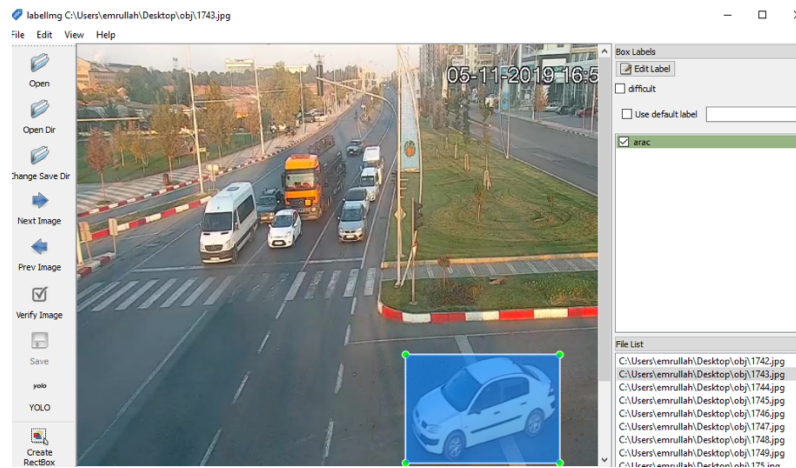


Figure 3. Labeling of the data

2.3. Training the Model

Google Colab was preferred for training. Google Colab environment was used because it provides training with CPU, Tesla K80 GPU and TPU. Since convolutional neural network is used for training, GPU environment is preferred. Before starting the training, Darknet files and pre-trained weights for YOLOV3 are loaded into the system. In the Yolov3.cfg file, the number of classes is determined as 1, the number of filters 18, and max_batches 2000 steps 1600, 1800, respectively. As seen in Figure 4, the training was completed with 1400 iterations. At the beginning of the training, the error rate decreased from 18 to 0.69. In other words, improvements were seen from the beginning to the end of the training. Appropriate weights were determined at the end of the training.

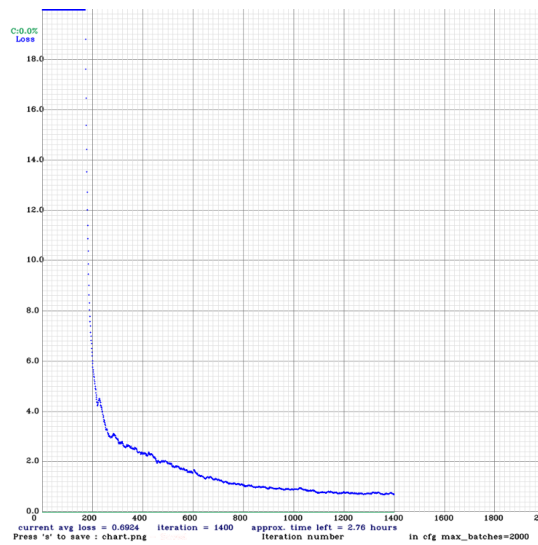


Figure 4. The training iteration graph of the model

After the training was completed, the weights and data were tested and the prediction event was realized in 91.383000 milliseconds. Figure 5 shows the testing process of the model.

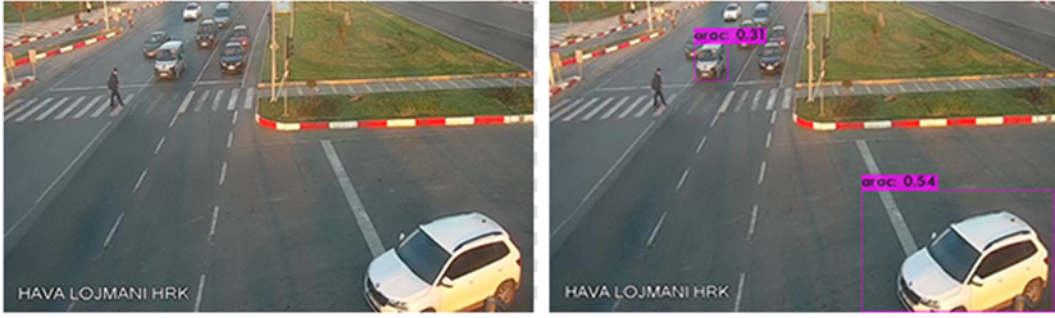


Figure 5. Testing the model

2.4. Image Processing Based Intersection Management System

In intersection applications where there is a traffic light, traffic signaling systems are formed with fixed light durations. The red and green light durations are determined beforehand, and traffic flows at fixed times. However, this system, which is applied due to the increasing vehicle density, eliminates problems such as time loss, environmental pollution and economic loss caused by unnecessary waiting times. With the developed system, the vehicles waiting at the red light at the intersections are counted and the green light durations are determined dynamically. Image Processing Based Intersection Management System interface was implemented using CSharp programming language. Yolov3 algorithm was preferred as a deep learning algorithm. Aluros of yolov3, a real-time object detection algorithm in Image Processing Based Intersection Management System. The Yolo csharp library is used. Image Processing Based Intersection Management System is shown in Figure 6.

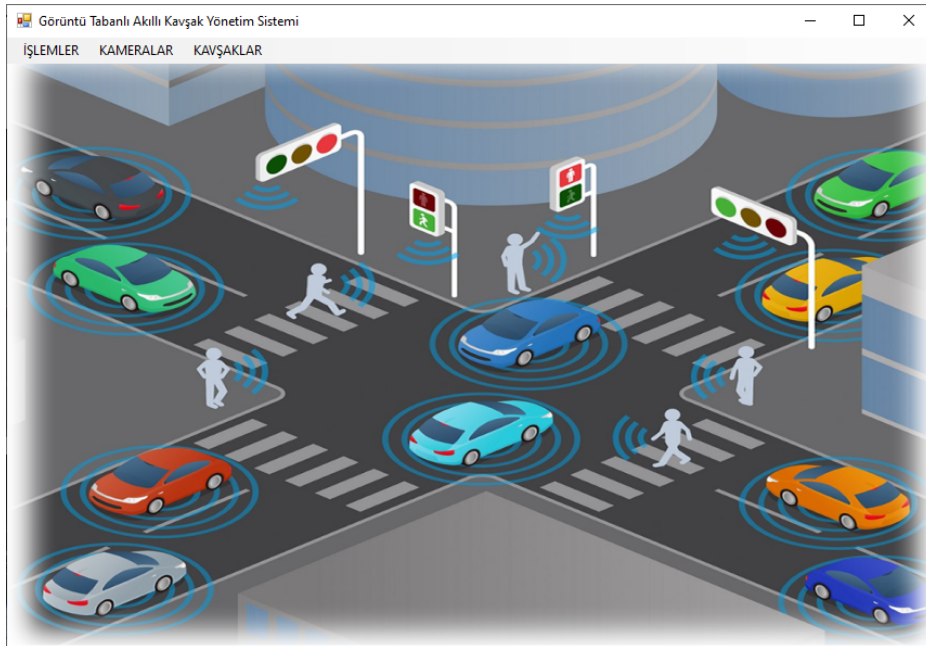


Figure 6. The training iteration graph of the model

In this study, intersection images of the smart intersection application used by Malatya Metropolitan Municipality are used as test data. As seen in Figure 7, the video images taken from the vehicle counting cameras at the intersections were converted to the appropriate resolution and transferred to the system we created. With the prepared application, it has been observed that the intersection light durations work dynamically according to the number of vehicles from the images given to the system at a four-light intersection. When the system first started,

the first lamp at the intersection started with a green light and the light duration was determined as $t_1=15$ seconds. The lights of the other second, third and fourth lamps were assigned as red and their light durations were assigned as $t_2=200$, $t_3=200$ and $t_4=200$. The aim here is to determine the green light duration of the second lamp, which comes after it, before the green light period of the first lamp ends. Taking an image from the intersection over the designed system is shown in Figure 7.

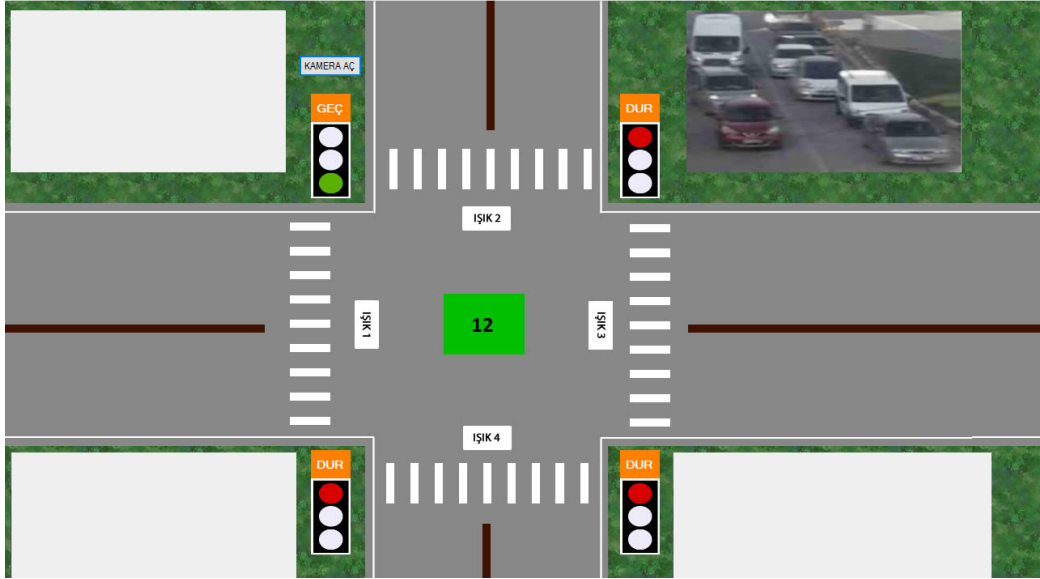


Figure 7. Getting an image of the intersection

Since the light durations in dynamic intersection systems differ according to each situation, the waiting or crossing times are not shown on the traffic boards. Here, when the green light duration of the first light reaches the seventh second determined by us, the images of the vehicles waiting at the red light of the second light are sent to the system. The system performs the counting of waiting vehicles with object recognition detection using a deep learning algorithm.

3. Results and discussion

In this study, a simulation of the dynamical realization of traffic light signaling was carried out with the image processing technique used in smart intersection systems. In this system, deep learning method was used to determine the number of vehicles waiting at the light. Learning weights were created with a loss value of 0.6924 in the training made on the yolov3 algorithm for the data created in the method implemented. By using these weights on the system, it is ensured that the light durations at the intersection are adjusted dynamically, not statically.

In Table 1, features such as location information, width and height of detected objects are shown. It is possible to access this information from within the system. In Table 2, green light durations are given according to the number of vehicles at the lights. After the number of vehicles in the image is determined, this value is sent to the green light duration method.

Table 1. Properties of detected objects

Type	Confidence Value	Horizontal Position	Vertical Position	Width	Height
car	0,563400387763	198	110	96	109
car	0,351490288972	179	92	151	182

car	0,346583276987	137	72	63	97
car	0,287773132324	23	121	93	128
car	0,477845072746	189	101	86	91

Table 2. Green light times according to the number of vehicles

Number of Vehicles	Green Light Duration
Number of Vehicles ≥ 0 or Number of Vehicles < 15	15 second
Number of Vehicles ≥ 15 or Number of Vehicles < 25	25 second
Number of Vehicles ≥ 25	40 second

Especially today, the success rate of deep learning algorithms in object recognition is very good. With the model we prepared, it was seen from the pictures given to the system at an intersection consisting of four lights, that the system showed a great deal of accuracy in the detection and number of vehicles. Here, a particularly good camera system should be chosen. In vehicle counting, green light times are determined instantly according to the number of vehicles, thus ensuring a fast traffic flow. Thanks to the speed of the Yolov3 algorithm in instant object detection, the system works without hesitation.

Imaging-based smart intersection application system work machines are used [18]. In classical processes, attributes are determined and displayed by processes such as graying, masking, and backgrounding. In the deep method used, it is realized by the convolutional nerve. It is to achieve great success in time and feature extraction. In the videonet selection planned in 2012 [19], deep learning in AlexNet [20] achieved great success with an error rate of %15 and it is realized with a high planned between % 95 - 100 within millimeters of the real-time planned image during the working time.

Intelligent intersection systems are both easy to install and easy to maintain with image processing systems. When you see which road is busy at the intersection, the green light duration can be increased by intervening only the light duration of that road. Thanks to this system, it helps to realize not only light durations but also many other functions. They are systems that can be used especially in urban security applications. For example, these systems are used in operations such as finding a stolen vehicle or tracking and finding a wanted plate.

Resources

- [1] Yaldiz, F. (2010). Development of image-based vehicle detection system in traffic automation and implementation with FPGA.
- [2] Jadhav, P., Kelkar, P., Patil, K., & Thorat, S. (2016). Smart traffic control system using image processing. *International Research Journal of Engineering and Technology (IRJET)*, 3(3), 2395-0056.
- [3] Pazar, Ş., Bulut, M., & Uysal, C. (2020). Development of Artificial Intelligence Based Vehicle Detection System. *Journal of Scientific, Technology and Engineering Research*, 1(1), 31-37.
- [4] Tan, Z. (2019). Vehicle classification with the help of deep learning (Master's thesis, Firat University, Institute of Science and Technology).
- [5] Alyuruk, M. (2020). Chapter 18 Intelligent Transportation Systems and the Future of Transportation. *Transforming Professions and Industries in the Digital Future*.
- [6] Azimjonov, J. (2021). Development of real-time vision-based traffic flow information computing systems for intersections and highways.
- [7] Bulbul, H. (2020). Real Time Vehicle Detection Using Deep Learning Methods.
- [8] Dikbayir, H. S., & Bulbul, H. I. (2020). Real Time Vehicle Detection Using Deep Learning Methods. *Tubaw Science Journal*, 13(3), 1-14.
- [9] Oguzhan, A. (2021) Autonomous traffic lights control and optimization, Istanbul University.
- [10] Azimjonov, J. (2021). Development of real-time vision-based traffic flow information computing systems for intersections and highways.

- [11] Tunc, I., Elmas, O., Edem, A., Koroglu, A., Akmesse, S., & Soylemez, M. (2021) Traffic Light Signalling with Deep Q Learning Technique.
- [12] Krishna, B. H., Patra, P. S. K., & Kalpana, G. (2021, July). Real Time Traffic Light Controlling System Using Morphological Operators and Fuzzy Logic. In *Journal of Physics: Conference Series* (Vol. 1964, No. 6, p. 062061). IOP Publishing.
- [13] Nam, D., Lavanya, R., Jayakrishnan, R., Yang, I., & Jeon, W. H. (2020). A deep learning approach for estimating traffic density using data obtained from connected and autonomous probes. *Sensors*, 20(17), 4824.
- [14] Chandrasekara, W. A. C. J. K., Rathnayaka, R. M. K. T., & Chathuranga, L. L. G. (2020, December). A Real-Time Density-Based Traffic Signal Control System. In *2020 5th International Conference on Information Technology Research (ICITR)* (pp. 1-6). IEEE.
- [15] Anas, A. M., Terzioglu, H., & Durdu, A. (2020). Intelligent Traffic Signalling Control Using Petri Nets. *Artificial Intelligence*, 3(1), 1-13.
- [16] Osman, T., Psyche, S. S., Ferdous, J. S., & Zaman, H. U. (2017, January). Intelligent traffic management system for cross section of roads using computer vision. In *2017 IEEE 7th Annual Computing and Communication Workshop and Conference (CCWC)* (pp. 1-7). IEEE.
- [17] Khooban, M. H., Vafamand, N., Liaghat, A., & Dragicevic, T. (2017). An optimal general type-2 fuzzy controller for Urban Traffic Network. *ISA transactions*, 66, 335-343.
- [18] Ferhat Y., Development of image-based vehicle detection system in traffic automation and realization with fpga, 2010.
- [19] Özkan I., Erhan U. Deep Learning and Deep Learning Models Used in Image Analysis, Gaziosmanpasa Journal of Scientific Research, 2017.
- [20] Krizhevsky, A., Sutskever, I., and Hinton, G. E. (2012). 25th International Conference on Neural Information Processing Systems. ImageNet Classification with Deep Convolutional, 1097–1105. Lake Tahoe, Nevada: NIPS'12 Proceedings.

Photo-electrical Characterization of New CuAlNi/n-Si/Al Schottky Photodiode Fabricated by Coating Thin-film Smart Material

Oktay KARADUMAN¹, Canan Aksu CANBAY^{2*}

¹ Department of Physics, Science Faculty, Firat University, Elazig, TURKEY

¹ o.karaduman@firat.edu.tr, ^{2*} caksu@firat.edu.tr

(Geliş/Received: 26/04/2022;

Kabul/Accepted: 02/08/2022)

Abstract: Micro/nano scale thin-film shape memory alloys (SMAs) have been used in many different miniaturized systems. Using them as thin-film metal components in fabrication of Schottky photodiodes has started a few years ago. In this work, a new SMA-photodiode device with CuAlNi/n-Si/Al structure was produced by coating nano-thick CuAlNi SMA film onto n-Si wafer substrate via thermal evaporation. The photoelectrical I-V, C-V and I-t photodiode signalization tests were performed under dark and varied artificial light power intensities in room conditions. It was observed that the new device exhibited photoconductive, photovoltaic and capacitive behaviors. By using conventional I-V method, the diode parameters such as electrical ideality factor (n), Schottky barrier height (ϕ_b) and rectification ratio (RR) of the produced photodiode for the condition of dark environment were computed as 12.5, 0.599 eV and 1266, respectively. As good figure of merits, the photodiode's performance parameters of responsivity (R_{ph}), photosensitivity (%PS) and specific detectivity (D^*) maxima values determined for at -5 V reverse voltage bias and under 100 mW/cm² of light power intensity condition are as 0.030 A/W (or 30 mA/W), 18693 and 1.33×10^{10} Jones, respectively. The current conduction mechanism analysis revealed that the space charge limited conduction (SCLC) mechanism is the dominant current conduction mechanism. By the drawn reverse squared C²-V plots, the values of diffusion potential (V_d), donor concentration (N_D), Fermi level (E_F) and also barrier height (ϕ_b) were determined for the SMA-photodiode. The results indicated that the new SMA-photodiode device can be useful in optoelectronic communication systems and photosensing applications.

Keywords: Schottky photodiode, thin-film shape memory alloy, space charge limited current, photosensitivity, detectivity.

İnce Film Akıllı Malzeme Kaplamasıyla Üretilen Yeni CuAlNi/n-Si/Al Schottky Fotodiyotunun Foto-elektriksel Karakterizasyonu

Öz: Mikro/nano ölçekli ince-film şekil hafızalı alaşımlar (ŞHA'lar) birçok farklı minyatürize sistemde kullanılmıştır. Bunların Schottky fotodiyotların üretimlerinde ince-film metal bileşenleri olarak kullanılmaları da henüz birkaç yıl önce başlamıştır. Bu çalışmada, termal buharlaştırma ile n-Si yonga üzerine nano-kalınlıklı CuAlNi ŞHA film kaplanarak CuAlNi/n-Si/Al yapısı şeklinde yeni bir ŞHA-fotodiyot aygıtı üretilmiştir. Fotoelektriksel I-V, I-t ve C-V fotodiyot karakterizasyon testleri oda sıcaklığında, karanlıkta ve farklı yapay ışık gücü yoğunluklarında gerçekleştirilmiştir. Yeni aygıtın fotoiletken, fotovoltajik ve kapasitif davranışlar sergilediği gözlemlenmiştir. Geleneksel I-V yöntemi kullanılarak, üretilen fotodiyotun karanlık ortam koşulu için elektriksel idealite faktörü (n), Schottky engel yüksekliği (ϕ_b) ve doğrultma oranı (RR) gibi diyet parametreleri sırasıyla 12.5, 0.599 eV ve 1266 olarak hesaplanmıştır. İyi başarımlı değerleri olarak, fotodiyotun performans parametrelerinden responsivite (R_{ph}), fotosensitivite (%PS) ve spesifik dedektivite (D^*) parametrelerinin maksimum değerleri -5 V ters beslem voltajında ve 100 mW/cm² ışık gücü yoğunluğu koşulunda belirlenmiş olup sırasıyla 0.030 A/W (veya 30 mA/W), 18693 ve 1.33×10^{10} Jones şeklindedir. Akım iletim mekanizması analizi, uzay yükü sınırlı iletim (SCLC) mekanizmasının baskın akım iletim mekanizması olduğunu ortaya koymuştur. Çizilen ters kare C²-V grafikleri ile, ŞHA-fotodiyot için donör konsantrasyonu (N_D), difüzyon potansiyeli (V_d), Fermi seviyesi (E_F) ve ayrıca bariyer yüksekliği (ϕ_b) değerleri belirlendi. Sonuçlar, yeni üretilen ŞHA-fotodiyot aygıtının optoelektronik iletişim sistemlerinde ve fotosensör uygulamalarında faydalı olabileceğine işaret etmiştir.

Anahtar kelimeler: Schottky fotodiyot, ince-film şekil hafızalı alaşım, uzay yükü sınırlı akım, fotosensitivite, dedektivite.

1. Introduction

Shape memory alloys (SMAs) are a unique smart materials group which have been extensively studied and are ever-increasingly used in many technological and industrial applications [1–11] today due to the shape memory effect (SME) and superelasticity (SE) properties [2] of these highly functional smart alloys. SME is a shape remembering or strain recovery mechanism that occurs as a macroscopic geometric shape change of a SMA when its temperature is changed after mechanically deformed. Such a macro-shape change is a sum of all micro-

* Corresponding author: caksu@firat.edu.tr. ORCID Number of authors: ¹ 0000-0002-6947-7590, ² 0000-0002-5151-4576

crystallographic changes occurring in SMA by an atomically diffusionless and isothermal solid-solid phase transformation called as martensitic transformation (MT). It occurs between two different solid phases existing at different temperatures called as martensite (product or cold) phase and austenite (parent or hot) phase. NiTi, Cu-based and Fe-based SMAs are three main group of SMAs. Among these the equiatomic NiTi SMAs are the most commercially used ones due to the superior SME and SE properties, albeit they are expensive. Therefore, the cheaper Cu-based SMAs plus with higher thermal and electrical conductivity values than NiTi ones have attracted researchers and been studied to improve them for developing alternative to NiTi SMAs [12–19].

Micro or nano sized thin film shape memory alloys (SMAs) have been already used in many different micro and nano electromechanical systems (M/NEMS) such as microactuators, microvalves, micropumps and mass, temperature or force sensors [1,6,7,10,11,20–30]. SMA thin films can be patterned with standard lithography techniques thus they can be integrated into MEMS devices [30]. Apart from usual thermomechanical MEMS actuator and sensors, coating of thin film SMAs as metal contact layers on semiconductor (silicon) wafers in Schottky diodes have been started in 1990's [25,31,32]. Since a few years ago, photodiodes were also produced by coating Cu-based SMA thin films on silicon wafers [23,28,33–36] for the first time and good photodiode performances, photocapacitance and current rectifying and other diode properties were achieved. For example, in one [23] of these works made on fabrication of a Au/CuAlMnV/n-Si/Al diode by using a nano-layer of thin film CuAlMnV shape memory alloy they reported that a 6.3 of ideality factor, a 0.54 eV of barrier height in dark condition, a photocurrent sensitive to illumination intensity and linearly increases with increasing illumination intensity and also a capacitance and a conductivity varying strongly with frequency changes. In another work [33] made on a CuAlMnNi/p-Si/Al quadrant photodiode a 2.72 of ideality factor, a 0.65 eV of barrier height for dark condition, and similar light-induced photocurrent generation and frequency dependent capacitance characteristics were reported. In else one [34] made on CuAlMn±Cr/p-Si/Al photodiodes, a minimum 2.03 value of ideality factor, the maxima 12480.33 of rectification ratio and 0.59 eV of barrier height values, and similar photosensitive and capacitive features were reported. The thin film SMAs used in these kind of works were Cu-based SMAs because their thermal and electrical conductivities are higher than NiTi SMAs withal Cu-based SMAs are proper for silicon in terms of metal work function, too, which is important in building a semiconductor/metal contact.

However, the number of these new research works made on SMA-photodiodes are very few and plainly insufficient. Also the spectrum of the types and alloy compositions of SMAs used as thin films in these works are still very diminutive. So, there are more and more explorative works that can be done upon such kind photodiodes with thin film SMA layer components. Mostly because the work function of SMAs, interface and photodiode/diode characteristics are sensitively depended on the type and composition of SMAs used as thin films in these kind of photodiodes. Works with different Cu-based SMAs, different alloy compositions or other many combinations of components and conditions have not been made yet. Being inspired by these motivations, in the study presented here, it is aimed to fabricate and characterize a nano thin film shape memory alloy layered CuAlNi/n-Si/Al photodiode with using a different type of shape memory alloy (a CuAlNi HTSMA) than the ones reported in the literature. Also, due to their inexpensive production cost and high resistance to the degradation of functional properties that occurred during the aging processes [12], the CuAlNi SMAs are one SMA group among the two most commercially used Cu-rich SMAs (the other is CuZnAl group), which is important in terms of practicality and accessibility in the related potential photodiode applications.

In this work, a new SMA-photodiode structured as Schottky type CuAlNi/n-Si/Al junction contact was produced by coating of CuAlNi SMA on an n-type silicon (n-Si) via thermal evaporation and by performing the photoelectrical I-V, I-t and C-V characterization measurements the photodiode properties of the device were revealed.

2. Experimental

In this experimental research study, the CuAlNi shape-memory-alloy with an atomical Cu-25.04Al-3.88Ni (at%) chemical composition from using the powders of the highly pure (~99.9) Cu, Al, and Ni alloying elements was previously fabricated as ribbons (with ~5 mm wideness and 15 µm thickness) by melt spinning method without applying a post-homogenization process. More details about the production process and thermo-structural DSC, DTA and XRD characterization results of this CuAlNi high temperature SMA (HTSMA) were given in the previous work [37]. In the fabrication process of the new Schottky type CuAlNi/n-Si/Al metal/semiconductor (MS) junction contact photodiode for coating CuAlNi SMA and Al metal driblets in sequence onto the back (ohmic) and polished front (Schottky) sides of an n-Si wafer a Nanovak labeled thermal evaporation system was operated. Before making coatings for building these MS contacts, the n-Si wafer and metal driblets were cleaned via the standard cleaning treatment. This standard cleaning method consists of washing by ultrasonic bathing

sequentially in media of water (distilled), acetone and then ethyl alcohol (for 5 min in each medium), etching the wafer in (1:10 ml) HF:H₂O solution for ~30 s, washing by distilled-water and desiccating it by spraying nitrogen gas. Under a chamber pressure of 2×10^{-6} Pa in evaporator, the backside of the wafer was coated by 150 nm thickness of Al metal film layer and thus the ohmic n-Si/Al contact structure was built and then this was annealed under constant nitrogen gas flow at 570 °C for 5 min long for making diffusion of n-Si and Al surfaces one another. Then by shadowing the front face of the n-Si wafer with a proper splashy mask with small circular holes, the Schottky top diode contact on the bright front face of n-Si was built by evaporating a CuAlNi SMA metal piece to form 150 nm thickness of a thin film CuAlNi SMA layer. Each one of the diode's top-contact CuAlNi spots marked off by mask holes has an area (A) of 0.785×10^{-2} cm². By using FYM-7000 and FYM-9000 model FYTRONIX lable Solar Simulator electronic characterization systems, the photo-electrical characterization of the produced device was carried out by performing current-voltage (I-V), capacitance-voltage (C-V) and current-time (I-t) measurements under dark and varied artificial day light power intensities in room conditions. The fabricated SMA-photodiode structure was schematically presented in Figure 1.

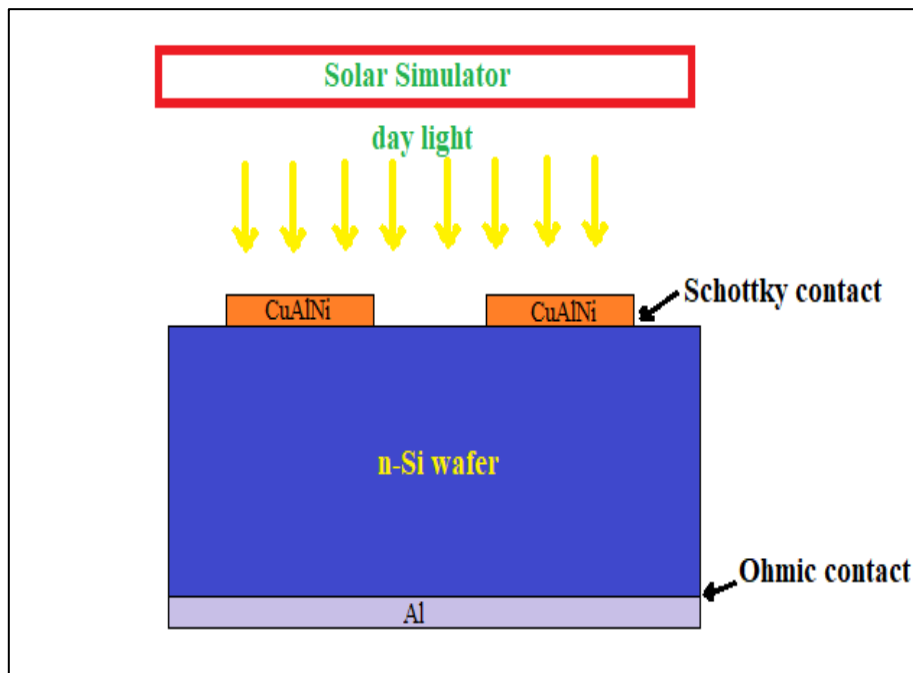


Figure 1. A schematic presentation of the fabricated CuAlNi/n-Si/Al SMA-photodiode structure.

3. Results and Discussions

The characterization measurements findings obtained for CuAlNi shape memory alloy and CuAlNi/n-Si/Al photodiode were given below as following in succession.

The DSC curve of the ribbon CuAlNi alloy obtained at a single heating-cooling rate (25 °C/min) is presented as both DSC heat-flow (mW) vs. temperature (°C) and heat flow vs. time (min.) graphics in Figure 2-a and -b, respectively. On these graphics of same DSC curve at between ~192 °C and ~293 °C, the downward endothermic peak seen on heating the alloy and the correspondent upward exothermic peak seen on cooling the alloy indicate the reverse martensite-to-austenite (M→A) and direct austenite-to-martensite (A→M) martensitic phase transformations, respectively. This reversible solid-solid phase reaction demonstrates that the CuAlNi alloy has a shape memory effect property. The alloy is a high temperature SMA due to its transformation temperatures are above 100 °C.

The thermodynamical parameters such as the start and finish temperatures (M_s , M_f , A_s and A_f) of the martensite and austenite phases, hysteresis gap ($A_s - M_f$), maximum M→A transformation peak temperature (A_{max}), equilibrium temperature (T_0), and the enthalpy change (ΔH) and entropy change (ΔS) values related to the M→A transformation of the CuAlNi alloy were listed in Table 1. Among these values, the T_0 and $\Delta S_{M \rightarrow A}$ values were determined by using $T_0 = 0.5 \times (A_f + M_s)$ and $\Delta S_{M \rightarrow A} = \Delta H_{M \rightarrow A} / T_0$ relations [15,28].

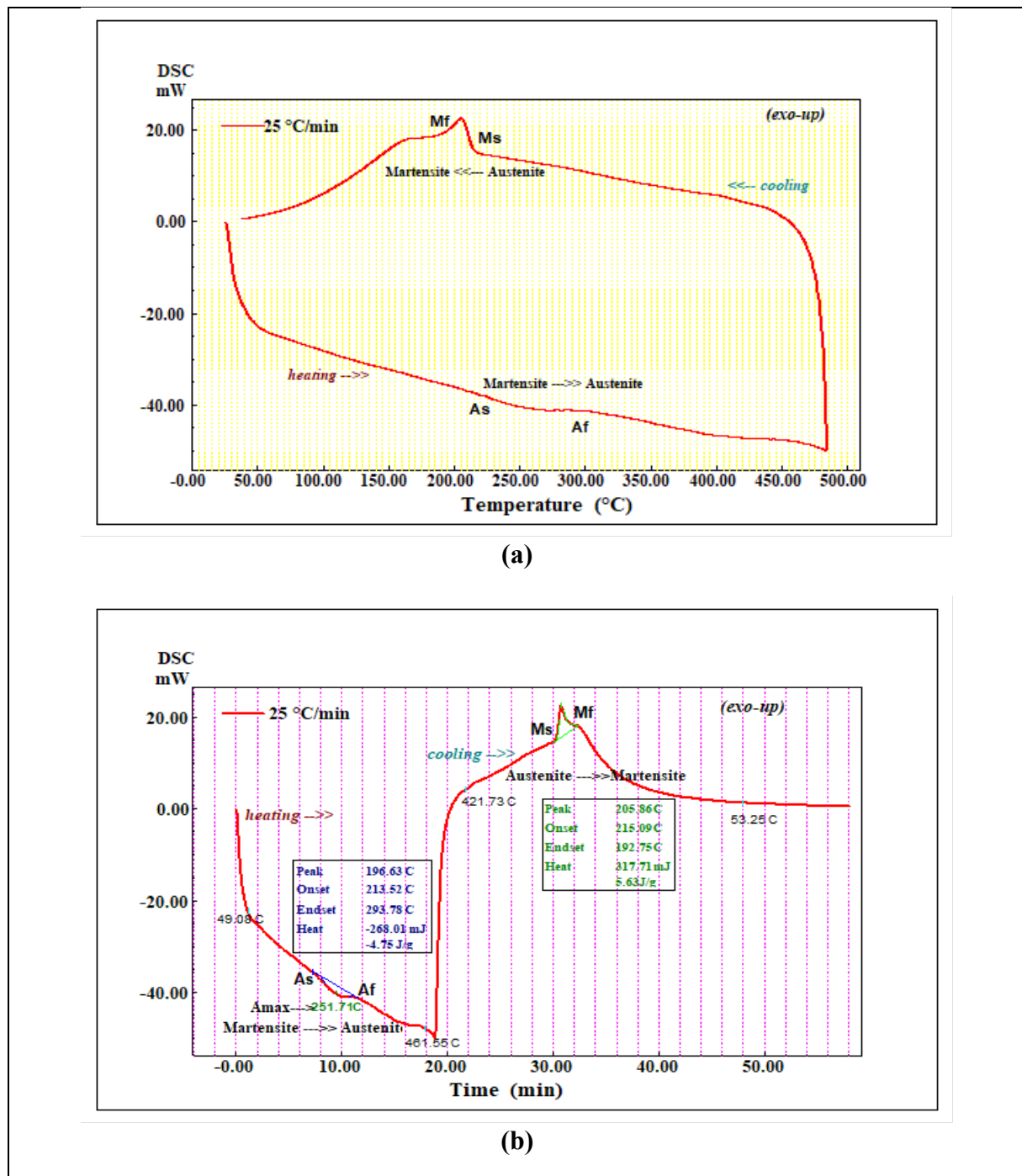


Figure 2. The DSC curve of the CuAlNi alloy as on x-axis of a) temperature and b) time.

Table 1. The thermodynamical parameters and martensitic transformation temperatures of the CuAlNi alloy.

Heating/cooling rate (C/min)	A_s (°C)	A_r (°C)	A_{max} (°C)	M_s (°C)	M_r (°C)	A_s-M_r (°C)	T_0 (°C)	$\Delta H_{M \rightarrow A}$ (J/g)	$\Delta S_{M \rightarrow A}$ (J/g°C)
25	213.52	293.78	251.71	215.09	192.75	20.77	254.44	4.75	0.01867

The thermal response cycling heating/cooling pattern of the alloy in high temperature region shown as DTA curve obtained between room temperature and 900 °C by 25 °C/min of heating-cooling rate can be seen in Figure 3. On this DTA curve, the sequential phase transitions of $\beta 1'(+\gamma 1')$ \rightarrow $\beta 1$ (or B1) \rightarrow $\beta 2$ (metastable) \rightarrow $\gamma 2+\alpha$ (precipitation) \rightarrow eutectoid reaction \rightarrow B2(ordered) \rightarrow A2 (disordered) were observed on heating the alloy, which transitions are a common similar behavior of copper-based shape memory alloys [15,19,38].

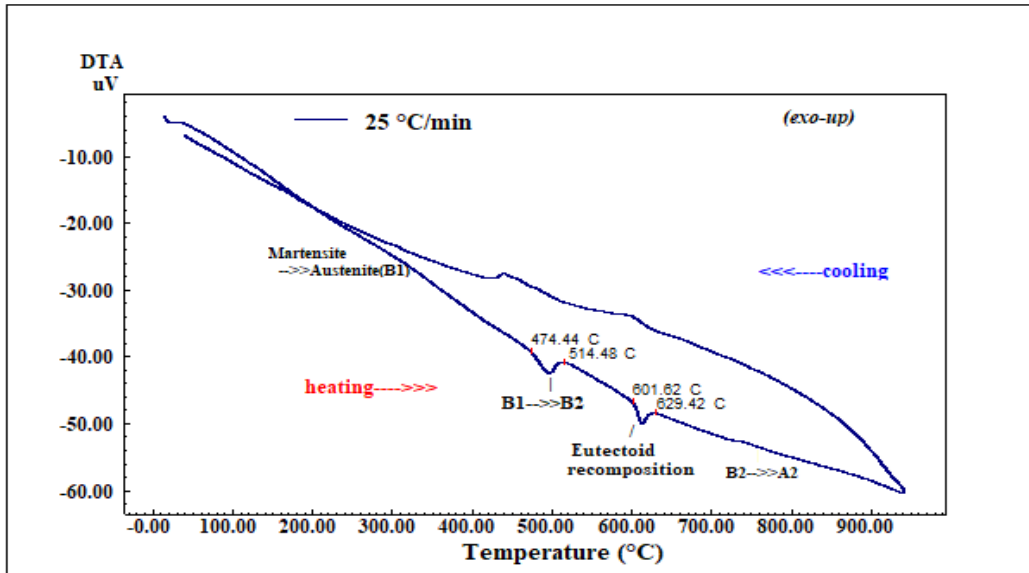


Figure 3. The DTA curve of the CuAlNi shape memory alloy.

The X-ray diffraction pattern of the CuAlNi alloy obtained at room temperature by using $\text{CuK}\alpha$ radiation is presented in Figure 4. As seen on this crystallograph, the martensite phase of $\gamma 1'(211)$ peak is the highest and this peak with the other $\gamma 1'$ and $\beta 1'$ martensite peaks [15,16,28,33,37] indicate the formation of a structure which is underlying mechanism of shape memory effect property of the CuAlNi alloy. The $\beta 1$ and $\gamma 1$, $\gamma 2$, and α -Cu precipitates are the other appeared peaks on the pattern [37]. All of these many small XRD peaks demonstrate that the CuAlNi alloy has a highly polycrystalline structure caused from not making a post-heat-treatment (homogenization) after obtaining ribbon alloy by melt spinning process.

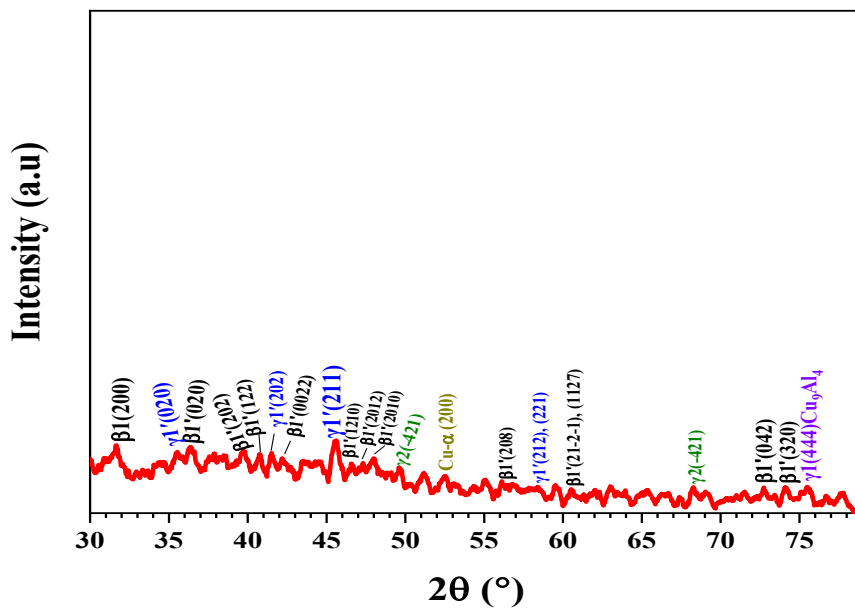


Figure 4. The XRD diffraction pattern CuAlNi alloy.

The photo-electrical I - V graphics of the novel CuAlNi/n-Si/Al photodiode as in semi-log mode obtained under darkness and varied step-increasing artificial day light power intensity conditions are presented in Figure 5. As seen on these plots, the SMA-photodiode rectifies the current; it lets current to flow under forward bias and does not under reverse bias except a low leakage (saturation) current under all conditions. It also shows acute photoconductive photosensitiveness under the all light conditions by crescendo photocurrents in reverse bias current [23,28,33,35,39]. This photocurrent generation and raise in the negative voltage (reverse) bias by light exposure confirms that the fabricated photodevice has photodiode properties. This photocurrent generation occurs by excitation of the valance band electrons by the absorbed incoming photons with enough energies ($h\nu \geq E_g$) beamed from the the solar simulator I-V measuring device. The photo-excited electrons leave holes behind when they pass to the conduction band and this photoelectrical phenomenon (electron-hole pair generation) is named as the photoelectric effect. The reverse bias current in dark is seen as some zig-zag noisy but the illuminated reverse bias currents are highly stable. Moreover, the forward bias current is seen also increased by the effect of light power. All of these findings indicate that the new device has good photoconductive and photovoltaic properties.

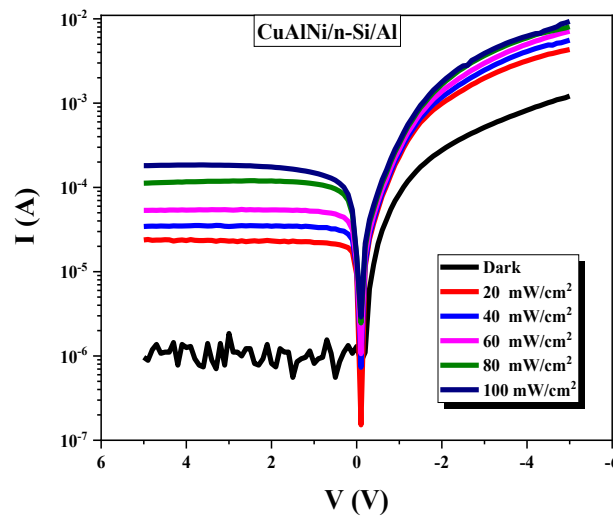


Figure 5: The semi-log I - V plots of the fabricated CuAlNi/n-Si/Al SMA-photodiode obtained under the conditions of dark and different light power intensities.

One of the electrical diode parameters is current rectifying exponent, RR. This ratio is the rate of the absolute current values at a definite absolute-equal negative and positive voltage ($\pm V$) couple. It was found by using $RR_{\pm V} = I_V/I_{-V}$ formula [28]. The value of RR for the SMA-photodiode at ± 5.0 V was determined as 1266 for dark condition and 52 for 100 mW/cm^2 of light power condition. Close RR values were reported in some other similar works [28, 34,36]. Generally, I - V plot at low voltages of forward bias is linear, however when the applying voltage is raised, deviations from this linearity occurs mainly by the impact of the interfacial layer, interface states (in CuAlNi/n-Si interface) and series resistance (R_s) [40].

For a Schottky (photo)diode the relationship between current and voltage elucidated by the conventional thermionic emission (TE) charge transport mechanism theory is defined by the equation [28,41] (for $V > 3kT/q$ condition) given as below;

$$I = I_0 \exp\left(\frac{q(V-IR_s)}{nkT} - 1\right). \quad (1)$$

where; k refers to the Boltzmann constant, $V-IR_s$ stands for the voltage that drops across the metal-semiconductor junction diode, q is charge of electron, T is temperature ($T= 300$ K), n refers to the unitless ideality factor parameter of the diode, I_0 is the reverse saturation current obtained from the intersecting of linear segment of $\ln(I)$ - V plot in forward bias region. The saturation current I_0 is expressed as below;

$$I_0 = AA^*T^2 \exp\left(-\frac{q\phi_b}{kT}\right) \quad (2)$$

where; ϕ_b refers to the Schottky barrier height (SBH) of the CuAlNi/n-Si/Al SMA-photodiode (at $V=0$), A^* is Richardson invariant (for n-Si the theoretical value of A^* is $112 \text{ A}\cdot\text{cm}^{-2}\text{K}^{-2}$) [41,42], and A stands for the CuAlNi top-contact diode area ($=0.785 \times 10^{-2} \text{ cm}^2$) of the manufactured CuAlNi/n-Si/Al photodiode. The n ideality factor values were computed by substituting the slope quantities of the linear fragments of the $\ln(I)$ - V plots (in the positive biased voltage side) of the SMA-photodiode in the following formula;

$$n = \frac{q}{kT} \left(\frac{dV}{d(\ln I)} \right) \quad (3)$$

The ideality factor n of the CuAlNi/n-Si/Al photodiode was computed as 12.5 for darkness condition and 13.3 for 100 mW/cm^2 power of illuminated condition and these n values are higher than the ideal value ($n=1$). The deviations occurring in n values from the value of ideal one (1) are attributed to the influences of non-uniform distribution of charges in the interface, interface states, impurities, the inhomogeneity of SBH across the junction [28,43,44]. The value of the SBH (ϕ_b) for the signalized photodiode consisting thin-film CuAlNi SMA top-layer can be calculated by using the following formula [28];

$$\phi_b = \frac{kT}{q} \ln \left(\frac{AA^*T^2}{I_0} \right) \quad (4)$$

The ϕ_b value for the CuAlNi/n-Si/Al photodiode was computed as 0.599 eV for dark condition and 0.566 for 100 mW/cm^2 power of illuminated condition. As seen, the n , ϕ_b and RR values of the produced SMA-photodiode are found changed by the light effect. These changes occurred most probably because of the carrier generation-recombination induced by the incident luminous effect and the effect of interface states in the interface of CuAlNi/n-Si Schottky contact [28,45].

One of the most important figure of merits of a photodiode is its responsivity (R_{ph}) parameter that reveals the photo-detecting performance of a photodiode viz; how that device absorbs and reacts to the incident light. R_{ph} is the rate of the generated output photocurrent to the power of incoming light and can be calculated by using $R_{ph}=I_{ph}/P \cdot A_{eff}$ formula [46], where I_{ph} stands for the net photocurrent ($I_{ph} = I_{light} - I_{dark}$), P refers to the incoming light power intensity, and A_{eff} is the effectively enlightened area (6 mm^2) of the produced photodiode. For at -5 V of reverse bias, the net photocurrent R_{ph} responsivity values of the manufactured SMA-photodiode under 20 mW/cm^2 and 100 mW/cm^2 of light power intensities were found as 0.019 A/W and 0.030 A/W (or 19 mA/W and 30 mA/W), respectively. These responsivity values are found similar to those reported in some recent works [46,47]. Moreover, in this work, even higher responsivity values could be achieved by applying larger light power intensities than 100 mW/cm^2 as far as the limit of the SMA-photodiode device [28].

Another photodiode parameter is the photosensitivity parameter, which is defined as a measure of the photodiode's ability to absorb incoming light. It is a unitless parameter and represented as PS or percent %PS. The better the photodiode can absorb light, the greater its photosensitivity. A formula [28,44] to determine the %PS photosensitivity parameter is given as $\%PS = [(I_{ph} - I_d) \times 100] / I_d$, where I_d is dark current. For at -5 V and under 100 mW/cm^2 light power condition, the photosensitivity %PS value of the SMA-photodiode was found as 18693 and this value is consistent with some recent literature values [28,44,48].

Specific detectivity (D^*) is another figure of merit for a photodiode and it is defined as the weak light (signal) detection capability of a photodiode [28]. For shot-noise limit condition, the detectivity D^* value of the device normalized by the effective diode area (A_{eff}) can be calculated by $D^*=R_{ph}/(2qI_d/A_{eff})^{1/2}$ formula [28,49], where q is electron charge. The higher detectivity a photodiode has, the more sensitively it can detect weak signals. The photodiodes with high detectivities can be used in optoelectronic communication systems. For at -5 V and under 100 mW/cm^2 light power condition, the D^* value of the SMA-photodiode was calculated as 1.33×10^{10} Jones and this value is in accordance with some recently reported literature values [28,44,48,49].

In MS Schottky contacts the current is not conducted by thermionic emission mechanism at forward bias due to the absence of a potential barrier and depletion layer. The current conduction mechanisms that must be dominant in the produced SMA-photodiode during at forward voltage bias and under dark condition were investigated by making SCLC (space charge limited current) analysis [50–52], which is made according to $I \propto V^m$ power law relationship. To make this analysis, under dark condition the forward bias $\ln(I)$ - $\ln(V)$ graphic of the produced SMA-photodiode was drawn and given in Figure 6. The slope (m) values found for the linear parts of this graphic are defined by the current conduction mechanisms regions as; the I.Region ($m<1$) is electron tunneling region due to low voltages, (the II.Region ($m=1$, $I \propto V$) is ohmic conduction but not found here so instead) the II.Region ($m=2$, $I \propto V^2$) is trap free SCLC conduction (all traps are filled) and this region is also called as super ohmic or

super linear conduction, the III.Region ($m > 2$, $I \propto V^m$) is SCLC with trap effect and lastly the IV.Region ($1 < m < 2$, $I \propto V^{-1.5}$ or $I \propto \exp(V)$) is SCLC based on recombination-tunneling mechanisms.

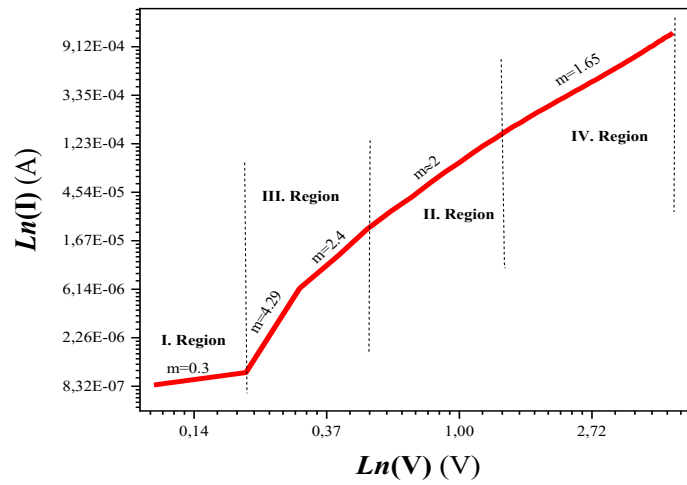


Figure 6. The regions of dominant current conduction mechanisms on the double logarithmic $Ln(I)$ - $Ln(V)$ current-voltage graphic of the CuAlNi/n-Si/Al SMA-photodiode at forward bias and under dark.

To set apart of carrier charges generated by the photovoltaic effect of the SMA-photodiode the dynamic (time-dependent) photocurrent response also called as transient photocurrent (TPC) measurement was performed on SMA-photodiode. The obtained TPC patterns of the novel photodiode under increasing light power intensities were given in Figure 7. On these patterns, upon the light is turned on each time, the photocurrent rapidly ascends a higher altitude due to the light induced generation of the excess charge carriers and remains barely constant till the light off. Each time the light is put out, the photocurrent comes down to its initial level like rapidly again. Such swift downfalls on these curves occur due to the excess carriers and trapped carriers recombination in the deep levels [28,33,53].

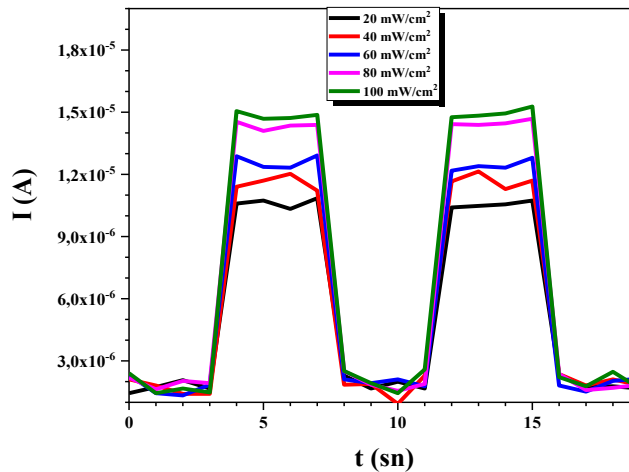


Figure 7. The characteristic photoreactive time-dependent I-t (TPC) curves of the produced CuAlNi/n-Si/Al photodiode as its response to the different P (mW/cm^2) light power intensities.

The capacitance-voltage (C-V) curves of the photodiode obtained at different step frequencies are presented in Figure 8 (due to the opposite probe poles used in the C-V measurement the left voltage side in this figure is actually reverse bias region). According to these C-V curves, the capacitance of the SMA-photodiode changes by change of frequency and applied voltage [28, 33-36, 54-56]. The higher frequency, the lower capacitance. Because the electrons cannot chase the ac current at high frequencies and therefore they don't contribute to the total

capacitance at high frequencies [23, 54-56]. The capacitance of the photodiode becomes zero in the forward bias region at all frequencies.

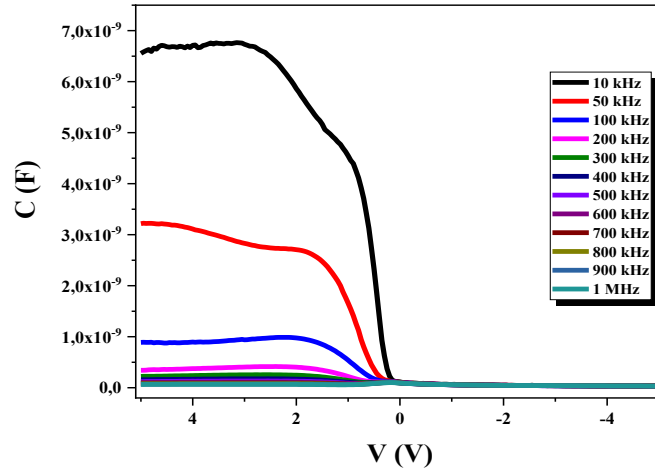


Figure 8. The characteristic capacitance-voltage (C - V) curves of the produced CuAlNi/n-Si/Al photodiode obtained at different frequencies.

By plotting the inverse squared capacitance-voltage (C^{-2} - V) curves of the SMA-photodiode as given in Figure 9 some other electrical parameters can be determined at the reverse bias (negative voltage) region. The values of these parameters were calculated by using the linear fit value obtained from the graphic at 1 MHz. The capacitance of depletion layer is expressed by the formula [28] given as below;

$$C^{-2} = \frac{2(V_d + V)}{q\epsilon_0\epsilon_s A^2 N_D} \quad (5)$$

where; N_D is concentration of non-compensated ionized donor atoms, V_d refers to diffusion potential, A is diode area, q is electron charge, ϵ_s (=11.8 for n-Si) is permittivity of the semiconductor and ϵ_0 is permittivity of space. The values of N_D and V_d are determined by the slope and linear extrapolation of the C^{-2} - V plot to the x -axis (voltage). The donor concentration N_D can be calculated by the following formula [28];

$$N_D = \frac{2}{q\epsilon_0\epsilon_s A^2} \left[\frac{d(C^{-2})}{dV} \right]^{-1} \quad (6)$$

The values of N_d and V_d at 1 MHz were determined as 1.25×10^{15} [28] and 0.875 V, respectively. Plus, the Schottky barrier height ϕ_b can be also calculated from the C^{-2} - V method by using the formula given as below;

$$\phi_b = \frac{V_d}{n} + \frac{kT}{q} \ln \left(\frac{N_C}{N_D} \right) \quad (7)$$

where; N_C refers to the effective density of states in the conduction band of n-Si substrate ($N_C = 2.8 \times 10^{19} \text{ cm}^{-3}$). By this method, the value of ϕ_b was found as 0.330 eV and this value was found lower than the conventional 0.599 eV value found by I - V method. This difference is due to the coating CuAlNi alloy metal layer onto n-Si without use of an insulator interlayer which makes the capacitance of the produced device lower than those of the diodes (MIS) with insulator interlayer [28]. Moreover, the effective Fermi energy (E_F) was determined as 0.260 eV by using $E_F = \phi_b - (V_d/n)$ formula, and it was found as 0.529 eV from the conventional I - V method [28].

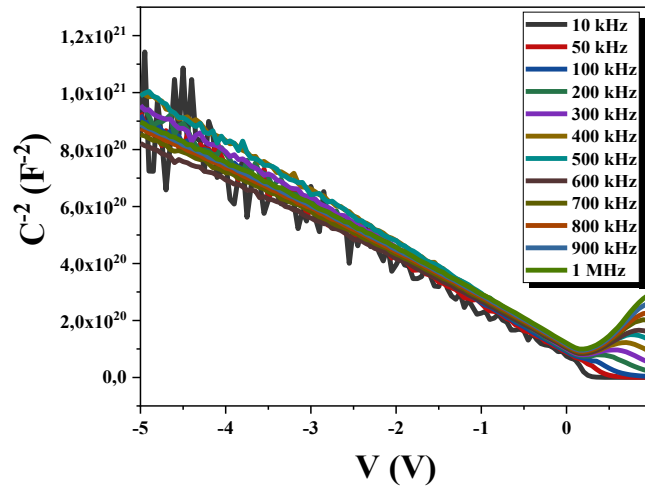


Figure 9. Multiple C^{-2} - V graphs of CuAlNi/n-Si/Al SMA-photodiode at different frequencies.

4. Conclusions

In this work, the new MS Schottky type CuAlNi/n-Si/Al SMA-photodiode was successfully fabricated by coating nano-thick CuAlNi shape memory alloy thin film as top diode metal contact onto n-Si substrate using thermal evaporation method. The CuAlNi alloy was classified as a high temperature shape memory alloy with a high polycrystalline structure including martensite phases. The photo-electrical I-V, I-t and C-V measurements were carried out for characterization of the SMA-photodiode device. The electrical ideality factor, Schottky barrier height and rectification ratio diode parameters of the produced device were determined from the I-V method as 12.5, 0.599 eV and 1266, respectively. The high ideality factor deviated from unity was caused mainly from the presence of interface states, non-uniform distribution of the interface charges and barrier inhomogeneity across the CuAlNi/n-Si contact. The SCLC current conduction mechanisms were found as the dominant current conduction mechanisms at forward bias and in dark condition. The produced SMA-photodiode showed remarkable photoconductive and photovoltaic profile and very well photodiode figure of merits such as a huge photosensitivity (%PS) value of 18693, a specific detectivity of $\sim 10^{10}$ Jones and a responsivity of 0.030 A/W by the effect of applied artificial solar light. These merits show that the produced SMA-photodiode can be used in photosensor and optical communication systems. It was observed that the electrons cannot follow the applied ac voltage at the high frequencies of C-V tests made on the SMA-photodiode. All of the results showed that this novel CuAlNi/n-Si/Al photodiode can be potentially used in photodiode, photosensor, optoelectronic communication systems, photovoltaic etc. applications and also in M/NEMs applications where light-induced actuating-sensing mechanism is based on.

Acknowledgements

This research work is a part of Ph.D. thesis works of Oktay KARADUMAN supervised by Prof. Dr. Canan Aksu CANBAY at Firat University, Faculty of Science, Department of Physics and was financially supported by FÜBAP, Project No: FF.21.14. O.K. wrote the article, implemented the experiments and C.A.C. wrote the article.

References

- [1] J. Mohd Jani, M. Leary, A. Subic, M.A. Gibson, A review of shape memory alloy research, applications and opportunities, *Materials and Design*. 56 (2014) 1078–1113. <https://doi.org/10.1016/j.matdes.2013.11.084>.
- [2] K. Otsuka, C.M. Wayman, *Shape memory materials*, Cambridge University Press, 1999.
- [3] A. Concilio, V. Antonucci, F. Auricchio, L. Lecce, E. (Eds.). Sacco, *Shape Memory Alloy Engineering*, 2nd ed., Elsevier, 2021. <https://doi.org/10.1016/C2018-0-02430-5>.
- [4] J. Ma, I. Karaman, R.D. Noebe, High temperature shape memory alloys, *International Materials Reviews*. 55 (2010) 257–315. <https://doi.org/10.1179/095066010X12646898728363>.
- [5] A. Rao, A.R. Srinivasa, J.N. Reddy, *Introduction to shape memory alloys*, SpringerBriefs in Applied Sciences and Technology. (2015) 1–31. https://doi.org/10.1007/978-3-319-03188-0_1.

- [6] Y.Q. Fu, J.K. Luo, A.J. Flewitt, W.M. Huang, S. Zhang, H.J. Du, W.I. Milne, Thin film shape memory alloys and microactuators, *Int. J. Computational Materials Science and Surface Engineering*. 2 (2009) 208–226. <https://doi.org/10.1504/IJCMSE.2009.027483>.
- [7] P. Krulevitch, A.P. Lee, P.B. Ramsey, J.C. Trevino, J. Hamilton, M. Allen, Thin film shape memory alloy microactuators, 1996. <https://doi.org/10.1109/84.546407>.
- [8] E. Patoor, D.C. Lagoudas, P.B. Entchev, L.C. Brinson, X. Gao, Shape memory alloys, Part I: General properties and modeling of single crystals, *Mechanics of Materials*. 38 (2006) 391–429. <https://doi.org/10.1016/j.mechmat.2005.05.027>.
- [9] J.M. San Juan, M.L. N6, C.A. Schuh, Superelasticity and shape memory in micro- and nanometer-scale pillars, *Advanced Materials*. 20 (2008) 272–278. <https://doi.org/10.1002/adma.200701527>.
- [10] N. Choudhary, D. Kaur, Shape memory alloy thin films and heterostructures for MEMS applications: A review, *Sensors and Actuators, A: Physical*. 242 (2016) 162–181. <https://doi.org/10.1016/j.sna.2016.02.026>.
- [11] I. Stachiv, E. Alarcon, M. Lamac, Shape memory alloys and polymers for mems/nems applications: Review on recent findings and challenges in design, preparation, and characterization, *Metals (Basel)*. 11 (2021) 1–28. <https://doi.org/10.3390/met11030415>.
- [12] S. Najah Saud Al-Humairi, Cu-Based Shape Memory Alloys: Modified Structures and Their Related Properties, in: *Recent Advancements in the Metallurgical Engineering and Electrodeposition*, IntechOpen, 2020. <https://doi.org/10.5772/intechopen.86193>.
- [13] R. Dasgupta, A look into Cu-based shape memory alloys: Present scenario and future prospects, *Journal of Materials Research*. 29 (2014) 1681–1698. <https://doi.org/10.1557/jmr.2014.189>.
- [14] K.K. Alaneme, J.U. Anaele, E.A. Okotete, Martensite aging phenomena in Cu-based alloys: Effects on structural transformation, mechanical and shape memory properties: A critical review, *Sci Afr*. 12 (2021). <https://doi.org/10.1016/j.sciaf.2021.e00760>.
- [15] C.A. Canbay, O. Karaduman, N. Ünlü, S.A. Baiz, İ. Özkul, Heat treatment and quenching media effects on the thermodynamical, thermoelastical and structural characteristics of a new Cu-based quaternary shape memory alloy, *Composites Part B: Engineering*. 174 (2019) 106940. <https://doi.org/10.1016/j.compositesb.2019.106940>.
- [16] O. Karaduman, C. Aksu Canbay, N. Ünlü, S. Özkul, Analysis of a newly composed Cu-Al-Mn SMA showing acute SME characteristics, in: *AIP Conference Proceedings*, American Institute of Physics Inc., 2019. <https://doi.org/10.1063/1.5135437>.
- [17] S.N. Saud, E. Hamzah, T.A. Abu Bakar, A. Abdolahi, Influence of addition of carbon nanotubes on structure-properties of Cu-Al-Ni shape memory alloys, *Materials Science and Technology (United Kingdom)*. 30 (2014) 458–464. <https://doi.org/10.1179/1743284713Y.0000000379>.
- [18] U.S. Mallik, V. Sampath, Influence of quaternary alloying additions on transformation temperatures and shape memory properties of Cu-Al-Mn shape memory alloy, *Journal of Alloys and Compounds*. 469 (2009) 156–163. <https://doi.org/10.1016/j.jallcom.2008.01.128>.
- [19] R.O. Ferreira, L.S. Silva, R.A.G. Silva, Thermal behavior of as-annealed CuAlMnAgZr alloys, *Journal of Thermal Analysis and Calorimetry*. 146 (2021) 595–600. <https://doi.org/10.1007/s10973-020-10002-8>.
- [20] S. Karthick, S. Shalini, S.S. Mani Prabu, K. Suhel, A. Vandan, C. Puneet, S. Manoj Kumar, R. Venkatesh, I.A. Palani, Influence of quaternary alloying addition on transformation temperatures and shape memory properties of Cu–Al–Mn shape memory alloy coated optical fiber, *Measurement: Journal of the International Measurement Confederation*. 153 (2020). <https://doi.org/10.1016/j.measurement.2019.107379>.
- [21] Y. Motemani, P.J.S. Buenconsejo, A. Ludwig, Recent Developments in High-Temperature Shape Memory Thin Films, *Shape Memory and Superelasticity*. 1 (2015). <https://doi.org/10.1007/s40830-015-0041-0>.
- [22] Y.Q. Fu, J.K. Luo, W.M. Huang, A.J. Flewitt, W.I. Milne, Thin film shape memory alloys for optical sensing applications, *Journal of Physics: Conference Series*. 76 (2007). <https://doi.org/10.1088/1742-6596/76/1/012032>.
- [23] C.A. Canbay, A. Tatarođlu, W.A. Farooq, A. Dere, A. Karabulut, M. Atif, A. Hanif, CuAlMnV shape memory alloy thin film based photosensitive diode, *Materials Science in Semiconductor Processing*. 107 (2020) 104858. <https://doi.org/10.1016/J.MSSP.2019.104858>.
- [24] A. Isalgue, V. Torra, J.-L. Seguin, M. Bendahan, J.M. Amigo, V. Esteve-Cano, Shape memory NiTi thin films deposited at low temperature, *Materials Science and Engineering A*. 273–275 (1999) 717–721. [https://doi.org/10.1016/S0921-5093\(99\)00403-7](https://doi.org/10.1016/S0921-5093(99)00403-7).
- [25] J.A. Walker, K.J. Gabriel, M. Mehregany, Thin-film processing of TiNi shape memory alloy, *Sensors and Actuators A: Physical*. 21 (1990). [https://doi.org/10.1016/0924-4247\(90\)85047-8](https://doi.org/10.1016/0924-4247(90)85047-8).
- [26] M. Bendahan, J.L. Seguin, D. Lollman, H. Carchano, New type of Schottky barriers using NiTi shape memory alloy films, *Thin Solid Films*. 294 (1997) 278–280. [https://doi.org/10.1016/S0040-6090\(96\)09230-9](https://doi.org/10.1016/S0040-6090(96)09230-9).
- [27] M. Geetha, K. Dhanalakshmi, S. Jayachandran, I.A. Palani, V. Sathish Kumar, Analysis of actuation characteristics of CuAlNiMn/Polyimide thin film shape memory alloy, *Materials Today: Proceedings*. 46 (2021) 9580–9585. <https://doi.org/10.1016/j.matpr.2020.04.689>.
- [28] C.A. Canbay, O. Karaduman, The photo response properties of shape memory alloy thin film based photodiode, *Journal of Molecular Structure*. 1235 (2021) 130263. <https://doi.org/10.1016/j.molstruc.2021.130263>.
- [29] Q. Pan, C. Cho, The Investigation of a Shape Memory Alloy Micro-Damper for MEMS Applications, *Sensors*. 7 (2007). <https://doi.org/10.3390/s7091887>.

- [30] M. Kabla, E. Ben-David, D. Shilo, A novel shape memory alloy microactuator for large in-plane strokes and forces, *Smart Materials and Structures*. 25 (2016). <https://doi.org/10.1088/0964-1726/25/7/075020>.
- [31] K.R.C. Gisser, J.D. Busch, A.D. Johnson, A.B. Ellis, Oriented nickel-titanium shape memory alloy films prepared by annealing during deposition, *Applied Physics Letters*. 61 (1992) 1632–1634. <https://doi.org/10.1063/1.108434>.
- [32] A.P. Jardine, H. Zhang, L.D. Wasielesky, Investigations into the thin-film fabrication of intermetallic NiTi, *Mat. Res. Soc. Symp. Proc.* 187 (1990) 181–186. <https://doi.org/10.1557/PROC-187-181>.
- [33] C.A. Canbay, A. Tataroglu, A. Dere, A. Al-Ghamdi, F. Yakuphanoglu, A new shape memory alloy film/p-Si solar light four quadrant detector for solar tracking applications, *Journal of Alloys and Compounds*. 688 (2016) 762–768. <https://doi.org/10.1016/J.JALLCOM.2016.07.087>.
- [34] C. Aksu Canbay, A. Dere, K. Mensah-Darkwa, A. Al-Ghamdi, Z. Karagoz Genç, R.K. Gupta, F. Yakuphanoglu, New type of Schottky diode-based Cu–Al–Mn–Cr shape memory material films, *Applied Physics A: Materials Science and Processing*. 122 (2016). <https://doi.org/10.1007/s00339-016-0208-3>.
- [35] C.A. Canbay, A. Tataroğlu, A. Dere, A.G. Al-Sehemi, A. Karabulut, A.A. Al-Ghamdi, F. Yakuphanoglu, Electrical, kinetic and photoelectrical properties of CuAlMnMg shape memory alloy/n-Si Schottky diode, *Journal of Alloys and Compounds*. 888 (2021) 161600. <https://doi.org/10.1016/J.JALLCOM.2021.161600>.
- [36] E. Aldirmaz, A. Tataroğlu, A. Dere, M. Güler, E. Güler, A. Karabulut, F. Yakuphanoglu, Cu-Al-Mn shape memory alloy based Schottky diode formed on Si, *Physica B: Condensed Matter*. 560 (2019) 261–266. <https://doi.org/10.1016/j.physb.2018.12.024>.
- [37] O. Karaduman, İ. Özkul, C.A. Canbay, Shape memory effect characterization of a ternary CuAlNi high temperature SMA ribbons produced by melt spinning method, *Advanced Engineering Science*. 1 (2021) 26–33. <http://publish.mersin.edu.tr/index.php/ades>.
- [38] C.A. Canbay, O. Karaduman, N. Ünlü, İ. Özkul, M.A. Çiçek, Energetic Behavior Study in Phase Transformations of High Temperature Cu–Al–X (X: Mn, Te, Sn, Hf) Shape Memory Alloys, *Transactions of the Indian Institute of Metals*. (2021). <https://doi.org/10.1007/S12666-021-02241-6>.
- [39] E. Aldirmaz, M. Guler, E. Guler, A. Dere, A. Tataroğlu, A.G. Al-Sehemi, A.A. Al-Ghamdi, F. Yakuphanoglu, A shape memory alloy based on photodiode for optoelectronic applications, *Journal of Alloys and Compounds*. 743 (2018) 227–233. <https://doi.org/10.1016/J.JALLCOM.2018.01.380>.
- [40] P. Cova, A. Singh, A. Medina, R.A. Masut, Effect of doping on the forward current-transport mechanisms in a metal–insulator–semiconductor contact to InP:Zn grown by metal organic vapor phase epitaxy, *Solid-State Electronics*. 42 (1998) 477–485. [https://doi.org/10.1016/S0038-1101\(97\)00250-5](https://doi.org/10.1016/S0038-1101(97)00250-5).
- [41] S.M. Sze, K.N. Kwok, *Physics of Semiconductor Devices*, 3rd ed., John Wiley Sons Inc., Hoboken, New Jersey, 2006.
- [42] A. Tataroğlu, F.Z. Pür, The Richardson constant and barrier inhomogeneity at Au/Si 3N4/n-Si (MIS) Schottky diodes, *Physica Scripta*. 88 (2013). <https://doi.org/10.1088/0031-8949/88/01/015801>.
- [43] S. Riazimehr, S. Kataria, J.M. Gonzalez-Medina, S. Wagner, M. Shaygan, S. Suckow, F.G. Ruiz, O. Engström, A. Godoy, M.C. Lemme, High Responsivity and Quantum Efficiency of Graphene/Silicon Photodiodes Achieved by Interdigitating Schottky and Gated Regions, *ACS Photonics*. 6 (2019) 107–115. <https://doi.org/10.1021/acsp Photonics.8b00951>.
- [44] V. Balasubramani, J. Chandrasekaran, T.D. Nguyen, S. Maruthamuthu, R. Marnadu, P. Vivek, S. Sugarthi, Colossal photosensitive boost in Schottky diode behaviour with Ce-V2O5 interfaced layer of MIS structure, *Sensors and Actuators, A: Physical*. 315 (2020). <https://doi.org/10.1016/j.sna.2020.112333>.
- [45] S. Ruzgar, M. Caglar, Fabrication and characterization of solution processed Al/Sn:ZnO/p-Si photodiodes, *Materials Science in Semiconductor Processing*. 115 (2020) 105076. <https://doi.org/10.1016/j.mssp.2020.105076>.
- [46] A.G. Imer, E. Kaya, A. Dere, A.G. Al-Sehemi, A.A. Al-Ghamdi, A. Karabulut, F. Yakuphanoglu, Illumination impact on the electrical characteristics of Au/Sunset Yellow/n-Si/Au hybrid Schottky diode, *Journal of Materials Science: Materials in Electronics*. 31 (2020) 14665–14673. <https://doi.org/10.1007/s10854-020-04029-8>.
- [47] P. Vivek, J. Chandrasekaran, R. Marnadu, S. Maruthamuthu, Fabrication of Illumination-Dependent Cu/p-Si Schottky Barrier Diodes by Sandwiching MoO₃ Nanoplates as an Interfacial Layer via JNSP Technique, (n.d.). <https://doi.org/10.1007/s11664-020-08137-3>.
- [48] V. Balasubramani, J. Chandrasekaran, V. Manikandan, T.K. Le, R. Marnadu, P. Vivek, Upgraded photosensitivity under the influence of Yb doped on V2O5 thin films as an interfacial layer in MIS type Schottky barrier diode as photodiode application, *Journal of Solid State Chemistry*. 301 (2021). <https://doi.org/10.1016/j.jssc.2021.122289>.
- [49] U.Y. Won, B.H. Lee, Y.R. Kim, W.T. Kang, I. Lee, J.E. Kim, Y.H. Lee, W.J. Yu, Efficient photovoltaic effect in graphene/h-BN/silicon heterostructure self-powered photodetector, *Nano Research*. 14 (2021) 1967–1972. <https://doi.org/10.1007/s12274-020-2866-x>.
- [50] F. Gul, A simplified method to determine carrier transport mechanisms of metal-oxide resistive random access memory (RRAM) devices, in: *Materials Today: Proceedings*, Elsevier Ltd, 2021: pp. 6976–6978. <https://doi.org/10.1016/j.matpr.2021.03.274>.
- [51] Z. Çaldıran, M. Şinoforoğlu, Ö. Metin, Ş. Aydoğan, K. Meral, Space charge limited current mechanism (SCLC) in the graphene oxide-Fe3O4 nanocomposites/n-Si heterojunctions, *Journal of Alloys and Compounds*. 631 (2015) 261–265. <https://doi.org/10.1016/j.jallcom.2015.01.117>.
- [52] F.C. Chiu, A review on conduction mechanisms in dielectric films, *Advances in Materials Science and Engineering*. 2014 (2014). <https://doi.org/10.1155/2014/578168>.

- [53] C.A. Arredondo, G. Gordillo, Photoconductive and electrical transport properties of AgInSe₂ thin films prepared by co-evaporation, *Physica B: Condensed Matter*. 405 (2010) 3694–3699. <https://doi.org/10.1016/j.physb.2010.05.068>.
- [54] N. Shiwakoti, A. Bobby, K. Asokan, B. Antony, Temperature dependent dielectric studies of Ni/n-GaP Schottky diodes by capacitance and conductance measurements, *Materials Science in Semiconductor Processing*. 42 (2016) 378–382. <https://doi.org/10.1016/j.mssp.2015.11.010>.
- [55] E. Gürgeç, A. Dıkıcı, F. Aslan, Investigation of structural, electrical and photoresponse properties of composite based Al/NiO: CdO/p-Si/Al photodiodes, *Physica B: Condensed Matter*. 639 (2022) 413981. <https://doi.org/10.1016/j.physb.2022.413981>.
- [56] E. GÜRGENÇ, A. DİKİCİ, F. ASLAN, Production and Characterization of Al/NiO:ZnO/p-Si/Al Composite Photodiodes for Solar Energy Tracking Systems, *Turkish Journal of Science and Technology*. (2022). <https://doi.org/10.55525/tjst.1071332>.

Some Quantum Integral Inequalities Based on Left-Right Quantum Integrals

Mehmet KUNT¹, Abdul Wakil BAIDAR², Zeynep ŞANLI^{3*}

¹ Department of Mathematics, Faculty of Sciences, Karadeniz Technical University, Trabzon, Turkey

² Kabul University, Department of Mathematics, Kabul, Afghanistan

³ Department of Mathematics, Faculty of Sciences and Letters, Mersin University, Mersin, Turkey

¹mkunt@ktu.edu.tr, ² baidarmath87@gmail.com, ^{3*}zeynepshanli@mersin.edu.tr

(Geliş/Received: 04/05/2022;

Kabul/Accepted: 27/06/2022)

Abstract: In this work, the concepts of quantum derivative and quantum integral were renamed to be the left quantum derivative and the left definite quantum integral. Symmetrically to the left, a new quantum derivative (the right) and definite quantum integral (the right) were defined. Some properties of these new concepts were investigated and as well as according to do these new concepts some inaccuracies in quantum integral inequalities were corrected. Moreover, some new quantum Hermite-Hadamard type inequalities were established.

Key words: Quantum derivative, quantum integral, integral inequalities, convex functions.

Sol Sağ Kuantum İntegrallerine Dayalı Bazı Kuantum İntegral Eşitsizlikleri

Öz: Bu çalışmada, kuantum türevi ve kuantum integrali kavramları, sol kuantum türevi ve sol kuantum belirli integrali olarak yeniden adlandırıldı. Sola simetrik olarak, yeni bir kuantum türevi (sağ) ve belirli kuantum integrali (sağ) tanımlandı. Bu kavramların bazı özellikleri araştırıldı ve buna göre bu yeni kuantum integral eşitsizliklerindeki bazı yanlışlıklar düzeltildi. Ayrıca, bazı yeni kuantum Hermite-Hadamard tipi eşitsizlikler kuruldu.

Anahtar kelimeler: Kuantum türev, kuantum integral, integral eşitsizlikleri, konveks fonksiyonlar.

1. INTRODUCTION

A function $f: J \subseteq \mathbb{R} \rightarrow \mathbb{R}$ is said to be convex on J if the following inequality

$$f(tx + (1-t)y) \leq tf(x) + (1-t)f(y)$$

holds for all $x, y \in J$ and $t \in [0,1]$.

One of the most useful inequalities for convex functions is Hermite-Hadamard's inequality, due to its geometrical importance and applications, which is described as follows:

Let $f: J \subseteq \mathbb{R} \rightarrow \mathbb{R}$ be a convex function on the interval of real numbers and $a, b \in J$ with $a < b$.

Then

$$(1.1) \quad f\left(\frac{a+b}{2}\right) \leq \frac{1}{b-a} \int_a^b f(t) dt \leq \frac{f(a)+f(b)}{2}.$$

This inequality has been widely studied in different ways and different forms in the theory of integral inequalities. It is indispensable to mention the papers [14], which are leading the studies over the past twenty years. In [14], the authors gave an identity to obtain trapezoid type error estimations. Following, researchers continued to work to obtain error estimates such as midpoint, Ostrowski, Simpson, Bullen, Newton, etc. and to improved existing inequalities. Many generalizations of this paper have been done by considering different types of functions or various types of integrals. In recent years, generalizations of these studies in quantum calculus theory have been widely researched. For some studies in this regard, the reader is refer to [1]-[4], [6]-[13], [18]-[25], [27]-[36].

However, since the quantum integral is different from the Riemann integral in some properties, some inaccuracies in some of these studies arise. For instance, in [22, Lemma 3.1], the authors gave an identity to obtain quantum analogues of Ostrowski type inequalities. To prove this identity, using similar proving argument with its Riemann integral form, the authors proved the following identity:

$$(1.2) \quad \frac{(x-a)^2}{b-a} \int_0^1 t {}_a D_q f(tx + (1-t)a) {}_0 d_q t = \frac{x-a}{q(b-a)} f(x) - \frac{1}{q(b-a)} \int_a^x f(u) {}_a d_q t.$$

After that, they assumed symmetrically to (1.2) the following identity could be held:

$$(1.3) \quad \frac{(b-x)^2}{b-a} \int_0^1 t {}_a D_q f(tx + (1-t)b) {}_0 d_q t = \frac{b-x}{q(b-a)} f(x) - \frac{1}{q(b-a)} \int_x^b f(u) {}_a d_q t.$$

(see [22, equalities (3.2) and (3.3)]). But the current quantum derivative and integral definitions are not sufficient to satisfy (1.3). In fact, the reason for this problem is that there is no substitution rule in the quantum integral, and the quantum integral is not similar to the Riemann integral for some aspects.

In our investigations, we realized that the existing quantum derivative and integral concepts are not sufficient to overcome these problems. It is known that conjugate concepts of left and right fractional integrals are widely used to derive fractional integral inequalities. Considering that a similar situation can be useful for quantum integral inequalities, we have found that it is necessary to give symmetric concepts which are conjugate to the concepts of quantum derivative and integral.

In this context, the main motivation of this study is to introduce new quantum derivative and integral concepts which are symmetrical to the known and to examine some of their properties. Using them, we will solve some inaccuracies encountered in quantum integral inequalities. In addition, similar to fractional integral inequalities, some quantum type integral inequalities will be obtained by using two symmetric quantum derivatives and integrals concepts together. Also, in the last section, we will use these two conjugate concepts together to obtain quantum analogs of some trapezoid type integral inequalities posed in paper [16]. We think that this new method will be used effectively and widely in future studies.

2. PRELIMINARIES

In this section, we recall some previously known concepts.

In [30,31], Tariboon and Ntouyas introduced the concepts of quantum derivative and definite quantum integral for the functions of defined on an arbitrary finite intervals as follows:

Definition 2.1. [30,31] A function $f(t)$ defined on $[a, b]$ is called quantum differentiable on $(a, b]$ with the following expression:

$$(2.1) \quad {}_a D_q f(t) = \frac{f(t) - f(qt + (1-q)a)}{(1-q)(t-a)} \in \mathbb{R}, \quad t \neq a,$$

and quantum differentiable on $t = a$, if the following limit exists:

$${}_a D_q f(a) = \lim_{t \rightarrow a^+} {}_a D_q f(t),$$

for any $a < b$ (See also [19]).

Clearly, if $a = 0$ in (2.1), then ${}_0 D_q f(t) = D_q f(t)$ where $D_q f(t)$ is familiar quantum derivative given by the following expression:

$$(2.2) \quad D_q f(t) = \frac{f(t) - f(qt)}{(1-q)t}, \quad t \neq 0,$$

$$D_q f(0) = \lim_{t \rightarrow 0^+} D_q f(t),$$

where f is defined on the interval $[a, 0]$. (see also [5,17])

Definition 2.2. [30,31] Let $f(t)$ be a function defined on $[a, b]$. Then the definite quantum integral of $f(t)$ on $[a, b]$ is delineated as:

$$(2.3) \quad \int_a^b f(t) {}_a d_q t = (1-q)(b-a) \sum_{n=0}^{\infty} q^n f(q^n b + (1-q^n)a).$$

If the series in the right-hand side of (2.3) is convergence, then $\int_a^b f(t) {}_a d_q t$ is exist, i.e., $f(t)$ is quantum integrable on $[a, b]$. For any $c \in (a, b)$

$$(2.4) \quad \int_c^b f(t) {}_a d_q t = \int_a^b f(t) {}_a d_q t - \int_a^c f(t) {}_a d_q t,$$

if the series in the right-hand side of (2.4) is convergence. (See also [19]).

Clearly, if $a = 0$, in (2.3), then $\int_0^b f(t) d_q t$ is familiar definite quantum integral (see [5,17]) on $[0, b]$ such as

$$\int_0^b f(t) {}_0 d_q t = \int_0^b f(t) d_q t = (1 - q)b \sum_{n=0}^{\infty} q^n f(q^n b).$$

Lemma 2.1. [19] Let $f: [a, b] \rightarrow \mathbb{R}$ be a differentiable funtion. Then we have

$$(2.5) \quad \lim_{q \rightarrow 1^-} {}_a D_q f(t) = \frac{df(t)}{dt}.$$

Lemma 2.2. [19] Let $f: [a, b] \rightarrow \mathbb{R}$ be an arbitrary function. Provided that $\int_a^b f(t) dt$ converges, then we have

$$(2.6) \quad \lim_{q \rightarrow 1^-} \int_a^b f(t) {}_a d_q t = \int_a^b f(t) dt.$$

By using the Definitions 2.1 and 2.2, in [7], the authors present the quantum Hermite-Hadamard inequality (in [32], the authors proved the same inequality with the fewer assumptions and shorter method) as follows:

Theorem 2.1. Let $f: [a, b] \rightarrow \mathbb{R}$ be a convex function and $0 < q < 1$. Then we have

$$(2.7) \quad f\left(\frac{qa+b}{1+q}\right) \leq \frac{1}{b-a} \int_a^b f(t) {}_a d_q t \leq \frac{qf(a)+f(b)}{1+q}.$$

We will use the following notations and names to avoid confusion:

The left quantum derivative on $[a, b]$ for (2.1):

$${}_a^+ D_q f(t) = {}_a D_q f(t) = \frac{f(t) - f(qt + (1-q)a)}{(1-q)(t-a)}, \quad t \neq a.$$

The left definite quantum integral on $[a, b]$ for (2.3):

$$\int_a^b f(t) {}_a^+ d_q = \int_a^b f(t) {}_a d_q = (1 - q)(b - a) \sum_{n=0}^{\infty} q^n f(q^n b + (1 - q^n)a).$$

The left definite quantum integral on $[0, b]$ for (2.1):

$$\int_0^b f(t) {}_0^+ d_q = \int_0^b f(t) {}_0 d_q = (1 - q)b \sum_{n=0}^{\infty} q^n f(q^n b).$$

The left quantum integral on Hermite-Hadamard ineququality for (2.7)

$$f\left(\frac{qa+b}{1+q}\right) \leq \frac{1}{b-a} \int_a^b f(t) {}_a^+ d_q t \leq \frac{qf(a)+f(b)}{1+q}.$$

3. THE RIGHT QUANTUM DERIVATIVE AND THE RIGHT QUANTUM INTEGRAL ON FINITE INTERVALS

To begin with, we should point out that definitions and some results in this section are given in [13] independently of us.

Let $f(t)$ be a function defined on $[a, b]$. It is clear that $qt + (1 - q)b \in [a, b]$ for all $t \in [a, b]$. It means that $f(t) - f(qt + (1 - q)b)$ is a real number for all $t \in [a, b]$. Hence, $\frac{f(t) - f(qt + (1 - q)b)}{(1 - q)(t - b)}$ is a real number and always exist for all $t \in [a, b]$. Symmetrically to Definition 2.1, we can introduce the following definition of quantum derivative:

Definition 3.1. A function $f(t)$ defined on $[a, b]$ is called the right quantum differentiable on $t \in [a, b)$ with the following expression:

$$(3.1) \quad {}_b^-D_q f(t) := \frac{f(t) - f(qt + (1 - q)b)}{(1 - q)(t - b)}, \quad t \neq b,$$

and the right quantum differentiable on $t = b$, if the following limit exists:

$${}_b^-D_q f(b) = \lim_{t \rightarrow b^-} {}_b^-D_q f(t).$$

Clearly, if $b = 0$ in (3.1), then ${}_0^-D_q f(t) = D_q f(t)$ where $D_q f(t)$ is familiar quantum derivative given in (2.2) of the function defined on the interval $[a, 0]$.

The question is that similar property as stated in Lemma 2.1 can be given or not for the right quantum derivative. The answer is positive and follows:

Lemma 3.1. Let $f: [a, b] \rightarrow \mathbb{R}$ be a differentiable function. Then

$$(3.2) \quad \lim_{q \rightarrow 1^-} {}_b^-D_q f(t) = \frac{df(t)}{dt}.$$

Proof. Since f is differentiable on $[a, b]$, clearly

$$(3.3) \quad \lim_{h \rightarrow 0^+} \frac{f(t+h) - f(t)}{h} = \lim_{h \rightarrow 0^-} \frac{f(t+h) - f(t)}{h} = \lim_{h \rightarrow 0} \frac{f(t+h) - f(t)}{h} = \frac{df(t)}{dt},$$

for all $t \in (a, b)$ and

$$\frac{df(a^+)}{dt} = \lim_{h \rightarrow 0^+} \frac{f(a+h) - f(a)}{h},$$

$$\frac{df(b^-)}{dt} = \lim_{h \rightarrow 0^-} \frac{f(b+h) - f(b)}{h}.$$

Since $0 < q < 1$, $(1 - q)(t - b) < 0$, for all $a < t < b$. Changing variable in (3.1) as $(1 - q)(t - b) = -h$, then $q \rightarrow 1^-$ we have $h \rightarrow 0^+$ and $qt + (1 - q)b = t + h$. Using (3.3),

$$(3.4) \quad \begin{aligned} \lim_{q \rightarrow 1^-} {}_b^-D_q f(t) &= \lim_{q \rightarrow 1^-} \frac{f(t) - f(qt + (1 - q)b)}{(1 - q)(t - b)} \\ &= \lim_{h \rightarrow 0^+} \frac{f(t) - f(t+h)}{-h} \\ &= \lim_{h \rightarrow 0^+} \frac{f(t+h) - f(t)}{h} \\ &= \lim_{h \rightarrow 0} \frac{f(t+h) - f(t)}{h} \end{aligned}$$

$$= \frac{df(t)}{dt},$$

for all $t \in (a, b)$.

For $t = a$, similarly to (3.4).

$$\begin{aligned} \lim_{q \rightarrow 1^-} {}_b D_q f(a) &= \lim_{q \rightarrow 1^-} \frac{f(a) - f(qa + (1-q)b)}{(1-q)(a-b)} \\ &= \lim_{h \rightarrow 0^+} \frac{f(a) - f(a+h)}{-h} \\ &= \lim_{h \rightarrow 0^+} \frac{f(a+h) - f(a)}{h} \\ &= \frac{df(a^+)}{dt}, \end{aligned}$$

On the other hand, for $t = b$,

$$\begin{aligned} \lim_{q \rightarrow 1^-} {}_b D_q f(a) &= \lim_{q \rightarrow 1^-} \lim_{t \rightarrow b^-} {}_b D_q f(t) \\ &= \lim_{q \rightarrow b^-} \lim_{q \rightarrow 1^-} {}_b D_q f(t) \\ &= \lim_{t \rightarrow b^-} \left(\frac{df(t)}{dt} \right) \\ &= \lim_{t \rightarrow b^-} \lim_{h \rightarrow 0} \frac{f(t+h) - f(t)}{h} \\ &= \lim_{t \rightarrow b^-} \lim_{h \rightarrow 0^-} \frac{f(t+h) - f(t)}{h} \\ &= \lim_{h \rightarrow 0^-} \lim_{t \rightarrow b^-} \frac{f(t+h) - f(t)}{h} \\ &= \lim_{h \rightarrow 0^-} \frac{f(b+h) - f(b)}{h} \\ &= \frac{df(b^-)}{dt}, \end{aligned}$$

which completes the proof. ■

It is known that in classical quantum derivative $D_q t^n = [n]_q t^{n-1}$ where $[n]_q = \frac{1-q^n}{1-q}$. The symmetric property in the right quantum derivative as follows:

Example 1. Let $f: [a, b] \rightarrow \mathbb{R}$, $f(t) = (t - b)^n$ for $n \in \mathbb{N}$, then

$$\begin{aligned} {}_b D_q f(t) &= {}_b D_q f(t - b)^n = \frac{(t-b)^n - ((qt + (1-q)b) - b)^n}{(1-q)(t-b)} \\ &= \frac{(b-t)^n - q^n (b-t)^n}{(1-q)(t-b)} \\ &= \frac{1-q^n}{1-q} (t - b)^{n-1} \\ &= [n]_q (t - b)^{n-1} \end{aligned}$$

Theorem 3.1. Let $f, g: [a, b] \rightarrow \mathbb{R}$ arbitrary functions, $\lambda \in \mathbb{R}$ constant, then

- (i) ${}_b-D_q[f(t) + g(t)] = {}_b-D_qf(t) + {}_b-D_qg(t)$, for all $t \in [a, b]$,
- (ii) ${}_b-D_q\lambda f(t) = \lambda {}_b-D_qf(t)$, for all $t \in [a, b]$,
- (iii) ${}_b-D_q(fg)(t) = f(t) {}_b-D_qg(t) + g(qt + (1 - q)b) {}_b-D_qf(t)$, for all $t \in [a, b]$,
- (iv) ${}_b-D_q\left(\frac{f}{g}\right)(t) = \frac{g(t) {}_b-D_qf(t) - f(t) {}_b-D_qg(t)}{g(t)g(qt+(1-q)b)}$,

for all $t \in [a, b] \setminus \{t: g(t)g(qt + (1 - q)b) \neq 0\}$.

Proof. It is omitted because the proof is quite easy and similar to the proof of [30, Theorem 3.1].

Definition 3.2. Let $f(t)$ be a function defined on $[a, b]$. Then the n th order right quantum derivative of $f(t)$ for $n \in \mathbb{N}$ is defined as

$$(3.5) \quad {}_b-D_q^n f(t) = {}_b-D_q({}_b-D_q^{n-1} f(t)) .$$

For the definition of the right definite quantum integral the following shift operator is used.

$$K_q F(t) := F(qt + (1 - q)b).$$

By Mathematical induction, we have $K_q^n F(t)$ can be written as

$$K_q^n F(t) = \begin{cases} K_q(K_q^{n-1} F)(t) = F(q^n t + (1 - q^n)b) & , n \in \mathbb{N} \\ F(t) & , n = 0 \end{cases} .$$

According to the Definition 3.1 and $K_q F(t)$

$${}_b-D_q F(t) = \frac{F(t) - F(qt + (1 - q)b)}{(1 - q)(t - b)} = \frac{1 - K_q}{(1 - q)(t - b)} F(t) = f(t).$$

It implies that the right quantum antiderivative of $F(t)$ can be expressed as :

$$F(t) = (1 - q) \frac{1}{1 - K_q} [(t - b)f(t)].$$

By using the geometric series expansion, the right quantum antiderivative of $f(t)$ can be written as:

$$(3.6) \quad \begin{aligned} F(t) &= (1 - q) \sum_{n=0}^{\infty} K_q^n [(t - b)f(t)] \\ &= (1 - q) \sum_{n=0}^{\infty} [(q^n t + (1 - q^n)b) - b] f(q^n t + (1 - q^n)b) \\ &= (1 - q)(t - b) \sum_{n=0}^{\infty} q^n f(q^n t + (1 - q^n)b), \end{aligned}$$

provided that if the series in the right-hand side of (3.6) converges. Symmetrically to Definition 2.2, definite quantum integral can be defined as follows:

Definition 3.3. Let $f(t)$ be a function defined on $[a, b]$. Then the right definite quantum integral of $f(t)$ on $[a, b]$ is described as:

$$(3.7) \quad \int_a^b f(t) {}_b-d_q t = F(b) - F(a) = (1 - q)(b - a) \sum_{n=0}^{\infty} q^n f(q^n a + (1 - q^n)b) .$$

If the series in right hand side of (3.7) is convergence, then $\int_a^b f(t) {}_b-d_q t$ is exist, i.e., $f(t)$ is right quantum integrable on $[a, b]$. For any $c \in (a, b)$

$$(3.8) \quad \int_a^c f(t) {}_b-d_q t = \int_a^b f(t) {}_b-d_q t - \int_c^b f(t) {}_b-d_q t ,$$

if the series in right hand side of (3.8) is convergence.

If $b = 0$ in (3.7), then

$$(3.9) \quad \int_a^0 f(t) {}_0-d_q t = (1-q)(-a) \sum_{n=0}^{\infty} q^n f(q^n a).$$

It is called as the right definite quantum integral of f on $[a, 0]$.

The question is that similar property as stated in Lemma 2.2 can be given or not for the right definite quantum integral on $[a, b]$. The answer is positive and as follows:

Lemma 3.2. Let $f: [a, b] \rightarrow \mathbb{R}$ be an arbitrary function. Provided that if $\int_a^b f(t) dt$ converges, then

$$(3.10) \quad \lim_{q \rightarrow 1^-} \int_a^b f(t) {}_b-d_q t = \int_a^b f(t) dt .$$

Proof. Let $\int_a^b f(t) dt$ converges, then $\int_0^1 f(ta + (1-t)b) dt$ converges also. Hence, by using Lemma 2.2, we have

$$\begin{aligned} \lim_{q \rightarrow 1^-} \int_a^b f(t) {}_b-d_q t &= \lim_{q \rightarrow 1^-} (1-q)(b-a) \sum_{n=0}^{\infty} q^n f(q^n a + (1-q^n)b) \\ &= (b-a) \lim_{q \rightarrow 1^-} \int_0^1 f(ta + (1-t)b) {}_0+d_q t \\ &= (b-a) \int_0^1 f(ta + (1-t)b) dt \\ &= \int_a^b f(t) dt. \end{aligned}$$

Some properties of the right definite quantum integral similar to the [30, Theorem 3.2, Theorem 3.3] are discussed in the following theorem. ■

Theorem 3.2. Let $f: [a, b] \rightarrow \mathbb{R}$ be arbitrary functions, $\lambda \in \mathbb{R}$ be a constant, then

- (i) $\int_a^b [f(t) + g(t)] {}_b-d_q t = \int_a^b f(t) {}_b-d_q t + \int_a^b g(t) {}_b-d_q t ,$
- (ii) $\int_a^b \lambda f(t) {}_b-d_q t = \lambda \int_a^b f(t) {}_b-d_q t ,$
- (iii) ${}_b-D_q \int_t^b f(s) {}_b-d_q s = -f(t) ,$ if f is right quantum integrable on $[t, b]$ for all $t \in [a, b]$,
- (iv) $\int_t^b {}_b-D_q f(s) {}_b-d_q s = f(b) - f(t) ,$ for all $t \in [a, b]$, if f is continuous on $[a, b]$,
- (v) $\int_t^b f(s) {}_b-D_q g(s) {}_b-d_q s = (fg)(b) - (fg)(t) - \int_t^b g(qs + (1-q)b) {}_b-D_q f(s) {}_b-d_q s ,$ if f is right quantum integrable on $[t, b]$ for all $t \in [a, b]$.

Proof. The proof of (i) and (ii) follows by direct computation by Definition 3.3.

(iii) Using Definitions 3.1 and 3.3, then

$$\begin{aligned} &{}_b-D_q \int_t^b f(s) {}_b-d_q s \\ &= \frac{\int_t^b f(s) {}_b-d_q s - \int_{qt+(1-q)b}^b f(s) {}_b-d_q s}{(1-q)(t-b)} \\ &= \frac{\left[- (1-q)(b-(qt+(1-q)b)) \sum_{n=0}^{\infty} q^n f(q^n (qt+(1-q)b) + (1-q^n)b) \right]}{(1-q)(t-b)} \end{aligned}$$

$$\begin{aligned}
 &= \frac{(b-t)\sum_{n=0}^{\infty} q^n f(q^n t + (1-q^n)b) - q(b-t)\sum_{n=0}^{\infty} q^n f(q^{n+1}t + (1-q^{n+1})b)}{(t-b)} \\
 &= \sum_{n=1}^{\infty} q^n f(q^n t + (1-q^n)b) - \sum_{n=0}^{\infty} q^n f(q^n t + (1-q^n)b) \\
 &= -f(t).
 \end{aligned}$$

(iv) Similarly to (iii), we have

$$\begin{aligned}
 &\int_t^b {}_b D_q f(s) {}_b d_q s \\
 &= \int_t^b \frac{f(s) - f(qs + (1-q)b)}{(1-q)(s-b)} {}_b d_q s \\
 &= \frac{1}{(1-q)} \left[\int_t^b \frac{f(s)}{s-b} {}_b d_q s - \int_t^b \frac{f(qs + (1-q)b)}{s-b} {}_b d_q s \right] \\
 &= \frac{1}{(1-q)} \left[(1-q)(b-t) \sum_{n=0}^{\infty} q^n \frac{f(q^n t + (1-q^n)b)}{(q^n t + (1-q^n)b - b)} \right. \\
 &\quad \left. - (1-q)(b-t) \sum_{n=0}^{\infty} q^n \frac{f(q(q^n t + (1-q^n)b) + (1-q)b)}{(q^n t + (1-q^n)b - b)} \right] \\
 &= (b-t) \sum_{n=0}^{\infty} q^n \frac{f(q^n t + (1-q^n)b)}{q^n(t-b)} - (b-t) \sum_{n=0}^{\infty} q^n \frac{f(q^{n+1}t + (1-q^{n+1})b)}{(q^n(t-b))} \\
 &= \sum_{n=0}^{\infty} f(q^{n+1}t + (1-q^{n+1})b) - \sum_{n=0}^{\infty} f(q^n t + (1-q^n)b) \\
 &= \lim_{k \rightarrow \infty} [f(q^{k+1}t + (1-q^{k+1})b) - f(t)] \quad (\text{Since } f(t) \text{ is continuous}) \\
 &= f(b) - f(t).
 \end{aligned}$$

(v) Using Theorem 3.1 (ii), we have

$$(3.11) \quad f(s) {}_b D_q g(s) = {}_b D_q (fg)(s) - g(qs + (1-q)b) {}_b D_q f(s).$$

Taking the right definite quantum integral of (3.11) on $[t, b]$, it gives that

$$(3.12) \quad \int_t^b f(s) {}_b D_q g(s) {}_b d_s = \int_t^b {}_b D_q (fg)(s) {}_b d_s - \int_t^b g(qs + (1-q)b) {}_b D_q f(s) {}_b d_s.$$

If the previous result is used in (3.12), then the desired result is obtained. ■

4. CORRECTION OF “QUANTUM OSTROWSKI INEQUALITIES FOR DIFFERENTIABLE CONVEX FUNCTIONS”

In this section the right quantum derivative and the right quantum integral are used to correct the identity given in [22, Lemma 3.1].

Lemma 4.1. Let $f: [a, b] \rightarrow \mathbb{R}$ be an arbitrary function with ${}_a D_q f$ and ${}_b D_q f$ are left quantum integrable on $[a, b]$, then we have

$$\begin{aligned}
 (4.1) \quad & f(x) - \frac{1}{b-a} \left[\int_a^x f(t) {}_{a+}d_q t + \int_x^b f(t) {}_{b-}d_q t \right] \\
 &= \frac{q(x-a)^2}{b-a} \int_0^1 t {}_{a+}D_q f(tx + (1-t)a) {}_{0+}d_q t \\
 &\quad - \frac{q(b-x)^2}{b-a} \int_0^1 t {}_{b-}D_q f(tx + (1-t)b) {}_{0+}d_q t
 \end{aligned}$$

for all $x \in [a, b]$.

Proof. From [22, Lemma 3.1] , we have

$$(4.2) \quad = \frac{q(x-a)^2}{b-a} \int_0^1 t {}_{a+}D_q f(tx + (1-t)a) {}_{0+}d_q t = \frac{x-a}{b-a} f(x) - \frac{1}{b-a} \int_a^x f(t) {}_{a+}d_q t .$$

Similarly, we have

$$\begin{aligned}
 (4.3) \quad & - \frac{q(b-x)^2}{b-a} \int_0^1 t {}_{b-}D_q f(tx + (1-t)b) {}_{0+}d_q t \\
 &= - \frac{q(b-x)^2}{b-a} \int_0^1 t \frac{f(tx+(1-t)b)-f(tx+(1-tq)b)}{(1-q)t(x-b)} {}_{0+}d_q t \\
 &= \frac{q(b-x)}{(b-a)(1-q)} \left[\int_0^1 f(tx + (1-t)b) {}_{0+}d_q t - \int_0^1 f(tx + (1-tq)b) {}_{0+}d_q t \right] \\
 &= \frac{q(b-x)}{(b-a)(1-q)} \left[(1-q) \sum_{n=0}^{\infty} q^n f(q^n x + (1-q^n)b) \right. \\
 &\quad \left. - (1-q) \sum_{n=0}^{\infty} q^n f(q^{n+1}x + (1-q^{n+1})b) \right] \\
 &= \frac{q(b-x)}{(b-a)} \left[\sum_{n=0}^{\infty} q^n f(q^n x + (1-q^n)b) - \frac{1}{q} \sum_{n=1}^{\infty} q^n f(q^n x + (1-q^n)b) \right] \\
 &= \frac{q(b-x)}{(b-a)} \left[\sum_{n=0}^{\infty} q^n f(q^n x + (1-q^n)b) - \frac{1}{q} \sum_{n=0}^{\infty} q^n f(q^n x + (1-q^n)b) + \frac{f(x)}{q} \right] \\
 &= \frac{q(b-x)}{(b-a)} \left[\left(1 - \frac{1}{q} \right) \sum_{n=0}^{\infty} q^n f(q^n x + (1-q^n)b) + \frac{f(x)}{q} \right] \\
 &= \frac{(b-x)}{(b-a)} f(x) - \frac{1}{b-a} \left[(1-q)(b-x) \sum_{n=0}^{\infty} q^n f(q^n x + (1-q^n)b) \right] \\
 &= \frac{(b-x)}{(b-a)} f(x) - \frac{1}{b-a} \int_x^b f(t) {}_{b-}d_q t .
 \end{aligned}$$

Summing (4.2) and (4.3), we get (4.1). ■

By using Lemma 4.1, [22, Theorem 3.1 and Theorem 3.2] are corrected as follows:

Theorem 4.1. (Correction to [22, Theorem 3.1]) Let $f: [a, b] \rightarrow \mathbb{R}$ be an arbitrary function with ${}_{a+}D_q f$ and ${}_{b-}D_q f$ are left quantum integrable on $[a, b]$. If $|{}_{a+}D_q f|$ and $|{}_{b-}D_q f|$ are convex functions, $|{}_{a+}D_q f(x)| \leq M$ and $|{}_{b-}D_q f(x)| \leq M$ for all $x \in [a, b]$, then we have

$$(4.4) \quad \left| f(x) - \frac{1}{b-a} \left[\int_a^x f(t) {}_{a+}d_q t + \int_x^b f(t) {}_{b-}d_q t \right] \right| \leq \frac{qM[(x-a)^2+(b-x)^2]}{(b-a)(1+q)} .$$

Theorem 4.2. (Correction to [22, Theorem 3.2]) Let $f: [a, b] \rightarrow \mathbb{R}$ be an arbitrary function with ${}_a^+D_q f$ and ${}_b^-D_q f$ are left quantum integrable on $[a, b]$. If $|{}_a^+D_q f|^r$ and $|{}_b^-D_q f|^r$ are convex functions for $p, r > 1, \frac{1}{p} + \frac{1}{r} = 1$, $|{}_a^+D_q f(x)| \leq M$ and $|{}_b^-D_q f(x)| \leq M$ for all $x \in [a, b]$, then we have

$$(4.5) \quad \left| f(x) - \frac{1}{b-a} \left[\int_a^x f(t) {}_a^+d_q t + \int_x^b f(t) {}_b^-d_q t \right] \right| \leq \frac{qM[(x-a)^2+(b-x)^2]}{(b-a)} \left(\frac{1-q}{1-q^{p+1}} \right)^{\frac{1}{p}}.$$

5. SOME NEW QUANTUM INTEGRAL INEQUALITIES

In this section, new quantum Hermite-Hadamard type inequalities are investigated with respect to the left and right definite quantum integrals.

Theorem 5.1. Let $f: [a, b] \rightarrow \mathbb{R}$ be a convex function and $0 < q < 1$. Then we have

$$(5.1) \quad f\left(\frac{a+b}{2}\right) \leq \frac{1}{2(b-a)} \left[\int_a^b f(t) {}_a^+d_q t + \int_a^b f(t) {}_b^-d_q t \right] \leq \frac{f(a)+f(b)}{2}.$$

Proof. Clearly

$$(5.2) \quad \begin{aligned} \int_0^1 f(tb + (1-t)a) {}_0^+d_q &= (1-q) \sum_{n=0}^{\infty} q^n f(q^n b + (1-q^n)a) \\ &= \frac{1}{b-a} [(1-q)(b-a) \sum_{n=0}^{\infty} q^n f(q^n b + (1-q^n)a)] \\ &= \frac{1}{b-a} \int_a^b f(t) {}_a^+d_q t, \end{aligned}$$

$$(5.3) \quad \begin{aligned} \int_0^1 f(ta + (1-t)b) {}_0^+d_q &= (1-q) \sum_{n=0}^{\infty} q^n f(q^n a + (1-q^n)b) \\ &= \frac{1}{b-a} [(1-q)(b-a) \sum_{n=0}^{\infty} q^n f(q^n a + (1-q^n)b)] \\ &= \frac{1}{b-a} \int_a^b f(t) {}_b^-d_q t, \end{aligned}$$

Since $f(t)$ is a convex function on $[a, b]$, then we have

$$(5.4) \quad f\left(\frac{a+b}{2}\right) \leq \frac{1}{2} [f(tb + (1-t)a) + f(ta + (1-t)b)] \leq \frac{f(a)+f(b)}{2},$$

for all $t \in [0,1]$. Taking the left definite quantum integral on all sides of the inequalities (5.4) over $[0,1]$, using (5.2) and (5.3), we have (5.1). ■

Similarly to Theorem 2.1, the right quantum Hermite-Hadamard inequality can be given as follows:

Theorem 5.2. Let $f: [a, b] \rightarrow \mathbb{R}$ be a convex function and $0 < q < 1$. Then we have

$$(5.5) \quad f\left(\frac{a+qb}{1+q}\right) \leq \frac{1}{b-a} \int_a^b f(t) {}_b^-d_q t \leq \frac{f(a)+qf(b)}{1+q}.$$

Proof. It is omitted because the proof is similar to the proof of Theorem 2.1.

In the following quantum Hermite-Hadamard type inequalities, the left and right quantum integrals are used together.

Theorem 5.3. Let $f: [a, b] \rightarrow \mathbb{R}$ be a convex function and $0 < q < 1$. Then we have

$$(5.6) \quad \frac{f\left(\frac{qa+b}{1+q}\right)+f\left(\frac{a+qb}{1+q}\right)}{2} \leq \frac{1}{2(b-a)} \left[\int_a^b f(t) {}_{a+}d_q t + \int_a^b f(t) {}_{b-}d_q t \right] \leq \frac{f(a)+f(b)}{2}.$$

Proof. Adding (2.7) and (5.5) side by side and multiplying the final inequality by $\frac{1}{2}$, implies (5.6) ■

Remark 5.1. Since any convex function $f(t)$ and $0 < q < 1$. we have $f\left(\frac{a+b}{2}\right) \leq \frac{f\left(\frac{qa+b}{1+q}\right)+f\left(\frac{a+qb}{1+q}\right)}{2}$, i.e., (5.6) is better than (5.1).

Theorem 5.4. Let $f, g : [a, b] \rightarrow [0, \infty)$ be the right quantum integrable functions on $[a, b]$ for $0 < q < 1$, $r, s > 1$ and $\frac{1}{r} + \frac{1}{s} = 1$. Then we have :

$$(5.7) \quad \int_a^b f(t)g(t) {}_{b-}d_q t \leq \left(\int_a^b f^r(t) {}_{b-}d_q t \right)^{1/r} \left(\int_a^b g^s(t) {}_{b-}d_q t \right)^{1/s}.$$

Proof. Using classical Hölder inequality for sum and Definition 3.3,

$$\begin{aligned} \int_a^b f(t)g(t) {}_{b-}d_q &= (1-q)(b-a) \sum_{n=0}^{\infty} q^n f(q^n a + (1-q^n)b)g(q^n a + (1-q^n)b) \\ &= (1-q)(b-a) \\ &\quad \times \sum_{n=0}^{\infty} \left[(q^n)^{1/r} f(q^n a + (1-q^n)b) \right] \left[(q^n)^{1/s} g(q^n a + (1-q^n)b) \right] \\ &\leq (1-q)(b-a) \left(\sum_{n=0}^{\infty} q^n f^r(q^n a + (1-q^n)b) \right)^{1/r} \\ &\quad \times \left(\sum_{n=0}^{\infty} q^n g^s(q^n a + (1-q^n)b) \right)^{1/s} \\ &= \left((1-q)(b-a) \sum_{n=0}^{\infty} q^n f^r(q^n a + (1-q^n)b) \right)^{1/r} \\ &\quad \times \left((1-q)(b-a) \sum_{n=0}^{\infty} q^n g^s(q^n a + (1-q^n)b) \right)^{1/s} \\ &= \left(\int_a^b f^r(t) {}_{b-}d_q t \right)^{1/r} \left(\int_a^b g^s(t) {}_{b-}d_q t \right)^{1/s}. \end{aligned}$$

The proof is completed. ■

Theorem 5.5. Let $f : [a, b] \rightarrow \mathbb{R}$ be a right quantum differentiable function for $0 < q < 1$ and ${}_{b-}D_q f \in L_\infty[a, b]$, then we have

$$(5.8) \quad \left| (b-a) \frac{f(a)+f(b)}{2} - \int_a^b f(qt + (1-q)b) {}_{b-}d_q t \right| \leq \frac{(b-a)^2}{2(1+q)} \| {}_{b-}D_q f \|_\infty,$$

where $\| {}_{b-}D_q f \|_\infty = \sup_{t \in [a,b]} | {}_{b-}D_q f(t) |$.

Proof. Using Theorem 3.2 (v) (The right quantum partial integration formula), we get

$$(5.9) \quad \begin{aligned} &\int_a^b \left(\frac{a+b}{2} - t \right) {}_{b-}D_q f(t) {}_{b-}d_q t \\ &= \left[\left(\frac{a+b}{2} - t \right) f(t) \right] (b) - \left[\left(\frac{a+b}{2} - t \right) f(t) \right] (a) \end{aligned}$$

$$\begin{aligned}
 & - \int_a^b f(qt + (1-q)b) {}_{b-D_q} \left(\frac{a+b}{2} - t \right) {}_{b-d_q} s \\
 & = - \frac{(b-a)}{2} f(a) - \frac{(b-a)}{2} f(b) + \int_a^b f(qt + (1-q)b) {}_{b-d_q} s \\
 & = -(b-a) \frac{f(a)+f(b)}{2} + \int_a^b f(qt + (1-q)b) {}_{b-d_q} s .
 \end{aligned}$$

Then from (5.9), we have

$$\begin{aligned}
 (5.10) \quad & \left| (b-a) \frac{f(a)+f(b)}{2} - \int_a^b f(qt + (1-q)b) {}_{b-d_q} s \right| \\
 & \leq \int_a^b \left| \frac{a+b}{2} - t \right| | {}_{b-D_q} f(t) | {}_{b-d_q} t \\
 & \leq \int_a^b \left| \frac{a+b}{2} - t \right| \| {}_{b-D_q} f \|_\infty {}_{b-d_q} s \\
 & = \| {}_{b-D_q} f \|_\infty \int_a^b \left| \frac{a+b}{2} - t \right| {}_{b-d_q} s .
 \end{aligned}$$

Calculating the following right quantum integral,

$$\begin{aligned}
 (5.11) \quad & \int_a^b \left| \frac{a+b}{2} - t \right| {}_{b-d_q} t \\
 & = \left[\int_a^{\frac{a+b}{2}} \left(\frac{a+b}{2} - t \right) {}_{b-d_q} t + \int_{\frac{a+b}{2}}^b \left(t - \frac{a+b}{2} \right) {}_{b-d_q} t \right] \\
 & = \left[\int_a^{\frac{a+b}{2}} \left(\frac{a+b}{2} - t \right) {}_{b-d_q} t + 2 \int_{\frac{a+b}{2}}^b \left(t - \frac{a+b}{2} \right) {}_{b-d_q} t \right] \\
 & = \left[\begin{array}{l} (1-q)(b-a) \sum_{n=0}^{\infty} q^n \left[\left(\frac{a+b}{2} - (q^n a + (1-q^n)b) \right) \right] \\ + 2(1-q) \left(b - \frac{a+b}{2} \right) \sum_{n=0}^{\infty} q^n \left[\left(q^n \frac{a+b}{2} + (1-q^n)b \right) - \frac{a+b}{2} \right] \end{array} \right] \\
 & = \left[\begin{array}{l} (1-q)(b-a) \left[\frac{a+b}{2} \sum_{n=0}^{\infty} q^n - a \sum_{n=0}^{\infty} q^{2n} - b \sum_{n=0}^{\infty} q^n + b \sum_{n=0}^{\infty} q^{2n} \right] \\ + 2(1-q) \left(b - \frac{a+b}{2} \right) \left[\frac{a+b}{2} \sum_{n=0}^{\infty} q^{2n} + b \sum_{n=0}^{\infty} q^n - b \sum_{n=0}^{\infty} q^{2n} - \frac{a+b}{2} \sum_{n=0}^{\infty} q^n \right] \end{array} \right] \\
 & = \left[\begin{array}{l} (b-a) \left[\frac{a+b}{2} - \frac{a}{1+q} - b + \frac{b}{1+q} \right] \\ + 2 \left(b - \frac{a+b}{2} \right) \left[\frac{a+b}{2(1+q)} + b - \frac{b}{1+q} - \frac{a+b}{2} \right] \end{array} \right] \\
 & = \left[(b-a)^2 \left[\frac{1}{1+q} - \frac{1}{2} \right] + (b-a)^2 \left[\frac{1}{2} - \frac{1}{2(1+q)} \right] \right] \\
 & = \frac{(b-a)^2}{2(1+q)} .
 \end{aligned}$$

The desired inequality is obtained from combining (5.10) and (5.11), we have (5.8). This completes the proof.

■

6. CONCLUSION

Quantum integral inequalities on an arbitrary finite interval is widely studied in the papers [6,7], [18]-[36] and some others. From now on, they should be considered as the left quantum integral inequalities. Definitions of the right quantum derivative and the right definite quantum integral are bear a torch to many asymmetric investigations. Using the left and right quantum integrals together could give interesting results.

Competing interests

The authors declare that they have no competing interests.

Authors' contributions

The authors contributed equally to the writing of this paper. The authors read and approved the final manuscript.

Funding

Not applicable

Acknowledgements

Not applicable

Availability of Data and Materials

Data sharing not applicable to this article as no datasets were generated or analyzed during the current study.

REFERENCES

- [1] Ali MA, Abbas M, Budak H, Agarwal P, Murtaza G, Chu YM. New quantum boundaries for quantum Simpson's and quantum Newton's type inequalities for preinvex functions. *Advances in Difference Equations* 2021; 2021(2): 1-21.
- [2] Ali M, Budak H, Abbas M, Chu YM. Quantum Hermite-Hadamard-type inequalities for functions with convex absolute values of second q^b -derivatives. *Advances in Difference Equations* 2021; 2021(1): 1-12.
- [3] Ali MA, Budak H, Zhang Z, Yıldırım H. Some new Simpson's type inequalities for coordinated convex functions in quantum calculus. *Mathematical Methods in the Applied Sciences* 2021; 44(6): 4515-4540.
- [4] Ali MA, Chu YM, Budak H, Akkurt A, Yıldırım H, Zahid MA. Quantum variant of Montgomery identity and Ostrowski-type inequalities for the mappings of two variables. *Advance in Difference Equations*, 2021; 2021(1): 1-26.
- [5] Annaby MH, Mansour ZS. *q-Fractional Calculus and Equations*: Springer, Heidelberg, 2012.
- [6] Alp N, Sarıkaya MZ. A new definition and properties of quantum integral which calls \bar{q} -integral. *Konuralp J Math* 2017; 5 (2):146-159.
- [7] Alp N, Sarıkaya MZ, Kunt M, İşcan İ. q -Hermite Hadamard inequalities and quantum estimates for midpoint type inequalities via convex and quasi-convex functions. *J King Saud Univ Sci* 2018; 30 (2): 193-203.
- [8] Awan MU, Talib S, Kashuri A, Noor MA, Chu YM. Estimates of quantum bounds pertaining to new q -integral identity with applications. *Advances in Difference Equations* 2020; 2020(1): 1-15.
- [9] Awan MU, Talib S, Kashuri A, Noor MA, Noor KI, Chu YM. A new q -integral identity and estimation of its bounds involving generalized exponentially μ -preinvex functions. *Advances in Difference Equations* 2020; 2020(1): 1-12.
- [10] Budak H, Ali MA, Tarhanacı M. Some new quantum Hermite-Hadamard-like inequalities for coordinated convex functions. *Journal of Optimization Theory and Applications* 2020; 189(3): 899-910.
- [11] Budak H, Ali MA, Tunç T. Quantum Ostrowski-type integral inequalities for functions of two variables. *Mathematical Methods in the Applied Sciences* 2020.
- [12] Budak H, Erden S, Ali MA. Simpson and Newton Type inequalities for convex functions via newly defined quantum integrals. *Mathematical Methods in the Applied Sciences* 2021; 44(1): 378-390.
- [13] Bermudo S, Korus P, Valdes JEN. On q -Hermite-Hadamard inequalities for general convex functions, *Acta Math Hungar* 2020; 162 (1): 364-374
- [14] Dragomir SS, Agarwal R. Two inequalities for differentiable mappings and applications to special means of real numbers and to trapezoidal formula. *Applied Mathematics Letters* 1998; 11(5): 91-95
- [15] Erden S, İftikhar S, Delavar MR, Kumam P, Thounthong P, Kumam W. On generalizations of some inequalities for convex functions via quantum integrals. *Revista de la Real Academia de Ciencias Exactas, Físicas y Naturales. Serie A. Matemáticas* 2020; 114(3): 1-15.
- [16] Kavurmacı H, Avci M, Özdemir ME. New inequalities of Hermite-Hadamard type for convex functions with applications. *Journal of Inequalities and Applications* 2011; 2011(1): 1-11.
- [17] Kac V, Cheung P. *Quantum calculus*: Springer 2001.
- [18] Kunt M, İşcan İ, Alp N, Sarıkaya MZ. (p, q) -Hermite-Hadamard inequalities and (p, q) -estimates for midpoint type

- inequalities via convex and quasi-convex functions, RACSAM 2018; 112: 969-992.
- [19] Kunt M, Kashuri A, Du TS, Baidar AW. Quantum Montgomery identity and some new quantum integral inequalities, AIMS Math. 2020; 5(6): 5439-5457.
- [20] Kunt M, Latif MA, İşcan İ, Dragomir SS. Quantum Hermite-Hadamard type inequality and some estimates of quantum midpoint type inequalities for double integrals. Sigma J Eng Nat Sci. 2019; 37(1): 207-223.
- [21] Khan MA, Mohammad N, Nwaeze ER, Chu YM. Quantum Hermite-Hadamard inequality by means of a Green function. Advances in Difference Equations 2020; 2020(1): 1-20.
- [22] Noor MA, Awan MU, Noor KI, Quantum Ostrowski inequalities for q -differentiable convex functions. J Math Inequal. 2016; 10(4):1013-1018.
- [23] Noor MA, Noor KI, Awan MU. Some quantum estimates for Hermite-Hadamard inequalities. Appl Marth Comput 2015; 251: 675-679.
- [24] Noor MA, Noor KI, Awan MU. Some quantum integral inequalities via preinvex functions. Appl Math Comput 2015; 269: 242-251.
- [25] Prabseang J, Nonlaopon K, Ntouyas SK. On the refinement of quantum Hermite-Hadamard inequalities for continuous convex functions. J Math Inequal 2020; 14(3): 875-885.
- [26] Pearce CE, Pearic J. Inequalities for differentiable mappings with application to special means and quadrature formulae. Applied Mathematics Letters 2000; 13(2): 51-55.
- [27] Rashid S, Butt SI, Kanwal S, Ahmad H, Wang MK. Quantum Integral Inequalities with Respect to Raina's Function via Coordinated Generalized-Convex Functions with Applications. Journal of Function Spaces 2021.
- [28] Sudsutad , Ntouyas SK, Tariboon T. Quantum integral inequalities for convex functions. J Math Inequal 2015; 9(3): 781-793.
- [29] Tunç M, Gov E, Balgeçti S. Simpson type quantum integral inequalities for convex functions. Miskolc Math Notes 2018; 19 (1): 649-664.
- [30] Tariboon J, Ntouyas SK. Quantum calculus on finite intervals and applications to impulsive difference equations. Adv Difference Equ 2013; 282:1-19.
- [31] Tariboon J, Ntouyas SK. Quantum integral inequalities on finite intervals. J Inequal Appl 2014; 121: 1-13.
- [32] Zhang T, Du TS, Wang H, Shen YJ. Different types of quantum integral inequalities via (α, m) -convexity. J Inequal Appl 2018; 264: 1-24.
- [33] Vivas-Cortez M, Aamir Ali, M, Kashuri A, Bashir Sial I, Zhang Z. Some new Newton's type integral inequalities for coordinated convex functions in quantum calculus. Symmetry 2020; 12(9): 1476.
- [34] Vivas-Cortez M, Kashuri A, Liko R, Hernandez JE. Some new q -integral inequalities using generalized quantum Montgomery identity via preinvex functions. Symmetry 2020; 12(4): 553.
- [35] You X, Kara H, Budak H, Kalsoom H. Quantum Inequalities of Hermite-Hadamard Type for-Convex Functions. Journal of Mathematics 2021.
- [36] Zhuang H, Liu W, Park J. Some quantum estimates of Hermite-Hadamard inequalities for quasi-convex functions. Math 2019; 7(2): 1-18.

Dynamic Response of Concentrically Braced Steel Frames to Pulse Period in Near-Fault Ground Motions

Zeliha TONYALI¹, Muhammet YURDAKUL², Hasan SESLİ^{3*}

¹ Department of Civil Engineering, The Faculty of Engineering and Architecture, Recep Tayyip Erdoğan University, Rize, Turkey

² Department of Civil Engineering, The Faculty of Technology, Karadeniz Technical University, Trabzon, Turkey

³ Department of Civil Engineering, The Faculty of Engineering, Yalova University, Yalova, Turkey

¹ zeliha.tonyali@erdogan.edu.tr, ² m.yurdakul@ktu.edu.tr, ³ hasan.sesli@yalova.edu.tr

(Geliş/Received: 06/05/2022;

Kabul/Accepted: 02/08/2022)

Abstract: Steel braced frame systems (SBFs) having high stiffness and high strength are commonly utilized due to their resistance to lateral seismic forces in regions with high seismicity. In this study, concentrically braced frames (CBFs) having different bracing configurations are used to obtain the significance of the pulse period associated with near-fault (NF) ground motion by time-history dynamic analysis. Besides, far-fault (FF) ground motions are also used to compare with NF ground motion results according to changing bracing configurations. To achieve dynamic responses of steel frames with different concentric bracings under NF ground motions, which especially have small, medium, and long pulse periods, 3-story and 4-span CBFs having different bracing configurations were selected as an example. 4 FF and 12 NF ground motions having different pulse durations were chosen to evaluate the dynamic response of concentrically braced frames. The results showed that peak ground acceleration (PGA) could be identified as a key parameter that controls the response of braced frames under FF ground motions. In addition, the ratio of the pulse duration to the first mode period is the dominant parameter when this ratio is only greater than 1.0 under the NF ground motions.

Key words: Dynamic response, pulse period, near-fault, concentric bracing, steel frames.

Merkezi Çaprazlı Çelik Çerçevelerin Yakın-Fay Yer Hareketlerinin Darbe Periyoduna Dinamik Tepkisi

Öz: Hem yüksek rijitliğe hem de yüksek dayanıma sahip olan çelik çaprazlı çerçeve sistemler, depremselliğin yüksek olduğu bölgelerde yanal sismik yüklerle karşı gösterdikleri performans nedeniyle yaygın olarak kullanılmaktadır. Bu çalışmada, yakın fay yer hareketi ile ilişkili olan darbe periyotlarının farklı çapraz konfigürasyonlarına sahip merkezi çaprazlı çerçevelerin üzerindeki etkisini ortaya koymak için zaman tanım alanında dinamik analizler gerçekleştirilmiştir. Bununla birlikte, farklı çapraz konfigürasyonlarının yakın fay yer hareketi altındaki davranışlarının değerlendirilebilmesi için uzak fay yer hareketleri de dikkate alınmıştır. Özellikle küçük, orta ve uzun darbe periyotlarına sahip yakın fay yer hareketleri altında farklı merkezi çaprazlara sahip çelik çerçevelerin dinamik tepkilerini elde etmek için farklı çapraz konfigürasyonlarına sahip 3 katlı ve 4 açıklıklı merkezi gergili çerçeveler uygulama çalışması olarak seçilmiştir. Merkezi çaprazlı çerçevelerin dinamik tepkisini değerlendirmek için farklı darbe sürelerine sahip 4 uzak fay ve 12 yakın fay yer hareketi kullanılmıştır. Sonuçlar, en büyük yer ivmesi değerinin (PGA) uzak fay yer hareketleri altında çaprazlı çerçevelerin tepkisini kontrol eden bir anahtar parametre olarak tanımlanabileceğini göstermiştir. Yakın fay yer hareketlerinde ise darbe periyodunun birinci mod titreşim periyoduna oranının (T_p/T_1) sadece 1.0 değerinden büyük olduğu durumlarda etkin parametre olduğu belirlenmiştir.

Anahtar kelimeler: Dinamik davranış, darbe periyodu, yakın fay, merkezi çapraz, çelik çerçeveler.

1. Introduction

Several research has been carried out to assure the safety of steel building structures exposed to lateral loads like earthquakes and winds, in recent years. Different studies have been carried out for steel frame systems according to these studies. One of the most common of these applications accepted by the current seismic codes is steel braced frames. Braces used in the moment-resisting frame systems (MRFs) are widely used in both concentrically braced frames (CBFs) and eccentrically braced frames (EBFs). A bracing member is used to increase the stiffness of the CBFs laterally axes cross in a single point in the connections between beams. However, the axes in EBFs do not intersect in a single node or point. Elements with large cross-sectional dimensions should be used to ensure adequate rigidity in MRFs. However, in the case of the use of the braces, the stiffness for the

* Corresponding author: hasan.sesli@yalova.edu.tr. ORCID Number of authors: ¹ 0000-0002-6637-7949, ² 0000-0002-3904-3206, ³ 0000-0003-3328-5922

frame systems may be ensured, the displacements and drifts are kept at a desirable level, and also a more economical solution is provided.

When the last decades of studies are surveyed, there are many studies on steel braced frame (SBF) systems. Martinelli et al. [1] investigated the dynamic behavior of CBFs under different earthquake ground excitations. A six-story MRF designed according to Eurocode 8 was analyzed and compared with the results of CBFs. Analysis results showed that CBFs were more effective than MRFs. Balendra and Huang [2] presented a study to determine the ductility and over-strength of split X-braced and reverse V-braced frames designed according to BS5950. As a result of the study, although the over-strength factors and the ductility factors were nearly identical, the response modification factor was reduced depending on the number of stories. Kim and Choi [3] presented a comparative study with reverse V-type CBF and ordinary CBF systems. In the study, ductility, over-strength, and response modification factors were investigated depending on story heights and bays. Dicleli and Mehta [4] studied non-buckling EBFs. To assess the performance of non-buckling EBFs, time history and static pushover analysis were executed. The results of the analysis were compared to the results of CBFs. It is obtained that non-buckling EBFs have less damage than CBFs. Khandelwal et al. [5] used a verified computational simulation on a 10-story building to investigate the progressive collapse resistance of SBFs. Their study showed that the CBF is sensitive to progressive collapse compared to the EBF. Coffield and Adeli [6] studied the structural response of 3D SBFs under blast loading. In the comparative study, three different frame systems were considered, such as MRF, CBF, and EBF. Shiravand and Shabani [7] investigated nonlinear dynamic analysis of 3D structural models of special moment frames, CBFs, and EBFs with 10, 5, and 3 stories under blast loadings. The performance levels, ductility ratios, plastic hinge rotations, and flexural moments obtained from the analysis compared with each other. The results of the analysis showed that EBFs are generally more effective than other systems under burst loads. Qi et al. [8] investigated the seismic performance of EBFs with K-shape and V-shape braced systems designed regarding the Chinese Seismic Design Code. Although V-shape braces were more effective for seismicity, K-shape braces were found to have a lower capacity against seismic loadings. Larijan et al. [9] assessed the developing collapse of steel buildings along with CBF and EBF. Braced bays were investigated for bay numbers and the locations of braces. It has been obtained that the X-braced and reverse V-braced frame systems offer a better strength capacity for progressive collapse, according to a study of both two and three braced bays in the external frames. Bosco et al. [10] proposed a design procedure for MRF and EBF according to Eurocode 8, and dynamic analysis was performed to develop the procedure for buildings founded on soft and hard soil. Karsaz and Tosee [11] examined the seismic performance of 5, 10, and 15-story steel buildings using braces with MRF and different CBF under different earthquake ground excitations. The analysis result showed that X-braced systems have better performance for initial stiffness and yield stress for low-rise buildings, whereas mid-and high-rise buildings with EBF have the least damage and higher ductility performance under an earthquake. It has been observed that the performance of the building with EBF will increase when the story heights are increased. Yaman and Ağcakoca [12] determined the structural performance of some types of CBF shear walls having regular and irregular geometry in steel buildings. It has been observed that the diagonal CBF steel system has more energy absorption capacity than the reverse V-braced shear wall system. Faroughi et al. [13] examined the effects of the number and the location of the braced bays. Nonlinear analysis was performed on five- and eight-story buildings. It has been shown that the number of bays is less effective than the position of braced bays in terms of redundancy and the height of the building is effective in determining the number of braced bays. Additionally, it is not advised to place the bracing solely around the outside of the plan for dual structural systems. Altan [14] performed a static and dynamic analysis of CBF and EBF systems having 5, 10 and 15-story steel structures defined in the Turkish Earthquake Code 2018. It is concluded that eccentrically reverse V-braced systems are more effective than the other bracing systems for stiffness and ductility. Yao et al. [15] aimed to the enhancement of the energy dissipation capacity of prefabricated tension-only concentrically braced beam-through frames (BTFs). The effects of link length, link section, and bracing angle are investigated on seven full-scale eccentrically braced BTFs. Short links improved the load capacity and stiffness of frames, whereas the increment in bracing angle leads to reduce ductility. Haji et al. [16] investigated a new type of EBF and proposed the truss-shaped brace. It is concluded from the analysis that the hollow square cross-sections are very effective for strength and dissipation of energy. Barbagallo et al. [17] investigated the behavior of anti-buckling braces and bi-stage yield buckling braces of CBF and EBF designed according to Eurocode 8. Rouhi and Hamidi [18] used a performance-based plastic design to investigate the influence of forward-directivity on EBFs. To that end 6, 12, and 18-story EBFs were analyzed under NF ground excitations using ETABS software. Allowable drift limits of the EBF frames designed according to the current code were exceeded under NF earthquakes with a forward directivity effect. Gürsoy and Yılmaz [19] investigated the behavior of different EBFs and MRSFs under earthquake excitation. As a result of their study, they showed that models with EBFs are safer than MRSFs.

The results of these research studies showed that although analyses were conducted using various CBFs, the behavior of these frame systems subjected to NF has not comprehensively been studied yet. In this study, aiming to fill this gap, different types of CBFs [20] and MRFs were investigated under ordinary FF ground excitations and NF ground excitations with variable pulse durations. The analysis results of the models having different braced arrangements have been compared for three types of NF and one type of FF earthquake motion sets.

2. NF Ground Motions

One of the most significant dynamic stresses on buildings is strong ground excitation. For the structures, the effects of its characteristics are much more important than the magnitude of an earthquake. Its effects depend on variables such as the amplitude, duration, and frequency content of the ground excitation, as well as the mass of the structure, the natural period, damping, and stiffness. Ground excitations in the NF region can differ greatly from those of FF earthquakes further away from the epicenter.

NF ground excitations are defined as ground vibrations that take place within 20 kilometers of the rupture [21-24]. The velocity pulse duration must be larger than 1.00 seconds and also the ratio of the peak ground velocity (PGV) to the peak ground acceleration (PGA) must be larger than 0.10 seconds [25]. The permanent ground displacements and long-period pulses seem obvious in NF ground excitations. This feature is not visible in recordings gathered in FF regions [26].

NF ground excitations can be categorized as having or not having a pulse signal. Because it is simpler to recognize the pulse from the velocity waveforms, they are used to identify the pulse signals [27]. Figure 1 depicts velocity time series for comparing the NF ground excitation with and without a pulse signal.

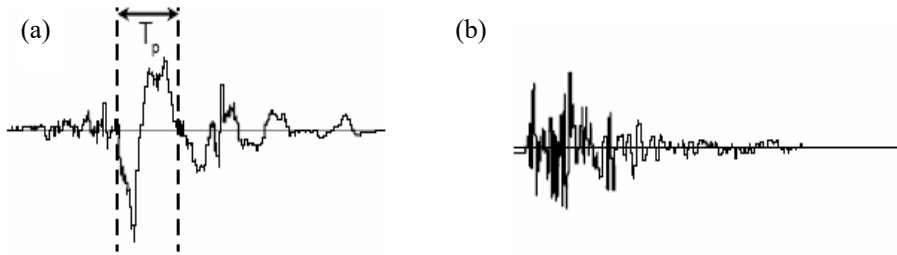


Figure 1. Velocity time series with a pulse (a) and without pulse (b) signals.

Fundamentally, the important response parameters for the structures are the peak values of ground displacement (PGD), velocity (PGV), and acceleration (PGA). NF ground excitations with long-period pulses have a high PGV/PGA ratio, which significantly impacts their responses [28]. The pulse amplitude and duration increase displacements and drift demands. When compared to FF movements, the velocity-sensitive spectral region for NF recordings is substantially narrower, while the acceleration-sensitive and displacement-sensitive sections are much wider. NF ground excitations required a greater strength demand than FF motions for the same ductility factor. The reaction for both NF and FF ground movements became identical if the periods were normalized to the transition time of the acceleration-sensitive area [29]. Resonance can considerably increase the demands on a structure if the pulse period and the fundamental period of the structure are aligned [30]. Much demand can be required for a structure under a large number of remarkable cycles. Fortunately, only one or two remarkable cycles occur mostly in the case of forward-directivity. The pulse period is the period at which the ratio of the spectral velocity of the peak-to-peak velocity (PPV) pulse to the median spectral velocity from the Next Generation Attenuation (NGA) models is at a maximum [31]. PPV is also the difference between the two peaks in a single motion cycle.

T_p/T_1 is a critical number which is a ratio of the pulse duration to the first mode period for specifying the structural response under NF ground excitations with pulse or pulse-like motions [27,32-33]. Although the earthquake motion records with T_p/T_1 have larger mode effects and maximum reaction at higher stories, the short period structures under the records with a large pulse have a maximum ductility demand in bottom stories [32].

In the present study, an MRF and different types of CBFs given in TBEC-2018 [20] were subjected to two types of ground excitation records, which are NF ground excitation having different pulse durations and ordinary FF records. The period of the pulse (extracted pulse, T_p) is identified as the time needed to complete a full velocity cycle and is obtained in the velocity time history (VTH) of the selected ground excitations. The duration of extracted pulse period is considered by selecting a proper NF ground excitation and selected motions are also

classified sets as large, medium, and small pulses as shown in Table 1. The large, medium and small pulse periods are respectively over 3 sec., a range of about 1.5 sec. and about 2.9 sec., and smaller than about 1.2 sec. Besides, every record set given in Table 1 which contained three types of NF and one type of FF earthquake motion, which are nearly the same PGV/PGA .

In addition, the original VTH of ground excitations with the associated extracted pulses for all types of selected motions are given in Figures 2-4. The pulse velocities associated with selected motions are drawn [34] software according to the method proposed by Kardoutsou et al. [35]. It can be seen easily in Figure 2 that the extracted pulse for NF small pulse covers substantially the entire time history as compared to the NF medium (Figure 3) and NF large (Figure 4) pulses.

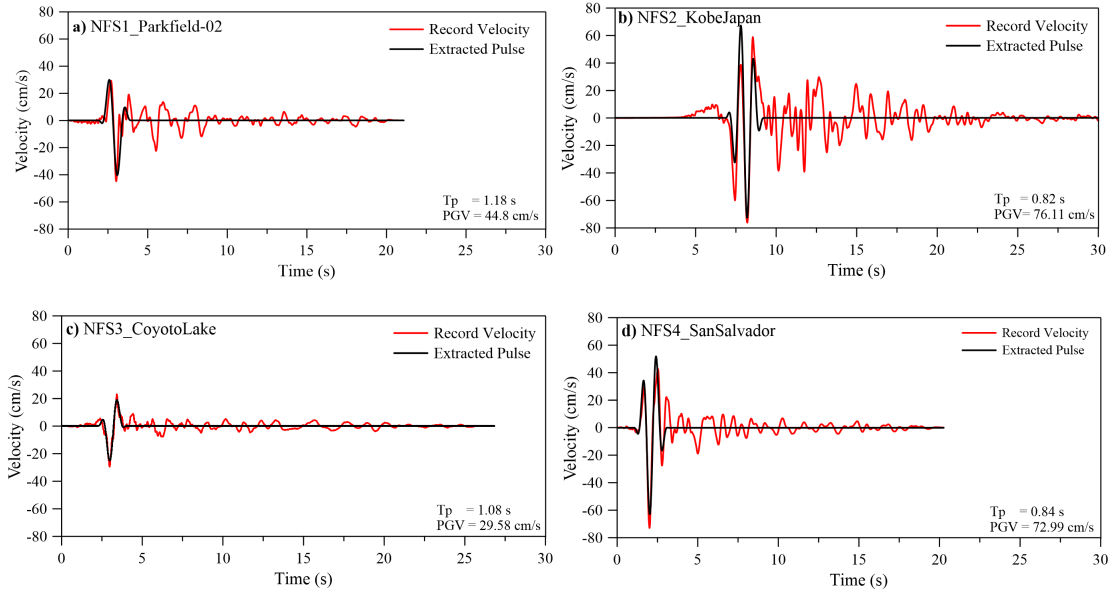


Figure 2. VTHs of NF small pulse.

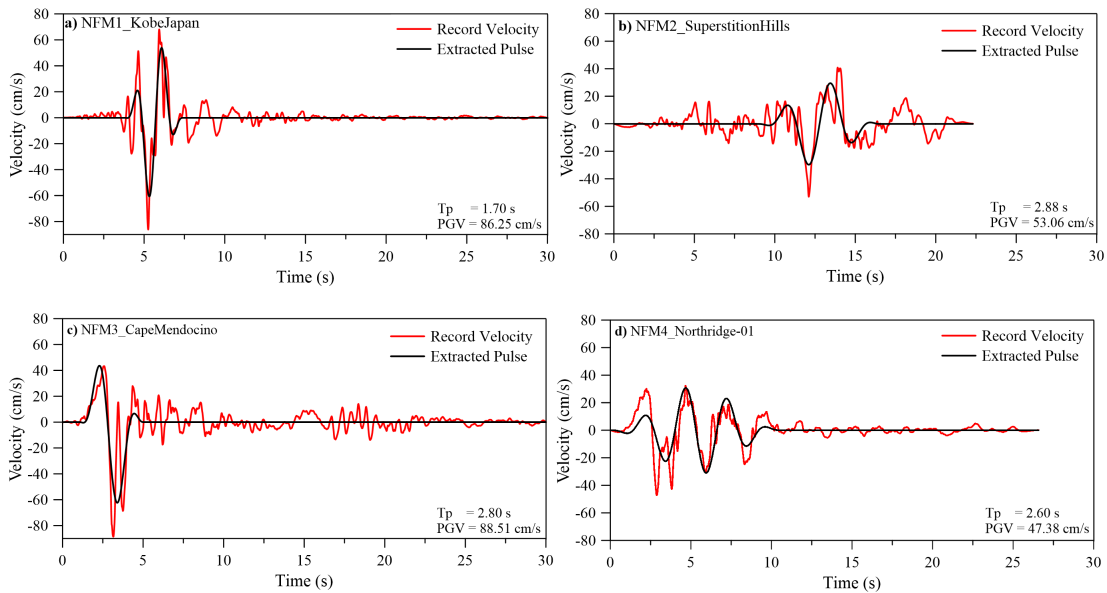


Figure 3. VTHs of NF medium pulse.

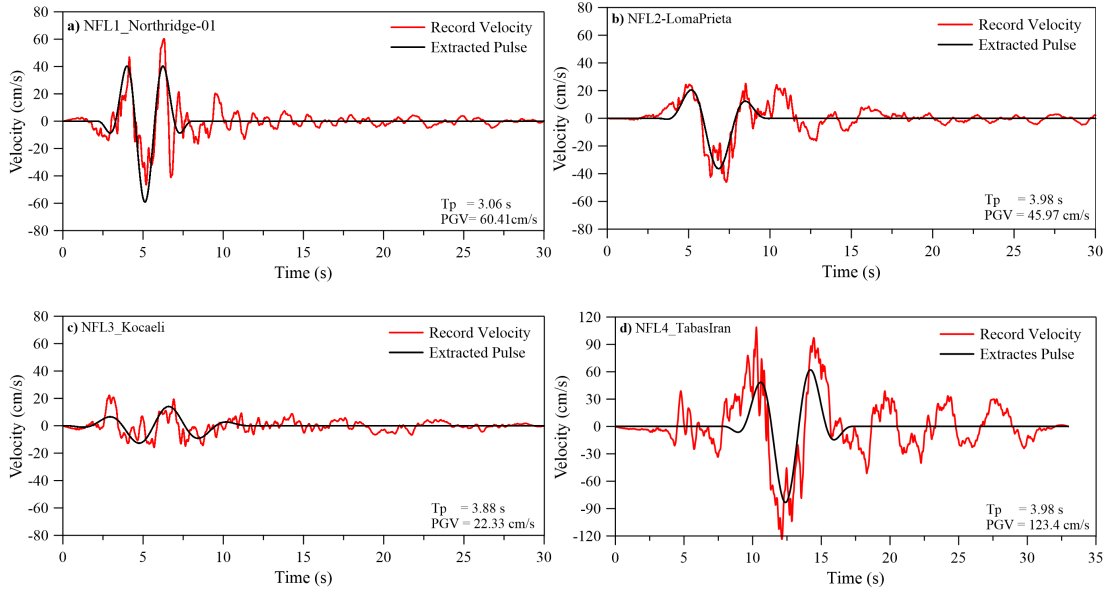


Figure 4. VTHs of NF large pulse.

Table 1. Dynamic characteristics of selected ground motions [36]

Motion Type	RSN	Earthquake	M_w	Station	R_{rup} (km)	PGA (g)	PGV (cm/s)	$\frac{PGV}{PGA}$	T_p (sec)
NFL*	1085	Northridge-01	6.69	Sylmar - Converter Sta East	5.19	0.449	60.41	0.14	3.06
	802	Loma Prieta	6.93	Saratoga - Aloha Ave	8.50	0.326	45.97	0.14	3.98
	1165	Kocaeli, Turkey	7.51	İzmit	7.21	0.165	22.33	0.14	3.88
	143	Tabas, Iran	7.35	Tabas	2.05	0.862	123.4	0.15	3.98
NFM*	1013	Northridge-01	6.69	LA Dam	5.92	0.324	47.38	0.15	2.60
	1119	Kobe, Japan	6.90	Takarazuka	0.27	0.614	86.25	0.14	1.70
	723	Superstition Hills-02	6.54	Parachute Test Site	0.95	0.384	53.06	0.14	2.88
	828	Cape Mendocino	7.01	Petrolia	8.18	0.662	88.51	0.14	2.80
NFS*	4100	Parkfield-02, CA	6.00	Parkfield - Cholame 2WA	3.01	0.373	44.80	0.12	1.18
	1106	Kobe, Japan	6.90	KJMA	0.96	0.630	76.11	0.12	0.82
	569	San Salvador	5.80	National Geographical Inst	6.99	0.534	72.99	0.14	0.84
	148	Coyote Lake	5.74	Gilroy Array #3	7.42	0.256	29.58	0.12	1.08
FF*	491	Taiwan SMART1(33)	5.80	SMART1 O01	41.99	0.049	2.02	0.04	-
	5802	Iwate, Japan	6.90	Yokote O Morimachi	44.86	0.219	8.49	0.04	-
	6949	Darfield, New Zealand	7.00	PEEC	53.75	0.117	4.59	0.04	-
	436	Borah Peak, ID-01	6.88	CPP-601	82.60	0.040	1.60	0.04	-

NFL* NF ground motions (large-pulse period)
 NFM* NF ground motions (medium-pulse period)
 NFS* NF ground motions (small-pulse period)
 FF* FF ground motions

3. Structures Description and Modeling

The geometric details of the structures considered for linear time-history analyses are demonstrated in Figure 5. The MRF system is expressed as an unbraced frame system in this study. The different five frame types [20] were selected and designed according to AISC360-16 [37]. Each model has three stories and 4-span in the x-

direction, the span length and the story height are 6 m and 3 m, respectively. The dynamic analyses were carried out using SAP2000 [38] under FF and NF earthquake ground excitations considered models of the study. The models consist of an unbraced frame system and the five braced models of CBFs defined in [20]. The braces are located on the two side spans of the structure in CBFs as shown in Figure 5. The frames are represented on the x-z plane since the linear time history analyses are done in plane. The profile sections used are given in Table 2. Young's modulus was taken as 2.1×10^5 MPa. S275 [37] steel material type was used in the considered models.

Table 2. Section details for the model

<i>Story</i>	<i>Beam</i>	<i>Column</i>	<i>Diagonal</i>
1	HE120A	HE140A	HE120A
2			
3			

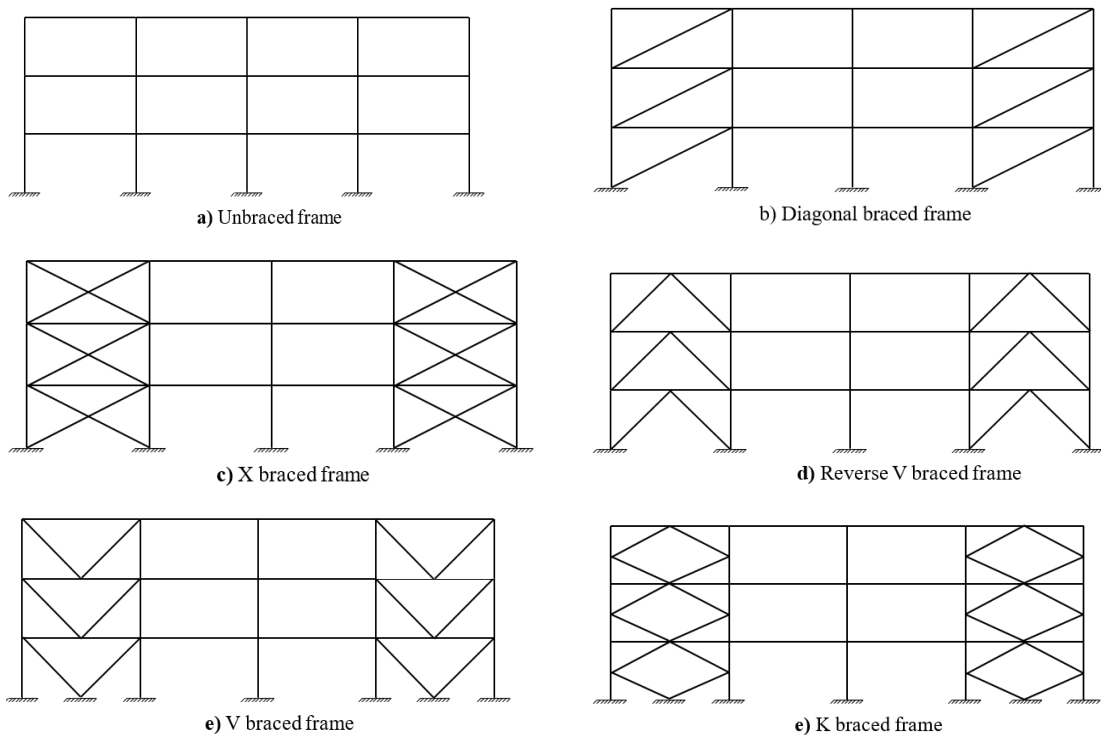


Figure 5. Typical unbraced and concentrically braced steel frame systems.

4. Results and Discussion

Firstly, the behavior of the unbraced steel frame system subjected to four different ground excitations categories consisting of NF and FF was investigated. As a result of the modal analysis, the fundamental period values of the unbraced steel frame and structural models having different steel braced types, performed according to the mode coupling method are given in Table 3.

The unbraced frame system has the largest dominant period while the reverse V-braced frame system has the smallest period as can be seen from Table 3. This shows that the period values are significantly reduced with the use of brace elements in the structural models. This finding shows that the period values of the steel braced frame models decrease with the increase in the rigidity of the structure caused by using steel brace elements.

As a part of the analysis's results interpretation, NFL, MFM, and NFS abbreviations used in the figures are NF large pulse, NF medium pulse, and NF small pulse, respectively. The maximum floor displacements of the unbraced frame system under the earthquake categories are given in Figure 6. The maximum story displacements that were obtained under the Iwate-Japan earthquake ground excitation were higher than those of other ground excitations, as can be seen from Figure 6-a. The other FF ground excitations with much smaller PGA values

compared to the Iwate-Japan earthquake motion (PGA=0.219g) record caused very small displacements close to each other. By examining four NF records with small pulses (NFS), the Kobe-Japan earthquake record motion having a higher PGA value (0.630g) has a noticeable effect on the story displacements (Figure 6-b). All results of the NF effects are much greater than FF ground excitations. The parameter PGA of the motions has been very effective than pulse duration (T_p) and PGV/PGA values for the displacements. Therefore, the maximum story displacement values are obtained from Kobe-Japan, San-Salvador, Parkfield-02, and Coyote-Lake earthquakes for NFS pulses, respectively. For category NFM (Figure 6-c), the higher displacements are obtained from Kobe-Japan earthquake record motions with smaller pulse duration. Since the PGA values of the Northridge-01 and Superstition-Hills earthquake record motions are smaller than the Kobe-Japan and San-Salvador earthquake motions, which have also the largest pulse duration less maximum story displacements are obtained compared to other earthquakes. Considering Figure 6-d, in the Tabas-Iran earthquake having a greater PGA value (0.862g), the maximum and the largest story displacements occurred. Although the Kocaeli Earthquake has a large impact duration, braced frame systems are subject to smaller storey displacements under the Kocaeli earthquake, which has a smaller PGA (0.165g) than other earthquake ground excitations.

Table 3. The periods depend on the vibration modes of the considered models

Models	Fundamental Period (sec.)		
	1 st Mode	2 nd Mode	3 rd Mode
Unbraced frame	0.3615	0.1076	0.0583
Diagonally braced frame	0.0540	0.0190	0.0156
X-braced frame	0.0404	0.0168	0.0166
Reverse V-braced frame	0.0368	0.0160	0.0150
V-braced frame	0.0454	0.0169	0.0164
K-braced frame	0.0407	0.0325	0.0325

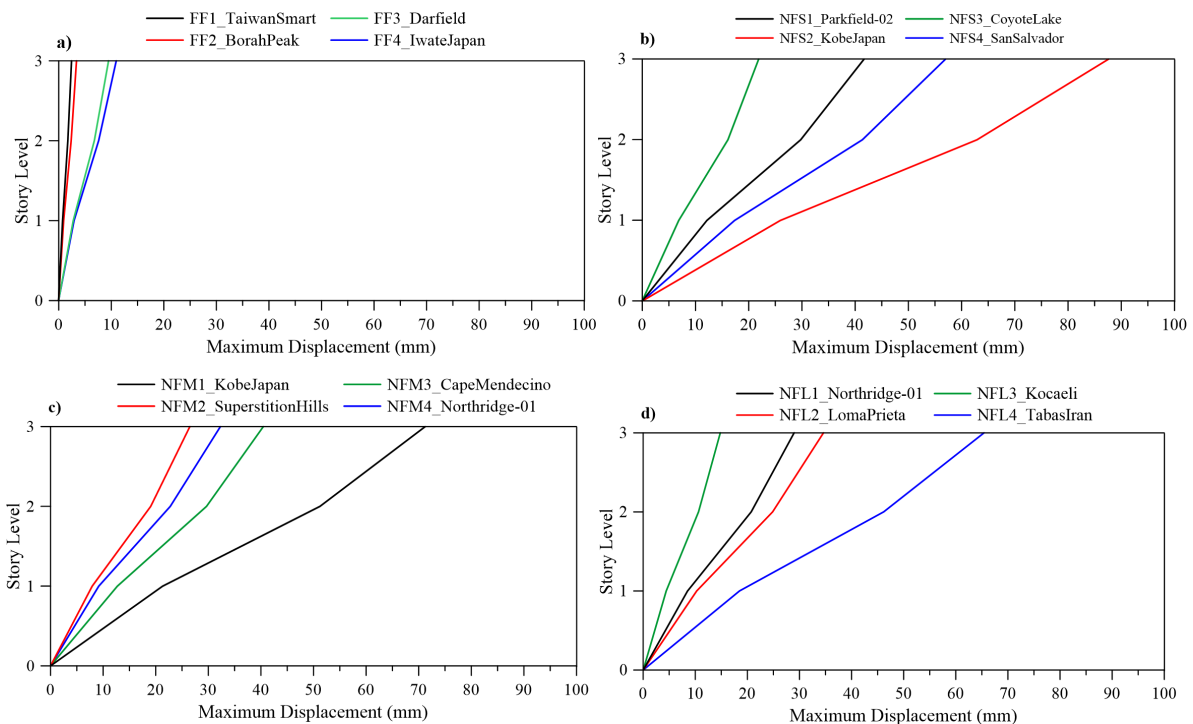


Figure 6. Maximum lateral displacement for the unbraced frame system.

Iwate-Japan earthquake ground excitation, which has higher results than those of other FF ground excitations. The other FF ground excitations having much smaller PGA values as compared to the Iwate-Japan earthquake motion record caused very small displacements and have close displacements. By examining NFS pulse results (Figure 7-

b), although the story displacements up to the 2nd story are close to each other in the Kobe and Salvador earthquakes, they are different at the 3rd story. While the largest story displacement in the unbraced system is in the Kobe earthquake, the story displacements in the diagonal frame system are close to each other. By examining NFM pulse results (Figure 7-c), the Cape Mendocino earthquake record motion having a higher PGA value has a noticeable effect on the story displacements. All results are nearly greater than FF ground excitations. Therefore, the maximum story displacement values are obtained from Cape Mendocino, Kobe Japan, Superstition Hills, and Northridge earthquakes, respectively. While the largest story displacement in the unbraced system is in the Kobe earthquake, the largest story displacement in the diagonal frame system is in the Cape Mendocino earthquake. It can be depicted from Figure 7-d that the Tabas-Iran earthquake having a greater PGA gave larger maximum story displacements for the diagonal steel frame system. The PGA values have been very effective than pulse duration for the story displacements. Besides, the maximum story displacement values are obtained from Tabas-Iran, Northridge, Loma Prieta, and Kocaeli earthquakes, respectively. As in the unbraced system, the largest story displacement is observed in the Iran Tabas earthquake.

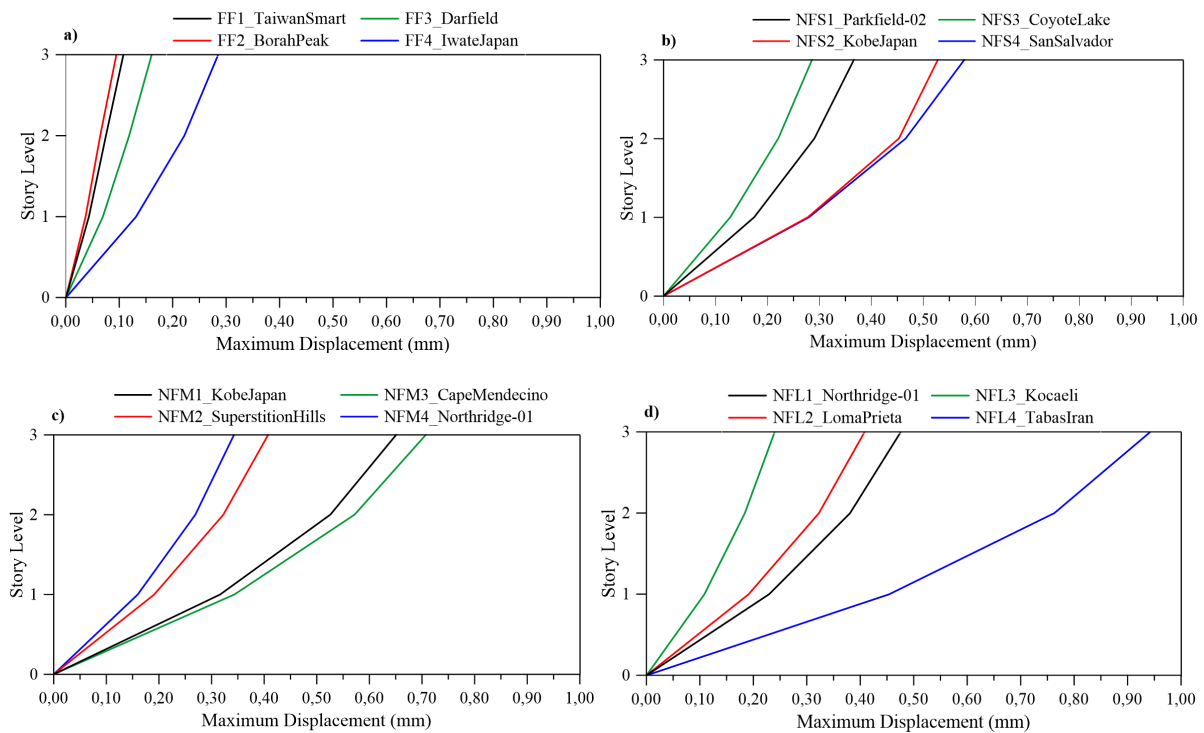


Figure 7. Maximum lateral displacement for the diagonally braced frame system.

The maximum story displacements for the X-braced frame are given in Figure 8. As it can be seen from Figure 8-a, the maximum story displacements of the X-braced frame system are obtained under the Iwate-Japan earthquake for FF ground excitations. The other FF ground excitations having much smaller PGA values compared to the Iwate-Japan earthquake record caused very small displacements and have close displacements. By examining NFS pulse results (Figure 8-b), the maximum story displacement occurred Kobe Japan earthquake having the biggest PGA in the X-braced frame system. The PGA values have been very effective than pulse duration for the story displacements. The story displacements in the X-braced frame are quite small compared to the unbraced system. In the NFM pulse results (Figure 8-c), the Cape Mendocino earthquake record motion having a higher PGA value (0.662g) has been quite effective on the maximum story displacements. All results for NF are much greater than FF ground excitations. Having nearly the same PGV/PGA motions, the maximum story displacement values are obtained from Cape Mendocino, Kobe Japan, Superstition Hills, and Northridge earthquakes, respectively. While the largest story displacement in the unbraced system is in the Kobe earthquake, the largest story displacement in the X-braced frame system is in the Cape Mendocino earthquake. It can be depicted from Figure 8-d that the Tabas-Iran earthquake having a greater PGA result in larger story displacements for the X-braced frame system. Also, the maximum story displacement values were obtained from Tabas-Iran,

Northridge, Loma Prieta, and Kocaeli earthquakes, respectively. As in the unbraced system, the largest story displacement is observed in the Tabas-Iran earthquake in the X-braced frame system.

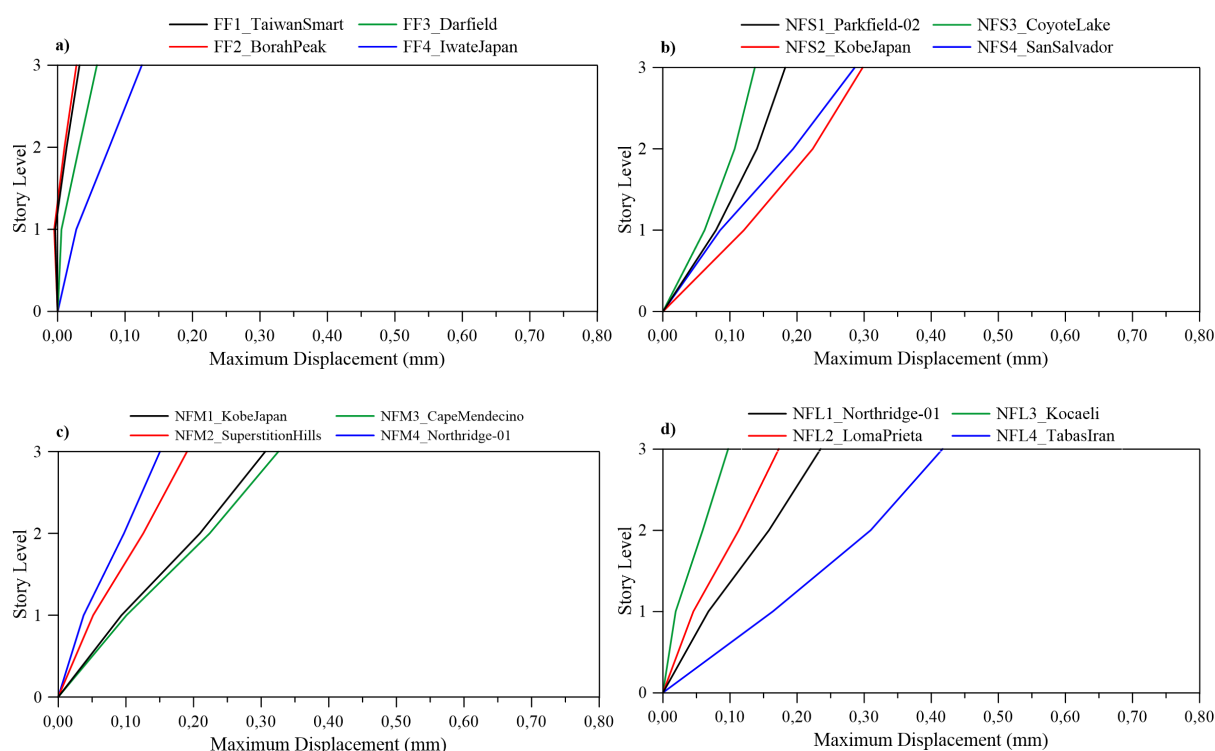


Figure 8. Maximum lateral displacement for the X-braced frame system.

The variation of lateral displacements at every floor level of the reverse V-braced steel frame system is presented in Figure 9. As can be seen in Figure 9-a that the maximum displacements occur under Iwate-Japan earthquake ground excitation like in the unbraced frame, whereas the Darfield-New Zealand earthquake lost effects on the lateral displacements. When the reverse V-braced steel frame system is subjected to four NF records with NFS pulse in Figure 9-b, it is clear that the lateral displacements obtain from the Kobe-Japan and the San Salvador earthquakes, which caused a larger displacement and had less pulses, come close to the lateral displacements obtained from the Parkfield-02 and Coyote-Lake record motions. Figure 9-c shows that the Superstition-Hills and Cape-Mendocino earthquake record motions which had large velocity pulse duration were very effective compared to the unbraced frame. However, the Kobe-Japan earthquake which caused larger displacements on the unbraced frame has not had larger displacements since it had a smaller velocity pulse duration. It can be depicted from Figure 9-d that the Tabas-Iran earthquake having a greater PGA and pulse duration results in larger maximum story displacements for the reverse V-braced steel frame system. Although the displacements obtained from the Loma-Prieta Earthquake have decreased, the lateral displacements for the Northridge-01 earthquake have considerably increased compared to the unbraced frame system.

The maximum story displacement results deal with the V-braced steel frame system under different earthquake motions are presented in Figure 10. Although the similarities observed in the other frames are also seen in this frame, Figure 10-a shows that the Iwate-Japan earthquake ground excitation greatly increases efficiency in the V-braced frame compared to the others. From Figure 10-b, it is observed that Kobe-Japan has less pulses and larger PGA values cause larger displacements same as the San Salvador earthquake, but it lost effectiveness compared to the unbraced frame system. Figure 10-c illustrated that the Kobe-Japan earthquake, which has a smaller velocity pulse duration, has not larger displacements compared to the unbraced frame, and also the Cape-Mendocino earthquake which has a larger velocity pulse duration and a larger PGA value results in the maximum lateral displacements. It can be seen from Figure 10-d that the Tabas-Iran earthquake having a greater PGA and pulse duration caused the large structural demand for the V-braced steel frame system. The Loma-Prieta

earthquake lost the efficiency of structural behavior of the V-braced steel frame system compared to the unbraced frame system.

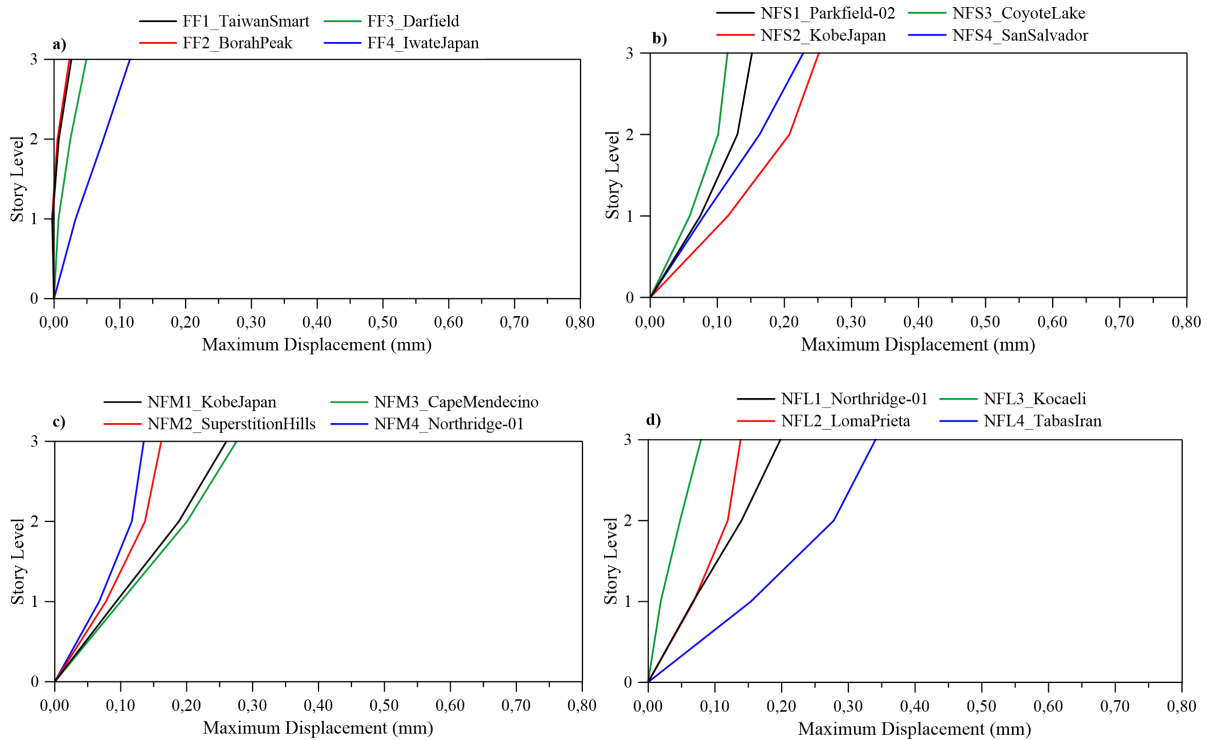


Figure 9. Maximum lateral displacement for the reverse V-braced frame system.

The results of analysis obtained from the K-braced frame system for FF earthquakes showed that the results are obtained as similar to the unbraced frame system, but the Darfield Earthquake gave less lateral displacement compared to the unbraced frame system (Figure 11-a). It can be said that PGA values are very effective for FF earthquakes. The investigation of the lateral displacements of K-braced frame systems under near-fault earthquake motions with small pulse duration present that the Kobe-Japan earthquake which has a small pulse duration compared to the other had less effect on the structural behavior according to the unbraced frame system (Figure 11-b). According to Figure 11-c, the Kobe-Japan earthquake lost the efficiency in structural behavior compared to the unbraced since this motion has a low pulse duration. Whereas the Cape-Mendocino and the Superstition Hills-02 earthquakes have a low effect on the unbraced frame system, these record motions, which have large pulse durations, caused an increase in the displacements of the K-braced frame systems. When Figure 11-d is examined, the Tabas-Iran earthquake is very effective on the structural behavior of the K-braced frame system same as unbraced frame system. The Loma-Prieta Earthquake is not effective on the structural behavior of the K-braced steel frame system compared to the unbraced frame system.

Figure 12 shows the relationship between different frame systems and FF earthquake motions for the maximum displacements of the top floor. When the first-mode periods of vibrations given in Table 3 are considered, all results obtained from six-different frame systems depend on the first-mode periods of vibrations. The Iwate-Japan and the Darfield-New Zealand earthquakes have large PGA values in the FF earthquakes. The maximum top floor displacements are obtained as 10.98 mm, 0.285 mm, 0.125 mm, 0.115 mm, 0.207 mm, and 0.134 mm under the Iwate-Japan earthquake for unbraced, diagonal braced, X-braced, reverse V-braced, V-braced, K-braced, respectively. Similarly, the top floor displacements are as 9.51 mm, 0.16 mm, 0.058 mm, 0.049 mm, 0.097 mm, and 0.062 mm for the Darfield-New Zealand earthquake. The percentage variations in displacements derived from two record motions were 13%, 44%, 54%, 57%, 53% and 54%, respectively. For the FF earthquakes, PGA values and the stiffness are the effective parameters for steel frame systems, and also as long as the stiffness of the system is increased, the structural demands are increased depending on PGA values.

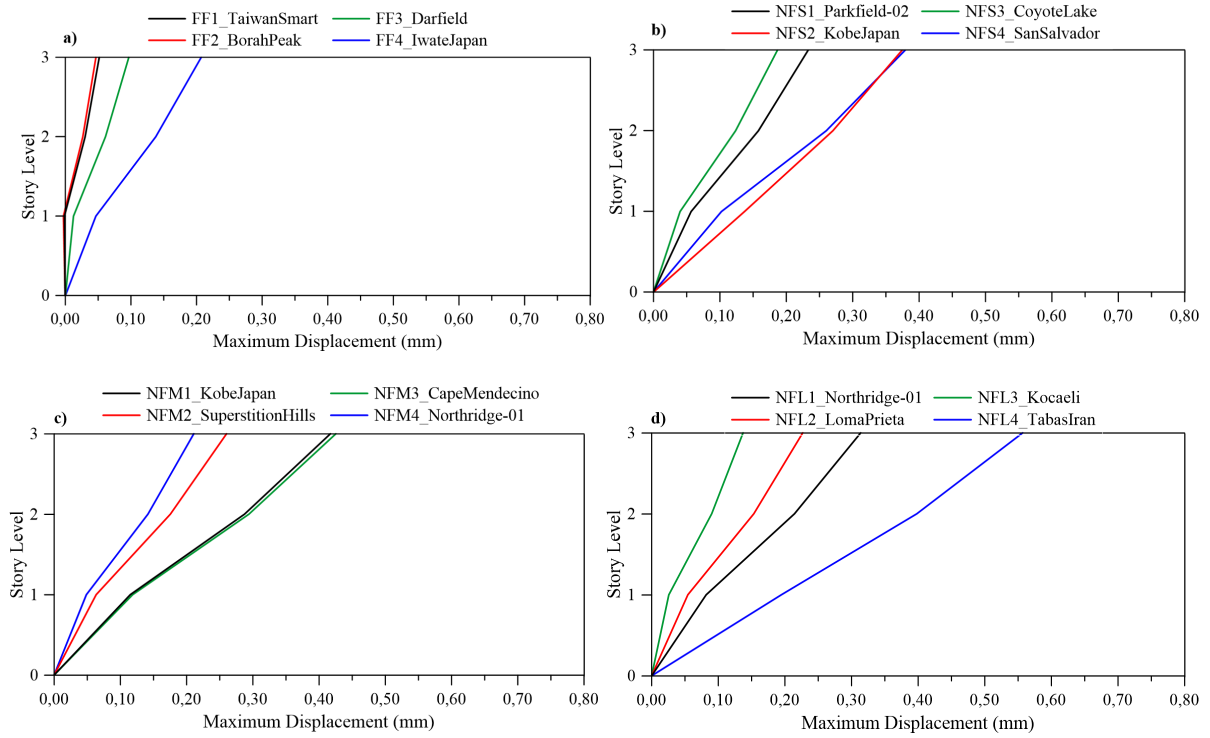


Figure 10. Maximum lateral displacement for the V-braced frame system.

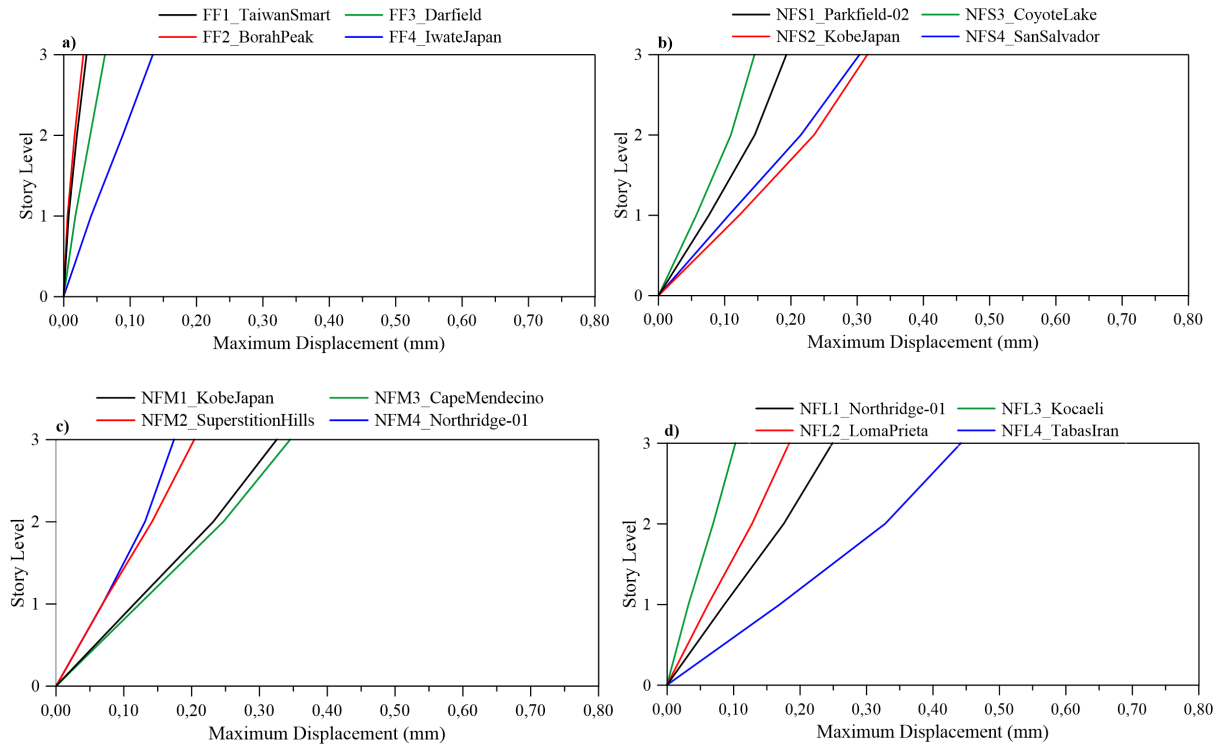


Figure 11. Maximum lateral displacement for the K-braced frame system.

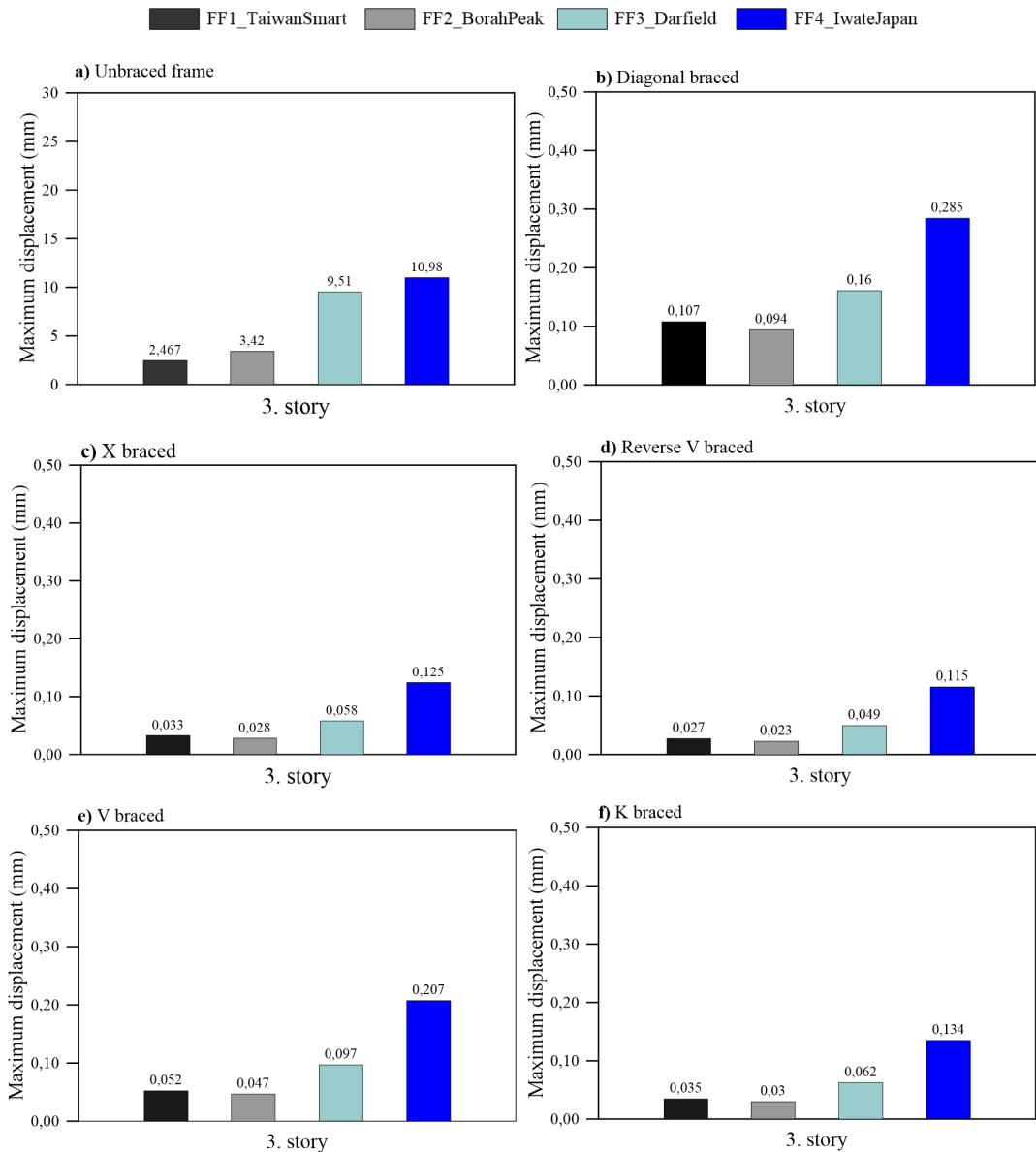


Figure 12. Maximum horizontal displacements considering different bracing models for the FF.

The maximum displacements of top floors for the considered models are compared according to NFS pulse duration in Figure 13. Kobe-Japan and San-Salvador earthquakes have both large PGA values and lower pulse duration compared to other earthquakes with small pulses. For this record motions, the variations in displacements are -35%, 9.60%, -4%, -9.20%, 1% and -3.80% according to the results of Kobe-Japan earthquake. When the diagonal braced frame system, which is the more flexible braced system, is compared to the reverse V-braced system, which is a most stiff system, in considering to first mode period, the variation in percentage is 58%, 52%, 60% and 60% for the Parkfield-02, Kobe-Japan, Coyote-Lake, and San-Salvador, respectively. The Kobe-Japan earthquake having a large PGA is very effective on the reverse V-braced system, which is a very stiff braced system. While the unbraced frame system has a 26% variation in the top floor displacements under the Parkfield-02 and San-Salvador earthquakes, the variation in the top floor displacements are 36%, 36%, 33%, 38%, 36% for diagonal, X-braced, reverse V-braced, V-braced and K-braced frame systems, respectively. PGA values are significant parameter in the systems for the NFS pulse motions.

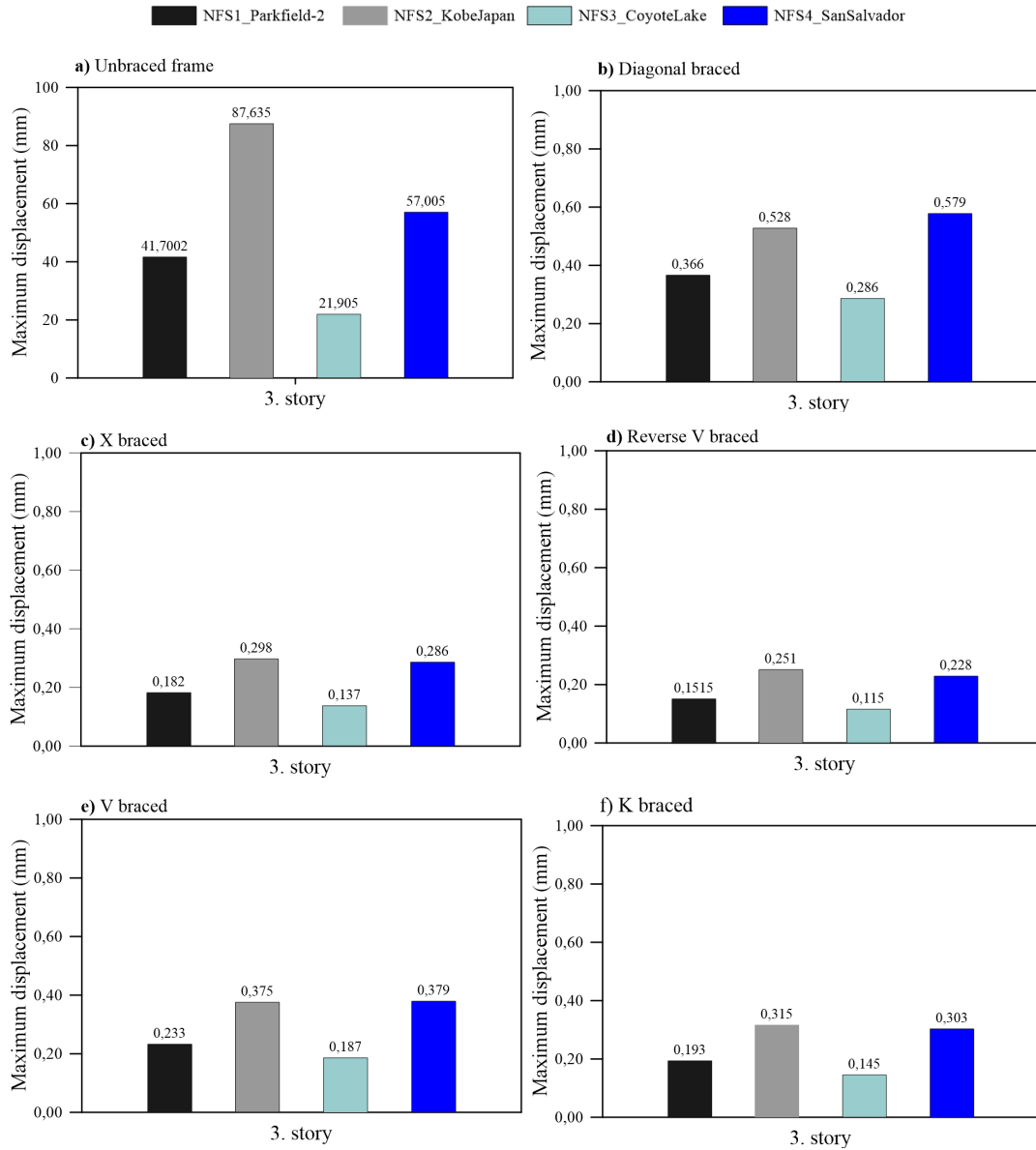


Figure 13. Maximum horizontal displacements considering different bracing models for the NFS.

The effect of NFM pulse motions on the maximum displacements of the top floor for the considered models is compared in Figure 14. The Cape-Mendocino earthquake, which has a larger pulse duration and the Kobe-Japan earthquake has nearly the same PGA values. The variations in displacements obtained from the Cape-Mendocino earthquake according to the Kobe-Japan earthquake are -43.28%, 8.60%, 6.53%, 6.15%, 1.92%, 6.15% for unbraced, diagonally braced, X-braced, reverse V-braced, V-braced, K-braced, respectively. The diagonal braced frame system is very sensitive to the pulse duration. Although a diagonal braced frame system has a large vibration natural period, the V-braced frame system is less affected under pulse duration. Except for the unbraced frame system, all braced frame systems are affected by pulse duration under the Cape-Mendocino earthquake. Furthermore, the Superstition-Hills earthquake is very effective on the braced frame systems compared to the Northridge-01 record motion.

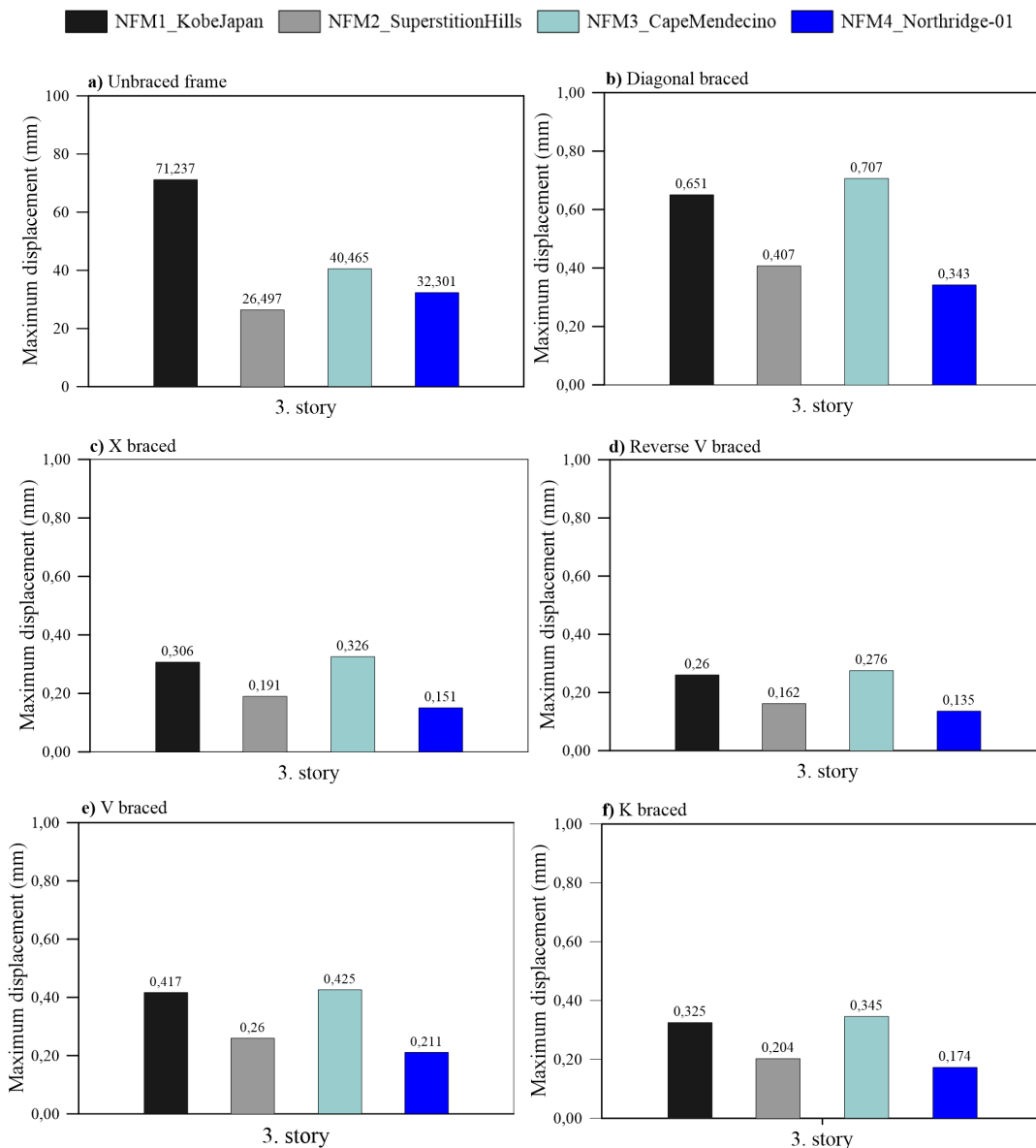


Figure 14. Maximum horizontal displacements considering different bracing models for the NFM.

For the unbraced frame system in Figure 14, the maximum top floor displacements obtained from the Northridge-01 record motion are greater than the displacements obtained from the Superstition-Hills. However, the Superstition-Hills earthquake result in greater maximum displacements compared to the Northridge-01 record motion. Under the Superstition-Hills earthquake, the maximum top floor displacements are 26.497 mm, 0.407 mm, 0.191 mm, 0.162 mm, 0.26 mm, 0.204 mm for the unbraced, diagonally braced, X-braced, reverse V-braced, V-braced, K-braced, respectively. In addition, the maximum top floor displacements are 32.301 mm, 0.343 mm, 0.151 mm, 0.135 mm, 0.211 mm, 0.174 mm under the Northridge-01 record motions, respectively. When the results obtained under the Superstition-Hills and Northridge-01 record motions are considered, the variations are as 21.90%, -15.72%, -20.94%, -16.67%, -18.85% and -14.70% for all systems, respectively. The Superstition-Hills and the Cape-Mendocino earthquakes have nearly the same pulse duration, but these record motions have quite different PGA values. While the top floor displacements are respectively obtained as 26.497 mm, 0.407 mm, 0.191 mm, 0.162 mm, 0.260 mm, 0.204 mm for all frames under the Superstition-Hills earthquake, the top floor displacements were respectively obtained as 40.405 mm, 0.707 mm, 0.326 mm, 0.276 mm, 0.425 mm, 0.345 mm for all frames under the Cape-Mendocino earthquake. The variations in top floor displacements for the Superstition-Hills and the Cape-Mendocino earthquakes are 52.48%, 73.71%, 70.68%, 70.37%, 63.46%, and

69.12% for all systems, respectively. While the unbraced frames have a structural demand under the earthquakes with large PGA values, the structural behavior of the braced systems is increased under the earthquakes with a pulse.

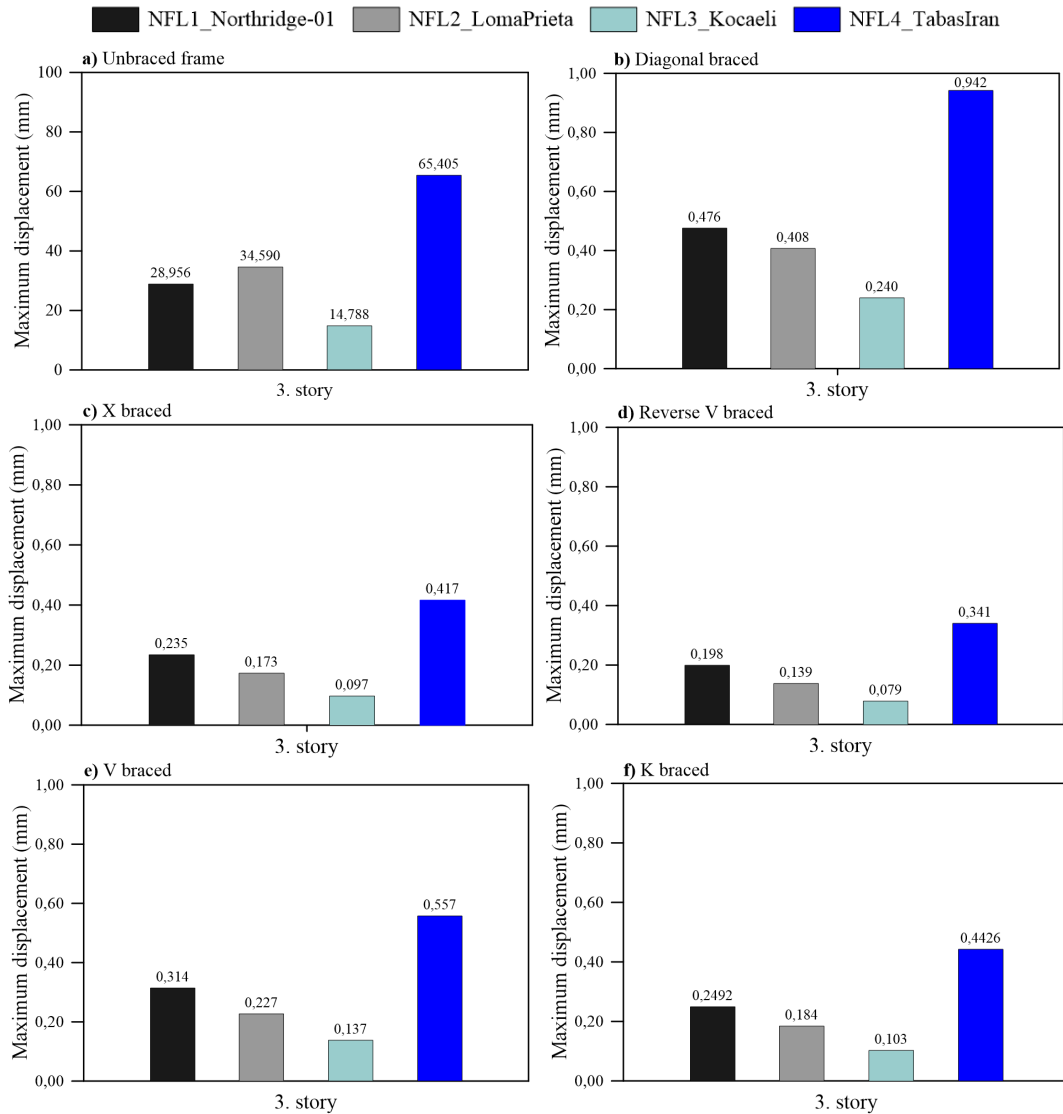


Figure 15. Maximum horizontal displacements considering different bracing models for the NFL.

The maximum top floor displacements under the NFL pulse motions are shown in Figure 15. The displacements for all frame systems are respectively obtained as 65.405 mm, 0.942 mm, 0.417 mm, 0.341 mm, 0.557 mm, and 0.443 mm under the Tabas-Iran earthquake, which has a large pulse and PGA value. Under the Loma-Prieta earthquake, which has a 3.98 s of pulse duration, the maximum top displacements are as 34.59 mm, 0.408 mm, 0.173 mm, 0.139 mm, 0.227 mm, and 0.184 mm for all frames, respectively. Likewise, the displacements are as 14.788 mm, 0.24 mm, 0.097 mm, 0.079 mm, 0.137 mm, and 0.103 mm under the Kocaeli-İzmit ground excitation, respectively. These ground excitations have nearly the same pulse duration and different PGA values. The displacement variation between the Tabas-Iran and Loma-Prieta earthquakes are 89%, 130%, 141%, 162%, 145%, and 141% for all frames, respectively. Moreover, the displacement variation between the Tabas-Iran and Kocaeli earthquakes is 343%, 290%, 329%, 331%, 306%, and 330% for all frames, respectively. In this manner, the low PGA values cause to lost efficiency according to the period of the structures but as long as PGA values are increased, the period effect has been very effective on structures for the NFL pulse motion.

In a general discussion, the triple displacement values for Loma-Prieta (NFL)-Northridge-01 (NFM)-Parkfield-02 (NFS) record motions are obtained as 34.59 mm-32.30 mm-41.70 mm, 0.408 mm-0.343 mm-0.366

mm, 0.173 mm-0.151 mm-0.182 mm, 0.139 mm-0.135 mm-0.151 mm, 0.227 mm-0.221 mm-0.233 mm and 0.184 mm-0.174 mm-0.193 mm for all frames, respectively. The double displacement values for Kobe-Japan (NFM) and Kobe-Japan (NFS) record motions are as 71.24 mm-87.64 mm, 0.65 mm-0.528 mm, 0.31 mm-0.30 mm, 0.26 mm-0.25 mm, 0.42 mm-0.38 mm, 0.33 mm-0.32 mm, for all frames, respectively. The double displacement values for Cape-Mendocino (NFM) and Kobe-Japan (NFS) record motions are as 40.50 mm-87.64 mm, 0.71 mm-0.528 mm, 0.33 mm-0.30 mm, 0.28 mm-0.25 mm, 0.43 mm-0.38 mm, 0.35 mm-0.32 mm, for all frames, respectively.

5. Conclusions and Recommendations

In the TBEC-2018, six different resisting frame systems have been suggested for steel structures such as moment resisting frame (unbraced frames), diagonally braced, X-braced, and reverse V-braced, V-braced, and K-braced. A comparison of the linear dynamic response characteristics of steel frame structures consisting of different resisting frame systems subjected to NF ground excitations which include pulse signals or have large velocity pulse duration is carried out in this study. For this purpose, a 3-story steel frame model composed of MRF and (CBFs) are analyzed using four different record motion sets, which are FF earthquakes, NF earthquakes with a small pulse (as an about 1 s), NF earthquakes with a medium pulse (as an about 2.80 s) and NF earthquakes with a large pulse (as an about 4 s). The investigation of the dynamic behavior of different steel resisting frames systems under pulse-like NF excitation has led to the following conclusions:

- The effects of PGA values on stiff systems are significant compared to flexible systems. Even though reverse V-braced systems, which have the lowest first mode period of vibration, occur minimum floor displacements under FF record motions, these systems are sensitive to PGA values. If the first mode period of vibration decreased, an increment in PGA values caused to larger structural demand. PGA could be identified as a key parameter that controls the response of braced frames under FF ground excitations.
- Although the diagonally braced frame systems have a larger first mode period of vibration according to other braced frames, these braced frames are not much affected under PGA for FF ground excitations.
- If NF ground excitations are taken into consideration as having a small pulse duration, which is only greater than the first mode period of bracing systems, it can be remarked that the ratio of T_p/T_1 is a dominant parameter even if PGA values are very large.
- Although the pulse duration, which is greater than the first mode period of vibration, is a dominant factor, but the rate of T_p/T_1 does not have a remarkable change on the structural demands as distinct from PGA values in consequence of the low first mode period of vibration.
- Although all braced systems have nearly same first mode period, especially diagonally braced and V-braced frame systems, which have a larger first mode period, are more sensitive to a pulse duration of ground excitations.

The results obtained from V-braced and reverse V-braced frame systems showed that the eccentricity can be more significant in eccentrically braced frames under pulse-like ground excitations. Future studies should examine the response of the pulse duration of ground excitations using nonlinear analysis of structures and fuse mechanisms instead of braces.

References

- [1] Martinelli L, Mulas MG, Perotti F. The seismic response of concentrically braced moment-resisting steel frames. *Earthquake Engineering & Structural Dynamics* 1996; 25: 1275-1299.
- [2] Balendra T, Huang X. Overstrength and ductility factors for steel frames designed according to BS 5950. *Journal of Structural Engineering* 2003;129: 1019-1035.
- [3] Kim J, Choi H. Response modification factors of chevron-braced frames. *Engineering Structures* 2005; 27(2): 285-300.
- [4] Dicleli M, Mehta A. Seismic performance of a special type of single-story eccentrically braced steel frame. *Advances in Structural Engineering* 2008; 11(1): 35-51.
- [5] Khandelwal K, El-Tawil S, Sadek F. Progressive collapse analysis of seismically designed steel braced frames. *Journal of Constructional Steel Research* 2009; 65(3): 699-708.
- [6] Coffield A, Adeli H. An investigation of the effectiveness of the framing systems in steel structures subjected to blast loading. *Journal of Civil Engineering Management* 2014; 20(6): 767-777.

- [7] Shiravand MR, Shabani MJ. The effect of oblique blast loadings on moment and braced frames in steel structures. *Advances in Structural Engineering* 2016; 19(4): 563-580.
- [8] Qi Y, Li W, Feng N. Seismic collapse probability of eccentrically braced steel frames. *Steel and Composite Structures* 2017; 24: 37-52.
- [9] Larijan RJ, Nasserabadi HD, Aghayan I. Progressive collapse analysis of buildings with concentric and eccentric braced frames. *Structural engineering and mechanics* 2017; 61(6): 755-763.
- [10] Bosco M, Marino E, Rossi P. A design procedure for dual eccentrically braced-moment resisting frames in the framework of Eurocode 8. *Engineering structures* 2017; 130: 198-215.
- [11] Karsaz K, Tosee SVR. A comparative study on the behavior of steel moment-resisting frames with different bracing systems based on a response-based damage index. *Civil Engineering Journal* 2018; 4(6), 1354-1373.
- [12] Yaman Z, Ağcakoca E. Performance Analysis of Circular Sieve Owner Center Steel Crosses. *Sakarya University Journal of Science* 2018; 22(2): 340-349.
- [13] Faroughi A, Sarvghad Moghadam A, Ghanooni Bagha M. The Effects of Number and Location of Bracing Bays on Redundancy of Eccentrically-Braced Steel Moment Frames. *Journal of Structural and Construction Engineering* 2021; 8(8): 5-20.
- [14] Altan Y. Merkezi ve dışmerkez çaprazlı çelik bina yapılarında deprem performansının belirlenmesi, Master thesis, İstanbul Gelişim University, Fen Bilimleri Enstitüsü, 2020.
- [15] Yao Z, Wang W, Fang C, Zhang Z. An experimental study on eccentrically braced beam-through steel frames with replaceable shear links. *Engineering Structures* 2020; 206:110185.
- [16] Haji M, Azarhomayun F, Ghiami Azad AR. Numerical investigation of truss-shaped braces in eccentrically braced steel frames. *Magazine of Civil Engineering* 2021; 2(102): 10208.
- [17] Barbagallo F, Bosco M, Marino EM, Rossi PP. Seismic performance and cost comparative analysis of steel braced frames designed in the framework of EC8. *Engineering Structures* 2021; 240: 112379.
- [18] Rouhi A, Hamidi H. Development of performance based plastic design of EBF steel structures subjected to forward directivity effect. *International Journal of Steel Structures* 2021; 21(3):1092-1107.
- [19] Gürsoy Ş, Yılmaz A. Dış Merkezi Çelik Çapraz Tiplerinin Çerçeve Davranışına ve Yapı Maliyetine Etkisinin İncelenmesi. *Düzce Üniversitesi Bilim ve Teknoloji Dergisi* 2021; 9(5): 1766-1781.
- [20] TBEC 2018. Turkish building earthquake code. Ministry of Environment and Urbanization of Turkey, Ankara, Turkey.
- [21] Mahmoud S, Alqarni A, Saliba J, Ibrahim AH, Diab H. Influence of floor system on seismic behavior of RC buildings to forward directivity and fling-step in the near-fault region. *Structures* 2021; 30: 803-817.
- [22] Somerville PG. Magnitude scaling of the near fault rupture directivity pulse. *Physics of the earth and planetary interiors* 2003; 137: 201-212.
- [23] Yang D, Pan J, Li G. Interstory drift ratio of building structures subjected to near-fault ground motions based on generalized drift spectral analysis. *Soil Dynamics and Earthquake Engineering* 2010; 30(11): 1182-1197.
- [24] Zou D, Han H, Liu J, Yang D, Kong X. 2017. Seismic failure analysis for a high concrete face rockfill dam subjected to near-fault pulse-like ground motions. *Soil Dynamics and Earthquake Engineering* 2017; 98: 235-243.
- [25] Liao WI, Loh, CH, Lee, BH. Comparison of dynamic response of isolated and non-isolated continuous girder bridges subjected to near-fault ground motions. *Engineering Structures* 2004; 26(14): 2173-2183.
- [26] Alavi B, Krawinkler H. Effects of near-fault ground motions on frame structures, John A. Blume Earthquake Engineering Center Stanford. 2001.
- [27] Akkar S, Yazgan U, Gülkan P. Drift estimates in frame buildings subjected to near-fault ground motions. *Journal of Structural Engineering* 2005; 131(7):1014-1024.
- [28] Malhotra PK. Response of buildings to near-field pulse-like ground motions. *Earthquake Engineering and Structural Dynamics* 1999; 28(11), 1309-1326.
- [29] Chopra AK, Chintanapakdee C. Comparing response of SDF systems to near-fault and far-fault earthquake motions in the context of spectral regions. *Earthquake engineering and structural dynamics* 2001; 30(12): 1769-1789.
- [30] Anderson JC, Bertero VV. Uncertainties in establishing design earthquakes. *Journal of Structural Engineering* 1987; 113(8): 1709-1724.
- [31] Hayden C, Bray J, Abrahamson N, Acevedo-Cabrera A. Selection of near-fault pulse motions for use in design. 15th International World Conference on Earthquake Engineering; 2012; Lisboa.
- [32] Alavi B, Krawinkler H. The behavior of moment-resisting frame structures subjected to near-fault ground motions. *Earthquake engineering and structural dynamics* 2004; 33(6): 687-706.
- [33] Güneş N, Ulucan ZÇ. Nonlinear dynamic response of a tall building to near-fault pulse-like ground motions. *Bulletin of Earthquake Engineering* 2019; 17(6): 2989-3013.
- [34] Seissoft 2022. SeismoSignal-Signal Processing of Strong Motion Data.
- [35] Kardoutsou V, Taflampas I, Psycharis. A new pulse indicator for the classification of ground motions. *Bulletin of the Seismological Society of America* 2017; 107(3): 1356-1364.
- [36] PEER 2022. Ground motions Database Pacific Earthquake Engineering Research Center. University of California, California.
- [37] ANSI, B. AISC 360-16, specification for structural steel buildings. Chicago AISC, 2016.
- [38] Computers and Structures Inc. SAP2000: Static and Dynamic Finite Element Analysis of Structures, Berkeley, CA, U.S.A.

Improving the Flux-Weakening Capability of Interior Permanent Magnet Machines by Number of Turns Changing Methodology

Tayfun GÜNDOĞDU^{1*}

Department of Electrical and Electronic Engineering, Faculty of Engineering, Hakkari University, Hakkari, Turkey
^{*1} tayfungundogdu@hakkari.edu.tr

(Geliş/Received: 01/06/2022;

Kabul/Accepted: 20/08/2022)

Abstract: In this paper, an interior permanent magnet (IPM) machine having two sets of windings with different number of turns is developed to improve the limited flux-weakening (FW) capability and efficiency, simultaneously. The flux-adjustable range appears to be somewhat limited because of the limited maximum inverter voltage and high magnetic saturation, which degrades the FW capability. To address its restricted FW capability, a unique winding-switching concept is introduced, in which auxiliary coils with lower turns alternately function as the secondary armature winding, resulting in flux-linkage reduction within the same phase. Winding topologies, design considerations, the FW principle, and FW computations have all been addressed. To validate the feasibility of the proposed FW enhancement strategy, a co-simulation procedure based on the 2D finite element method (FEM) and MatLab codes is used to determine the steady-state and FW performance characteristics of IPM machines with various winding topologies. All steady-state and FW performance characteristics of the conventional IPM machine and the proposed IPM machines have been compared quantitatively. Furthermore, to ensure the accuracy of the analytical and numerical calculations provided in this study, the predicted efficiency map of the original Toyota Prius 2010 IPM machine is validated using the efficiency measurements provided.

Key words: Flux-weakening capability, IPM machines, winding switching method, turn number variation, efficiency map.

Gömülü Tip Mıknatıslı Makinaların Sipir Sayısı Değişirme Metodolojisi ile Akı Zayıflatma Kapasitesinin Geliştirilmesi

Öz: Bu çalışmada, sınırlı akı zayıflatma (AZ) kapasitesi ve verimi aynı anda arttırabilmek için farklı sipir sayılarına sahip birbirinden izole iki adet sargısı olan bir gömülü tip kalıcı mıknatıslı (IPM) makina geliştirilmiştir. Akı ayarlayabilme aralığı, AZ kapasitesini düşüren sınırlı maksimum inverter gerilimi ve yüksek manyetik doygunluk nedeniyle sınırlanmaktadır. Kısıtlı AZ kabiliyetini geliştirmek için, ana sargıya göre daha düşük sipir sayısına sahip yardımcı bobinlerin sistematik olarak anahtarlanması ile akı bağlantısının azalmasını sağlayan benzersiz bir sarım-anahtarlama konsepti tanıtılmıştır. Sargı topolojileri, tasarım hususları, AZ ilkesi ve hesaplamaları tümüyle ele alınmıştır. Önerilen AZ kapasitesi geliştirme stratejisinin uygulanabilirliğini doğrulamak için, çeşitli sargı topolojilerine sahip IPM makinelerinin kararlı durum ve AZ performans özelliklerini belirlemek için 2-boyutlu sonlu elemanlar yöntemine (SEY) ve MatLab kodlarına dayalı bir ortak simülasyon prosedürü kullanılmıştır. Klasik ve önerilen IPM makinalarının tüm kararlı durum ve AZ performans özellikleri nicel olarak karşılaştırılmıştır. Ayrıca, bu çalışmada sağlanan analitik ve sayısal hesaplamaların doğruluğunu sağlamak için, orijinal Toyota Prius 2010 IPM makinasının öngörülen verimlilik haritası, sağlanan verimlilik ölçümleri kullanılarak doğrulanmıştır.

Anahtar kelimeler: Akı zayıflatma kapasitesi, IPM makinalar, sargı değişirme yöntemi, sipir sayısı değişimi, verim haritası.

1. Introduction

Permanent magnet synchronous machines (PMSMs) have gained popularity in recent years due to their benefits such as high efficiency, high torque density, high torque to current ratio, low weight, and high-power factor. The PMSMs are especially well-suited for the use of electric vehicle (EV) and traction applications in order to reduce system volume and weight. In most EVs, a battery is employed as an energy storage and power source, with a limited output voltage. A direct drive system replaces the gear box to reduce energy loss. As a result, PMSMs are typically required to operate at high speed and flux-weakening (FW) regions, particularly in traction systems.

Inability to adjust the fixed PM field limits PMSM applications at constant-power operating ranges [1]. To provide a wide speed range, a large minus d -axis current is required to generate demagnetizing magnetic flux. This

* Corresponding author: tayfungundogdu@hakkari.edu.tr. ORCID Number of the author: [0000-0002-7150-1860](https://orcid.org/0000-0002-7150-1860).

demagnetizing magnetic flux cancels out some of the reversible magnetic flux produced by PMs. The effective air gap magnetic flux is lowered, and the PMSM speed range is widened [1], [2].

Flux weakening control techniques are frequently used to drive the PMSMs and to increase the speed range. However, due to inverter constraints on maximum current and voltage [1]–[6], the speed range may be constrained and unsuitable for some applications, such as EV. Furthermore, the FW obtained with this technique raises the risk of irreversible PM demagnetization and copper losses in the windings. As a consequence, variable flux concepts have been established [7] for improved flux weakening capabilities and enhanced speed range expansion while maintaining high efficiency. The PM flux level can be regulated via electrical, mechanical, or other approaches to broaden the speed range and enhance the PMSMs' flux weakening capabilities. Many hybrid excitation machines, or PM machines with electrical or mechanical variable flux techniques, have been developed during the past 15 years [8–20]. IPM, homopolar and bipolar embedded PM, hybrid excited, consequent pole PM, and other synchronous PM devices are all subject to the same flux control paradigm [12]–[19]. In the axial flux surface-mounted PM machines presented in [21, 22], the PM flux-linkage is adjusted by the relative movement of two separate windings. Radial flux surface-mounted PM machines can be altered to be capable of changing the PM flux linkage by splitting the rotor into two separate portions [23]. Similarly, the interior PM machine's flux barriers can be filled with movable ferromagnetic material fragments to modify the PM flux-linkage while it is in operation [24–26]. Moreover, the doubly salient machine makes use of moveable ferromagnetic parts that are outside of the stator to create a short-circuit route for the PM flux [27]. Memory motors [28], another type of variable flux machine, have been proposed as using several flux weakening methods. The use of AlNiCo magnets, which can be magnetized and demagnetized with a short current pulse in the d-axis direction, enables for the modification of PMs remanence, allowing for flux weakening and strengthening during machine operation [29–32]. Furthermore, by adjusting the winding connection or the number of turns per phase, the pole-changing and double-winding set machines enable variable flux capability [33], [34]. Basically, PM machines have pioneered the concept of winding switching or altering, such as the wye/delta transformation [33].

Winding switching is the most basic, low-cost, and adaptable of the methods discussed above. However, it frequently needs machine rewinding, which raises the cost. The requirement for more switches, gating circuits, and a more complex control board raises the cost of the drive. The switching transient (torque, current, and/or voltage pulsations), which might damage the stator windings or inverter, is another drawback of this method. Several research [33–36] have addressed this issue and proved the feasibility of winding changeover during machine operation. In addition, it has been shown that the high-pulsations in voltage or current can be eliminated by implementing a zero-crossing voltage or current control method [37], [38].

This research attempted to provide a unique winding-switching/changing concept, corresponding to the change of phase winding groups with a different number of turns, in order to improve the IPM machine's limited FW capability and overall efficiency, simultaneously. To change the machine's operating mode, two independent winding groups per phase, namely main and auxiliary windings with differing number of turns, have been created and functionally switched. As a consequence, high-speed back EMF will be decreased, reducing the inverter rating required and extending the available adjustable speed range. Thanks to the proposed winding switching mechanism, three different operating modes, namely constant torque (highest-torque) mode, moderate FW mode, and deep FW (highest-speed) mode, are achieved. The physical and operating specifications of the Toyota Prius 2010 IPM machine were employed as key design parameters. The winding topologies, design considerations, the FW principle, and the FW computations have all been addressed. In order to confirm the feasibility of the proposed FW enhancement technique, a co-simulation algorithm, consisting of the 2D finite element method (FEM) and MatLab, is employed to calculate the steady and flux-weakening performance of the IPM machines having different winding topologies. The steady-state characteristics listed below have been investigated and compared for different switching modes:

- Harmonic analysis of air gap flux density waveform;
- Harmonic analysis of flux linkage waveform;
- Harmonic analysis of Back-EMF waveform;
- Electromagnetic torque waveform;
- Machine losses and efficiency;
- Flux density and flux line distributions.

As for the FW characteristics the followings have been investigated and compared for different switching modes:

- Torque-speed curves;
- Power-speed curves;
- Efficiency maps;

- Inverter current-speed and voltage-speed curves.

Finally, to be able to validate the numerical and analytical calculations, the predicted efficiency map of the original Toyota Prius 2010 IPM machine is verified through the efficiency measurements provided by [39].

2. Number of Turns Changing (Winding-Switching) Concept

A double-fed IPM machine is proposed in [40] to achieve improved FW characteristics. It has been reported that the obtained FW and efficiency characteristics of the dual-fed IPM machine is satisfactory. Although the winding topology proposed in [40] is similar to the winding topology proposed in this study, it requires two separate inverters to supply the windings. Although the winding topology proposed in [40] is similar to the winding topology proposed in this study, it requires two separate inverters to supply the windings. Therefore, the cost of the FW enhancement approach described in [40] is much greater than the cost of the method described in this work.

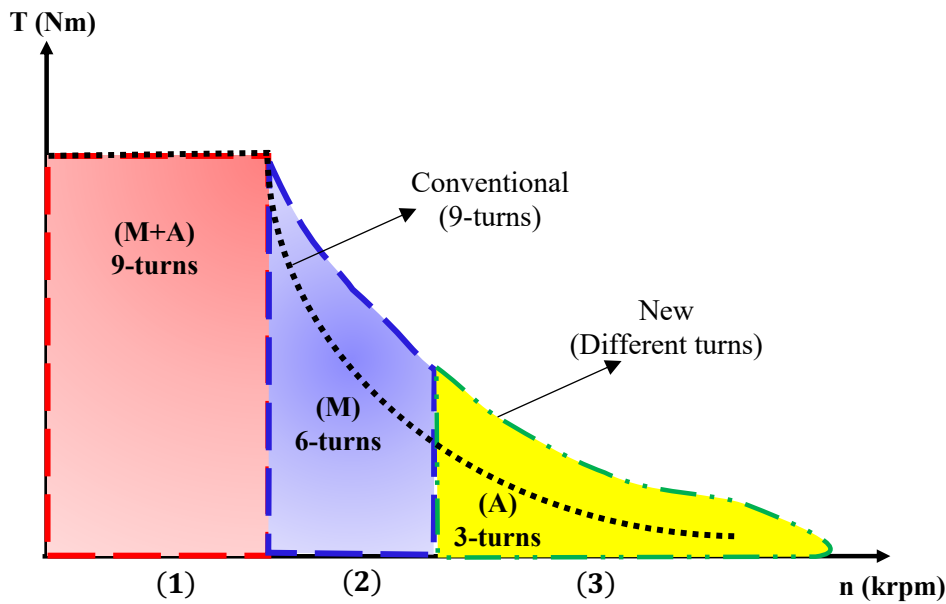


Figure 1. Principle torque-speed curve showing the improved FW characteristic.

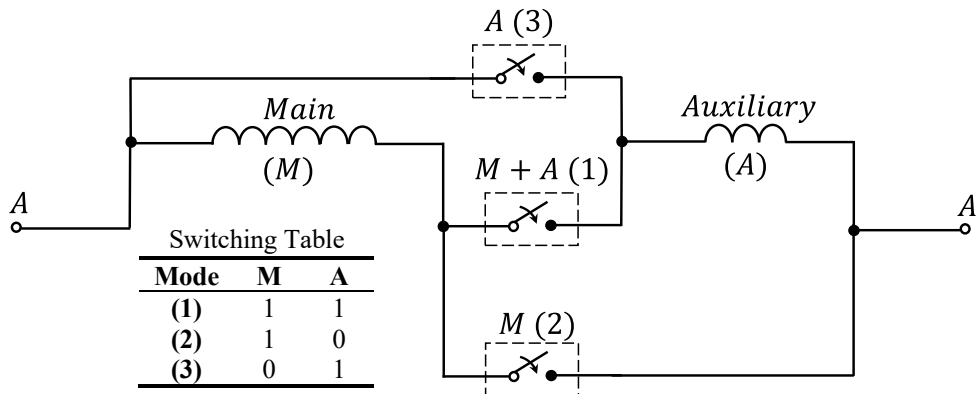


Figure 2. One phase connection diagram of main and auxiliary windings according to their switching order.

Instead of utilizing additional inverters, it requires electronic switches such as IGBT in order to change the turn number per phase during the operation. The basic principle is that to be able to weaken the main flux, the number of turns has been reduced instead of producing an additional opposite-direction flux. The principle torque-speed curve and corresponding winding connection diagram are shown in Figure 1 and Figure 2, respectively. Considering the switching table shown in Figure 2, three different operating modes can be achieved. Once both windings are activated (case#1), the machine operates at constant torque region. If only the main winding is

activated (case#2), the machine operates at moderate torque/speed region. Alternatively, if only the auxiliary winding is activated (case#3), the machine operates at deep FW region.

Some key advantages of the turn-changing concept are presented as follows:

- ✓ Does not require an additional inverter;
- ✓ Does not consume power to weaken the flux;
- ✓ Does not produce additional copper loss;
- ✓ Depending on the number of turn shares of the main and auxiliary windings, it is possible to increase the power up to the maximum limits of the inverted at the very-high speed operations.

3. Design Specifications and Analysis Method

In this section, to be able to verify the calculations, the number of turns changing method has been directly utilized for the original IPM machine design. To examine the effects of various turning sharing between the main and auxiliary windings, a M/A: 8/3 and a M/A: 7/4 version of Toyota Prius IPM machine are designed. M/A: 8/3 indicates that turn-changing IPM machine with 8-turns for main winding and 3-turns for auxiliary windings. In the similar manner, the M/A: 7/4 indicates that the main windings have 7-turns and the auxiliary windings have 4-turns. The total turn number per phase, which is 11-turns, kept the same for all the designs. The design specifications of the considered machines are listed in Table 1 and the cross-sectional views of the machines are shown in Figure 3. The coefficients of flux linkage, inductance, and power loss were estimated parametrically using 2D, non-linear, time-stepping FEM. Using the hybrid FW control approach, these parameters are entered into a MatLab program for analytical FW computation.

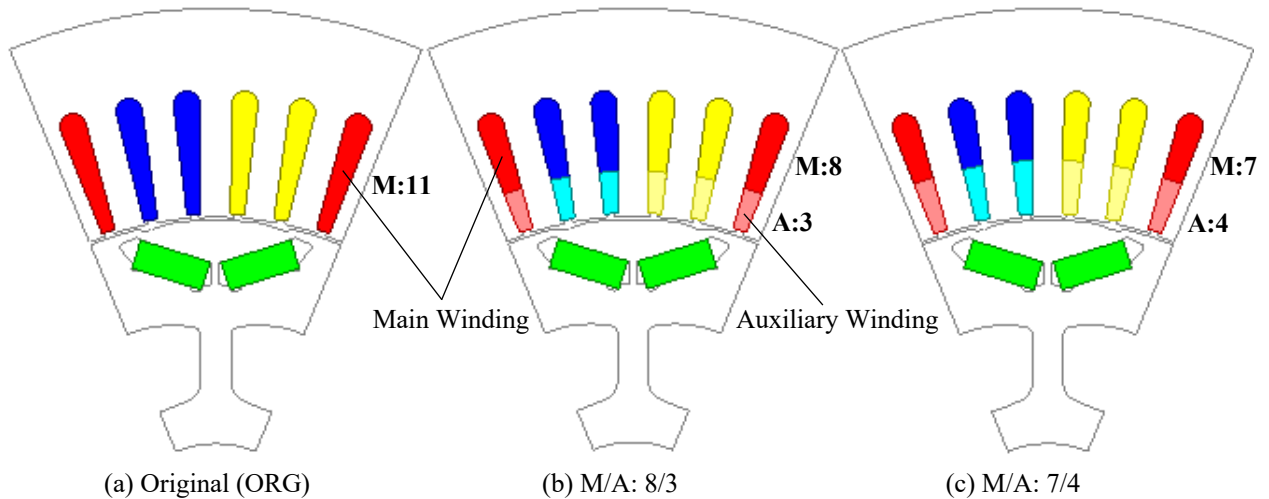


Figure 3. 2-D cross-sectional views of the original and proposed IPM machines with turn changing topology.

One of the main limitations of IPM drives is the restricted excitation. When the inverter's voltage limit u_{max} is reached, as shown in Equation (1), the back-EMF of the IPM machine rises with rotor speed in the constant-torque region. Equation (2) states that the machine rating limits the maximum current (i_{max}), whereas the inverter rating limits the maximum voltage. The corresponding d - and q -axis voltages are expressed in Equations (3) and (4), respectively. Usually, the operating mode of a machine is determined according to the base speed n_b (see Equation (5)) of the machine. As a result, the control approach is relatively straightforward: the maximum torque per ampere (MTPA) technique is used to control the machine if it operates below the base speed. Moreover, if it exceeds the base speed, then it is controlled by the FW control algorithm, which searches for the optimal current angle γ , delivering the maximum torque available. Furthermore, the correlation between the electromagnetic torque T_e and γ is expressed in Equation (6).

$$V_d^2 + V_q^2 \leq u_{max}^2 \quad (1)$$

$$i_d^2 + i_q^2 \leq i_{max}^2 \quad (2)$$

$$V_d = R_s i_d - \omega_s L_q i_q \quad (3)$$

$$V_q = R_s i_q + \omega_s (L_d i_d + \lambda_{pm}) \quad (4)$$

$$n_b = \frac{120}{2\pi P} \frac{u_{max}}{\sqrt{(\lambda_{pm} - L_d i_d)^2 + (L_q i_q)^2}} \quad (5)$$

$$T_e = 0.5P[\lambda_{pm} i_s \cos \gamma + 0.5(L_d - L_q) i_s^2 \sin 2\gamma] \quad (6)$$

In Equations between (1) and (6); V_d , V_q , i_d , i_q , L_d , and L_q are the voltage, current, and inductance of d - and q -axes, respectively. R_s , i_s , ω_s , λ_{pm} , and P are the phase resistance, current vector, angular speed, flux linkage of PMs, and pole number, respectively. For the FW calculations, the dq equivalent circuit of the IPM machine is employed. More details about the FW algorithm employed in this study can be found in [41].

Table 1 Design Specifications

Parameter	unit	ORG	M/A: 8/3	M/A: 7/4
Stator Outer Diameter	mm		264	
Stator Inner Diameter	mm		161.9	
Stator axial length	mm		50.8	
Rotor Inner Diameter	mm		51	
Air-gap	mm		0.73	
Number of Slot			48	
Turns per coil		11	8+3	7+4
Parallel brunches			1	
Coils in series per phase		8	8+8	8+8
Number of turns per phase		88	64+24	56+32
Slot fill factor			0.448	
Stator slot height	mm		26.753	
Stator tooth width	mm		7.55	
Stator slot radius	mm		3.447	
Stator slot opening width	mm		1.9	
Stator slot opening height	mm		0.85	
Outer bridge thickness (Ribs)	mm		1.836	
Inner bridge thickness	mm		1.863	
O1 (length of the PM positions to origin)	mm		63.141	
B1 (length between the PMs on q)	mm		12.806	
PM dimensions (W× T)	mm ²		17.88065×7.16	
Core Material			Steel 1010	
Hysteresis loss coefficient (K_h)			179.04	
Classical loss coefficient (K_c)			0.375	
Excess loss coefficient (K_e)			0.262	
Mass density (ρ)	kg/m ³		7650	
Stacking factor (K_{fe})			0.93	
PM material			NdFeB35	
Permeability			1.05	
Conductivity (σ)	s/m		625000	
Coercivity (H_c)	A/m		-932193.2381	
Mass density ρ	kg/m ³		7400	

4. Steady-State Performance Characteristics at Full Load

The steady-state analyses of the considered machines are presented as follows. To be able to find the ideal current angle γ delivering the maximum time-averaged torque, parametric analyses, including variations of d and q axes currents, flux linkages, and torque, have been performed, and the results are illustrated in Figure 4. It can be observed that the maximum torque is achieved at 45° .

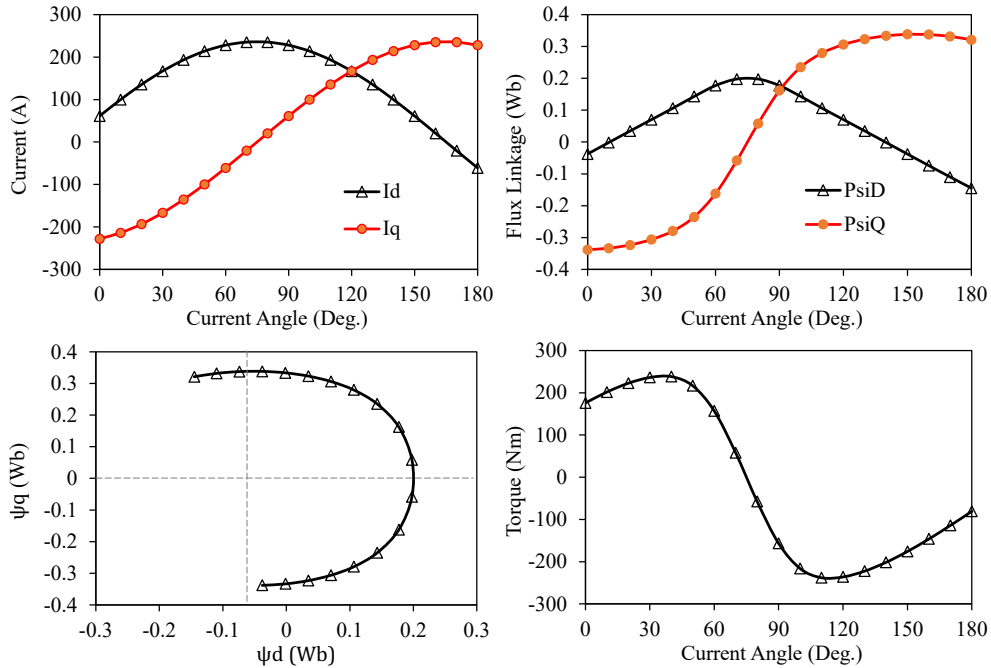
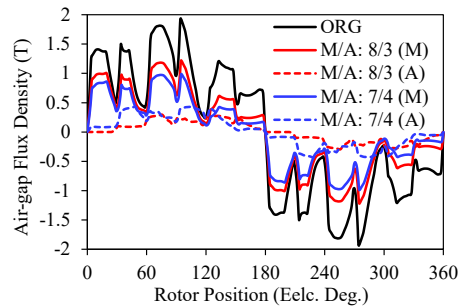
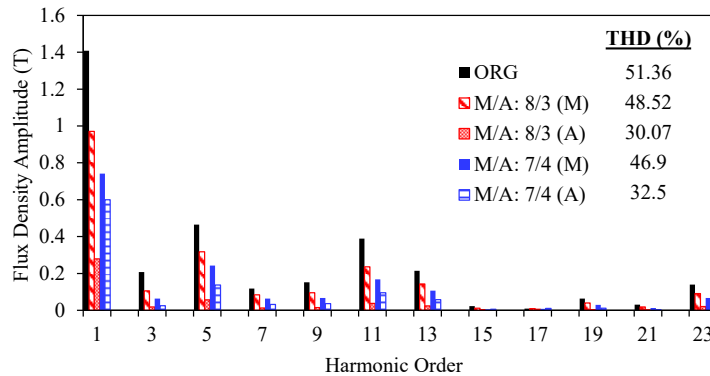


Figure 4. Determination of the optimal current angle for full load analyses.



(a)



(b)

Figure 5. Air-gap flux density distributions and their harmonic spectra.

The results of the harmonic analysis of the air-gap flux density waveform illustrated in Figure 5. As clearly seen, the amplitude of the flux density changes as a function of turn number. As expected, the original design 'ORG' with 11-turns per slot has the highest air-gap flux density, whilst the turn-changing design with 3-turns 'M/A: 8/3 (A)' has the lowest air-gap flux density amplitude. Note that the numbers inside of the brackets indicate the number of turns for the main 'M' and auxiliary 'A' windings, respectively. The waveform distortion levels are fairly severe, as can be observed from the waveforms, due to the combined influence of the winding MMF harmonics and the slotting effect.

The harmonic analysis results of the flux-linkage waveforms are shown in Figure 6. As expected, the ORG design has the highest flux-linkage amplitude while M/A: 8/3 (A) has the lowest. Therefore, it is conceivable to forecast how each design will function in the high-speed operating region by taking into account these flux-linkage amounts. It is clear that windings with fewer turns provide more torque and, as a result, more power in the deep FW region.

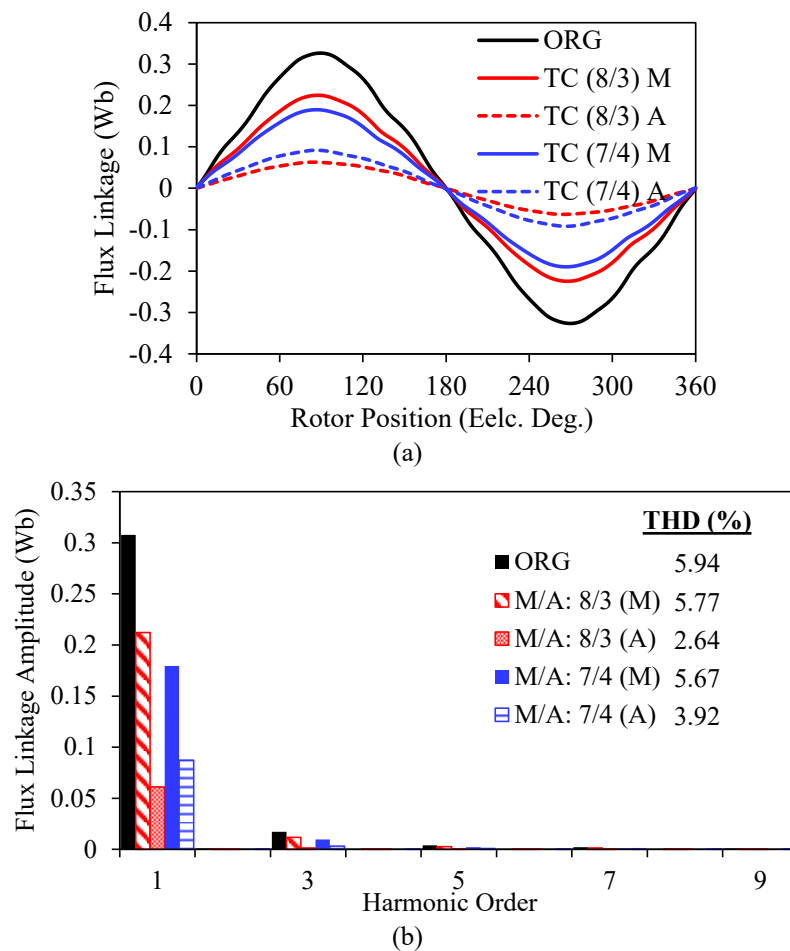


Figure 6. Flux-linkage waveforms and their harmonic spectra.

Figure 7 depicts phase 'A' back-EMF waveforms and harmonic spectra. When the air-gap flux density, flux-linkage, and back-EMF fundamental amplitudes are compared, it is clear that they have a fixed ratio dependent on the number of rotations. Figure 8 depicts the torque fluctuation with regard to rotor position. Given this figure, it is clear that if the Prius IPM machine is constructed with 8-turn main and 3-auxiliary turns (M/A: 8/3), the acquired torque in the deep FW area will be lower than that of the design with 7-turn main and 4-auxiliary turns (M/A: 7/4).

Figure 9 shows a comparison of the power losses of the considered IPM machines. The copper loss is the main loss component at 1000rpm and 236A operation conditions, as seen in the figure. Furthermore, the power loss levels vary based on the output power of the machines with varying rotations. The higher the power, the greater the loss, as expected.

The flux density and flux line distributions of the IPM machines for various operating modes (at different magnetization states) are illustrated in Figure 10 and Figure 11, respectively. As seen in the figures, as the number of turns is lowered, the induced voltage and flux-linkage are reduced, as is the machine's saturation level. It is also clear that as the number of spins is reduced, so are the flux lines traveling through the stator slots. The effective flux linkage fluctuates with the switched winding, which is mostly resulted in the substantial magnetic saturation of the stator teeth and rotor flux barrier bridges.

Table 2 summarizes the comparison of the steady-state performance characteristics of the original and proposed IPM machines.

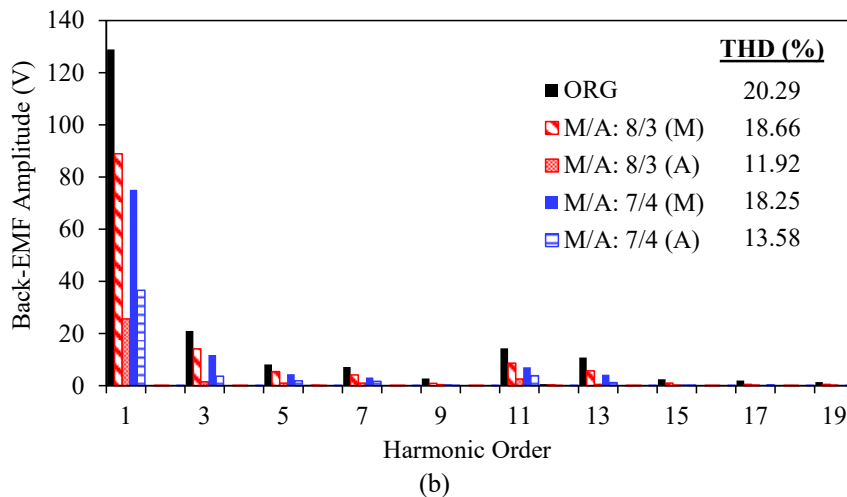
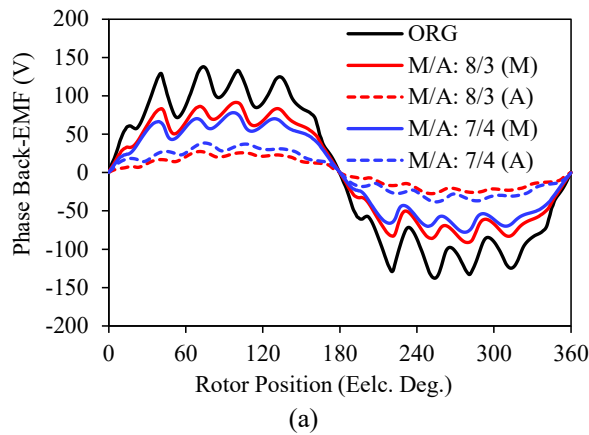


Figure 7 Phase 'A' back-EMF waveforms and their harmonic spectra.

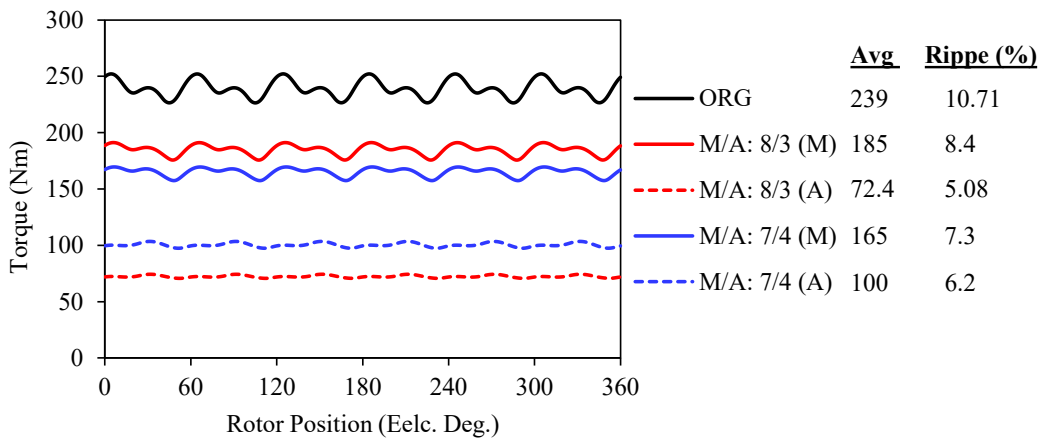


Figure 8 Torque against rotor position.

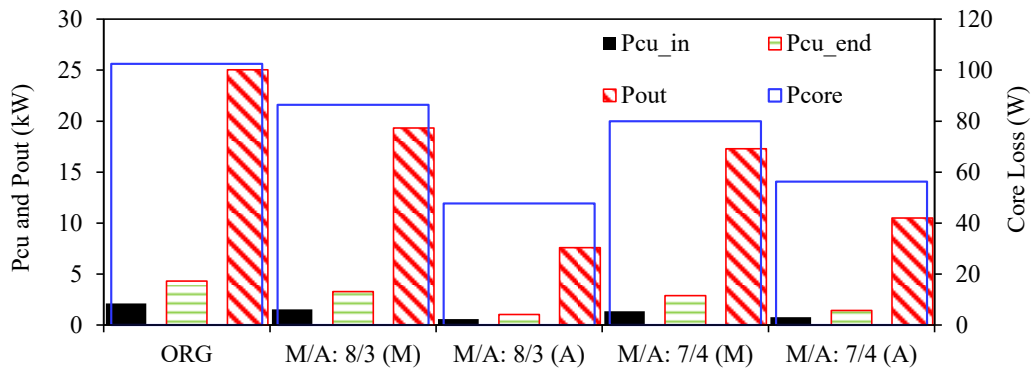


Figure 9 Comparison of power losses.

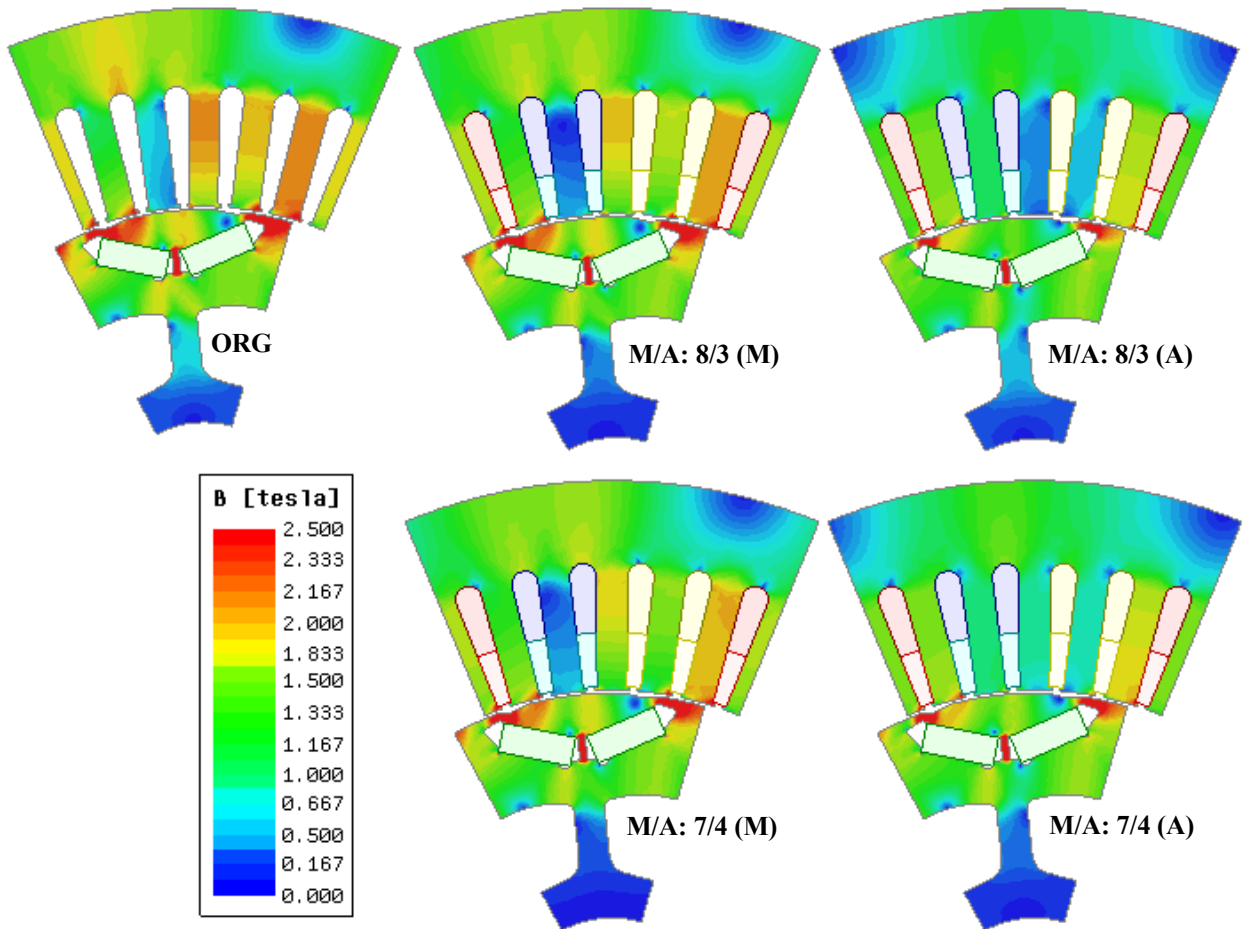


Figure 10 Flux density distributions.

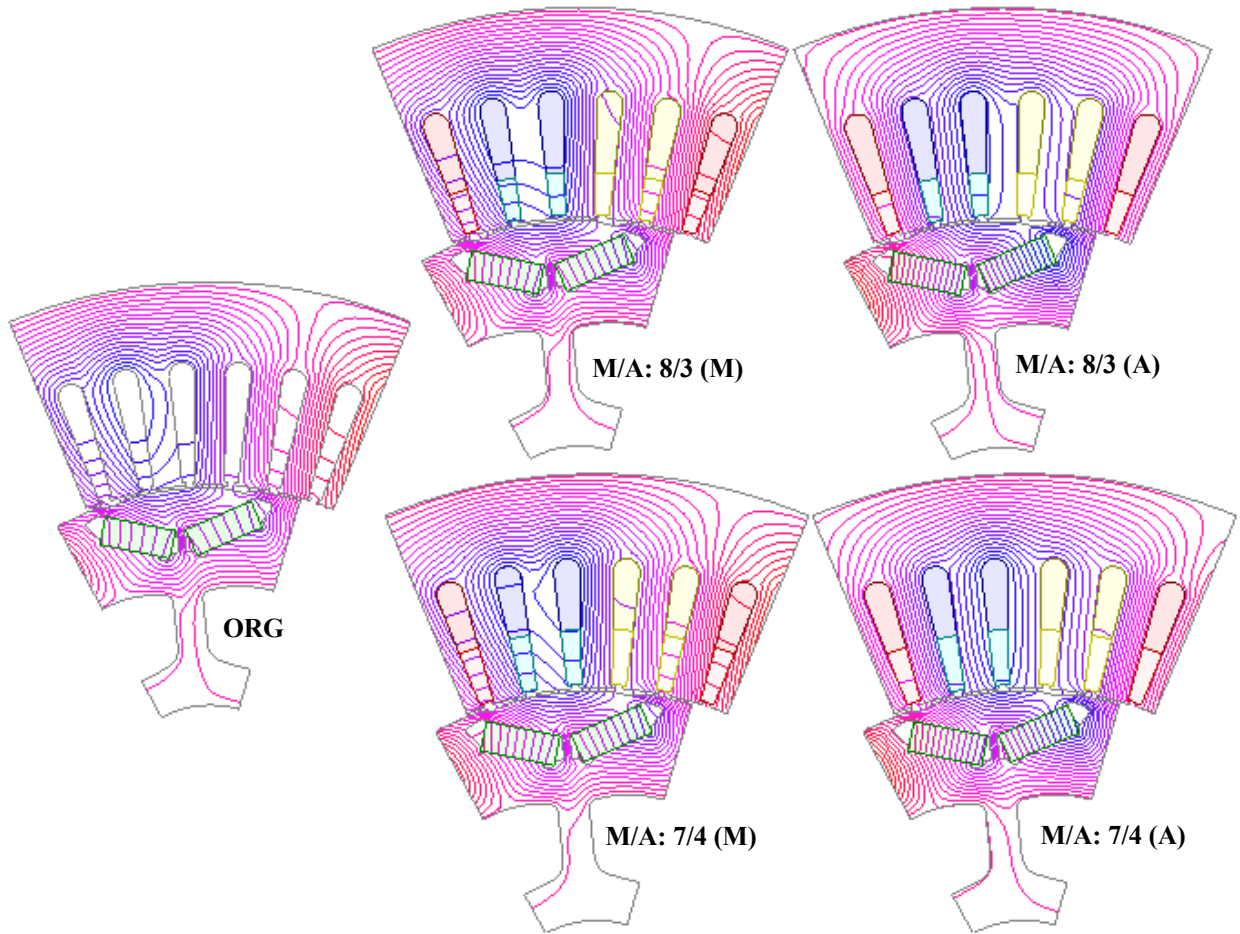


Figure 11 Flux line distributions.

Table 2 Comparison of key performance characteristics.

	ORG	M/A: 8/3 and M/A: 7/4			
		M8	A3	M7	A4
I_s (Apeak)		236			
n_s (rpm)		1000			
J_s (A/mm ²)		27.36			
Cur. Ang. (Deg.)	45	40	25	40	30
N_{ts}	11	8	3	7	4
N_{cs}		8			
N_{tp}	88	64	24	56	32
At	1836	1335	501	1168	668
R_{phase} (@21°C) (Ω)	0.077	0.0576	0.0194	0.0508	0.0262
k_f (%)		0.4482			
T (Nm) @	238.28	184.72	72.46	165.13	100.42
ΔT (%)	10.23	8.39	5.08	7.26	6.22
P_{out} (kW)	25.04	19.33	7.58	17.28	10.5
η (%)	78.68	84.51	69.12	84.63	77.53

5. Analysis of FW Characteristics

This section explored the effect of the number of turns on the FW performance of the considered IPM machines. Torque-speed, power-speed, and efficiency characteristics of the Toyota Prius 2010 IPM machine and its number of changing versions with different number of turns combinations per main and auxiliary windings have been investigated in this section. Since the ORG and M+A designs have the same total number of turns (i.e. 11-turns per slot) and geometric parameters, their electromagnetic properties are identical. The FW characteristics of the ORG and turn-changing designs have been compared as illustrated in Figure 12. As seen in the figure, thanks to the proposed method, it is possible to increase the torque and hence the power significantly at constant power and deep-flux weakening-regions. If the Toyota Prius IPM machine is designed with 8-turn main and 3-turn auxiliary windings M/A: 8/3, 275% higher power than that of the original design can be achieved in the deep FW region. If higher torque and power are required at the mid-constant-power region, then it is reasonable to design the windings with 7-turn and 4-turn for main and auxiliary windings (M/A: 7/4), respectively.

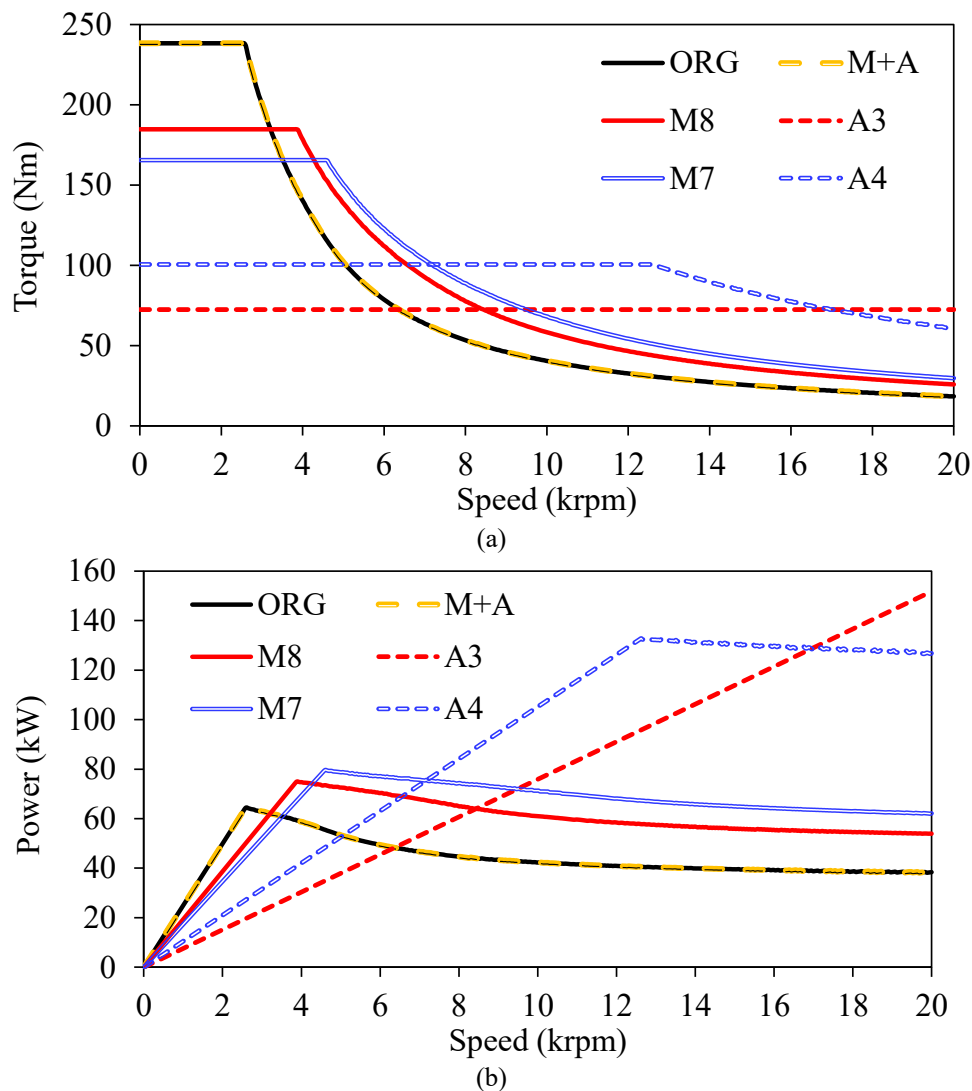
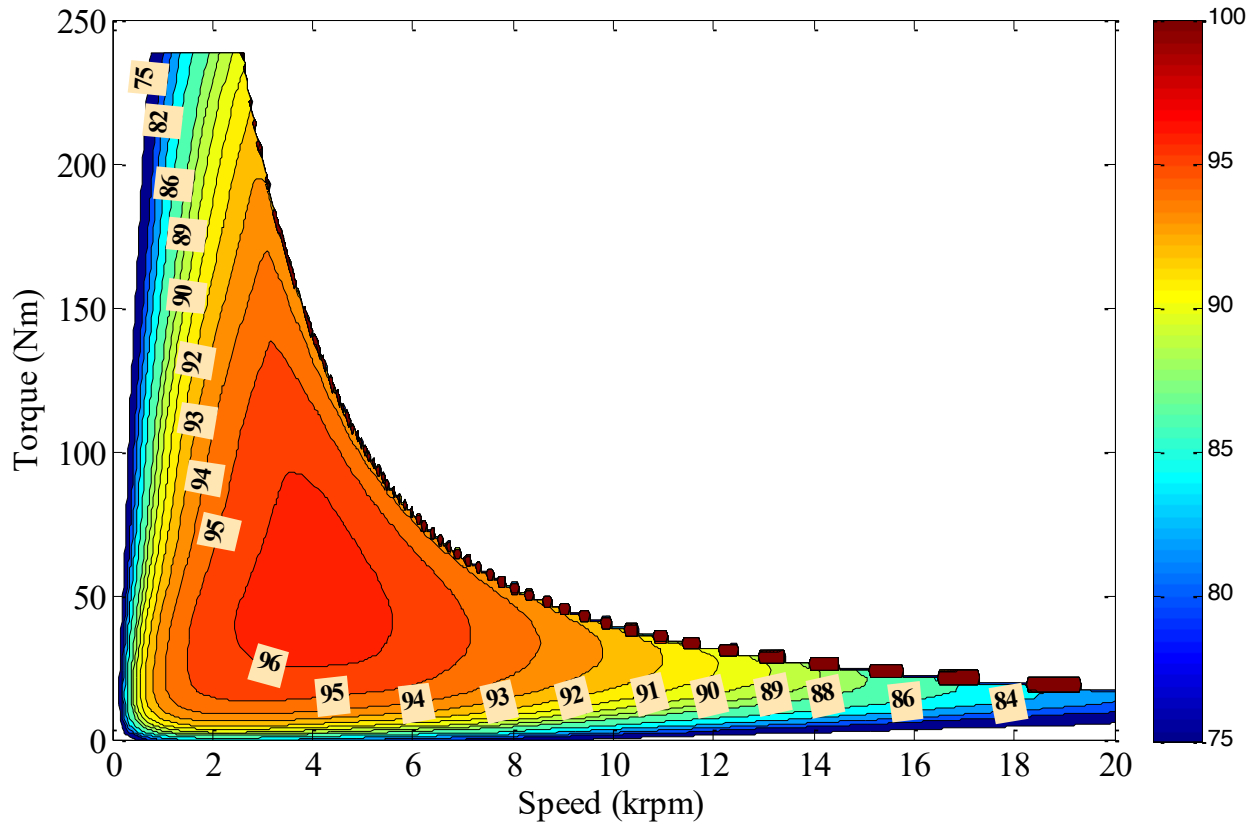
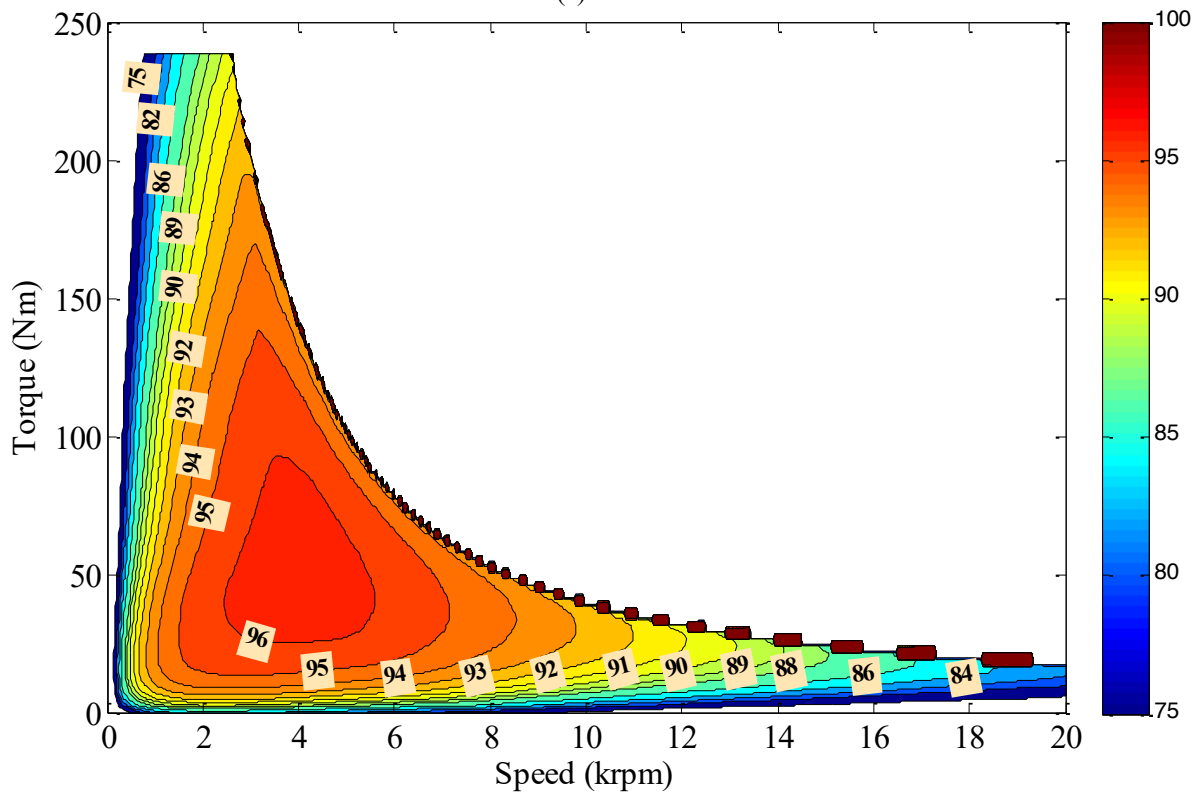


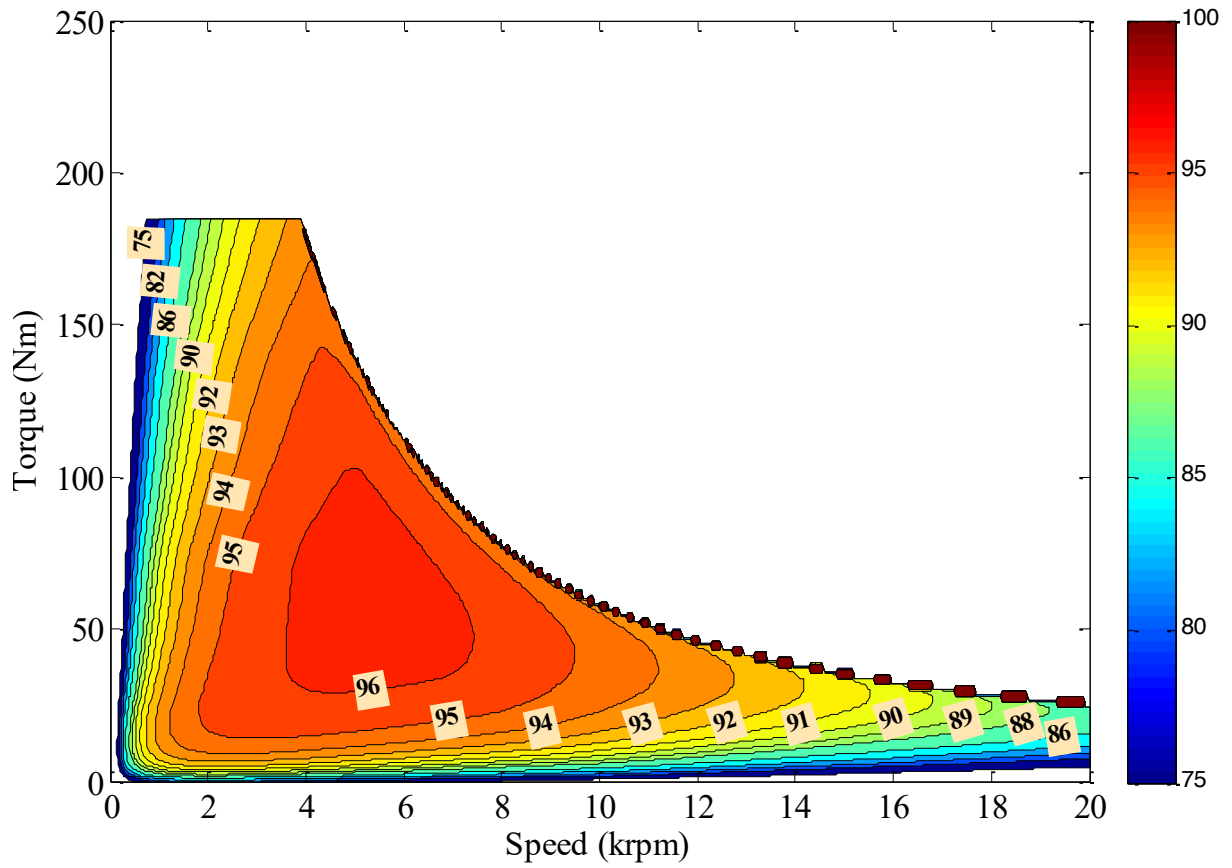
Figure 12 Comparison of FW performances of the IPM machines with different number of main and auxiliary turns.



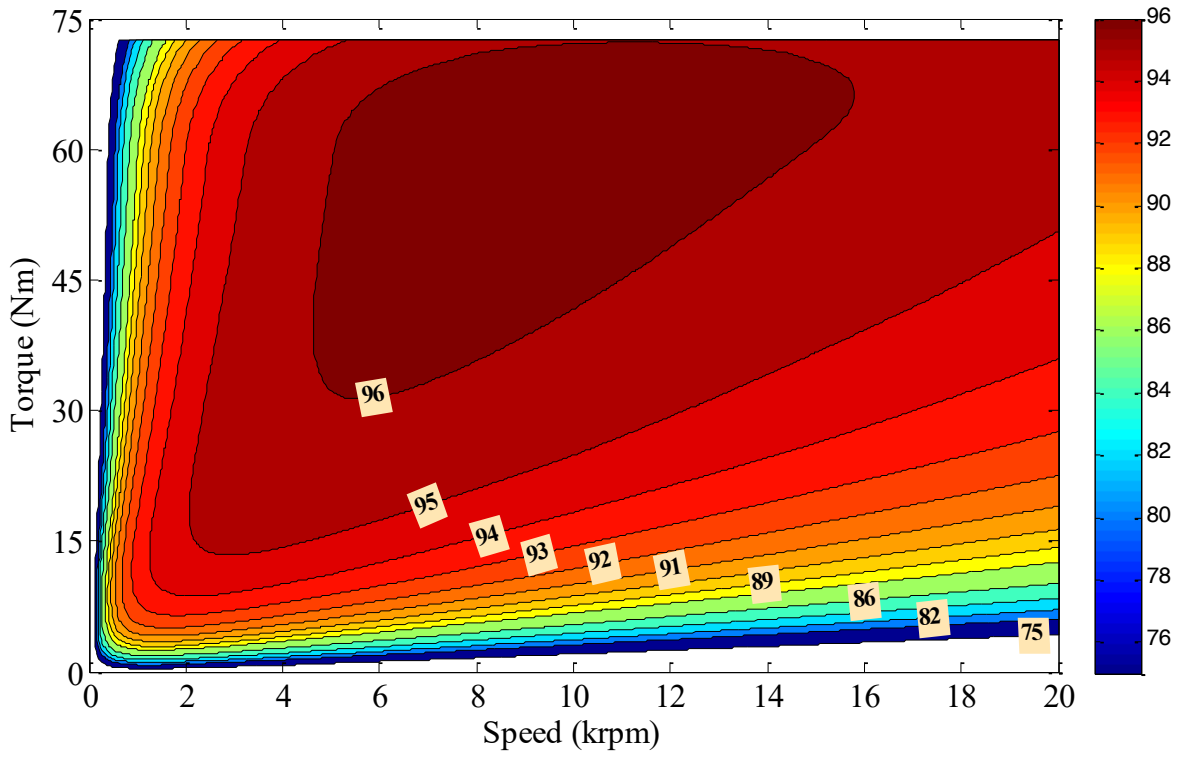
(a) ORG



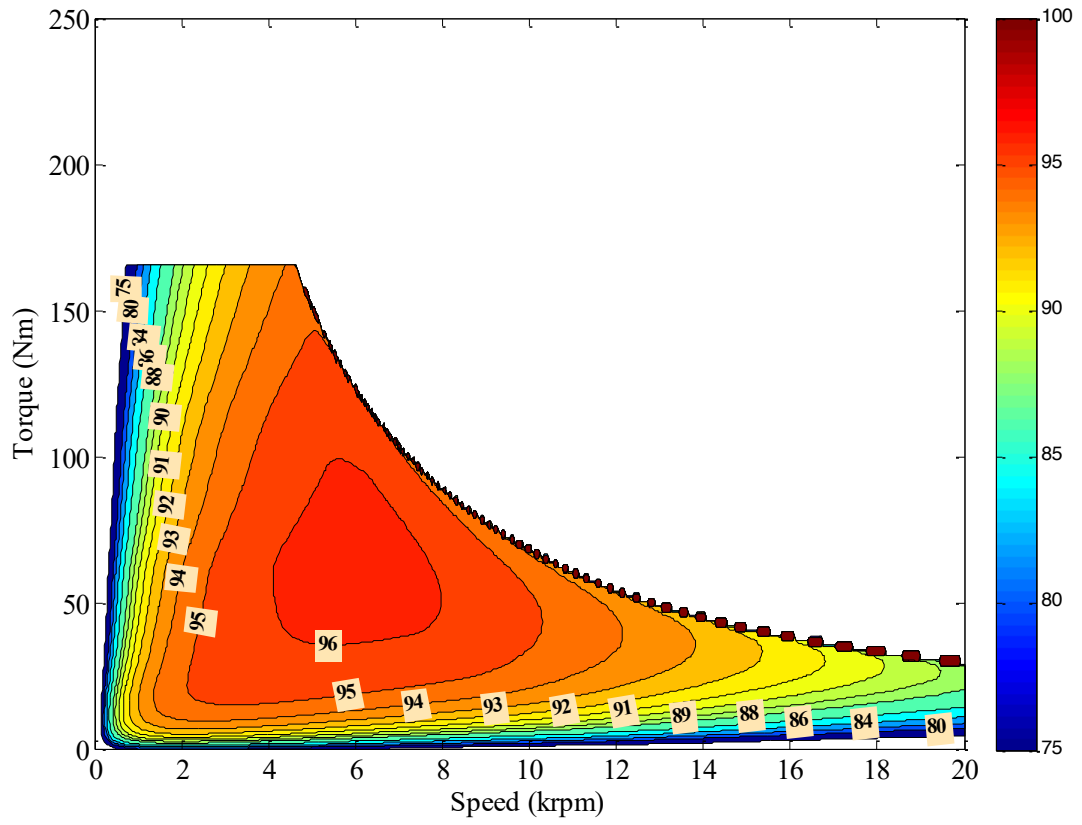
(b) M+A



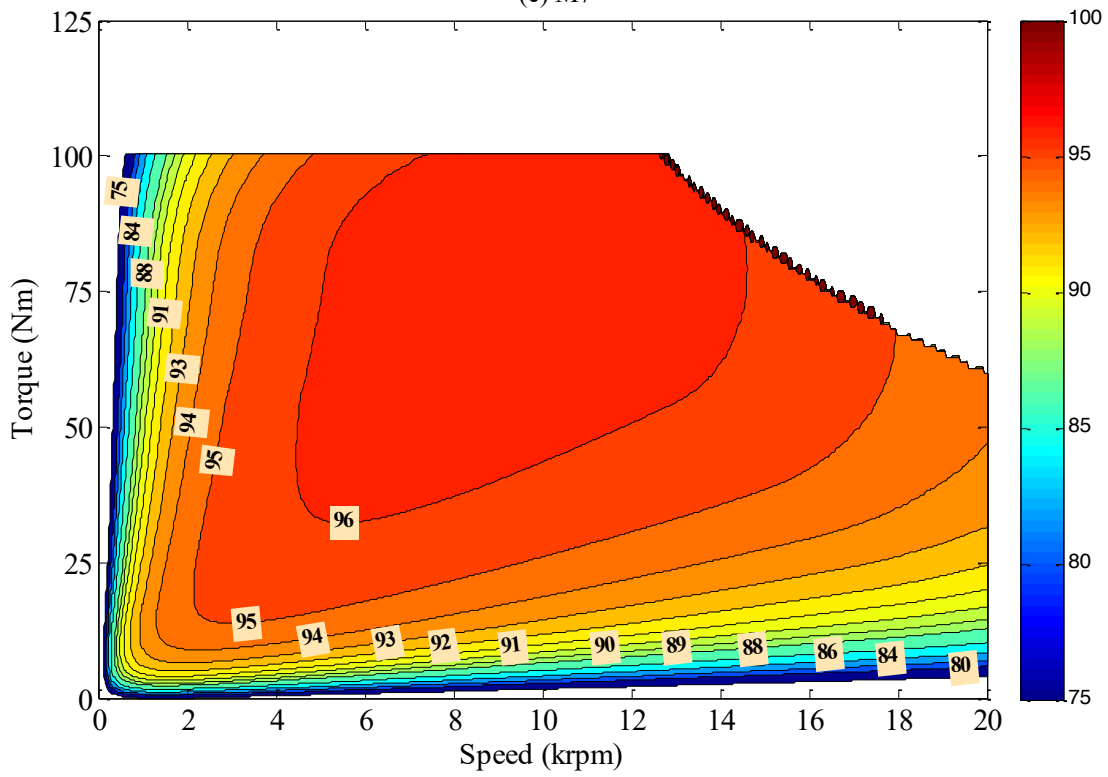
(c) M8



(d) A3



(e) M7



(f) A4

Figure 13 Comparison of efficiency maps of conventional and new IPM machines with different number of turn concept.

The calculated efficiency maps are illustrated in Figure 13. Mechanical losses, in addition to copper and core losses, have been considered during efficiency map calculations. Moreover, the winding resistor has been calculated for 100°C for the calculation of copper losses. It can be deduced that the suggested strategy has greatly improved the efficiency in high speed regions. Note that, in order to increase the efficiency at the low-speed and low-torque regions further, the diameter of the main and auxiliary windings should be increased together. Moreover, increasing the slot fill factor will also help to increase the overall efficiency. Alternatively, the efficiency of the mid-constant power and/or deep FW regions can be increased by changing the diameters of the main and auxiliary windings. However, this would cause a decrease in the efficiency in the constant-torque region. As shown in Figure 14, the performance characteristics of the designs' individual main and auxiliary winding activations have been integrated in order to evaluate the designs' whole-working condition. If the winding switches were activated at the correct time, the FW performance of the Prius IPM machine could be improved significantly thanks to the proposed turn-changing method.

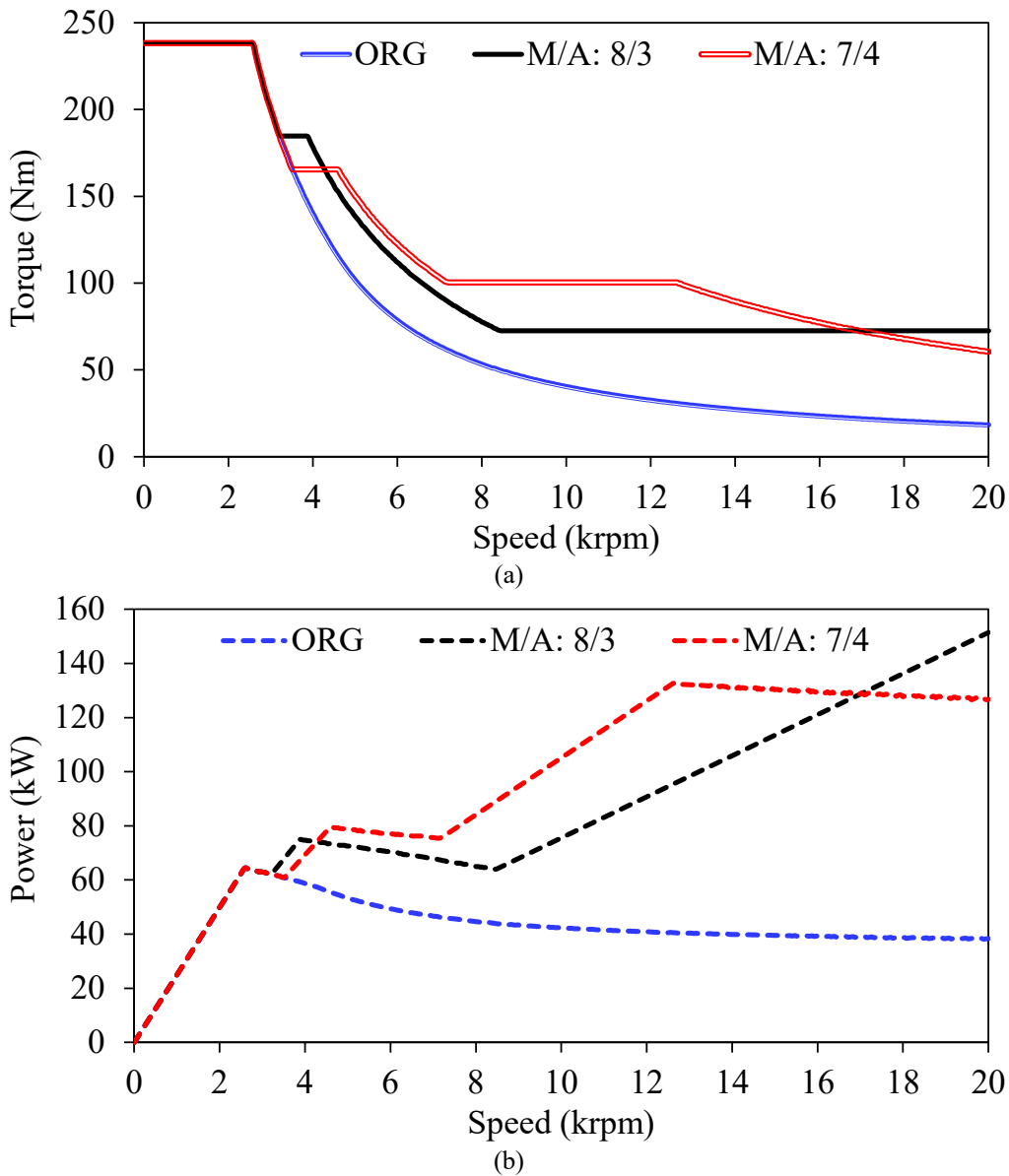
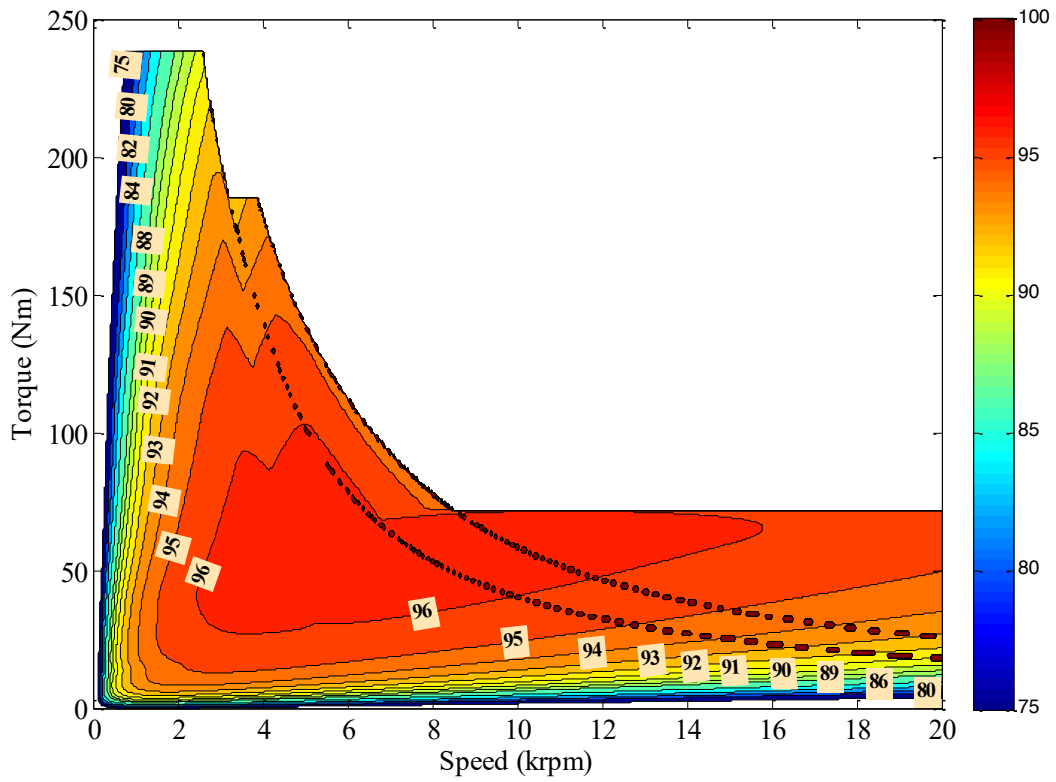
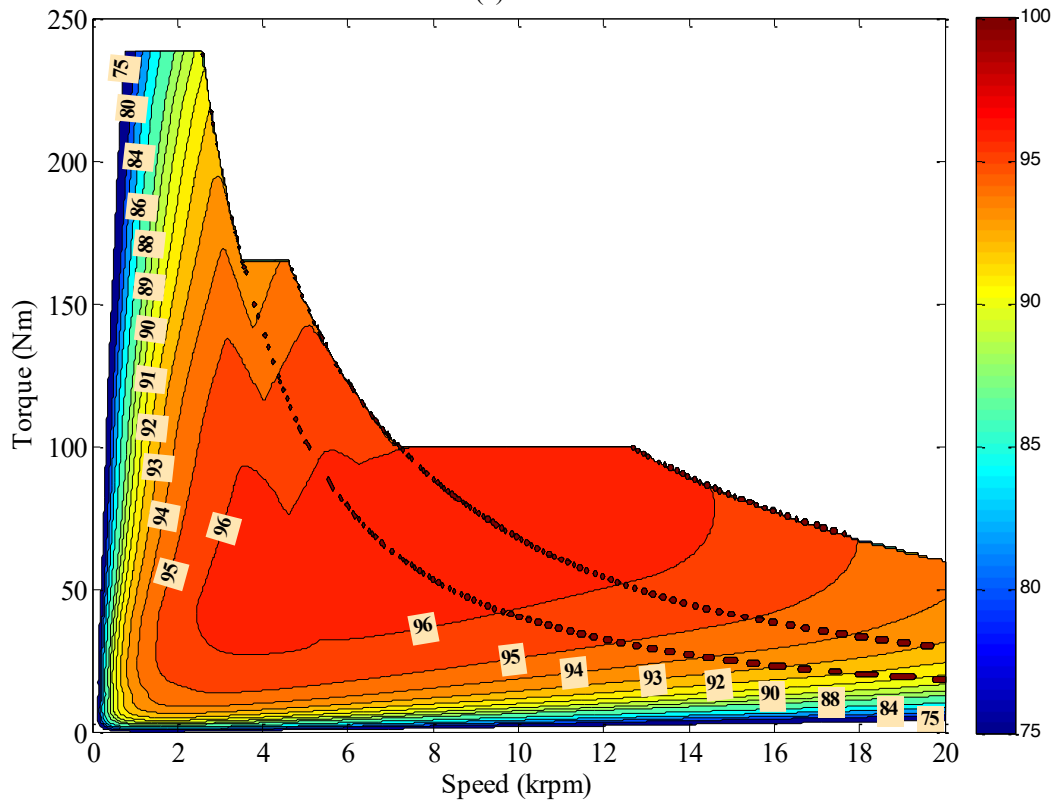


Figure 14 Comparison of torque- and power-speed characteristics of conventional (ORG), and new (M8/A3) and (M7/A4) IPM machines with number of turns switching concepts.



(a) M8/A3



(b) M7/A4

Figure 15 Comparison combined efficiency maps.

The combined versions of the efficiency maps are shown in Figure 15. The efficiency at constant power and in deep FW regions is fairly good in both scenarios, as indicated in the figure (M/A: 8/3 or M/A: 7/4). Conclusion: The deeper the FW region and the constant power region, the higher the torque, the better the efficiency.

Phase current and voltage changes with respect to speed are shown in Figure 16 to demonstrate that the current and voltage limitations have not been exceeded. It is clear that no operating point has exceeded the current or voltage restrictions. As a consequence, the torque and power in the high-speed operation areas may be greatly improved thanks to the turn number changing idea without going above the current and voltage restrictions of the inverter.

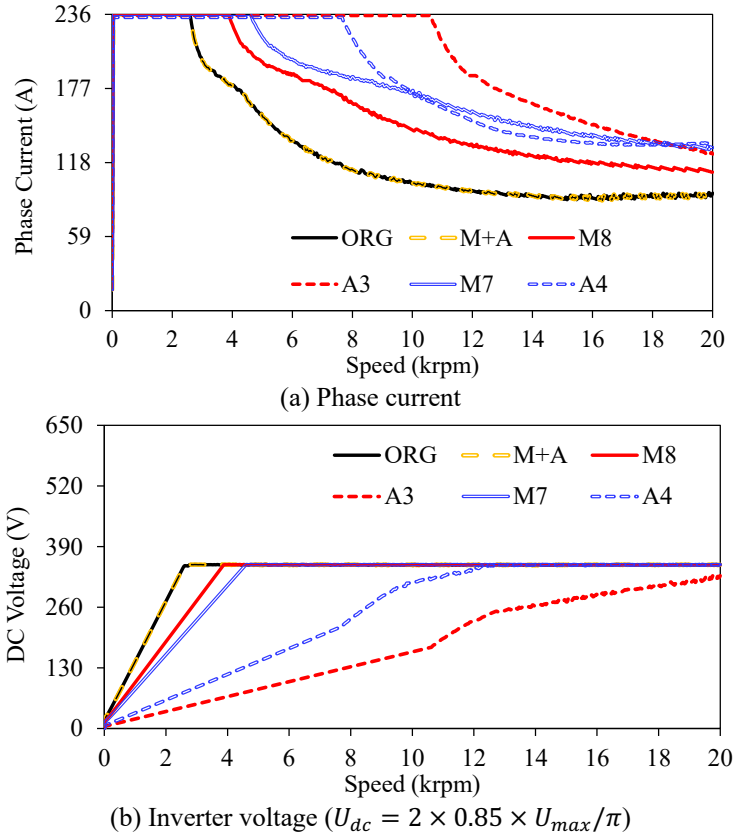


Figure 16 Variation of phase current and inverter DC voltage with respect to speed.

6. FW Characteristics Verification

In order to validate that the FW performance calculations are correct, the calculated FW performance of the Toyota Prius IPM machine with 236A peak phase current and $650V \times 2 \times 0.85 / \pi$ inverted voltage has been compared with the measured characteristics. The measurement results have been taken from the reports of Oak Ridge National Laboratory [39]. The calculated FW performance of the Prius IPM machine under the operation conditions given above is shown in Figure 17. As seen in the figure, the peak torque is about 238Nm and the peak power is 60kW.

The calculated and measured efficiency maps of the Prius IPM machine are illustrated in Figure 18. It is obvious that the measured efficiency map is obtained under lower phase current injection operation. However, as demonstrated in the Prius IPM machine's locked rotor test [39], the peak torque is approximately 200Nm when operating at 200A current.

As seen in the figure, the peak efficiency is 96% between about 2.5 and 6 krpm and 4.5 and 6.5krpm for calculated and measured, respectively. Furthermore, the operation region's efficiency levels exceeding 88 percent are dispersed throughout a considerable portion of the territory. It is obvious that operations using more current at the same number of phase turns cost less efficiently. However, as shown in Figure 13(c), when the number of turns is reduced from 11 to 8, an almost identical efficiency map to the measured one is obtained.

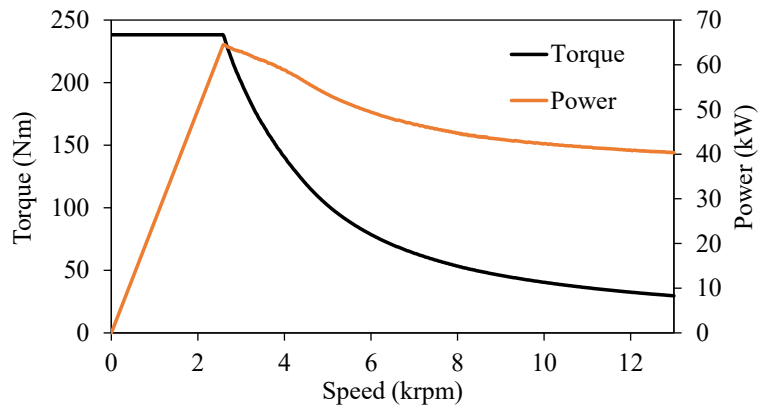
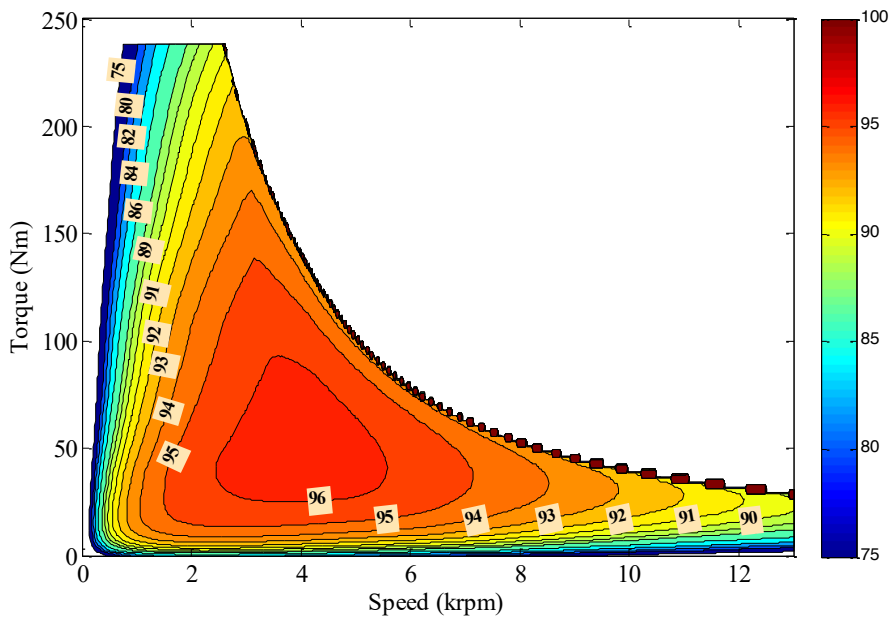
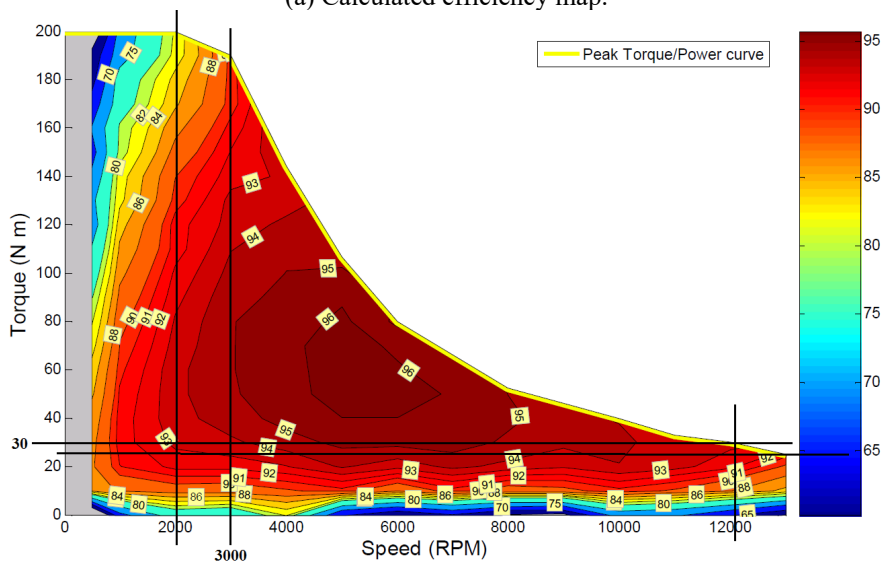


Figure 17 Torque- and power-speed characteristics of Prius IPM for 236A and $650V \times 2 \times 0.85/\pi$.



(a) Calculated efficiency map.



(b) Measured efficiency map [39].

Figure 18 Comparison of calculated and measured efficiency maps for Toyota Prius 2010 IPM machine.

7. Conclusions

This paper proposes and implements an unconventional winding-switching approach in IPM machines to improve FW capability and efficiency. The basic structure and working principle of the considered topology are explained. The main and auxiliary windings are activated based on the torque demand by simply changing the status of switches. Thus, the steady-state and FW performance of IPM machines having different number of turns in their main and auxiliary windings have been investigated in depth. The IPM machine topologies having winding-switching features are compared with Toyota Prius IPM machine's performance characteristics in order to reveal the merits/demerits of the proposed methodology. The following advantages have been achieved over the conventional IPM by implementing the proposed winding-switching approach to the IPM machines.

- Ability to adjust flux as a wide range: wide FW capability;
- Significantly improved FW performance characteristics: substantially high power at high speed;
- Move the highest efficient region from the high torque to the low torque at the constant torque region;
- Move the highest efficient region from the high speed to the low-speed operating region;
- Overall high efficiency.

Moreover, the predicted efficiency map of the original Toyota Prius 2010 IPM machine is verified using the efficiency measurements provided to ensure the accuracy of the analytical and numerical calculations offered in this work.

References

- [1] Jans TM. Flux-weakening regime operation of an interior permanent magnet synchronous motor drive. *IEEE Trans. Ind. Appl.* 1987; IA-23(4): 681-689.
- [2] Sebastian T, Siemon GR. Operating limits of inverter-driven permanent magnet motor drives. *IEEE Trans. Ind. Applicat.* 1987; 23: 327-333.
- [3] Schiferl RF, Lipo TA. Power capability of salient pole permanent magnet synchronous motor in variable speed drive applications. *IEEE Trans. Ind. Applicat.* 1990; 26: 115-123.
- [4] Sneyers B, Novotny DW, Lipo TA. Field weakening in buried permanent magnet Ac motor drives. *IEEE Trans. Ind. Applicat.* 1985; 21: 398-407.
- [5] Lawler S, Bailey M, McKeever W. Extended constant power speed range of the brushless DC motor through dual mode inverter control. 2001. Oak Ridge National Lab., UT-Battelle, LLC, USA.
- [6] Bailey M, et al. Dual mode inverter control test verification. 2001. Oak Ridge National Lab., UT-Battelle, LLC, ORNUTM-20001172.
- [7] Ostovic V. Memory motors—a new class of controllable flux PM machines for a true wide speed operation. In: *IEEE Ind. Appl. Conf.*; Oct. 2001; Chicago, IL, USA. pp. 2577-2584.
- [8] Hemmati S, Barigh M. A new approach for field weakening in a surface mounted permanent magnet synchronous motor by winding switching. *27th Iranian Conf. Elect. Eng. (ICEE'19)*; May 2019; Yazd, Iran. pp. 509-514.
- [9] Hemmati S, Lipo TA. Field weakening of a surface mounted permanent magnet motor by winding switching. *Int. Symp. Power Electron, Elect. Drives, Auto. Motion*; Jun. 2012; Sorrento, Italy. pp. 736-740.
- [10] Sin S, Roshanzamir A, Kwon B. I. Improvement of the Constant-Power Speed Range of Surface-Permanent Magnet Machine Using Winding Switching. *IEEE Access* 2021; 9: 32298-32309.
- [11] Im SH, Park GM, Gu BG. Novel Winding Changeover Method for A High Efficiency AC Motor Drive. *IEEE Energy Convers. Cong. Expo. (ECCE'19)*; Oct. 2019; Baltimore, MD, USA. pp. 2347-2352.
- [12] Vido L, Amara Y, Gabsi M, Lecrivain M, Chabot F. Compared performances of homopolar and bipolar hybrid excitation synchronous machines. *Proc. IEEE Ind. Appl. Conf.*; Oct. 2005; Hong Kong, China. pp. 1555–1560.
- [13] Vido L, Amara Y, Gabsi M, Lecrivain M, Chabot F. Homopolar and bipolar hybrid excitation synchronous machines. *IEEE Int. Conf. Elect. Mach. Drives*; May 2005; San Antonio, TX, USA. pp. 1212–1218.
- [14] Chan CC, Chau KT, Jiang JZ, Xia W, Zhu M, Zhang R. Novel permanent magnet motor drives for electric vehicles. *IEEE Trans. Ind. Electron.*, 1996; 43(2): 331–339.
- [15] Tapia JA, Leonardi F, Lipo TA. Consequent-pole permanent magnet machine with extended field-weakening capability. *IEEE Trans. Ind. Appl.* 2003; 39(6): 1704–1709.
- [16] Luo X, Lipo TA. A synchronous/permanent magnet hybrid AC machine. *IEEE Trans. Energy Convers.* 2000; 15(2): 203–210.
- [17] Fodorean D, Djerdir A, Viorel IA, Miraoui A. A double excited synchronous machine for direct drive application—Design and prototype tests. *IEEE Trans. Energy Convers.* 2007; 22(3): 656–665.
- [18] Li Y, Lipo T. A. A doubly salient permanent magnet motor capable of field weakening. *Proc. IEEE Power Electron. Spec. Conf.*; Jun. 1995; Atlanta, GA, USA. pp. 565–571.

- [19] Kosaka T, Kano Y, Matsui N, Pollock C. A novel multi-pole permanent magnet synchronous machine with SMC bypass core for magnet flux and SMC field-pole core with toroidal coil for independent field strengthening/weakening. Proc. Eur. Conf. Power Electron. Appl.; Sep. 2005; Dresden, Germany. pp. 1–10.
- [20] Zhu ZQ, Al-Ani M. MJ, Liu X, Lee B. A Mechanical Flux Weakening Method for Switched Flux Permanent Magnet Machines. IEEE Trans. Energy Convers 2015; 30(2): 806-815.
- [21] Capponi FG, Donato G, Caricchi F. Recent advances in axial-flux permanent-magnet machine technology. IEEE Trans. Ind. Appl. 2012; 48(6): 2190–2205.
- [22] Capponi FG, Terrigi R, Caricchi F, Ferraro L. Active output voltage regulation for an ironless axial-flux PM automotive alternator with electromechanical flux weakening. IEEE Trans. Ind. Appl. 2009; 45(5): 1785–1793.
- [23] Zhou G, Miyazaki T, Kawamata S, Kaneko D, Hino N. Development of variable magnetic flux motor suitable for electric vehicle. In: Proc. Int. Power Electron. Conf.; Jun. 2010; Sapporo, Japan. pp. 2171–2174.
- [24] Lei M, Sanada M, Morimoto S, Takeda Y, Matsui N. High efficiency adjustable speed control of IPMSM with variable permanent magnet flux linkage. In: Proc. Conf. Rec. IEEE IAS Annu. Meeting; Oct. 1999; Phoenix, AZ, USA. pp. 881–887.
- [25] Lei M, Sanada M, Morimoto S, Takeda Y. Advantages of IPMSM with adjustable PM armature flux linkage in efficiency improvement an operating range extension. In: Proc. Power Convers. Conf.; Apr. 2002; Osaka, Japan. pp. 136–141.
- [26] Kou B, Li C, Cheng S. Flux-weakening-characteristic analysis of a new permanent-magnet synchronous motor used for electric vehicles. IEEE Trans. Plasma Sci. 2011; 39(1): 511–515.
- [27] Shakal A, Yuefeng L, Lipo TA. A permanent magnet AC machine structure with true field weakening capability. In: Proc. IEEE Int. Symp. Ind. Electron.; Jun. 1993; Budapest, Hungary. pp. 19–24.
- [28] Ostovic V. Memory motor. IEEE Trans. Ind. Appl. 2003; 9(1): 52–61.
- [29] Ostovic V. Pole-changing permanent magnet machines. IEEE Trans. Ind. Appl. 2002; 38(6): 1493–1499.
- [30] Hengchuan L, Heyun L, Zhu ZQ, Mingming H, Ping J. Permanent magnet remagnetizing physics of a variable flux memory motor. IEEE Trans. Magn. 2010; 46(6): 1679–1682.
- [31] Yu C, Chau K.T. Design, analysis, and control of DC-excited memory motor. IEEE Trans. Energy Convers. 2011; 26(2): 479–489.
- [32] Yu C, Chau KT, Liu X, Jiang JZ. A flux-mnemonic permanent magnet brushless motor for electric vehicles. IEEE J. Appl. Phys. 2008; 103(7): 103–106.
- [33] Swamy MM, Kume T, Maemura A, Morimoto S. Extended high speed operation via electronic winding-change method for AC motors. IEEE Trans. Ind. Appl. 2006; 42(3): 742–752.
- [34] Ilhan E, Gysen BLJ, Paulides JJH, Lomonova EA. Analytical hybrid model for flux switching permanent magnet machines. IEEE Trans. Magn. 2010; 46(6): 1762–1765.
- [35] Copt F, Raujo DM, Koechli C, Perriard Y. Current control strategy for dynamic winding reconfiguration of slotless brushless DC motors. IEEE Trans. Ind. Appl. 2019; 55(1): 417–425.
- [36] Im SH, Gu BG. A snubberless solid-state tap changer for permanent magnet synchronous motors. IEEE Trans. Power Electron. 2020. 35(11): 12143–12152.
- [37] He S, Li Q, Tong R, Shi G. Transformer economic operation control system based on zero-crossing switching; In: IEEE Advanced Inform. Technol. Electron. Autom. Control Conf. (IAEAC'15); Dec. 2015; Chongqing, China. pp. 508-512.
- [38] Nian H, Zhou Y. Investigation and Suppression of Current Zero Crossing Phenomenon for a Semicontrolled Open-Winding PMSG System. IEEE Trans. Power Electron. 2017; 32(1): 602-612.
- [39] Olszewski M. Evaluation of the 2010 Toyota Prius hybrid synergy drive system. 2011; Oak Ridge Nat. Lab. U.S. Dept. Energy.
- [40] Gundogdu T. Design and Analysis of Double Fed Interior Permanent Magnet Machines for Traction Applications. In: 2022 IEEE IAS Global Conf. Emerging Technol. (GlobConET'22); May 2022; Arad, Romania. pp. 1-8.
- [41] Gundogdu T, Komurgoz G. Influence of design parameters on flux-weakening performance of interior permanent magnet machines with novel semi-overlapping windings. IET Elect. Power Appl. 2020; 14: 2547-2563.

Optimized YOLOv4 Algorithm for Car Detection in Traffic Flow

Alzubair Alqaraghuli¹, Oğuz Ata^{2*}

¹ Information Technology, Computer Engineering, Altinbas University, Istanbul, Türkiye

² Information Technology, Computer Engineering, Altinbas University, Istanbul, Türkiye

¹zubairk53@gmail.com, ^{2*}oguzata@gmail.com

(Geliş/Received: 30/05/2022;

Kabul/Accepted: 02/08/2022)

Abstract: The vehicle detection accuracy and actual in images and videos appear to be very tough and critical duties in a key technology traffic system. Specifically, under convoluted traffic conditions. As a result, the presented study proposes single-stage deep neural networks YOLOv4-3L, YOLOv4-2L, YOLOv4-GB, and YOLOv3-GB. After optimizing the network structure by adding more layers in the right positions with the right amount of filters, the dataset will be repaired and the noise reduced before being sent to the mentoring. This research will be applied to YOLOv3 and YOLOv4. In this study the OA-Dataset is collect and used, the data set is manually labeled with the care of different weathers and scenarios, as well as for end-to-end training of the network. Around the same time, optimized YOLOv4 and YOLOv3 demonstrate a significant degree of accuracy with 99.68 % and precision of 91 %. The speed and detection accuracy of this algorithm are found to be higher than that of previous algorithms.

Key words: Car Detection, The Traffic Flow, YOLOv4, Deep learning.

Trafik Akışında Araba Algılama için Optimize Edilmiş YOLOv4 Algoritması

Öz: Görüntülerde ve videolarda araç algılama doğruluğu ve gerçekliği, önemli bir teknoloji trafik sisteminde çok zor ve kritik görevler gibi görünmektedir. Özellikle, kıvrımlı trafik koşulları altında. Sonuç olarak, sunulan çalışma tek aşamalı derin sinir ağları YOLOv4-3L, YOLOv4-2L, YOLOv4-GB ve YOLOv3-GB önermektedir. Doğru miktarda filtre ile doğru pozisyonlara daha fazla katman ekleyerek ağ yapısını optimize ettikten sonra, veri seti onarılacak ve mentorluğa gönderilmeden önce gürültü azaltılacaktır. Bu araştırma YOLOv3 ve YOLOv4'e uygulanacaktır. Bu çalışmada OA-Dataset toplanmış ve kullanılmış, veri seti farklı hava koşulları ve senaryolar dikkate alınarak ve ayrıca ağır uçtan uca eğitimi için manuel olarak etiketlenmiştir. Aynı zamanda, optimize edilmiş YOLOv4 ve YOLOv3, %99,68 ve %91 hassasiyetle önemli derecede doğruluk gösterir. Bu algoritmanın hızı ve algılama doğruluğu, önceki algoritmalarından daha yüksek bulunmuştur.

Anahtar kelimeler: Araba algılama, Trafik akışı, YOLOv4 modeli, Derin öğrenme.

1. Introduction

With all of the changes in people's lives, city growth has accelerated, resulting in a large increase in the number of private cars. As a result, traffic congestion has become a major issue that impacts people's lives. The intelligent transportation system (ITS), the traffic with a good accuracy predictions may present basic information to make a decision to the traffic administration. As a result, in smart cities, high-accuracy traffic transmission estimate is seen as a critical component of evolving smart transmission systems. The main task in traffic prediction is the accurate and rapid detection of cars in traffic videos or images, Therefore, it is really substantial to find an algorithm that can produce correct detection and real-time recognition of cars [1]. The presented study aims to sort the conventional detection methods in the following: - Xu et al. found out distinct factors that are able to pull out the features from the zone of interest which are nominated in the pictures then by training a classifier, will apply the detection, Unfortunately, due to the sensor's complexity, these techniques will decrease accuracy[2]. Qiu et al. used visual detection, which is based on inter-frame and visual flow variations. Visual flow has good accuracy, but the problem with visual flow is the slow detection speed, even though the inter-frame difference process is fast but not very accurate[3]. Felzenszwalb et al. suggested a method called "the classification of sliding window", the first step of this method is sliding the windows to pull out features of the region of interest after that the second step is applying a classifier to get detection on the target by using the support-vector machine (SVM). This method requires a lot of calculation that leads to slow speed in detection [4].while , Kenan Mu et al.

* Corresponding author: oguzata@gmail.com ORCID Number of authors: ¹ 0000-0002-6117-8051, ² 0000-0003-4511-7694

used a method called edge detection, but the process of edge detection can be affected by noise and background intervention which means inaccurate detection [5]. The above-mentioned target detection approaches necessitate a lot of calculations, which results in slow detection speeds, as well as a lack of generality in the field of feature extraction.

In the last few years, with the fast developments in artificial intelligence technologies and computer vision, new methods of object detection algorithms have been investigated, these methods are based on deep learning, the convolutional neural networks (CNN) is considered to be very convenient and the feature extraction of the images has strong generalization [6]. These days, there are two major methods of object detection in deep learning: the first is the algorithm that combines candidate region suggestions and convolutional neural networks, exemplified by spatial pyramid pooling (SPP)-net [7], and Region-Based Convolutional Neural Networks (R-CNN) [8], the second one is You Only Look Once (YOLO)[9-12] [10][11][12], and Single Shot MultiBox Detector chain (SSD) [13]. These algorithms convert detection issues into case of regression by employing deep learning. The R-CNN algorithm uses feature extractor to select region suggestion boxes, which improves object detection accuracy. However, due to the scaled candidate box and the large number of calculations, the process takes a long time, resulting in the loss of image feature information. In the R-CNN, there is a problem with the size of the fixed input layer, the SPP-net algorithm solved this problem by using a pyramid pooling layer. But this will lead to cumbersome training steps and every step generate a ratio of errors due to the SVM classification and the convolutional neural network should be trained separately. As a result of that, it will take a long time for training and a large space from the hard disk due to the large number of feature files that are saved after the training. The rapid R-CNN algorithm which is merging the specifications of SPP-net into the R-CNN has solved some problems like test time, long training and large space occupation, etc. But it still depends on the selective search method to find the extraction of the particular box, so that means the problem of time-consuming still exists [14]. By replacing the selective search (SS) with the RPN(region proposal networks), the Faster R-CNN back end and the region frame extraction candidate are integrated with convolutional neural network model, as a result, the candidate region extraction time will be short in the Faster R-CNN [15]. The first truly end-to-end object detection algorithm is Faster R-CNN. However, its real-time object detection speed is far from the requirement. YOLO chain is a network algorithm based on regression which uses a full map for training and it returns both object category and object frame at diverse positions. To train the network, the algorithm of YOLO employs a method rely on the frame area algorithm of the candidate. For the training, YOLO employs the full image then returns both object category and object frame at various positions, using the steps that the researcher mentioned makes it a lot simpler to fastly differentiate the background area from objects however it is susceptible to errors of position to enhance the structure of the YOLO network model YOLOv2 employ methods, and due to these methods the speed of detection improved. The network of YOLOv2 is simple, even with it enhancing the speed but it does not make the detection more accurate. YOLOv3 employs the idea of Feature Pyramid Networks(FPN) to achieve multi-scale predictions [16] and for extracting the image features, YOLOv3 uses the ideas of the deep residual network(ResNet) to achieve equilibrium between the speed of detection and the detection accuracy [17]. YOLOv4 Is much better than the last versions of YOLO in speed and performance. YOLOv4 uses a bag of freebies and it's a method that is used to enhance the training without any cost from the hardware, also to improve the accuracy of detection, YOLOv4 use collection of modules. These modules excess the inference cost by little amount but it has a good effect on the detection accuracy. The presented study suggests some changes to the structure of the YOLOv4 to optimize it, in this study, the researcher investigate optimized YOLOv4-2L, YOLOv4-3L, YOLOv4-GB, and YOLOv3-GB for tracking and detecting vehicles in traffics. Optimized modules of YOLO is based on the YOLOv4 algorithm, the researcher adds more layers and fixes the data set befor training the model to enhance the YOLOv4 detection system performance on traffics.

2. Principle and Composition of Traffic Detectoin System

Many researchers in field indicates that the characterization of traffic state studies can be gathered into some categories like determination of average speed, determination of traffic flow parameters, and detection of the congestion location [18]. The detection system of traffics consists of an image preprocessing module, the module of video image acquisition, the module of vehicle flows statistics, and the module of vehicle detection and identification. All the detection system modules are displayed in figure 1.

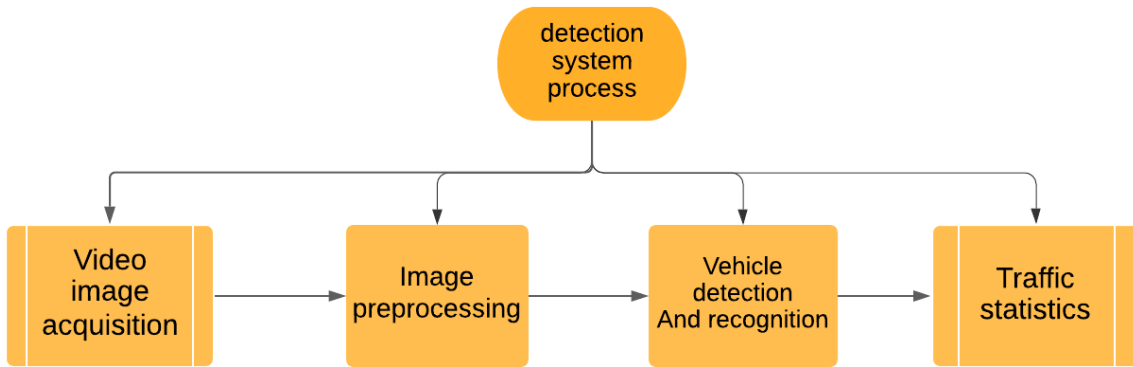


Figure 1. The process of Detection System

The core of the system is the module of vehicle detection and recognition because it recognizes and locates the vehicle in video images. To combine recognition and object position into one, which needs to take the requirements of recognition accuracy and speed detection into consideration, the researcher uses YOLOv4 for vehicles detection and recognition. YOLOv4 is the updated YOLO, so it has advantages in detection accuracy, fast speed, and accurate positioning. On previous versions of YOLO, YOLOv4 uses CSPDarknet53 as Backbone and the CSPDarknet53 is an updated version of Darknet-53. It is based on concepts from CSPNet, they use this kind of the darknet to increase gradient path, reduce memory traffic and balance computation of each layer. YOLOv4 uses Spatial Pyramid Pooling (SPP) as the Neck. And the Head of YOLOv4 is YOLOv3. The present research hotspot is YOLOv4, in figure 2 the YOLOv4 network structure is shown.

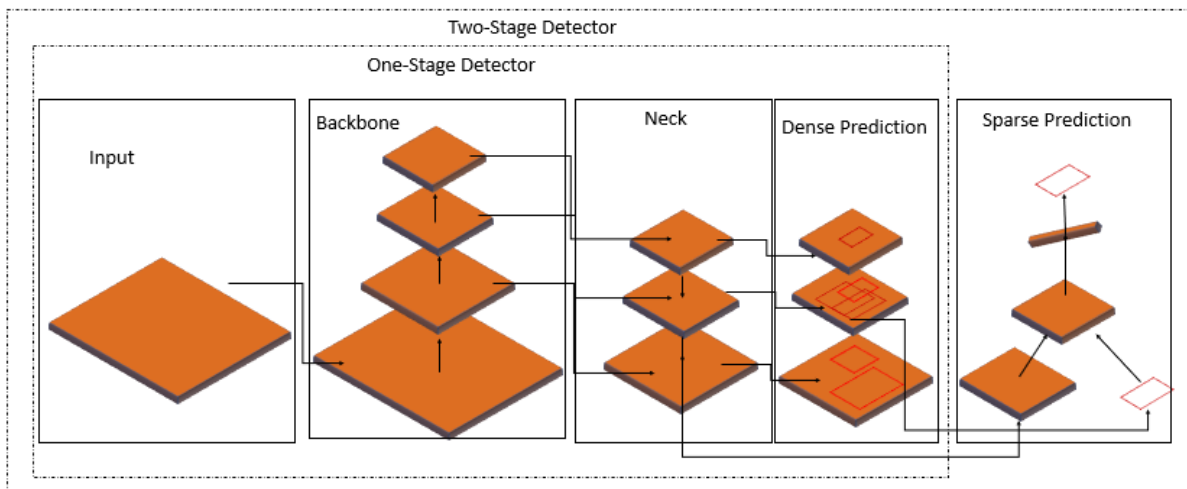


Figure 2. YOLOv4 Network Structure

2.1 YOLOv4 Structure Optimization

YOLOv4 uses CSPdarknet-53 and CSPdarknet-53 consists of convolutional layers. So as what has been done in YOLO 9000, the study finds out that increasing the number of layers helps to enhance the accuracy of the detection, the presented study suggests doing the same with YOLOv4. In the structure of YOLO. There are three layers responsible for the detection, so in the first optimization, the researcher adds one layer before the first detection layer and one more layer before the third detection layer. These layers contain a specified amount of filters, and this study revealed that when the model is trained, the detection accuracy improved. In the second

optimization, the researcher added three layers, one before the first YOLO layer, which is responsible for detection, and two layers before the third detection layer, and the detection rate increased.

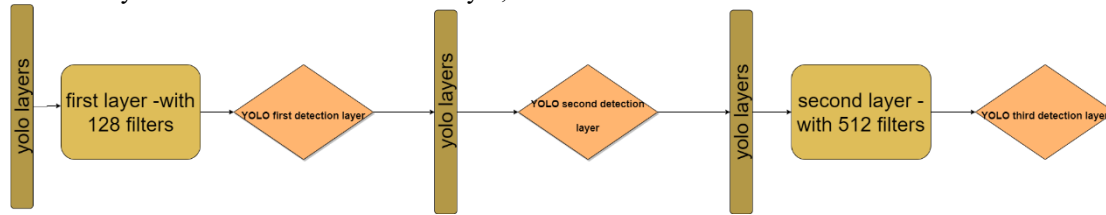


Figure 3. YOLOv4_2L

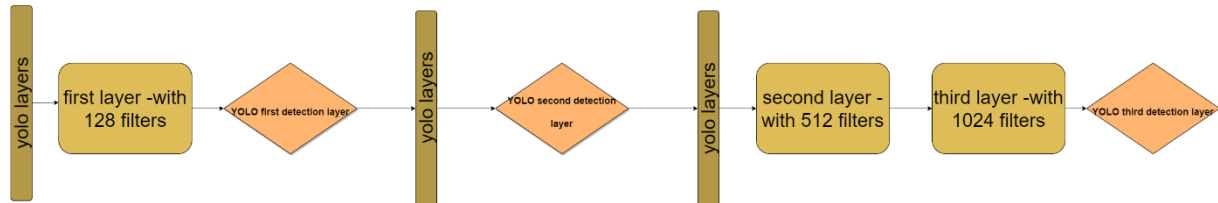


Figure 4. YOLOv4_3L

figures 3 – 4 shows that the optimization of the structure are YOLO first detection layer, YOLO second detection layer, and YOLO third detection layer refers to the layers that are responsible for detection, the square shape refers to the new layers that the researcher adds, in addition to the original layers that represented by the long shape.

2.2 Dataset Optimization

E.Torpov et al. referred that the low rate of frames makes the detection of vehicle tracking not feasible, and image compression and low image quality can add more noise to the images[19]. The dataset is a really important part that plays an essential role in the YOLO. The presented study decides to clear the images from the noise before labeling and importing them. The procedure is to apply the Gaussian filter on the images using the open-cv library in python, the gaussian filter will remove the noise from the images[20].

2.3 Making the Dataset

If the study aims to examine real-world traffic, it should use images from real-world traffic with data set called (DETRAC). Furthermore, it is a large-scale detection and tracking data set that is used to detect and track vehicles. This data set is chosen since it is derived from real footage of traffic on highways and bridges in locations such as Tianjin and Beijing. A total of 6203 images from the data set are manually tagged. This data set contains a variety of meteorological conditions. Images of the sun, rain, clouds, and night, as well as their height and angle, are all different.

- 1) The collecting images is done with different weather situations, dusk images, rainy images, and daytime images, the images are taken from the dataset of DETRAC, the number of images is 6203 images;
- 2) To make training set the researcher randomly extracts 80% of the dataset.
- 3) To make testing set the researcher randomly extracts 20% of the dataset.
- 4) 6203 images can be called as the OA. Dataset in the current study.

To label each vehicle in the training set, testing set images and use the labelling tool and when label the vehicle on the images an XML file will be created. The XML file saves the information of labeling for the next training. Five values will be saved in the XML file. The first value is an individual number that refers to the type of the class. So if there are two classes, for example, gender classes, (0) will refer to male and 1 will refer to female, but in our case, there is only one class which is vehicle so the individual number will be 0, the rest values will be decimal numbers. These numbers will refer to the location of the vehicle, the first one is for X center coordinate, the second decimal number refer to Y center coordinate, the third decimal number refer to width, and the final decimal number refers to the height.

3. Analysis and Results of Experiment

3.1. The Paltform

In the presented study, it used Windows 10 system, and PyCharm environment, also python 3.7. is used under the Darknet framework, the YOLOv4 algorithm is applied. NVIDIA RTX 3070 graphic card is used to accelerate training and the processor is Ryzen 7 5800H.

3.2. Network Training

The model multiple times is used to conduct the results, first, the trained model for 30,000 iterations but the results are not good , it found out that the more iteration steps are not a good choice to improve the detection accuracy, so it is used for only 4000 iterations. In the first 1000 iterations, the average loss was so high then it starts to get down slowly and it reaches 2.0 at 1100-1500, at 1500-2500 the average lose was 1.0 then it goes to 0.9 at 3000-3500 and at 3500-4000 it reaches 0.8-0.7, and that was the best average loss in the study, it gives us a really good accuracy. the tests with YOLOv4, YOLOv4-2L, and YOLOv4-3L, with YOLOv4-GB, YOLOv3, and YOLOv3-GB. The researcher uses part of our data set and it contains 200 images, these images contain vehicles in different positions, the training is done with 2000 iterations, it is also found out that if the training increases, it will not make a big difference the results are almost the same.

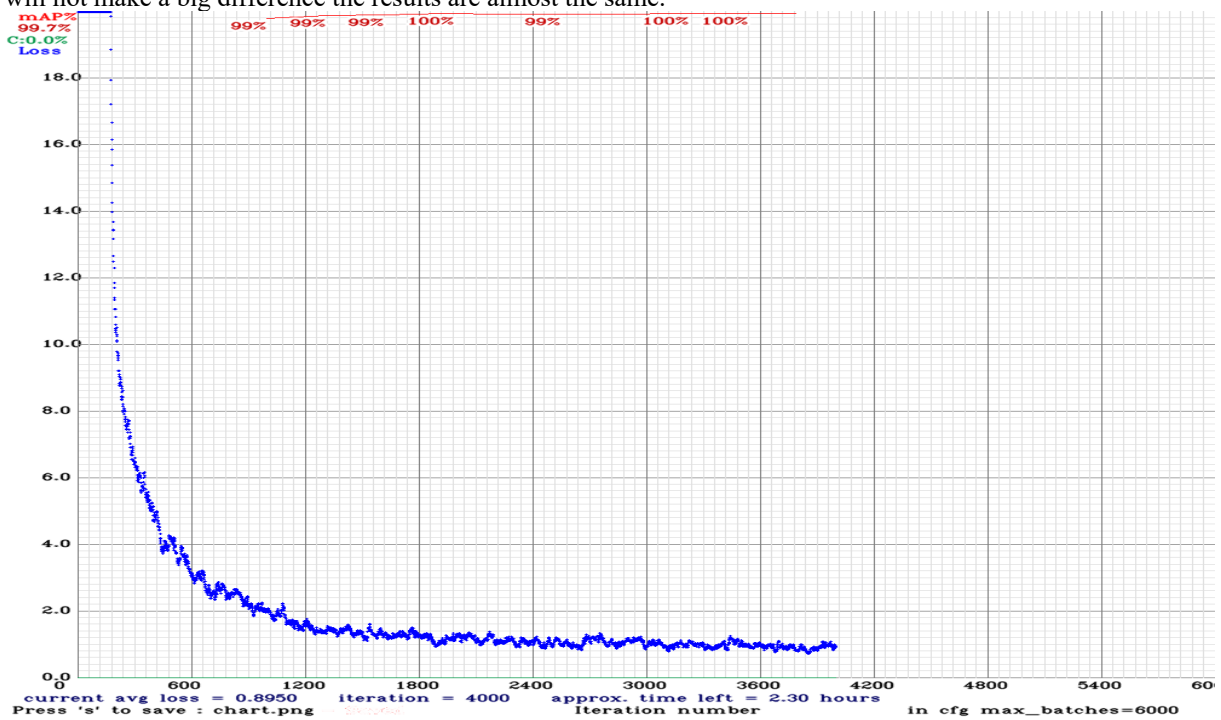


Figure 5. YOLOv4-2L Training Chart

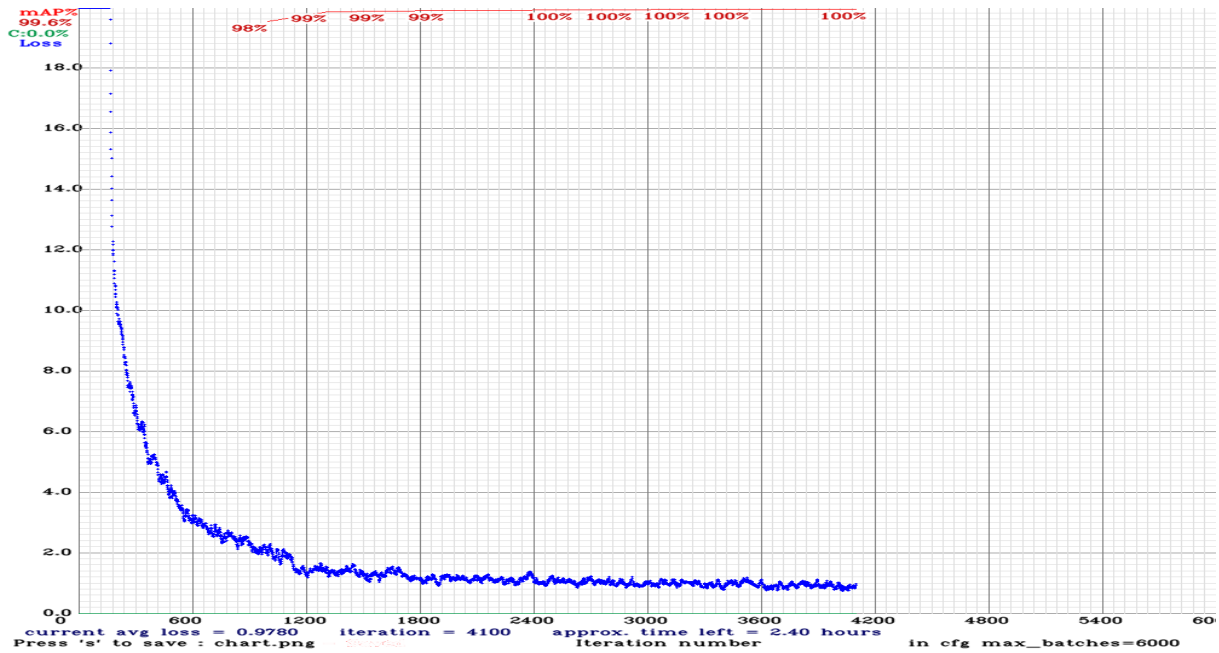


Figure 5. YOLOv4-3L Training Chart

3.3. Evaluation Parameters

To make sure of the efficiency of optimized YOLOv4, the particular tests are used on dataset, analyzing the experimental data, and compression of the experimental results. In the monitoring processes, some problems may occur like false detection and missed detection. As evaluation parameters, Precision, Recall, and mAP(mean average precision) are also used to fulfill the required results. The Precision mean accuracy which refers to the proportion of the accurately detected vehicles to all number of detected vehicles. And the Recall implies the review rate which means the proportion of the number of detected vehicles to the aggregate number of vehicles in the dataset. Equations are displayed below :

$$Precision = \frac{TP}{TP+FP} \quad (1)$$

$$Recall = \frac{TP}{TP+FN} \quad (2)$$

The (TP) refers to True Positive which is the correct vehicles detection number, the (TN) mean True Negative which refers to the correct backgrounds detection number, the (FP) refers to False Negative which indicates detection missed number.

3.4 Setup of YOLO Architecture

Here the names of the modified YOLO will be explained in details.

- YOLOv4-2L : this name refers to the optimized YOLOv4 with extra two layers in the structure of YOLOv4, these layers contain filters, 128 filters in the first layer and 512 filters in the second.
- YOLOv4-3L : this name refers to the second optimized YOLOv4 with extra three layers in the structure of YOLOv4, these layers also contain filters, exactly 128, 512 and 1024 filters to the first, second and third layer successively.
- YOLOv4-GB and YOLOv3-GB : these names refers to YOLO with fixed data set.

4. The Analysis of Comparison Results of Different Algorithms

The Precision, Recall, and mAP (Mean Average Precision) of the presented study are compared with other models. results are displayed in Table 1.

Table 1. Comparative Between Presented Study and Other Studies

	The Precision	The Recall	Accuracy
YOLOv4 (Original)[12]	90%	100%	99.67%
YOLOv4-2L(Presented Study)	89%	100%	99.68%
YOLOv4-3L(Presented Study)	91%	100%	99.67%
YOLOv4-GB(Presented Study)	97%	100%	99.98%
YOLOv3(Original)[11]	97%	100%	99.97%
YOLOv3-GB(Presented Study)	97%	100%	99.97%
YOLOv3-DL(Previous Study)[1]	96%	98%	98.83%

From table 1 it appears that the accuracy has increased in comparison with other studies that are indicated that the current study can detect more vehicles in the image and difficult positions like vehicles which are far away from the detection camera.



Figure 7. YOLOv4

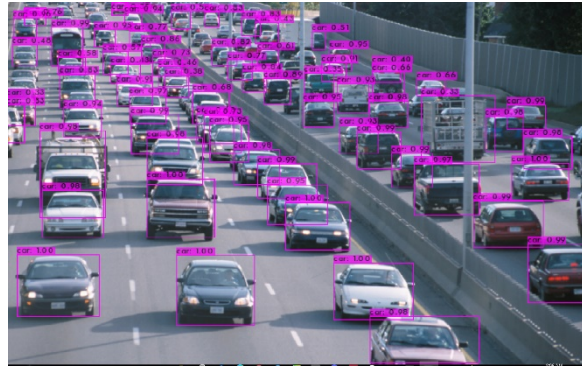


Figure 8. YOLOv4-2L



Figure 9. YOLOv4-3L



Figure 10. YOLOv4-GB

The figures(7-8-9-10) above shows the results of YOLO object detection method and the optimized YOLOv4 with indicating that the presented study shows massive accuracy compared to the original study.

4.1 Video Analysis and Comparison

To experience the detection accuracy of the presented study in a video stream, the study is applied on a vehicle driving video and the length of the video is 30s while, the test results are shown as a follow in Table2. The presented studies's accuracy rate is higher than other studies.

Table 2. Video Comparison

	AVG-FPS
YOLOv4 (Original)[12]	62.0
YOLOv4-2L (Presented Study)	62.5
YOLOv4-3L (Presented Study)	60
YOLOv4-GB (Presented Study)	62.2
YOLOv3 (Original)[11]	63.3
YOLOv3-GB (Presented Study)	63.1

The test results shows that it took a different amount of time to count the vehicles per frame depending on the algorithm used within study, furthermore, the presented study is nearly similar to the real traffic. The current study is compared to other studie's results like YOLOv3 and YOLOv4, that are indicated the video monitoring accuracy rate of the traffic flow has increased.

5. Conclusion

Due to the limitation in YOLOv4, the current study finds out that the detecting far-away object is hard with noticing that YOLOv4 may miss the detection if there are more vehicles or when the vehicles are different in size, and that will affect the accuracy rate of the traffic flow prediction and statistics information. By using the presented study, the high accuracy rate of traffic flow statistics could be produced, and the results are conducted by using the presented study is ultimately based to the real number of vehicles in images. The results show that the YOLOv4 can be improved in the accuracy rate of traffic monitoring and in real-time.

References

- [1] Y. Q. Huang, J. C. Zheng, S. D. Sun, C. F. Yang, and J. Liu, "Optimized YOLOv3 algorithm and its application in traffic flow detections," *Appl. Sci.*, vol. 10, no. 9, May 2020, doi: 10.3390/app10093079.
- [2] Y. Xu, G. Yu, Y. Wang, X. Wu, and Y. Ma, "A hybrid vehicle detection method based on viola-jones and HOG + SVM from UAV images," *Sensors (Switzerland)*, vol. 16, no. 8, 2016, doi: 10.3390/s16081325.
- [3] Q. J. Qiu, L. Yong, and D. W. Cai, "Vehicle detection based on LBP features of the Haar-like Characteristics," *Proc. World Congr. Intell. Control Autom.*, vol. 2015-March, no. March, pp. 1050–1055, 2015, doi: 10.1109/WCICA.2014.7052862.
- [4] P. F. Felzenszwalb, R. B. Girshick, D. Mcallester, and D. Ramanan, "Object Detection With Partbase," *IEEE Trans. Pattern Anal. Mach. Intell.*, vol. 32, no. 9, pp. 1627–1645, 2010.
- [5] K. Mu, F. Hui, X. Zhao, and C. Prehofer, "Multiscale edge fusion for vehicle detection based on difference of Gaussian," *Optik (Stuttg.)*, vol. 127, no. 11, pp. 4794–4798, 2016, doi: 10.1016/j.ijleo.2016.01.017.
- [6] K. S. Choi, J. S. Shin, J. J. Lee, Y. S. Kim, S. B. Kim, and C. W. Kim, "In vitro trans-differentiation of rat mesenchymal cells into insulin-producing cells by rat pancreatic extract," *Biochem. Biophys. Res. Commun.*, vol. 330, no. 4, pp. 1299–1305, 2005, doi: 10.1016/j.bbrc.2005.03.111.
- [7] K. He, X. Zhang, S. Ren, and J. Sun, "Spatial Pyramid Pooling in Deep Convolutional Networks for Visual Recognition," *IEEE Trans. Pattern Anal. Mach. Intell.*, vol. 37, no. 9, pp. 1904–1916, 2015, doi: 10.1109/TPAMI.2015.2389824.
- [8] R. Girshick, J. Donahue, T. Darrell, J. Malik, U. C. Berkeley, and J. Malik, "1043.0690," *Proc. IEEE Comput. Soc. Conf. Comput. Vis. Pattern Recognit.*, vol. 1, p. 5000, 2014, doi: 10.1109/CVPR.2014.81.
- [9] J. Redmon, S. Divvala, R. Girshick, and A. Farhadi, "You Only Look Once: Unified, Real-Time Object Detection." [Online]. Available: <https://goo.gl/bEs6Cj>.
- [10] J. Redmon and A. Farhadi, "YOLO9000: Better, Faster, Stronger." [Online]. Available: <http://pjreddie.com/yolo9000/>.
- [11] J. Redmon and A. Farhadi, "YOLOv3: An Incremental Improvement." [Online]. Available: <https://pjreddie.com/yolo/>.
- [12] A. Bochkovskiy, C.-Y. Wang, and H.-Y. M. Liao, "YOLOv4: Optimal Speed and Accuracy of Object Detection," 2020, [Online]. Available: <http://arxiv.org/abs/2004.10934>.

- [13] V. Thakar, H. Saini, W. Ahmed, M. M. Soltani, A. Aly, and J. Y. Yu, "Efficient Single-Shot Multibox Detector for Construction Site Monitoring," *2018 IEEE Int. Smart Cities Conf. ISC2 2018*, no. 1, p. 77, 2019, doi: 10.1109/ISC2.2018.8656929.
- [14] J. Liu, Y. Huang, J. Peng, J. Yao, and L. Wang, "Fast Object Detection at Constrained Energy," *IEEE Trans. Emerg. Top. Comput.*, vol. 6, no. 3, pp. 409–416, 2018, doi: 10.1109/TETC.2016.2577538.
- [15] S. Ren, K. He, and R. Girshick, "Faster R-CNN : Towards Real-Time Object Detection with Region Proposal Networks," pp. 1–9.
- [16] F. B. Tesema, J. Lin, J. Ou, H. Wu, and W. Zhu, "Feature Fusing of Feature Pyramid Network for Multi-Scale Pedestrian Detection," *2018 15th Int. Comput. Conf. Wavelet Act. Media Technol. Inf. Process. ICCWAMTIP 2018*, no. 1, pp. 10–13, 2019, doi: 10.1109/ICCWAMTIP.2018.8632614.
- [17] V. Sangeetha and K. J. R. Prasad, "Syntheses of novel derivatives of 2-acetylfuro[2,3-a]carbazoles, benzo[1,2-b]-1,4-thiazepino[2,3-a]carbazoles and 1-acetyloxycarbazole-2- carbaldehydes," *Indian J. Chem. - Sect. B Org. Med. Chem.*, vol. 45, no. 8, pp. 1951–1954, 2006, doi: 10.1002/chin.200650130.
- [18] Y. Liu, "Big Data Technology and Its Analysis of Application in Urban Intelligent Transportation System," *Proc. - 3rd Int. Conf. Intell. Transp. Big Data Smart City, ICITBS 2018*, vol. 2018-Janua, pp. 17–19, 2018, doi: 10.1109/ICITBS.2018.00012.
- [19] E. Toropov, L. Gui, S. Zhang, S. Kottur, and J. M. F. Moura, "TRAFFIC FLOW FROM A LOW FRAME RATE CITY CAMERA Electrical and Computer Engineering Pittsburgh , PA , USA Instituto Superior Técnico Instituto de Sistemas e Robótica Lisbon , Portugal," *Int. Conf. Image Process.*, pp. 3802–3806, 2015.
- [20] "Gaussian filtering • Significant values," pp. 18–32, 2010.

Automatic Diagnosis of Snoring Sounds with the Developed Artificial Intelligence-based Hybrid Model

Muhammed YILDIRIM^{1*}

¹ Department of Computer Engineering, Faculty of Engineering and Natural Sciences, Malatya Turgut Ozal University, Malatya, Turkey

*¹ muhammed.yildirim@ozal.edu.tr

(Geliş/Received: 07/06/2022;

Kabul/Accepted: 02/08/2022)

Abstract: Sleep patterns and sleep continuity have a great impact on people's quality of life. The sound of snoring both reduces the sleep quality of the snorer and disturbs other people in the environment. Interpretation of sleep signals by experts and diagnosis of the disease is a difficult and costly process. Therefore, in the study, an artificial intelligence-based hybrid model was developed for the classification of snoring sounds. In the proposed method, first of all, sound signals were converted into images using the Mel-spectrogram method. The feature maps of the obtained images were obtained using Alexnet and Resnet101 architectures. After combining the feature maps that are different in each architecture, dimension reduction was made using the NCA dimension reduction method. The feature map optimized using the NCA method was classified in the Bilayered Neural Network. In addition, spectrogram images were classified with 8 different CNN models to compare the performance of the proposed model. Later, in order to test the performance of the proposed model, feature maps were obtained using the MFCC method and the obtained feature maps were classified in different classifiers. The accuracy value obtained in the proposed model is 99.5%.

Key words: Deep Learning, Classifiers, CNN, MFCC, Snoring, Spectrogram

Geliştirilen Yapay Zeka Tabanlı Hibrit Model ile Horlama Seslerinin Otomatik Teşhisi

Öz: Uyku düzeni ve uyku devamlılığı insanların yaşam kalitesi üzerinde büyük bir etkiye sahiptir. Horlama sesi hem horlayanın uyku kalitesini düşürür hem de çevredeki diğer insanların rahatsız eder. Uyku sinyallerinin uzmanlar tarafından yorumlanması ve hastalığın teşhisi zor ve maliyetli bir süreçtir. Bu nedenle çalışmada horlama seslerinin sınıflandırılması için yapay zekâ tabanlı hibrit bir model geliştirilmiştir. Önerilen yöntemde öncelikle ses sinyalleri Mel-spektrum yöntemi kullanılarak görüntüye dönüştürülmüştür. Elde edilen görüntülerin öznelik haritaları Alexnet ve Resnet101 mimarileri kullanılarak elde edilmiştir. Her mimaride farklı olan özellik haritaları birleştirildikten sonra NCA boyut indirgeme yöntemi kullanılarak boyut indirgeme yapılmıştır. NCA yöntemi kullanılarak optimize edilen özellik haritası, İki Katmanlı Sinir Ağı'nda sınıflandırılmıştır. Ayrıca önerilen modelin performansını karşılaştırmak için spektrum görüntüleri 8 farklı CNN modeli ile sınıflandırılmıştır. Daha sonra, önerilen modelin performansını test etmek için MFCC yöntemi kullanılarak öznelik haritaları elde edilmiş ve elde edilen öznelik haritaları farklı sınıflandırıcılarda sınıflandırılmıştır. Önerilen modelde elde edilen doğruluk değeri %99,5'tir.

Anahtar kelimeler: Derin Öğrenme, Sınıflandırıcılar, CNN, MFCC, Horlama, Spectrogram

1. Introduction

Quality sleep has a great impact on people's daily lives. While snoring that occurs during sleep reduces the sleep quality of people, it can be a precursor to some diseases. Snoring not only affects the snorer's sleep quality, but it also affects the sleep quality of those in the same environment [1]. Snoring is caused by the relaxation of the muscles surrounding the throat during sleep. Since the relaxation of the muscles surrounding the throat narrows the airway, the vibrations that cause snoring are triggered. Snoring is most common when you're lying on your back. It is possible to reduce the snoring problem by lying on its side, but it is not a sure solution [2, 3].

Snoring caused by severe sleep apnea has a 40% higher risk of death than other people. Snoring not only disturbs the people around us, it can also be a sign of serious diseases. Severe sleep apnea, stroke, heart diseases, reflux, fatigue, mental health problems, headache, and sexual reluctance are some of these diseases. Mild and moderate sleep disorders can also cause problems such as heart diseases and sexual reluctance [4-6].

It is of great importance to classify the sounds that people make during sleep in order to improve sleep quality. These sounds should be recorded under the control of a sleep specialist and diagnosed accordingly. This is a time-consuming, costly and difficult process. This study, it is aimed to develop a computer-assisted artificial

* Corresponding author: muhammed.yildirim@ozal.edu.tr ORCID Number of authors: ¹ 0000-0003-1866-4721

intelligence-based hybrid model that will help the specialist to diagnose and classify voice data quickly. Thanks to this developed computer-aided system, snoring sounds will be classified more quickly and accurately.

1.1. Related Works

There are studies in the literature for the diagnosis of snoring sounds. Khan et al. [7] proposed a CNN-based model for the classification of snoring sounds in their paper. The data set used in the study consists of two classes, snoring and non-snoring. The researchers obtained an accuracy value of 96% in this study.

Jiang et al. proposed a LSTM-DNN-CNN based model to classify snoring sounds. In the study, feature extraction was performed with the Mel-spectrogram method. The researchers stated that they obtained an accuracy value of 95.07% in this study [8].

Cavusoglu et al. developed a new data set to classify snoring and non-snoring sounds in their study. Feature extraction of the sound signals in the data set was performed using the Sub-band spectral energy method. The researchers classified the feature maps they obtained using the linear regression method. The accuracy value obtained in this study was 90.2% [9].

Dafna et al. used feature extraction methods such as MFCCs, LPCs, and SED in this study. The researchers classified the feature maps they obtained in the Adaboost classifier. In the study, a high accuracy value of 98.2% was obtained. The data set used in this study consists of two classes, snoring and non-snoring sounds [10].

In the method, they developed to classify snoring and non-snoring sounds in this study, Wang et al. obtained an accuracy value of 94.5% in the SVM classifier. In this study, different methods were preferred for feature extraction. The threshold method and linear and nonlinear feature extraction methods are some of them [11].

Lim et al. used recurrent neural networks to classify snoring and non-snoring sounds in their study. In this study, many methods were used for feature extraction. STFT and MFCC are some of these methods. In this study, the researchers obtained an accuracy value of 98.9% [12].

Arsenali et al., while classifying snoring and non-snoring sounds in their study, performed feature extraction using the MFCC method. The accuracy value obtained in this study, which was carried out using Recurrent Neural Networks, was 95% [13].

Shen et al. used MFCC, LPMFCC, and LPC methods for feature extraction while classifying snoring sounds in their study. The feature maps obtained using the MFCC method were classified in CNN and LSTM networks. When the feature map obtained using the MFCC method is classified in the LSTM network, an accuracy value of 87% was obtained [14].

1.2. Contributions and Innovations

- This study, it is aimed to classify snoring sounds, which is a serious problem today.
- Two different methods were used in the study. In the first, the feature maps obtained by the MFCC method were classified in different supervised classifiers.
- In the second method, a hybrid model is proposed. In the proposed model, first of all, sound signals were converted into images by the Mel-spectrogram method. Then, Alexnet and Resnet101 architectures were used as the basis and feature maps were obtained. The obtained feature maps were concatenated and different features of the same data were brought together.
- NCA size reduction method was applied to the combined feature map. In this way, since unnecessary features are eliminated, the training time of the model is shortened.
- In the final stage of the proposed hybrid model, the optimized feature map is classified in the Bilayer Neural Network.
- In the study, the feature map obtained using the MFCC method was classified in 6 different classifiers, and the images obtained using the Mel-spectrogram method were classified using 8 different pre-trained models. When the obtained results were evaluated, it was observed that the most successful model was the proposed hybrid model.
- In the proposed hybrid model, the accuracy value attained is 99.5 %. This result indicates that the proposed model can be utilized to diagnose snoring sounds.

1.3. Organization of Paper

In the first part of the paper, general information was given and the contribution and innovations of the study to the literature were discussed. In the second part, the material and methods section is examined, in this section the data set used in the paper, deep models, spectrogram method, classifiers, and NCA method are discussed. In

addition, the hybrid model developed for the classification of snoring sounds is examined in this section. The results obtained using different methods and models are presented in the third part, the discussion section in the fourth section, and the conclusion section in the last part.

2. Material and Methods

In this section, the data set used in the paper, deep models, spectrogram method, classifiers, NCA, and the proposed hybrid model is examined. The rough diagram of the proposed hybrid model is given in Figure 1.

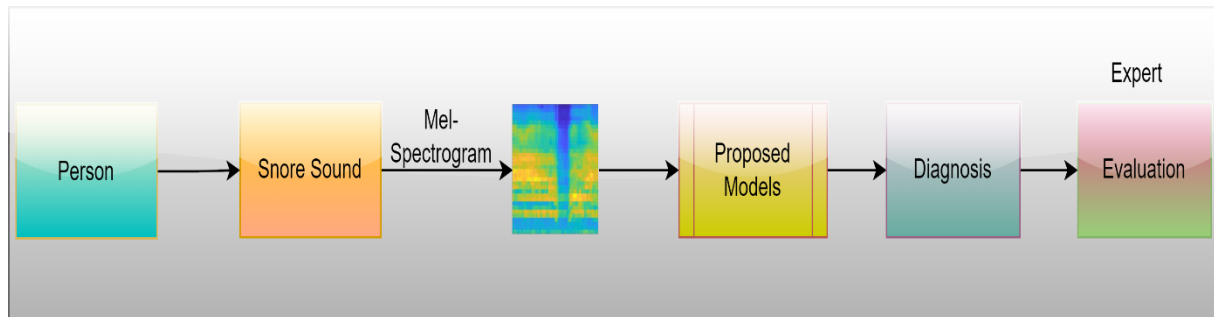


Figure 1. The rough working manner of the developed hybrid method

2.1. Data Set

A public data set was used in the study. The dataset used in the study consists of two classes, snoring and non-snoring. There are 500 sound files in each class. Each sound data is 1 second and these data have the extension “.wav” [7]. In Figure 2, sound data is shown as a signal.

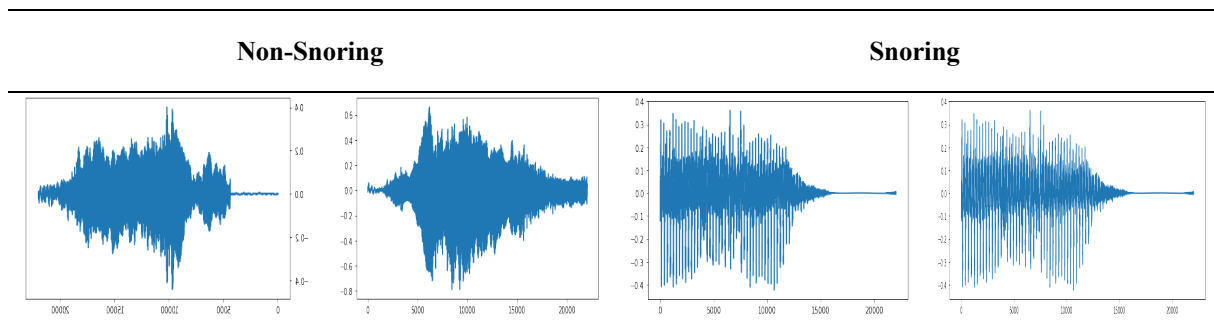


Figure 2. Examples of sound signals

While the first two images in Figure 1 belong to the Non-snoring class, the third and fourth images belong to the snoring class.

2.2. Spectrogram, Deep Models and NCA

The spectrogram is a visual heat map that represents the signal time on the horizontal axis and the signal frequency on the vertical axis as it changes with time. It is possible to define the spectrogram briefly as a visual representation of a time-varying sound signal [15, 16]. In this paper, the Mel-Spectrogram method was preferred to work with spectrograms of sound signals. Examples of spectrograms obtained using sound signals are presented in Figure 3.

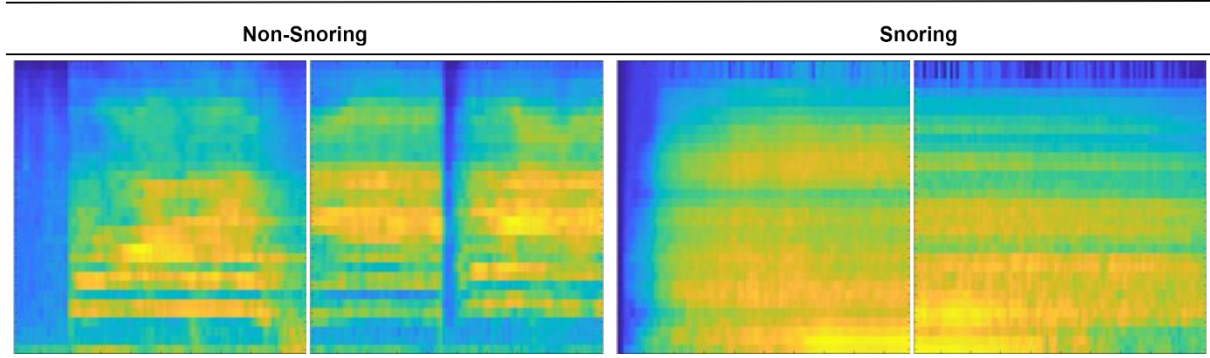


Figure 3. Spectrogram examples

In order to test the performance of the hybrid model proposed in the study, the obtained spectrogram data were also classified with deep methods accepted in the literature. 8 different deep methods were used in the paper. The first one is the Alexnet, which makes a great contribution to the popularity of deep learning. The Alexnet won the ILSVRC ImageNet competition in 2012 [17]. Darknet53 architecture is one of the current architectures of recent years. This architecture was developed based on the Darknet19 and Resnet architectures in YoloV2 [18]. In Resnet architecture, on the other hand, the gradient problem is tried to be solved by using Residual blocks. This model, created by He et al., was the winner of the ILSVRC ImageNet competition in 2015 [19]. The Densenet201 architecture developed by Huang et al. is different from other architectures in terms of the use of activation functions. The original data is maintained in all types of layers in the Densenet201 architecture, in addition to the activations from preceding layers [20]. Googlenet, which won the ILSVRC ImageNet competition in 2014, is another architecture employed in the study. This approach is one of the first to abandon the sequential arrangement of layers [21]. The Mobilenet architecture developed by Howard et al. is a architecture mostly suggested for mobile applications. In this model, the researchers aimed to develop a model with fewer parameters, high performance, and working speed [22]. The InceptionV3 model, developed by Szegedy et al., consists of 3 parts. This model has a convolution block, an initial block, and a classification block [23]. The last model used in the study is the Efficientnetb0 model. This model is a current and popular model developed in recent years. In this model, in addition to the depth factor, the concepts of width and resolution are also discussed for the first time [24].

NCA dimension reduction was preferred to reduce the size of the feature maps get in the proposed hybrid model. Thanks to the NCA dimension reduction method, unnecessary features in the feature map are eliminated. This step allows the training time of the proposed hybrid model to be completed in a shorter time [25, 26].

2.3. MFCC and Classifiers

While the first method used in the study is the spectrogram method, another method is the MFCC method. With the MFCC method, direct feature maps were obtained without converting the sound data into images. The MFCC method is a method that extracts feature from sound signals and is frequently used in the literature. Thanks to this method, it is possible to work directly on sound signals. The MFCC method used in this study to diagnose snoring sounds was first used by Davis and Mermelstein in 1980 [27]. The MFCC method uses the Hamming window technique to shape the sound signal and divide it into smaller windows. Spectrum is produced for each frame using the Fast Fourier transform and the filter bank is weighted. Finally, the MFCC vector is obtained by using the Logarithm and Discrete Cosine transformations. Filter banks are obtained using equation 1.

$$H_m(k) = \begin{cases} 0 & k < f(m-1) \\ \frac{k - f(m-1)}{f(m) - f(m-1)} & f(m-1) \leq k \leq f(m) \\ \frac{f(m+1) - k}{f(m+1) - f(m)} & f(m) \leq k \leq f(m+1) \\ 0 & k > f(m+1) \end{cases} \quad (\text{Eq.1.})$$

In Equation 1, M represents the desired number of filters and f shows the list of frequencies. The MFCC method is a method that is frequently used especially in biomedical studies [28, 29]. The block diagram of the MFCC method is given in Figure 4.

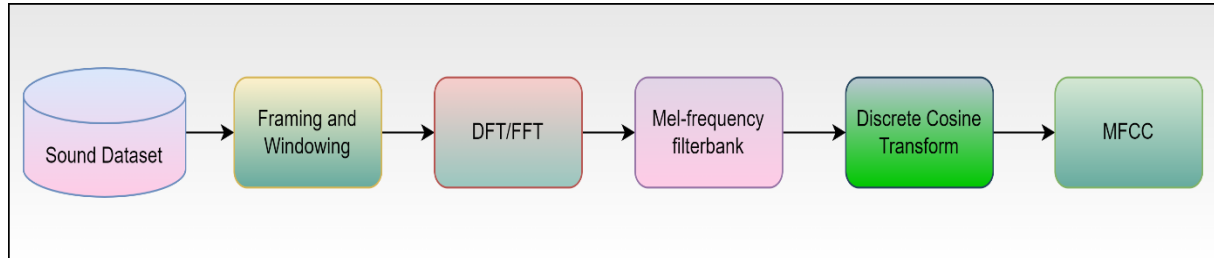


Figure 4. The block diagram of the MFCC method

The feature map obtained using the MFCC method was classified in 6 different supervised classifiers. Classifiers known in the literature were used in the study. These classifiers are Naïve Bayes [30], Support Vector Machine (SVM) [31], Logistic Regression [32], k-nearest neighborhood (KNN) [33], Gradient Boosting [34], and Random Forest [35].

2.4. Proposed Model

In the proposed model, first of all, sound signals were converted into images by the Mel-spectrogram method. The feature maps of the images in the acquired spectrogram data set were obtained using the Alexnet and Resnet101 architectures. These architectures extract feature maps with different features from the same data set. Therefore, these two architectures are used as the basis in the proposed hybrid model. The feature maps obtained using the Alexnet and Resnet101 architectures were combined. In this way, different features of the same image are brought side by side. NCA size reduction method was used to optimize the features in this feature map. In this way, the new size of the 1000x2000 feature map has become 1000x500. This allows the developed model to be trained in a shorter time. Finally, the optimized feature map is classified in the Bilayered Neural Network. Figure 5 depicts the suggested model's block diagram.

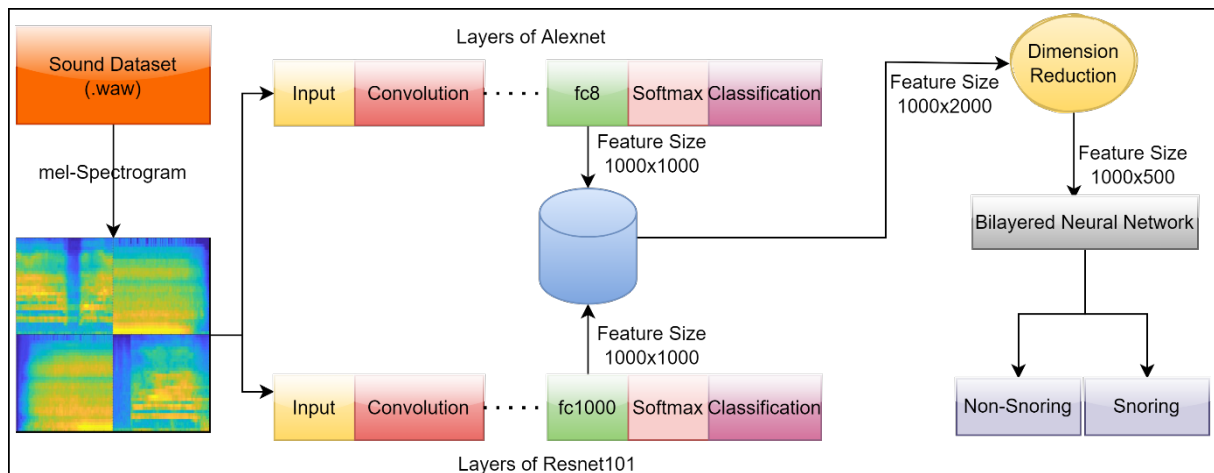


Figure 5. The suggested model's block diagram

Looking at Figure 5, the feature maps of the data set were obtained from the "fc8" layer of the Alexnet architecture, while it was obtained from the "fc1000" layer of the Resnet101 architecture. While the number of features obtained in both architectures was 1000, this number increased to 2000 after the merge process. After NCA size reduction, this number has decreased to 500 and has been classified in the Bilayered Neural Network.

3.Application Results

Matlab and Python environments were used in the implementation. Two different methods were used to diagnose snoring sounds. In the first method, sound signals were converted into images using the Mel-spectrogram method. Then, the obtained spectrogram images were first classified into 8 different classifiers and the proposed hybrid model. In the second method used in the study, feature maps were extracted using the MFCC method. The feature maps produced in the MFCC method were classified into 8 different classifiers. Confusion matrices are presented in detail in the study in order to compare the results obtained in different models and the proposed hybrid model using different methods [36].

3.1. Results obtained in deep models

In this study, first of all, sound signals were converted into images by using the Mel-spectrogram method. Obtained spectrogram images were classified using 8 different deep models accepted in the literature. 80% of the data in the data set was used in the training process of the models, and 20% in the testing phase of the models. Table 1 shows the accuracy rates obtained in deep models.

Table 1. Accuracy rates in state-of-the-art models

Alexnet	Darknet53	Resnet101	Densenet201
90%	89%	89%	88.5%
Googlenet	MobilenetV2	InceptionV3	Efficientnetb0
88%	88%	88%	87%

When the accuracy values obtained in Table 1 are examined, the accuracy rate obtained in Alexnet architecture is 90%, while 89% accuracy in Darknet53 and Resnet101 architecture, 88.5% in Densenet201 architecture, 88% in Googlenet, MobilenetV2, and InceptionV3 architectures and 87% in Efficientnetb0 architecture. In classifying spectrogram images, the most successful deep model was Alexnet with 90% accuracy, while the most unsuccessful deep model was Efficientnetb0 with 87% accuracy. Confusion matrices obtained using deep models are given in Figure 6.

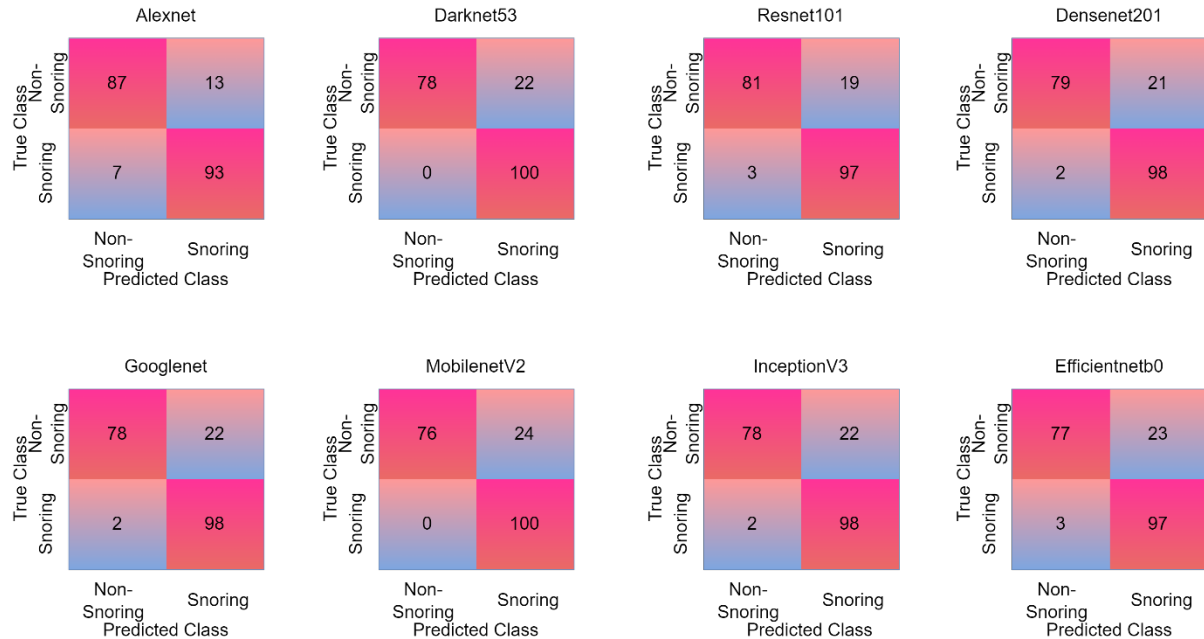


Figure 6. Confusion matrix in state-of-the-art models

In Figure 6, it is seen that Alexnet architecture makes the most successful classification. While the Alexnet architecture correctly predicted 180 of 200 test data, it predicted 20 test data incorrectly. While there is a balance in the number of data that the Alexnet architecture predicts incorrectly, the rate of predicting the data belonging to the Snore class as if it belongs to the Normal class is much higher in other architectures. Among the 8 models used in the study, the model that made the most incorrect predictions were the Efficientnetb0 model. While this model predicted 174 of 200 test data correctly, it predicted 26 of them incorrectly. If deep models are to be used to detect snoring sounds, it would be more appropriate to use Alexnet architecture.

3.2. Classification of feature maps obtained by MFCC method in classifiers

The second method used to diagnose snoring sounds is the MFCC method. With the MFCC method, the feature map of the sound signals was obtained and classified in different classifiers. The obtained accuracy values are presented in Table 2.

Table 2. MFCC + Classifiers

Naive Bayes	SVM	Logistic Regression
82.5%	87.5%	89%
KNN	Gradient Boosting	Random Forest
96%	96%	98%

The feature map produced in the MFCC method was classified in 6 different supervised classifiers. The Random Forest classifier achieved the greatest accuracy of 98% among these classifiers. The Naive Bayes classifier had the lowest accuracy rating of 82.5%. Confusion matrices obtained in supervised classifiers are given in Figure 7.

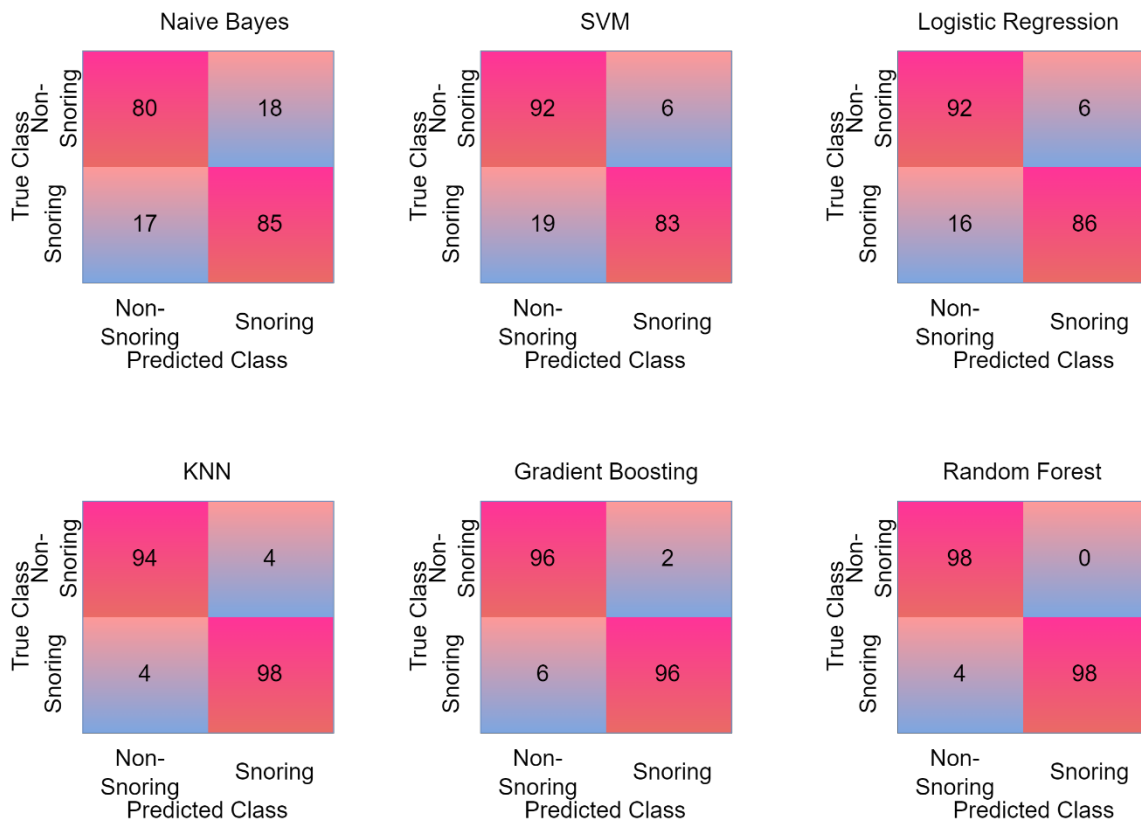


Figure 7. MFCC + Classifiers

The Random Forest classifier is clearly the most successful, as shown in Figure 7. Random Forest classifier predicted 196 out of 200 test data correctly and predicted 4 test data incorrectly. The data that the Random Forest classifier predicted incorrectly belonged to the Snoring class and was predicted as non-snoring by the model. The model with the most incorrect predictions was Naive Bayes. Naive Bayes guessed correctly 165 of 200 test images and mispredicted 35 of them.

3.3. Proposed Model

A hybrid model is proposed for diagnosing snoring sounds with a high success rate. Alexnet and Resnet101 architectures were utilized as the foundation for the proposed hybrid model, and feature maps of the data in the data set were obtained. Since the feature maps of each architecture are different from each other, different features were obtained from the same data set. After the obtained feature maps were combined, unnecessary features were eliminated using the NCA method. Finally, the optimized feature map is classified in the Bilayered Neural Network. The confusion matrix obtained in the proposed method is shown in Figure 8.

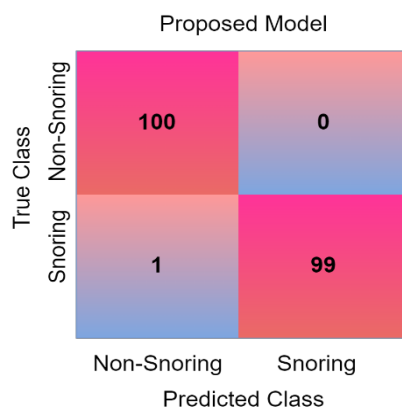


Figure 8. Confusion matrix of the proposed method

Figure 8 shows that the suggested model correctly identifies 199 of the 200 test data while wrongly classifying one. While the data that the proposed model misclassified belonged to the snoring class, the proposed model incorrectly predicted this data as non-snoring. The performance metrics of the proposed model are given in Table 3.

Table 3. Performance measurement parameters of the proposed model

Accuracy%	Sensitivity%	Specificity%	False Positive Rate%	False Discovery Rate%
99.50	99.01	100	0	0
False Negative Rate%	Negative Predictive Value%	Precision%	F1 Score%	Matthews Correlation Coefficient%
0.99	99	100	99.50	99

It is observed that the model proposed in Table 3 has achieved high success in classifying snoring sounds. the proposed model, it is seen that a 99.5% Accuracy value, 99.01% Sensitivity value, and 100% Specificity value are obtained in the process of diagnosing snoring sounds. ROC curves obtained in the proposed model are given in Figure 9.

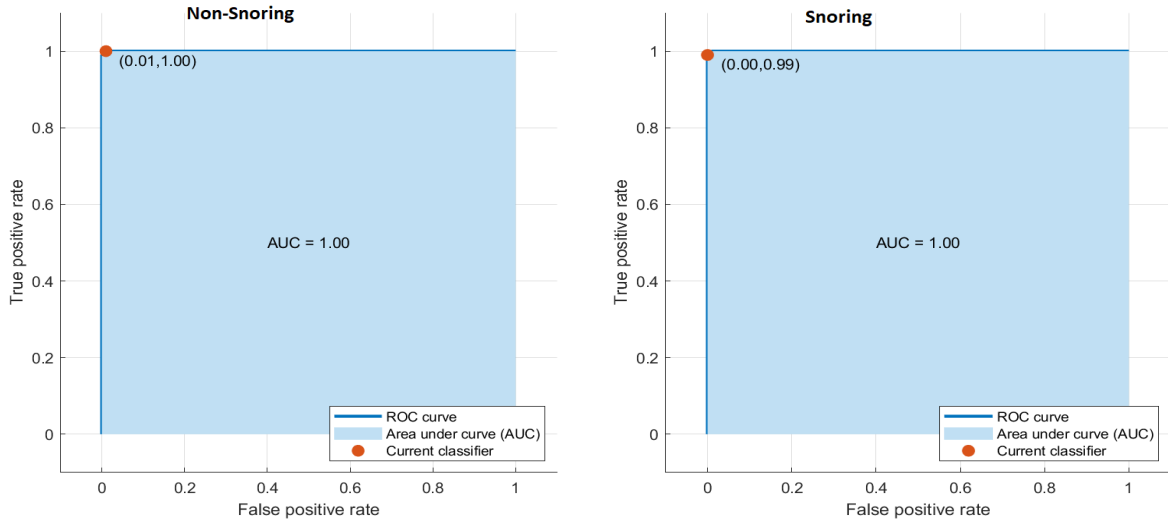


Figure 9. ROC Curves of Proposed model

When the ROC curves shown in Figure 9 are observed, the success of the proposed method in diagnosing snoring sounds can be observed.

4. Discussion

Snoring is a common sleep problem in humans. This problem has a negative effect on the sleep pattern of the person and their partner. Snoring can cause various diseases when left untreated. Because the amount of oxygen in the blood may decrease during snoring. Heart diseases, fatigue, diabetes, stroke, and psychological problems are some of the disorders that can be caused by snoring [37, 38]. Since snoring is a problem that can be treated, it will be faster and easier to detect this ailment thanks to computer-aided systems. In this study, a hybrid model was developed to diagnose snoring sounds. In the developed model, feature extraction was done with two different deep models and these feature maps were combined. In this way, different features of the sound signals in the data set are brought together. In order to make the proposed model work faster, the size reduction process was performed. NCA method was preferred for this process. The proposed hybrid model is compared with similar studies performed for the classification of snoring sounds in Table 4.

Table 4. Studies for the diagnosis of snoring sounds

Study	Classes	Method	Accuracy
Khan et al. [7]	Snoring, Non-snoring	Proposed CNN based model	96%
Jiang et al. [8]	Snoring, Non-snoring	LSTM, DNN, CNN, Mel-spectrogram	95.07%
Cavusoglu et al. [9]	Snoring, Non-snoring	Sub-band spectral energy	90.2%
Dafna et al. [10]	Snoring,	MFCC, LPC, Adaboost	98.2%

	Non-snoring		
Wang et al. [11]	Snoring, Non-snoring	Linear and non-linear feature extraction methods, SVM	94.5%
Lim et al. [12]	Snoring, Non-snoring	STFT, MFCC	98.9%
Arsenali et al. [13]	Snoring, Non-snoring	MFCC, Recurrent Neural Network	95%
Shen et al. [14]	Snoring, Non-snoring	MFCC, LPMFCC, LPC, CNN, LSTM	87%
Proposed Model	Snoring, Non-snoring	Spectrogram, deep models, NCA, Bilayered Neural Network	99.5%

It is seen in Table 4 that the proposed model has reached the highest accuracy value. In the proposed model, no metaheuristic optimization algorithm or a genetic algorithm type method is preferred to increase the performance rate. Feature selection was performed automatically with the NCA method. In addition, in the proposed hybrid model, deep models are only used for feature extraction. No time was spent training these models. At the same time, results were obtained by using 8 different deep models in the study. Among these results, Alexnet architecture obtained the highest accuracy rate with 90% accuracy. The proposed model has been more successful than these models.

The proposed model has many advantages as well as some disadvantages. The main limitations are the small number of data used in the study and the inability to collect data from patients from different regions. One of our goals is to collect data with the help of more experts from different centers and to design a model that can serve over the internet. In addition, it is among our aims to apply the developed model to other sound data sets.

5. Conclusion

Snoring sounds are a serious problem that can disrupt the sleep patterns of people and others around them. If this problem is not treated, it can cause other diseases. Recording snoring sounds by experts is both time-consuming and costly. This study, it is aimed to automatically diagnose snoring sounds with the hybrid model proposed. In the proposed model, Alexnet and Resnet101 architectures are used for feature extraction. Since no training process is performed with these architectures in the proposed hybrid model, the proposed model is much faster than the CNN models. In addition, the feature map has been optimized by using the NCA dimension reduction method so that the proposed model can be trained in a faster time. A high accuracy value of 99.5% was obtained in the proposed hybrid model.

Funding

No funding was received from anywhere in this study.

Conflict of Interest

The authors declare no conflict of interest.

Acknowledgments

We thank the owner of the data set for sharing the data set used in the study.

References

- [1] Veiga, A., et al. An IoT-based smart pillow for sleep quality monitoring in AAL environments. in 2018 Third International Conference on Fog and Mobile Edge Computing (FMEC). 2018. IEEE.
- [2] Oksenberg, A. and D.S. Silverberg, The effect of body posture on sleep-related breathing disorders: facts and therapeutic implications. *Sleep medicine reviews*, 1998. 2(3): p. 139-162.
- [3] Kwekkeboom, K.L., et al., The role of inflammation in the pain, fatigue, and sleep disturbance symptom cluster in advanced cancer. *Journal of pain and symptom management*, 2018. 55(5): p. 1286-1295.
- [4] <https://www.everydayhealth.com/news/eleven-health-risks-snoring/>.
- [5] Jodaki, K., et al., Effect of rosa damascene aromatherapy on anxiety and sleep quality in cardiac patients: A randomized controlled trial. *Complementary Therapies in Clinical Practice*, 2021. 42: p. 101299.
- [6] Tietjens, J.R., et al., Obstructive sleep apnea in cardiovascular disease: a review of the literature and proposed multidisciplinary clinical management strategy. *Journal of the American Heart Association*, 2019. 8(1): p. e010440.
- [7] Khan, T., A deep learning model for snoring detection and vibration notification using a smart wearable gadget. *Electronics*, 2019. 8(9): p. 987.
- [8] Jiang, Y., J. Peng, and X. Zhang, Automatic snoring sounds detection from sleep sounds based on deep learning. *Physical and engineering sciences in medicine*, 2020. 43(2): p. 679-689.
- [9] Cavusoglu, M., et al., An efficient method for snore/nonsnore classification of sleep sounds. *Physiological measurement*, 2007. 28(8): p. 841.
- [10] Dafna, E., A. Tarasiuk, and Y. Zigel, Automatic detection of whole night snoring events using non-contact microphone. *PLoS one*, 2013. 8(12): p. e84139.
- [11] Wang, C., et al., Automatic snoring sounds detection from sleep sounds via multi-features analysis. *Australasian physical & engineering sciences in medicine*, 2017. 40(1): p. 127-135.
- [12] Lim, S.J., et al., Classification of snoring sound based on a recurrent neural network. *Expert Systems with Applications*, 2019. 123: p. 237-245.
- [13] Arsenali, B., et al. Recurrent neural network for classification of snoring and non-snoring sound events. in 2018 40th Annual International Conference of the IEEE Engineering in Medicine and Biology Society (EMBC). 2018. IEEE.
- [14] Shen, F., et al., Detection of Snore from OSAHS Patients Based on Deep Learning. *Journal of Healthcare Engineering*, 2020. 2020.
- [15] Skoczylas, A., et al., Belt conveyors rollers diagnostics based on acoustic signal collected using autonomous legged inspection robot. *Applied Sciences*, 2021. 11(5): p. 2299.
- [16] Bhatti, F.A., et al., Shared spectrum monitoring using deep learning. *IEEE Transactions on Cognitive Communications and Networking*, 2021. 7(4): p. 1171-1185.
- [17] Krizhevsky, A., I. Sutskever, and G.E. Hinton, Imagenet classification with deep convolutional neural networks. *Advances in neural information processing systems*, 2012. 25.
- [18] Redmon, J. and A. Farhadi, Yolov3: An incremental improvement. *arXiv preprint arXiv:1804.02767*, 2018.
- [19] He, K., et al. Deep residual learning for image recognition. in *Proceedings of the IEEE conference on computer vision and pattern recognition*. 2016.
- [20] Huang, G., et al. Densely connected convolutional networks. in *Proceedings of the IEEE conference on computer vision and pattern recognition*. 2017.
- [21] Szegedy, C., et al. Going deeper with convolutions. in *Proceedings of the IEEE conference on computer vision and pattern recognition*. 2015.
- [22] Howard, A.G., et al., Mobilenets: Efficient convolutional neural networks for mobile vision applications. *arXiv preprint arXiv:1704.04861*, 2017.
- [23] Szegedy, C., et al. Rethinking the inception architecture for computer vision. in *Proceedings of the IEEE conference on computer vision and pattern recognition*. 2016.
- [24] Tan, M. and Q. Le. Efficientnet: Rethinking model scaling for convolutional neural networks. in *International conference on machine learning*. 2019. PMLR.
- [25] Eroğlu, O. and M. Yildirim, Automatic detection of eardrum otoendoscopic images in patients with otitis media using hybrid-based deep models. *International Journal of Imaging Systems and Technology*, 2022. 32(3): p. 717-727.
- [26] Bingol, H. (2022). NCA-based hybrid convolutional neural network model for classification of cervical cancer on gauss-enhanced pap-smear images. *International Journal of Imaging Systems and Technology*.
- [27] Davis, S. and P. Mermelstein, Comparison of parametric representations for monosyllabic word recognition in continuously spoken sentences. *IEEE transactions on acoustics, speech, and signal processing*, 1980. 28(4): p. 357-366.
- [28] Deng, M., et al., Heart sound classification based on improved MFCC features and convolutional recurrent neural networks. *Neural Networks*, 2020. 130: p. 22-32.
- [29] Karan, B., S.S. Sahu, and K. Mahto, Parkinson disease prediction using intrinsic mode function based features from speech signal. *Biocybernetics and Biomedical Engineering*, 2020. 40(1): p. 249-264.

- [30] Rish, I. An empirical study of the naive Bayes classifier. in IJCAI 2001 workshop on empirical methods in artificial intelligence. 2001.
- [31] Joachims, T., 11 Making Large-Scale Support Vector Machine Learning Practical. *Advances in kernel methods: support vector learning*, 1999: p. 169.
- [32] Kleinbaum, D.G., et al., *Logistic regression*. 2002: Springer.
- [33] Keller, J.M., M.R. Gray, and J.A. Givens, A fuzzy k-nearest neighbor algorithm. *IEEE transactions on systems, man, and cybernetics*, 1985(4): p. 580-585.
- [34] Friedman, J.H., Greedy function approximation: a gradient boosting machine. *Annals of statistics*, 2001: p. 1189-1232.
- [35] Liaw, A. and M. Wiener, Classification and regression by randomForest. *R news*, 2002. 2(3): p. 18-22.
- [36] Eroglu, Y., et al., Diagnosis and grading of vesicoureteral reflux on voiding cystourethrography images in children using a deep hybrid model. *Computer Methods and Programs in Biomedicine*, 2021. 210: p. 106369.
- [37] Brockmann, P.E., et al., Reduced sleep spindle activity in children with primary snoring. *Sleep Medicine*, 2020. 65: p. 142-146.
- [38] Macarthur, K.E., et al., Dissociation between objectively quantified snoring and sleep quality. *American Journal of Otolaryngology*, 2020. 41(1): p. 102283.

A Deep Learning-Based Technique for Diagnosing Retinal Disease by Using Optical Coherence Tomography (OCT) Images

M. Emin SAHİN^{1*}

¹Department of Computer Engineering, Engineering and Architecture Faculty, Yozgat Bozok University, Yozgat, Turkey

*emin.sahin@bozok.edu.tr

(Geliş/Received: 09/06/2022;

Kabul/Accepted: 20/06/2022)

Abstract: The retina layer is the most complex and sensitive part of the eye, and disorders that affect it have a big impact on people's lives. The Optical Coherence Tomography (OCT) imaging technology can be used to diagnose diseases that are caused by pathological alterations in the retina. The importance of early diagnosis in the management of these illnesses cannot be overstated. In this article, an approach based on convolutional neural networks (CNN), a deep learning method, is presented for the detection of retinal disorders from OCT images. A new CNN architecture has been developed for disease diagnosis and classification. The proposed method has been found to have an accuracy rate of 94% in the detection of retinal disorders. The results are obtained by comparing the proposed CNN network model in a deep learning application used in classification with the MobileNet50 network model in the literature. The evaluation parameter values for models trained using the 5-fold cross validation approach for each type of disease in the retinal OCT image dataset are also submitted. The proposed method can clearly be utilized as a decision-making tool to assist clinicians in diagnosing retinal illnesses in a clinical context based on its effectiveness thus far.

Key words: Classification, CNN, Deep Learning, OCT, Retina

Optik koherens tomografi (OCT) görüntülerini kullanarak retina hastalığını teşhis etmek için derin öğrenmeye dayalı bir teknik

Öz: Retina tabakası, gözün en karmaşık ve hassas kısmıdır ve onu etkileyen rahatsızlıkların insanların yaşamları üzerinde büyük etkisi vardır. Optik Koherens Tomografi (OCT) görüntüleme teknolojisi, retinadaki patolojik değişiklikler nedeniyle ortaya çıkan hastalıkları teşhis etmek için kullanılabilir. Bu hastalıkların tedavisinde erken teşhisin önemi yadsınamaz. Bu makalede, OCT görüntülerinden retina bozukluklarının tespiti için bir derin öğrenme yöntemi olan konvolüsyonel sinir ağlarına (CNN) dayalı bir yaklaşım sunulmaktadır. Hastalık tespiti ve sınıflandırması için yeni bir CNN mimarisi geliştirilmiştir. Önerilen yöntemin retina bozukluklarının belirlenmesinde %94 doğruluk oranına sahip olduğu bulunmuştur. Sınıflandırma için bir derin öğrenme uygulamasında, önerilen CNN ağ modeli literatürde mevcut olan MobileNet50 ağ modeli ile karşılaştırılmakta ve sonuçlar verilmektedir. Retinal OCT görüntüleri veri setindeki her hastalık türü için 5 katlı çapraz doğrulama yaklaşımı kullanılarak eğitilen modeller için değerlendirme parametresi değerleri de sunulur. Önerilen yöntem, şimdiye kadarki etkinliğine dayalı olarak, klinik bağlamda retina hastalıklarını teşhis etmede klinisyenlere yardımcı olacak bir karar verme aracı olarak açıkça kullanılabilir.

Anahtar kelimeler: CNN, Derin Öğrenme, OCT, Retina, Sınıflandırma

1. Introduction

The eye layer, which includes nerve fibers that are directly attached to the brain and give vision, is made up of light and color-sensitive cells and is referred to as the retina. Vision loss and blindness can result from defects in the retina. At the same time, it is known that retinal diseases cause diseases such as heart diseases and hypertension, as well as their effect on the sense of sight [1]. The importance of early identification and treatment in preventing or minimizing such adverse outcomes cannot be overstated. Age related macular degeneration (AMD), drusen, diabetic retinopathy (DR), diabetic macular edema (DME) and myopic choroidal neovascularization (CNV) can be given as examples of important retinal diseases.

Corresponding author: emin.sahin@bozok.edu.tr. ORCID Number of author: 0000-0001-7729-990X

According to studies, the number of people living with macular degeneration is expected to reach 288 million worldwide by 2040 [2]. Soft drusen, which is a deposit of granular or amorphous material, is considered a precursor to AMD [3]. The severity of the disease in dry AMD depends on the number, size, and density of drusen lesions. Dry AMD has progressed to wet AMD, which is a more advanced form of the disease. Another kind of retinal

illness is diabetic retinopathy, which is described as damage to the blood vessels in the retina caused by diabetes or high blood pressure. It is a progressive eye disease that affects a large proportion of working-age adults [4]. Lastly, CNV is caused by insufficient growth of blood vessels at the back of the eye. It is a very common disease that causes vision loss and threatens vision. Through a rupture in Bruch's membrane, new blood vessels emerge from the choroid and develop into the subretinal pigment epithelium, or subretinal space [2]. Over time, these vessels may burst, causing bleeding and fluid leakage into the retina [5].

In the literature, researchers in the field of ophthalmology have tried many methods to facilitate the early diagnosis and diagnosis of retinal disorders. From OCT images, AMD proposed a classification method based on linear SVM techniques, including scale-invariant feature transformation, to detect DME diseases and normal status [6]. In another study, OCT images were used to create a computer-aided diagnosis model that could tell the difference between AMD, DME, and a healthy macula [7]. In addition, a computer-aided diagnostic system using a deep learning-based multi-scale convolutional expert mix ensemble model has been presented in the literature. They reported the detection of two common types of AMD and DME pathologies in the retina and the normal state of the retina [8].

Li et al. developed an application based on convolutional neural networks (CNN) to determine CNV, DME and dry type AMD diseases in the retina. OCT images of 5,319 adult patients are used in this study. It was evaluated in their study utilizing the ImageNet database's pre-trained VGG-16 CNN architecture. With the transfer learning method, the weights of the VGG-16 network are retrained with the images taken from the patients. As a result of this study, an estimation accuracy of 98.6% was obtained in the diagnosis of retinal diseases from OCT images [9]. Mishra et al. used OCT images and CNN's ResNet50 architecture to diagnose AMD and DME diseases in the retina. They wanted to apply a technique termed multilevel dual attention mechanism (DAM) to CNN layers in their work. They were able to assess both the unique coarse and fine aspects of the OCT input pictures and display them to the literature using this method. As a result of this experiment, they obtained 99.97% accuracy from the Duke database used [10].

Motozawa and colleagues used two computational deep learning models to investigate the diagnosis of AMD illness and submitted their findings to the literature. Two CNN models are created in this study. As a result of the experiment, the first CNN architecture gave 99.0% accuracy for the diagnosis of AMD disease. The second CNN model is successful in detecting exudative findings with an accuracy of 93.8% [11]. Najeeb et al. focused on the possibility of detecting and classifying retinal diseases through OCT images. Included in the study are CNV, DME and drusen diseases. When the results were examined, it was observed that the proposed system could detect retinal diseases with a sensitivity of 95.66% [12]. Wang et al. studied a dual-trained two-stream CNN model for the investigation of wet AMD and dry AMD. As a result of this study, two single-mode models are superior to single-mode models with an accuracy rate of 94.2% [13]. In the literature review, networks with high computational cost and usually pre-trained are used in deep neural network-based studies.

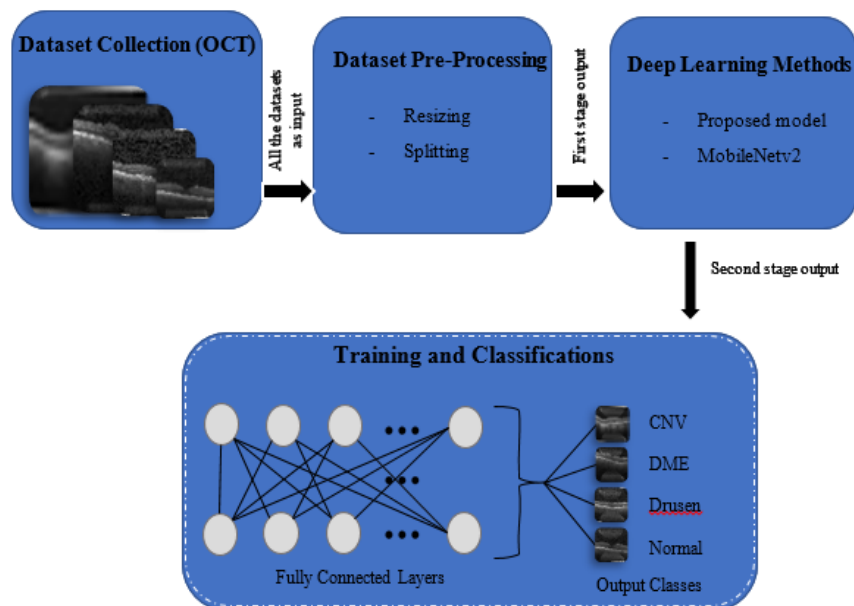


Figure 1. The block diagram of the study

Therefore, it is necessary to develop innovative methods that can improve accuracy while keeping the mesh size as small as possible. In this study, a system for automatic classification of retinal diseases is proposed using OCT images subjected to CNN architecture. The block diagram of the study is given in Fig.1. The following is a summary of the paper's structure. The dataset and deep learning models are described in Section 2. The created

deep learning application models' parameters are presented. In section 3, deep learning classifiers' work and outputs and also assessment measures including accuracy, recall, precision, and F1-scores are discussed. K-fold results are also given in that section. Finally, the advantages and success rate of the proposed model, and recommendations for future research are given in section 4.

2. Material and Methods

2.1. Dataset

Retinal optical coherence tomography (OCT) is a method for capturing high-resolution retinal images of the patients.

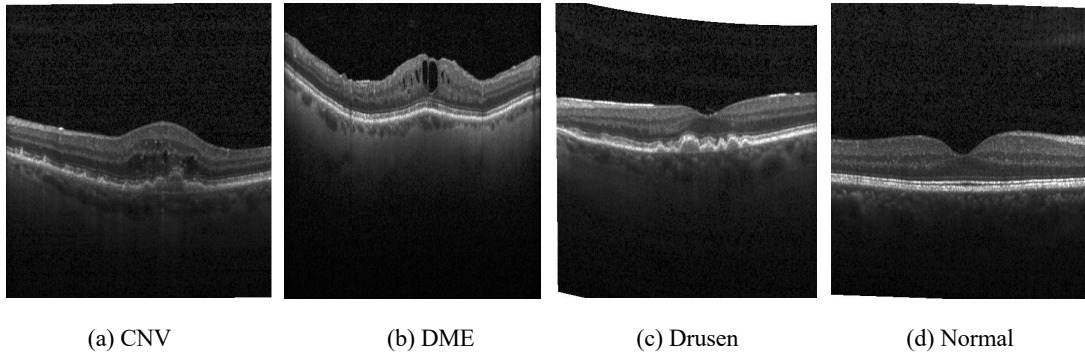


Figure 2. Examples of each class from the dataset.

The OCT images used in the project were obtained from adult patients from the Eye Institute database at the University of California San Diego Shiley Eye Institute, California Retinal Research Foundation, and Medical Center Ophthalmology Associates in Shanghai. In this study, training and testing of the model is done by Kermany et al. publicly available optical coherence tomography image dataset is used [14]. Examples of each class from the dataset are shown in Fig. 2.

Table 1. Total and number of images used in the dataset.

No	Case Name	Total Images	Used Images
1	CNV	37455	2500
2	DME	11598	2500
3	Drusen	8916	2500
4	Normal	26615	2500

The dataset is organized into three folders (train, test, and validation) with its own subdirectory for each image type (CNV, DME, Drusen, Normal). It has 84,495 X-Ray images (jpeg) divided into four categories: CNV, DME, Drusen, and Normal. A total of 10,000 data are taken, with 2,500 for each class used in the testing and training process. The sum of images in the dataset and the number of images used are given in Table 1.

2.2. Deep learning

The term "deep learning" refers to a category of machine learning algorithms that are used to program computers to think and act in ways that are analogous to those of humans. In other words, it is a method of learning and decision-making that attempts to emulate the human brain's functioning [15], [16].

Neural networks, progressive probability models, and unsupervised and supervised feature learning algorithms are all part of the deep learning family, and their applications are growing by the day. The research areas of deep learning are at the intersection of artificial intelligence, graph modeling, optimization, pattern recognition and signal processing [15]. The most common deep learning architectures such as Convolutional Neural Networks (CNN), Deep Belief Networks, Deep Auto-Encoders and Recurrent Neural Networks-RNNs are given below with subheadings.

2.2.1. Convolutional neural network models (CNN)

Convolutional Neural Networks (CNNs) are special types of multi-layered neural networks. The visual cortex inspired a convolutional neural network design that is analogous to the connecting structure of neurons in the human brain. Individual neurons here only respond to stimuli in the receptive part, which is a small part of the visual field. CNN is made up of neurons having weights and biases that may be learned. Each neuron in the system gets some input and, if desired, outputs it non-linearly via a dot product. Classification, localization, detection, segmentation, and recording of medical images are all tasks that CNNs excel at. While the earliest research employing CNN was published towards the end of the 1970s, Lo et al. reported one of the first studies based on medical images using CNN in 1995 [17].

2.2.2. Proposed CNN model

In this section, the proposed convolution-based CNN model to detect retinal diseases from OCT images is analysed. The CNN model is designed using the sequential model of the Keras library. In order to reduce the overfitting situations that may occur, dropout layers with different densities have been added to the model. The ReLu activation function, which is frequently used in image processing, is used as the activation function. Fig. 3 depicts the proposed CNN network design.

The network architecture consists of the convolution layer, maximum pooling, dropout, and a classification layer. A set of convolution and max pooling layers act as feature extractors. The network architecture consists of convolution layers and maximum pooling layers, respectively. There are also dropout layers in the model. Proposed CNN model structure parameters are demonstrated in Table 2.

Table 2. Proposed CNN model structure parameters.

Layer (type)	Output Shape	Parameters
Conv2D	222 x 222 x 32	896
MaxPooling2D	111 x 111 x 32	0
Dropout	111 x 111 x 32	0
Conv2D	109 x 109 x 64	18496
MaxPooling2D	54 x 54 x 64	0
Dropout	54 x 54 x 64	0
Conv2D	52 x 52 x 64	36928
MaxPooling2D	26 x 26 x 64	0
Dropout	26 x 26 x 64	0
Conv2D	24 x 24 x 128	73856
MaxPooling2D	12 x 12 x 128	0
Dropout	12 x 12 x 128	0
Conv2D	10 x 10 x 256	295168
MaxPooling2D	5 x 5 x 256	0
Dropout	5 x 5 x 256	0
Flatten	6400	0
Dense	4	25604
Total Params: 450.948		
Trainable Params: 450.948		
Non-trainable Params: 0		

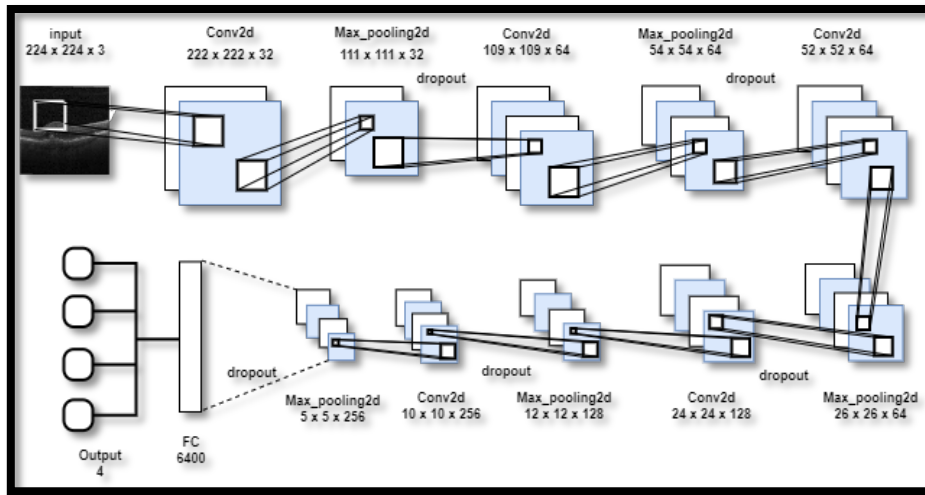


Figure 3. Proposed CNN architecture.

3. Experimental Results

In this study, besides the CNN model, the MobileNetv2 network architecture, which has been pre-trained with the ImageNet dataset and has proven its performance, is used. For these two models, the optimization algorithm is chosen as Adam, and the initial learning rate is 0.0001. The performance metric is accuracy and the loss function is categorical_crossentropy. Training data for each model is trained in 150 epochs in the form of 100 batch sizes. Then, the trained model is tested with the test data. From the testing of CNN and MobileNetv2 models, 94% and 90% accuracy are obtained, respectively.

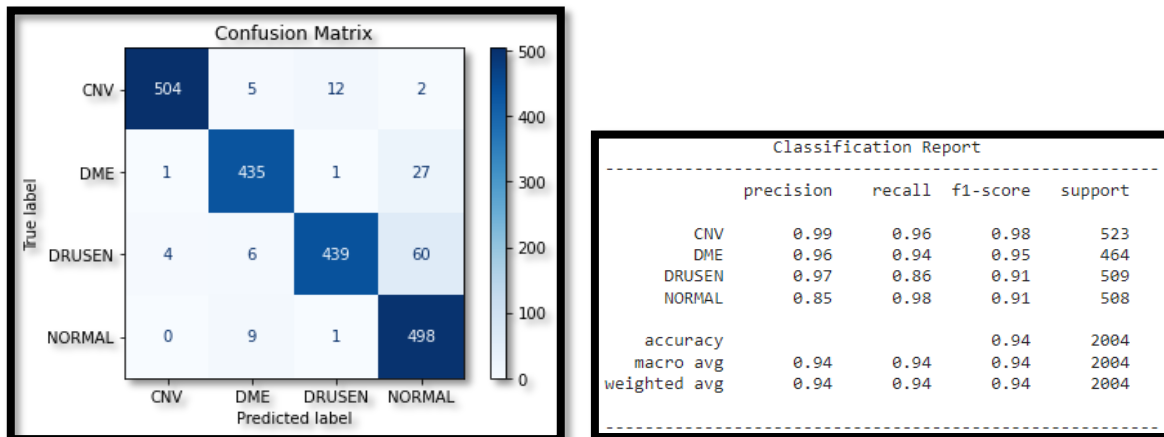


Figure 4. Confusion matrix and classification report of the proposed CNN model.

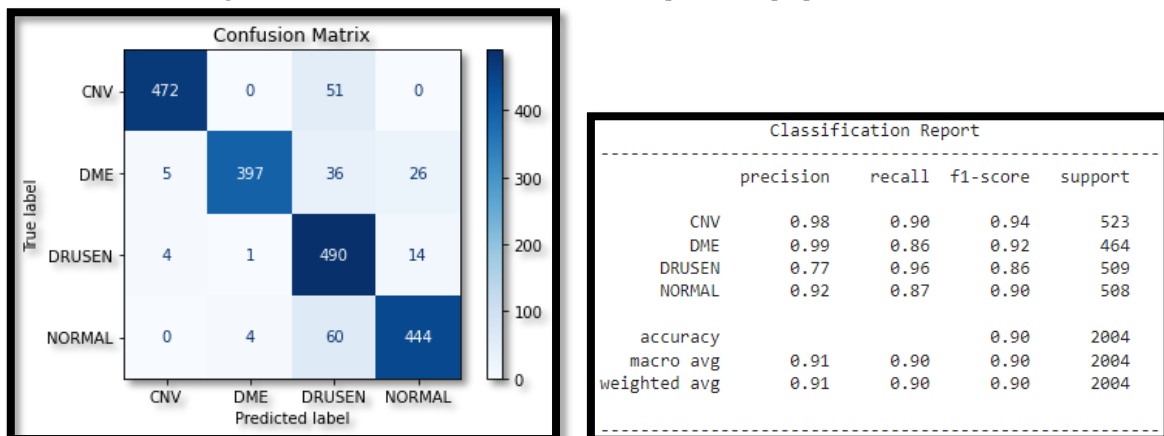


Figure 5. Confusion matrix and classification report of the MobileNetv2 model.

The classification estimation results for each model are presented in the complexity matrix and classification reports are given in Figs. 4 and 5, respectively. With a confidence interval of 96 percent, accuracy, precision, recall, and Area Under a Curve (AUC) metrics are used to assess the performance of the network models, and a comparison is made between models to select the best model in terms of performance. The number of correctly classified photos divided by the total number of test images provides precision. The model's ability to identify abnormal from normal in retinal OCT images is evaluated using receiver operating characteristic (ROC) curves. AUC is used to summarize the diagnostic accuracy of each parameter. The higher the AUC of the active model ranging from 0.5 to 1, the better its performance is.

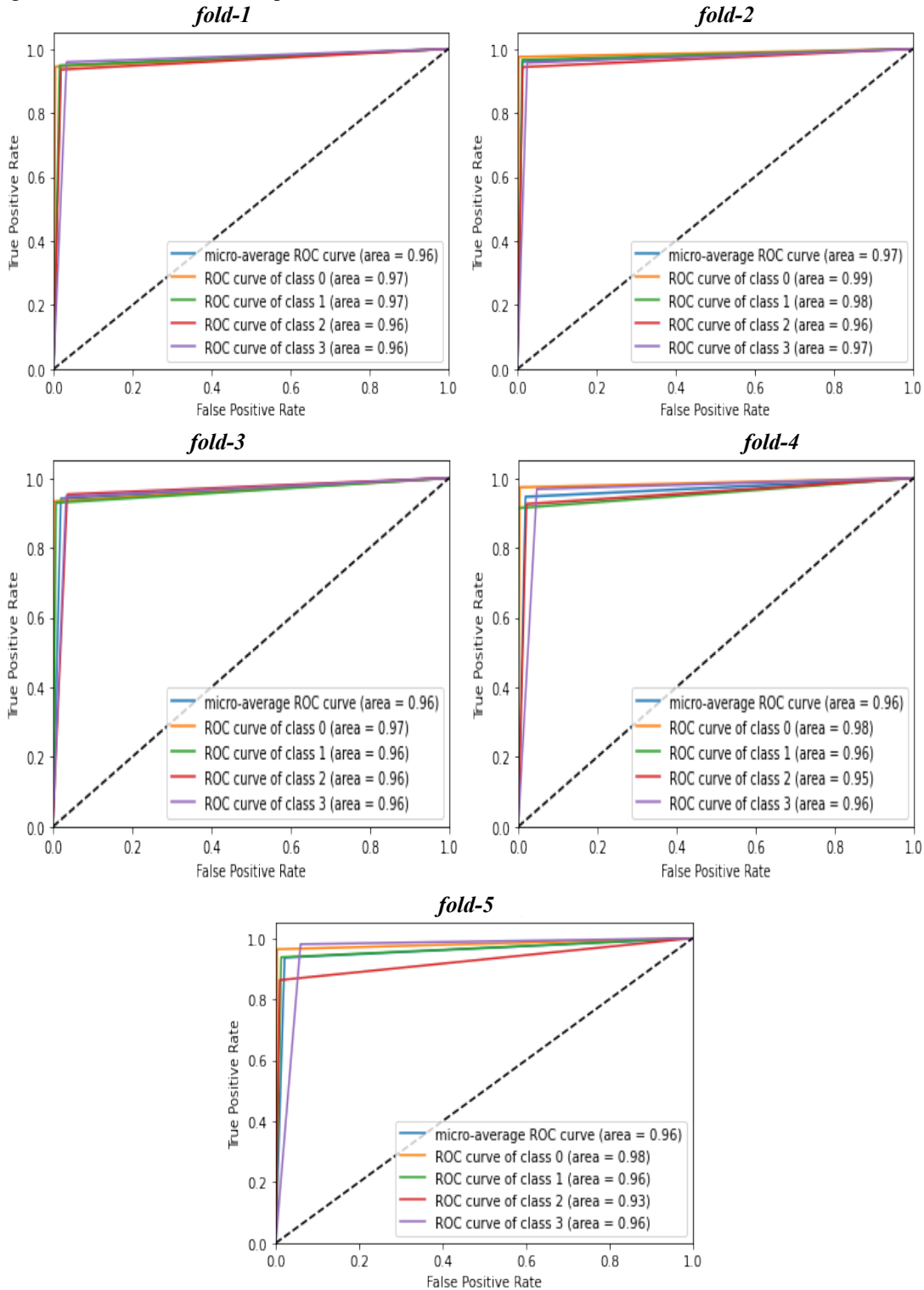


Figure 6. ROC graphs for 5 folds of the proposed CNN model.

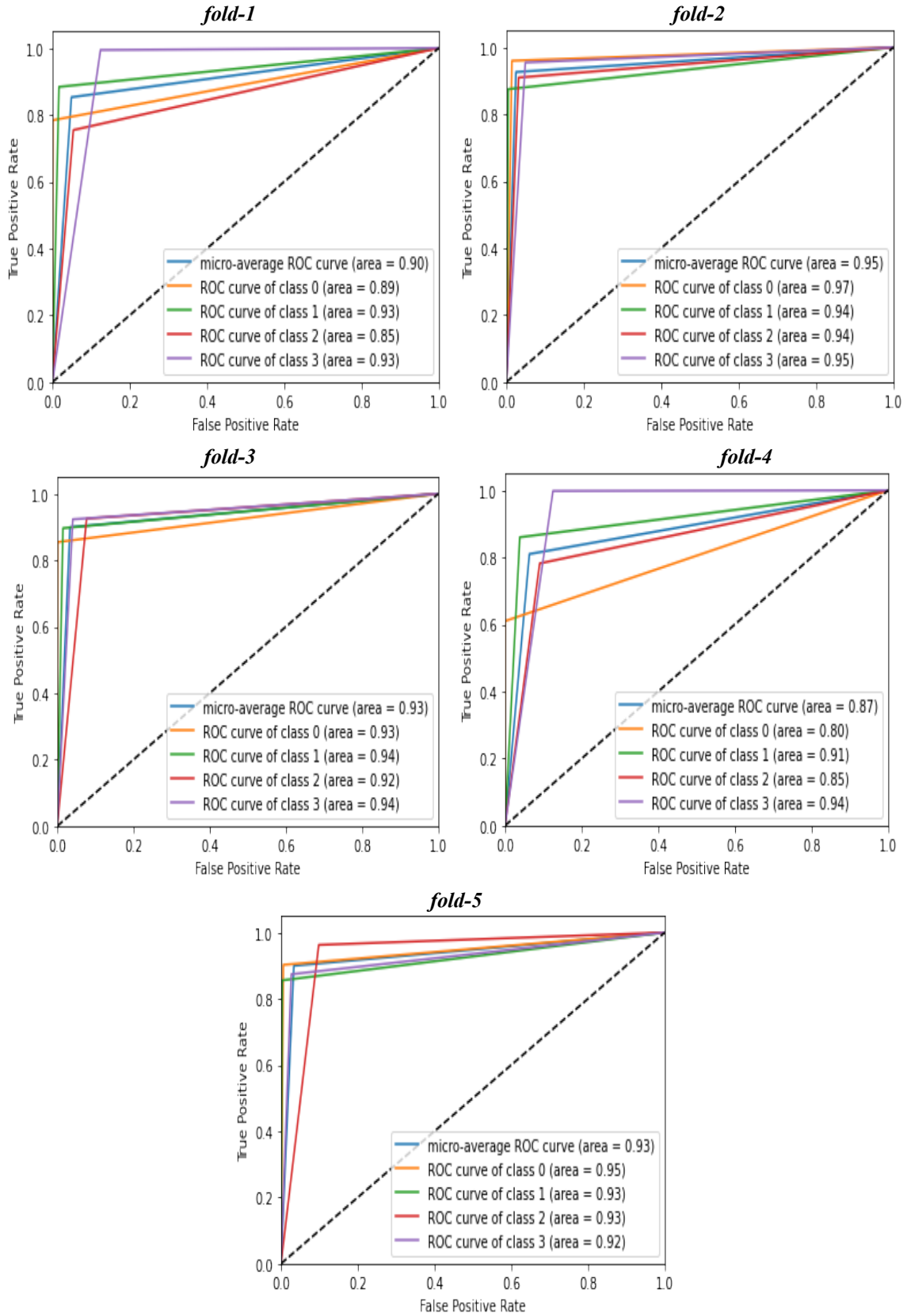


Figure 7. ROC graphs for 5 folds of the MobileNetv2 model.

The test dataset is used to evaluate the model's performance. The CNN model scored 0.94 accuracy, 0.94 precision, and 0.94 recall in a multiclass evaluation of CNV, DME, Drusen, and Normal. A ROC curve is

constructed to achieve the capacity to distinguish normal from 3 abnormals. A high AUC of 0.96 is obtained with the results of testing. The MobileNetv2 model, on the other hand, reached 0.90 accuracy, 0.91 precision and 0.90 recall. The AUC of 0.93 is obtained with the results of testing. ROC graphs for 5-folds of CNN and MobileNetv2 models are given in Figs. 6 and 7, respectively.

The evaluation parameter values of the models trained using the 5-fold cross-validation strategy for each infection type in the Retinal OCT Images dataset are given in Table 2. While the first model, the CNN model, provided 0.94 accuracy, 0.94 precision, 0.94 recall and 0.94 F1-score, the second model, MobileNetv2, achieved 0.90 accuracy, 0.91 precision, 0.90 recall and 0.90 F1-score. When these results are evaluated, it is observed that the CNN model is the better. In addition, the accuracy, precision, recall and F1-score obtained as a result of 5-fold cross validation for the two models are taken separately for each fold and are reflected in the graphs shown in Figs. 8 and 9. Performance of network models are given in Table 3. The accuracy graph and the loss graph of the system are illustrated in Figs. 10 and 11, respectively.

Table 3. Performances of network models

Number	Network	Accuracy(%)	Precision(%)	Recall(%)	F1-Score(%)
1	CNN	94	94	94	94
2	MobileNetv2	90	91	90	90

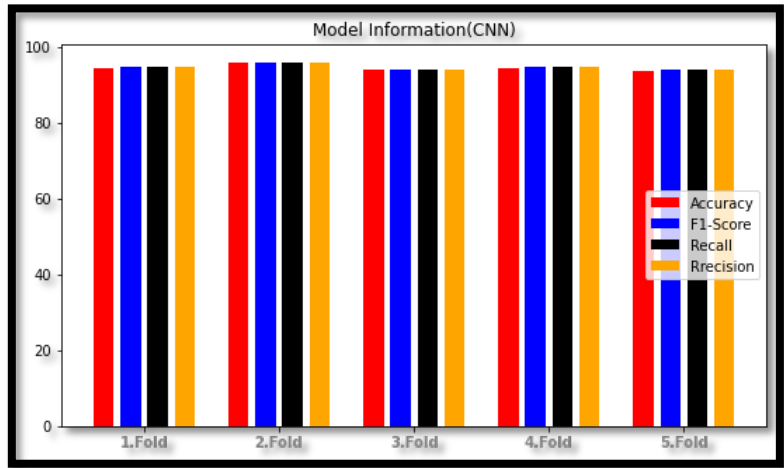


Figure 8. Infographic of proposed CNN model.

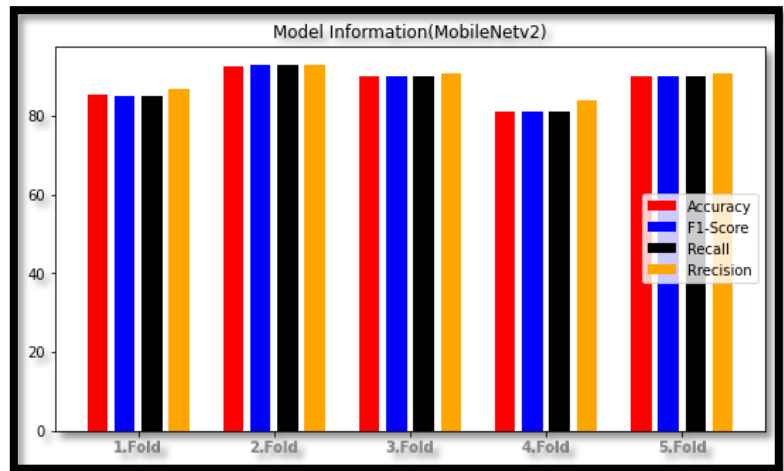


Figure 9. Infographic of the MobileNetv2 model.

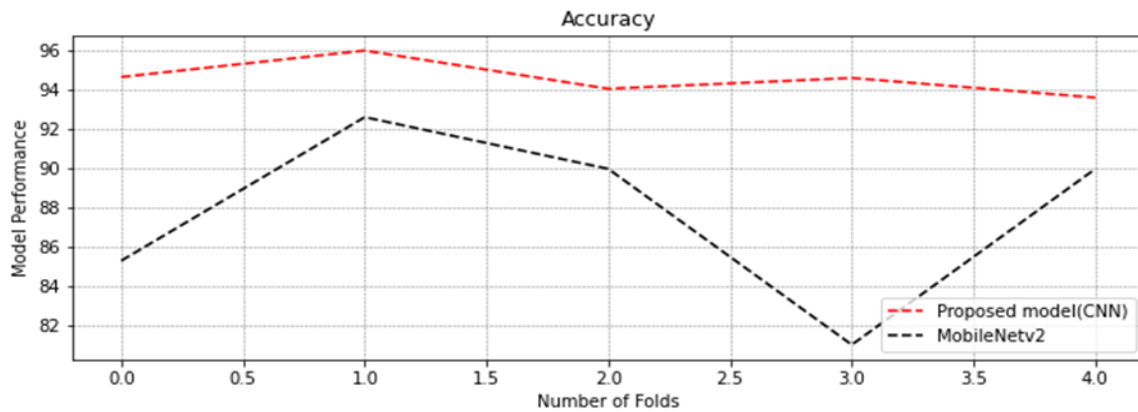


Figure 10. Accuracy graph of the system.

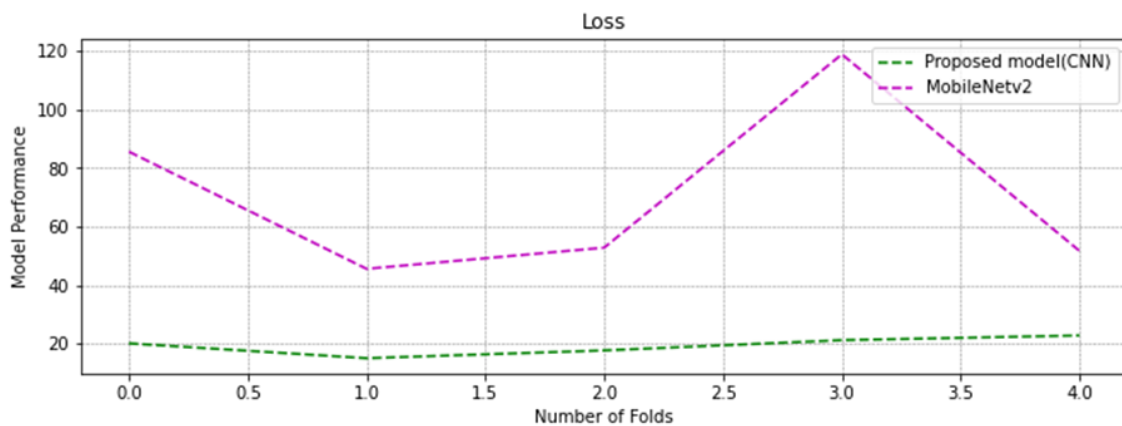


Figure 11. Loss graph of the system.

4. Discussion

Globally, there are more retinal diseases, and technological advancements have made it simpler to identify and treat these diseases. Cost, expert mistakes, timing, technological infrastructure, and other factors can all have a negative effect on the disease's diagnosis and treatment. This study's objective is to suggest a method for accurately identifying retinal diseases while reducing error rates. In this study, the applicability of neural network models based on retinal OCT datasets in the detection of various retinal illnesses is evaluated and examined. The publicly accessible OCT dataset is used to evaluate the performance of the proposed and selected neural networks. Two different neural network topologies (the proposed CNN and the MobileNetv2 model) are tested and appraised. Accuracy, recall, precision, and AUC are used as evaluation criteria to show the ROC curve and confusion matrix of each neural network. The proposed CNN model achieves higher results than MobileNet with an accuracy rate of 94% and an AUC value of 0.96 as a result of k-layer cross-validation methods (5 folds) in the data set used. When examining and comparing the studies conducted for OCT diagnosis and classification in the literature with our proposed model, it becomes clear that the proposed model performs more satisfactorily than some architectures and less accuracy rate than others [17], [18]. Our study has limitations; the fact that OCT datasets are not very common in the literature and especially the lack of labelled data is a significant challenge. In addition, the external generalizability of the system can be demonstrated with the datasets to be trained using images from several academic centers. Future work will include expanding the number of diagnoses using all images from a macular OCT scan, including images from different OCT manufacturers, and validation of OCT scans from other institutions.

5. Conclusions

Retinal diseases are one of the most critical variables affecting human life quality. Degeneration of the retina is the most common cause of retinal diseases. With the advancement of technology, tremendous progress in

acquiring images in medicine has recently been made. OCT imaging techniques are commonly utilized in ophthalmology to diagnose retinal disorders. A deep learning-based technique for diagnosing eye problems from OCT images is proposed in this article. A CNN architecture with five convolution layers has been created for this purpose. Deep learning adaptation has been shown to improve image classification with a high accuracy of 94%. The proposed CNN network model is compared to the MobileNet50 network model available in the literature in a deep learning application for classification, and their results are provided. The paper also includes the evaluation parameter values for the models trained using the 5 fold cross-validation approach for each infection type in the retinal OCT Images dataset. In short, it provides ophthalmologists with a new easy and efficient way to diagnose and detect previous stages of the disease.

References

- [1] Miranda, M., & Romero, F. J. (2019). Antioxidants and Retinal Diseases. *Antioxidants*, 8(12), 604.
- [2] Berrimi, M., & Moussaoui, A. (2020, October). Deep learning for identifying and classifying retinal diseases. In *2020 2nd International Conference on Computer and Information Sciences (ICCIS)* (pp. 1-6). IEEE.
- [3] Sunija, A. P., Kar, S., Gayathri, S., Gopi, V. P., & Palanisamy, P. (2021). Octnet: A lightweight cnn for retinal disease classification from optical coherence tomography images. *Computer methods and programs in biomedicine*, 200, 105877.
- [4] Abidalkareem, A. J., Abd, M. A., Ibrahim, A. K., Zhuang, H., Altaher, A. S., & Ali, A. M. (2020, July). Diabetic retinopathy (DR) severity level classification using multimodel convolutional neural networks. In *2020 42nd Annual International Conference of the IEEE Engineering in Medicine & Biology Society (EMBC)* (pp. 1404-1407). IEEE.
- [5] Wang, J., Hormel, T. T., Gao, L., Zang, P., Guo, Y., Wang, X., ... & Jia, Y. (2020). Automated diagnosis and segmentation of choroidal neovascularization in OCT angiography using deep learning. *Biomedical Optics Express*, 11(2), 927-944.
- [6] Sun, Y., Li, S., & Sun, Z. (2017). Fully automated macular pathology detection in retina optical coherence tomography images using sparse coding and dictionary learning. *Journal of biomedical optics*, 22(1), 016012.
- [7] Wang, Y., Zhang, Y., Yao, Z., Zhao, R., & Zhou, F. (2016). Machine learning based detection of age-related macular degeneration (AMD) and diabetic macular edema (DME) from optical coherence tomography (OCT) images. *Biomedical optics express*, 7(12), 4928-4940.
- [8] Rasti, R., Rabbani, H., Mehridehnavi, A., & Hajizadeh, F. (2017). Macular OCT classification using a multi-scale convolutional neural network ensemble. *IEEE transactions on medical imaging*, 37(4), 1024-1034.
- [9] Li, F., Chen, H., Liu, Z., Zhang, X., & Wu, Z. (2019). Fully automated detection of retinal disorders by image-based deep learning. *Graefé's Archive for Clinical and Experimental Ophthalmology*, 257(3), 495-505.
- [10] Mishra, S. S., Mandal, B., & Puhan, N. B. (2019). Multi-level dual-attention based CNN for macular optical coherence tomography classification. *IEEE Signal Processing Letters*, 26(12), 1793-1797.
- [11] Motozawa, N., An, G., Takagi, S., Kitahata, S., Mandai, M., Hirami, Y., ... & Kurimoto, Y. (2019). Optical coherence tomography-based deep-learning models for classifying normal and age-related macular degeneration and exudative and non-exudative age-related macular degeneration changes. *Ophthalmology and therapy*, 8(4), 527-539.
- [12] Najeeb, S., Sharmile, N., Khan, M. S., Sahin, I., Islam, M. T., & Bhuiyan, M. I. H. (2018, December). Classification of retinal diseases from OCT scans using convolutional neural networks. In *2018 10th International Conference on Electrical and Computer Engineering (ICECE)* (pp. 465-468). IEEE.
- [13] Wang, W., Xu, Z., Yu, W., Zhao, J., Yang, J., He, F., ... & Li, X. (2019, October). Two-stream CNN with loose pair training for multi-modal AMD categorization. In *International Conference on Medical Image Computing and Computer-Assisted Intervention* (pp. 156-164). Springer, Cham.
- [14] Kermany D, Zhang K, Goldbaum M, 2018, Large Dataset of Labeled Optical Coherence Tomography (Oct) and Chest X-Ray Images, Mendeley Data.
- [15] Deng, L., & Yu, D. (2014). Deep learning: methods and applications. *Foundations and trends in signal processing*, 7(3-4), 197-387.
- [16] Sahin, M. E., Ulutas, H., & Esra, Yuce. A deep learning approach for detecting pneumonia in chest X-rays. *Avrupa Bilim ve Teknoloji Dergisi*, (28), 562-567.
- [17] Lo, S. C., Lou, S. L., Lin, J. S., Freedman, M. T., Chien, M. V., & Mun, S. K. (1995). Artificial convolution neural network techniques and applications for lung nodule detection. *IEEE transactions on medical imaging*, 14(4), 711-718.
- [18] Lee, C. S., Baughman, D. M., & Lee, A. Y. (2017). Deep learning is effective for classifying normal versus age-related macular degeneration OCT images. *Ophthalmology Retina*, 1(4), 322-327.
- [19] Toğaçar, M., Ergen, B., & Tümen, V. (2022). Use of dominant activations obtained by processing OCT images with the CNNs and slime mold method in retinal disease detection. *Biocybernetics and Biomedical Engineering*.

Loxodromes On Twisted Surfaces in Euclidean 3-Space

Mustafa ALTIN^{1*}

¹ Technical Sciences Vocational School, Bingöl University, Bingöl, Türkiye

*1 maltin@bingol.edu.tr

(Geliş/Received: 28/06/2022;

Kabul/Accepted: 31/08/2022)

Abstract: In the present paper, loxodromes, which cut all meridians and parallels of twisted surfaces (that can be considered as a generalization of rotational surfaces) at a constant angle, have been studied in Euclidean 3-space and also some examples have been constructed to visualize and support our theory.

Key words: Loxodromes, meridian, twisted surface.

Öklidyen 3-Uzayında Twisted Yüzeyler Üzerinde Loksodromlar

Öz: Bu makalede, Öklidyen 3-uzayında twisted yüzeylerin (ki bunlar dönel yüzeylerin bir genelleştirilmesi olarak düşünülebilir) tüm meridyen ve paralellerini sabit bir açı ile kesen loksodromlar çalışıldı ve ayrıca görselleştirmek ve teorimizi desteklemek için bazı örnekler inşa edildi.

Anahtar kelimeler: Loksodromlar, meridyen, twisted yüzeyler.

1. General Information and Basic Concepts

Loxodromes (also known as rhumb lines) correspond to the curves which intersect all of the meridians at a constant angle on the Earth (see Figure 1). An aircraft flying and a ship sailing on a fixed magnetic compass course move along a curve. Here the course is a rhumb and the curve is a loxodrome. Generally, a loxodrome is not a great circle, thus it does not measure the shortest distance between two points on the Earth. However, loxodromes are important in navigation and they should be known by aircraft pilots and sailors [1].

If the shape of the Earth is approximated by a sphere, then the loxodrome is a logarithmic spiral that cuts all meridians at the same angle and asymptotically approaches the Earth's poles but never meets them. Since maritime surface navigation defines the course as the angle between the current meridian and the longitudinal direction of the ship, it may be concluded that the loxodrome is the curve of the constant course, which means that whenever navigating on an unchanging course we are navigating according to a loxodrome [11].

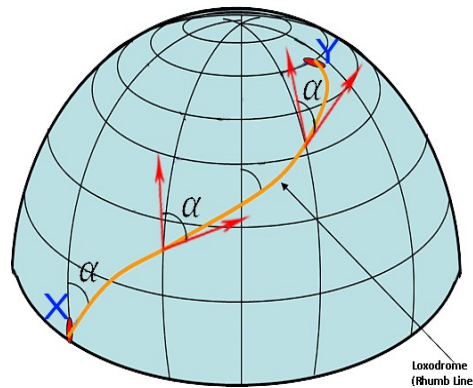


Figure 1. Loxodrome on Earth

In this context, there are lots of studies about loxodromes in Euclidean and Minkowskian spaces. For instance, the differential equations of loxodromes on a sphere, spheroid, rotational surface, helicoidal surface and canal surface in Euclidean 3-space have been given in [11], [13], [12], [2] and [3], respectively. Also, in [4] and [5], spacelike and timelike loxodromes on rotational surface and in [6], differential equations of the spacelike

Loxodromes On Twisted Surfaces in Euclidean 3-Space

loxodromes on the helicoidal surfaces in Lorentz-Minkowski 3-space have been given.

Now, we recall some basic notions about curves and twisted surfaces in Euclidean 3-space E^3 .

For two vectors $\vec{u} = (u_1, u_2, u_3)$ and $\vec{v} = (v_1, v_2, v_3)$ in E^3 the inner product of these vectors and the norm of the vector \vec{u} are defined by

$$\langle \vec{u}, \vec{v} \rangle = u_1 v_1 + u_2 v_2 + u_3 v_3 \quad (1)$$

and

$$\|\vec{u}\| = \sqrt{\langle \vec{u}, \vec{u} \rangle}, \quad (2)$$

respectively. We say that \vec{u} is a unit vector, if $\|\vec{u}\| = 1$.

The arc-length of a regular curve $\alpha: I \subset \mathbb{R} \rightarrow E^3, s \rightarrow \alpha(s)$, between s_0 and s is

$$t(s) = \int_{s_0}^s \|\alpha'(s)\| ds. \quad (3)$$

Then the parameter $t \in J \subset \mathbb{R}$ is determined as $\|\alpha'(s)\| = 1$.

Also, the angle ϕ ($0 < \phi < \pi$) between the vectors \vec{u} and \vec{v} is

$$\cos \phi = \frac{\langle \vec{u}, \vec{v} \rangle}{\|\vec{u}\| \|\vec{v}\|}. \quad (4)$$

Here, we recall the definition and parametrization of twisted surfaces in E^3 (for detail, see [8]).

A twisted surface in E^3 is obtained by rotating a planar curve α in its supporting plane while this plane itself is rotated about some containing straight line. Without loss of generality, the coordinate system can be chosen in such a way that the xz -plane corresponds with the plane supporting the planar curve with the z -axis as its containing rotation axis and that the straight line through the point $(a, 0, 0)$ parallel with the y -axis acts as rotation axis for the planar curve.

Firstly, let us apply the rotation about the straight line through the point $(a, 0, 0)$ parallel with the y -axis to the profile curve $\alpha(y) = (f(y), 0, g(y))$, (f and g are real-valued functions) and next apply the rotation about the z -axis to the obtained surface. Then, up to a transformation, we get the parametrization of the twisted surface in E^3

$$T(x, y) = \begin{pmatrix} (a + f(y) \cos(bx) - g(y) \sin(bx)) \cos x, \\ (a + f(y) \cos(bx) - g(y) \sin(bx)) \sin x, \\ f(y) \sin(bx) + g(y) \cos(bx) \end{pmatrix}. \quad (5)$$

Here, the presence of the factor $b \in \mathbb{R}$ allows for differences in the rotation speed of both rotations and it is obvious from the construction that, if we take $b = 0$, then the twisted surface reduces to a surface of revolution. Thus, the twisted surfaces can be considered as generalizations of surfaces of revolution.

After giving the definition of the twisted surfaces, twisted surfaces with null rotation axis in Minkowski 3-space have been studied in [9] and twisted surfaces with vanishing curvature in Galilean 3-space have been classified in [7]. Also, in [10], the twisted surfaces in pseudo-Galilean space have been studied.

In this paper, we have studied loxodromes on twisted surfaces in Euclidean 3-space and also we have constructed some examples to visualize and support our results.

2. Loxodromes on Twisted Surfaces in E^3

In this section, we obtain the equations of loxodromes on the twisted surfaces in E^3 .

Let T be the twisted surface which parametrized as (5). Then the coefficients of first fundamental form of the twisted surface T are obtained by

$$g_{11} = \frac{1}{2} \begin{pmatrix} 2a^2 + (1 + 2b^2 + \cos(2bx))f^2 + (1 + 2b^2 - \cos(2bx))g^2, \\ -4agsin(bx) + 4f \cos(bx)(a - g \sin(bx)) \end{pmatrix},$$

$$\begin{aligned} g_{12} &= g_{21} = b(fg' - f'g), \\ g_{22} &= f'^2 + g'^2, \end{aligned} \tag{6}$$

where $g_{11} = \langle T_x, T_x \rangle$, $g_{12} = g_{21} = \langle T_x, T_y \rangle$, $g_{22} = \langle T_y, T_y \rangle$, $f = f(y)$, $g = g(y)$, $f' = \frac{df(y)}{dy}$ and $g' = \frac{dg(y)}{dy}$.

Also, we know that the first fundamental form in the base $\{M_x, M_y\}$ for a surface $M(x, y)$ is given by

$$ds^2 = g_{11}dx^2 + 2g_{12}dxdy + g_{22}dy^2, \tag{7}$$

where g_{ij} are the coefficients of the first fundamental form of M . So, from (6) and (7), we can write the first fundamental form of the twisted surface (5) as

$$ds^2 = \left(\begin{aligned} &a^2 - 2agsin(bx) + 2fcos(bx)(a - gsin(bx)) \\ &+ \frac{1}{2}((1 + 2b^2 + cos(2bx))f^2 + (1 + 2b^2 - cos(2bx))g^2) \end{aligned} \right) dx^2 + 2b(fg' - f'g)dxdy + (f'^2 + g'^2)dy^2 \tag{8}$$

and from (8), the arc-length of any curve on the twisted surface between x_1 and x_2 is given by

$$s = \left| \int_{x_1}^{x_2} \sqrt{\begin{aligned} &\left(a^2 - 2agsin(bx) + 2fcos(bx)(a - gsin(bx)) \right. \\ &\left. + \frac{1}{2}((1 + 2b^2 + cos(2bx))f^2 + (1 + 2b^2 - cos(2bx))g^2) \right. \\ &\left. + 2b(fg' - f'g)\frac{dy}{dx} + (f'^2 + g'^2)\left(\frac{dy}{dx}\right)^2 \right)} dx \right|. \tag{9}$$

Furthermore, a curve γ is called a loxodrome on the twisted surface T in E^3 if it cuts all meridians (y constant) (or parallels (x constant)) of T at a constant angle.

Now, let us suppose that $\gamma(t) = T(x(t), y(t))$; i.e. $\gamma(t)$ is a curve on the twisted surface T . With respect to the local base $\{T_x, T_y\}$, the vector $\gamma'(t)$ has the coordinates (x', y') and the vector T_x has the coordinates $(1, 0)$. At the point $p = T(x, y)$; where the loxodrome cuts the meridians at a constant angle; we get

$$cos\phi = \frac{\langle T_x, \gamma'(t) \rangle}{\|T_x\| \|\gamma'(t)\|} = \frac{g_{11}dx + g_{12}dy}{\sqrt{g_{11}^2 dx^2 + 2g_{11}g_{12}dxdy + g_{11}g_{22}dy^2}}. \tag{10}$$

Therefore, keeping in mind (10) we get

$$g_{11}^2 sin^2\phi dx^2 + 2g_{11}g_{12} sin^2\phi dxdy + (g_{12}^2 - g_{11}g_{22} cos^2\phi) dy^2 = 0 \tag{11}$$

and so,

$$\frac{dy}{dx} = \frac{-2g_{11}g_{12} sin^2\phi \mp g_{11}\sqrt{g_{11}g_{12} - g_{11}^2} sin(2\phi)}{2(g_{12}^2 - g_{11}g_{22} cos^2\phi)}. \tag{12}$$

Hence from (6) and (12), the loxodrome on the twisted surface (5) must satisfy

$$\frac{dy}{dx} = - \frac{\left(\begin{aligned} &2b(fg' - f'g) sin\phi \\ &\mp 2cos\phi \sqrt{\begin{aligned} &-b^2(fg' - f'g)^2 + \\ &(a^2 - 2agsin(bx) + 2fcos(bx)(a - gsin(bx))) \end{aligned}} \right) \times \left(\begin{aligned} &\frac{1}{2}((1 + 2b^2 + cos(2bx))f^2 \\ &+ (1 + 2b^2 - cos(2bx))g^2) \end{aligned} \right)}{\begin{aligned} &(2a^2 + (1 + 2b^2 + cos(2bx))f^2 + (1 + 2b^2 - cos(2bx))g^2) sin\phi \\ &- 4agsin(bx) + 4fcos(bx)(a - gsin(bx)) \end{aligned}} \tag{13}$$

Now, we give some examples to support our results that obtained in the paper.

Loxodromes On Twisted Surfaces in Euclidean 3-Space

Example 1. Taking the profile curve as $\alpha(y) = (y, 0, 0)$, the twisted surface (5) becomes

$$T(x, y) = ((a + y \cos(bx)) \cos x, (a + y \cos(bx)) \sin x, y \sin(bx)). \quad (14)$$

From (13) (we take \mp in this equation as $-$), we get the differential equation of the loxodrome on the twisted surface (14) for $a = 0$ and $b = \frac{1}{2}$ as

$$\frac{dy}{dx} = \frac{y \sqrt{2 \cos x + 3 \tan \phi}}{2}. \quad (15)$$

Thus, we write

$$\frac{dy}{y} = \frac{\sqrt{2 \cos x + 3 \tan \phi}}{2} dx$$

and by integrating both sides of this equation, we get

$$\ln y = \int_{x_0}^x \frac{\sqrt{2 \cos x + 3 \tan \phi}}{2} dx. \quad (16)$$

Putting $x_0 = 0$ in (16), we reach that

$$y = y(x) = e^{\sqrt{5} \text{EllipticE}\left[\frac{x}{2}, \frac{4}{5}\right] \tan \phi}. \quad (17)$$

Now, if we take $\phi = \frac{\pi}{6}$ and $x \in (-2\pi, 2\pi)$, we get $y \in (0.0476989, 20.9649)$. Thus, the loxodrome which lies on the twisted surface (14) is obtained as

$$\gamma(x) = e^{\sqrt{\frac{5}{3}} \text{EllipticE}\left[\frac{x}{2}, \frac{4}{5}\right]} \cdot \left(\cos\left(\frac{x}{2}\right) \cos x, \cos\left(\frac{x}{2}\right) \sin x, \sin\left(\frac{x}{2}\right) \right). \quad (18)$$

Also, the arc-length of our loxodrome (18) is approximately equal to 41.8343. The twisted surface (14), meridian for $y = 15$ and the loxodrome (18) can be seen in Figure 2.

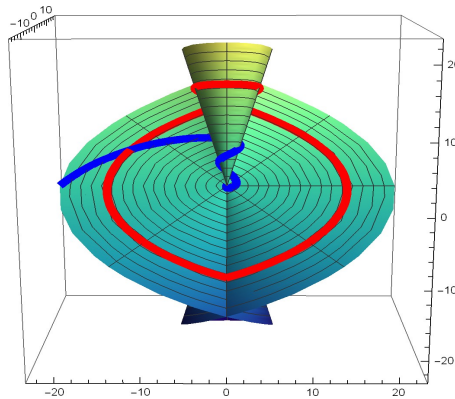


Figure 2. Twisted surface (14), Meridian (red) and Loxodrome (blue)

Example 2. For the profile curve $\alpha(y) = (\cos y, 0, \sin y)$ the twisted surface (5) is

$$T(x, y) = \begin{pmatrix} (a + \cos y \cos(bx) - \sin y \sin(bx)) \cos x, \\ (a + \cos y \cos(bx) - \sin y \sin(bx)) \sin x, \\ \cos y \sin(bx) + \sin y \cos(bx) \end{pmatrix}. \quad (19)$$

If we take $a = 1$ and $b = 0$ then from (13) (we take $\bar{\Gamma}$ in this equation as $-$), we have

$$\frac{dy}{dx} = 2 \cos^2\left(\frac{y}{2}\right) \tan \phi \quad (20)$$

and hence

$$\frac{dy}{2 \cos^2\left(\frac{y}{2}\right)} = \tan \phi dx \quad (21)$$

and by integrating both sides of this equation, we get

$$\tan\left(\frac{y}{2}\right) = \int_{x_0}^x \tan \phi dx. \quad (22)$$

Taking $x_0 = 0$ in (22), we arrive at

$$y = y(x) = 2 (\arctan(x \tan \phi) + c\pi), \quad c \in \mathbb{Z}. \quad (23)$$

Here, if we take $c = 0$, $\phi = \frac{\pi}{4}$ and $x \in (-\pi, \pi)$ we have $y \in (-2.52525, 2.52525)$. Thus, the loxodrome which lies on the twisted surface (19) is obtained as

$$\gamma(x) = ((1 + \cos(2\arctan x)) \cos x, (1 + \cos(2\arctan x)) \sin x, \sin(2\arctan x)). \quad (24)$$

Also, the arc-length of our loxodrome (24) is approximately equal to 7.1425. One can see the twisted surface (19), meridian for $y = 1$ and the loxodrome (24) in Figure 3.

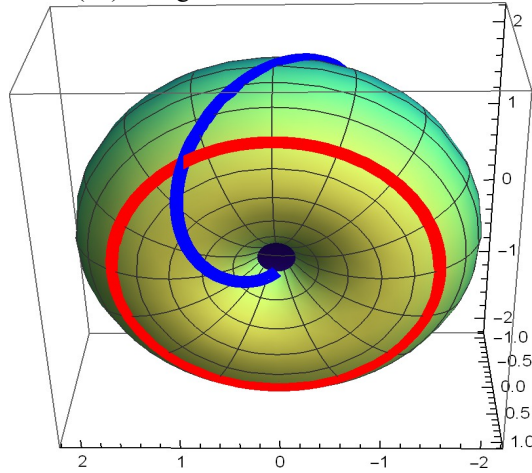


Figure 3. Twisted surface (2.14), Meridian (red) and Loxodrome (blue)

Furthermore, from the definition of the angle θ between the loxodrome and any parallel ($x=\text{constant}$), we have

$$\cos \theta = \frac{\langle \gamma'(t), T_y \rangle}{\|\gamma'(t)\| \|T_y\|} = \frac{g_{12} dx + g_{22} dy}{\sqrt{g_{11}g_{22} dx^2 + 2g_{12}g_{22} dx dy + g_{22}^2 dy^2}}. \quad (25)$$

From (25), we get

$$(g_{11}g_{22} \cos^2 \theta - g_{12}^2) dx^2 - 2g_{12}g_{22} \sin^2 \theta dx dy - g_{22}^2 \sin^2 \theta dy^2 = 0 \quad (26)$$

and so,

Loxodromes On Twisted Surfaces in Euclidean 3-Space

$$\frac{dx}{dy} = \frac{-2g_{12}g_{22} \sin^2 \theta \pm g_{22} \sqrt{g_{11}g_{22} - g_{12}^2} \sin(2\theta)}{2(g_{12}^2 - g_{11}g_{22} \cos^2 \theta)}. \quad (27)$$

Therefore, the loxodrome on the twisted surface must

$$\frac{dx}{dy} = \frac{\left(\mp 2 \cos \theta \sqrt{\frac{2b \sin \theta (f'g - fg')}{-b^2(gf' - fg')^2} + \left(\begin{array}{l} a^2 - 2ag \sin(bx) + 2f \cos(bx)(a - g \sin(bx)) \\ + \frac{1}{2} (1 + 2b^2 + \cos(2bx)) f^2 \\ + (1 + 2b^2 - \cos(2bx)) g^2 \end{array} \right) (f'^2 + g'^2)}{2b^2 (f'g - fg')^2} \right) (f'^2 + g'^2) \sin \theta}{\left(\begin{array}{l} 2a^2 - 4ag \sin(bx) + 4f \cos(bx)(a - g \sin(bx)) \\ + (1 + 2b^2 + \cos(2bx)) f^2 + (1 + 2b^2 - \cos(2bx)) g^2 \end{array} \right) (f'^2 + g'^2) \cos^2 \theta} \right)}. \quad (28)$$

Now, let us give an example for the loxodrome which cuts the parallels of the twisted surface at a constant angle.

Example 3. Let us take the profile curve as $\alpha(y) = (\cos^2 y, 0, \sin^2 y)$. Then, the twisted surface (5) is

$$T(x, y) = \begin{pmatrix} (a + \cos^2 y \cos(bx) - \sin^2 y \sin(bx)) \cos x, \\ (a + \cos^2 y \cos(bx) - \sin^2 y \sin(bx)) \sin x, \\ \cos^2 y \sin(bx) + \sin^2 y \cos(bx) \end{pmatrix}. \quad (29)$$

Putting $a = -1$ and $b = 0$, from (28) (we take \mp in this equation as $-$), we get

$$\frac{dx}{dy} = 2\sqrt{2} \cot y \tan \theta \quad (30)$$

which gives

$$dx = 2\sqrt{2} \cot y \tan \theta dy.$$

Thus, by integrating both sides of the equation

$$x = \int_{y_0}^y 2\sqrt{2} \cot y \tan \theta dy. \quad (31)$$

For $y_0 = \frac{\pi}{2}$, we reach that

$$x = x(y) = 2\sqrt{2} \ln(\sin y) \tan \theta. \quad (32)$$

Here, by taking $\theta = \frac{\pi}{3}$ and $y \in (\frac{\pi}{16}, \frac{2\pi}{3})$, we have $x \in (-8.00637, -0.704674)$. Therefore, we obtain the loxodrome which lies on the twisted surface (29) as

$$\delta(y) = (-\sin^2 y \cos(2\sqrt{6} \ln(\sin y)), -\sin^2 y \sin(2\sqrt{6} \ln(\sin y)), \sin^2 y). \quad (33)$$

Also, the arc-length of the loxodrome (33) is approximately equal to 3.42788. One can see the twisted surface (29), meridian for $x = -1$ and the loxodrome (33) in Figure 4.

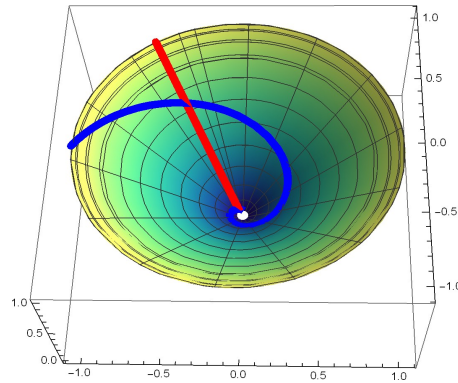


Figure 4. Twisted surface (29), Meridian (red) and Loxodrome (blue)

References

- [1] Alexander J. Loxodromes: a rhumb way to go, *Math. Mag* 2004; 77(5): 349–356.
- [2] Babaarslan M, Yaylı Y. Differential Equation of the Loxodrome on a Helicoidal Surface, *The Journal of Navigation* 2015; 68; 962–970.
- [3] Babaarslan M, Loxodromes on Canal Surfaces in Euclidean 3-Space, *Ann. Sofia Univ. Fac. Math and Inf.* 2016; 103: 97–103.
- [4] Babaarslan M, Yaylı Y. Space-like loxodromes on rotational surfaces in Minkowski 3-space, *J. Math. Anal. Appl* 2014; 409; 288–298.
- [5] Babaarslan M, Munteanu M.I. Timelike loxodromes on rotational surfaces in Minkowski 3-space, *Annals of the Alexandru Ioan Cuza University-Mathematics*, 2015; DOI: 10.2478/aicu-2013-0021.
- [6] Babaarslan M, Kayacik M. Differential Equations of the Space-Like Loxodromes on the Helicoidal Surfaces, *Differ Equ Dyn Syst* 2020; 28(2): 495–512.
- [7] Dede M, Ekici C, Goemans W, Ünlütürk Y. Twisted surfaces with vanishing curvature in Galilean 3-space, *International Journal of Geometric Methods in Modern Physics*, 2018; 15(1).
- [8] Goemans W, Van de Woestyne I. Twisted surfaces in Euclidean and Minkowski 3-space, *Pure and Applied Differential Geometry*, Joeri Van der Veken, Ignace Van de Woestyne, Leopold Verstraelen and Luc Vrancken (Editors), Shaker Verlag (Aachen, Germany) 2013; 143-151.
- [9] Goemans W, Van de Woestyne I. Twisted Surfaces with Null Rotation Axis in Minkowski 3-Space, *Results in Mathematics*, (2016; 70: 81–93.
- [10] Kazan A, Karadağ H.B. Twisted Surfaces in the Pseudo-Galilean Space, *NTMSCI* 2017; 5(4): 72-79.
- [11] Kos S, Vranic D, Zec D. Differential Equation of a Loxodrome on a Sphere, *The Journal of Navigation* 1999; 52: 418–420.
- [12] Kos S, Filjar R, Hess M, Differential equation of the loxodrome on a rotational surface, *ION ITM Conference*, 2009; Anaheim, California, USA.
- [13] Petrovic M. Differential Equation of a Loxodrome on the Spheroid, "Naše more" 2007; 54(3-4): 87-89.

Active Face Spoof Detection Using Image Distortion Analysis

Betul AY^{1*}, Peter ANTHONY²

^{1,2} Department of Computer Engineering, Faculty of Engineering, Firat University, Elazig, Turkiye

*¹ betulay@firat.edu.tr, ² pettony1@gmail.com

(Geliş/Received: 08/07/2022;

Kabul/Accepted: 15/08/2022)

Abstract: With the rising use of facial recognition systems in a range of real-world scenarios and applications, attackers are also increasing their efforts, with a number of spoofing techniques emerging. As a result, developing a reliable spoof detection mechanism is critical. Active-based techniques have been shown to be good at finding spoofs, but they have a number of problems, such as being intrusive, expensive, hard to compute, not being able to be used in many situations, and usually needing extra hardware. This research presented an active-based robust spoof detection technique capable of detecting a wide range of media or 2D attacks while being less intrusive, less expensive, low in complexity, and more generalizable than other active-based techniques. It doesn't require any additional hardware, so it can easily be integrated into current systems. The distortion variations of video frames of the user's face collected at varying distances from the camera are analyzed to detect spoofing. Both the legitimate and spoof attack datasets were created using real-world facial photo and video data. The proposed approach achieved a spoof detection accuracy of 98.18% using both machine learning classifiers and a deep learning model, with an equal error rate and a half total error rate as low as 0.023 and 0.021, respectively.

Key words: Face Anti-spoofing, Face Spoof Detection, Face Recognition, Biometrics, Image Distortion Analysis.

Yüz Tanıma Sistemleri İçin Kararlı Aktif Tabanlı Yüz Sahteciliği Tespiti

Öz: Bir dizi gerçek dünya senaryosu ve uygulamasında yüz tanıma sistemlerinin artan kullanımıyla birlikte, yeni ortaya çıkan farklı sahtecilik teknikleri kullanarak saldırganlar da çabalarını artırmaktadır. Bunun sonucu olarak, güvenilir bir sahtecilik tespit mekanizması geliştirmek kritik öneme sahiptir. Aktif tabanlı tekniklerin sahtekarlıkları bulmada iyi olduğu gösterilmiş olsa da bunların, müdahaleci, pahalı, hesaplanması zor olmaları, birçok durumda kullanılamamaları ve genellikle ekstra donanım ihtiyacı duymaları gibi bir takım sorunları vardır. Bu çalışma, daha az müdahaleci, düşük maliyetli, karmaşıklığı düşük ve diğer aktif tabanlı tekniklerden daha genelleştirilebilen, çok çeşitli medya veya 2D saldırıları tespit edebilen aktif tabanlı sağlam bir sahtekarlık algılama tekniği sunmaktadır. Önerilen yöntem herhangi bir ek donanım gerektirmez, bu nedenle mevcut sistemlere kolayca entegre edilebilir. Kullanıcının yüzünün kamera yardımıyla farklı mesafelerden elde edilen video karelerindeki bozulma değişimleri, sahtekarlığı tespit etmek için analiz edilmiştir. Hem gerçek hem de sahte saldırı veri kümeleri, gerçek dünyadan yüz fotoğrafı ve video verileri kullanılarak oluşturulmuştur. Önerilen yaklaşım, hem makine öğrenimi sınıflandırıcıları hem de derin öğrenme modeli kullanılarak, sırasıyla 0,023 ve 0,021 kadar düşük bir hata oranı ve yarı toplam hata oranıyla %98,18'lik bir sahtekarlık algılama doğruluğu elde etmiştir.

Anahtar kelimeler: Yüz Sahteciliğine Karşı Koruma, Yüz Sahteciliği Algılama, Yüz Tanıma, Biyometri, Görüntü Bozulma Analizi.

1. Introduction

Face recognition is one of the most widely used biometric systems today, and its use has increased dramatically and rapidly over the last decade. Facial recognition, after fingerprints, is the second most frequently used biometric technology in the world, according to the International Biometric Group (IBG) [1]. This rising popularity is attributed to the fact that it is more convenient, contactless, and non-invasive than other biometric systems like fingerprint and iris [2,3]. Face recognition is also a biometric system that has a wider functioning range and application potential than others [4]. Unfortunately, the majority of existing facial recognition systems are vulnerable to spoof attacks.

A spoofing attack occurs when a phony piece of evidence is provided to a biometric system for authentication, resulting in false approval [5–8]. Face spoofing is the act of masking a person's face in order to get around a biometric system and acquire unauthorized access or privileges. Face photographs or videos of a person can now be easily obtained through social media or shot from afar without the individual's consent [9]. This is accomplished by simply presenting or replaying illegally obtained photographs or videos. As efforts to combat spoofing operations have increased, spoofing artifacts have morphed into a variety of methods.

* Corresponding author: betulay@firat.edu.tr. ORCID Number of authors: ¹ 0000-0002-3060-0432, ² 0000-0002-9010-3075

Face anti-spoofing, also known as face spoof detection, is the challenge of preventing fraudulent face verification. Despite the fact that the problem of face spoof detection has been around for over a decade [10], it did not undergo a genuine revolution until around the year 2010 under the European project TABULA RASA, which was focused on biometric spoof threats [11]. Another element that has contributed to significant progress in creating approaches for identifying face spoofing attacks is the compilation and sharing of publicly available face spoof datasets. This has relieved researchers of the burden of data collection, allowing them to focus on developing viable ways to counter various types of attacks [12–15].

These important factors have resulted in the release of numerous strategies for preventing both 2D and 3D face spoofing attacks. For spoof detection, researchers have proposed a number of approaches, ranging from the use of motion cues [16–18] to the current deep learning approaches [19,20] with competitive performance. Face spoof detection techniques can be divided into two categories: active and passive. The mode of enrollment, or the approach utilized to acquire the user's data, differentiates between the two types. Active techniques have proven to be quite reliable, with good anti-spoofing capabilities. Active techniques, on the other hand, involve user participation, which makes them intrusive and limits their applicability. Some active techniques, such as multi-modal [21,22] and sensor-level approaches [18], might be computationally challenging and costly due to the additional hardware required. A semi-active strategy is proposed here, with less intrusiveness and interaction, a wider application range, no additional hardware requirements, and hence a lower cost.

The possibility of image distortion caused by the proximity of the face to the camera in combating face spoof attempts is investigated in this paper. The decision to use image distortion analysis (IDA) for spoof detection is based on three findings:

- The typical photographic phenomena of face distortion in video when the camera is very close to the face, which is caused by the uneven 3D-surface of the human face, as contrast to the flat surface of 2D materials such as prints and screens.
- Image distortion has had a lot of success in the field of biometrics and security systems for finger print spoof detection [23], steganalysis [24,25], and facial liveness detection [2,26].
- When the camera gets closer to an object, that object grows in size faster than things in the background. A scatter plot of measured pixel intensity versus distance to the camera revealed an exponential falloff in intensity with distance from the camera in a study by Bryson et al [27]. This is due to the fact that the item and the background image create an uneven 3D surface. 2D attacks have flat surfaces, so when filmed by the camera, a different observation is predicted.

This study aims at employing image distortion for developing a robust active face spoof detection technique that is less intrusive, less expensive, and more generic than current active-based approaches and requires no additional hardware.

2. Related Literature

The utilization of image distortion features as a descriptor for face spoof detection has been broadly adopted. Authors have devised a number of methodologies based on image distortion analysis (IDA) and found encouraging results.

Image distortion analysis feature vector was constructed in [2] by combining four (4) separate distortion features, including chromatic moment, color diversity, specular reflectance features, and blurriness features, to create a strategy against printed photo and replay attacks. For differentiating real and fake faces, an ensemble classifier made up of multiple support vector machines (SVM) was used to learn these characteristics. The same features were retrieved by the authors in [26] using the four IDA features from the MSU-MFSD dataset, which include printed photo and replay attacks. Training using SVM and an artificial neural network yielded 94.4% and 88.9% accuracy, respectively. Even though they used a non-intrusive approach, their spoof detection performance is not reliable enough for real-world use.

There have also been other active-based techniques proposed. The authors of [28] generated NIR differential (NIRD) images using an active near-infrared (NIR) light source. To achieve spoof detection, they used two separate features based on NIRD images. The pixel consistency between facial and non-facial regions was studied, and context signals were used to distinguish faked faces from real ones. Although their method proved effective in detecting spoofs, it is limited in terms of applicability because it involves the use of additional hardware and it is also quite intrusive. The authors of [29] proposed a multi-spectral imaging approach that used both visible (VIS) and near-infrared (NIR) spectra for imaging. The authors in [30] integrate face and voice. A user is required to present his/her voice and also speak. A specialized piece of hardware was utilized in [16] to capture pupil orientation as a clue for liveness assessment. In an approach in [1], to ascertain liveness, the user is asked to open

and close his mouth or blink his eyelids. All of these active-based approaches suffer from some or all of the issues that active approaches encounter, such as the need for additional hardware, high intrusiveness, high cost, computational complexity, and reduced ability to fit into existing systems, among others.

Distinctively, the approach proposed in this research work computes the distortion changes between a user's face captured at two different distances to deliver a robust active spoof detection technique, yet less intrusive and less expensive. The authors in [31] propose a method that is similar to the one given in this paper, but their method requires eight (8) face frames at varied distances from the camera for a single sample, and the feature is represented by a 7 by 2147 matrix. The method provided in this paper, on the other hand, requires just two frames to be represented in a vector space. Furthermore, the technique does not require additional hardware, making it easy to integrate into existing systems.

3. Methodology

3.1 System Model Design

The system architecture in this work is organized into three core modules, as shown in Figure 1: the Frames Selection Module, the Distortion Feature Extraction Module, and the Classification Module. Face videos are fed into the frame selection module, and two frames are chosen from each of two facial videos captured at varying distances from the camera. The Feature extraction module then extracts a number of facial landmarks from each frame and computes features about how the distortion of the face evolves over time. Finally, the classification module uses the obtained features to perform binary classification to discriminate between fake and real faces.

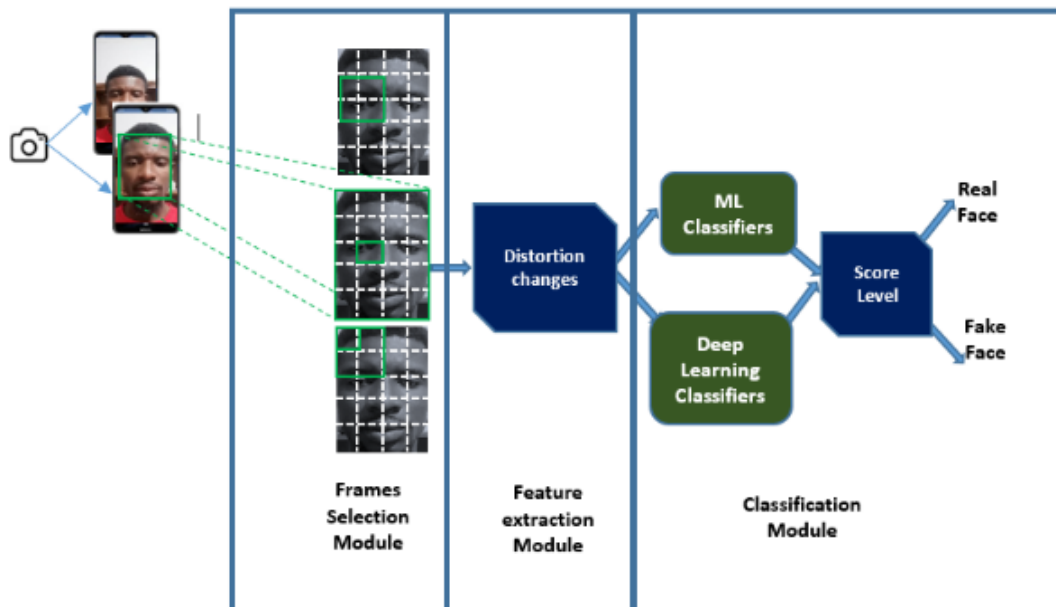


Figure 0. Workflow design for the proposed approach.

3.1.1 Frame selection module

At first, as the user's face approaches or moves away from the mobile device, the device's camera captures two video clips at two different specified distances between the camera and the user's face, referred to as D1 and D2. A number of frames of the user's face are contained in each video. Using Dlib face detector [32], the frame selection module then detects and extracts a K-sequence of frames (D1f1, D1f2, ..., D1fk) and (D2f1, D2f2, ..., D2fk) from the video frames captured at distances D1 and D2, respectively. The frames are then paired D1fi and D2fi, for $i=(1,2,\dots, k)$.

3.1.2 Feature extraction module

Using the extracted frames $D1fi$ and $D2fi$ as input, the feature extraction module detects a number of facial landmarks and calculates the geometric distances (d) between the different facial landmarks in each frame, as well as the relative distance (r) between the two frames ($D1fi$ and $D2fi$) which form the feature vector for detecting distortion changes in the face frames. From each video frame, 68 facial landmarks are detected using the Dlib 68 facial landmark predictor [33]. As shown in Figure 2, the 68 facial landmarks are spread out over the face and include:

- The chin region with 17 points
- The eyebrows region with 10 points, 5 points for each eyebrow
- The nose stem region with 4 points
- Below nose with 5 points
- The eyes region with 12 point, 6 point for each eye
- And the lips or mouth region with 20 points,

The 68 face landmarks are denoted as $(p_1, p_2, \dots, p_{68})$ where $p_i = (x_i, y_i)$ is the coordinate.

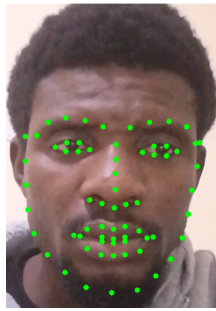


Figure 2. A face with detected landmarks using Dlib 68 point facial landmarks detector.

The facial distortion is captured for each paired frame $D1fi$ and $D2fi$, $i=(1,2,\dots, k)$ by first computing the geometric distance between any two facial landmarks p_s and p_t for each frame using the formula below:

$$d = \sqrt{(x_s - x_t)^2 + (y_s - y_t)^2} \quad (1)$$

Where $s, t \in \{1, 2, \dots, 68\}$ and $s \neq t$.

Each frame's 68 facial landmarks resulted in 2278 pairwise distances $d_1, d_2, \dots, d_{2278}$. The geometric vector (geo) = $(d_1, d_2, \dots, d_{2278}, w, h)$ is formed by concatenating the 2278 pairwise distances with the width (w) and height (h) of the detected face. The relative distance between the paired frames $D1fi$ and $D2fi$ is then calculated using the formula: $r = (r_1, r_2, \dots, r_{2278}, rw, rh)$, where:

$$r_j = \frac{d_{D1,i}}{d_{D2,i}} \quad (2)$$

for $i = 1, 2, \dots, 2278$.

$$rw = \frac{w_{D1}}{w_{D2}} \quad (3)$$

$$rh = \frac{h_{D1}}{h_{D2}} \quad (4)$$

Therefore, each pairwise selected frame $D1fi$ and $D2fi$ is represented by a 1×2280 feature vector (FV).

3.1.3 Classification module

Finally, in the classification module uses classification algorithms to determine whether the feature vector (FV) was taken from a genuine face or a spoof attack. For comparison, four different models, including machine learning models (Linear Discriminant Analysis, Support Vector Machine, and K-Nearest Neighbor) and deep learning models (Convolutional Neural Network) were employed. Details of the models are discussed below:

Support Vector Machines (SVM): An SVM is a supervised learning-based classifier with a generalized model for conducting binary classifications. Nonlinear classification tasks can also be completed using the kernel approach. SVM is frequently used to solve face recognition problems due to its exceptional sparsity and robustness properties [34]. The maximum margin hyperplane of the learning samples' solution is the Support Vector Machine's decision boundary. SVM also uses hinge loss functions to calculate empirical risks and add regularization terms to the solution system in order to maximize structural risks. Face spoof detection is typically thought of as a binary classification task, and SVMs are classifiers with a lot of promise for handling it. It is important to note that this study used a hand-crafted feature-based approach to get a very large feature size, and Support Vector Machines are very good at learning from datasets with high dimensions.

Linear Discriminant Analysis (LDA): Linear discriminant analysis (LDA) has been widely used in face recognition as a supervised approach [35], as well as in face presentation attack detection [36]. LDA can be used to reduce dimensionality and classify data. The goal of LDA is to identify an appropriate projection in the projective feature space that maximizes the between-class scatter matrix while minimizing the within-class scatter matrix. In the past, image data was frequently used directly as a classification input, but when dealing with high-dimensional face data, linear discriminant analysis frequently suffers from a limited sample size problem. It is assumed that LDA is a good fit because the hand-crafted feature-based technique used in this work produced large, high-dimensional features.

K-Nearest Neighbor (KNN): Among machine learning classifiers, the KNN classifier is thought to have the simplest approach. The authors of [37] used Local Binary Pattern descriptors to approach the spoof detection problem; analysis of their results suggests that KNN fared better in terms of accuracy and execution time. In a similar spirit, the authors in [38] used the Eigen vector approach to extract characteristics. Their findings also reveal that KNN outperforms SVM in terms of accuracy and execution time. For comparison, KNN is also used in this study.

Convolutional Neural Network (CNN): Deep learning can be used to generate promising results in the field of computer vision, and it has been shown to be useful in solving the challenge of face spoof detection [39].

Table 1. Summary of the CNN architecture employed

Layer No	Layer type	Activation Function	Value
1	Convolution (Conv1D)	Relu	Unit=32, Kernel size=3
2	MaxPooling1D	None	Stride= 2
3	Dropout	None	0.4
4	Flatten	None	None
5	Dense	Relu	Unit=1024
6	Dropout	None	0.4
7	Dense	Sigmoid	Unit=2

The CNN architecture employed in this research is as follows: To extract various features from input images, a 1-dimensional convolutional layer (Conv1D) with 32 units as the input layer and an input dimension of (2280 x1) is used. To learn and approximate the relationship between network variables, the kernel of the input layer is set to 3 using a Relu activation function. Then, in order to reduce computational costs, a Maxpooling stride 2 is used to reduce the size of the feature map obtained from the Convolutional layer. The third layer has 1024 units and is fully connected. Finally, the output layer is a fully-connected layer with two units and a sigmoid function

(due to the binary classification). To combat overfitting, two Dropout layers with a 0.4 value were added. The first fully-connected layer comes after the pooling layer, and the second comes after the pooling layer. Just before the fully connected layer, a flatten layer is added. The model is tuned at a learning rate of 0.001 and decay of $1e-6$ using the Adam optimizer. In Table 1, the model's summary is provided.

3.2 Data Collection and Dataset Generation

This section explains the complete data gathering procedure as well as the methodologies used to generate the datasets. The genuine photo dataset, the printed-photo attack dataset, the screen-photo attack dataset, and the replay attack dataset are the four datasets that will be discussed.

3.2.1 Data collection

Eighty (80) volunteers were used to collect data for this study, with 56 men and 22 women making up the group. Volunteers range in age from 15 to 40 years of age.

We collect selfie facial recordings from participants in two distinct device positions, with the face covering the middle of the image. Each participant is asked to capture two 1080HD frontal face video clips at 24fps (frames per second) selfies with his or her phone held at controlled distances D1 and D2 from his or her face. The video clips at each distance are 3 seconds long, with each frame measuring 1920×1080 pixels and the face filling the middle of the frame. The capturing at two predefined distances (20 cm and 50 cm) from the device camera are aided by a simple interface program built in python (see Figure 3, 4 and 5). Initially, the participant holds the phone and tries to fit his face into the elliptical shape on the interface (see Figure 3). Once the face is fitted to the elliptical shape (implying a 50 cm distance between the face and the camera), the program automatically takes 3 seconds of facial video frames and adjusts the settings for the next distance, as illustrated in Figure 4. and Figure 5. The elliptical shape increases automatically to capture the face at a closer range (20 cm). Each participant provides a set of two facial video data (at $D1 = 20$ cm and $D2 = 50$ cm).

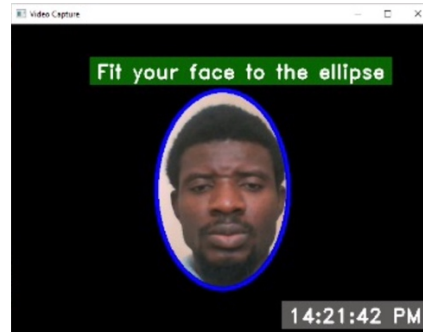


Figure 3. Interface with ellipse set to capture face at 50cm away from the camera.

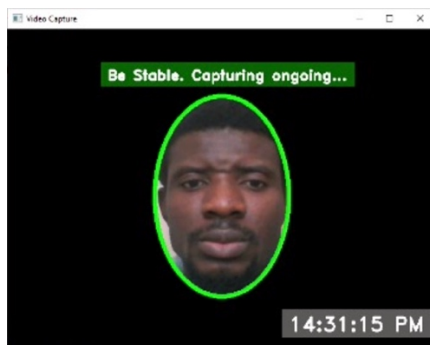


Figure 4. Interface capturing detected face at 50 cm away from the camera.

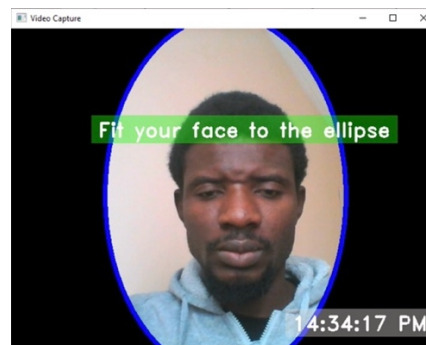


Figure 5. Interface with ellipse set to capture face at 20 cm away from the camera

Image samples from the data obtained are shown in Figure 6. Face photos on the left were obtained at a distance of 20 cm between the face and the camera, whereas the photos on the right were acquired at a distance of 50 cm between the face and the camera.



Figure 6. Sample face images from the dataset

3.2.2 Dataset generation

In this study, four different dataset classes were generated, including real and fake cases: The legitimate dataset, the printed-photo-attack dataset, the screen-photo-attack dataset, and the replay-attack dataset were created from the facial videos and photos collected.

Legitimate Dataset: The genuine dataset comprises of facial videos collected while using a mobile phone with the help of the capture control interface program from a distance of $D1 = 20$ cm to a distance of $D2 = 50$ cm. As a result, the genuine dataset contains eighty (80) videos for $D1 = 20$ cm and eighty (80) videos for $D2 = 50$ cm. That's a total of 80 paired videos.

Printed-Photo Attack Dataset: For the printed photo attack, one facial frame is manually extracted from each participant's frontal facial video clips taken at distance of 50cm from the camera. The images captured at 50 cm were chosen because of the obvious distortion that would be visible on the face image at 20 cm, and the majority of people will not disclose their facial photos/videos shot at such a close range as 20 cm. The extracted facial frames are printed on photo quality paper using a high-quality industrial Direct Impression printer. This makes the size of the face similar to that of a real face. Finally, using the mobile phone and the capture control interface program, each of the printed images is recaptured for three seconds at 24 frames per second, at distances of $D1 = 20$ and $D2 = 50$ cm. There are 80 paired videos in total in the printed-photo attack dataset (80 for $D1 = 20$ cm and 80 for $D2 = 50$ for each photo).

Screen photo-attack dataset: For the screen-photo attack dataset, the manually extracted facial frames from frontal facial video clips captured at distance $D = 50$ cm between the camera and face, are displayed to the controlled

capture system as described in section 5.2.1 using a mobile device. the system records 2 videos for each image at controlled distance $D1=20$ and $D2=50$ cm, each for 3 seconds at 24fps. In total, the screen-photo attack dataset consists of 80 pairwise videos (that is 80 for $D1=20$ cm and 80 for $D2=50$ for each photo).

Replay-Attack Dataset. We used frontal facial video clips collected from each participant at a fixed distance of 50 cm between the camera and their face for the replay attack dataset. Each video clip is played in loop mode using a mobile device before being presented to the controlled capture system, which consists of a mobile phone and the interface program. The replay device is moved closer or farther away from the camera until the facial region fits within the ellipse, and then the video is recorded. For each replayed video, the system records two facial video clips at a controlled distance of $D1 = 20$ cm and $D2 = 50$ cm, each for 3 seconds at 24 frames per second. Hence, a total of 80 pairwise videos (that is, 80 for $D1 = 20$ cm and 80 for $D2 = 50$ for each photo) are generated for the replay-attack dataset.

3.3 Evaluation metrics

Kanika and Jaspreet [40] outlined five characteristics that are typically utilized in face spoof detection evaluation: FRR (false rejection rate), FAR (false acceptance rate), EER (equal error rate), HTER (half total error rate), and accuracy. These parameters aid in identifying serious threats posed by a spoofing database to any face recognition system. These metrics are calculated using following results:

- TP (True Positive): The number of attacks that have been identified as attacks.
- TN (True Negative): The number of authentic samples that have been identified correctly as genuine.
- FP (False Positive): The number of legitimate samples that are incorrectly identified as fake.
- FN (False Negative): The number of attacks that have been identified as genuine samples.

3.3.1 False Acceptance Rate (FAR)

The false acceptance rate, or FAR, is a measure of the tendency that a biometric security system may accept an unauthorized user's access attempt wrongly. It's simply the percentage of times an unauthorized person's face is accepted erroneously. The FAR of a system is commonly calculated by dividing the number of false acceptances by the number of identification tries. The following is the FAR formula:

$$FAR = FP / (FP + TN).$$

3.3.2 False Rejection Rate (FRR)

The false rejection rate is a measure of a biometric system's likelihood of wrongfully rejecting or refusing access to a legitimate user. It's just the percentage of authorized users whose identification is wrongly rejected. The FRR of a system is commonly calculated by dividing the number of erroneous rejections by the number of identification tries. The formula is as follows: $FRR = FN / (TP + FN)$

3.3.3 Equal Error Rate (EER)

A lower false acceptance rate (FAR) will lead to a higher false rejection rate (FRR), and vice versa. The Equal Error Rate refers to the point where the lines meet (EER). The EER is the point of equality in FAR and FRR, as shown in Figure 3.8. Equal Error Rate refers to an algorithmic method of error margin in which false rejections and false acceptances are equalized. This rate is the result's common value, or common ground. The smaller the error margin, the more precise the biometric system is. In terms of misleading data, it's just a mathematical means of scoring out errors and error margins.

EER is very important for figuring out how accurate data is and comparing the results of two systems

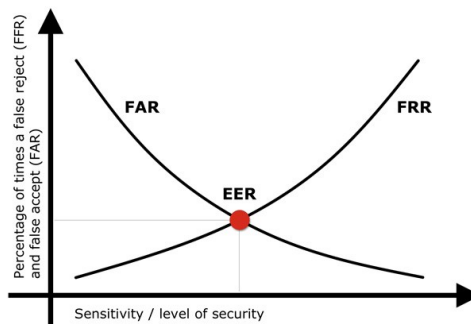


Figure 7. Illustration of EER derived from the plot of FAR vs FRR

If the false acceptance rate is reduced to the bare minimum, the false rejection rate is likely to increase. In other words, the more secure the access control system is, the less convenient it will be because users will be wrongly rejected by it. As a result, choosing between FAR and FRR is a personal decision that will result in either a more secure (but less user-friendly) or less secure system (but more user-friendly). There are few systems on the market that can provide a high level of security while still providing user-friendly access management. If a company doesn't have a system like this, user comfort usually comes before security [41].

3.3.4 Half Total Error Rate (HTER)

The half total error rate is an error rate that is equal to the sum of the FAR and FRR error rates. The HTER formula is as follows: $HTER = (FAR + FRR)/2$.

HTERs or other variations of HTERs are used in most biometric systems for measurement and comparison. It should be noted that in most benchmark databases used in biometric system literature, there is a significant imbalance between the number of genuine and fake accesses. It is most likely due to the fact that obtaining the former is more expensive than obtaining the latter. This imbalance explains why HTER, rather than the usual classification error used in machine learning literatures, is used for model comparison [42].

3.3.5 Accuracy

The ratio of correctly predicted samples to total predictions is used to determine the accuracy of a biometric system. It is calculated as follows:

$$\text{Accuracy} = (TP + TN) / (TP + TN + FP + FN).$$

It's worth noting that the lower the EER or HTER, the better the detection result.

4. Results And Discussion

4.1 Experimental Setup

To ascertain the authenticity of a face, the frame selection module takes K-frames from each paired facial video collected at distances $D1 = 20$ cm and $D2 = 50$ cm as mentioned in section 3.2. The feature extraction module then extracts the features, generating a vector of 1×2280 for each paired frame $D1fi$ and $D2fi$, for $i = (1, 2, \dots, K)$, K is set to 30 for attack samples in this investigation, while K is set to 60 for genuine samples. This is to avoid a situation where the classes are unbalanced. As a result, 30 samples are taken from each pairwise video of attack instances, resulting in $30 \times 80 = 2400$ samples for each spoof case, for a total of $2400 \times 3 = 7200$ (printed-photo, screen-photo, and replay attack) samples for the attack dataset. The legitimate dataset also generates $60 \times 80 = 4800$ samples for real videos. There are a total of 12,000 samples, which makes a matrix of 12000×2280 for real and fake data samples.

Three experiments were carried out to verify the effectiveness of our approach. First, the full dataset of 12000 samples was trained using four distinct models (SVM, LDA, K-NN, and CNN models) in a 3:1 ratio for training and testing (9000 and 3000, respectively). In section 4.2, the findings are provided.

Secondly, the datasets for each spoof case are supplied to the trained models for classification in order to gain insight into their performance based on different spoof examples. The figures in section 4.3 indicate the results.

Finally, each model is saved and a simple program is created to evaluate all of the models in real time using the saved models and the video capture control system described in section 2.2. (see Figure 5,6 and 7). The models were presented with live faces as well as all of the spoof cases.

4.2 Results

We trained four models with the dataset. SVM, LDA, K-NN, and CNN. Figure 8 provides accuracy results for these models for three types of spoof attacks: printed photo, screen photo and replay video attacks.

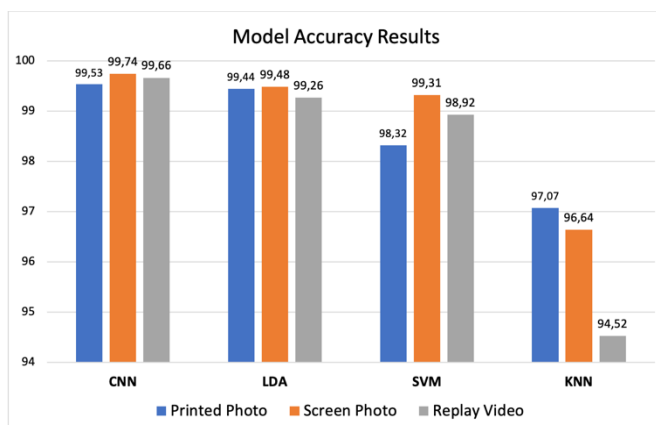


Figure 8. Model Accuracy Results

4.2.1 SVM Classifier Results

The SVM classifier is trained on the main dataset, which contains 12000 samples, 4800 of which are valid and 7200 of which are spoof cases. The SVM classifier had an accuracy of 96.07 percent, as shown in Table 4.1. This demonstrates the model's overall ability to correctly detect both real and fake faces. It also has 0.053 and 0.031 FAR and FRR, respectively. With a false acceptance rate of 0.053, the model is expected to wrongly accept or provide access to 53 unauthorized users in a sample of 1000. Similarly, a false rejection rate of 0.031 means that the model can correctly accept 969 authentic faces out of 1000, while failing in only 31 situations. This also demonstrates that the SVM model's capacity to accurately recognize real faces is slightly superior to its ability to correctly identify spoof cases. The model also achieved an EER and HTER of 0.034 and 0.042, respectively, which are good indicators of performance because of the lower the EER and HTER, the better.

In the second experiment, the SVM model is put to the test on individual fake cases to see how well it does. As shown in Figure 8, the results show that it is better at finding screen-photo threats than printed-photo and replay attacks.

4.2.2 Results from LDA Classifier

The accuracy of 98.03%, FAR and FRR of 0.022 and 0.018, respectively, revealed by linear discriminant analysis, demonstrates an excellent performance across all parameters. This indicates that just 22 illegal individuals are likely to be mistakenly accepted or granted access in a sample of 1000. Similarly, a false rejection rate of 0.018 means that the model is likely to reject or refuse access to as few as 18 authorized users in a sample of 1000 authentic faces. EER and HTER values of 0.014 and 0.020, respectively, show how robust the model is (See Table 2).

Figure 8 reveals that Linear Discriminant Analysis performs somewhat better in detecting screen photo attacks, followed by printed-photo attacks, and least in replay attacks, with an accuracy of 99.44 percent, 99.48 percent, and 99.26 percent, respectively, in the unit testing.

4.2.4 Results from KNN Classifier

With an accuracy of 92.90%, FAR and FRR of 0.082 and 0.062, respectively, the K-NN classifier has the worst performance (See Table 2). When given a sample of 1000 real and spoof faces, a false prediction of 82 and 63 is expected for each. The low performance could be due to the dataset's high dimensionality. This correlates to the fact that, while K nearest neighbors (KNN) is one of the simplest nonparametric classifiers, its accuracy is impacted by nuisance features in high-dimensional settings [43].

In the unit testing phase, the K-NN classifier, in contrast to other classifiers that were more robust in detecting screen-photo attacks, had its best performance in printed-photo attacks with 97.07%, which is slightly better than its performance in screen-photo and replay attacks, with 96.64 % and 94.52 % accuracy, respectively (See Figure 8).

4.2.4 Results from CNN Model

The CNN model is trained with the architecture described in Table 3.1, with the learning rate set to 0.001, weight decay set to $1e-6$, and the maximum iteration set to 100. The CNN model performed the best, as shown in Table 2, with an accuracy of 98.18% and FAR and FRR of 0.036 and 0.007, respectively. An FRR of 0.007 indicates that the model has strong recall for real samples. The CNN model also got EER and HTER values of 0.023 and 0.021, respectively, which shows very good performance.

In the unit testing phase, the CNN model performed better in the screen-photo attack than in the other two attacks, as shown in Figure 8, with an accuracy of 99.74%, 99.66%, and 99.53% for screen-photo attack, replay attack, and printed-photo attacks, respectively.

4.2.5 Validation on Real-Life Test Scenario

Based on each test case, the results of the real-time test cases using the saved trained models and the capture control system is presented. Figures 9 is the output of live test on a live face. Whereas, Figure 10, 11 and 12 are the output of the live tests using the spoof cases.

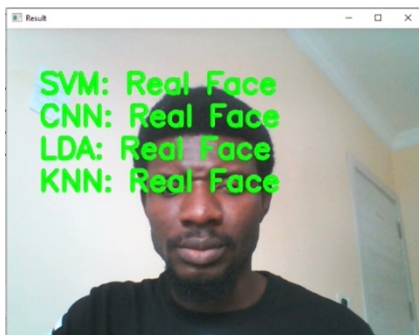


Figure 9. Result of the models on live face.

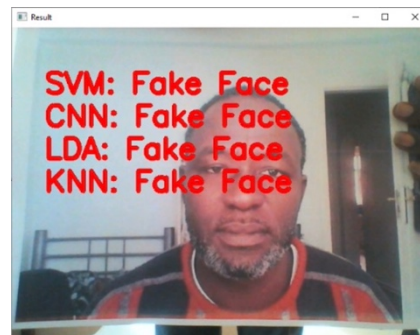


Figure 10. Result of the models on printed-photo attack

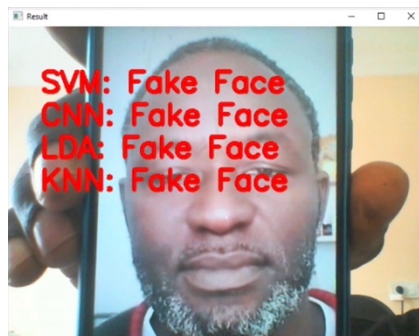


Figure 11. Result of the models on screen-photo attack

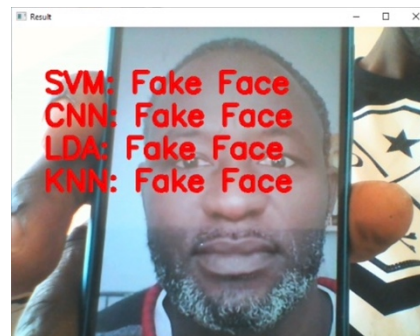


Figure 12. Result of the models on replay attack

4.3 Comparison of The Model Performances

Table 2 provides a comparison of the performances of all models across all five metrics for evaluation. Values in bold indicate the best performance on each metric.

Table 2. Comparison of the model performances across five metrics

Model	Accuracy	FAR	FRR	EER	HTER
SVM	96.07%	0.053	0.031	0.034	0.042
LDA	98.03%	0.022	0.018	0.014	0.020
KNN	92.90%	0.082	0.063	0.053	0.073
CNN	98.18%	0.036	0.007	0.023	0.021
Best Performance	98.18%	0.022	0.007	0.014	0.020

The saved models were also evaluated against time. For prediction, each model is provided an input of 2400 data samples. Figure 13 depicts their results. The LDA model is incredibly fast, with the best performance in terms of time spent by predicting the 2400 samples in about 490 milliseconds. The CNN model has the longest execution time of 10.901 seconds. SVM and KNN performance in terms of execution time are nearly the same, with 3.712 seconds and 3.869 seconds for SVM and LDA, respectively.

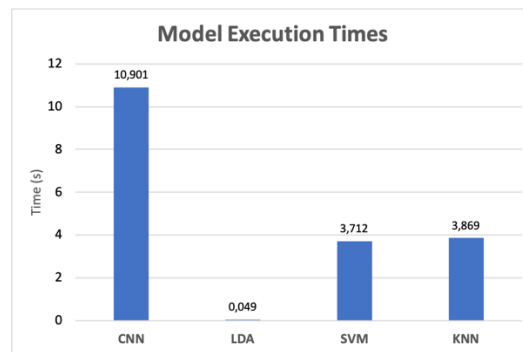


Figure 13. Results of the models performances against time taken for prediction

4.4 Discussion

The results reported in this work demonstrated that the strategy proposed in this study is resilient and thus practical, with all models above 92 percent accuracy. The CNN model and the LDA classifier are at the top of the list. Based on the performance evaluation of the four models over the five metrics, the CNN model outperformed the others in two of the measures, with accuracy and false rejection rate (FRR) of 98.18 percent and 0.007, respectively. That is, given a set of data samples, the CNN model will yield a greater accuracy rate, and the likelihood of blocking access or wrongly rejecting an authorized user is extremely low, as demonstrated by an FRR of 0.007, demonstrating that only 7 erroneous rejections are expected in a sample of 1000. The linear discriminant analysis, on the other hand, surpassed the others in terms of three other measures, FAR, EER, and HTER, with values of 0.022, 0.014, and 0.020, respectively. Although the CNN has a very low FRR, it has a much larger FAR, which is why it is defeated by the LDA in EER and HTER values. A lower EER suggests a healthy FAR/FRR margin.

In contrast to the results provided in [37] and [38], where KNN performed better than other classifiers, KNN had the lowest performance across all measures in this study. This is consistent with the authors' belief in [43] that in the presence of a high dimensional feature space, KNN performance is hampered by nuisance features.

CNN performed the worst in the execution time test, with 10.901 seconds of execution time over 2400 samples predicted. LDA performed the best, with an execution time of 0.049 seconds (490 milliseconds) for the

2400 samples. The rapid and good performance of LDA is attributable to the reduction in dimensionality, which is not the case with other models.

Table 3. Comparison of other approaches with the proposed approach

Technique	Category	Strength	Limitation	Performance
Fusion of face and Voice [30]	Active	<ul style="list-style-type: none"> • Very robust • Can detect 3D attacks 	<ul style="list-style-type: none"> • Highly Intrusive • Extra Hardware requirement • Low application range • Expensive • Computational complexity 	FAR=0.017 FRR= 0.011 FTC= 0.031 EER= 0.01
Pupil tracking using led sensor[16]	Active	<ul style="list-style-type: none"> • Robust against print attacks 	<ul style="list-style-type: none"> • Intrusive • Helpless in cut-photo and replay attacks • Extra Hardware requirement • Cannot easily fit into existing system • Time consuming 	-
DoG[13]	Passive	<ul style="list-style-type: none"> • Fast response time • Non-Intrusive 	<ul style="list-style-type: none"> • Poor generalization (Vulnerable to variation in acquisition) 	EER=0.17
Ensemble of Texture descriptors (LBP+GDP+GLTP+LDiP+LGBPHS+LPQ)	Passive	<ul style="list-style-type: none"> • Non-Intrusive 	<ul style="list-style-type: none"> • Computational complexity • Poor generalization • Limited to 2D attacks 	RR= 0.98.39 FRR= 0.49
3D sensor [18]	Passive	<ul style="list-style-type: none"> • Robust • Non-intrusive 	<ul style="list-style-type: none"> • Time complexity • Require extra hardware • Helpless in 3D attacks • Cannot fit into existing systems easily 	Accuracy=100%
Eye-blinking and Mouth movement[1]	Active	<ul style="list-style-type: none"> • Robust against • No extra hardware required • Less expensive 	<ul style="list-style-type: none"> • Intrusive • Weak in detecting cut-photo and replay attacks • Slow response time 	-
Face and Finger print[21]	Active	<ul style="list-style-type: none"> • Very robust • Captures 3D attacks 	<ul style="list-style-type: none"> • Highly Intrusive • Extra Hardware requirement • Low generalization ability • Expensive 	EER=0.012
Facial distortion changes	Active	<ul style="list-style-type: none"> • Robust • No extra hardware requirement • Less expensive 	<ul style="list-style-type: none"> • Intrusive • Computational complexity 	Accuracy= 99.48%
Temporal and depth information	Passive	<ul style="list-style-type: none"> • Robust • Non-intrusive 	<ul style="list-style-type: none"> • Computational Complexity • Require extra hardware • Helpless in 3D attacks • Cannot fit into existing systems easily 	Intra DB: ACER= 0.73 on SiW; ACER= 1.3 on OULU-NPU Cross DB: HTER = 17.5 on Replay Attack DB; HTER = 24.0 on CASIA-MFSD
Proposed approach	Active	<ul style="list-style-type: none"> • Can easily fit into existing system • Less intrusive • No extra hardware requirement • Less expensive • Robust • Less complexity 	<ul style="list-style-type: none"> • Intrusive • Limited to 2D attacks 	Accuracy=98.18% FAR=0.036 FRR=0.007 EER=0.023 HTER=0.021

A useful question to pose is, "In this scenario, which model should be picked between CNN and LDA?" The truth is that it is determined by the aim and priority of the system to be built or deployed. Some system objectives may emphasize FAR while others may prioritize FRR. As a result, the choice of FAR or FRR is a question of

preference, resulting in either a more secure (but less user-friendly) or less secure (but more user-friendly) system [41]. Consider the following scenario: you want to avoid people queuing at the entry since the system is not working properly (false rejection). In such instances, users may accept that convenience takes precedence. However, when users assume a high level of security, the situation is reversed. However, when it comes to biometric systems, a low equal error rate should be taken into account.

In comparison to the efforts in [31], which are closer to the one proposed in this study, while they achieved slightly higher accuracy, a single sample is represented by a 7×2147 matrix as a feature set taken from 8 frames at different distances in their technique. In contrast, the approach suggested in this work requires only two frames recorded at 20 cm and 50 cm from the camera to create the feature vector for a single sample. As a result, their approach becomes more computationally complex and time-intensive.

Table 4.6 further clearly shows the benefits of the proposed approach over existing active-based approaches. In [30] and [21], where face recognition is paired with voice or fingerprint recognition, a user is additionally asked to speak or present his or her fingerprint, which is collected using an audio device or fingerprint reader. Although they are relatively resistant to all types of face spoof attacks, they are very intrusive and require additional hardware such as a fingerprint scanner, which is also costly. Whereas with the suggested solution, no additional hardware is required, and it is less intrusive because a user will only need to move his face closer or farther, which is usual for users before any facial recognition system to do even without instruction. A user is asked to blink his/her eye and open and close his/her mouth in the effort presented in [1], which does not require extra hardware and tends to fit into existing systems. Unfortunately, it is quite intrusive and extremely vulnerable to cut-photo or replay attacks, whereas the approach provided here has achieved 99.66 percent accuracy against replay-attacks in the unit testing scenario. Furthermore, every user confronted with such a system is aware that the liveness test is based on blinking of the eye and movement of the mouth, and as such, it suggests the next point of action to the impostor, as opposed to the method proposed in this study, where the liveness cue is not obvious to the user.

Table 3 provides a comparison of the proposed approach to other approaches while highlighting their strength and limitations.

5. Conclusion

This study is inspired by the common phenomenon in photography of distortion of faces in video where the camera and the face are in close proximity, which is caused by the uneven 3D surface of the human face, and proposed a face spoof detection approach that uses the distortion changes of video frames of user's faces captured at different distances from the camera to deliver a robust active-based spoof detection while being less intrusive, less expensive, and with more application range.

An analytical experiment was carried out and assessed across five metrics to verify the effectiveness of the approach: accuracy, FAR, FRR, EER, and HTER. The results demonstrate excellent and competitive performance, with the best performances in CNN and LDA models, with accuracy = 98.18%, EER = 0.023, HTER = 0.021 and accuracy = 98.03%, EER = 0.022, HTER = 0.020, respectively. Hence, it is obvious that the approach proposed in this study is practical, and the handcrafted features are discriminative enough against 2D attacks and can be investigated further against other types of attacks, such as 3D attacks. It is also worth noting that the proposed approach has various advantages over alternative active-based approaches, such as reduced intrusiveness, no additional hardware required, fast response time, lower computing complexity, and ease of integration into existing systems.

Finally, despite the variety of threats, spoof detection tasks are typically viewed and approached as binary classification problems. As such, it is recommended that future research handle spoof detection in terms of multi-class classification, taking into account the various types of attacks. Feedback on the most prevalent types of attacks faced by the facial recognition system can thus be collected, analyzed, and used for further research and development. Cases of previously unknown or emerging threats can also be tracked.

References

- [1] A. Singh, P. Joshi, G.C. Nandi, Face recognition with liveness detection using eye and mouth movement, 2014 Int. Conf. Signal Propag. Comput. Technol. (ICSPCT 2014). (2014) 592–597.
- [2] D. Wen, H. Han, A.K. Jain, Face Spoof Detection With Image Distortion Analysis, *IEEE Trans. Inf. Forensics Secur.* 10 (2015) 746–761. <https://doi.org/10.1109/TIFS.2015.2400395>.
- [3] L. Sun, G. Pan, Z. Wu, S. Lao, Blinking-Based Live Face Detection Using Conditional Random Fields, in: S.-W. Lee, S.Z. Li (Eds.), *Adv. Biometrics*, Springer Berlin Heidelberg, Berlin, Heidelberg, 2007: pp. 252–260.
- [4] C.N. Karson, Spontaneous eye-blink rates and dopaminergic systems., *Brain.* 106 (Pt 3) (1983) 643–653.

- https://www.unboundmedicine.com/medline/citation/6640274/Spontaneous_eye_blink_rates_and_dopaminergic_systems.
- [5] S. Kumar, S. Singh, J. Kumar, A comparative study on face spoofing attacks, in: 2017 Int. Conf. Comput. Commun. Autom., 2017: pp. 1104–1108. <https://doi.org/10.1109/CCAA.2017.8229961>.
 - [6] J. Galbally, S. Marcel, J. Fierrez, Biometric Antispoofing Methods: A Survey in Face Recognition, *IEEE Access*. 2 (2014) 1530–1552. <https://doi.org/10.1109/ACCESS.2014.2381273>.
 - [7] D. Menotti, G. Chiachia, A. Pinto, W.R. Schwartz, H. Pedrini, A.X. Falcão, A. Rocha, Deep Representations for Iris, Face, and Fingerprint Spoofing Detection, *IEEE Trans. Inf. Forensics Secur.* 10 (2015) 864–879. <https://doi.org/10.1109/TIFS.2015.2398817>.
 - [8] A. Pinto, W. Schwartz, H. Pedrini, A. Rocha, Using Visual Rhythms for Detecting Video-Based Facial Spoof Attacks, *Inf. Forensics Secur. IEEE Trans.* 10 (2015) 1025–1038. <https://doi.org/10.1109/TIFS.2015.2395139>.
 - [9] J. Yang, Z. Lei, D. Yi, S.Z. Li, Person-Specific Face Antispoofing With Subject Domain Adaptation, *IEEE Trans. Inf. Forensics Secur.* 10 (2015) 797–809. <https://doi.org/10.1109/TIFS.2015.2403306>.
 - [10] I. Pavlidis, P. Symosek, The imaging issue in an automatic face/disguise detection system, in: *Proc. IEEE Work. Comput. Vis. Beyond Visible Spectr. Methods Appl. (Cat. No.PR00640)*, 2000: pp. 15–24. <https://doi.org/10.1109/CVBVS.2000.855246>.
 - [11] R. TABULA, “Trusted biometrics under spoofing attacks,” <Http://Www.Tabularasa-Euproject.Org/>. (n.d.).
 - [12] I. Chingovska, A. Anjos, S. Marcel, On the effectiveness of local binary patterns in face anti-spoofing, 2012 BIOSIG - Proc. Int. Conf. Biometrics Spec. Interes. Gr. (2012) 1–7.
 - [13] Z. Zhang, J. Yan, S. Liu, Z. Lei, D. Yi, S. Li, A face antispoofing database with diverse attacks, 2012 5th IAPR Int. Conf. Biometrics. (2012) 26–31.
 - [14] X. Tan, Y. Li, J. Liu, L. Jiang, Face Liveness Detection from a Single Image with Sparse Low Rank Bilinear Discriminative Model, in: K. Daniilidis, P. Maragos, N. Paragios (Eds.), *Comput. Vis. -- ECCV 2010*, Springer Berlin Heidelberg, Berlin, Heidelberg, 2010: pp. 504–517.
 - [15] N. Erdogmus, S. Marcel, Spoofing in 2D Face Recognition with 3D Masks and Anti-spoofing with Kinect, in: *Biometrics Theory, Appl. Syst.*, 2013.
 - [16] M. Killioğlu, M. Taşkıran, N. Kahraman, Anti-spoofing in face recognition with liveness detection using pupil tracking, in: 2017 IEEE 15th Int. Symp. Appl. Mach. Intell. Informatics, 2017: pp. 87–92. <https://doi.org/10.1109/SAMI.2017.7880281>.
 - [17] T. Dhawanpatil, B. Joglekar, A Review Spoof Face Recognition Using LBP Descriptor, in: A.K. Somani, S. Srivastava, A. Mundra, S. Rawat (Eds.), *Proc. First Int. Conf. Smart Syst. Innov. Comput.*, Springer Singapore, Singapore, 2018: pp. 661–668. https://doi.org/https://doi.org/10.1007/978-981-10-5828-8_63.
 - [18] G. Albakri, S. Alghowinem, The Effectiveness of Depth Data in Liveness Face Authentication Using 3D Sensor Cameras@, *Sensors (Basel)*. 19 (2019).
 - [19] Y. Ma, L. Wu, Z. Li, F. liu, A novel face presentation attack detection scheme based on multi-regional convolutional neural networks, *Pattern Recognit. Lett.* 131 (2020) 261–267.
 - [20] L. Feng, L.-M. Po, Y. Li, X. Xu, F. Yuan, T.C.-H. Cheung, K.-W. Cheung, Integration of image quality and motion cues for face anti-spoofing: A neural network approach, *J. Vis. Commun. Image Represent.* 38 (2016) 451–460. <https://doi.org/https://doi.org/10.1016/j.jvcir.2016.03.019>.
 - [21] P. Wild, P. Radu, L. Chen, J. Ferryman, Robust multimodal face and fingerprint fusion in the presence of spoofing attacks, *Pattern Recognit.* 50 (2016) 17–25. <https://doi.org/https://doi.org/10.1016/j.patcog.2015.08.007>.
 - [22] B. Geng, C. Lang, J. Xing, S. Feng, W. Jun, MFAD: A Multi-modality Face Anti-spoofing Dataset, in: 2019: pp. 214–225. https://doi.org/10.1007/978-3-030-29911-8_17.
 - [23] T. Chugh, A.K. Jain, Fingerprint Spoof Detection: Temporal Analysis of Image Sequence, *CoRR*. abs/1912.0 (2019). <http://arxiv.org/abs/1912.08240>.
 - [24] V. Holub, J. Fridrich, Digital Image Steganography Using Universal Distortion, in: *IH MMSec 2013 - Proc. 2013 ACM Inf. Hiding Multimed. Secur. Work.*, 2013. <https://doi.org/10.1145/2482513.2482514>.
 - [25] J. Cheng, A.C. Kot, S. Rahardja, Steganalysis of Binary Cartoon Image using Distortion Measure, in: 2007 IEEE Int. Conf. Acoust. Speech Signal Process. - ICASSP '07, 2007: pp. II-261-II-264. <https://doi.org/10.1109/ICASSP.2007.366222>.
 - [26] P.P.D. Raval, R.R. Sedamkar, S. Kulkarni, Face Spoofing Detection Using Image Distortion Features, in: 2017.
 - [27] M. Bryson, M. Johnson-Roberson, O. Pizarro, S. Williams, Colour-Consistent Structure-from-Motion Models using Underwater Imagery, in: 2012. <https://doi.org/10.15607/RSS.2012.VIII.005>.
 - [28] X. Sun, L. Huang, C. Liu, Context based face spoofing detection using active near-infrared images, in: 2016: pp. 4262–4267. <https://doi.org/10.1109/ICPR.2016.7900303>.
 - [29] Mohamed, Shaimaa, Ghoneim, Amr, Youssif, Aliaa, Visible/Infrared face spoofing detection using texture descriptors, *MATEC Web Conf.* 292 (2019) 4006. <https://doi.org/10.1051/mateconf/201929204006>.
 - [30] B.R. Naidu, P.V.G.D. Reddy, Fusion of face and voice for a multimodal biometric recognition system, *Int. J. Eng. Adv. Technol.* 8 (2019) 506–515.
 - [31] Y. Li, Z. Wang, Y. Li, R. Deng, B. Chen, W. Meng, H. Li, A Closer Look Tells More: A Facial Distortion Based Liveness Detection for Face Authentication, in: *Proc. 2019 ACM Asia Conf. Comput. Commun. Secur.*, Association for Computing Machinery, New York, NY, USA, 2019: pp. 241–246. <https://doi.org/10.1145/3321705.3329850>.

- [32] Dlib Python API Tutorials [Electronic resource] – Access mode: <http://dlib.net/python/index.html>, (n.d.). <http://dlib.net/python/index.html>.
- [33] D.E. King, Dlib-ml: A Machine Learning Toolkit, *J. Mach. Learn. Res.* 10 (2009) 1755–1758.
- [34] E. Osuna, R. Freund, F. Girosit, Training support vector machines: an application to face detection, in: *Proc. IEEE Comput. Soc. Conf. Comput. Vis. Pattern Recognit.*, 1997: pp. 130–136.
- [35] H. Yu, J. Yang, A direct LDA algorithm for high-dimensional data—with application to face recognition, *Pattern Recognit.* 34 (2001) 2067–2070.
- [36] S. Bharadwaj, T.I. Dhamecha, M. Vatsa, R. Singh, Computationally efficient face spoofing detection with motion magnification, in: *Proc. IEEE Conf. Comput. Vis. Pattern Recognit. Work.*, 2013: pp. 105–110.
- [37] C. Priyanka, Sharma; Neha, Spoofing Face Detection using LBP Descriptor and KNN Classifier in Image Processing, *Int. J. Recent Technol. Eng. Volume-8* (n.d.).
- [38] K. Samrity, Saini; Kiranpreet, KNN Classification for the Face Spoof Detection, *Int. J. Sci. Eng. Res. Volume 10* (n.d.) 1101–1106.
- [39] Y. Du, T. Qiao, M. Xu, N. Zheng, Towards Face Presentation Attack Detection Based on Residual Color Texture Representation, *Secur. Commun. Networks.* 2021 (2021) 6652727. <https://doi.org/10.1155/2021/6652727>.
- [40] Kanika kalihal ; Jaspreet Kaur, A Review on Different Face Spoof Detection Techniques in Biometric Systems, *Int. J. Sci. Res. Eng. Trends. Volume 5* (n.d.).
- [41] RecogTech, FAR and FRR: security level versus user convenience, <https://www.recogtech.com/en/knowledge-base/security-level-versus-user-convenience>, (Retrieved on 31st/01/2022). (n.d.) (Retrieved on 31st/01/2022).
- [42] S. Bengio, J. Mariéthoz, A Statistical Significance Test for Person Authentication, *Speak. Lang. Recognit. Work.* (2004).
- [43] H. Raeisi Shahraki, S. Pourahmad, N. Zare, K Important Neighbors: A Novel Approach to Binary Classification in High Dimensional Data, *Biomed Res. Int.* 2017 (2017) 7560807. <https://doi.org/10.1155/2017/7560807>.

Genetic Algorithm-Based Optimization of Mass Customization Using Hyperledger Fabric Blockchain

Nursena BAYGIN^{1*}, Mehmet KARAKOSE²

¹ Department of Computer Engineering, Kafkas University, Kars, Turkey

² Department of Computer Engineering, Firat University, Elazig, Turkey

*¹ nbaygin@kafkas.edu.tr, ² mkarakose@firat.edu.tr

(Geliş/Received: 18/07/2022;

Kabul/Accepted: 20/08/2022)

Abstract: With the developing technology, the production model, which is structured in line with user requests, has become a very popular topic. This production model, which expresses individualization, has become increasingly common. For this reason, it attracts the attention of many researchers and company executives. At this point, studies are concentrated on the concept of mass customization, which expresses personalized production. Considering the related studies, various difficulties are encountered in this production model on issues such as cooperation, trust, and optimization. In this proposed method, a blockchain-based platform is designed to solve the problems of cooperation and trust, one of the most important problems of mass customization. In addition, in this study, the problem of optimization of the production and supply chain process in the manufacturing sector has been examined. This process includes reaching from the producer to the consumer and many parameters. Therefore, the optimization of this process is a very difficult problem. A two-stage system has been proposed to find a solution to this problem. In the first stage, a reliable platform was created by bringing together service providers and buyers in the manufacturing sector with blockchain. In the second stage, the most suitable parties were selected by a genetic algorithm.

Key words: Blockchain, Smart Contract, Genetic Algorithm, Mass Customization.

Hyperledger Fabric Blok Zincirini Kullanarak Kitlesele Özelleştirme Genetik Algoritma Tabanlı Optimizasyonu

Öz: Gelişen teknoloji ile birlikte kullanıcı istekleri doğrultusunda yapılandırılan üretim modeli oldukça popüler bir konu haline gelmiştir. Bireyselleşmeyi ifade eden bu üretim modeli giderek yaygınlaşmaktadır. Bu nedenle birçok araştırmacının ve şirket yöneticisinin ilgisini çekmektedir. Bu noktada, kişiselleştirilmiş üretimi ifade eden kitlesele özelleştirme kavramı üzerinde çalışmalar yoğunlaşmaktadır. İlgili çalışmalara bakıldığında bu üretim modelinde işbirliği, güven, optimizasyon gibi konularda çeşitli zorluklarla karşılaşmaktadır. Önerilen bu yöntem de kitlesele özelleştirme en önemli sorunlarından işbirliği ve güven problemlerini çözmek için blok zincir tabanlı bir platform tasarlanmıştır. Ayrıca bu çalışmada imalat sektöründe üretim ve tedarik zinciri sürecinin optimizasyonu problem incelenmiştir. Bu süreç üreticiden tüketiciye ulaşmayı ve birçok parametreyi içermektedir. Bu nedenle, bu sürecin optimizasyonu çok zor bir problemdir. Bu soruna çözüm bulmak için iki aşamalı bir sistem önerilmiştir. İlk aşamada blockchain ile imalat sektöründe hizmet verenler ve alıcılar bir araya getirilerek güvenilir bir platform oluşturulmuştur. Daha sonra ikinci aşamada, genetik algoritma ile en uygun taraflar seçilmiştir.

Anahtar kelimeler: Blockchain, Akıllı Sözleşme, Genetik Algoritma, Kitlesele Özelleştirme.

1. Introduction

With the developing technology, it is seen that traditional production models have been replaced by sectors that act in line with consumer demands and expectations [1–4]. Meeting consumer demands in optimum conditions and thus ensuring consumer satisfaction is the key to the success of the company. In customer-oriented production models, intersectoral studies provide higher efficiency. Therefore, there is a need for a cross-sectoral collaborative platform in today's customization paradigm. It is seen that the manufacturing sector is experiencing a transition from centralized production to decentralized production on a global scale [5]. In collaborative production models in the industry, it means that stakeholders are/will carry out dynamic interactions and transactions. However, many difficulties are encountered in the transition of the stakeholders serving in the sector to the collaborative customization production model (for example, price fluctuation, product diversity, consumer participation,

* Corresponding author: nbaygin@kafkas.edu.tr. ORCID Number of authors: ¹ 0000-0003-4457-5503, ² 0000-0002-3276-3788

production flexibility, etc.) [6,7]. With mass customization (MC), increasing demand, costs, and lead-time complexities increase. Consistent approaches are required when designing the product to ensure consumer demands, minimize cost and shorten lead time [8–10].

Blockchain, which has been very popular recently, offers a transparent, cryptographic, and reliable platform where consensus independent from authority is ensured with its decentralized structure [11–13]. It also enables shareholders to make decisions and set rules together in a commercial environment where trust is extremely important. It is anticipated that this new system will serve the market in many ways, with its feature that increases competition and provides a consensus protocol [14–16]. In traditional centralized customizations, the available resources of the producers are defined and the consumers choose them in line with their needs [17–19]. In this case, optimum consumer-producer matching does not occur. The proposed method is aimed to ensure that the stakeholder materials defined on a decentralized platform are matched to the user requirements at the optimum level. Another disadvantage of traditional methods is that consumer needs are obtained through surveys. With this proposed study, it is ensured that those who serve on a platform where consumer needs are met with blockchain can make inferences about the demands.

This study, it is aimed to carry out the optimum ordering process. There are various studies on supply chain scheduling optimization in MC in the literature. In the proposed models, it is seen that one or more objective functions are usually specified. It is aimed to minimize cost and maximize service level [20–22]. However, as far as we know, there is no study in the literature on the optimization of both the supply process and the production process. The problem we should be most concerned with here is the planning optimization from the production process to the supply chain in MC. Unlike the supply chain scheduling process, the scheduling process in MC contains complex parameters. In this research, a two-stage distribution network including multiple suppliers, manufacturers, retailers, and distributors is designed. It is aimed to provide optimum timing and service. The first stage is aimed to find the optimum manufacturer, supplier, retailer, and distributor. In the second stage, it is investigated whether these stakeholders will meet the requirements of the product created by the consumer. At this stage, it is ensured that optimum stakeholders work together on a common platform through the blockchain. The resulting multi-objective integer programming cannot be solved by exact methods [23]. Therefore, a multi-objective genetic algorithm is used to solve this problem.

The contribution of this research is the proposal of a consortium blockchain-based system in which the cooperation of mass customization actors in the manufacturing sector is ensured. A platform where all actors and consumers in the supply chain are registered is used in the system. It is aimed to ensure the optimum selection of service (supplier, producer, distributor...) and service-receiving (consumer) actors with genetic algorithms and to bring collaborators together. In this study, in which the consumer-oriented production model is adopted, optimization and blockchain integration is aimed. The remainder of the article is organized as follows. In Section 2, the theoretical background is given about the topics used in the proposed study. The proposed method is presented in Section 3. In Section 4, the results of the proposed method are given.

2. Theoretical Background

1.1. Genetic algorithm

The genetic algorithm (GA), first introduced by Holland in 1975, is a group computational process model. With this algorithm, an optimal solution to a particular problem is sought, inspired by the survival principle of chromosomes. Figure 1 shows the steps of the GA. In this method, a random population consisting of sequences of numbers is first created. This population consists of individuals, individuals from chromosomes, and chromosomes from genes. Then, the population is subjected to the determined fitness function, and fitness results close to the optimal solution are determined. It consists of three stages: selection, crossover, and mutation. In the selection process, the parent individual is selected according to the fitness values of the individuals in the population. In the crossover process, certain parts of the parent individuals obtained by the selection process are replaced. In this way, individuals with new characteristics that are not in the population are obtained. In the mutation process, any gene of the newly formed individual is subjected to the process of changing [23–25].

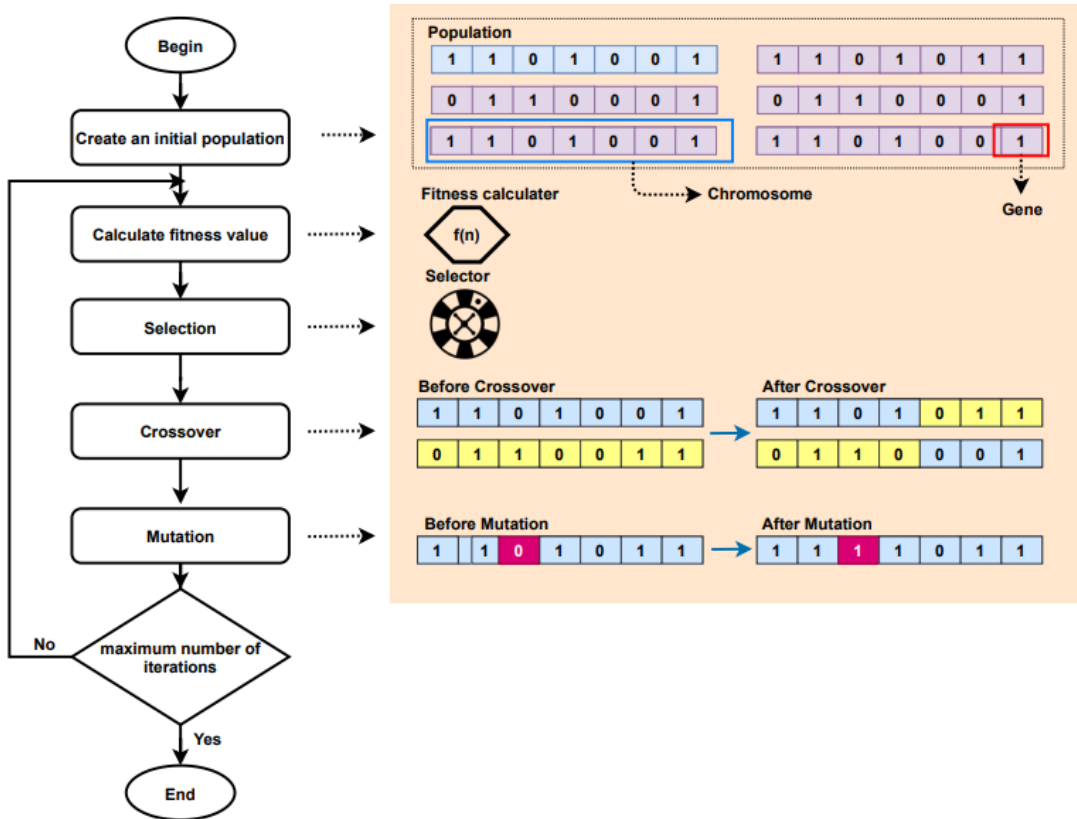


Figure 1. Genetic algorithm

1.2. Genetic algorithm in the manufacturing industry

With the widespread use of the MC-based production model, global production has shifted from traditional offline platforms to online platforms [26]. While product production is carried out from a single point in traditional platforms, it is carried out from independent points in service-oriented production models. By creating an online platform, service providers can work together under a single roof. With new generation technologies, the online participation of customers in the production process can be ensured [27]. In addition, models of product production can be developed collaboratively by service providers and customers. Consumer demands are at the forefront when producing personalized products. Meeting various customized product requirements complicates production processes. The process, which is complicated in an online production model, can be optimized with a GA and suitable solutions can be obtained.

MC in the manufacturing industry is a typical NP-Hard problem. The solution set created by the join process grows exponentially. Therefore, high-performance production models that meet customer demands are a challenging problem for academic and industry researchers [28]. In addition, timing problems in the production process reveal a very complex structure. GA is widely used in task scheduling strategies research. In a study in the literature, optimization was presented in terms of determining task completion and transmission times as a timing strategy. The simulation results proved the efficiency of the algorithm [29]. There are two objective functions in a proposed study. The first is aimed at optimizing transportation, holding, and purchasing costs. Transport costs increase in direct proportion as the distance increases. In this function, the aim is to solve the minimum cost with minimum distance. The other objective function, is to ensure that the products are produced with minimum cost. For this purpose, the optimum solution will be found at the shortest distance and in the case of the minimum bid. During planning, a mathematical model was created to determine the amount of product that needs to be shipped between two locations [23].

3. Blockchain Application Proposed for Mass Customization

In general, the manufacturing sector is divided into two categories: service recipients and service providers. Service recipients can be users, while a manufacturer who can request raw materials can also be service recipients. Service providers are actors such as manufacturers, suppliers, and retailers in general. The production and supply process has a very important place in the manufacturing sector. Therefore, the optimization of these processes is critical in terms of efficiency. In this study, a proposal has been made to realize an optimum process. For this purpose, as seen in Figure 2, information such as raw material, retail support, and distribution support are recorded on the platform. In addition, customer requests are received over the blockchain. In line with this information, it is aimed to produce an optimum process by using GA. Then, the service providers registered in the blockchain are selected with the help of this optimum solution process result.

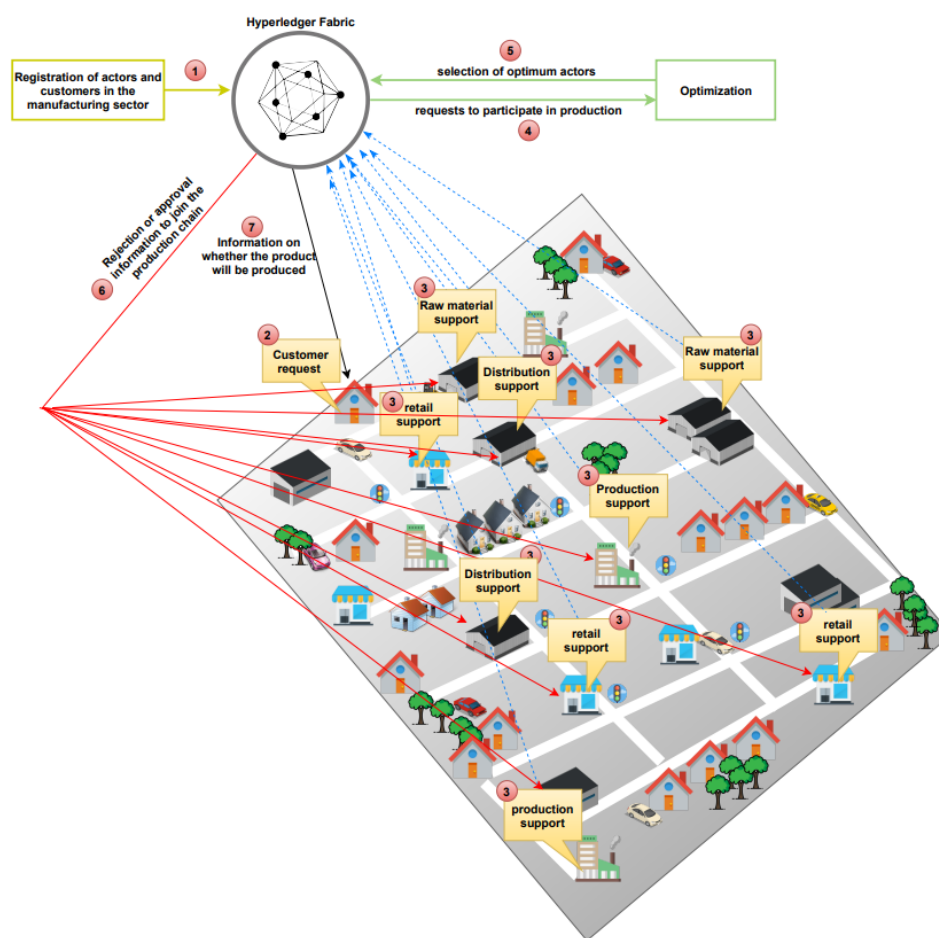


Figure 2. Proposed method

It is seen that companies with similar policies tend to do more business with each other. In addition, there are various difficulties in communication to ensure cooperation. This means that there is a need for an environment that will bring actors together to do a common business and implement the same policy. For this purpose, blockchain technology, which offers a traceable and reliable common environment, is proposed in this study. With

the smart contract feature, a platform is offered where actors can create common rules where they can unite on a common denominator.

3.1. Multihost deployment

The proposed method accommodates multiple users. Therefore, as shown in Figure 3, a 4-organization network design is first simulated on a virtual machine. The connection between the channel in the created system and these organizations is provided. With this channel, the business logic in the smart contract will be distributed. Raft algorithm was used as the consensus algorithm and 3 orderers were defined. The structure of the organizations is the same, and a single peer is suggested as both anchor and committing peers. It has the couch database, which is a peer status database, and smart contracts. A certificate authority is defined for each organization and orderer service. The Docker Swarm network will enable organizations in the virtual machine to communicate effectively with each other. As seen in the registry, smart contracts, and certificates are defined on each machine. Organizations can perform workflows, queries, and transactions defined in smart contracts with the help of the channel.

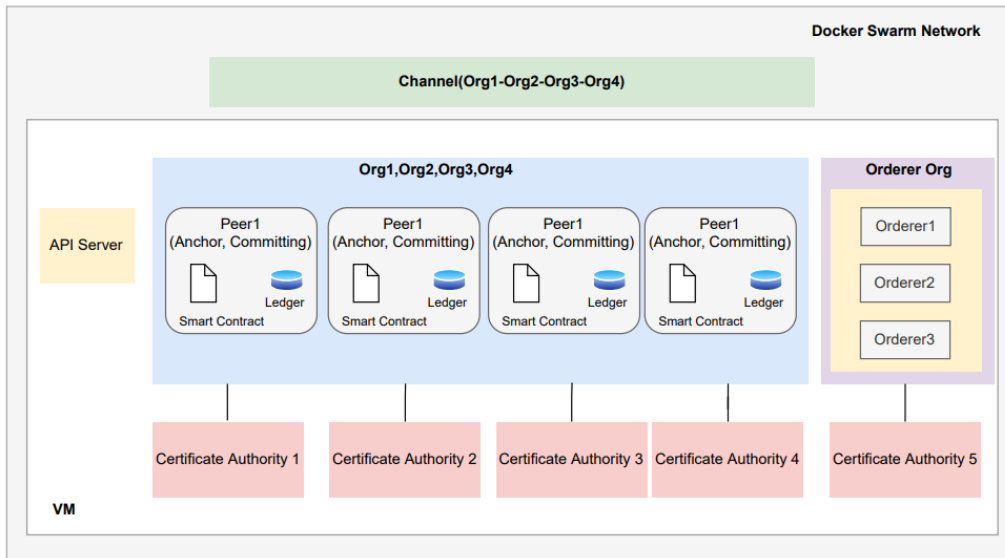


Figure 3. Virtual machine and network settings

As can be seen in Figure 4, crypto materials must be created for all participants. Certificate authority services should be run for all organizations. In Hyperledger Fabric, each organization is represented by a Membership Service Provider. MSP is the Hyperledger Fabric component that defines the membership processes of the participants.

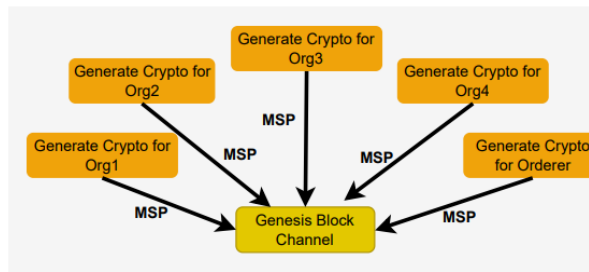


Figure 4. Creation of Crypto materials for organizations

Verification of each organization’s identity and signature is required for MSP configuration. For this purpose, the authentication process and the boot of the network must be performed.

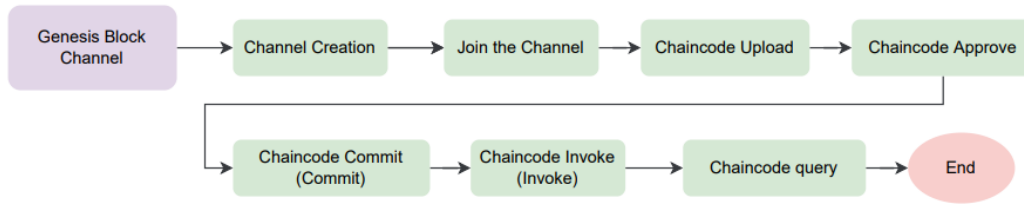


Figure 5. Channel creation and chaincode operations

As can be seen in Figure 5, the genesis block must be created first. Afterward, the channel is created and the participation of the participants is ensured. Participants must have the same organization. Thus, unauthorized access from outside is prevented. After the channel is created and the participants are defined to the channel, the chain code is uploaded to each participant. The uploaded chain code is submitted for the approval of the participants. Each participant must approve and commit. Then the chain is activated by calling the code. Finally, a query is made on the chain code, and the transactions in this section are terminated.

3.2. Mathematical model and optimization of supply chain

In the production sector, where the competitive environment is developing, producing in line with user requests provides an important advantage. In addition, it is an important factor that suppliers deliver the product in the right quantity, at the right time, and to the right place [30]. Products are temporarily stored before being delivered to warehouses. Considering the capacity constraints of warehouses, it is of great importance to have a system where they can buy the required amount of goods on time. The warehouses of suppliers and retailers have limitations on capacity, holding, and delivery capacities [11,31–34].

After the product enters the production process, it is included in the procurement process shown in Figure 6. First, the supplier provides the raw material guarantee for the product. It then manufactures the product for the manufacturer. The product produced is bought by the retailer. The received product is sent to the distributor for distribution. Finally, the distributor delivers the product to the customer.

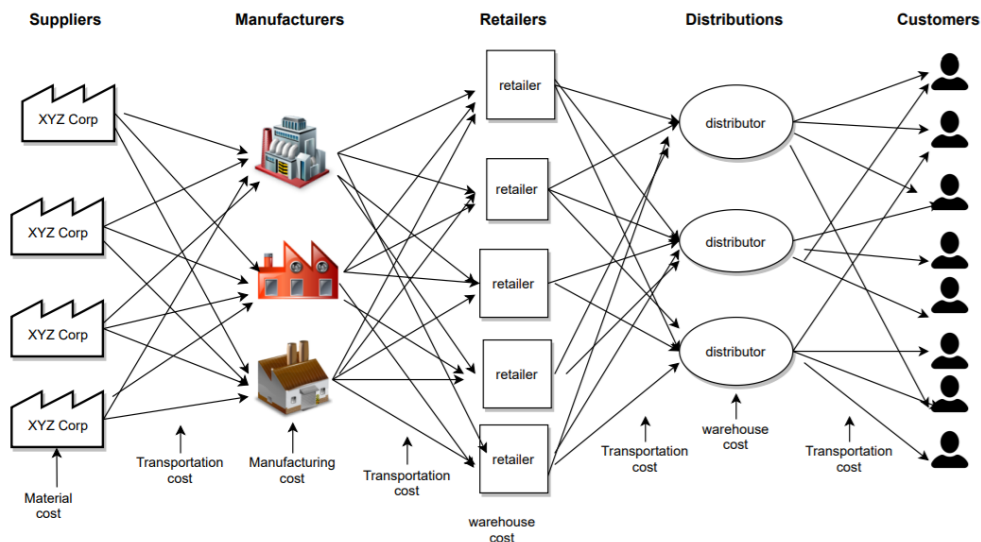


Figure 6. Product supply chain

As seen in Table 1, costs are encountered during the product supply and production process. This proposed study, it is aimed to minimize these costs. This table contains explanations of the equation parameters to be used in the optimization process. The parties, product, and number of parties in MCare defined. In addition, transportation, holding, supply, and production costs are specified.

Table 1. Explanations of model assumption, indexes, and parameters

Parameters	Explanations	
z	The customer index	$z=1,2,\dots,Z$
i	The supplier index	$i=1,2,\dots,I$
j	The producer index	$j=1,2,\dots,J$
k	The retailer index	$k=1,2,\dots,K$
l	The distributor index	$l=1,2,\dots,L$
p	The product index	$p=1,2,\dots,P$
t	The period index	$t=1,2,\dots,T$
w	The raw materials index	$w=1,2,\dots,W$
Z	Total number of customers	
I	Total number of suppliers	
J	Total number of producers	
K	Total number of retails	
L	Total number of distributors	
P	Total number of products	
T	Total number of periods	
W	Total number of raw materials	
a_{ijp}	Cost of transporting product p from supplier i to producer j	Approach 1
b_{jkp}	Cost of transporting product p from producer j to retailer k	
c_{klp}	Cost of transporting product p from retailer k to distributor l	
x_{kzp}	Cost of transporting product p from distributor l to customer z	
s_{ipw}	Cost of raw material procurement w of product p of supplier i	Approach 2
f_{jp}	Cost of producer j to produce product p	
g_{kpt}	The cost of k retailers to hold product p in period t	Approach 3
q_{lpt}	The cost of distributor l of hold product p in period t	
d_{ijpt}	Time to move product p from supplier i to producer j	Approach 4
e_{jkpt}	Time to move product p from producer j to retail k	
f_{klpt}	Time to move product p from retailer k to distributor l	
o_{tzip}	Time to move product p from distributor l to customer z	
y_{pijt}	The amount of product p transported from supplier i to producer j in period t	Approach 5
u_{pjkt}	The amount of product p transported from producer j to retailer k in period t	
h_{pklt}	The amount of product p transported from retailer k to distributor l in period t	

In this proposed method, the values of F_1, F_2, F_3 , and F_4 in equations (1), (2), (3), and (4) represent transportation cost, supply cost, holding cost, and production time. That is, they are fitness functions to find service providers that will meet the minimum level. F_1, F_2, F_3 , and F_4 values are calculated with the fitness function offered

by the GA and it is aimed to find the optimum values. Since the value of F_5 in equation (5) expresses the amount of product transport, the maximum transport situation will make the system more efficient.

Approach 1

The values of F_1 , in equation (1) represent transportation costs. This equation, it is aimed to find the minimum shipping cost. It covers the transportation process from the procurement process to the customer. For this purpose, optimum 4 transportation costs are calculated.

$$\text{Min } F_1 = a_{ijp} + b_{jkp} + c_{klp} + x_{kzp} \quad (1)$$

Approach 2

The values of F_2 , in equation (2) represent the supply cost. The aim is to adjust the raw material and production cost of the product to be produced to a minimum.

$$\text{Min } F_2 = s_{ipw} + f_{jp} \quad (2)$$

Approach 3

The values of F_3 , in equation (3) represent the holding cost. The aim is to ensure that the holding cost of the product is minimal. Therefore, it is aimed to choose optimum parties with low holding costs.

$$\text{Min } F_3 = g_{kpt} + q_{lpt} \quad (3)$$

Approach 4

The values of F_4 , in equation (4) represent the production time. The aim is to keep the shipping time of the product to a minimum. For this reason, parties that will provide quick access are selected.

$$\text{Min } F_4 = d_{ijpt} + e_{jkpt} + f_{klpt} + o_{lzpt} \quad (4)$$

Approach 5

The values of F_5 , in equation (5) represent the amount of product. In this equation, the aim is to select the optimum sides that will ensure maximum product transport.

$$\text{Max } F_5 = y_{pijt} + u_{pjkt} + h_{pklt} \quad (5)$$

This proposed study, it is aimed to bring together the parties in a collaborative working group under optimum conditions. The optimization methodology of the GA was examined and its compatibility with the blockchain was reviewed. In addition, this study, it is aimed to minimize the costs and time with the optimum solution provided by the GA. It refers to a large-scale problem such as the supply chain. Therefore, the combination of blockchain and supply chain is designed with a multi-objective GA.

4. Conclusion

In this proposed study, the problems encountered in the production and supply chain process in the manufacturing sector are examined and a solution-oriented approach to these problems is presented. In addition, the shortcomings of MC in the literature were investigated. When the studies in the literature are examined, it is understood that one of the biggest obstacles to the realization of MC is cooperation and trust. At this point,

blockchain will bring the parties together, cooperate and provide security with its cryptological structure. For this purpose, the Hyperledger Fabric blockchain used in business networks was used. Thus, it was aimed to create a platform with common policies. Another problem with MC is optimization in the purchasing process. For this purpose, it is aimed to select the most optimal parties among the parties brought together with the blockchain. In this study, in which a GA, which is one of the optimization methods, was used, more than one objective function was defined and a solution was sought for a difficult problem such as the supply chain. As far as we know, there is no study in the literature covering the production process and supply process. With this method we recommend, that the process of a product from raw material supply to its delivery to the customer has been defined and optimum results have been tried to be found. This work is a recommendation and has some shortcomings in the case of a real-time application. For example, the parameters in the supply chain are very diverse and this study is based on basic parameters. The feasibility of MC is not impossible, but it is difficult and involves many parameters. In addition, companies are cautious as blockchain is a new technology. Future works, it is aimed to design the necessary layers, smart contracts, and network models for a Hyperledger-based application.

References

- [1] Qi Y, Mao Z, Zhang M, Guo H. Manufacturing Practices and Servitization: The Role of Mass Customization and Product Innovation Capabilities. *Int. J. Prod. Econ.* 2020; 228(January 2019): 107747.
- [2] Kotha S. Mass Customization: Implementing the Emerging Paradigm for Competitive Advantage. *Strateg. Manag. J.* 1995; 16(S1): 21–42.
- [3] Da Silveira G, Borenstein D, Fogliatto FS. Mass Customization: Literature Review and Research Directions. *Int. J. Prod. Econ.* 2001; 72(1): 1–13.
- [4] Pallant JL, Sands S, Karpen IO. The 4Cs of Mass Customization in Service Industries: A Customer Lens. *J. Serv. Mark.* 2020; 34(4): 499–511.
- [5] Kumar G, Saha R, Lal C, Conti M. Internet-of-Forensic (IoF): A Blockchain Based Digital Forensics Framework for IoT Applications. *Futur. Gener. Comput. Syst.* 2021; 120: 13–25.
- [6] Mourtzis D, Doukas M, Psarommatis F. A Multi-Criteria Evaluation of Centralized and Decentralized Production Networks in a Highly Customer-Driven Environment. *CIRP Ann. - Manuf. Technol.* 2012; 61(1): 427–430.
- [7] Bonnin Roca J, Vaishnav P, Laureijs RE, Mendonça J, Fuchs ERH. Technology Cost Drivers for a Potential Transition to Decentralized Manufacturing. *Addit. Manuf.* 2019; 28(December 2018): 136–151.
- [8] Zhu X, Shi J, Huang S, Zhang B. Consensus-Oriented Cloud Manufacturing Based on Blockchain Technology: An Exploratory Study. *Pervasive Mob. Comput.* 2020; 62: 101113.
- [9] Zhang M, Lettice F, Zhao X. The Impact of Social Capital on Mass Customisation and Product Innovation Capabilities. *Int. J. Prod. Res.* 2015; 53(17): 5251–5264.
- [10] Ullah I, Narain R. Achieving Mass Customization Capability: The Roles of Flexible Manufacturing Competence and Workforce Management Practices. *J. Adv. Manag. Res.* 2020; 18(2): 273–296.
- [11] Pournader M, Shi Y, Seuring S, Koh SCL. Blockchain Applications in Supply Chains, Transport and Logistics: A Systematic Review of the Literature. *Int. J. Prod. Res.* 2020; 58(7): 2063–2081.
- [12] Vacca A, Di Sorbo A, Visaggio CA, Canfora G. A Systematic Literature Review of Blockchain and Smart Contract Development: Techniques, Tools, and Open Challenges. *J. Syst. Softw.* 2020; 174: 110891.
- [13] Prashanth Joshi A, Han M, Wang Y. A Survey on Security and Privacy Issues of Blockchain Technology. *Math. Found. Comput.* 2018; 1(2): 121–147.
- [14] Issaoui Y, Khat A, Bahnasse A, Ouajji H. Smart Logistics: Blockchain Trends and Applications. *J. Ubiquitous Syst. Pervasive Networks* 2020; 12(2): 09–15.
- [15] Lin IC, Liao TC. A Survey of Blockchain Security Issues and Challenges. *Int. J. Netw. Secur.* 2017; 19(5): 653–659.
- [16] Wang H, Zheng Z, Xie S, Dai HN, Chen X. Blockchain Challenges and Opportunities: A Survey. *Int. J. Web Grid Serv.* 2018; 14(4): 352.
- [17] Zhou Y, Xiong G, Nyberg T, Mohajeri B, Bao S. Social Manufacturing Realizing Personalization Production: A State-of-the-Art Review. *Proc. - 2016 IEEE Int. Conf. Serv. Oper. Logist. Informatics, SOLI 2016* 2016: 7–11.
- [18] Aheleroff S, Zhong RY, Xu X. A Digital Twin Reference for Mass Personalization in Industry 4.0. *Procedia CIRP* 2020; 93: 228–233.
- [19] Iarovyi S, Lastra JLM, Haber R, del Toro R. From Artificial Cognitive Systems and Open Architectures to Cognitive Manufacturing Systems. In: 2015 {IEEE} 13th Int. Conf. Ind. Informatics. *IEEE* 2015.
- [20] Jin M, Wang H, Zhang Q, Zeng Y. Supply Chain Optimization Based on Chain Management and Mass Customization. *Inf. Syst. E-Bus. Manag.* 2020; 18(4): 647–664.
- [21] Yao J, Liu L. Optimization Analysis of Supply Chain Scheduling in Mass Customization. *Int. J. Prod. Econ.* 2009; 117(1): 197–211.
- [22] Liu C, Yao J. Dynamic Supply Chain Integration Optimization in Service Mass Customization. *Comput. Ind. Eng.*

- 2018; 120(November 2017): 42–52.
- [23] Farahani RZ, Elahipanah M. A Genetic Algorithm to Optimize the Total Cost and Service Level for Just-in-Time Distribution in a Supply Chain. *Int. J. Prod. Econ.* 2008; 111(2): 229–243.
- [24] Katoch S, Chauhan SS, Kumar V. A Review on Genetic Algorithm: Past, Present, and Future, vol. 80. *Multimedia Tools and Applications* 2021.
- [25] Mureddu M, Ghiani E, Pilo F. Smart Grid Optimization with Blockchain Based Decentralized Genetic Algorithm. *IEEE Power Energy Soc. Gen. Meet.* 2020; 2020-Augus.
- [26] Cheng Y, Tao F, Zhao D, Zhang L. Modeling of Manufacturing Service Supply–Demand Matching Hypernetwork in Service-Oriented Manufacturing Systems. *Robot. Comput. Integr. Manuf.* 2017; 45: 59–72.
- [27] Tao F, Cheng J, Cheng Y, Gu S, Zheng T, Yang H. SDMSim: A Manufacturing Service Supply–Demand Matching Simulator under Cloud Environment. *Robot. Comput. Integr. Manuf.* 2017; 45: 34–46.
- [28] Liu Z, Wang L, Li X, Pang S. A Multi-Attribute Personalized Recommendation Method for Manufacturing Service Composition with Combining Collaborative Filtering and Genetic Algorithm. *J. Manuf. Syst.* 2021; 58(PA): 348–364.
- [29] Zhang G, Zhang Y, Xu X, Zhong RY. An Augmented Lagrangian Coordination Method for Optimal Allocation of Cloud Manufacturing Services. *J. Manuf. Syst.* 2018; 48: 122–133.
- [30] Wang W, Fung RYK, Chai Y. Approach of Just-in-Time Distribution Requirements Planning for Supply Chain Management. *Int. J. Prod. Econ.* 2004; 91(2): 101–107.
- [31] . SAA. Blockchain Ready Manufacturing Supply Chain Using Distributed Ledger. *Int. J. Res. Eng. Technol.* 2016; 05(09): 1–10.
- [32] Tian F. An Agri-Food Supply Chain Traceability System for China Based on RFID & Blockchain Technology. 2016 13th Int. Conf. Serv. Syst. Serv. Manag. ICSSSM 2016 2016: 1–6.
- [33] Biswas K, Muthukkumarasamy V, Tan WL. Blockchain Based Wine Supply Chain Traceability System. *Proc. 2017 Futur. Technol. Conf.* 2017; (December): 56–62.
- [34] Breese JL, Park S-J, Ganesh V. Blockchain Technology Adoption In Supply Change Management : Two Theoretical Perspectives. *Issues Inf. Syst.* 2019; 20(2): 140–150.

Dynamic Analysis of Historical Masonry Arch Bridges under Different Earthquakes:

The Case of Murat Bey Bridge

Elif Gözde ÇUBUK¹, Erkut SAYIN^{1*}, Alper ÖZMEN²

¹ İnşaat Mühendisliği, Fırat Üniversitesi, Mühendislik Fakültesi, Elazığ, Türkiye
² İnşaat Mühendisliği, İnönü Üniversitesi, Mühendislik Fakültesi, Malatya, Türkiye
¹elifcubuk4@gmail.com, ^{*}1esayin@firat.edu.tr, ²alper.ozmen@inonu.edu.tr

(Geliş/Received: 21/05/2022;

Kabul/Accepted: 04/06/2022)

Abstract: Historical structures, which constitute an important part of our cultural heritage, should be well protected and carried into the future. Masonry arch bridges are significant part of these structures. In this study, the single-span Murat Bey Bridge in the province of Kütahya, built in 1460, was studied as a numerical application. Firstly, three dimensional finite element model of the bridge was constituted with SAP2000 finite element program. Static analysis of the bridge under its own weight was carried out. The modal analysis method was used to obtain the dynamic characteristics of the bridge. Then, time-history analysis method was applied for seismic evaluation of the bridge. For this purpose, the acceleration records of the 1998 Adana, 2003 Bingöl, 2011 Van and 2020 Elazığ earthquakes were taken into consideration. As a result of the dynamic analyses carried out, the displacement and stress graphs occurring on the bridge were examined. The highest displacement and stress values on the historical bridge were obtained from the acceleration records of the 2011 Van earthquake.

Key words: Historical masonry bridges, finite elements, dynamic analysis.

Tarihi Yığma Köprülerin Farklı Depremler Altında Dinamik Analizi: Murat Bey Köprüsü Örneği

Öz: Kültürel mirasımızın önemli bir parçası olan tarihi yapılar en iyi şekilde korunmalı ve geleceğe taşınmalıdır. Yığma kemer köprüleri tarihi yapıların önemli bir kısmını oluşturur. Bu çalışmada, Kütahya ilinde 1460 yılında inşa edilmiş tek açıklıklı Murat Bey köprüsü sayısal uygulama olarak dikkate alınmıştır. İlk olarak köprü'nün üç boyutlu modeli SAP2000 sonlu eleman programı yardımıyla oluşturulmuştur. Köprü'nün statik analizi kendi ağırlığı altında yapılmıştır. Dinamik karakteristikleri ise modal analiz metodu ile elde edilmiştir. Daha sonra köprü'nün sismik değerlendirilmesi için zaman tanım alanı metodu kullanılmıştır. Bu amaçla, 1998 Adana, 2003 Bingöl, 2011 Van ve 2020 Elazığ depremleri dikkate alınmıştır. Dinamik analizler sonucunda köprü'den elde edilen yerdeğiştirme ve gerilme grafikleri elde edilmiştir. Köprüde en büyük yerdeğiştirme ve gerilme değerleri 2011 Van depremi ivme kayıtlarından elde edilmiştir.

Anahtar kelimeler: Tarihi yığma köprüler, sonlu elemanlar, dinamik analiz.

1. Introduction

Historical structures are an important part of the cultural heritage. In Turkey, there are many historical structures such as bridges, mosques, churches etc. reached today from the Roman, Byzantine, Seljuk and Ottoman periods. Protection and transfer to the next generation of these structures is important. These historical structures can be damaged or ruined under earthquake, wind and traffic loads. Many of them are located in medium or high seismic areas. Also, these structures are exposed to large earthquake forces because they are heavy and rigid. In order to protect structural integrity of these structures, assessment of the seismic behaviour of these structures is necessary. Historical masonry bridges are one of the most important part of transportation, commercial and architecture since the ancient times. These bridges which are important historical structures of a country were built in different spans, shapes and sizes in the world. Also, these bridges are still valuable components of transportation systems in many countries. They constituted a large part of Europe's road and railway bridge stock. According to the Sustainable Bridges project, more than 40% of railway bridges and 25% of the existing road bridges are masonry arch bridges [1]. In Turkey, an important percentage of masonry arch bridges in the railway network, such that 6966 of the 24196 culverts and 245 of the 2012 railway bridges are made of masonry material. Also, there are 2063 masonry arch bridges in the road network [2]. Although there were many masonry bridges in

** Corresponding author: esayin@firat.edu.tr. Yazarların ORCID Numarası: ¹ 0000-0001-9566-7200, ^{1*} 0000-0003-0266-759X, ² 0000-0003-1335-3780

Turkey, studies on these structures are relatively rare when compare the other structures. Accurate analysis methods are necessary to protect and restoration of historical bridges.

Different studies were performed about structural assessment and behaviour of historical masonry structures in the literature. Frunzio et al. [3] evaluated the results of a three dimensional finite element model analysis of a stone masonry arch bridge built in the Roman age, performed involving non-linear material behaviour, in which the structural role of the spandrel walls and filling was involved. Milan and Lourenço [4] evaluated the nonlinear behaviour of three dimensional of two masonry arch bridges through finite element code. Sayın et al. [5] generated the historical Uzunok Bridge with three dimensional finite element and they assessed linear and nonlinear analyses of the bridge. Altunışık et al. [6] assessed the arch thickness effect on the structural behaviour of masonry arch bridges under live and dead loads. As a case study, they selected Göderni historical arch bridge in Turkey. Güllü and Jaf [7] investigated soil structure interaction effect on a historical masonry stone arch bridge. For this purpose, they were evaluated the Mataracı Bridge with three dimensional nonlinear time history analyses. Özmen and Sayın [8] evaluated the seismic behaviour of the historical masonry Dudpınar Bridge under the 2003 Bingöl earthquake. As a result of the study, the maximum and minimum principal stresses were occurred at right and left arch base of the bridge and the maximum displacement was obtained at the top of the bridge. Sevim et al. [9] investigated linear dynamic analyses of two historical masonry arch bridges with operational modal analysis. Hökelekli and Yılmaz [10] examined the in-plane and out-of-plane non-linear structural responses of the spandrel walls of a historical masonry bridge in Bartın-Turkey. Sakcalı et al. [11] investigated historical Irgandı Bridge which is located in Bursa. They evaluated seismic behaviour of the bridge by linear dynamic analysis. Şeker and Gökçe [12] studied behaviour of Hundi Hatun (Kunç) Bridge located in Amasya city under the effect of increasing traffic loads. Analyses were carried out according to the most unfavourable situation. Radnić et al. [13] investigated static and dynamic analysis of the old stone bridge in Mostar. They assessed influence of vertical load, temperature change and seismic action. Gönen et al. [14] investigated stress contours and displacement values of the historical Murat bridge under dead loads. For this purpose, linear elastic response of the bridge was evaluated. Güllü [15] investigated Cendere Bridge under earthquake effects. Firstly, 3D finite element model of the bridge was consisted using solid element and the earthquake behaviour of the bridge was investigated with time-history analysis for linear elastic behaviour. Özodabaş and Artan [16] carried out a study to investigate historical Muş Murat Bridge. Stress regions of the bridge was investigated after earthquake, flood, and traffic loads. Akın et al. [17] assessed the seismic behaviour of a historical masonry bridge under different damping types. For this purpose, mass proportional, stiffness proportional and Rayleigh damping types were used. 1992 Tunceli earthquake acceleration records were used as seismic effect.

This paper presents the seismic behaviour of historical Murat Bey Bridge. The bridge was evaluated under 1998 Adana, 2003 Bingöl, 2011 Van and 2020 Elazığ earthquakes acceleration records. For this purpose, the historical bridge was constructed with three dimensional finite element model by SAP2000 finite element software and seismic behaviour of the bridge was investigated. Also, the displacement and stress graphs occurring on the bridge were examined after the dynamic analysis.

2. Historical Masonry Bridges

Arch is a structural form that is frequently used in masonry structures. It can span large distances and it generally subjected to compressive forces because of its geometric form. For this reason, it is the most preferred form. Stone and brick are the main construction materials for the masonry structures and arches because they have high compressive strength. There have been serious developments in arch forms over time. Different cultures and civilizations used various arch forms in order to both functional and decorative purposes. Some of the preliminary examples of arches were dated back to 3000 BC found in the Sumerian underground tombs located in Mesopotamia. Although it is not certain whether it was the Sumerians who discovered the arch form, the Romans put them to good use in both efficient and amazing ways. The ancient Romans constructed stone arches for bridges and aqueducts to across obstacles. Due to the geographical location and rich cultural heritage, Turkey has many historical structures and also stone masonry arch bridges. In Turkey, the best examples of bridge architecture were constructed in the 16th century of Master Builder Sinan [18]. Many masonry bridges of various sizes, shapes and materials were built from past to present. These masonry bridges have different parts. The main part of masonry arch bridges is spandrel wall, arch, backfill and foundation. Arch is the significant segment of historical structures. Also, one of the oldest architectural forms used for the historical structures. Typical components of masonry arch bridges are shown in Figure 1.

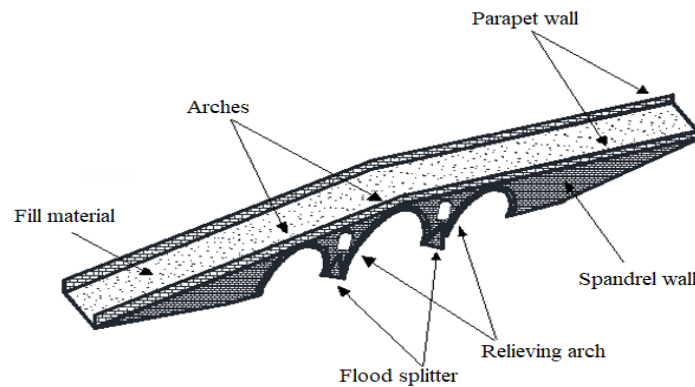


Figure 1. Typical components of masonry arch bridge

3. Description of the bridge and structural analysis

Numerical modeling of masonry structures is complex due to the interaction between masonry units and the mortar. Masonry is a heterogeneous material which exhibits distinct directional properties due to the mortar joints which act as planes of weakness. Finite element method is frequently used to numerical modelling of masonry structures. For modelling historical masonry structures, three modelling techniques are commonly used. According to the size of the structural system, detailed micro, simplified micro and macro modeling techniques have been frequently used in the modeling of masonry unit. These modelling techniques are given in Figure 2.

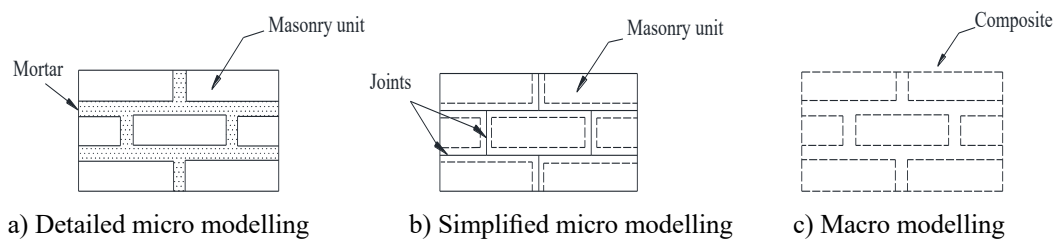


Figure 2. Modelling techniques of masonry structures [19]

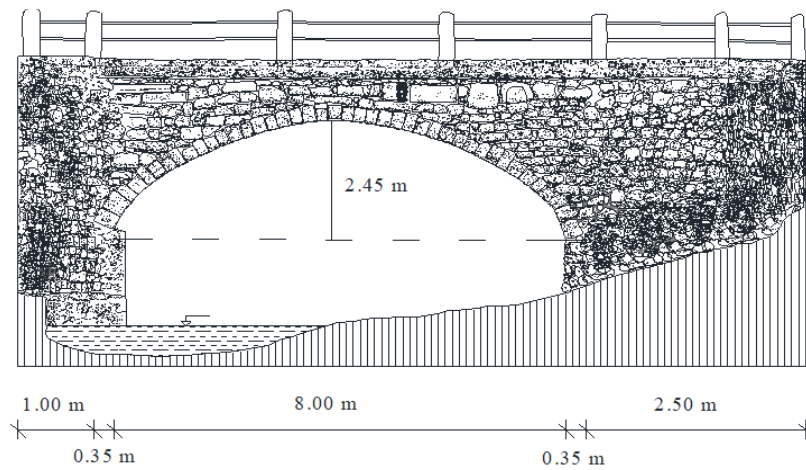
Masonry unit and mortar materials are modelled separately in the detailed micro modelling. Although this is a precise modelling technique, the time required for the analysis of the complete structure takes very long. For this reason, it is preferred for the analysis of small buildings or parts of large structures. In the simplified micro modelling, dimensions of masonry unit are extended as much as half thickness of the mortar. Thereby, the masonry units are separated from each other with interface lines and the mortar layer is neglected. Masonry unit and mortar is considered as a homogenized domain in the macro modelling [19]. When the literature is reviewed, it can be seen that macro-modelling was used to model full-scale historical structures because of its low computational effort [20-23].

The case study structure is the historical Murat Bey Bridge in Kütahya, Turkey. It was built in 1460 during the Ottoman period. It has single arch. The arch is made of cut stones and other parts of rubble stone. The bridge is 12.20 m long and 4.70 m wide, 2.45 m in height and span of 8 m. The thickness of spandrel walls and arch are 0.45 m and 0.35 m, respectively. Also, there are balustrades on both sides of the bridge. The bridge is good condition and open to vehicular and pedestrian traffic nowadays (Fig. 3). The section properties of Murat Bey Bridge were shown in Figure 4.

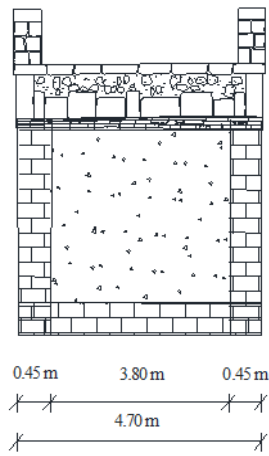
Dynamic Analysis of Historical Masonry Bridges under Different Earthquakes:
The Case of Murat Bey Bridge



Figure 3. Murat Bey Bridge



a) Plan view



b) Section view

Fig. 4. Geometrical properties of Murat Bey Bridge

Three dimensional (3D) model of the bridge was generated by using SAP2000 program (Figure 5). This program can be used for linear and non-linear analyses of 3D model of the structures. 5796 nodal points and 4580 solid elements were used in the finite element model of the historical bridge. The nodal point 131 on the top of the bridge was also given in the Figure 5. Also, all degrees of freedom were taken into account to be fixed at the foundation level in the finite element model of the bridge.

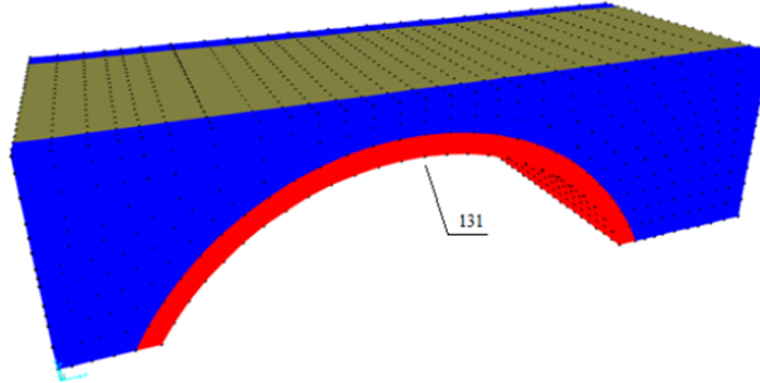


Fig. 5. Three dimensional finite element model of the Murat Bey Bridge

The bridge was modelled with the macro-modelling where the structure is considered as an isotropic and homogeneous material. Arch, spandrel wall and filling material were considered as three different material properties. It is not easy to determine the material properties of historical structures. Also, historical structures are important and sensitive structures therefore it may be inconvenient to take test samples from these structures. For this reason, similar material properties in the relevant literature were used (Table 1) [24-25]. Compressive strength of the stone material was considered as 20 MPa. Also, it was assumed that tensile strength of stone is 1/10 of compressive strength in accordance with previous studies [26].

Table.1. Material properties of Murat Bey Bridge

Material	Elasticity modulus (kN/m ²)	Density (t/m ³)	Poisson ratio
Arch material	2.5E6	2.3	0.2
Spandrel walls	2E6	2.2	0.2
Filling material	1.2E6	1.4	0.2

Firstly, static analysis of the bridge under dead load was carried out. Maximum displacement under dead load obtained at the vertical axis (z axis) on the middle of the bridge arch span. Maximum displacement of the marked point in Figure 5 was obtained as 0.569 mm in z direction. The deformed shape of the bridge was presented in Figure 6.

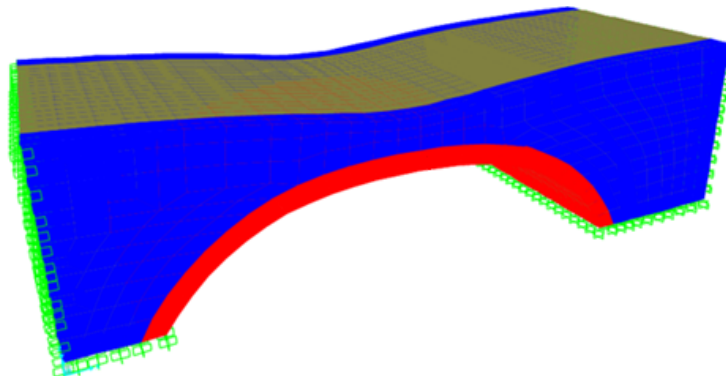


Fig. 6. Deformed shape of the bridge under its own weight

At the end of the static analysis, the maximum tensile and compressive stresses contours of the bridge were presented in Figure 7. Maximum tensile and compressive stress occurred as 162.89 kPa and 431.35 kPa, respectively. These high stress contours were marked in the circle in Figure 7.

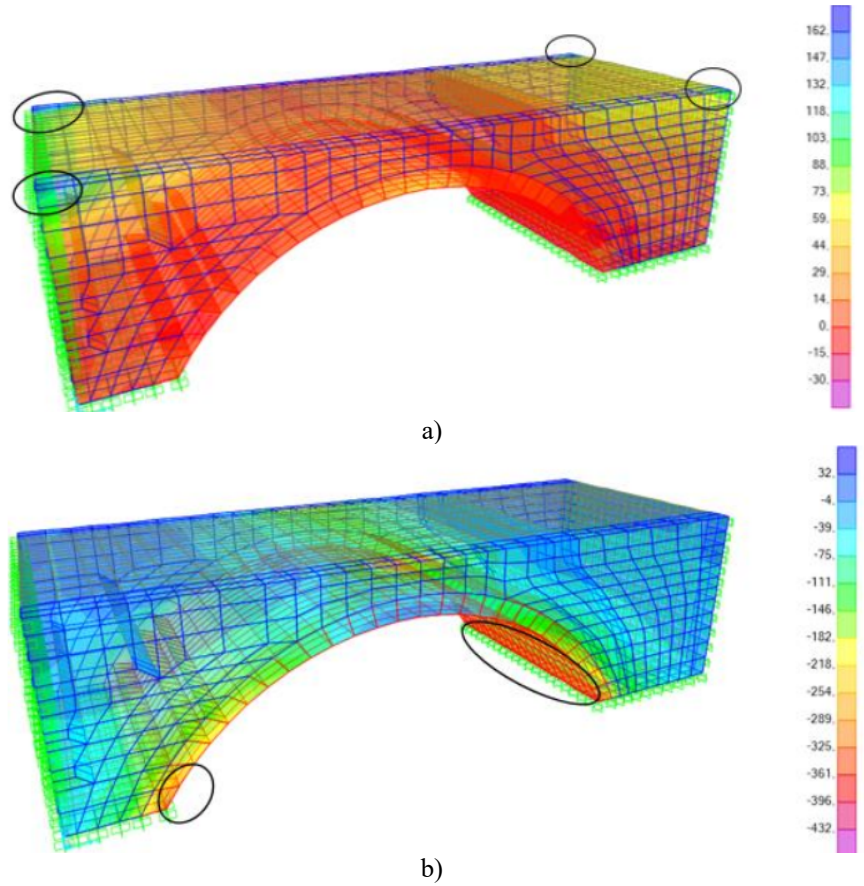
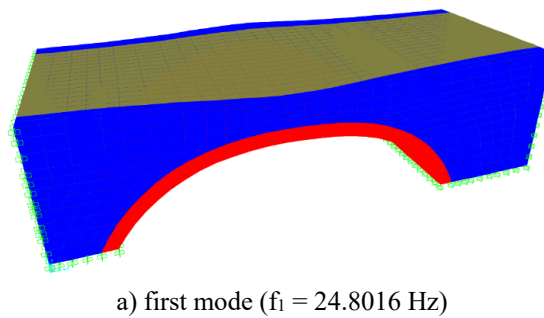
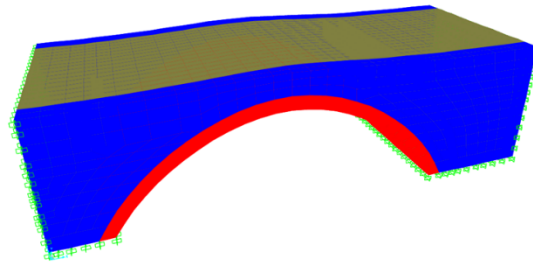


Fig. 7. Static analysis a) maximum tensile contour b) maximum compressive contour

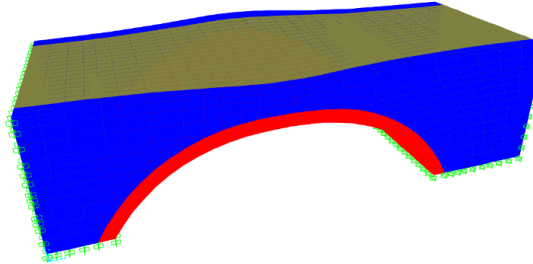
Modal analysis was performed to determine the dynamic characteristics of the Murat Bey Bridge. In this analysis, mode shapes, free vibration periods and mass participation ratios of the structures were acquired. In the analysis, 5% damping ratio was used for the Rayleigh damping coefficients [27-29]. Dynamic characteristics were calculated for the first 100 modes. Mass participation ratio was found greater than 90% for the first 100 modes. The first three modes of the bridge obtained from the modal analysis were shown in Fig. 8.



a) first mode ($f_1 = 24.8016$ Hz)



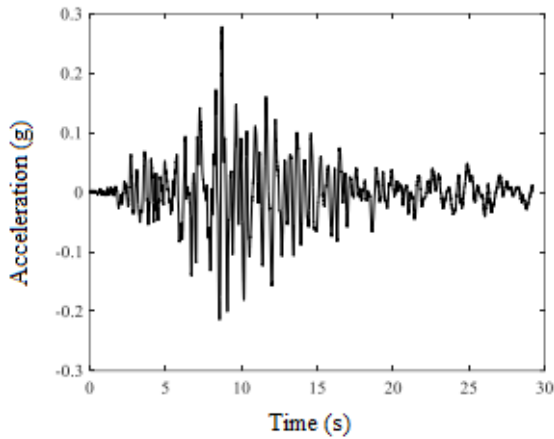
b) second mode ($f_2 = 24.8694$ Hz)



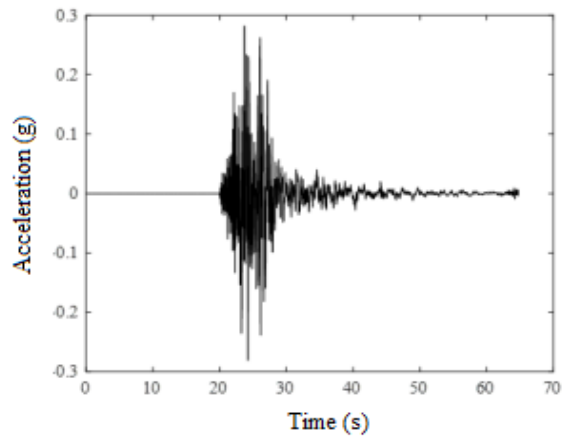
c) third mode ($f_3 = 34.0892$ Hz)

Fig. 8. First three mode shapes and frequencies of the bridge

For the dynamic analysis of the bridge, 1998 Adana, 2003 Bingöl, 2011 Van and 2020 Elazığ earthquakes acceleration records were used (Fig. 9). East-West component of the earthquakes were applied in the flow (y) direction of the bridge. In the dynamic analysis, the most effective 20 seconds of earthquake acceleration records were used because of the large memory required. The integration step was selected as 0.01 sec. Also, HHT- α method was considered for solution of equilibrium of motion.



a) 1998 Adana



b) 2003 Bingöl

Dynamic Analysis of Historical Masonry Bridges under Different Earthquakes:
The Case of Murat Bey Bridge

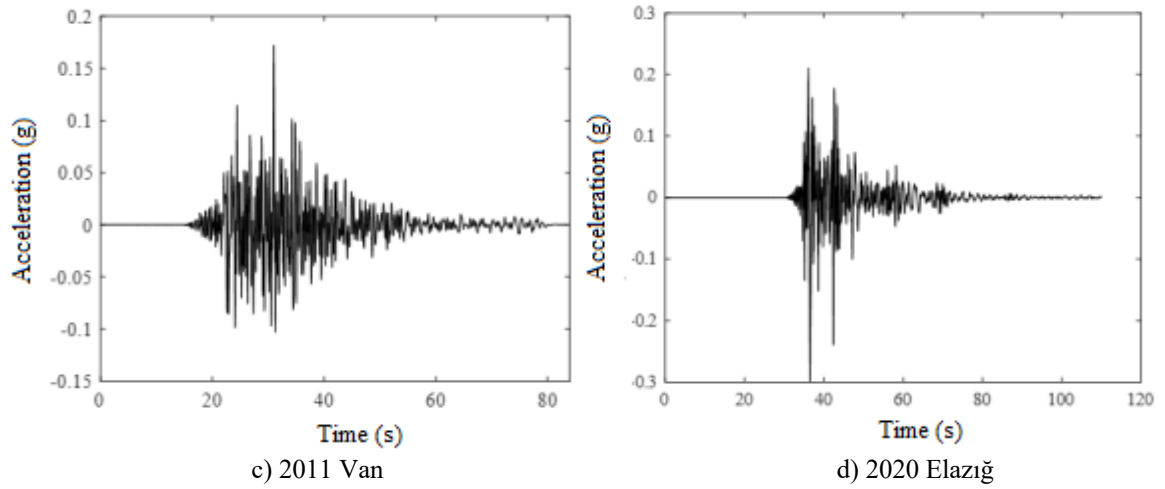
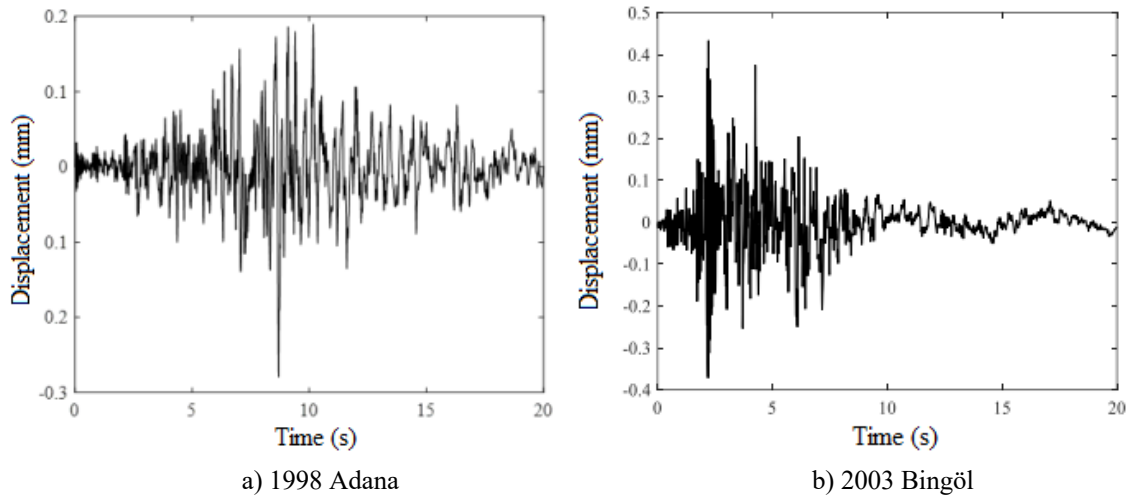


Fig. 9. East-West component of the selected earthquakes

These selected earthquake acceleration records were scaled according to bridge's location. For the scaling parameters, the earthquake level of seismic ground motion was chosen as DD-2, representing a 10% probability of exceedance in 50 years (475 years return period) [30]. After the dynamic analysis, the horizontal displacements (flow direction) for the node 131 were obtained. The time histories of the displacements subjected to the selected earthquakes were given in Fig. 10. These displacement values for 1998 Adana, 2003 Bingöl, 2011 Van and 2020 Elazığ earthquakes were obtained as 0.279 mm, 0.434 mm, 0.468 mm and 0.303 mm, respectively.



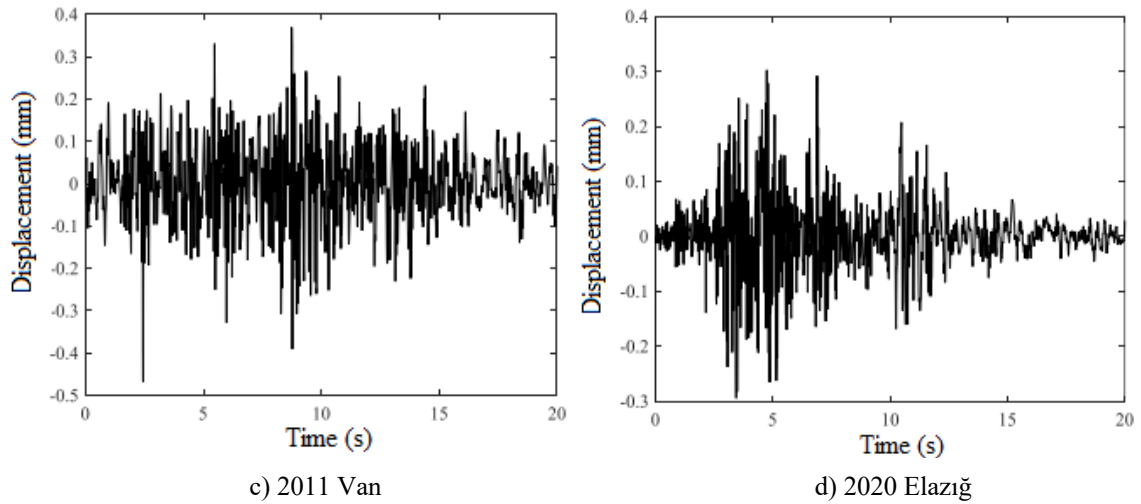


Fig. 10. Time history graph of the nodal point 131

All these displacement values for the nodal point 131 were given in Figure 11. As shown in Fig. 11, the highest displacement value was occurred for the 2011 Van earthquake.

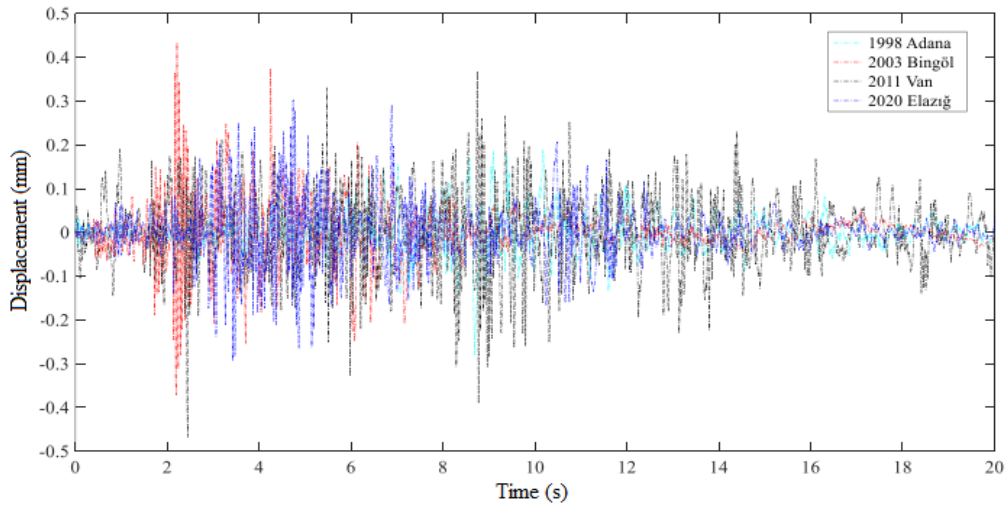
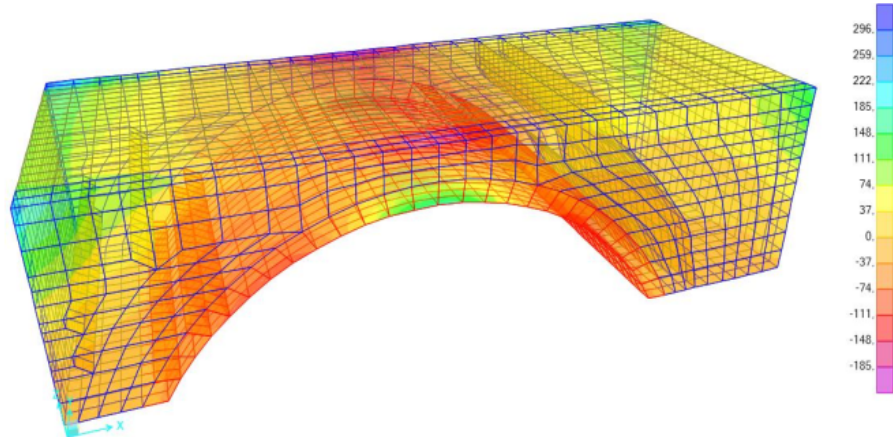


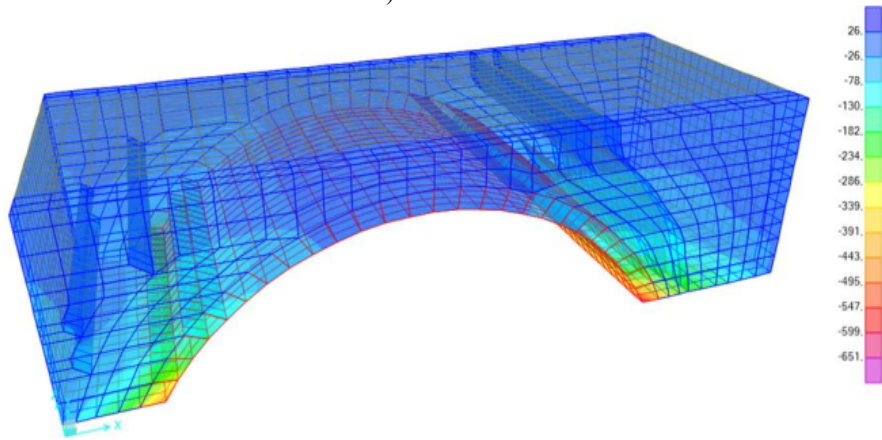
Fig. 11. Time history graph of the nodal point 131 for all selected earthquakes

Also, the time histories of the maximum and minimum stress contours of the bridge subjected to the selected earthquakes were obtained. In the dynamic analyses, dead load of the bridge was considered with the earthquake load. When the 1998 Adana earthquake was considered, maximum and minimum stress contours of the historical bridge were obtained as Figure 12.

Dynamic Analysis of Historical Masonry Bridges under Different Earthquakes:
The Case of Murat Bey Bridge



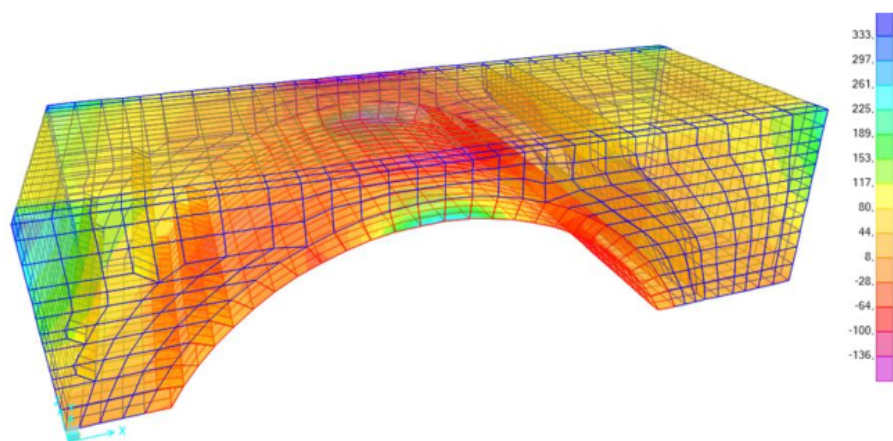
a) maximum



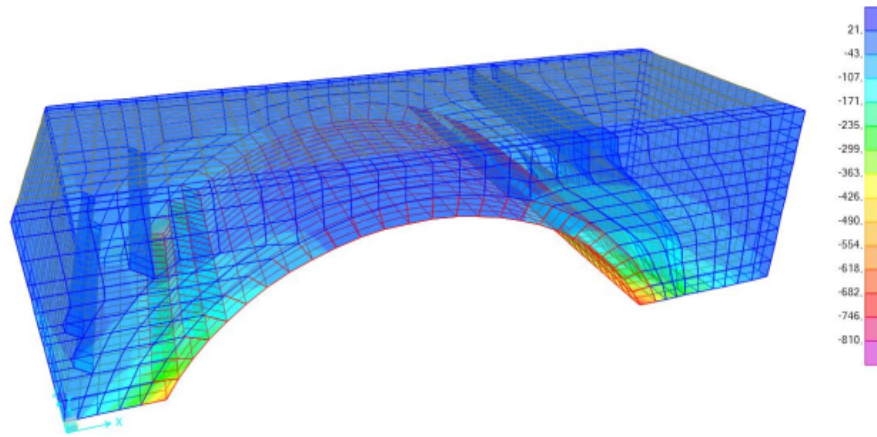
b) minimum

Fig. 12. Stress contours of the bridge for 1998 Adana earthquake

In this analysis, maximum and minimum stress values were achieved as 295.82 and -650.81 kPa, respectively. For the 2003 Bingöl earthquake acceleration records, maximum and minimum stress contours of the bridge were shown in Figure 13.



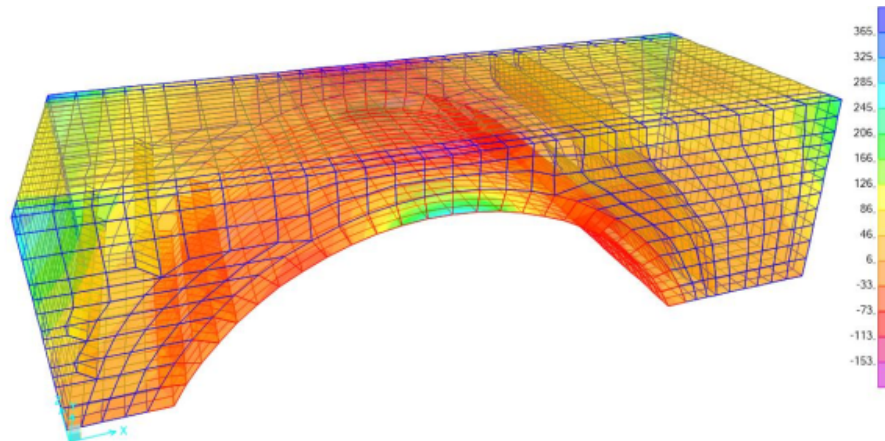
a) maximum



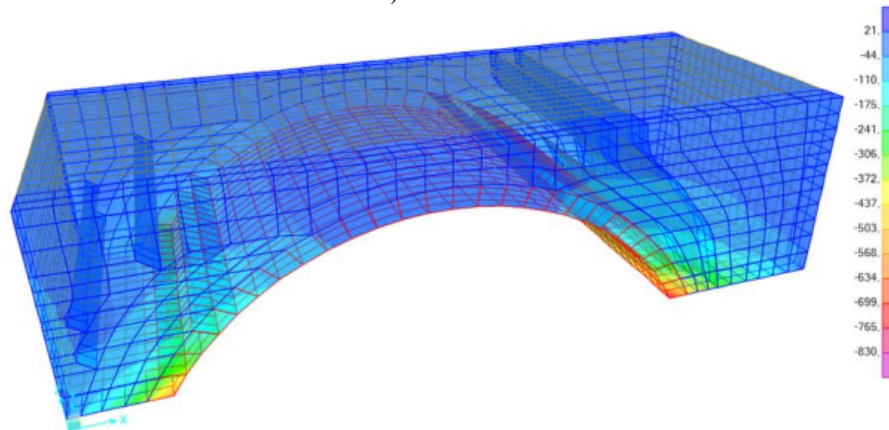
b) minimum

Fig. 13. Stress contours of the bridge for 2003 Bingöl earthquake

As seen in Figure 13, the maximum and minimum stress values were acquired as 332.50 and -809.08 kPa for 2003 Bingöl earthquake, respectively. When the 2011 Van earthquake was evaluated, maximum and minimum stress contours of the bridge were obtained as Figure 14. In this analysis, maximum and minimum stress values were achieved as 364.77 and -829.33 kPa, respectively.



a) maximum



b) minimum

Fig. 14. Stress contours of the bridge for 2011 Van earthquake

Also, maximum and minimum stress contours of the bridge were shown in Figure 15 for the 2020 Elazığ earthquake acceleration records. As seen in Figure 15, the maximum and minimum stress values were obtained as 295.72 and -662.40 kPa, respectively.

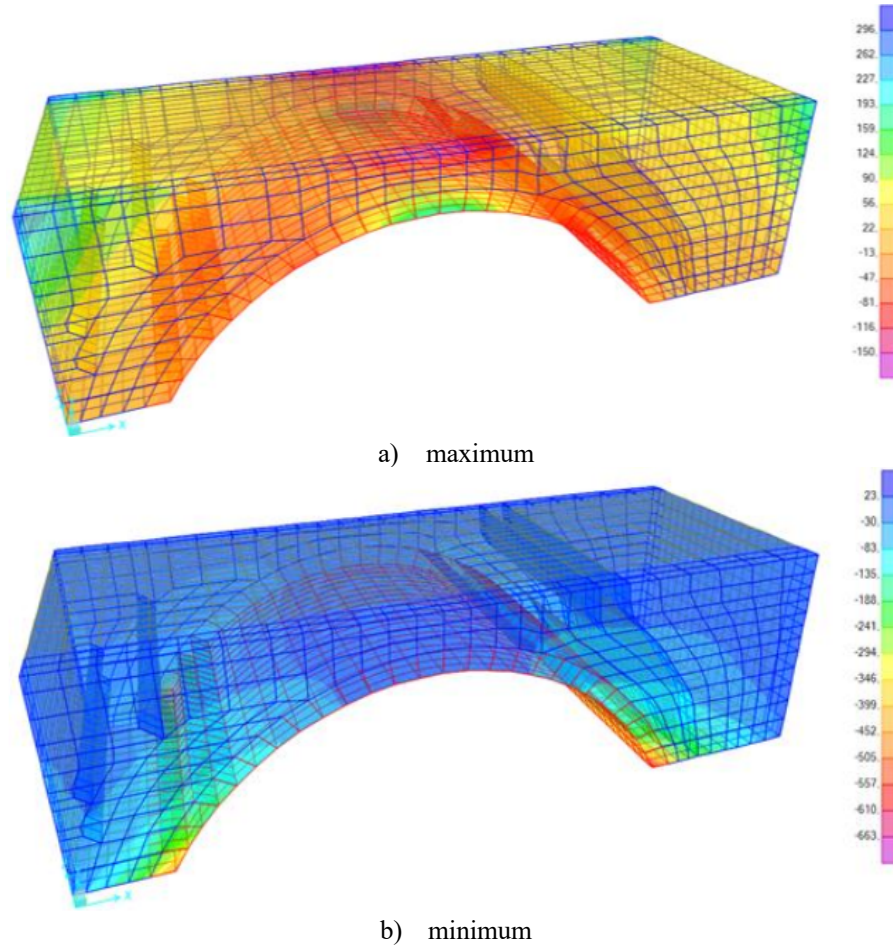


Fig. 15. Stress contours of the bridge for 2020 Elazığ earthquake

When all the earthquake accelerations used in the analysis were evaluated, the highest stress values were obtained for the 2011 Van earthquake.

4. Conclusions

This paper aimed to investigate the dynamic analysis of historical masonry bridge. As a numerical application, the single-span Murat Bey Bridge built in 1460 located in Kütahya was selected. SAP2000 finite element software was used to constitute three dimensional finite element model of the bridge. Natural frequencies, period and mode shapes of the bridge determined by modal analysis. In the dynamic analysis, 5% damping ratio was used for the Rayleigh damping coefficients and seismic evaluation was investigated using 1998 Adana, 2003 Bingöl, 2011 Van and 2020 Elazığ earthquakes. The displacement values and stress contours of the bridge were investigated for these selected earthquakes. The highest displacement value was obtained as 0.468 mm at 2011 Van earthquake. Also, maximum and minimum stress contours of the bridge were investigated for the selected earthquakes with dynamic analysis. It is possible to see that high compressive stresses were concentrated arch base of the bridge. Also, it was seen that tensile stresses reached higher values in the regions where spandrel walls connect side slopes. The highest stress values were achieved at 2011 Van earthquake. However, the obtained compressive and tensile stresses as a result of the dynamic analysis were below the compressive and tensile stress considered in the study.

References

- [1] Bell B. Sustainable Bridges – Assessment for Future Traffic Demands and Longer Lives. European Railway Bridge Demography. 2004.
- [2] Gönen S, Soyöz S. Seismic analysis of a masonry arch bridge using multiple methodologies. Engineering Structures 2021; <https://doi.org/10.1016/j.engstruct.2020.111354>.
- [3] Frunzio G, Monaco M, Gesualdo A. 3D F.E.M. analysis of a Roman arch bridge, Historical Constructions. P.B.Lourenço, P.Roca (Eds.), 591-598, Guimarães, 2001.
- [4] Milan G, Lourenço PB. 3D non-linear behaviour of masonry arch bridges. Computers and Structures 2012; 110–111: 133–150.
- [5] Sayın E, Calayır Y, Karaton M. Nonlinear seismic analysis of historical Uzunok Bridge. Seventh National Conference on Earthquake Engineering, 30 May-3 June, Istanbul, Turkey, 2011 (in Turkish).
- [6] Altunışık, AC, Kanbur, B, Genç, AF. The effect of arch geometry on the structural behaviour of masonry bridges. Smart Structures and System 2015; 1: 1-20.
- [7] Güllü H, Jaf HS. Full 3D nonlinear time history analysis of dynamic soil–structure interaction for a historical masonry arch bridge. Environmental Earth Sciences 2016; 75(11): 1-17.
- [8] Özmen A, Sayın E. Seismic assessment of a historical masonry arch bridge. Journal of Structural Engineering & Applied Mechanics 2018; 1(2): 95–104.
- [9] Sevim B, Bayraktar A, Altunışık AC, Atamtürktür S, Birinci F. Finite element model calibration effects on the earthquake response of masonry arch bridges. Finite Elements in Analysis and Design 2011; 47: 621-634.
- [10] Hokelekli E., Yılmaz BN. Effect of cohesive contact of backfill with arch and spandrel walls of a historical masonry arch bridge on seismic response. Periodica Polytechnica Civil Engineering 2019; 63(3): 926-937.
- [11] Sakcalı GB, Gönül A, Yüksel İ. Seismic behaviour of historical masonry bridges: The case study of Irgandi Bridge. International Journal of Architectural Engineering Technology 2019; 6: 24-32.
- [12] Şeker BŞ, Gökçe M. Tarihi Hundi Hatun (Kunç) köprüsünün artan trafik yükü altında davranışının incelenmesi. Uluslararası Mühendislik Araştırma ve Geliştirme Dergisi 2021; 13(2): 496-507.
- [13] Radnić J, Harapin A, Smilović M, Grgić N, Glibić M. Static and dynamic analysis of the old stone bridge in Mostar. Građevinar, 2012; 8: 655-665.
- [14] Gonen H, Dogan M, Karacasu M, Ozbasaran H, Gokdemir H. Structural failures in retrofit historical Murat masonry arch bridge. Eng. Fail. Anal., 2013; 35: 334-342.
- [15] Güllü H. Tarihi yağma yapıları Cendere köprüsünün deprem etkisinin incelenmesi. ÖHÜ Müh. Bilim. Derg. 2018; 7(1): 245-259.
- [16] Özodabaş A, Artan C. Determination of stress and deformation zones of historical Mus Murat Bridge. BSEU Journal of Science 2021; 8(1): 413-429.
- [17] Akın K, Sayın E, Özmen A. Farklı sönüm tipleri altında tarihi yağma köprülerinin sismik tepkilerinin değerlendirilmesi. Fırat Üniversitesi Müh. Bil. Dergisi 2022; 34(1): 45-59.
- [18] Toker S, Ünay Aİ. Kemerli taş köprülerinin matematiksel modellenmesi ve sonlu elemanlar yöntemiyle analizi. G.Ü. Fen Bilimleri Dergisi 2004; 17(2): 129-139.
- [19] Lourenço, P. B., Computational strategies for masonry structures, Delft University of Technology, Netherlands, 1996.
- [20] Usta, P, Bozdağ, Ö. Tarihi Başdurak camisinin deprem analizi. Pamukkale University Journal of Engineering Sciences 2021; 27(3): 244–250.
- [21] Özmen A, Sayın E. Tarihi yağma bir köprüünün deprem davranışının değerlendirilmesi. NÖHÜ Müh. Bilim. Derg. 2020; 9(2): 956-965.
- [22] Homaei F, Yazdani M. The probabilistic seismic assessment of aged concrete arch bridges: The role of soil-structure interaction. Structures 2020; 28: 894-904.
- [23] Ercan E, Nuhoglu A. Identification of historical Veziragasi aqueduct using the operational modal analysis, The Scientific World Journal, Article ID: 518608, 2014.
- [24] Bayraktar A, Altunışık AC, Türker T, Sevim B. Tarihi köprülerin deprem davranışına sonlu eleman model iyileştirilmesinin etkisi. Altıncı Ulusal Deprem Mühendisliği Konferansı, İstanbul, Türkiye, 2007.
- [25] Pela L, Aprile A, Benedetti A. Seismic assessment of masonry arch bridges. Engineering Structures 2009; 31: 1777- 1788.
- [26] Turer A, Boz B. Computer modelling and seismic performance assessment of historic Aspendos theatre in Antalya, Turkey. Engineering Structures 2008; 30(8): 2127-2139.
- [27] Sayın E. Nonlinear seismic response of a masonry arch bridge. Earthquakes and Structures 2016; 10(2): 483–494.
- [28] Özmen A, Sayın E. Seismic response of a historical masonry bridge under near and far-fault ground motions. Periodica Polytechnica Civil Engineering 2021; 65(3): 946–958.
- [29] Altunışık AC, Genç AF. Earthquake response of heavily damaged historical masonry mosques after restoration. Natural Hazards and Earth System Sciences 2017; 17(10): 1811–1821.
- [30] TBEC, 2018 Turkish Building Earthquake Code, Ministry of Public Works and Settlement.

Response Surface Methodology to Optimize the Yield of Alkyd Resin from Jatropha (*Jatropha Curcas*) and Sesame (*Sesamum Indicum*) Seed Oils Using CaCO₃ as Catalyst

Aliru Olajide MUSTAPHA^{1*}, Simeon Gbenga OLADELE², Salihu Folorunsho ADISA³

^{1,2,3}Department of Chemical, Geological and Physical Sciences, Faculty of Pure and Applied Sciences, Kwara State University Malete, Ilorin, Kwara State, Nigeria

^{1*} aliru.mustapha@kwasu.edu.ng, ² oladelesimeon@aol.com, ³ funzy4life@gmail.com

(Geliş/Received: 31/05/2022;

Kabul/Accepted: 08/08/2022)

Abstract: The low-cost feedstocks such as sesame (*sesamum indicum*) and jatropha (*jatropha curcas*) seed oils were utilized to optimize the yield of alkyd resins. The experimentally selected input factors ranges in the molar ratios of oil:glycerol (0.3 – 1), phthalic anhydride: glycerol (1 – 3), and catalyst (0.5–1.5 wt. %) for optimization were established using the response surface methodology (RSM) of Box Behken model to improve the alkyd resin yield factors. The optimization solution utilizing CaCO₃ catalysts, and a combination of other process factors evaluated, as well as the corresponding desirability functions, was found using analysis of variance (ANOVA) results for refined sesame alkyd resin (RSAR) and refined jatropha alkyd resin (RJAR). The RSAR optimization using a CaCO₃ concentration of 1.5 wt. % at a molar ratios of oil:glycerol (1.0:1.0) and phthalic anhydride:glycerol (3.0:1.0), while the RJAR at a similar catalyst concentration of 1.5 wt. %, molar ratio of oil:glycerol (1.0:1.0), and phthalic anhydride:glycerol (2.8:1.0) were observed for the alkyd resin optimization for the two processes. At these reaction conditions, the predicted and experimental biodiesel yield were 48.26 % and 47.29 % for RSAR and 62.07 % and 61.61 % for RJAR, respectively which shows less than 0.5% variations in both cases.

Key words: vegetable-oils, alkyd resin; optimization; jatropha; sesame

Katalizör Olarak CaCO₃ Kullanan Jatropha (*Jatropha Curcas*) ve Susam (*Sesamum Indicum*) Tohum Yağlarından Alkid Reçinesinin Görünümünü Optimize Etmek için Tepki Yüzey Metodolojisi

Öz: Alkid reçinelerinin verimini optimize etmek için susam (*sesamum indicum*) ve jatropha (*jatropha curcas*) tohum yağları gibi düşük maliyetli hammaddeler kullanılmıştır. Optimizasyon için yağ:gliserol (0,3 – 1), fitalik anhidrit: gliserol (1 – 3) ve katalizörün (% 0,5–1,5 ağırlık) molar oranlarında deneysel olarak seçilen girdi faktörleri aralıkları yanıt yüzeyi metodolojisi kullanılarak oluşturulmuştur (Alkid reçine verim faktörlerini iyileştirmek için Box Behken modelinin RSM). CaCO₃ katalizörlerini kullanan optimizasyon çözümü ve değerlendirilen diğer işlem faktörlerinin yanı sıra karşılık gelen arzu edilebilirlik fonksiyonlarının bir kombinasyonu, rafine susam alkid reçinesi (RSAR) ve rafine jatrofa alkid reçinesi (RJAR) için varyans analizi (ANOVA) sonuçları kullanılarak bulundu. . Ağırlıkça 1.5 CaCO₃ konsantrasyonu kullanılarak RSAR optimizasyonu. yağ:gliserol (1.0:1.0) ve fitalik anhidrit:gliserol (3.0:1.0) molar oranlarında %, RJAR ise ağırlıkça 1.5 benzer bir katalizör konsantrasyonunda. İki işlem için alkid reçinesi optimizasyonu için %, yağ:gliserol (1.0:1.0) ve fitalik anhidrit:gliserol (2.8:1.0) molar oranı gözlemlendi. Bu reaksiyon koşullarında, öngörülen ve deneysel biyodizel verimi, RSAR için sırasıyla %48.26 ve %47.29 ve RJAR için %62.07 ve %61.61'dir ve bu, her iki durumda da %0.5'ten daha az varyasyon gösterir.

* Corresponding author: aliru.mustapha@kwasu.edu.ng ORCID Number of authors: ¹ 0000-0002-6071-4342

1. Introduction:

Due to increased awareness of environmental concerns around the world, the use of renewable resources in various fields of polymer applications has proliferated day by day. Naturally, renewable resources have many advantages, such as feed availability, environmentally friendly nature, and low cost [1]. Nigeria's extensive forest resources and farmland yield a range of oil-bearing products sowing plants. For the manufacture of diverse polymeric resins, such as polyester, epoxy, polyurethane, amide polyester, etc several seed oils were employed. [2]. Main seed oil traditionally used to make such resins is linseed, castor, soybean, sunflower, safflower, tung, coconut, etc. These resins were used in the various fields of application like paint, coating, adhesives, and composite binder. Avocados are of commercial value and are cultivated worldwide in tropical Mediterranean climates. They have fleshy, green-skinned bodies, it can be shaped like a pear, an egg, or a sphere. The self-pollinating, avocado trees are propagated by grafting to preserve a projected quality and quantity of fruit [3,4].

According to Aigbodion, *et al.* [5,6], alkyds are important basic ingredients for making a variety of surface coatings because they act as binders.. In the surface-coating industry, vegetable oils are widely used in the production of oil-modified alkyd resin. The rising expense of traditional vegetable oils used in coatings, which contributed to price increases in finished coating products such as paints and lacquers, has led alkyd chemists to hunt for other, but less expensive, sources of surface-coating vegetable oils. [7]. The oil chosen for alkyd production appears to have a profound impact on the properties of the saturated bond amount presumably contributing to its non-dryness properties. Aigbodion and Okieimen [5], and Ikhuoria, *et al.* [8] studied the castor oil-modified alkyd resin production and characterization drying air for surface coatings.

Muturi-Nwangi, *et al.* [9], documented synthesis of alkyd resins using a partially and completely epoxidized vernonia oil, linseed oil, and soybean oil. The less yellowing property demonstrated the completely epoxidized linseed oil, and this yellowing of a vegetable oil could be managed by reducing the amount of unsaturation. Gogte and Sarwadekar [4] proved that alkyd resin prepared in conjunction with castor oil, from fractionated rice bran oil was of very good quality. The result showed that rice bran oil allowed for the use of maleic acid without the danger of the prepared resin being gelled. Igwe and Ogbobe [10], studied alkyd resin synthesis using melon seed, and oils from rubber seed. The results revealed that in the synthesis of alkyd resins, linseed may be replaced by rubber seed oil and soybean oils. Melon seed oil was shown to be a good substitute for linseed oil and soya bean oil in the synthesis of various alkyd resins.. The epoxidized soybean seed oil had greater potential for use in the formulation of surface coating based on drying movie resources. The alkyd resins derived from both altered and epoxidized soybeans modified alkyd soybean resins showed excellent chemical and alkaline resistance. By processes of alcoholysis-polyesterification Alkyd resins containing jojoba seed oil were created by Shaker *et al.* [11]. Also, Box *et al.* [12] developed Response Surface Methodology (RSM), which is based on computer simulations or experimental observations [13-15]. This study used response surface methods to provide the best analysis of factors on alkyd resin yields from jatropha and sesame seed oils.

2. Materials and Methods

2.1 Seed Collection and Extraction

The sesame and jatropha seeds were collected in farms and markets in Ilorin, Kwara State, Nigeria. A 40g of freeze dried raw crushed sample was placed in a beaker with 200 mL n-hexane and agitated at 300 rpm for 20 hours at 45 °C for n-hexane extraction. To prevent the solvent from evaporating, the lip of the beaker was securely closed with aluminum foil paper. The hexane solution was filtered with 125 mm grade filter paper after extraction and evaporated at 400°C in a rotary vacuum evaporator. Until examination, the extracted oil was kept at room temperature (20°C).

2.2. Refinement of the crude oils

This was a crucial step in the manufacturing of alkyd resins because it allowed for the removal of contaminants like phosphorus compounds, which were necessary for successful trans-esterification. Degumming, alkaline, and bleaching treatments were used in the refining process [16-18].

2.3. Two stage - alky resin preparation – alcoholysis and esterification

Alcoholysis stage

The reactor was charged with 2 grams of CaCO₃ (catalyst) and 50 grams of each oil. The mixture was then heated to roughly 120 °C. A 20g glycerol was added at 120 oC and heated to 230-250 °C (the alcoholysis stage high temperature was deliberate to break the vegetable oil to monoglyceride and diglycerides , which in turn was

further broken down to two monoglycerides before esterification) with vigorous agitation for 30 minutes to cause trans-esterification of triglyceride into a mixture of mono- and diglyceride oils. Alcoholysis was completed when a sample of the combination formed became soluble in 1 to 3 liters of anhydrous methanol, providing a clear solution. To ensure a seamless transition to the esterification stage, the reaction temperature was reduced to 140°C.

Esterification stage

After 30 minutes, the temperature was lowered to 150 oC, and 25g phthalic anhydride, then xylene, were added. To increase the resin's molecular weight, the esterification water is withdrawn at regular intervals before the temperature is raised to 245 °C with stirring.. By heating the bulk to temperatures above 250 °C and stirring continuously, water was extracted along with the unreacted acid. The 5 hour reaction procedure was monitored by monitoring the acid number and viscosity on a regular basis. When the resulting solution became viscous and the acid value dropped below 10, it was stopped. Titrating to the phenolphthalein end point (1:1) with a 0.1M KOH solution after dissolving in a mixture of toluene and ethanol was used to determine the acid value of in-process samples taken at intervals [19].

2.4 Optimization of seed oil-based alkyd resins

The Process optimization is necessary not only to ensure or detect the best reaction parameters for a better yield or intended response, but also to provide high-quality products with shorter drying times, acceptable color, low production costs, and so on. The amount of time it takes for the product to dry is crucial to its quality. Additionally, lowering the product's cost by reducing reaction time and temperature is constantly taken into account. The MRS optimization method will be used to optimize the process, and the criterion feature will be used to input the required value for obtaining a targeted response. [20].

2.5 Experimental designs for yield optimization

The design of experiments (DoE) was established using RSM with a design input to measure the outputs or response. The DoE input variables used are: glycerol/oil molar ratio (M_1), catalyst (C), temperature (T), and glycerol/phthalic molar ratio (M_2). The three factors and three levels of a Box-Behnken Design (BBD) was adopted Box and Behnken [21]. The selected experimental factors and their ranges for optimization are glycerol/phthalic molar ratio (1-3), reaction NaOH catalyst (0.5–1.5 wt. %), reaction temperature (200 – 260 ° C), and glycerol/oil molar ratio (0.3-1), while the pressure was kept constant. The expected measurable outputs are yield as shown in Table 1 contains the variable ranges to cover the intervals.

Table 1. Experimental design levels with independent variables

Inputs	Notation	Levels		
		-1	0	+1
Phthalic/Glycerol	Phyt/Gly	1	2	3
Catalyst	Cat	0.5	1	1.5
Oil/Glycerol	Oil/Glyc	0.3	0.65	1

3. Results and Discussion

3.1 Using response surface methodology to optimize alkyd resin yields.

A design matrix (inputs) must be created in order to measure the reaction of outputs; a Box-Behnken design (BBD) with three variables and three levels was used. The following input factors were used to create the design of experiments (DoE): Oil-to-Glycerol ratio (Oil/Gly), Phthalic-to-Glycerol ratio (Phy/Gly), and C: Catalyst-to-Glycerol ratio (Phy/Gly) (Cat.) The following were the factors that were chosen for optimization ranges based on experiments: The factor ranges spanned the intervals that were typically used in the literatures: Oil/Glyc (0.3–1), Phyt/Gly (1–3), and catalyst (0.5–1.5 wt. %) [22].

3.1.1 Refined jatropha-based alkyd resin

In this case, 17 experiments were needed to convert the entire range of choices and choose the optimal alkyd resin manufacturing procedure. The design matrix displays the number of experiments as well as the associated values for each variable combination (Table 2).

Table 2. Design experimental matrix at different input variables

Run	Factor 1	Factor 2	Factor3	Response	
	A:Oil/Glyc	B:Phyt/Gly	C:Cat	Actual	Predicted
1	1	2	1.5	55.8	56.64
2	0.65	2	1	22.4	22.40
3	0.65	2	1	22.4	22.40
4	0.3	1	1	5.15	4.94
5	0.65	2	1	22.4	22.40
6	0.65	3	0.5	43.2	42.42
7	0.3	2	0.5	14.65	13.81
8	0.65	2	1	22.4	22.40
9	0.65	3	1.5	46.6	45.55
10	1	3	1	58.7	58.91
11	0.65	1	1.5	30.48	31.26
12	0.65	1	0.5	25.69	26.74
13	1	1	1	50.55	48.93
14	0.3	2	1.5	18.37	17.80
15	0.3	3	1	23.29	24.91
16	0.65	2	1	22.4	22.40
17	1	2	0.5	52.4	52.97

Analysis of variance

These equations show the second order polynomial functions that were obtained to model yield

$$\text{Yield} = +31.47181 + 12.94745\text{oil/glyc} - 13.59679\text{phyt/gly} - 54.38536\text{cat} - 7.13571\text{oil/glyc*phyt/gly} - 0.457143\text{oil/glyc*cat} - 0.695000\text{phyt/gly*cat} + 44.22449\text{oil/glyc}^2 + 6.60500\text{phyt/gly}^2 + 29.95000\text{cat}^2 \quad (1)$$

The oil/glyc*phyt/gly, oil/glyc*cat, and phyt/gly*cat reflect the linear interaction effects between the refined jatropha oil/glycerol, phthalic/glycerol, and catalyst, respectively. The respective process variables' quadratic effects are oil/glyc², phyt/gly², and cat².

Table 3 shows how the regression equation was utilized to calculate the projected response.

It can be seen that all of the data points cluster together towards the straight y=x line. This indicates that the quadratic regression model developed was capable of accurately and confidently predicting the jatropha seed oil alkyd resin optimization process. As a result, this equation can be applied to both prediction and design.

Table 3. ANOVA Table for the “yield” quadratic model

Source	Sum of Squares	Df	Mean Square	F-value	p-value	
						(prob > F)
Model	4150.88	9	461.21	297.84	< 0.0001	significant
A-Oil/Glyc	3041.61	1	3041.61	1964.20	< 0.0001	
B-Phyt/Gly	448.80	1	448.80	289.82	< 0.0001	
C-Cat	29.30	1	29.30	18.92	0.0034	
AB	24.95	1	24.95	16.11	0.0051	
AC	0.0256	1	0.0256	0.0165	0.9013	
BC	0.4830	1	0.4830	0.3119	0.5939	
A ²	123.58	1	123.58	79.80	< 0.0001	
B ²	183.69	1	183.69	118.62	< 0.0001	
C ²	236.05	1	236.05	152.44	< 0.0001	
Residual	10.84	7	1.55			
Lack of Fit	10.84	3	3.61			
Pure Error	0.0000	4	0.0000			
Cor Total	4161.72	16				

The scatter diagrams show alignment of the predicted with the actual yields, viscosity and specific gravity as shown in Table 2 and Figure 1.

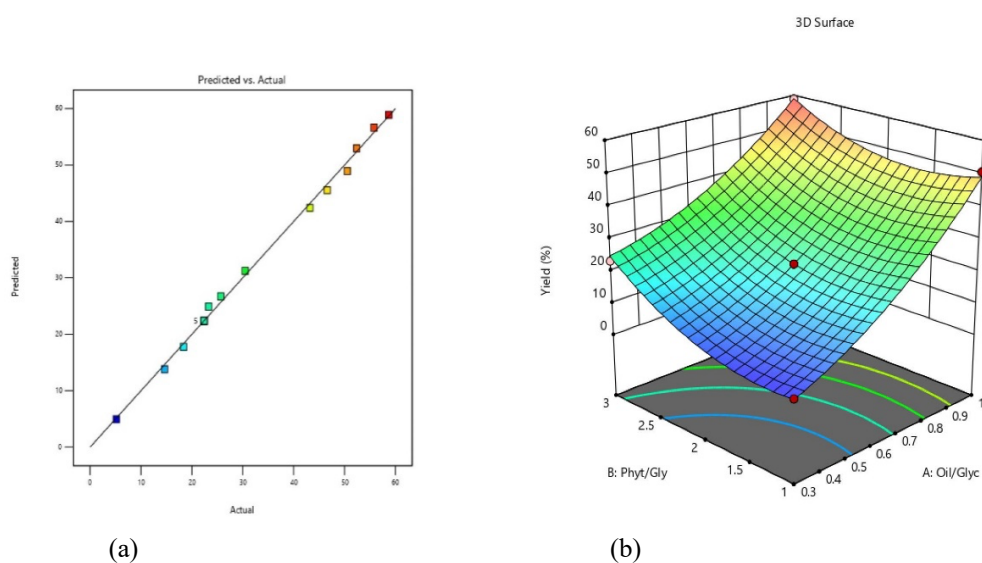


Figure 1. Scatter diagram of (a) yield and (b) corresponding 3D surfaces

Table 4. Constraints

Name	Goal	Lower Limit	Upper Limit	Lower Weight	Upper Weight	Importance
A:Oil/Glyc	maximize	0.3	1	1	1	5
B:Phyt/Gly	maximize	1	3	1	1	3
C:Cat	maximize	0.5	1.5	1	1	3
Yield	maximize	5.15	58.7	1	1	3

Saponification, (mg/KOH)	148.42±0.27	182.55±0.2
--------------------------	-------------	------------

Table 5. Optimization solution found according to RJAR optimization scenario

Number	Oil/Glyc	Phyt/Gly	Cat	Yield	Desirability	
1	1.000	2.621	1.500	62.066	0.932	Selected
2	1.000	2.628	1.500	62.162	0.932	
3	1.000	2.618	1.500	62.025	0.932	
4	1.000	2.642	1.500	62.345	0.932	
5	1.000	2.602	1.500	61.824	0.932	

Tables 2–4 illustrate the desirability functions for three separate criteria utilizing various input parameters (oil/glyc; phyt/gly; and CaCO₃ catalyst) and the combination of processes that were evaluated. Table 5 shows the optimization solutions discovered for the alkyd resin optimization scenario. The findings of the analysis of variance (ANOVA) revealed that catalyst dosages, oil/glycerol, and phthalic/glycerol molar ratios were critical factors in the formation of alkyd resin. The optimization solution yield was 62.066 %, with the selected overall desirability of 0.932, using the average input variables of catalyst (1.5 g), oil/glyc (1.0), and phyt/gly (2.621). Ikhuoria, *et al.* (2004), published studies on the enhancement of rubber seed oil methyl esters were used to make alkyd resins.. Methyl ester was more popular in rubber seed oil promising in alkyd resin growth, compared to rubber seed oil. Aghaie *et al.* [23] prepared alkyd resin with soybean oil fatty acid and compared the resin's properties with the resin made with other vegetable oils. The jathropa alkyd resin acid value decreased to 6.005±0.395 (mg/KOH), while alkyd resin viscosity improved to 10.88±0.042 (cp, 30 °C) in the polymerization reaction to condensation after 5 hr. The production of soybean seed oil modified alkyd resins and epoxidized soybean oil was reported by Kyenge *et al.* [24]. The molecular weights increased from the jathropa oil (763.34 gmol⁻¹) to jathropa resin (1118.52 gmol⁻¹) with the saponification value of 148.42±0.27 (mg/KOH)

3.1.2 Refined sesame based alkyd resin

In this situation, 17 tests were also required to convert the complete range of options and select the best alkyd resin production method. The number of experiments and the related values for the combination of variables are shown in the design matrix (Table 6).

Table 6: Design experimental matrix at different input factors

Std	Run	Factor 1 A:Oil/Glyc	Factor 2 B:Phyt/Gly	Factor3 C:Cat	Response Yield %	
					Actual	Predicted
8	1	1	2	1.5	50.55	51.96
14	2	0.65	2	1	38.55	38.55
13	3	0.65	2	1	38.55	38.55
1	4	0.3	1	1	4.35	9.34
15	5	0.65	2	1	38.55	38.55
10	6	0.65	3	0.5	24.9	30.60
5	7	0.3	2	0.5	16.21	14.80
17	8	0.65	2	1	38.55	38.55
12	9	0.65	3	1.5	25.29	28.88

4	10	1	3	1	59.285	54.29
11	11	0.65	1	1.5	28.52	22.82
9	12	0.65	1	0.5	24.68	21.09
2	13	1	1	1	45.25	49.55
7	14	0.3	2	1.5	9.415	10.12
3	15	0.3	3	1	24.47	20.17
16	16	0.65	2	1	38.55	38.55
6	17	1	2	0.5	47.995	47.29

Analysis of variance

These equations show the second order polynomial functions that were obtained to model yield.

$$\text{Yield} = -54.99454 + 48.50587\text{Oil/Glyc} + 29.25580\text{Phyt/Gly} + 54.76036\text{Cat} - 4.34643\text{Oil/Glyc*Phyt/Gly} + 13.35714 \text{ Oil/Glyc*Cat} - 1.72500\text{Phyt/Gly*Cat} - 0.066327\text{Oil/Glyc}^2 - 5.20312\text{Phyt/Gly}^2 - 29.99750\text{Cat}^2 \quad (2)$$

The oil/glyc*phyt/gly, oil/glyc*cat, and phyt/gly*cat reflect the linear interaction effects between the refined jatropha oil/glycerol, phthalic/glycerol, and catalyst, respectively. The respective process variables' quadratic effects are oil/glyc², phyt/gly², and cat².

Table 7 shows how the regression equation was utilized to calculate the projected response. It can be seen that all of the data points cluster together towards the straight y=x line. This indicates that the quadratic regression model developed was capable of accurately and confidently predicting the sesame seed oil alkyd resin optimization process. As a result, this equation can be applied to both prediction and design

Table 7. ANOVA Table for the “yield” quadratic model

Source	Sum of Squares	Df	Mean Square	F-value	p-value	
Model	3288.15	9	365.35	14.01	0.0011	significant
A-Oil/Glyc	2761.55	1	2761.55	105.86	< 0.0001	
B-Phyt/Gly	121.25	1	121.25	4.65	0.0680	
C-Cat	0.0000	1	0.0000	4.792E-07	0.9995	
AB	9.26	1	9.26	0.3549	0.5701	
AC	21.86	1	21.86	0.8378	0.3905	
BC	2.98	1	2.98	0.1141	0.7455	
A ²	0.0003	1	0.0003	0.0000	0.9975	
B ²	113.99	1	113.99	4.37	0.0749	
C ²	236.80	1	236.80	9.08	0.0196	
Residual	182.60	7	26.09			
Lack of Fit	182.60	3	60.87			
Pure Error	0.0000	4	0.0000			
Cor Total	3470.75	16				

The scatter diagrams show alignment of the predicted with the actual yields, viscosity and specific gravity as shown in Table 6 and Figure 2.

Response Surface Methodology to Optimize the Yield of Alkyd Resin from Jatropha (*Jatropha Curcas*) and Sesame (*Sesamum Indicum*) Seed Oils Using CaCO₃ as Catalyst

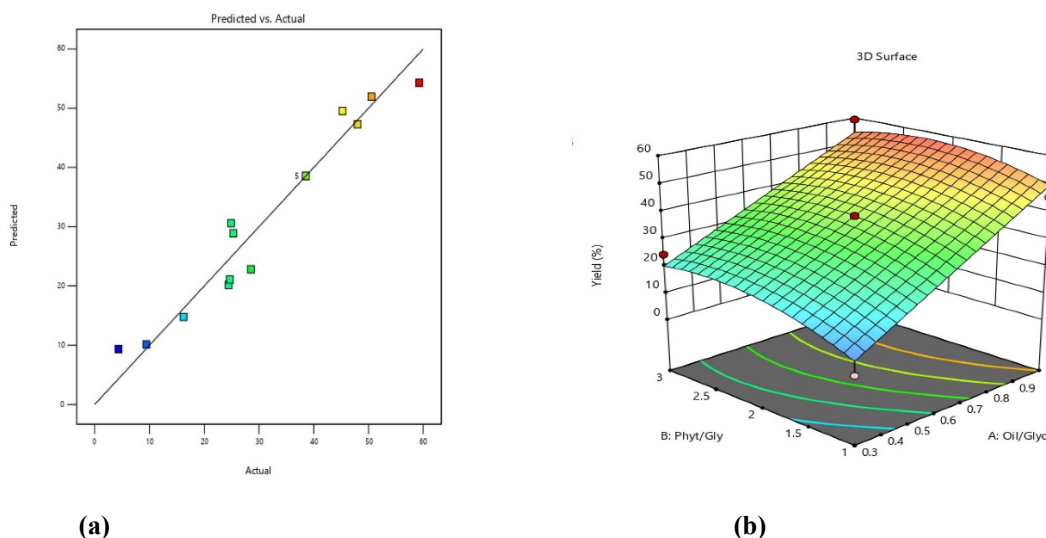


Figure 2. Scatter diagram: (a) yield and (b) with the corresponding 3D surface

Table 8: Constraints

Name	Goal	Lower Limit	Upper Limit	Lower Weight	Upper Weight	Importance
A:Oil/Glyc	maximize	0.3	1	1	1	3
B:Phyt/Gly	maximize	1	3	1	1	3
C:Cat	maximize	0.5	1.5	1	1	3

Table 8. Optimization solution found according to the RSAR optimization scenario

Number	Oil/Glyc	Phyt/Gly	Cat	Yield	Desirability
1	1.000	3.000	1.500	48.264	0.909 Selected
2	1.000	3.000	1.500	48.265	0.909
3	1.000	3.000	1.500	48.265	0.909
4	1.000	3.000	1.495	48.388	0.908
5	1.000	2.978	1.500	48.455	0.908

Tables 6–8 illustrate the desirability functions for three separate criteria utilizing various input parameters (oil/glyc; phyt/gly; and CaCO₃ catalyst) and the combination of processes that were evaluated. Table 9 shows the optimization solutions discovered for the alkyd resin optimization scenario. The findings of the analysis of variance (ANOVA) revealed that catalyst dosages, glycerol, and phthalic were critical factors in the formation of alkyd resin.

The optimization solution has alkyd resin yield of 48.264 % was obtained using the average input variables of catalyst (1.5 wt. %), oil/glyc (1.000), and phyt/gly (3.00), with the selected overall desirability of 0.909.

Table 9. Optimization solution found according to the RSAR optimization scenario

Sample	Oil/Glyc	Phyt/Gly	Cat	Yield	Desirability
RSAR	1.000	3.000	1.5	48.264	0.909 Selected
RJAR	1.000	2.621	1.5	62.066	0.932 Selected

Tables 10 demonstrate the optimization findings obtained from Tables 5 and 9 utilizing CaCO₃ catalysts and a combination of other process variables investigated, as well as the related desirability functions. The RSAR

optimization used CaCO₃ concentration of 1.5 wt. % at molar ratio of Oil/Glyc (1.0:1.0) and Phyt/Glyc (3.0:1.0) were computed and obtained 48.264 % yield with a desirability of 0.909, while the RJAR used a similar CaCO₃

Saponification, (mg/KOH)	148.42±0.27	182.55±0.2
--------------------------	-------------	------------

concentration of 1.5 wt. %, at molar ratio of Oil/Glyc (1.0/1.0) and Phyt/Glyc (2.621:1.0) to obtain 62.066 % yield with a desirability of 0.932. Average input factors such as catalyst concentration of 1.5 wt. %, molar ratio

of Oil/Glyc (1.0:1.0), and Phyt/Glyc (2.621:3.0) were observed during the alkyd resin optimization for the two procedures. The sesame alkyd resin acid value decreased to 8.53±0.12 (mg/KOH), while alkyd resin viscosity improved to 8.87±0.26 (cp, 30 °C) in the polymerization reaction to condensation after 5 hr. The molecular weights increased from the sesame oil (768.71 gmol⁻¹) to sesame resin (915.41 gmol⁻¹) with the saponification, value of 182.55±0.2 (mg/KOH).

Ibrahim, *et al.* [25], previously reported an alkyd resin production range of 2.56–23.93 %. However, when compared to the results for ordinary alkyd resin production in the literature [26-35], the optimized experimental yields reported in this work were both greater. We were able to obtain a successful combination of input variables using the Box–Behnken Design Response Surface Methodology, which resulted in better yields and quality that were comparable to commercially available alkyd resins, resulting in the study's novel outcomes.

3.2. The Fourier Transform Infrared (FT-IR) analysis of alkyd resins

The presence of an absorption band at 3461.74 cm⁻¹ in the RSAR FT-IR spectra (Figure 3 and 4) and Table 11 verifies the presence of hydroxyl group in the alkyd resin. A signal at 2920 cm⁻¹ indicated the presence of a C-H stretching vibration of a sp³ carbon or aliphatic compounds, whereas a signal at 1720.32 cm⁻¹ confirmed the presence of a C=O carbonyl functional group of a carbonyl compound, and an absorption band at 1448.02 cm⁻¹ indicated the presence of Sp³ (CH₃ bend) hybridized carbon of aliphatic compounds. The presence of C-O stretching vibration is indicated by the emergence of a peak at 1071.24 cm⁻¹.

Table 10. The FT-IR analysis of alkyd resin from RSAR, and RJAR

Frequency (cm ⁻¹)	Functional groups	Observed vibration bands/peaks (cm ⁻¹)	
		RSAR	RJAR
3600 – 3200	O–H stretching vibration (alcohol)	3461.74	3518.86
29500 - 2840	C-H aliphatic stretching vibration.	2920.32	2926.65
1750 – 1720	C=O stretching (ester)	1720.32	1710.82
1465 – 1440	- CH ₃ bend	1448.02	1448.02
1390 – 1365	O-CH ₂ bend	1384.70	1372.03
1200 – 1020	C-O stretching vibration	1071.24	1134.56

Response Surface Methodology to Optimize the Yield of Alkyd Resin from Jatropa (Jatropha Curcas) and Sesame (Sesamum Indicum) Seed Oils Using CaCO₃ as Catalyst

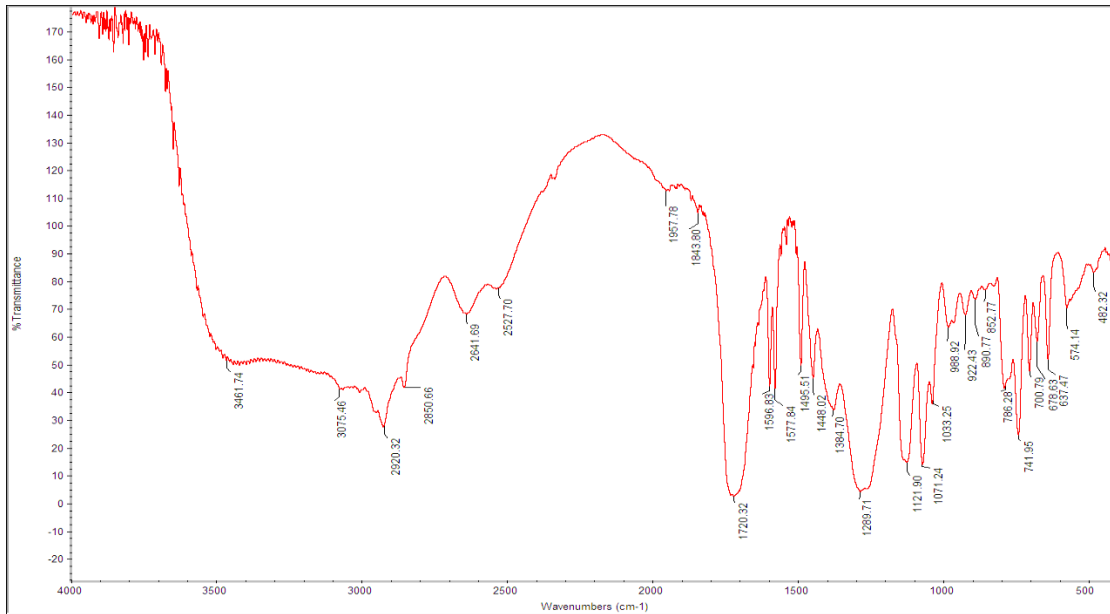


Figure 3. FTIR Spectra of the refined sesame based alkyd resin

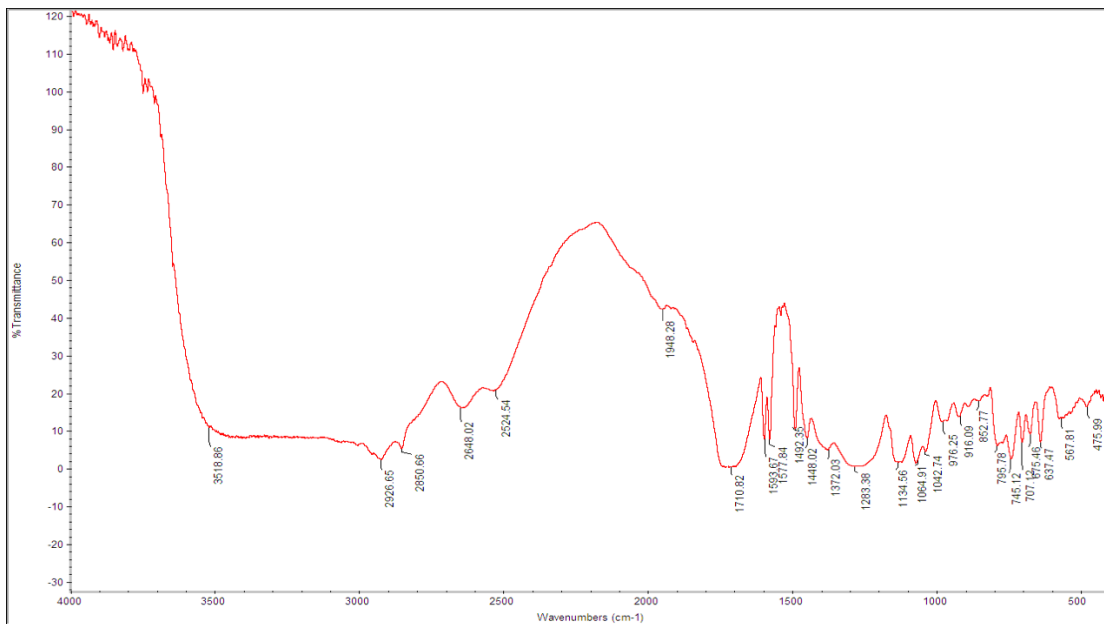


Figure 4. FTIR Spectra of the refined jatropa based alkyd resin

Table 11. Fatty acids profile of refined jatropha and sesame oils

Refined Jathropa oil			Refined sesame oil		
Composition	Saturation	Composition (%)	Composition	Saturation	Composition (%)
Acetic Acid	C ₂ H ₄ O ₂	1.92			
Octanoic Acid	C ₈ H ₁₆ O ₂	4.22			
Oleic Acid	C ₁₈ H ₃₄ O ₂	43.53			
n- Hexadecanoic Acid	C ₁₆ H ₃₂ O ₂	18.09			
Octadecanoic Acid	C ₁₈ H ₃₆ O ₂	8.76	Octadecanoic Acid	C ₁₈ H ₃₆ O ₂	6.83
Dodecanoic acid, methyl ester	C ₁₃ H ₂₆ O ₂	2.23			
Eicosanoic acid	C ₂₀ H ₄₀ O ₂	1.62			
6-Octadecenoic acid	C ₁₉ H ₃₆ O ₂	2.00	9, 17-Octadecadienoic acid	C ₁₈ H ₃₂ O ₂	89.52
9- Octadecenoic acid,	C ₁₉ H ₃₆ O ₂	1.61	9- Octadecenoic acid,	C ₁₉ H ₃₆ O ₂	3.65

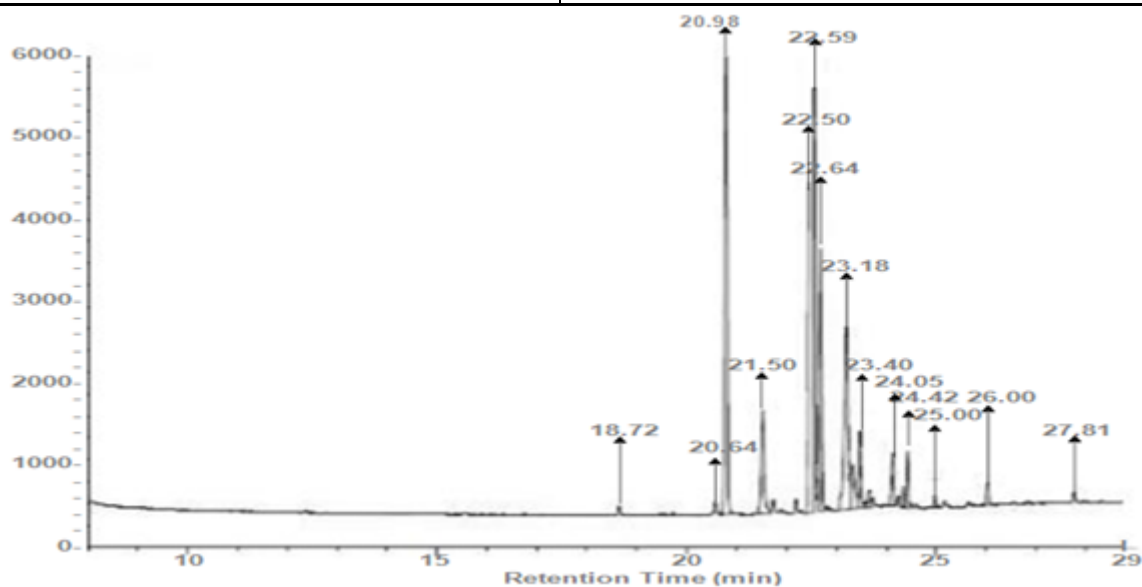


Figure 5. GC-MS Spectrum of refined jatropha oil

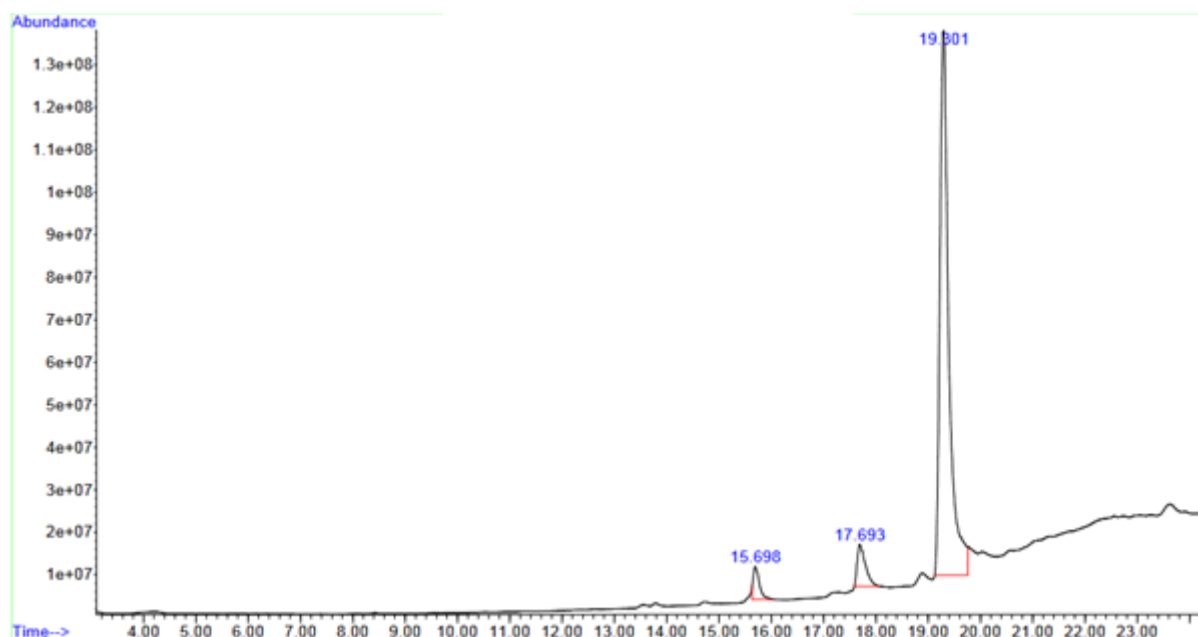


Figure 6. GC-MS Spectrum of refined jatropha oil

Figure 4 and Table 11 show the presence of an absorption band at 3518.86 cm^{-1} in RJAR's Fourier Transform Infrared (FTIR) spectra, indicating the presence of hydroxyl group in the alkyd resin. The appearance of a signal at 2926.65 cm^{-1} indicated the presence of C-H stretching vibration of a sp^3 carbon or aliphatic compounds, while the signal at 1710.82 cm^{-1} confirmed the presence of C=O carbonyl functional group of carbonyl compound, and the absorption band at 1448.02 cm^{-1} depicted the presence of sp^3 (CH_3 bend) hybridized carbon of aliphatic compounds. The development of a peak at 1134.24 cm^{-1} indicates the presence of C-O stretching vibration.

Table 12 contain the fatty acids profile of refined jatropha and sesame oils showed degree of unsaturation of different fatty acids with their corresponding gas chromatography spectral in figures 4 and 5, respectively. The oleic acid (43.53 %) and 9, 17-Octadecadienoic acid (89.52 %) observed as the most abundant.

5. Conclusion

The results from the ANOVA demonstrated that, although non edible seeds oil were different seeds, their molar ratio (oil/glycerol and glycerol/phthalic), speed, time and catalyst were vital factors that affects the yield of alkyd resin. Under these conditions, the highest alkyd resin yielded 62.066 % for RJAR and 48.263 % for RJAR, respectively. The experimental design for the alkyd resins that were produced resulted in increased yields and quality in industrial application.

The alkyd resin outputs generated from the two sets of combination variable tests were used to test the accuracy of the anticipated methodology. The optimized outputs of yield, viscosity, and Specific gravity quality data were gathered for these separate, diverse alkyd resins. The effects of calcium carbonate catalyst doses on the yield, viscosity, and specific gravity of alkyd resin produced from the RSAR and RJAR were major parameters that influenced the yield significantly, while the specific gravity and viscosity varied only marginally. The regression model supplied the multivariate analysis coefficients (R^2) as a variation of the mean, suggesting that the models were capable of good desirability.

5. References

[1] Aigbodion A, Okiemen F, Obazee E, Bakare I. O. Formation and Characterization of Paint Based on Alkyd Resin Derivative of *Ximenia americana* (Wild Olive) Seed Oil. *Progress in Organic Coatings*. 2003; 46; 28-3

- [2] Boruah M, Gogoi P, Adhikari B, Dolui S. Preparation and characterization of Jatropha curcas oil based alkyd resin suitable for surface coating. *Progress in Organic Coatings*. 2012; 74; 596-602
- [3] Gogte B, Dabhade S. Alkyd Based on Non Edible Oils Karanja Oil (Pongamia glabra) *Paint india*. 1977; 27; 17
- [4] Gogte B, Sarwadekar V. Fractionation of Rice Bran Oil, *Paint india*, 1996; 469(9); 31-34.
- [5] Aigbodion A, Okieimen F. Utilization of malenizedrubber seed oil and its alkyd resin as binders in water-borne coatings. *Progress in Organic Coatings* 2003; 46; 28-31.
- [6] Aigbodion A, Pillai C; Bakare I, Yahaya L. Effect of modification with cardonol-formaldehyde resin on the quality of rubber seed oil and its alkyds as binders in surface coating. *Paintindia*. 2001; 29; 39-42
- [7] Hlaing N, Mya O. Manufacture of Alkyd Resin from Castor Oil. *World Academy of Science and Engineering and Technology*. 2008; 24; 115-161.
- [8] Ikhuoria E, Maliki M, Okieimen F. Aigbodion A. Obazee, E.; Bakare, I., Synthesis and characterization of chlorinated rubber seed oil alkyd resins. *Progress in Organic Coatings* 2007; 59; 134-137.
- [9] Muturi-Mwangi P, Dirlikov S, Gitu P. Vernonia and Epoxidizes Linseed and Soyabean Oil as Low Yellowing Diluents in Alkyd Coatings. *Chemical Abstract*. 1994; 122; 216635.
- [10] Igwe I, Ogbobe O. Studies on the alcoholysis of some seed oils. *Journal of Applied Polymer Science*, 2000; 75; 1441.
- [11] Shaker N.O, Alian M.A, Elsayy M.M. Preparation, characterization and evaluation of jojoba seed oil-modified alkyd resins. *Pelagia Research Library*. 2012; 3(5); 1157-1162
- [12] Box, G.E.P, Hunter W.G, Hunter J.S. Statistics for Experimenters: An Introduction to Design, Data Analysis and Model Building. John Wiley and Sons Inc., New York, USA, ISBN-13: 9780471093152, 1978, 653
- [13] Isik O. An integrated probability-based approach for multiple response surface optimizations, Phd. Thesis, Old Dominion University, 2009, 107
- [14] Basha J. S. *et al*. Potential of utilization of renewable energy technologies in Gulf countries. *Sustainability*, 2021; 13(18); 10261.
- [15] Montgomery D, Runger G. Applied statistics and probability for engineers. John Wiley and Sons, Inc., 2011, 768.
- [16] Olaoluwa R.O, Abolanle S.A, John A. O. O, Efere M. O, Olatunji S. O, Adedayo M. S, Muib A. A, Oyedare M. A. Refining, Toxicology Study and Biodiesel Potentials of Used Vegetable Oils. *American Journal of Food Science and Technolog* 2017; 5(3); 78-88.
- [17] AOCS Official Method Cd 8-53., American Oil Chemists' Society. Champaign, Illinois, USA. 2006
- [18] AOAC. Official methods of analysis. Washington D.C., USA. Association of official analytical chemist 19th edition. 2012.
- [19] Ezugwu M. U. Synthesis and characterization of alkyd resin s from selected indigenous seeds, PhD Thesis, Federal University of Technology Owerri, 2017
- [20] Beg M. D, Islam M. R, Ahmed B, Yunus R. M, Abdullah A. Optimization of reaction parameters of esterification on the synthesis of palm oil-based alkyds using response surface methods. The 6th Global Conference on Polymer and Composite Materials Malaysia: *Materials Science and Engineering*. 2019, 634
- [21] Box, G.E.: Behnken, D.W. Some new three level designs for the study of quantitative variables, *Technometrics*, 1950, 2, 455-475
- [22] Mujtaba M.A, Masjuki H.H, Kalam M.A, Hwai C. O, Gul M, Farooq M, Manzoore E. *Renewable Energy*. 2020; 158; 202-214.

- [23] Aghaie H, Ilkani A, Sadat C. S. Utilization of Soyabean Fatty Acid for Synthesis of Alkyd Resin and Comparison of Properties with Other Vegetables Oils. Department of Chemistry, Science and Research Branch, Islamic Azad University, Tehran, Iran, 2012, 1-5.
- [24] Kyenge B, Anhwange B, Ageh J, Igbum G. Comparative analysis of soyabean seed oil modified alkyd resin and epoxidized soyabean seed oil modified alkyd resin. *International Journal of Modern Organic Chemistry*, 2012, 12, 66-71.
- [25] Ibrahim K. A, Abu-sbeih K. A, Al-Trawneh I, Bourghli L. Preparation and Characterization of Alkyd Resins of Jordan Valley Tomato Oil. *Journal of Polymers and the Environment*, 2014, 22, 4, 553–558.
- [26] Sujata B, Biswajit N, Bidangshri B, Bipul D, Pankaj S, Khemnath P, Sanjay B. Biodiesel production from mixed oils: A sustainable approach towards industrial biofuel production, *Chemical Engineering Journal Advances*, 2022; 10; 100284.
- [27] Patil P.D, Deng S. Optimization of biodiesel production from edible and nonedible vegetable oils. *Fuel*, 2009; 88; 6-1302.
- [28] Patil C.K, Jung D.W, Jirimali H.D, Baik J.H, Gite V.V, Hong S.C. Non-edible vegetable oil-based polyols in anticorrosive and antimicrobial polyurethane coatings. *Polymers* 2021; 13; 3149
- [29] Dubovik N.S, Matyas D.S, Dubovik S.A, Lyubushkin R.A. Method for controlling reaction mass parameters during the synthesis of alkyd resins, *Journal of Physics*, 2021: Conf Ser. 1926 012009
- [30] Beg M.D.H, Islam M.R, Ahmed B, Yunus R.M, Abdullah A. Optimization of reaction parameters of esterification on the synthesis of palm oil-based alkyds using response surface methods. *Materials Science and Engineering*, 2019; 634, Conf. Ser.634 012038
- [31] Ezeugo, J. O. Optimization of polycondensation process of alkyd resin synthesis from modified *Picralima nitida* seed oil suitable for surface coating of metal. *World Scientific News*, 2019; 62-90.
- [32] Ifijen I.H, Maliki M, Odiachi I.J, Aghedo O.N, Ohiocheoya E.B. Review on Solvents Based Alkyd Resins and Water Borne Alkyd Resins: Impacts of Modification on Their Coating Properties *Chemistry Africa*, 2022, 1 - 15.
- [33] Ikhuoria E, Aigbodion A, Okieimen F. Enhancing the quality of alkyd resins using methyl esters of rubber seed oil *Tropical Journal of Pharmaceutical Research*, 2004, 301, 311-317.
- [34] Leevijit T, Prateepchaikul G, Maliwan K, Mompiboon P, Okaew S, Eiadtrong S. Production, properties, and utilization of degummed/esterified mixed crude palm oil-diesel blends in an automotive engine without preheating. *Fuel*, 2016, 182.
- [35] Oladipo G, Ighodalo C, Eromosele I, Folarin O. Formation and characterization of paint based on alkyd resin derivative of *Ximenia americana* (wild olive) seed oil. *Environment and Natural Resources Research*, 2013; 3; 113-116.

COPYRIGHT RELEASE FORM

TURKISH JOURNAL OF SCIENCE AND TECHNOLOGY (TJST) Published by Firat University

Firat University, Fen Bilimleri Enstitüsü Müdürlüğü
Turkish Journal of Science & Technology Editörlüğü
Elazığ-TURKEY,
Manuscript title:

Full names of all authors (in order to appear on manuscript):

Name, address etc. of corresponding author:

ID Number: Telephone:

E-mail: Mobile phone:

The author(s) warrant(s) that:

- a) the manuscript submitted is his/her/their own original work;
- b) all authors participated in the work in a substantive way and are prepared to take public responsibility for the work;
- c) all authors have seen and approved the manuscript as submitted;
- d) the manuscript has not been published and is not being submitted or considered for publication elsewhere;
- e) the text, illustrations, and any other materials included in the manuscript do not infringe upon any existing copyright or other rights of anyone. Notwithstanding the above, the Contributor(s) or, if applicable the Contributor's Employer, retain(s) all proprietary rights other than copyright, such as

a) patent rights;

b) to use, free of charge, all parts of this article for the author's future works in books, lectures, classroom teaching or oral presentations;

c) the right to reproduce the article for their own purposes provided the copies are not offered for sale.

However, reproduction, posting, transmission or other distribution or use of the article or any material contained therein, in any medium as permitted hereunder, requires a citation to the Journal and appropriate credit to Firat University as publisher, suitable in form and content as follows:

Title of article, author(s), journal title and volume/issue, Copyright© year.

All materials related to manuscripts, accepted or rejected, including photographs, original figures etc., will be kept by Turkish Journal of Science and Technology editority for one year following the editor's decision. These materials will then be destroyed. I/We indemnify Firat University and the Editors of the Journals, and hold them harmless from any loss, expense or damage occasioned by a claim or suit by a third party for copyright infringement, or any suit arising out of any breach of the foregoing warranties as a result of publication of my/our article. I/We also warrant that the article contains no libelous or unlawful statements and does not contain material or instructions that might cause harm or injury.

This copyright form must be signed by all authors. Separate copies of the form (completed in full) may be submitted by authors located at different institutions; however, all signatures must be original.

ID number: ID number:

Full name (block letters) Full name (block letters)

Signature Date Signature Date

ID number: ID number:

Full name (block letters) Full name (block letters)

Signature Date Signature Date

ID number: ID number:

Turkish authors must supply their ID card number; foreign authors must supply their passport number (if possible)